# BIOCOMPATIBLE TUMOUR IMPLANT SYSTEMS: TOWARDS AN INTEGRATED BIOPHOTONIC SYSTEM

by
*OSCAR R. F. SILVESTRE*

DEPARTMENT OF INFECTION, IMMUNITY AND BIOCHEMISTRY
SCHOOL OF MEDICINE
CARDIFF UNIVERSITY

A thesis submitted to the School of Medicine, Cardiff University in partial fulfillment for the degree of Doctor of Philosophy

2011

# BIOCOMPATIBLE TUMOUR IMPLANT SYSTEMS: TOWARDS AN INTEGRATED BIOPHOTONIC SYSTEM

by
*OSCAR R. F. SILVESTRE*

DEPARTMENT OF INFECTION, IMMUNITY AND BIOCHEMISTRY
SCHOOL OF MEDICINE
CARDIFF UNIVERSITY

A thesis submitted to the School of Medicine, Cardiff University in partial fulfillment for the degree of Doctor of Philosophy

2011





ProQuest LLC
789 East Eisenhower Parkway
P.O. Box 1346
Ann Arbor, MI 48106-1346

## Declaration

This work has not previously been accepted in substance for any degree and is not concurrently submitted in candidature for any degree.

Signed ..César Silvestre..... (candidate) Date ..02/02/2011

**STATEMENT 1**

This thesis is being submitted in partial fulfillment of the requirements for the degree of PhD.

Signed ..César Silvestre..... (candidate) Date ..02/02/2011

**STATEMENT 2**

This thesis is the result of my own independent work/investigation, except where otherwise stated.
Other sources are acknowledged by explicit references.

Signed ..César Silvestre..... (candidate) Date ..02/02/2011

**STATEMENT 3**

I hereby give consent for my thesis, if accepted, to be available for photocopying and for inter-library loan, and for the title and summary to be made available to outside organisations.

Signed ..César Silvestre..... (candidate) Date ..02/02/2011

## Acknowledgements

I would like to thank all those who gave me their support throughout the course of this research, this exciting work is also in part due to them.

First I would like to thank all my supervisors Rachel Errington, Huw Summers and Paul Smith for their full support and invaluable advice. A very special word for my main supervisor Rachel Errington to whom I am going to be forever deeply grateful for her inspiration, unshakable support and guidance.

I wish to acknowledge the PhD funding support from Cardiff University – School of Medicine / School of Physics and Astronomy, under the Richard Whipp Interdisciplinary Studentship Scheme.

I would also like to express my thanks to the staff of the Departments of Pathology and Infection, Immunity and Biochemistry at Cardiff University for their help and advice. Especially I would like to acknowledge the elements of the group, namely: Sally Chappell, Janet Fisher, Marie Wiltshire, Kerenza Njoh, Imtiaz Khan, Hannah Tivey, Victoria Griesdoorn as well as Emeline Furon and Agurtzane Irizar on a personal note. Furthermore Nick White for the advice on the confocal, Jan Hobot and Gareth Edwards for the initial help with the electron microscopy and Peter Giles for the initial advice on the micro-arrays analysis.

Additional I would like to thank our collaborators from Swansea University for their valuable advice and good spirit and with whom I had the opportunity to closely work, namely Mark Holton and Martyn Brown plus I like to also thank Paul Rees. A word also for Christoph Kasseck (Ruhr-Universität Bochum) and Marcus Salmon (ViSen) for imaging my samples plus valuable suggestions and Steve Shnyder (University of Bradford) for the feedback on the hollow fiber protocol.

Last but not least, warm thanks to all my friends in Portugal, Wales and also spread all around the world, unfortunately there would not be enough space to mention all of their names here, but they know that I have them in my mind in these acknowledgements and I will always remember our good moments and their support.

Finally heartfelt thanks to all my family and brother for their ever present support.

*This thesis is dedicated to my beloved parents Joaquim and Emerita Silvestre for their unconditional support and for always believing in me*

...

*Cyflwynir y traethawd hwn i'm annwyl rieni Joaquim a Emerita Silvestre am eu cefnogaeth diamod a'u ffydd ynof bob amser*

...

*Esta tese é dedicada aos meus queridos pais Joaquim e Emerita Silvestre pelo seu apoio incondicional e por acreditarem sempre em mim*

## Summary

There is a need to perform comprehensive cell biology studies transferable across culture platforms using innovative cellular models. The higher purpose is to bridge the gap between *in vitro* cell culture and *in vivo* models.

In this thesis a significant advance is presented in the embedding of an innovative optical biophotonic capability for the dynamic interrogation and single cell tracking of human osteosarcoma cells encapsulated in the hollow fiber (HF) platform. Two approaches have been implemented: quantum dot (QD) nanoparticles providing proliferative and cell cycle readouts; and an in-fiber light illumination providing global features of particle and cell density.

An *in vitro* HF encapsulation model was developed and characterised against standard two-dimensional tissue culture (TC) using the human osteosarcoma U-2 OS cell line expressing a cell cycle fluorescent reporter (cyclin B1-GFP). Analysis of the packing and orientation of cells in the HF revealed that they grow like an anchorage dependent adherent layer. Overall cells in the fiber displayed a slower cell cycle traverse and a differential sensitivity to clinically relevant doses of the anticancer mitosis-inhibiting agent Taxol compared to cells under normal TC conditions.

Comprehensive gene profiling, with bioinformatics and ontology network analysis, showed that the HF cells presented high steroid related but low differentiation gene expression. Specific biomarkers were indentified, and it is suggested that the HF model displays features that are closer to an *in vivo* tumour.

A flow cytometry cell-tracking approach using QD labelling was validated and applied to the HF model for the first time. This represents an "embedded" biophotonic system where the QD sensors are integrated directly into the seeded cell population and then redistributed through the daughter cells, thus reflecting patterns of lineage expansion. This provides sub-population parameterized information on cell-cell heterogeneity and cell division.

A biophotonic HF prototype comprising the integration of direct coupled-light excitation in the HF was conceived, this revealed the potential and limitations to detect the presence of cells inside the HF lumen by analysing light attenuation changes.

Finally a "systems cytometry" acquisition concept has been proposed, comprising the use of embedded engineered nanoparticles as single cell "nano-memory" biophotonic intracellular probes.

# Table of contents

# List of figures

# List of tables

# List of supplementary information

## List of digital supplementary information (CD only)

Note the following supplementary information list is not present in the paper printed copy and is only available in the Thesis digital version on the attached CD.

**Supplementary Information 4.6-4–CD-PDF:** Single PDF file of the full network organic layout of the HFvsCON functional network cluster comparison analysis. (note: please zoom-in to 800%).

**Supplementary Information 4.6-7–CD-Files**: R script code used for the HFvsCON differential expression arrays analysis (see complete files):

...__ "HFvsCON_MicroArrayChip_R_Script.txt"
...__ "HFvsCON_MicroArrayChip_R_Script.R"
...__ "HFvsCON_MicroArrayChip_R_WorkSpace.RData"

**Supplementary Information 5.6-2–CD-Video:** Confocal time-lapse Video - QD705 track in U-2 OS cyclin B1-GFP cells (bar 20µm).

**Supplementary Information 5.6-3–CD-A3:** QD flow tracking Experiment_1 complete compilation of all the raw and analysed flow results sets (please zoom-in).

**Supplementary Information 5.6-4–CD-A3:** QD flow tracking Experiment_2 complete compilation of all the raw and analysed flow results sets (please zoom-in).

# Abbreviations

| | |
|---|---|
| A | amps |
| AB | alamarBlue |
| AC | alternating current |
| ADC | analog-to-digital converter |
| AMP | adenosine monophosphate |
| ATP | adenosine triphosphate |
| arb | arbitrary |
| au | arbitrary units |
| BMP | bone morphogenetic protein |
| BrdU | bromodeoxyuridine |
| CARS | coherent anti-Stokes Raman scattering |
| CBS | central biotechnology services |
| CCD | charge coupled device |
| CDF | cumulative distribution function |
| CF | confluency |
| CFDA-SE | carboxyfluorescein diacetate succinimidyl ester |
| CFSE | carboxyfluorescein succinimidyl ester |
| cm | centimetre |
| CMOS | complementary metal-oxide silicon |
| CO2 | carbon dioxide |
| CON | control |
| cyclin B1-GFP | cyclin B1 fused with enhanced Green Fluorescent Protein (eGFP) |
| DAVID | database for annotation, visualization and integrated discovery |
| dB | decibel |
| DC | direct current |
| DNA | deoxyribonucleic acid |
| DRAQ5 | 1,5-bis [2-(methylamino)ethyl]amino -4,8-dihydroxy anthracene-9,10-dione |
| EASE | expression analysis systematic explorer |
| EDTA | ethylene diaminetetraacetic acid |
| eGFP | enhanced Green Fluorescent Protein |
| EGTA | ethylene glycol tetraacetic acid |
| em | emission |
| ES | enrichment score |
| EtOH | ethanol |
| ex | excitation |
| FC | fold change |
| FCS | fetal calf serum |
| fdr | false discovery rate |
| FDR | false discovery rate |
| FITC | fluorescein isothiocyanate |

| | |
|---|---|
| GEO | gene expression omnibus |
| GFP | Green Fluorescent Protein |
| GO | gene ontology |
| GPCR | G protein-coupled receptors |
| GPS | global positioning system |
| | |
| h | hour |
| HEPES | 4-(2-hydroxyethyl)-1-piperazineethanesulfonic acid |
| HF-U2OS-GFP | hollow fiber U-2 OS cyclin B1-GFP *in vitro* cell culture model |
| Hz | Hertz |
| | |
| ID | inner diameter |
| IMT | inter-mitotic time |
| IVIS | in vivo imaging system |
| | |
| kDa | kiloDalton |
| KEGG | Kyoto encyclopedia of genes and genomes |
| | |
| lab | laboratory |
| LCTF | liquid crystal tunable filters |
| LED | light emitting diode |
| LNCaP | lymph node carcinoma of the prostate |
| | |
| m | milli |
| M | molar concentration |
| M2A | mouth to anus |
| mA | milliamps |
| MEA | modular enrichment analysis |
| MEMS | micro-electro-mechanical system |
| min | minutes |
| ml | millilitre |
| mm | millimetre |
| PVDF | polyvinylidene difluoride |
| MTT | 3-(4,5- dimethylthiazol-2-yl)-2,5-diphenyltetrazolium bromide |
| mW | milliwatt |
| | |
| NaCl | sodium chloride |
| nano-mbip | nano-memory biophotonic intracellular probe |
| NCBI | national center for biotechnology information |
| NCI | national cancer institute |
| NIR | near infra-red |
| nm | nanometers |
| | |
| $O_2$ | oxygen |
| OCT | optical coherence tomography |
| OD | outer diameter |
| | |
| p | photons |
| PBS | phosphate buffered saline |

| | |
|---|---|
| PC | personal computer |
| PEBBLE | probe encapsulated by biologically localized embedding |
| PEG | polyethylene glycol |
| PFA | paraformaldehyde |
| PI | propidium iodide |
| PMSF | PhenylMethylSulphonyl fluoride |
| PMT | photomultiplier tube |
| pp | page |
| PPi | pyrophosphayte |
| PSA | polysialic acid |
| PVDF | PolyVinyliDene Fluoride |
| | |
| QC | quality control |
| QD | quantum dots |
| QD705 | far-red quantum dot (705 nm emission) cell Qtracker® labelling kit |
| | |
| RF | radio frequency |
| RFID | radio frequency identification |
| RMA | robust multi-array average |
| RNA | ribonucleic acid |
| ROI | region of interest |
| rpm | rotation per minute |
| RT | room temperature |
| | |
| s | seconds |
| SD | standard deviation |
| sd | standard deviation |
| SEA | singular enrichment analysis |
| sec | seconds |
| SEM | scanning electron microscopy |
| SERS | surface-enhanced Raman scattering |
| sr | steradian |
| | |
| TC | tissue culture |
| TEM | transmission electro microscopy |
| tibmwi | tumour integrated biophotonic micro-device wireless implant |
| | |
| U-2 OS | human osteosarcoma cell line |
| U2OS-GFP | U-2 OS cell transfected with cyclin B1-GFP G2M cell cycle phase reporter |
| UHF | ultra high frequency |
| | |
| vol | volume |
| W | watt |
| WT | wild type |
| μ | micro |
| μm | micrometre |

# CHAPTER 1

# INTRODUCTION

# 1 INTRODUCTION

## 1.1 The hollow fibre (HF) implant

It is now becoming increasingly clear that traditional methods of cell culture, growth and manipulation on two-dimensional (2D) surfaces in cancer research are insufficient for the new challenges of cell biology and biochemistry, as well as for pharmaceutical assays. 2D cell cultures do not adequately represent the functions of three-dimensional (3D) real *in vivo* tissues that have extensive cell-cell and cell-matrix interactions, as well as markedly different diffusion/transport conditions. The developments in 3D *in vitro* models are continuously expanding our understanding of the tumour cells with an environment "closer" to an *in vivo* situation (Abbott 2003; Birgersdotter et al. 2005; Butcher et al. 2009; Feder-Mengus et al. 2008; Griffith and Swartz 2006; Weigelt and Bissell 2008; Yamada and Cukierman 2007).

There is a need for innovative tumour models that are capable not only of recreating distinct tumour-mimetic niches, but allow for *in vitro* and *in vivo* tumour modelling under well defined and reproducible conditions (Fischbach et al. 2007; Hutmacher 2010; Lee et al. 2008; Moreau et al. 2007). At the same time areal challenge is to develop interrogation techniques (e.g. imaging or biophotonic) that allow dynamic assays to monitor biological activity and therapeutic agents responses applied to both 2D and 3D *in vitro*, with relevance to *in vivo* whole animal pre-clinical research models and perhaps clinical situations (Cosgrove et al. 2008; Dothager et al. 2009; Kobayashi et al. 2010; Ntziachristos et al. 2005; Pampaloni et al. 2007; Provenzano et al. 2009; Qian et al. 2008; Sahai 2007; Weissleder and Pittet 2008).

In this thesis the Hollow Fiber (HF) implant (Hollingshead et al. 1995a) has been developed to emulate an encapsulation culture platform which addresses the above challenges. The HF implant was developed by Hollingshead et al. 1995a representing a technical innovation that emerged from the National Cancer Institute (NCI) anti-cancer drugs screening program, and was an evolution of previous techniques based on the cultivation and encapsulation of cells (Casciari et al. 1994; Lanza et al. 1991). The HF assay, as it is currently used at the NCI, is part of the drug screening process prior to the xenograft studies. In brief, tumours cells are grown

within a biocompatible encapsulation modified HF porous membrane, permeable to substances with a molecular weight <500 kDa, it therefore acts as a confined tubular 3D culture micro-environment. The "closed" HF can be surgically implanted in the animals host to examine the pharmacodynamics properties of the administered drug thus providing access to the HF compartments and allows for the evaluation of tumour responses to drug treatment.

The key goal of using the HF implant, to date, has been to decrease the time and cost, both financial and in the number of animals used, to evaluate initial efficacy and evidence of a compound's capacity to act across physiological barriers. Therefore this system is generally used as a pre-screening step before human xenograft testing is undertaken (Sharma et al. 2010). Due to the HF intrinsic characteristics, the application areas have also been expanded beyond of the role to undertake target-oriented biological assays in conjugation with, for example: microscopy and flow cytometry analysis of the HF retrieved cells to study in detail the drug action (Suggitt et al. 2004; Temmink et al. 2007) gene expression profiling (Wang et al. 2006; Wang et al. 2008) and more recently dynamic bioluminescence imaging interrogation (Hollingshead et al. 2004; Zhang et al. 2008a).

## 1.2 Statement of thesis challenges

The principles addressed in the introduction exploit the core HF features in conjugation with a biophotonic approach for bridging the gap between culture platforms (see Figure 1.1), these features include. First, the HF effectively represents a "transferable" cellular platform that can be manipulated *in vitro* and/or implanted into animals for pharmacodynamic/pharmacokinetics testing and importantly cells retrieved without external cell contamination for further processing and analysis of the changes to the discrete originally loaded population. Second as a 'bounded' cellular system or implant it provides a physical structure in which biophotonic components (i.e. nano-*sensors* or electronic *detectors*) can be included at a micro/macro level in order to continuously monitor the progress of tumour expansion or growth over time. This underlines the basis for an integrative imaging/cytometry approach to dynamically track cell proliferation and lineages across different platforms.

The challenge is to determine if this could be achieved using innovative biophotonics approaches. More specifically by employing novel fluorescence protein constructs or quantum dot nanoparticles the proliferative properties of the tumour cultures can be directly interpreted, including the response to anticancer agents. Thus providing biophotonic-readouts of proliferation that can be acquired in a transferable mode. Further by incorporating into the HF embedded coupled light delivery/detection the HF becomes a self reporting implant again with bounded optical and pharmacokinetic properties. The thesis focus is presented below (Figure 1.1) including the wider scientific context.

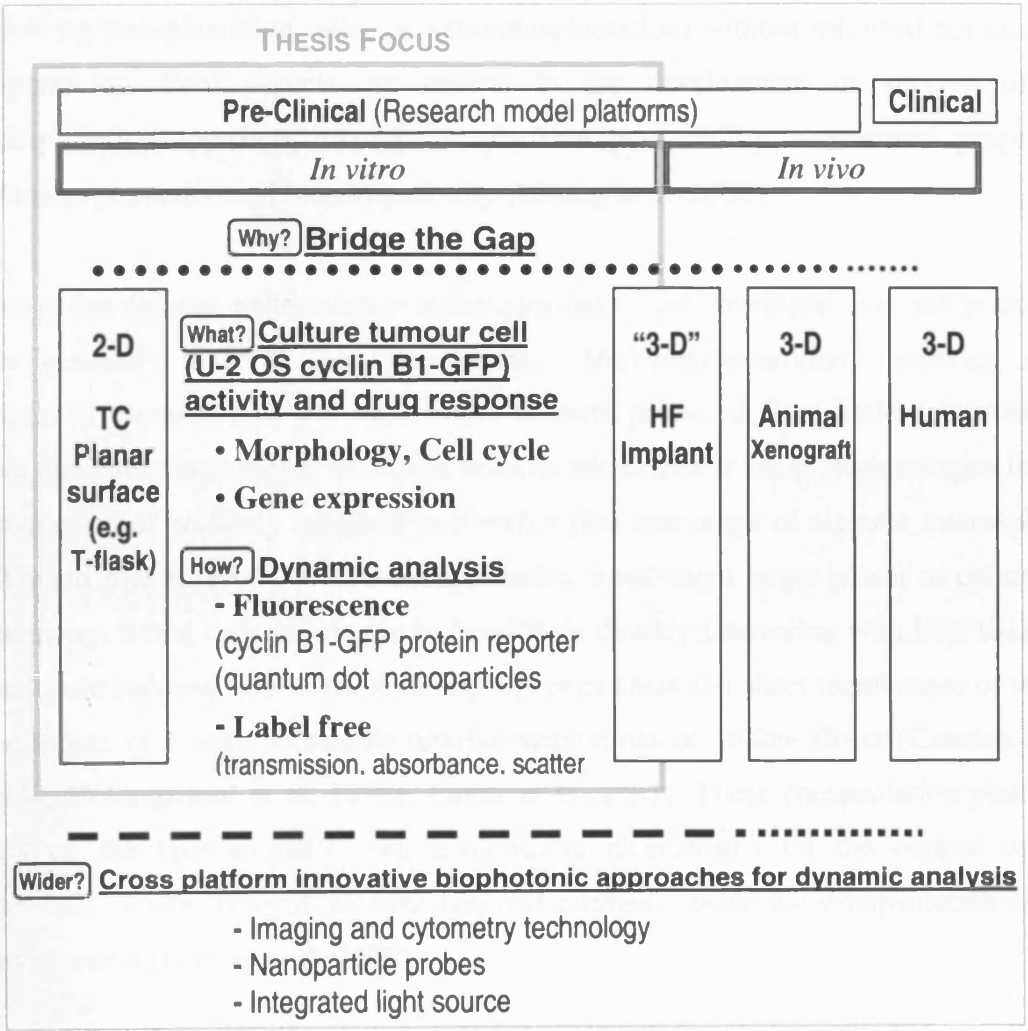


**Figure 1.1 – Overview of the thesis scientific focus.**

## 1.3 Principle to construct a tumour cell system providing a "degree of control"

### 1.3.1 Encapsulation systems

Cell encapsulation aims to entrap viable cells within the confines of matrices or semi-permeable membrane barriers. Encapsulation physically isolates a cell mass from an outside environment and aims to maintain normal cellular physiology within the permeable barrier. These methods have been developed based on the promise of its therapeutic usefulness for tissue transplantation (Lanza et al. 1991; Thanos et al. 2010) and also testing the *in vivo* activity of chemotherapeutic drugs (Gorelik et al. 1987). Transplanted cells are protected from immune rejection by the barrier, potentially allowing transplantation (allo- or xenotransplantation) without the need for immuno suppression. Four aspects are critical in the development or success of the encapsulation approach, namely the platform permeability, mechanical properties, immune protection and biocompatibility (Uludag et al. 2000).

Numerous cellular encapsulation techniques have been developed over the years, and are generally divided into two classes: *Micro-encapsulation*, involving small spherical capsules (0.3–1.5 mm), most of them produced from hydrogels matrices, like alginate. Some recent examples involve micro-fluidic "chip" technologies for the production of perfectly spherical and with a fine size range of alginate microspheres (Workman et al. 2007). *Macro-encapsulation*, involving a larger planar or cylindrical geometry, living cells physically isolated from directly interacting with host tissue by enclosure between two or more selectively permeable flat sheet membranes or within the lumen of a semi-permeable tubular membranes or hollow fibers (Casciari et al. 1994; Hollingshead et al. 1995a; Lanza et al. 1991). These encapsulation platforms rely on the host animal's own homeostatic mechanisms for the control of pH, metabolic waste removal, electrolytes, and nutrients inside the encapsulation micro-environment (Uludag et al. 2000).

HF membrane encapsulation is the primary focus of the present thesis. It is important to note that HF technologies have found a range of applications (Ulbricht 2006) including cell filtration and bioreactors culture systems (Uludag et al. 2000)

(described in the following section). The studies described in this thesis relate to the objective of using HF as an implant technology - introduced by Hollingshead et al. 1995a .

### 1.3.2 HF bioreactors cell culture systems

There are several culture bioreactors designs for mammalian tissue growth that meet the requirements of a wide variety of cell/tissue types and applications (Martin and Vermette 2005) including HF bioreactors. Generically a HF bioreactor consists of a closed vessel, normally a cylindrical module, filled with medium and mammalian cells into which a bundle of semi-permeable HFs is inserted, like the example of Figure 1.2-a.

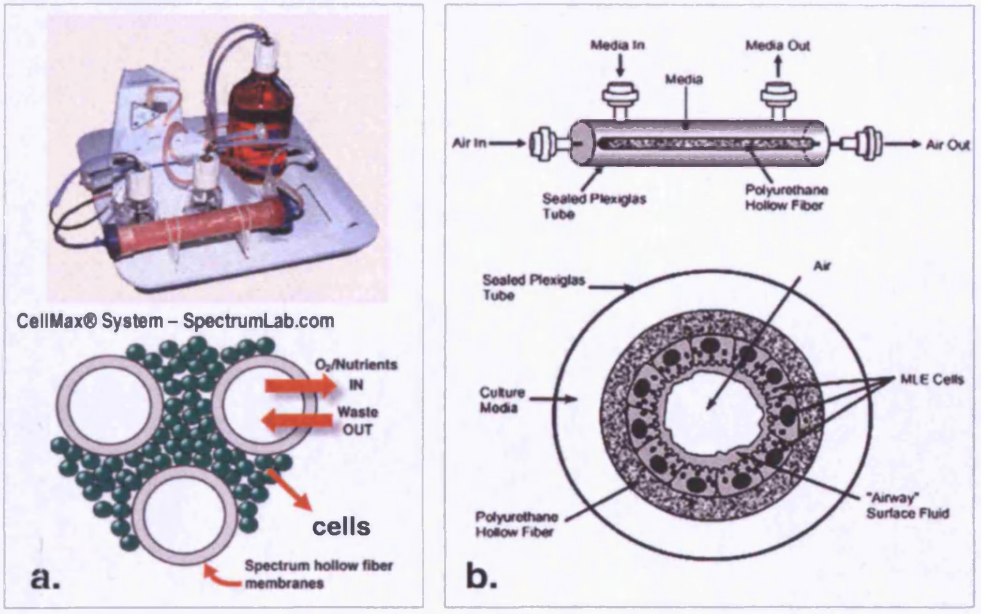


**Figure 1.2 – Examples of HF bioreactor culture systems.** **(a)** A cell perfusion bioreactor, the cell sits as a mass around the HF which are used to provide nutrients and remove the waste (adapted from (http://eu.spectrumlabs.com/cell/CellCulturing.html [2008]). **(b)** Schematic of selectively permeable HF air-liquid membrane culture system for murine lung epithelial (MLE) cells (reproduced from (Grek et al. 2009)).

The HFs provide nutrients to the cells that grow in the extra-fiber space (i.e. glucose, serum, $O_2$) and eliminate their metabolic waste by-products (i.e. lactic acid & $CO_2$) through a constant flow of pumped medium (Figure 1.2-a). Efficient exchange results in increased cell densities and higher yields of secreted product, allowing long culture

times and maintaining higher viability and cell morphology. This type of bioreactor is widely applied for the production of high value biological molecules/cells for pharmaceutical or research use, such as the production of cytokines (Lamers et al. 1999), monoclonal antibodies (Jain and Kumar 2008), recombinant proteins and viruses (Kalbfuss et al. 2007), hepatocyte culture (Schmelzer et al. 2010), extracorporeal hepatic assist devices (Chen and Palmer 2009; De Bartolo et al. 2009; Lu et al. 2005a) and rat bone marrow fibroblastic models (Ye et al. 2007).

The above HF bioreactor could also have the cells growing attached to the HF inner wall, with the nutrients in same manner supplied through the fibers and the waste disposal by outer-fiber medium. This type of culture configuration has been applied to specific endothelial cell models, where the cells attach to the inner wall surface are subject to a uniform shear stress which is directly proportional to the inner fiber flow rate, this is vital to maintain appropriate cell phenotype (Godara et al. 2008; Westmuckett et al. 2000). It is possible also to have two different types of cells growing in the bioreactor in co-culture models, one type inside the HF lumen and another in the extra-fiber space, for example as a model of the *in vitro* blood-brain barrier (Cucullo et al. 2008). Another HF model (Figure 1.2-b), consists of murine lung epithelial cells (MLE-15) culture in an semi-permeable HF within an air-liquid interface, with controlled airflow through the microfiber interior, trying to mimic the characteristics of a lung tissue micro-environment.

### 1.3.3 HF *In vivo* implant

#### 1.3.3.1 HF implant - NCI anticancer drugs screen

The development of a therapeutic agent is costly and time-consuming with thousands of potential agents needing to be evaluated every year. Since 1990, the NCI in the USA undertook the operation of a 60 cell line *in vitro* screen assay to define novel anticancer agents. The screening process began to generate anticancer drug candidates requiring further evaluation using *in vivo* models for the compounds identified as possessing some evidence of anti-proliferative activity *in vitro* (Decker et al. 2004).

Although various models using human tumors xenografted into immunocompromised mice have proved invaluable in chemotherapeutic agent development and assessment, they are accompanied by various limitations including high costs associated with large-scale screening, time, and the numbers of mice required. The empirical dosing and development of pharmacokinetic assays for each compound evaluated in xenograft models acts to greatly reduce the rate at which compounds could progress to the clinic (Decker et al. 2004; Hollingshead et al. 1995a; Suggitt and Bibby 2005).

To address this problem, Hollingshead et al. 1995a developed the HF assay. The HF assay is an *in vivo* test that involves the short-term growth of tumour cells within biocompatible polyvinylidene fluoride (PVDF) hollow fibres, permeable to substances with a molecular weight <500kDa, surgically implanted in mice. The NCI HF assay protocol (Figure 1.3) involves the *in vitro* culture (24-48 hours) of a panel of 12 cell lines inside HFs, followed by *in vivo* implantation at intraperitoneal (i.p.) and subcutaneous (s.c.) sites of nude mice. The assay has the potential to simultaneously evaluate compound efficacy against a maximum of six cell lines (three cell lines/fibres per site). Mice are treated with test compound at two doses for up to 4 days, fibres excised and the viable cell mass contained within the intact and closed HF are analyzed for cell viability using a modified 3-(4,5-dimethylthiazol-2-yl)-2,5-diphenyltetrazolium bromide dye conversion assay (MTT assay) (Alley et al. 1991; Hollingshead et al. 1995a).

The MTT assay is a quantitative colorimetric assay (measuring changes in absorbance) for estimating cell survival and proliferation (cell growth); it is extensively used for the screening of anticancer drugs (Hamid et al. 2004; Mueller et al. 2004; Vellonen et al. 2004). The MTT assay was first described and performed by Mosmann 1983 with later modifications suggested by Denizot and Lang 1986 . In living cells, the membrane permeable yellow MTT tetrazolium salt is reduced to purple formazan, which is membrane impermeable. MTT reduction is generally attributed to mitochondrial activity, but it has also been related to non-mitochondrial enzymes and as well as to endosomes and lysosomes (Berridge and Tan 1993; Liu et al. 1997). This reduction takes place only when the enzymes are active and thus the conversion can be directly related to the number of viable cells. The reduced formazan

trapped in the cells can be solubilised and the absorbance of the resulting solution (i.e. at 540nm) quantified by a spectrophotometer against a control (Alley et al. 1988).

The MTT assay has been widely used to quantify the viable cell fraction in the HF implant after anticancer drug screening conducted by the NCI (Decker et al. 2004; Hollingshead et al. 1995a; Hollingshead et al. 2005; Johnson et al. 2001) and in other HF studies (Hassan et al. 2001; Morrell et al. 2006; Suggitt et al. 2004; Temmink et al. 2007). In brief, the HF are retrieved from the host animal and placed in six-well plates with 1 ml of pre-warmed culture medium containing 1 mg MTT/ml. After a 4 hr incubation at 37°C, the culture medium is aspirated and the HF samples washed twice with normal saline containing 2.5% protamine sulfate solution and incubated overnight at 4°C. To quantify the MTT dye conversion to formazan, the fibers are cut in half and allowed to dry overnight. The formazan extracted from the cells of each HF sample with DMSO diethylsulfoxide with aliquots transferred to individual wells in 96 well plate and assessed for optical density (OD) at a wavelength of 540 nm on a plate reader (Alley et al. 1988; Hollingshead et al. 1995a). Usually the results are expressed in net cell growth ((mean $OD_{retrieval\ day}$ - mean $OD_{implantation\ day}$) / (mean $OD_{implantation\ day}$)) x 100% (Suggitt et al. 2004).

In the NCI screening the HF tested compounds are identified as 'active' using a detailed scoring system and optimal or near-optimal treatment regimens are indicated for subsequent testing using xenograft models (Hollingshead et al. 1995a; Johnson et al. 2001; Suggitt and Bibby 2005). Drugs that show efficacy in HF assays generally also show anti-tumour activity in xenografts studies (Decker et al. 2004; Johnson et al. 2001; Sharma et al. 2010).

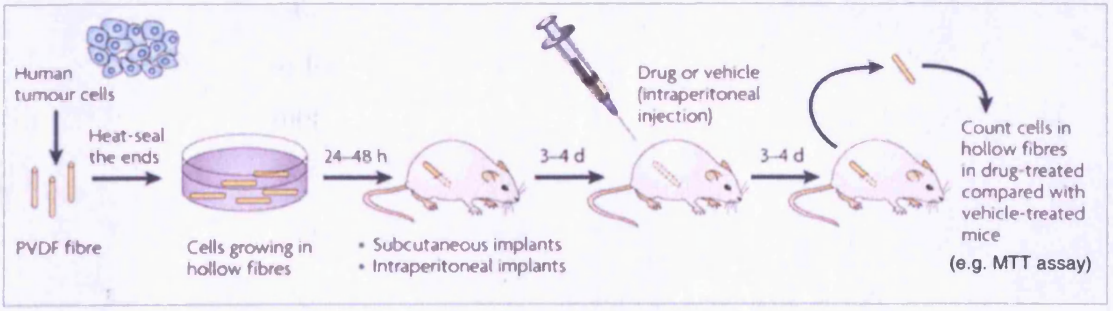


Figure 1.3 – The Hollow Fiber (HF) assay. Schematic of the NCI procedure for *in vivo* studies (adapted from (Sharma et al. 2010)).

### 1.3.3.2 HF implant - HF assay advantages versus xenograft model

The HF assay obviously does not replace traditional xenograft systems, in part because it does not replicate the complex interactions of tumour cells with normal host tissues. The value of the HF assay is in serving as an initial point of triage to indicate which compounds should be studied further in detailed xenograft studies.

In comparison with a traditional tumour xenograft model, the HF assay offers several additional advantages: 1) it allows retrieval of tumour cells uncontaminated by host cells for subsequent analysis; 2) it permits a shortened evaluation time and, therefore, reduces the consumption of test compounds; 3) there is no significant change in the volume of the implant or in the weight of the animal; 4) there is no limitation on cell type, therefore tumour cell lines that do not form tumours in animals can be evaluated; 5) it allows for multiplexing, where several HFs, each filled with a different cell type, can be implanted in one animal, and the in vivo effects of a test compound on these cell types can be evaluated simultaneously; 6) together these greatly reduce the number of animals for screening a compound; and 7) overall HF are a simpler and a cost-effective screening method to run (Decker et al. 2004; Sharma et al. 2010; Zhang et al. 2007; Zhang et al. 2004).

### 1.3.3.3 HF implant - applications beyond anticancer drugs screening

Although the use of the HF assay, as described previously, was based purely on cell growth analysis, the HF implant intrinsic characteristics presented further advantages. For example, the potential to selectively load and retrieve a "controlled" cell population from the HF for various types of biological analyses. The HF provides a well defined and reproducible assay conditions, which makes it possible to employ this system for specific cell studies and evaluate parameters that would be otherwise more difficult to analyse on a purely xenograft system.

Many authors have explored these opportunities to perform target-orientated approaches to the cells in the HF, through pharmacodynamic end point measurements, such as determining DNA damage induction, apoptosis, cell cycle perturbation and gene expression changes (Bishai and Karakousis 2006; Bridges et al. 2006; Hassan et al. 2001; Heindryckx et al. 2009; Jonsson et al. 2000; Liu et al. 2004; Sadar et al. 2002; Suggitt et al. 2004; Temmink et al. 2007; Wang et al. 2008).

For example, Hollingshead et al. 1995b were the first to have looked beyond cell survival assays as a measure of compound activity using the HF assay. Human lymphoid cells infected with the human immunodeficiency virus (HIV) were retrieved from fibres after treatment with antiviral agents, and levels of p24 cell membrane protein antigen and reverse transcriptase activity measured (Hollingshead et al. 1995b; Taggart et al. 2004).

The advantage of being able to retrieve a "pure" cell population from the HF, without host cell contamination, was particularly evident in studies on prostate cancer cells (Sadar et al. 2002; Wang et al. 2008), where the developed LNCaP HF model provided a means of obtaining pure populations of LNCaP cells for gene expression analysis during the different stages of progression to modified androgen dependency. A study by Suggitt et al. 2004 reported the use of HF to investigate the effects of the standard agents such as Taxol and combretastatin A1 phosphate on cell tubulin and the subsequent effects on cell cycle kinetics using laser confocal microscopy and flow cytometry (Suggitt et al. 2004). A recent study (Temmink et al. 2007), addressed the *in vivo* role of thymidine phosphorylase/platelet-derived endothelial cell growth factor in influencing the pharmacodynamic and cytotoxicity of a new fluoropyrimidine base drug formulation (TAS-102) in colon cancer cells, by the analysis of the cell cycle and apoptosis of the HF-retrieved cells using flow cytometry and histochemistry.

The HF platform is not intended to replace the more detailed biological models, such as transgenic or knockout animal models that allow insights into biology and pathogenesis. Further it cannot mimic the range of interactions of tumours with host tissues in terms of stromal or indeed immunological responses (Decker et al. 2004). In essence, the HF platform represents an attempt to establish a transferable *in vivo* and *in vitro* assay system with known performance. It attempts to combine both the *in vitro* qualities of easy manipulation and versatility, with some degree of the *in vivo* complexity. The HF therefore presents one option for a "controllable" tumour model within a confined micro-environment with free diffusion of cell nutrients/drugs/waste, which can be surgically implanted in the host were the test cells will continue to be easily accessible and confined on a defined "bounded vessel".

## 1.4 Principle "use of biophotonics to determine the context of a tumour cell in a HF"

### 1.4.1 Biophotonics introduction

Biophotonics, as defined by Prasad 2004 , deals with the interaction between light and biological matter, it involves the fusion of photonics and biology. The scope is wide, encompassing an interdisciplinary range of topics from chemistry, physics, biology, material science, informatics and engineering. It stands at the interphases of these disciplines. There is the promise that major technological breakthroughs, that utilize light to observe or manipulate biological matter, are more likely to occur through the integration four major existing technologies: lasers, photonics, nanotechnology and biotechnology. The wide range of applications include: photochemistry, vision, laser diagnostics and surgery, optical biopsy, photodynamic therapy, biosensors, flow cytometry, bioinformatics analysis, optical imaging of cells, 3D tissues, and organs. However, nearly all biophotonic applications are characterized by four basic components (Figure 1.4) (Molinaro 2010) - http://cbst.ucdavis.edu/education/courses/winter-2010-ist8a [2010]). In the current thesis these components can be conveniently as follows:

- *Light source* : generation of light via arc lamp, laser, LED (light emitting diode);
- *Target Subject*: cells growing in 2D and encapsulation environments;
- *Detector/Sensor*: light interactions detection with the subject via CCD (charge-coupled device) or photomultiplier tube; using fluorescent reporters and labels;
- *Interpreter:* translation of the light interaction signal into knowledge of the tumour proliferative system.

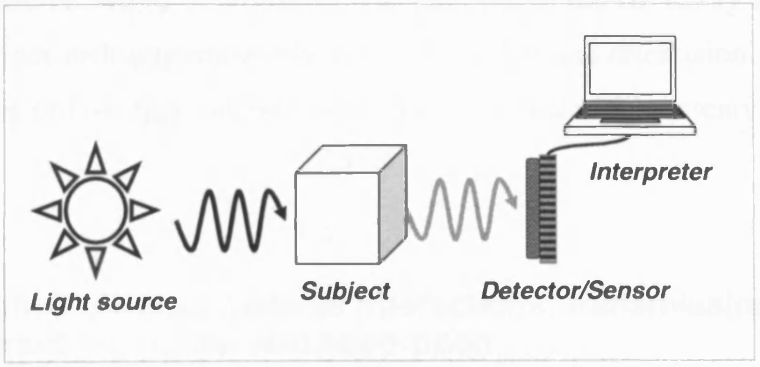


**Figure 1.4 – Schematic to show the linking of biophotonic components appropriate for HF applications** (adapted from (Molinaro 2010).

Indeed, in the current thesis classical commercial cytometric instrumentations have been exploited, each exemplifying the integration of the four biophotonic components (see chapter 2.4.1). For example, this includes a flow cytometer platform where a laser [*light source*] is directed onto a hydrodynamically focused stream of fluid to examine human osteosarcoma cells retrieved from the HF [*target subject*]. Photomultiplier tube (PMT) [*detectors*] are aligned with the light originating from the stream-laser focus point providing signals for forward scatter (monitoring an approximation of cell size), side scatter (cell granularity) and several other acquired spectrally distinct fluorescence emissions from cells labelled with reporter dyes, such as DRAQ5 and propidium iodide, or fluorescent proteins such as GFP [*sensors*]. These outputs are then [*interpreted*] using analysis software for multi-dimensional data to quantify biological features including the cell cycle. Spatial aspects of the cells [*target subject*] are then added to the complexity of the biophotonic-cytometry output using micro and macro-imaging dynamic assays techniques thus providing further contextual information.

Over and above the classical approach for undertaking cell-based assays the technical objectives of this thesis were to exploit the HF encapsulated platform features (introduced in the previous section) and integrate the biophotonic components to accumulate a signal that reflects proliferation and orientation of tumour cells in the HF. The first, was to integrate far-red fluorescent semi-conductor quantum dots (QD) functionalised so they could be taken up into live cells. The approach was to use this QD nanoparticles signal to obtain a parameterized proliferative history of cells in the HF. A second objective was to develop the concept of a micro-device where light is embedded [*source and detected*] directly at each end of the HF cavity and where cells perturb the light path according cell size, cell number and orientation. Therefore an understanding of how light interacts with biological material is essential to succeed in these objectives.

### 1.4.2 Light-biological material interactions: transmission, reflection, refraction, scatter and absorption

This section provides a brief overview of light interactions with biological material with emphasis on visible wavelengths. Light propagates as an electro-magnetic wave

with specific properties: frequency (number of cycles per unit time – hertz (Hz)), amplitude (amplitude is the height of the wave, being related to its energy) and wavelength (distance from peak to peak – nanometers (nm)); the light intensity is related to the number of waves or photons of light that arrive for example, at a detector. These waves could interact with matter molecules, consisting of atoms with electrons that vibrate at specific frequencies. Light can be ***transmitted, reflected, refracted, scattered and absorbed*** by the target *subject* molecules.

A schematic representation of the the interactions of light with biological matter when incident light encounters a point (P) at the boundary of two media with different refractive indexes is shown in Figure 1.5-a, this can be modified as follows for the hollow fiber context:

***Reflected*** light occurs at the interface between the two different media returning to the media from which it originated. This is one of the main principles behind the ability of optical fiber to keep light inside the fiber core acting as waveguide (Russell 2003). The light is guided down the core of the fibre by an optical cladding outer layer with a lower refractive index that traps the light in the optical fiber core and potentially this could be reproduced in the HF. ***Transmitted light*** through the sample matter (for example HF-encapsulated cells) being to some extent ***refracted*** at a different angle at the media interphase; ***scattered*** in all directions with the same wavelength but lower amplitude or ***absorbed*** by the molecules at specific wavelengths, resulting in a decrease of the ratio of incident light to emitted light at that wavelength (White and Errington 2005). This represents the main principle behind a cuvette spectrophotometer where using the amount of absorbed light at a particular wavelength for a specific molecule and by applying Beer's Law it is possible to calculate the molecule or compound concentration.

The light absorbed by a molecule results in increased vibrational and rotational energy of the inter-atomic bonds and/or promotion of electrons to higher energy levels. This energy may eventually be lost from the molecule through non-radiative transition. Alternatively, in the case of some specific chemical compounds, the energy in these excitation states may be emitted as fluorescence light (e.g. at visible wavelengths)

always with a higher wavelength (i.e. lower energy) that of the excitation incident light for single photon absorption events.

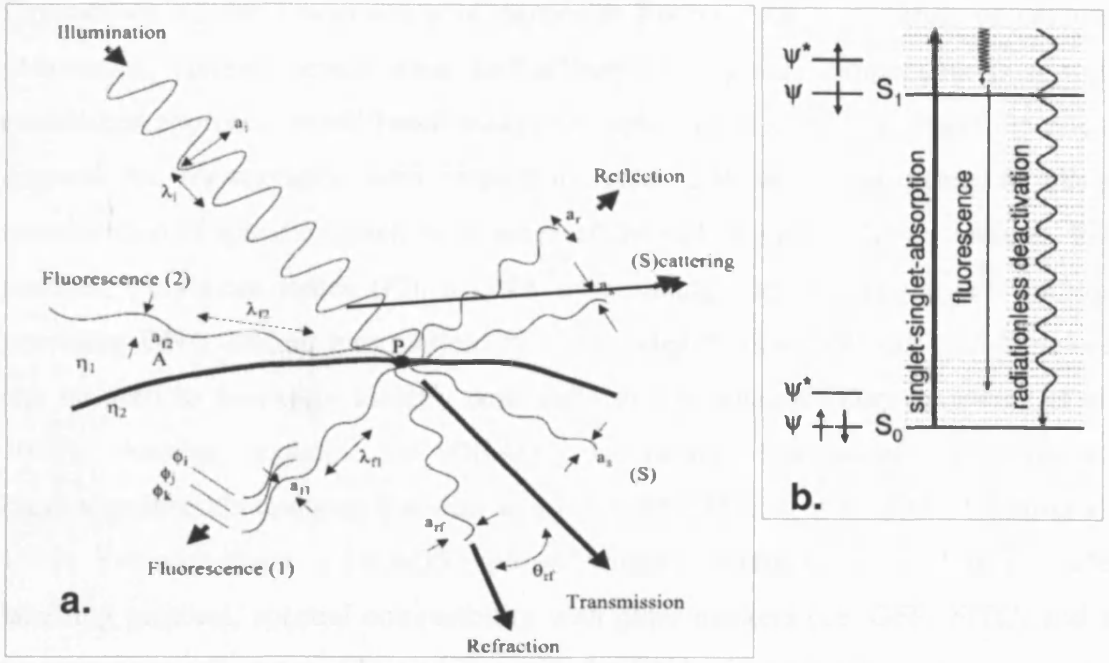


**Figure 1.5 – Schematic representation of important interactions of light with matter. (a)** Light of amplitude *ai* and wavelength $\lambda i$ encounters a point P at the boundary of two refractive index media ($\eta 1$ and $\eta 2$). Incident light can be reflected at the interface between two different media returning to the medium from which it originated; transmitter through the sample matter; refracted to an angle $\theta rf$ (given by Snell's Law) with amplitude *arf* or scattered in all directions with the same wavelength but lower amplitude (*as*). The light can also be absorbed moving the molecule electrons to higher energy levels with fluorescent light emitted in all directions, with a distinctive range of wavelengths and amplitudes ($\lambda f1$, $\lambda f2$, . . . and *af1*, *af2*, . ..). The fluorescence wavefront at any point shows a range of phases ($\Phi$i, $\Phi$j , $\Phi$k ...) (reproduced from (White and Errington 2005)). **(b)** Electron energy diagram, the horizontal lines represent the electron energy at the equilibrium position at the *So* ground state and excited state *S1* upon light absorption. The molecules can relax to the electronic *So* ground state by **(i)** non-radiative transition or **(ii)** emission of fluorescence light reporting a specific characteristic of some molecule (adapted from (Popp and Strehle 2006)).

### 1.4.3 Optical *in vitro and in vivo* imaging of cells with added contrast agents or probes

Fluorescent molecules are extensively used as probes or labels in both *in vitro and vivo* optical imaging acting as specific contrast agents to detect biological status or for the detection or localisation of features. A wide range of information sources exist for the selection of molecular probes, matched light sources and optical filter requirements (Shapiro 2004). There has been many new fluorophores with optimized

wavelength range, quantum yield and photostability, with some agents having binding affinities for macromolecular structures or discrete chemical entities or convenient distribution profiles for organelles (Giepmans et al. 2006; Smith et al. 2002). Exploitation of the functionality of particular fluorochromes, in terms of cellular penetration, compartmentalization and affinity for cellular components is a well established approach in cell-based assays. In high-content screening assays there is a demand for segmentation with respect to major cellular compartments to allow translocation of specific signals to be assessed through algorithm-driven routines. For instance, propidium iodide (PI), a DNA intercalating dye, depicts the cell nucleus providing DNA content information. PI is excluded from viable cells and therefore can be used to positively identify dead cells in a population (Darzynkiewicz et al. 1994). Another example is DRAQ5, a far-red fluorescent cell-permeant bisalkylaminoanthraquinone that acts as a DNA label (Smith et al. 2000; Smith et al. 1999). Key advantages of DRAQ5 exploited within the current study include a simple labelling protocol, spectral compatibility with other markers (i.e. GFP, FITC) and a capacity to rapidly enter and intercalate with the DNA of living cells.

However, for the studies conducted in this thesis there were several requirements for the fluorescent contrast agents to depict cell cycle, cell viability and global proliferative parameters on live proliferating cells over time. At the same time there was a need to consider the 'transferable' feature from *in vitro* to *in vivo* and the preference near infra-red (NIR) probes to ensure maximum photon collection; this is discussed in the next sections where the biophotonic integration into the HF is addressed. Clearly there is a move towards assays in which there is retention of functionality of cells and cross-platform analysis imaging/biophotonic solutions (Hutmacher 2010; Kobayashi et al. 2010; Ntziachristos et al. 2005; Pampaloni et al. 2007; Provenzano et al. 2009). This thesis focuses on dynamic proliferative signal readouts from live cells – specifically what could be termed as "tag and track" and therefore the implementation of contrast agent becomes more critical. .

### 1.4.3.1 Fluorescent probes properties for dynamic assays

There are many fluorescent optical probes specifically available for imaging live cells (Watson 2009). Probe properties have to allow repetitive time points acquisitions, perhaps inside the tissue of whole animal hosts, to show probe signal emission activity and location changes over time. The ratio between fluorescent probe signal and background (auto-fluorescence) noise is probably one of the major issues for fluorescent imaging in general, and for dynamic *in vivo* imaging in particular, due to the low probe concentration by volume necessary to balance unwanted biological perturbation against emission detection. In deep tissues the natural absorption and scattering of light acts to greatly attenuate and "blur" the emitted fluorescence light (Ballou et al. 2005) or any other photon originating or travelling through the tissue or organism (Ntziachristos 2006). For live cell imaging collecting and optimising for the fluorescence signal output is key since contrast can be described as:

$$contrast \propto \frac{s}{b+n} \quad \text{where} \quad n \propto \sqrt{(s+b)}$$ **Equation 1-1** (White and Errington 2005)

*s = average useful signal level (i.e. from biological feature(s) of interest); b=average background (i.e. from un-interesting features); n=noise (statistical variations in s and b).*

The ***brightness*** of a probe for live cell imaging is the ratio of the desired signal versus all possible reactions (i.e. number of fluorescence photons produced for each excitation photon) called the quantum efficiency or yield (White and Errington 2005). ***Photostability*** of the probe is a particular problem in time-lapse and caused by repetitive or/and high-intensity illumination conditions that lead to the photochemical destruction (bleaching) of the fluorophore, undermining the fluorescent signal readouts (White and Errington 2005). ***Bio-stability*** is related to the stability of the probe in biological environments. Molecular probes may be modified or metabolised by cells, particularly after internalization; the cellular environment influencing the optical properties to different degrees, providing a route for the development of biosensors or alternatively presenting a complication for the long-term tracking of cells. The requirement of ensuring that the probe does not interfere with the biology under question in simple terms this is related to probe toxicity and/or perturbation. The probe could be inherently toxic due its chemical composition (or its metabolites)

or yield a phototoxic effect, usually associated with the production of oxygen free radicals (Ballou et al. 2005).

Finally, the excitation ***wavelength*** should be matched with the absorption of the probe to maximize fluorescent signal. A key strategy for *in vivo* imaging is the use of NIR light. This is because hemoglobin (the principal absorber of visible light) plus water and lipids (the principal absorbers of infrared light) have their lowest absorption coefficients in the NIR region of around 650–900 nm. Imaging in this NIR region also has the added advantage of minimizing tissue auto-fluorescence, which can further improve target/background ratios (Kobayashi et al. 2010; Wagnieres et al. 1998; Weissleder and Ntziachristos 2003).

### 1.4.3.2 Technological advances in the biophotonic *interpreter* component

Advances in the development of biophotonic *interpreter* components, in the recent years, have been invaluable in expanding *in vitro* and especially *in vivo* imaging, converting images or scatter plots into knowledge. This includes developments in instrument hardware and analysis software, in particular mathematical models for describing of photon propagation in tissues. This drastically improves the capacity for obtaining dynamic biophotonic readouts in cells and tissue (see reviews (Bullen 2008; Leblond et al. 2010; Ntziachristos 2006; Ntziachristos et al. 2005). Furthermore a new future is emerging, related with the interconnection of all the generated imaging/biophotonic data with "-omic approaches" for a full integrated analysis of the biological circuits within a systems biology approach (Campbell et al. 2010; Hu et al. 2007; Megason and Fraser 2007; Peng 2008; Tarnok et al. 2010). Together with the technological progress of a full range of new probes and cell bio-sensors have been engineered to enable the tracking of living cells and organisms with corresponding readouts of many dynamic biological parameters (Giepmans et al. 2006; Kobayashi et al. 2010; Weissleder and Ntziachristos 2003). Some typical probes appropriate for tracking cell cycle and proliferation in tumour cells are described next.

### 1.4.3.3 Fluorescence – protein reporters

Genetically encoded fluorescent proteins come from a wide range of animals found in nature and have also been artificially optimized to present enhanced optical properties and emission wavelengths, including infra-red emission (Shcherbo et al. 2007; Shu et al. 2009). Typically these protein reporters are genetically encoded and must be transfected by the means of a vector into the host cells.

Green fluorescent protein (GFP) (Prasher et al. 1992) from the jellyfish *Aequorea victoria* was one of the first fluorescent proteins to be used for *in vivo* imaging, providing a genetic reporter or fused to endogenous proteins to monitor their localization, expression in living cells and organisms (Chalfie et al. 1994; Nasevicius and Ekker 2000; Tsien 1998). Many different mutants of GFP and other proteins have been engineered (Shaner et al. 2005), in order to improve their properties for *in vitro* and *in vivo* applications; including brightness, stability biological interference and wavelength, other properties such as protein expression and maturation efficiency in the transfected cells has also to be carefully evaluated. Probably one of the most widely used variant is the 'enhanced' GFP (eGFP). eGFP (excitation max. 488 nm, emission max. 507 nm) is a mutant of GFP with a 35-fold increase in fluorescence in relation to the wild-type (Cormack et al. 1996) with a re-engineered GFP gene sequence containing codons preferentially found in highly expressed human proteins (Chiu et al. 1996; Haas et al. 1996; Zhang et al. 1996), it presents the enhanced properties required for promoter driven reporter systems in transfected mammalian cells (Zhang et al. 1996). They have been effectively used in living cells (Muller-Taubenberger and Anderson 2007; Tsien 1998; Vordermark et al. 2001; Zimmer 2002), and small animal tumour models (Hoffman 2002; Okabe et al. 1997).

In this thesis the genetically engineered eGFP fused to the cyclin B1 promoter and including a destruction and nuclear locating signal provides a cell cycle stealth reporter that shadows endogenous cyclin B1 levels (GE_Healthcare 2003) (for a detailed description see section 1.6.1.2) (Thomas 2003; Thomas et al. 2005) tracking cells through the late cell cycle. In the current work the reporter is evaluated to obtain a cell cycle reading directly from HF encapsulated cells; its performance for macro-imaging the HF cells has been recently presented (Silvestre et al. 2009).

### 1.4.3.4 Fluorescence – semiconductor Quantum Dots (QD) particles

Semi-conductor nanocrystal quantum dots (QDs) with size-dependent optical and electrical properties were first illustrated by Alivisatos 1996 and their potential for ultra-sensitive biological detection was unravelled by Chan and Nie 1998 . QDs typically have a core/shell structure of 2-8 nm in diameter, normally the core is composed of heavy metal semiconductor crystalline compounds such as CdSe (Cadmium Selenide), CdTe (Cadmium telluride), InAs (Indium Arsenide) or PbSe (lead selenide) and a shell made of ZnS (Zinc sulphide). Due to their hydrophobicity QDs are not soluble in water or biocompatible. For use in aqueous environments they have to be additionally coated with a hydrophilic layer of different compositions, to ensure compatibility with physiological media (Michalet et al. 2005).

These nanocrytals present different light emission properties than traditional organic chemically synthesized dyes or fluorescent proteins. Briefly, the absorption of a photon with energy above the semiconductor band gap energy results in the creation of an electron-hole pair (or exciton), the absorption has an increased probability at higher energies (i.e., shorter wavelengths) and results in a broadband absorption spectrum. The unique optical properties of QDs include high absorbance, high quantum yield, narrow emission bands and large Stokes' shifts. The emission spectra of QDs can be tuned across a wide range by changing the size and composition of the QD core. The synthesis and engineering of QDs with different semi-conductor materials have expanded the range of possible emission wavelengths from the visible to the red and infrared regions (e.g. CdSe may be size-tuned to emit in the 450-650nm range, CdTe can emit in the 500-750nm range, whereas InAs or PbSe can emit above 800 nm) (Frasco and Chaniotakis 2010; Michalet et al. 2005). This makes it possible to simultaneous detected multiple targets at different wavelengths with a single excitation wavelength (Figure 1.6-a).

The advantages of using QDs in the place of traditional organic fluorophores have been widely reported (Jaiswal and Simon 2004; Resch-Genger et al. 2008). Firstly, they are highly photo-stable allowing long-term labelling of live cell populations (Hoshino et al. 2004; Parak et al. 2005). Secondly, QDs are far more chemically stable and are not so easily metabolised or degraded by the cell. Although, shown to have

minimum cytotoxic effects at some doses, any heavy metal leakage must be prevented, as the potential nanotoxicity in cells is still open to debate and seems to depend on their chemical nature and surface coating (Lewinski et al. 2008; Resch-Genger et al. 2008).

When conjugated with biomolecular ligands such as antibodies, peptides or small molecules (Figure 1.6-b), QDs can be used to target specific cellular or molecular compartments (Mattheakis et al. 2004). Today there is a high range of QD-based probes with unique optical properties and *bio-sensor* capabilities for live cell and *in vivo* applications (Frasco and Chaniotakis 2010; Rogach and Ogris 2010; Xing et al. 2009). This ranges from the "traditional" target-specific QD conjugates with monoclonal antibodies or peptides (Giepmans et al. 2006; Jaiswal et al. 2003) to self-illuminating QDs, in which the QD is excited by attached bioluminescent enzymes (luciferase) through resonant energy transfer (Yao et al. 2007; Zhang et al. 2006b).

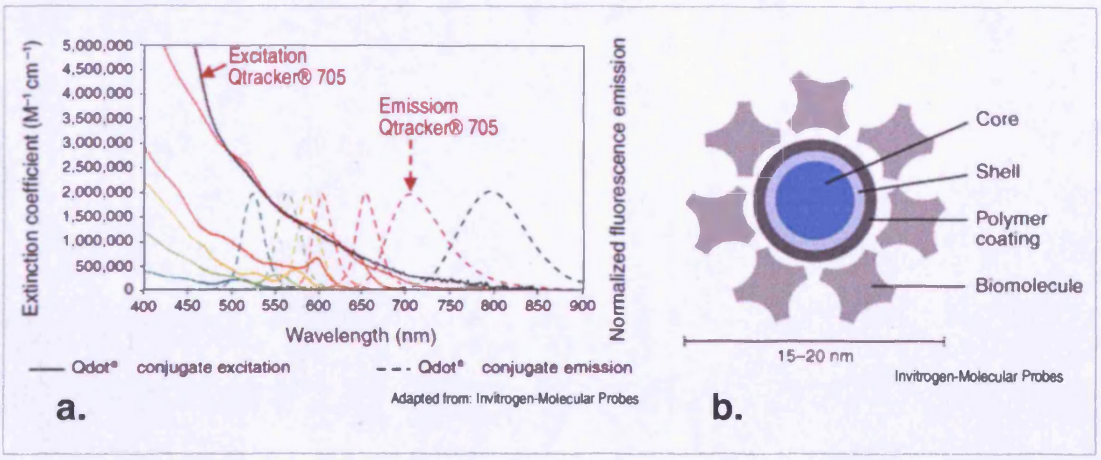


**Figure 1.6 – Properties of conjugated semiconductor quantum dots (QD). The QD used in the current thesis was bought commercially and chosen from the Qtracker® range.** (**a**) Excitation (solid line) and emission (dashed line) spectra of of these commercially available QDs, arrows highlight Qtracker®705 used in the current study. (**b**) Schematic of the QD nanocrystal conjugate to ensure biocompatibility. (adapted from: Invitrogen, The future of fluorescence-Qdot® nanocrystals, http://probes.invitrogen.com/media/publications/600.pdf [2007]).

### 1.4.3.5 Fluorescence – Qtracker 705 live cell labelling system

In the present thesis the QD studies employed a commercially available source (Invitrogen-Molecular Probes former Quantum Dot Corporation) of far-red (705 nm emission) CdTe/ZnS core-shell, (polyethylene glycol) PEG-coated QDs with

streptavidin linked to a biotinylated nine residue L-arginine peptide (biotin/9-arginine) that promotes cell internationalization (see spectra and schematic Figure 1.6-a and b). This QD peptide system cell internalization conjugate was developed by Lagerholm et al. 2004 , with a cell labelling kit commercial application called Qtracker® 705 (see Cat. No. Q25061MP, Invitrogen: http://products.invitrogen.com/ivgn/product/Q25061MP [2008]). This QD labelling system/kit will be referred in this thesis as QD705. The kit was used previously for live cell labelling (Buono et al. 2009; Fischer et al. 2009; Fotos et al. 2006; Lin et al. 2007; Machleidt et al. 2009; Murasawa et al. 2005; Rosen et al. 2007; Yang et al. 2009) and also in Cardiff in published studies (Brown et al. 2007; Chong et al. 2007; Njoh et al. 2007; Summers et al. 2008) and more recent publication connected with this thesis (Brown et al. 2010a; Errington et al. 2010; Holton et al. 2009).

### 1.4.4 HF platform optical imaging current "state of the art" biophotonics approaches

Until recently it has been necessary to retrieve the cells from inside the (host and) fiber for multiple end-point assays, not being possible to perform repetitive time point acquisitions of the same HF implanted in an animal during a study. This section deals with all the biophotonics related studies directly used in HF implants previously mentioned in the literature, focussing on the optical imaging approaches.

#### 1.4.4.1 HF optical imaging – bioluminescence

The feasibility of using tumours cells transfected with luciferase *in vitro* and also *in vivo* to provide a bioluminescent reporter based dynamic assay in the HF was first demonstrated by Hollingshead et al. 2004 and later further developed (Zhang et al. 2007; Zhang et al. 2008a; Zhang and Kaelin 2005; Zhang et al. 2004).

Bioluminescence represents a chemical reaction that occurs in a biological environment where of the "by-products" is actually light, without any need for excitation light as in the case of fluorescence. Similarly to the fluorescent proteins reporter systems, bioluminescent systems were genetically engineered and refined

from a range of natural occurring of organisms, including species of bacteria, marine organisms and insects (Wilson and Hastings 1998). Several gene constructs were developed and transfected to cells to be used as a reporter system. The most common enzyme/substrate pairing and also the most useful for *in vivo* imaging are the luciferases from the male firefly, *Photinus pyralis* (Dothager et al. 2009). The luciferase enzyme catalyses the following reaction: [ATP + luciferin substrate + $O_2 \rightarrow$ AMP + oxyuciferin +PPi + Light (photons)] in the presence of $Mg^{2+}$. Firefly luciferin normally produces light with maximum emission at 562 nm (Weissleder and Ntziachristos 2003). The application of bioluminescence to live animal imaging, namely pre-clinical research models, is an established technique and has been extensively reviewed (Contag and Bachmann 2002; Dothager et al. 2009; O'Neill et al. 2010; Welsh and Kay 2005)

It has been demonstrated (Hollingshead et al. 2004) that bioluminescence could be detected through the wall of the HF on subcutaneous implants and the capacity of cells within HF to support bioluminescence demonstrated that there was enough oxygenation of the contents of the fibre in spite of the lack of vascularisation. Furthermore, the bioluminescence in subcutaneous fibres following administration of the luciferin substrate demonstrated the speed with which small molecules substrates can be distributed systemically. Bioluminescence macro-imaging provides a variety of advantages to the evaluation of the *in vivo* efficacy of anti-cancer compounds in HF tumour implants: First, the ability to perform time series imaging of many animals simultaneously, using short exposure times (~1 min) using systems with cryogenically cooled CCD cameras that minimizes any electronics noise, thereby increasing its ability to detect very low levels of light (photon counting) (see chapter 2.6.4). Second, the capacity to engineer luciferase constructs reporters for specific promoters (i.e. transcriptional factors, fusion proteins). Third, the short half-life of the enzyme in mammalian tissues (about 3 h) and the non-toxic nature of the luciferin (Hollingshead et al. 2004).

Other studies further demonstrated the relevance of non-invasive *in vivo* bioluminescence imaging applied to the HF: A screening approach was applied that enabled a rapid and continuous evaluation of anti-cancer drugs (i.e. Taxotere and

Camptosar) inside the fiber without the need to retrieve the HF from the animal. The overall cell growth or proliferation could be followed by time point (i.e. each 4 days), up to 28 days, in the same HF implants and animals, using cells lines stably expressing luciferase (Zhang et al. 2007). The use of engineered luciferase reporter systems has allowed the monitoring for the activation of specific signalling pathways on *in vivo* tumour cells within an implanted HF, upon the administration of drugs, this is especially relevant for the study of drug molecular targets response (Zhang et al. 2007). This study dealt with the pharmacokinetics of cyclin-dependent kinase 2 (Cdk2) inhibitory drugs (i.e. Flavopiridol and R-roscovitine) responses, using p27-luciferase fused protein, considering that p27 is phosphorylated by Cdk2 (Zhang et al. 2004). Furthermore, Zhang et al. 2008a proposed a HF implant protocol for the systematic imaging of molecular pathways of interest using bioluminescent engineered reporter cells.

#### 1.4.4.2 HF optical imaging – other biophotonic approaches

A thorough examination of all available literature has revealed that, besides bioluminescence, there is virtually no mention of other bipohotonic dynamic *in vivo* techniques directly applied to the selected HF implants, this being also true for *in vitro* studies.

The exception was the fluorescent imaging of angiogenesis at HF implant sites *in vivo* (Zhang et al. 2007). Using the AngioSense750 probe, (MW=250kDa), a near-infrared fluorochrome ($ex._{max}$750nm / $em._{max}$780nm) long circulating labelled copolymer "blood pool probe", used for the localization and tracking of angiogenesis. Briefly, this probe is impermeable to intact normal vascular vessels while leaks from tumour vasculature and selectively accumulates in solid tumours. It was used to image the increase vascularisation around cell filled subcutaneous HF implants, demonstrating that the inside HF encapsulated cells can communicate with the host tissue.

Bioluminescence was so far the only imaging technique tool systematically used to interrogate *in vivo* HF implants. Although this technique has several advantages compared to fluorescence including practically inexistent background light

interference and greater sensitivity. However, it presents several disadvantages (for details see Figure 1.7), such as the dependence of exogenous administrated substrates plus limited wavelength and intensity of the emitted light (Choy et al. 2003; Contag and Bachmann 2002; Weissleder and Ntziachristos 2003). Also, identifying luciferase expressing cells (i.e. by flow cytometry) at the end of an experiment can be challenging (O'Neill et al. 2010).

## 1.5 Principle "to consider the requirement for bridging pre-clinical models and studying linked cellular features in different environments"

### 1.5.1 2D surface standard tissue culture limitation

The majority of adherent cell-based studies are routinely performed on 2D substrates such as plastic planar tissue culture (TC) multi-well plates, flasks and Petri dishes because of several factors, that include simplicity, convenience and high cell viability of 2D cultures. It is relatively simple to perform dynamic imaging on these culture platforms and they offer a coherent planar surface for imaging. However, standard types of cell culture systems have notably improved the understanding of basic cell biology and allow control over experiment and analysis parameters, but 2D systems also present severe limitations.

2D substrates are considerably limited in emulating the complex cell-cell and cell-matrix interactions, as well as the diffusion/transport conditions present in the 3D micro-environments of real live tissue. For example, 3D co-cultures used for derma-toxicity testing showed improved xenobiotic stress resistance to active agents when compared to the same cells cultured in 2D (Sun et al. 2006). Tissue cells connect not only to each other, but also to a support structure called the extracellular matrix. This contains proteins, such as collagen, elastin and laminin, that give tissues their mechanical properties and help to organize communication between cells embedded within the matrix; interactions within the extracellular matrix have essential roles in the regulation of cell behaviour and fate (see review (Geiger et al. 2001)). 2D cultures lack this structural mechano-architecture and of the complex and unique biochemical

and physical signals of the extracellular matrix environment characteristic of each cell type. These drawbacks can alter cell metabolism and reduce functionality, 2D culture substrates not only fall short of reproducing the complex and dynamic environments of the body tissues, but also are likely to misrepresent findings to some degree by forcing cells to adjust to an artificial flat, rigid surface.

Several studies have shown that cancer cells behave differently when comparing 2D versus 3D cell cultures that may help to explain for example the unsatisfactory results on clinical performance of a promising 2D models cancer drugs. For example it has been shown that antibodies against the cell surface receptor β1-integrin had different capacities to change the behaviour of tumour cells grown in a 3D human breast cancer model compared to 2D cultures. The 3D cells become non-tumourgenic and lose their abnormal shapes and patterns of growth contrary to the 2D counter-part (Weaver et al. 1997). One of the reasons behind this different behaviour is related to the cell apical–basal polarity orientation in the 3-D culture that altered the cells gene expression and biological responses. These findings have been further expanded by others (Abbott 2003; Weaver et al. 2002; Weigelt and Bissell 2008) where the tumour micro-environment is to be considered as a target in its own right.

In summary traditional methods of cell growth and manipulation on 2D surfaces overall and especially in cancer research have been shown to be insufficient for the new challenges of cell biology and biochemistry, as well as in pharmaceutical assays. This is why 3D systems are now at the forefront of development tissue engineering and cancer biology (for recent high impact reviews on this subject see (Fischbach et al. 2007; Hutmacher et al. 2010; Lee et al. 2008; van Staveren et al. 2009; Yamada and Cukierman 2007) (Fischbach et al. 2007; Hutmacher 2010; Lee et al. 2008; Moreau et al. 2007).

### 1.5.2 Examples of 3D cell culture systems for cancer studies

There is a wide range of 3D *in vitro* culture systems with different architectures and support materials, with applications in studies on regenerative medicine, stem cell

differentiation, organs morphogenesis and tumour models. Engineered tumour models that try to emulate more closely the 3D tissue structures are pertinent to study the mechanisms of aberrant 3D behaviour of proliferation and invasion associated with cancer and therefore provide an invaluable tool for the evaluation of anti-cancer drug candidates (Burdett et al. 2010; Fischbach et al. 2007). Some examples of 3D *in vitro* tumour models include:

*Tumour spheroids*: By far the most widely used 3D model (Ruei-Zhen and Hwan-You 2008), that corresponds to small, tightly bound cellular aggregate that tends to form when specific types of cells are maintained under non-adherent conditions. These aggregates can mimic tumour behaviour more effectively than regular 2-D cell cultures because spheroids, much tumours, usually contain both surface-exposed and deeply buried cells, proliferating and non-proliferating cells, and well-oxygenated and hypoxic cells (Cheng et al. 2009; Robertson et al. 2010).

*Gel embedding matrixes*: This approach uses gels as a substrate for 3D cell culture, some of these systems can also be included in the above spheroid models. The semi-solid substrate includes agarose, collagen, alginate or other gel biological formulation optimized to within possible promote cell differentiation, migration, and recreation of the *in vivo* cellular architecture as close has possible. One of the most used formulations is the commercial Matrigel matrix, to emulate a tissue basement membrane (BD-Matrigel™InvasionChamber 2010). It has been used in Matrigel cell invasion assay, with a modified "Boyden chamber" (Boyden 1962), the chamber consists of a well cell culture insert with an 8 μm pore size polymer membrane, the upper side of the membrane is uniformly coated with Matrigel matrix. Cells are seeded on the upper side in medium while in the lower chamber only medium of a different composition is added. The matrix provides a barrier to non-invasive cells while presenting an appropriate protein structure for invading cells to penetrate following the medium chemo-attractant gradient to the lower chamber (Walker et al. 2001). This has enabled the study of cell behaviour and expression of biomolecular markers associated with cell invasion in several studies (Han et al. 2008; Luu et al. 2005; Soncin et al. 2009; Xin et al. 2009). Although, considered as a 'true' 3D culture. The "real" 3D tumour studies with Matrigel can be traced to the works of (Debnath et al. 2003; Weaver et al. 2002; Weigelt and Bissell 2008) where cell growth and

organization formed hollow spherical-like clusters that replicate the numerous features of breast epithelium, including the formation of acini-like spheroids with a hollow lumen, apicobasal polarization of cells making up these acini and the basal deposition of basement membrane components.

*Other engineered 3D models:* Recent developments in tissue engineering and biomaterials fields have precipitated a series of advances in 3D culture system beyond the simple spheroid or gel matrixes. Tuneable and mechanically superior polymer matrices (i.e. scaffolds) have been developed as substrates for 3D cancer cells to provide a more well-defined architecture for tumour cell growth. Extensive review on this was previous performed (Burdett et al. 2010; Fischbach et al. 2007; Griffith and Swartz 2006). The most recent example of a new 3D culture technique has been development of a culture system based on magnetic cell levitation; performed in a hydrogel consisting of a mixture of several magnetic sensitive nanoparticles and filamentous, used to manipulate and cluster different cell types (Souza et al. 2010).

*The hollow fiber (HF)*: HF bioreactors provide for specialized 3D cell culture (section 1.3.2). While the HF implant presents a more "stand alone" culture system where the tumour cells grow inside a semi-permeable tubular confined structure, that can be used both *in vitro* and *in vivo* with all the advantages previously discussed (section 1.3.3.2). The HF implant platform has been recently discussed in context of other 3D systems (Sharma et al. 2010), the HF alongside other culture systems play an increasing important role to evaluate the therapeutic efficacy of candidate anticancer agents. The tumour cells grow inside a permeable tubular confined structure, where the porous membrane wall presents a physical barrier to contain the culture; as the cell mass develops evidence of a gradient of cell nutrients/waste between the interior and the outside also presumably develops (Casciari et al. 1994). This enhanced cell-cell, cell-wall proximity within the "tubular" HF encapsulated culture structure in some studies has resulted in different morphologies compared to standard 2D planar monolayer cultures (Bridges et al. 2006).

### 1.5.3 The HF a platform suitable for bridging the gap between pre-clinical culture systems.

Even though advantages of 3D culture have been demonstrated for some time, they still present some limitations and are not yet widely implemented in research. There are several reasons; first, the large deviation within 3D matrix structures and compositions lead to inconsistencies between cultures, preventing reproducible experimental data and proper systematic analysis. Second, normally these systems are more complex and present a high cost to run, which limits the feasibility of large-scale experiments. To compensate for these challenges, there is a need for the standardization of 3D matrixes surfaces, along with mass production manufacturing processes, to enable researchers to take full advantage of 3D cell culture potential (Lee et al. 2008).

The introduction and application of 3D culture systems brings-up the requirement to re-evaluate any results from standard 2D culture. So, for a rational transition it is vital to perform a systematic comparisons of the cell biology in 2D versus 3D cultures, in terms of morphology, metabolic and signalling activity, response to drugs and ultimately gene expression (Abbott 2003; Cosgrove et al. 2008; Fischbach et al. 2007). Bridging the gap between 2D and 3D *in vitro* models represents only a part of the problem when expanding to the more challenging task of linking standard pre-clinical cell culture to whole-animal *in vivo* systems (Hutmacher et al. 2010; Yamada and Cukierman 2007).

The detailed understanding of the cell biological responses and signalling pathways between these models will require application of systems-level biological approaches (Campbell et al. 2010; Hu et al. 2007; Khalil and Hill 2005; Kherlopian et al. 2008; Megason and Fraser 2007). These emerging approaches will further improve the ability to bridge the gap between *in vitro* systems and *in vivo*. Technologies paving the way include *in vitro* models that better reflect *in vivo* tumours, micro-fabricated devices of human physiology, and improved animal models. This will enable at the same time the discovery and research of several new factors that where not contemplated previously, namely in the cell response to changes of their micro-environment and to perturbations by cancer drugs or other agents.

The HF represents a natural 3D *in vitro* and *in vivo* platform to bridge the gap between traditional tissue culture and animals models. First, because it was developed and is still used mainly as a "fast-track" *in vivo* model, were the main advantages are the control of the seeded and retrieved cell population, allowing the easy transposition from *in vitro* culture to *in vivo*. Second, using this 3D platform it is possible to maintain and retrieve a "pure" cell population from the HF, because the HF encapsulated cell populations is physically separated form the host tissue on *in vivo* implants or other types of cell lines on *in vitro* co-culture systems. Third, although very simple and missing the specialized matrixes of other more advances 3D scaffolds, it represents a standardized well defined structure with minimal concerns of model/structure reproducibility. Finally, the HF assay is an established drug screening model, routinely used and therefore there is a rich data source already available to mine.

There have been some reports using histology to differentiate cell morphology/ organization adopted by specific cell lines compared between the HF *in vitro* and *in vivo* (Bridges et al. 2006). However, no systematic investigation has been undertaken changing a cell environment from a planar 2D standard surface to the 3D HF culture. An important question is how the HF culture modifies (or not) tumour cell morphology and packing, cellular proliferative behaviour *(Chapter 3)* and ultimately at the molecular level the gene expression profiles *(Chapter 4)*. At the same time consideration for the optical interrogation of the HF environment; multi-cellular packing needs to be considered for multi-modal imaging, expanding on the foundation studies where optical measurements have been undertaken and used to understand the changes in absorption and scattering as a response to growth and drug perturbation, like in spheroids models (Hargrave et al. 1996).

### 1.5.4 Examples of biophotonic and transferable approaches for pre-clinical cross platform studies in cancer research

The importance of linking different cell culture platforms in cancer research has been outlined above; the question now is what single cell tracking approaches are transferable across these platforms with the best results and highest data output.

Several end-point techniques, such as flow cytometry and micro-array analysis provide an important high-throughput cross-sectional 'snapshot' at a given time point reflecting cell population status. These represent static measurements and require disassembly of the tumour. Imaging technologies on the other hand provide the possibility of gaining dynamic live cell information in situ to record and track specific cell parameters. Furthermore, the imaging hardware and technology tools already pre-developed for interrogating standard flat 2D surfaces or whole animal imaging could be converted or applied to interrogate several 3D cultures systems (Yamada and Cukierman 2007) including the hollow fiber.

An extensive range of imaging or biophotonic approaches exist to monitor biological activity and therapeutic agents responses, applied to both 2D and 3D *in vitro*, with the emphasis to *in vivo* whole animal pre-clinical tumours models and also ultimately clinical studies. For recent reviews see (Griffith and Swartz 2006; Pampaloni et al. 2007; Provenzano et al. 2009; Sahai 2007; Weissleder and Pittet 2008) with some are more technological based (Burdett et al. 2010; Cosgrove et al. 2008; Leblond et al. 2010; Ntziachristos et al. 2005; Qian et al. 2008). In the next sections brief overviews of relevant imaging tools to the present study are presented, namely nanoparticle probes, fluorescent spectroscopy/tomography and flow cytometry.

#### 1.5.4.1 Nanoparticle probes in cancer studies acting as nano-tags and bio-sensors

The synthesis and development of all types of nanoparticles have been explored in many biological applications, with an ever increasing potential for innovation associated with multi-technological approaches, namely in biophotonics, and offer remarkable opportunities to study and regulate complex biological processes, including new therapeutics (Brown et al. 2010c). The biological applications of several types of nanomaterials and nanoparticles inside living cells has been recently reviewed in general (Gao and Xu 2009; Lee et al. 2009), concretely related to cancer diagnostic/therapeutic applications (Rogach and Ogris 2010; Scheinberg et al. 2010; Yong et al. 2009) and concerning only QDs application (Biju et al. 2010; Ho and Leong 2010; Rogach and Ogris 2010).

Overall, QD use with live cells can be divided into two main application areas that complement each other. First, QDs as "passive" nano-tags or labels for molecular and cell tracking in biological cancer studies, used as fluorescence contrast agents for imaging. Together with *fluorescence spectroscopy and tomography* technologies make them a preferential choice as a probe for multi-labelling in 2D and also 3D cultures or for more complex *in vivo* animal dynamic imaging. Second, acting as a multifunctional nanoplatform modified or functionalized to act as a sensor to report various biological cell metabolic responses, for example PEBBLE (probe encapsulated by biologically localized embedding) intracellular sensors (see (Lee et al. 2009) for recent review). Or acting as a nanoscale vehicle for the controlled delivery of agents or photodynamic therapy, targeting cancer cells (Schäfer-Korting et al. 2010). The only issue is that heavy metal-related nanotoxicity impairs QDs transition to clinical human applications (Kobayashi et al. 2010).

#### 1.5.4.2 Fluorescent spectroscopy/tomography of labelled cells and 3D tissue

These techniques take advantage of the range of contrast agents or probes available to enhance the detection of cell, organelles or specific biological parameter being interrogated. There are underlying differences and several issues between conduction dynamic fluorescence imaging *in vitro* and *in vivo* (Leblond et al. 2010; Ntziachristos et al. 2005; Pampaloni et al. 2007), being more pressing considering 3D systems.

*Fluorescence spectroscopy* is based on the analysis of the emitted (or absorbed) fluorescence from a sample (i.e. living cells/tissue). Normally it involves detection of cell/tissue auto-fluorescence background signal as well as the characteristic fluorescence emitted from the *target* of interest. In a typical set-up an optical fiber can be use to guide the excitation/emission light and scan a sample tissue through multiple-wavelengths using a monochromator. Although, these format provides a high resolution wavelength versus light intensity excitation/emission spectrum it doesn't provide any image structure. This approach has been used in several cancers studies (Brown et al. 2009).

Importantly fluorescent spectral based technologies are becoming integrated with micro/macroscopic imaging. Ideally when studying dynamic complex biological phenomena in cells and living tissues, besides image the sample as fast as possible, it's crucial to capture several channels (*multi-channel*), each corresponding to a wavelength range with the use of optical filters and PMT/CCD detector, or an entire spectrum (*multi-spectral*) witch provides wavelength versus light intensity resolution. Some of the most versatile systems in terms of multi-spectral imaging are equipped with liquid crystal tuneable filters (LCTF), which allow the acquisition of spectral ranges with a resolution that could be down to a few nanometres (Leblond et al. 2010). These technologies allow the interrogation of several probes associated with different biological targets simultaneous. Thus mathematic algorithms have been developed which are able to isolate the contribution of individual probes, including auto-fluorescence, enabling the producing of an "unmixed" output and enhancing the analysis of features otherwise un-detected.

The above fluorescent spectral imaging when associated with tomography techniques presents considerable enhancements to perform dynamic assays in 3D *in vitro* platforms or *in vivo* whole animals. *Fluorescence tomography* deals with the three-dimensional reconstruction of the internal distribution of fluorescent probes in deep-tissues (or 3D cultures) based on light measurements collected at the tissue surface boundary. One point of distinction of optical tomography compared with other tomographic high energy methods (i.e. positron emission tomography (PET)) is the multiple scatter interferences of both the excitation light and the fluorescence emission travelling back to the tissue surface detection area (see Figure 1.7). This introduces an intrinsic "blurring" in fluorescence images, an effect that is amplified the further away the fluorescent *target* is from the illumination/detection area at the surface of the tissue, and hence the main issue in deep-tissue optical imaging.

This is why optical tomography is generally heavily based on the mathematical physical models of light photon interactions and propagation within tissues. Together with technological advanced light sources, optics and detectors this allows deep-tissue three-dimensional reconstitution imaging with some spatial resolution, isolating the fluorophores probe signals, but the end results, though informative, still present several issues to overcome (Leblond et al. 2010; Ntziachristos 2006). Today, optical

micro and macroscopic multi-channel or/and multi-spectral imaging and tomographic reconstruction are routinely used with several pre-clinical and also clinical imaging commercially systems widely available (for reviews see (Kobayashi et al. 2010; Leblond et al. 2010; Rao et al. 2007; Weissleder and Pittet 2008).

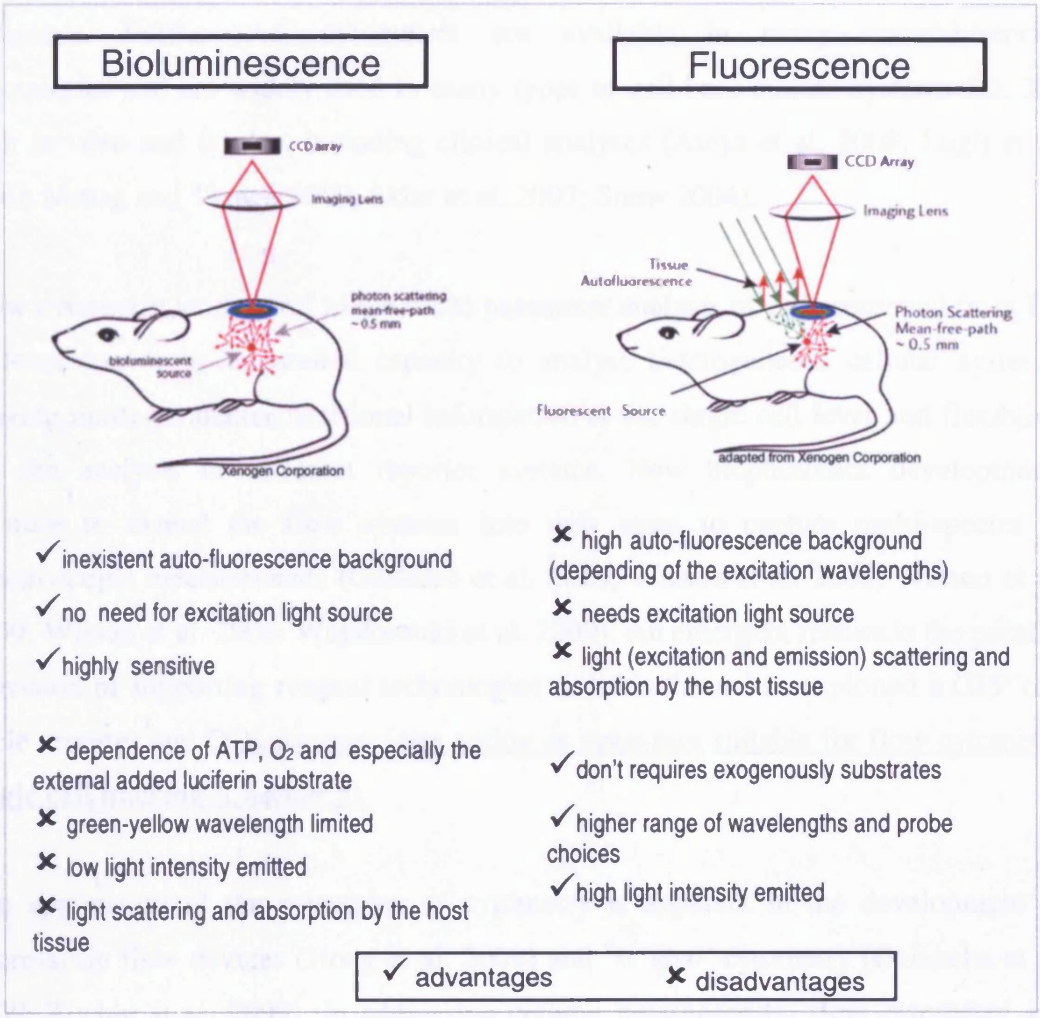


**Figure 1.7 – Comparison of non-invasive fluorescence and bioluminescence imaging using a small animal optical system, i.e. the In Vivo Imaging System (IVIS) used in the current study.** (adapted from: Xenogen Corporation, Living Image 2.50 Manual-2004 (http://www.umgcc.org/research/xenogen_sw_manual.pdf [2008])). For IVIS instrument technical details see chapter 2.6.4.

### 1.5.4.3 Flow cytometry

Multi-channel high-throughput acquisition represents one of the fundamental principles behind flow cytometry. The advantages of these technique include objective and precise single cell quantification, statistical precision, multi-parametric cross-

correlated data analysis and subset identification, sensitivity with high speed and generation of vast amount of data (Watson 1991). However the disadvantage is that the disaggregation of the tissue to obtain a single cell suspension is mandatory, making it essentially an end-point assay. Even so, flow cytometry presents outstanding features like a stable high data quality cross platform interrogation technique. Furthermore, cytometers are available in many research/service laboratories and are widely used in many types of cell-base culture systems 2D, 3D, both *in vitro* and *in vivo*, including clinical analyses (Ateya et al. 2008; Lugli et al. 2010; Mittag and Tarnok 2009; Sklar et al. 2007; Snow 2004).

Flow cytometry lends itself to the multi-parameter analysis of cells retrieved from HF systems due to its unparalled capacity to analyse heterogeneous cellular systems, provide multi-parameter functional information at the single cell level and flexibility for the analysis of different reporter systems. New biophotonics developments promise to extend the flow systems into new areas to capture multi-spectra or spectroscopic measurements (Goddard et al. 2010; Watson et al. 2008; Watson et al. 2009; Wilson et al. 2006; Wojakowski et al. 2009). An emergent feature is the parallel provision of supporting reagent technologies and this thesis has exploited a GFP cell cycle reporter and QDs nanoparticles acting as nano-tags suitable for flow cytometry single cell tracking *(Chapter 5).*

The application of the principles of cytometry is apparent in the development of micro-scale flow devices (Hong et al. 2009) and *'in vivo'* cytometry (Galanzha et al. 2008; Tuchin et al. 2009). In addressing cellular heterogeneity, flow cytometry and single cell analyses in general start to meet the aspiration to acquire systems levels insights from the molecular to the whole organism level in describing disease processes and revealing opportunities for therapeutic intervention. As a result there is an increasing recognition of the need to progress the 'flow of cytometry into systems biology' (Nolan and Yang 2007), a common aim being to bridge the molecular-cellular systems gap (Khan et al. 2007; Smith et al. 2007a; Smith et al. 2009). Here, both instrumentation and knowledge-from-data integration issues present significant challenges but if solved, will move flow cytometry to an interface with the wider and more complex systems biology frameworks. The HF model can be viewed as culture platform for such purposes.

### 1.5.5 Biophotonic component integrated into the HF - culture platform

Up to this point the described biophotonic approaches aim to interrogate cells using nano-scale probes (e.g. fluorescent proteins reporters and nanoparticles) and macro-scale technologies (e.g. imaging using microscopes or the IVIS200). But there might be a third way that can complement or work in parallel which embraces the implant opportunities of the HF and the potential offered by micro-technology based devices. Microsystems technologies for implantable applications are far ranging, (see (Receveur et al. 2007) from sensors, drug delivery devices to transducers and actuators used for long-term and temporary applications. Advances include the miniaturization of biophotonic components, such as *light source*, *detectors* and also wireless technology. This thesis (*Chapter 6*) deals with an initial preliminary study toward the development of a biophotonic micro-device approach; where components such as a *light source* and *detector* are "integrated" into the HF for direct "in-fiber" acquisition readouts. In other words this approach would potentially enable real time HF tumour cell behaviour acquisition and as an implant would maintain transferability to *in vivo* applications.

## 1.6 HF experimental parameters – model cell system and drug perturbations

In the present study the intent was to establish and characterize the HF 3D culture as a cross platform model appropriate for a systems biology approach where the culture is transferable from *in vitro* to *in vivo*. The concept was to develop and execute benchmark studies to establish a robust *in vitro* biophotonic-tumour model; and then to consider with our partners at Bradford University an *in vivo* implementation. The selected model cell line was the human osteosarcoma cell line U-2 OS and the cytotoxic model drugs were Taxol and Colcemid, all described in detail in the following sections.

### 1.6.1 Focus on the human osteosarcoma human cell line U-2 OS as an appropriate model system

The human osteosarcoma cell line U-2 OS (see next section) was selected for this study. It provides a wealth of *a priori* properties for a model cell system, as it has been extensively characterized *in vitro* culture (Lind et al. 1996; Pautke et al. 2004), presenting a relative homogeneous behaviour and genomic stability (Sihn et al. 2005) and therefore considered to be robust. U-2 OS cells were found to be negative for most osteoblastic markers (Pautke et al. 2004). Further extensive proteomics has been used to analyse the proteins of the U-2 OS cell line (Niforou et al. 2008) and therefore provides a foundation for conducting gene profiling as well as single cell characterisation. The U-2 OS cell line is routinely used for high-through-put analysis and drug screening (Vollmers et al. 2008), namely involving steroid receptor (Paruthiyil et al. 2009). Also, G protein-coupled receptors (GPCRs) have proven to be a rich source of therapeutic targets; therefore, finding compounds that regulate these receptors is a critical goal in drug discovery. The Transfluor technology (GPCR-MolecularDevices 2010) stably expressed in U-2 OS cells utilizes the redistribution of fluorescently labelled arrestins from the cytoplasm to agonist-occupied receptors at the plasma membrane to monitor quantitatively the activation or inactivation of GPCRs (Oakley et al. 2002). Also only few studies attempt to deal with this specific cell type in a mouse model (Manara et al. 2000). There is still the need for an *in vivo* animal model that incorporates all features of the human disease and can be used to more accurately study key genetic aberrations and also to develop anti-osteosarcoma agents (Dass et al. 2007; Ek et al. 2006). Finally, previous HF bioluminescence work (Zhang et al. 2004) used U-2 OS transfected cells with a p27-luciferase fused protein reporter to monitor Cdk2 activity *in vivo* and *in vitro*, but no major characterization was performed.

#### 1.6.1.1 Human osteosarcoma U-2 OS parental cell line

U-2 OS (ATCC HTB 96) is a human osteosarcoma cell line expressing wild type p53. (Ponten and Saksela 1967), isolated in 1964 from a moderately differentiated sarcoma of the tibia of a 15 year old female. Cells are positive for insulin-like growth factor I (IGF-I) and insulin-like growth factor II (IGF II) receptors and express a number of antigens (ATCC_HTB-96 2010). Alterations of the TP53 tumour suppressor gene

appear to be implicated in the tumorigenesis and progression of several types of human cancer, including different histologic subtypes of sarcomas. In U-2 OS cells the MDM2 copy number was normal, while the mRNA expression of both the TP53 and MDM2 genes was highly elevated (Florenes et al. 1994).

### 1.6.1.2 U-2 OS cyclin B1-GFP G2M cell cycle phase marker (U2OS-GFP)

For the purposes of this thesis the U-2 OS cells presented an additional benefit as they were transfected with the G2M cell cycle phase marker (GE Healthcare, UK), this reporter is based on the promoter of cyclin B1 fused with eGFP (cyclin B1-GFP) (GE_Healthcare 2003). The G2M cell cycle phase marker assay employs a non-destructive dynamic eGFP-based probe to report the position of individual cells in the cell cycle (Thomas et al. 2005). The construct probe (Figure 1.8-a) comprises cell cycle-dependent expression, destruction and localization elements from the gene for cyclin B1(Thomas 2003). This is a tightly-regulated cell cycle-dependent kinase that is expressed in late S-phase and is subsequently degraded during mitosis (Clute and Pines 1999; Morgan 2006) (Figure 1.8-b). By quantifying the location and fluorescence intensity of the expressed reporter molecule, the cell cycle position of individual cells can be resolved to distinct phases of the cell cycle by fluorescent microscopy (Figure 1.8-c and d) (GE_Healthcare 2003) and also by flow cytometry (Figure 1.8-d).

U-2 OS cell line stably transfected with cyclin B1-GFP G2M cell cycle phase marker (U2OS-GFP) has been compared to (Thomas et al. 2005) its non-transfected parental line for standard *in vitro* tissue culture. It was reported that the modified cell line expression of the eGFP cell cycle reporter does not perturb cell cycle kinetics, gene expression of key cell cycle control proteins and minimally perturbs gene expression in general. Analysis of the cell cycle duration and cell cycle phase distribution by cell growth assays and flow cytometry revealed that the two cell lines had identical doubling times and cell cycle distribution. eGFP fusion protein quantification indicates a reporter expression level equivalent to endogenous cyclin B1 (7000 copies/cell in G2) and microarray analysis showed a 0.9% (>2 fold at $p<0.001$ across 20 000 genes) difference in global gene expression levels between parental and cyclin B1-GFP expressing U-2 OS cells (Thomas et al. 2005).

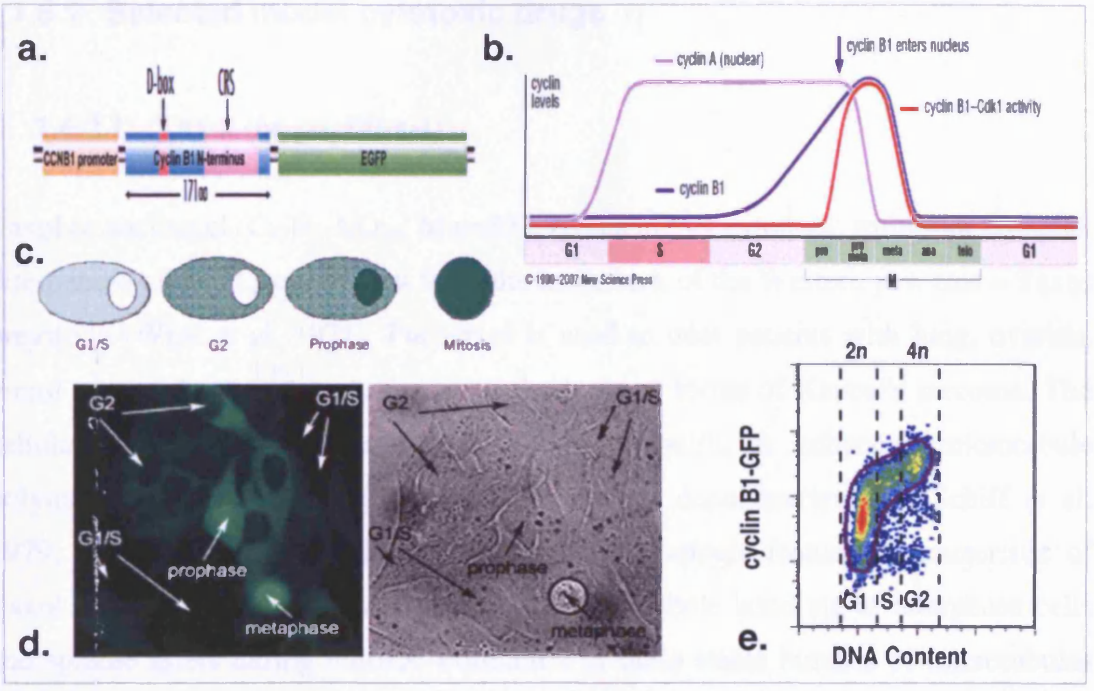


**Figure 1.8 – U-2 OS cyclin B1-GFP G2M cell cycle phase marker description. (a) The G2/M cell cycle phase marker construct**. eGFP synthesis is controlled by the cyclin B1(CCNB1) promoter, which limits production to late S and G2 phases, destruction of the reporter is controlled by the cyclin B1 D-box which mediates rapid degradation during mitosis. Location of the reporter is controlled by the cytoplasmic retention sequence (CRS) embedded in the N-terminal portion of cyclin B1 which localizes the reporter to the cytoplasm until the start of mitosis, when it translocates to the nucleus (adapted from (GE_Healthcare 2003; Thomas 2003)). **(b) Schematic to show typical mitotic cyclins levels in a somatic mammalian cell.** Details of cyclin B1 (dark purple line) changes with low levels in G1 and most of S, this increase at G2 and peaks during mitosis (adapted from (Morgan 2006)). **(c) Cell cycle-dependent reporter expression and location**. There are four different patterns that can be distinguished and assayed: cells that are in G1/S (non-fluorescent/dimly fluorescent in the cytoplasm), cells that are in G2 (high fluorescence in the cytoplasm), cells in prophase (signal translocation to include nucleus), cells during mitosis (highly fluorescent rounded cells) (adapted from (GE_Healthcare 2003)). **(d) Actual microscopy of U-2 OS cells expressing the cyclin B1-GFP reporter,** fluorescence (left panel) and transmission (right panel) images (adapted from (Chappell et al. 2008)). **(e) Typical U-2 OS cyclin B1-GFP flow cytometry profile of 10,000 cells.** A cyclin B1-GFP fluorescence density-plot plotted against the DNA content (DRAQ5), marked to indicate cell cycle phase (horizontal dashed lines).

The dual parameter readout (i.e. cyclin B1-GFP versus DNA content) of cell cycle parameters provides for high-resolution profiles of cell cycle status, including processes such as tetra-ploidisation traverse (Brown et al. 2010b; Smith et al. 2007b) are exploited in single-cell analysis of cells retrieved from the hollow fiber and attempted on the macro-analysis of the close fiber.

## 1.6.2 Selected model cytotoxic drugs

### 1.6.2.1 Taxol (or paclitaxel)

Taxol or paclitaxel ($C_{47}H_{51}NO_{14}$, Mw=853.9) is a highly cytotoxic antitumor complex diterpenoid alkaloid isolated first from the inner bark of the Western yew tree – Taxus brevifolia (Wani et al. 1971). Paclitaxel is used to treat patients with lung, ovarian, breast cancer, head and neck cancer, and advanced forms of Kaposi's sarcoma. The cellular target of Taxol was identified as tubulin, it enhances microtubule polymerization and stabilizes microtubules against depolymerization, (Schiff et al. 1979; Schiff and Horwitz 1980). Prominent morphologic features characteristic of Taxol treated cells include the formation of microtubule bundling in interphase cells and spindle asters during mitosis. Formation of these stable bundles of microtubules disrupts the normal dynamics of the tubulin/microtubule cytoskeleton and results in the arrest of cells in G2-M phase of the cell cycle and associated induction of apoptosis (Arnal and Wade 1995; Rowinsky et al. 1990).

However, Taxol action has proved more complex, depending on cell type, and drug dose (Allman et al. 2003; Chen and Horwitz 2002; Jordan et al. 1993; Jordan et al. 1996; Rieder and Maiato 2004; Torres and Horwitz 1998), plus transcriptional gene activation studies indicates that Taxol initiates apoptosis through multiple mechanisms (Wang et al. 2000). Exact biochemical mechanisms and timing of cell death in relation to progression through the cell cycle is still unclear (Gascoigne and Taylor 2009), see Figure 1.9 for an overview.

At high concentrations Taxol enhances microtubule polymerization and stabilizes microtubules against depolymerisation, leading to an increased microtubule polymer mass (Jordan et al. 1993) and causing massive microtubule damage, resulting in the activation of several pathways leading to apoptotic cell death (Wang et al. 2000). Whereas at low concentrations, Taxol mitotic arrest action mechanisms is related with the suppression of microtubule dynamics, with no changes in the microtubules polymer mass. This perturbs the formation of mitotic spindles, resulting in a cell cycle mitotic arrest (Jordan et al. 1993; Jordan and Wilson 2004).

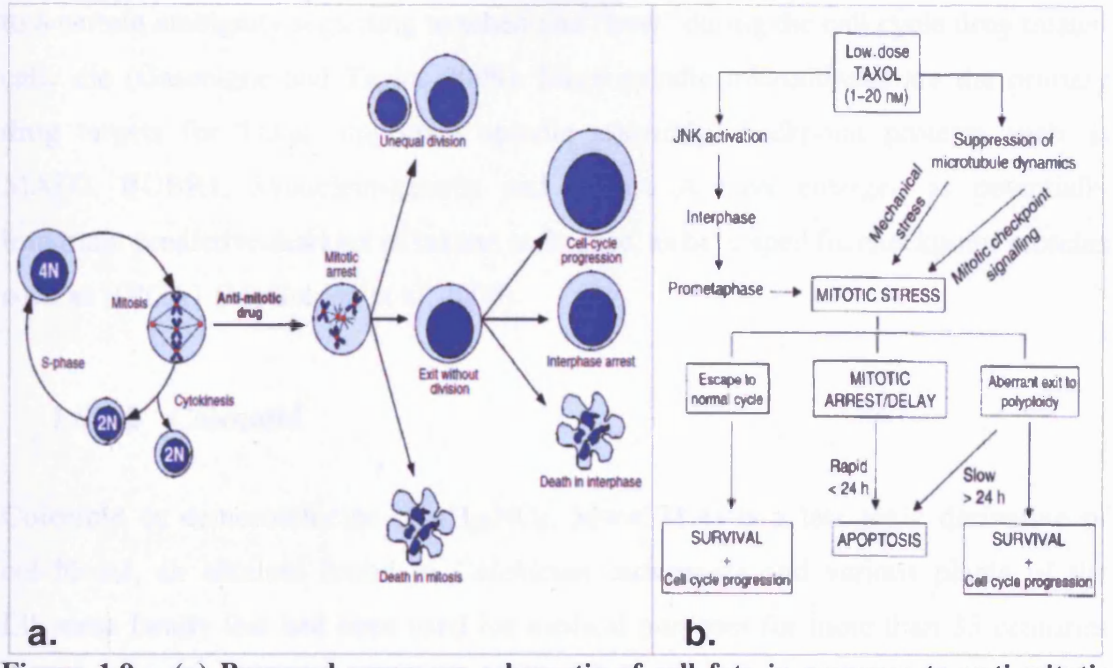


**Figure 1.9 – (a) Proposed summary schematic of cell fate in response to anti-mitotic drugs treatment such as Taxol.** The cell can arrest in mitosis due to chronic activation of the spindle-assembly checkpoint. They then undergo one of several fates. Cells die directly in mitosis or divide unequally to produce aneuploid daughter cells. Alternatively, cells exit mitosis not undergoing division. Then cells might die in interphase, arrest in interphase indefinitely or enter additional polyploidy in the absence of division (reproduced from (Gascoigne and Taylor 2009)). **(b) Proposed mechanism involved in cells treated with low concentrations of Taxol (1-20 nM).** Several biochemical events may lead to mitotic arrest and subsequent Taxol-induced cell death or survival (adapted from (Allman et al. 2003; Wang et al. 2000)).

The principal uncertainty at low Taxol concentrations lies on the precise mechanisms involved on the cell fate after this G2/M arrest (Wang et al. 2000). Previous studies showed that cells in the presence of low concentrations of Taxol (≤ 10 nM) resulted in abnormal chromosome segregation, leading to abnormal DNA content, cell size and aneuploidy (Chen and Horwitz 2002; Torres and Horwitz 1998). In summary (Figure 1.9), cells can undergo a rapid engagement of apoptosis and die directly in mitosis, divide unequally to produce aneuploid daughter cells or/and escape cell-cycle arrest continuing cycling or become apoptotic. Alternatively, cells might exit mitosis without undergoing division through an aberrant mitotic exit to a tetraploid state (referred here as G1tetra). In this case, cells might then experience a delayed engagement to apoptosis (>24h), arrest indefinitely in this phase or proceed to further polyploidy entering additional cell cycles (Allman et al. 2003; Brito and Rieder 2009; Gascoigne and Taylor 2009; Rieder and Maiato 2004; Smith et al. 2007b; Wang et al. 2000). In any one of the previous scenarios cell apoptosis is reported to occur, leading

to a certain ambiguity regarding to when and "how" during the cell cycle drug treated cells die (Gascoigne and Taylor 2009). Since spindle microtubules are the primary drug targets for Taxol, important spindle assembly checkpoint proteins such as MAD2, BUBR1, Synuclein-gamma and Aurora A have emerged as potentially important predictive markers of taxane resistance, as have specific checkpoint proteins such as BRCA1 (McGrogan et al. 2008).

### 1.6.2.2 Colcemid

Colcemid or demecolchicine ($C_{21}H_{25}NO_5$, Mw=371.4) is a less toxic derivative of colchicine, an alkaloid found in *Colehicum auturnnale* and various plants of the Liliaceae family that had been used for medical purposes for more than 35 centuries (Eigsti and Dustin 1955). Besides its use for treatment of gout and in (largely unsuccessful) trials as an anticancer chemotherapeutic agent, the active compound, colchicine, and its derivatives such as Colcemid have been widely used in cytogenetics.

By binding to tubulin dimer, the drug inhibits polymerization of microtubules. Since depolymerization is unaffected, the mitotic spindle rapidly dissociates or is not formed, and cycling cells accumulate in a prometaphase-like state, in many cases for an extended period. This mitosis response in the presence of these drugs was designated by (C-mitosis) (Hastie 1991; Jha et al. 1994; Rieder and Palazzo 1992; Sluder 1979; Taylor 1965). In a sufficient concentration this agent completely inhibits the formation of spindle microtubule. As a result, during nuclear envelope breakdown the chromosomes are released into the cytoplasm where they remain randomly dispersed throughout the prolonged period of C-mitosis (Rieder and Palazzo 1992). It's possibly for the cells, depending of the treatment conditions and type of cell line, with time to escape the mitosis block and enter the next cell cycle in the presence of the drug. Some cell lines never escape the block and die after some days, but in some cases, a significant proportion of the cells within a mitotic arrested population escape the block while others die in mitosis (Rieder and Palazzo 1992; Sherwood et al. 1994b). (Kung et al. 1990) previously showed that the ability of a cell type to survive C-mitosis is somewhat species specific, and is positively correlated with its ability to

degrade cyclin-B during the prolonged mitotic period, with some cell lines being ably to cycle (without dividing) with rise and fall of cyclin-B in a polyploidy state.

Due to the above mentioned prolonged mitotic block, Colcemid was used to perform cell cycle stathmokinetic calculations (Darzynkiewicz et al. 1987; Puck and Steffen 1963; Taylor 1965). Additionally, Colcemid was also used for cell cycle synchronization due to the fact that the removal of the drug provided synchronous G2/M cell populations (Sherwood et al. 1994a; Stubblef.E and Klevecz 1965; Uchiyama et al. 2004). However, the demonstrated drug-induced adverse metabolic perturbations and toxicity for the synchronized cells compromises the use of this and other microtubule-disrupting agents in synchronization methods (Davis et al. 2001; Urbani et al. 1995).

## 1.7 Statement of thesis aims

The overall aim of the thesis is to incorporate innovative biophotonics into the hollow fiber (HF) appropriate for tracking cell cycle and pharmacodynamic responses. The specific aims of this thesis are as follows:

***Aim_i*** - To establish and study the *in vitro* U-2 OS cyclin B1 GFP human osteosarcoma HF encapsulated model (HF–U2OS-GFP) parallel to the standard tissue culture (TC). Characterize and compare both of these model culture systems in relation to tumour cell morphology and biological behaviour, under normal proliferation and drug perturbation conditions, namely the action of Taxol and Colcemid (*Chapter 3*).

***Aim_ii*** - To perform gene expression profiling of the HF versus standard TC culture, interconnected with a "systems biology level" bioinformatics analysis, to ultimately evaluate the HF culture environment effect on the U-2 OS cells (*Chapter 4*).

***Aim_iii*** - To explore and validate a cross platform flow cytometry approach, tracking the consequences of introducing a nanoparticle presenting a conserved fluorescent signal, into a proliferative system. Thus providing quantitative generational information about the cell population in both the standard TC and the HF culture (*Chapter 5*).

***Aim_iv*** - To develop and assess the design of a hollow fiber format with embedded illumination for detecting particle and/or cell density (*Chapter 6*).

# CHAPTER 2

# MATERIALS AND METHODS

# 2 MATERIALS AND METHODS ..... 48

# 2 MATERIALS AND METHODS

All reagents were stored, handled and disposed of according to Cardiff University Health and Safety regulations and the guidelines recommended by the Material Safety Data sheets provided by the commercial suppliers. This Chapter provides an overview about the procedures and instrumentation used in this thesis. More information about specific methodologies and reagents linked with a focus area of investigation, are provided within the respective chapters.

## 2.1 Materials

All standard laboratory plastics (plates, dishes, T-flasks) consisted of tissue culture (TC) treated polystyrene with flat-bottoms from BD Falcon (Becton Dickinson Labware, Franklin Lakes, NJ, USA).

### 2.1.1 Hollow Fiber – porous PVDF

- Source: (cat. no. S9320101 Spectrum Laboratories, Inc, CellMax® Implant Membrane, Netherlands) - (http://eu.spectrapor.com/1/3/0.html [2007])

- Key features: Supplied like 34cm length dry sections, white (no added colour), inner diameter=1.0 mm, outer diameter=1.2 mm, made of porous Polyvinylidene Difluoride (PVDF) with 500 kD molecular weight cut-off value (CellMax_Spectrum_Labs 2009). See Figure 2.1 for structure details and Table 2.1 for porosity details. Standard PVDF polymer membrane presents a reflective index=1.42. PVDF itself is a mechanically strong, acid resistant, and chemically inert polymer, and is capable of binding proteins hydrophobically (Pluskal et al. 1986).

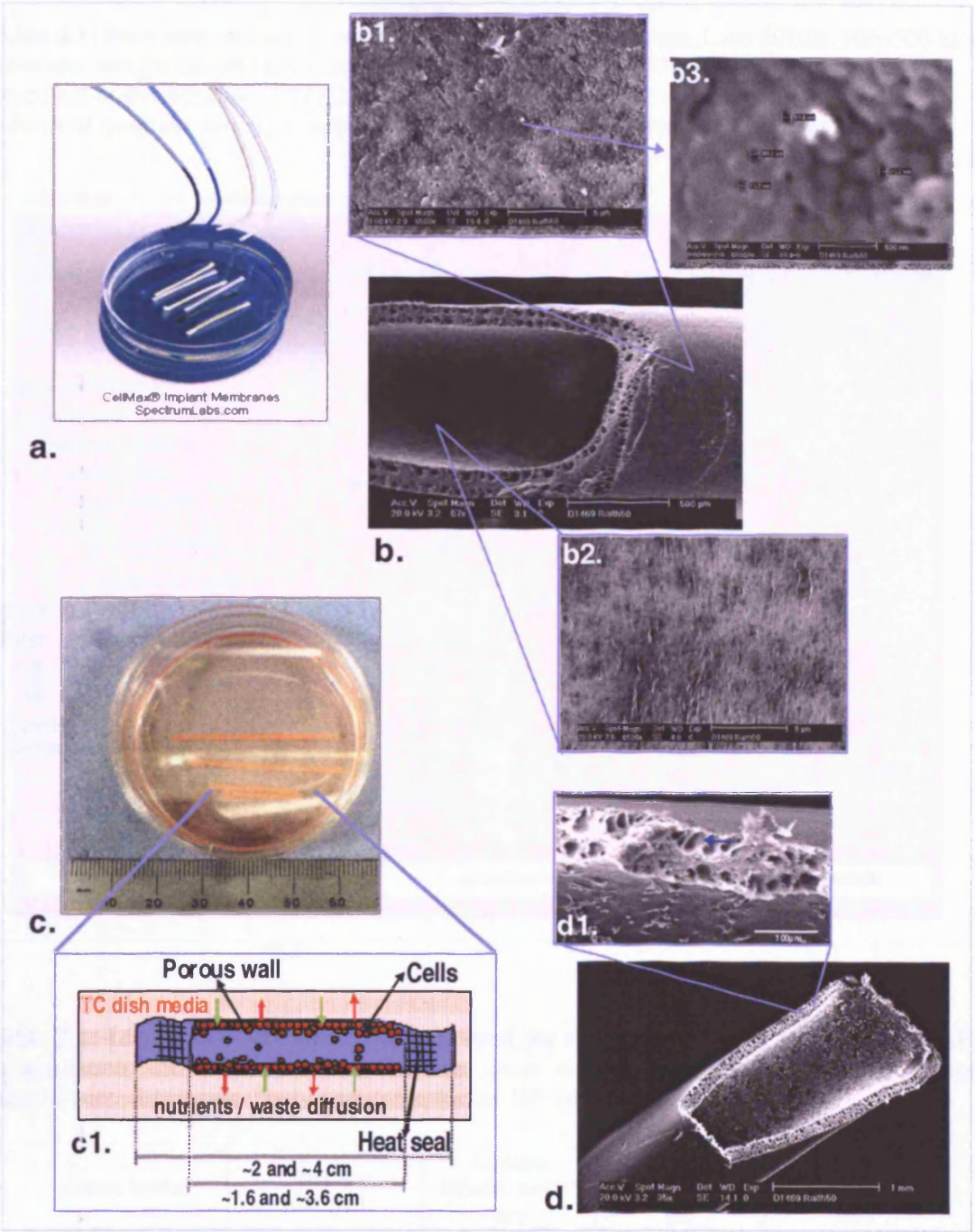


**Figure 2.1 – The Hollow fiber (HF).** **(a)** Full length HF as it comes from the manufacturer, colour use in the project - white (adapted from (CellMax_Spectrum_Labs 2009)). **(b)** Scanning electron microscopy (SEM) images, empty HF longitudinal-section (inner diameter 1.0 mm, outer diameter 1.2 mm) with details of the outer (b1) and inner (b2) wall surface and the small pores (b3) with a diameter of ~70-80 nm (bar represents 500, 5, 5 µm and 500nm, respectively). **(c) Typical culture conditions.** Example of closed HFs sections (i.e. heat sealed at both ends) approx. 2cm and 4cm length HFs, thus giving an available adherent cell inner surface length of 1.6 and 3.6 cm (0.50 and 1.13 $cm^2$ area) respectively, cultured in a 60 mm diameter TC dish. **(c1)** Schematic representation of the adherent cells inside the HF in culture with the exchange of nutrients and cell wastes through the pores with the outside TC media. **(d)** SEM image of a longitudinal-section cut HF containing a layer of adherent cells growing on the surface; **(d1)** higher magnification of cells on the fiber wall and of the inner pore structure, with detail of the large internal pores structure (arrow); (bar represents 1mm and 500µm, respectively).

**Table 2.1: Pore size comparative chart** (adapted from (Spectrum_Labs 2010)). HF=500 kDa molecular weight cut-off (green arrow); Taxol or paclitaxel (C47H51NO14, Mw=853.9); Colcemid or demecolcine (C21H25NO5, Mw=371.4) (both last - black arrow); Qtracker® individual quantum dots (QD) approx relative size 15-20 nm (purple arrow) (Invitrogen).

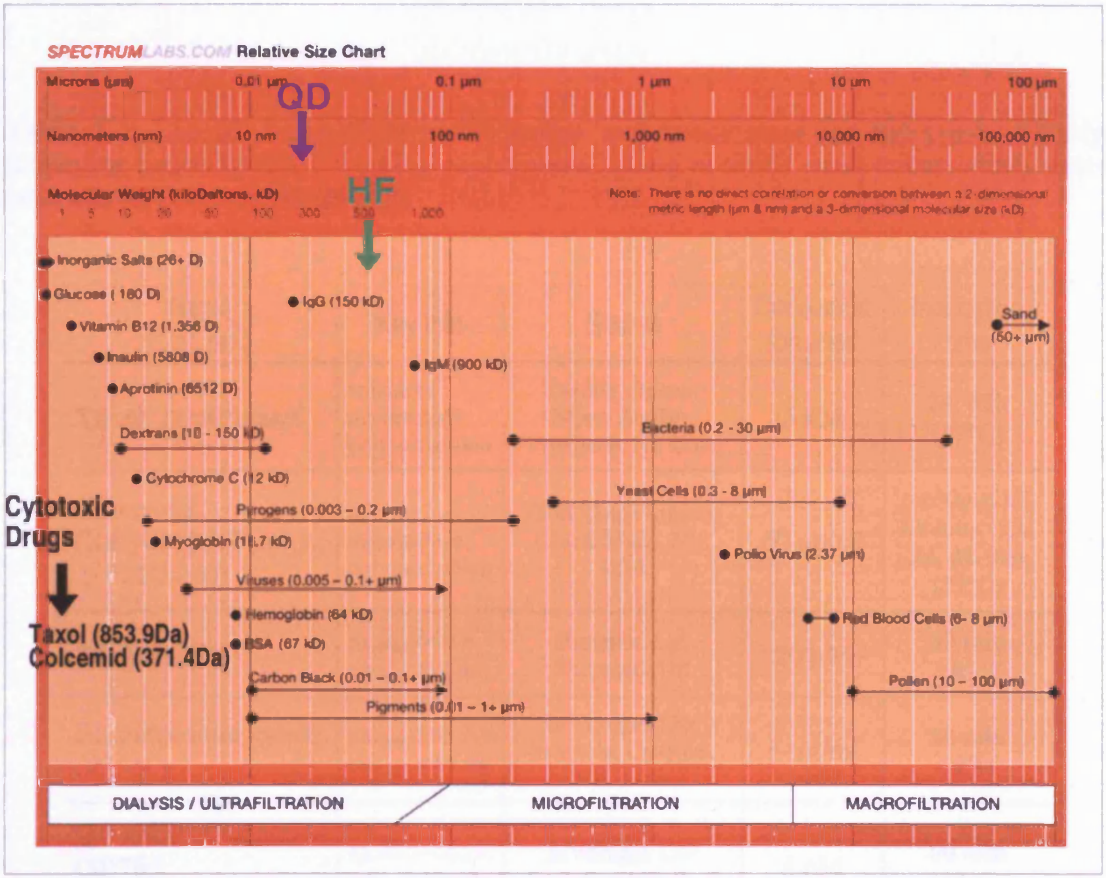


**Table 2.2: List of the cell culture systems used for the current study.** Hollow Fiber (HF) encapsulation and standard planar surface tissue culture (TC). Useful parameters and manufacturer dimension. *only applicable for the HF tubular matrix

| Culture System | Source (Cat. No.) | Available adherent length* (cm) | Tubular inner volume* (µl) | Growth surface area ($cm^2$) |
|---|---|---|---|---|
| HF 2cm length | Spectrum Laboratories, CellMax® (S9320101) | ~1.6 | ~12.6 | **~0.50** |
| HF 4cm length | | ~3.6 | ~28.3 | **~1.13** |
| 6 well TC plate | BD Falcon (353046) | - | - | **9.6** |
| 12 well TC plate | BD Falcon (353043) | - | - | **3.8** |
| 60 mm TC dish | BD Falcon (353002) | - | - | **21.3** |
| 100 mm TC dish | BD Falcon (353003) | - | - | **58.1** |
| 2 well Nunc 1.5 cover glass TC chambers | Nunc/Lab-TekII (155379) | - | - | **4.0** |

### 2.1.2 Drugs, fluorescent probes and beads

Drugs and fluorescent probes were prepared, stored and disposed of according to supplier instructions (see Table 2.3 for details)

**Table 2.3: List of drugs, fluorescent probes and beads used for the current study.** Regarding concentration – working experimental values normally used, except when stated otherwise. RT = room temperature

| Name (Cat. No.) | Key Info | Source | Concentration used | Incubation time |
|---|---|---|---|---|
| **Taxol** or paclitaxel | enhances microtubule polymerization | Taxol®, Bristol-Myers Squibb, Princeton, NJ, USA | 5 nM | **24, 48h (37°C)** |
| **Colcemid** (KaryoMAX® sol.) (15210-040) | inhibits microtubule polymerization | GIBCO-InVitrogen, Grand Island, NY, USA | 60 ng/ml | **multiple, i.e. 6h intervals, 24, 48, 96h (37°C)** |
| **DRAQ5** | $ex._{max}$ 646 / $em._{max}$697nm | Biostatus Ltd, Shepshed, UK | 20 µM | **10 min (RT)** |
| **PI**, propidium iodide (P3566) | $ex._{max}$ 535 / $em._{max}$617nm | InVitrogen Life Sciences, Carlsbad, CA, USA | 5 µg/ml | **10 min (RT)** |
| **Qtracker®705nm – QD705** (Q25061MP) | ex.405–665 / $em._{max}$705nm | InVitrogen Life Sciences | 4 nM | **60 min (37°C)** |
| **FluoroSpheres 6-peak** beads (K0110) | multiple ex./em. | Dako, Ely, UK | ~one to two drops in 1 ml | - |
| **Calibrite beads PE** (349502PE) | $ex._{max}$ 564 / $em._{max}$578nm | BD Bioscience, San Diego, CA, USA | ~one drop in 2 ml | - |
| **FluoSpheres 15µm** beads (F-8843) | $ex._{max}$645 / $em._{max}$680nm | InVitrogen Life Sciences | $5.0 \times 10^5$ beads/ml | - |
| **LinearFlow™ 6µm Calibration** beads (L-14819) **100% fluor** | $ex._{max}$ 633 / $em._{max}$660nm | InVitrogen Life Sciences | - | - |

## 2.2 Cell line and model culture conditions

### 2.2.1 General description and (stock) culture of U2OS-GFP cells

All experimental work was performed with the U-2 OS human osteosarcoma cell line stably transfected with cyclin B1 fused eGFP (U2OS-GFP) (GE_Healthcare 2003; Thomas 2003; Thomas et al. 2005) from the G2M Cell Cycle Phase Marker Assay (Amersham Biosciences, now GE Healthcare Life Sciences, Little Chalfont, UK) (see chapter 1.6.1.2 for details). The parental cell line was the U-2 OS (ATCC HTB-96) (Ponten and Saksela 1967).

The cell line was routinely cultured and split twice a week with, except when stated otherwise, with the following medium *10%McCoy's*: McCoy's 5A modified medium (Sigma, St Louis, MO, USA) supplemented with 10% fetal calf serum (FCS) (Autogen Bioclear, Calne, UK), 200 mM L-glutamine (Sigma), 10,000 units/ml penicillin/streptomycin 10 mg/ml (Sigma) and 800 ug/ml Genetcin Sulphate (G418) (Invitrogen). Variations of this medium include supplementing with 25 mM HEPES buffer (Sigma) (*10%McCoy's+25mM HEPES*) or the use of 20% FCS (*20%McCoy's*) with or without HEPES.

Cultures were maintained at 37°C under standard TC conditions in a humidified incubator with 5% CO2. All cell lines were generally passaged in T-75 vented flasks, as follows; the media was removed, the flask was rinsed with saline buffer or PBS (Dulbecco's Phosphate-Buffered Saline) (Invitrogen), aspirated and cells detached using Trypsin / ethylene diaminetetraacetic acid (EDTA) (Invitrogen), from now on only described as Trypsin. Detached cells were re-suspended in 10-15 ml of medium, and a new passage split taken from this suspension without centrifugation.

### 2.2.2 HF model – cell seeding and culture protocol

All the HF work was performed on *in vitro* culture, the HF's were not used for *in vivo* studies with implantation in to live animals. The Hollow Fiber U-2 OS cyclin B1-GFP *in vitro* adherent cell culture model (HF–U2OS-GFP) seeding protocol was adapted from the previous described for the standard HF assay (CellMax_Spectrum_Labs

2009; DTP-NCI 2009; Hollingshead et al. 1995b; Suggitt et al. 2004) and the protocol kindly supplied by Dr Steve Shnyder (ICT, Bradford University). The HF seeding and culture protocol modifications were performed to overcome several practical issues. Some of the major optimized new procedures introduced were:

First, the use of full medium with an additional 25 mM HEPES buffer in order to try to maintain a more stable cell medium pH during the loading and retrieval protocols to help minimize cell stress.

Second, the injection of the cell suspension into the HF with micro-pipette tips (100-200 µl) plugged into a serine/plastic pipette that fit on both ends of the HF., preventing or highly reducing the amount of cells suspension leaking from the HF in the loading protocol. Eliminating or at least reducing the amount of washing steps was important in order to prevent any problems with outer fiber cell contaminations that would "stick" to the HF outer wall and biologically contaminate the encapsulated population with exponential growth. Also it was important to minimize the amount of suspension cell volume used to load into a HF. Keeping control of the injection and avoiding any waste of cells was important for "precious" cell samples, like the QD705 labelled cells.

Third, the development and optimization of a basic cell retrieval and processing protocol, to efficiently obtain a HF cell suspension for analysis (namely flow cytometry), minimizing any possible adverse biological effects and interferences in the cyclin B1-GFP G2M cell cycle reporter system.

All the HF work was performed on *in vitro* culture, the HF's were not used for *in vivo* studies with implantation in to live animals.

The detailed protocols section are described in the next pages: the membrane activation and sterilization of the HF and the cell preparations had to be performed at least 4-5 days in advance of the actual HF cell loading. Gloves were used during all fiber manipulations, even prior to sterilization, to reduce transfer of body oils to the fibers and all the below procedures were performed in the laminar flow cabinet (hood) under sterile conditions.

#### 2.2.2.1 Membrane activation and sterilization of the HF

*1.* Dry 34 cm fibers were gently removed from the package and placed in a 500 ml glass column previous filled with 70% Ethanol (EtOH). The fibers were then individually flushed with 70% EtOH using a 10 ml syringe and 21 gauge blunt needle whilst the fibers were still inside the glass column. Care was taken to avoid and eliminate any air bubbles from inside the fibers.

*2.* The glass column with the 70% EtOH fibers was stored at room temperature (RT) with the lid sealed with parafilm. The fibers were allowed to soak for a minimum of 72 hours before the cell loading (they could be stored for weeks if necessary like this). The above procedure activated the HF membrane and also provided an acceptable level of HF sterilization.

#### 2.2.2.2 Cell preparation

Cells were split the previous week into T-75 flasks at densities that resulted in 70-90% confluency on the day of the experiment (roughly a T-75 flask will generate 3-4 ml of 1.0 x$10^6$ cell/ml in excess). Cells are fed the day before the experiment by removing half of the existing volume of medium and replacing with an equal volume of fresh medium with 20% FCS (*20%McCoy's*), (for the *HF cell loading protocol B*, medium contains 25mM HEPES).

#### 2.2.2.3 HF cell loading protocol_A

Due to the extensive and labour-intensive nature of this protocol, it was highly advisable to ensure all necessary materials/reagents were prepared and checked in advance. To minimize any cell stress effects, once the protocol was started it was continuous.

The general *HF cell loading protocol_A* was as follows:

*1.* On the day of the experiment the HFs stored in the glass column with 70% EtOH were rise with distilled water. Briefly, the HFs were transferred using a forceps (or by

hands with new and sterile gloves) from the glass column to a plastic box with lid (previously autoclaved or rinsed with 70% ethanol and dried) which is one quarter filled with sterile autoclaved distilled water. Each fiber was flushed individually with the distilled water using a 21 gauge blunt needle syringe and the box covered with the lid. Extra care was advised to not allow the HF to dry, otherwise the process had to be re-started from point 2.2.2.1, or if any HF becomes dry during or after cell loading it would have to be discarded.

*2.* The medium was removed from previously prepared T-75 cell flask(s) into a universal and centrifuge at 1300rpm for 10 min, the supernatant transferred into a second universal and place on ice (or at 4°C). This supernatant (termed ***conditioned medium***) was used to re-suspend the cells and/or added to the growth culture medium.

*3.* The T-75 cells were detached with Trypsin, re-suspended with 10 ml of 20%McCoy's fresh medium and transfered to a universal and centrifuged 10 min at 1000 rpm (4°C if available). The supernatant was discarded and the cells gently re-suspended in 4-5 ml (adjusted depending on the cell confluency) of *conditioned medium* and placed at 4°C (or on ice).

*4.* The suspension cells were counted using Z1-Coulter particle counter (Beckman Coulter, Fulton, California), adding the appropriate volume of *conditioned medium*, topped up with 20%McCoy's if necessary, to adjust the cells to the desired seeding concentration (normally ~1.0 x$10^6$ cell/ml) and is called the ***cell loading suspension***. Due to the length of time inherent to the execution of this present protocol, the *cell loading suspension* was stored at 4°C in a 20 ml universal.

*5.* The necessary number of 6 well plates (for 2cm length HF) or 60 mm TC dishes (for 4cm length HF) with minimum of 3 and 5 ml respectively of 10%McCoy's media was prepared and stored at 4°C. These were named ***washing medium plate/dishes*** and were used to wash out the fibers at the end after the heat sealing process.

Maximum care was taken in following standard good laboratory practice for working in the hood and spraying the external surfaces of each item coming to the hood with 70% EtOH.

*6.* The autoclaved steel tray was placed into the hood, this tray had a prior length scale (e.g. 1 cm masks to ~40-50 cm total) drawn on its centre surface. Other necessary items were also placed inside the hood such as the Fireboy burner, autoclaved sterile metal instruments box with lid (containing stainless steel forceps, scissors, smooth-jawed needle holders).

*7.* A 10 ml syringe was filled with *20%McCoy's* fresh 4°C cool medium, following this one 34 cm fiber was removed from the distilled water plastic box and placed in a wet line of medium near the drawn length scale of the tray. The HF was flushed with approx 2 ml of fresh cool medium. Immediately after a 5 ml syringe tube was filled with approx 2-3 ml of *cell loading suspension* Extra care was taken once this phase was reached to ensure that the loading was performed as quick as possible to keep the medium and cells as cool as possible.

*8.* The 5 ml syringe containing the *cell loading suspension* was attached to a 21 gauge blunt needle and the suspension gently mixed inside the syringe. The syringe needle was inserted into the end of the HF, allowing some air at the end of the tip to generate an air bubble. The *cell loading suspension* was then slowly injected into the HF, following the air bubble until the all of the fiber was loaded with cells.

*9.* The needle holder in the steel box was heated on the Fireboy burner flame for a few seconds (generally 3-5 seconds being adequate) and used to heat seal the HF by briefly clamping the end of the 34 cm HF with the needle holder, the other end attached to the needle was also sealed next. Following this the HF was heat sealed into 2 cm (or 4 cm) length sections using the scale marks on the tray, maintaining the HF as horizontal has possible and routinely covering the exterior of the fibers with 20%McCoy's fresh cool medium to prevent it from drying out.

*10.* Following this all HF 2 cm (or 4 cm) length sections were cut apart in the center of the heat seal, if necessary, the seal was re-heated to avoid any cell "leaks". The HF sections or segments were then placed in one of the *washing medium plate/dishes* with cool medium and moved well to well to wash off any loose cells contaminating the outside of the fiber.

*11.* Finally the washed HF sections were placed into a 6 well plate (for 2 cm HFs) or 60 mm TC dishes (for 4 cm HFs) filled with a vol. of 4 and 8 ml respectively of 20% or 10% FCS McCoy's fresh medium with a minimum of 1/4 of *conditioned medium* and incubated at 37°C in an humidified 5% $CO_2$ environment for the course of the different experiments.

The use of cooling and the adding of *conditioned medium* to re-suspend cells and supplement the HF initial growth culture medium seems to enhance cells survival and reduce cell stress during the loading procedure. Additional the HF encapsulated cells were growth without medium agitation during culture, with only free diffusion of the nutrients/wastes in/out the HF. Although medium agitation may have enhanced mass diffusion through the HF wall during culture, an non-agitation approach was selected because it was the more rational option to use to maintain stable culture conditions across experiments.

#### 2.2.2.4 HF cell loading protocol_B

This loading protocol represents a secondary further adaptation of the *HF cell loading protocol_A*. Overall both are extremely similar with two major differences in relation to the previous *cell loading protocol_A*. The *HF cell loading protocol_B* main differences was as follows:

First, all the 20% or 10% FCS McCoy's medium was complemented with 25 mM HEPES. Second, point *8* of the *cell loading protocol A* was replaced by the following:

*8.* Immediately prior to cell injection a micro-pipette tip (100-200 µl) firmly attached to a 1ml sterile plastic pipette was inserted into one end of the HF keeping it set in the horizontal position. A 5ml syringe with *cell loading suspension* was attached

to a micro-pipette tip (100-200 µl) with the help of a 0.5 cm length sterile tube section the suspension was gently mixed inside the syringe. The syringe tip was then tightly plugged to the end of the HF, allowing some air at the end of the tip to generate an air bubble. The *cell loading suspension* was then slowly injected in the HF, following the air bubble until the all of the fiber was loaded with cells. Although ~0.3 ml was the calculated volume of the 34 cm HF, an excess vol. of 0.4-0.5 ml was injected. The use of the above perfectly fitted tip set-up on both ends of the HF prevented any cells suspension leaking from the HF.

### 2.2.3 TC model – plating onto tissue culture substrate

Standard planar surface tissue culture (TC) samples were always prepared and run parallel to the HF culture experiments. These TC cell cultures were seeded normally after the HF loading with the same *cell loading suspension* stored at 4°C used to load the HFs described previously (in general with approx ~1.0 x$10^6$ cell/ml), with the same medium and conditions as the HF culture. The *cell loading suspension* 4°C storage time should be minimized as much as possible, a period of up to ~6h prior start seeding the TC plates/dishes may be acceptable.

The TC standard cultures were normally sub-divided into two groups:

*6 well plates or 60 mm TC dishes* were seeded with an appropriate volume of the *cell loading suspension* to obtain a low (50%CF) to "normal (70-80%CF) confluency (CF) at the time of the cell retrieval or experimental assay.

*12 well plates* were seeded with approx. 94 µl of the *cell loading suspension* in order to obtain a initial seeding value equivalent to calculated HF starting cell/area density (~2.5 x$10^4$cells/$cm^2$), given that the surface area of one well was approx the combined area of three 4 cm length HFs (3.8 $cm^2$). These samples usually presented a full confluency (≥100%CF) at the time of the cell retrieval or experimental assay.

### 2.2.4 HF model - retrieval of the cells from inside the close fiber

#### 2.2.4.1 HF retrieval protocol establishment and optimization

The present protocol was optimized specifically for this thesis. Most of the available references in the literature are related to MTT quantification, where the encapsulated cells are processed directly in the closed HF. The few papers that deal with actual adherent cell retrieval from inside the HF for other type of analysis (Bridges et al. 2006; Suggitt et al. 2004), such as flow cytometry, provided valuable insights but did not reveal to be entirely practical and efficient for the experiments in this thesis.

The evaluation of the tissue disaggregation/retrieval and processing protocol for flow cytometry is an importantly parameter to ensure standard, robust and data quality stability across culture platform studies, namely to compare the standard 2D TC versus the HF 3D encapsulation. Special for 3D cultures all the stress and even membrane damage to what cells may be subjected during retrieval may affect the biological features/viability and in this particular cell line the cyclin B1-GFP reporter signal. Trypsin retrieval protocol treatment was tested against the enzymatic free cell dissociation solution (Cat. No. C5914, Sigma), to detach the cells from the HF inner wall (Figure 2.2).

Although both treatments delivered similar number of cells on the Z1-Coulter counter (results nor showed), the non-enzymatic solution seems to enhanced PI positive cells (Figure 2.2-a) and increase cyclin B1-GFP protein leaking (Figure 2.2-b arrows). Overall the optimized HF Trypsin based cell procedure seem to produce acceptable reproducibility, low cell damage and cyclin B1-GFP profiles similar to standard high density TC Trypsin detached cells as demonstrated by the flow results. This appears to demonstrate that the following described optimized protocol was adequate for the HF–U2OS-GFP model live cell retrieval, processing and analysis by flow cytometry.

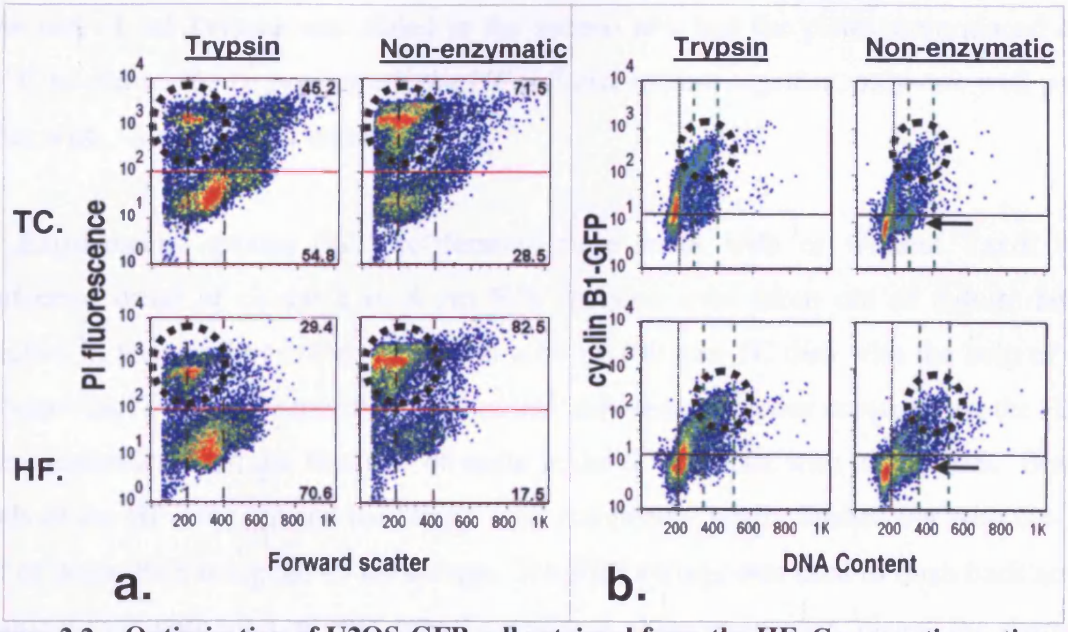


**Figure 2.2 – Optimisation of U2OS-GFP cell retrieval from the HF. Comparative action of Trypsin and non-enzymatic dissociation solution.** Retrieval protocols for (columns): **Trypsin** and **Non-enzymatic** solutions. Flow cytometry dot plots to identify: (**a**) Damaged/dead cells using propidium iodide (PI); dotted circle indicates non-viable fraction. (**b**) Cell cycle distribution using cyclin B1-GFP fluorescence density and DNA content (DRAQ5); dotted circle indicates G2/M fraction, arrows indicates accumulation of a non-reporting sub-fraction. Cell culture origin (rows): (**TC**) high confluency (≥100%CF) on standard tissue culture plate; (**HF**) All cell content retrieved from hollow fiber after 8 days culture (~90-100%CF).

### 2.2.4.2 HF cell retrieval protocol

Due to the labour intensive nature of the HF retrieval and processing methodology and especially because all *HF retrieved cell suspensions* were prepared and analysed live on the day of the experiment (except for SEM, cytospins and micro-arrays) all ancillary activities needed to be co-ordinated appropriately.

The general *HF retrieval protocol* was as follows:

*1.* The sterile metal sharps instruments box with lid (containing stainless steel forceps, scissors, 21 gauge blunt needle and scalpel) was placed on the hood, a different set of sharps was used for each of the HF groups (i.e. control and drug treatment) to avoid cross sample contamination. Two 10 ml syringes with the blunt needles were filled with warm PBS and Trypsin. Adequate numbers of 6 well plates were prepared. *1a. To separately process the two HF components* (adherent and easy flush-out loose components). Two types of solutions on each row of the 6 well were prepared, calculating one well of each group for each HF section. PBS was added to first 3 wells

row and ~1 ml Trypsin was added to the second row and the plates were placed at 37°C to warm. *1b. To process all the HF full cell content together,* only one well per fiber with ~1 ml Trypsin was necessary.

2. Experimental groups (i.e. proliferation time series with or without Taxol or Colcemid drug) of closed 2 or 4 cm HFs sections were taken out of culture and washed in warm saline buffer or PBS in a 60 or 100 mm TC dish with the help of a forceps. *2a.To process separately the two HF adherent and loose components*, the HF were transferred into the first row of wells in the 6 well plate with warm PBS. Both ends of the HF were cut and the "loose" cell component gently flushed out with 0.5-1 ml of warm PBS using the 10 ml syringe. The PBS syringe was used to flush back any residual cells with ~0.5 ml PBS into the well and at the same time "clean" the sharps for the next sample group. The HF cut sections were than transferred to the well below with Trypsin and cut into ~2-4 mm rings with scissors and help of the forceps. Similar to the PBS sharps, ~0.5 ml of the Trypsin syringe was used to flush and "clean" the sharps residual cells. *2b. To process all the HF full cell content together,* the same described above was used but all the HF ends cut, cell flush-out and rigs cut was perform in the Trypsin well.

*3.* The 6 well plate with the HFs rings were incubated for 5 min at 37°C, checked at the TC inverted microscope, mixed up-down 4-5 times with a P1000 micro-pipette slightly tilting the plate and further incubated for another 5 min at 37°C. After this incubation the cells on the wells were furthered mixed like above described and 1 ml of 20%McCoy's+25mM HEPES was added. Next the HFs rings were mixed again and transferred to a flow tube, followed by a further addition of 1 ml medium to wash-out any remaining cells from the well and pooled into the flow tube.

*4.* Each well of the 6 well plate with the individual HF cell retrieved samples (or each of the separated components) were pooled to a flow tube, topped-up with 20%McCoy's+25mM HEPES and centrifuged 5 min at 1000 rpm (4°C if available). The supernatant was vacuum aspirated /discarded and the pellet gently re-suspended in medium with appropriate vol. (0.8-1.2 ml) for flow cytometry and other measurements. Normally, a minimum vol. of 0.25ml (for ½ dilution) was used to cell counting using Z1 Coulter particle counter (Beckman Coulter) and a minimum vol of

0.5ml was used for flow. The *HF retrieved cell suspension* was normally in 20%McCoy's+25mM HEPES and kept at 4°C pending measurements.

### 2.2.5 TC model – retrieval of cells from tissue culture substrate

#### 2.2.5.1 TC retrieval protocol evaluation for single cell flow cytometry

The Trypsin retrieval protocol was evaluated in standard TC cultures at different confluency or densities (Figure 2.3).

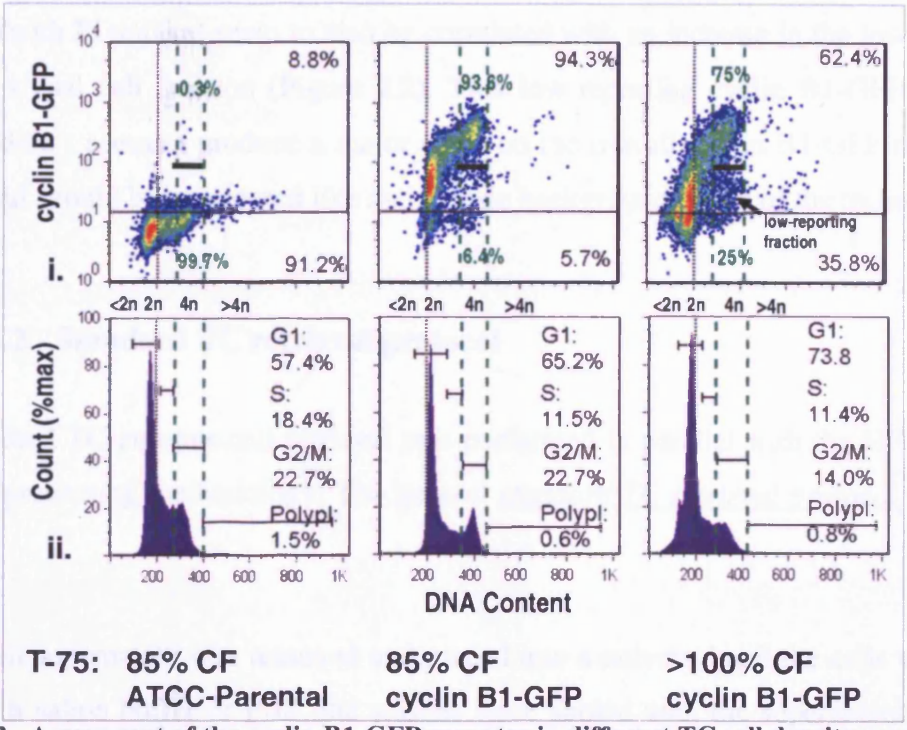


**Figure 2.3 –Assessment of the cyclin B1-GFP reporter in different TC cell density conditions.** Trypsin protocol was used for cell retrieval from a standard tissue culture flask (T-75). All the cell content was analysed by live cell flow cytometry. Assay type (depicted in rows): **(i) Reporter cyclin B1-GFP expression versus DNA content (DRAQ5).** Dot plots give detail of distribution. Full length solid horizontal black line separates the expressing from non-expressing fraction (corresponding percentages indicated in top and bottom corner). Vertical dotted green lines mark the boundaries of the G2/M fraction (corresponding percentages are indicated for high and low cyclin B1-GFP expression at ±80-90 arb. units, market by a horizontal black bar). **(ii) Cell cycle histograms to provide compartment analysis**. Manual calculated: G1,S,G2/M, >4nPolyploidy marking with corresponding percentages. Cell culture origin conditions (depicted in rows): **(85%CF ATCC-parental)** U-2 OS parental cell line (without the cyclin B1-GFP reporter) grown to 85% confluency; **(85%CF cyclin B1-GFP)** U2OS-GFP cells (containing the cyclin B1-GFP reporter) grown to 85% confluency and **(>100%CF cyclin B1-GFP)** as previous grown to above 100% confluency.

The normal 85%CF and high confluency 100%CF retrieved cells showed an increase in the frequency of low reporting cyclin B1-GFP (below ±80-90 arbitrary (arb.) units)

from 6.4% to 25% of the total G2/M population, respectively (Figure 2.3-i). Although it could not be totally excluded the possibility that some cell might have a perturbation of the transfected reporter system, the mostly likely explanation for the observed results seems to be related with the cells retrieval/processing protocol. It is conceivable that the retrieval protocol in the high confluent attach cells firmly hold together in comparing to low confluency, where most of the attach is to the plate surface, would increase the probability of more cells endured a potential membrane damage, resulting in cyclin B1-GFP protein leak out. This hypothesis is supported by the previous presented enzymatic free dissociation solution results were membrane damage (with PI uptake) seem to also be correlated with an increase in the low cyclin B1-GFP signal cell fraction (Figure 2.2). This low reporting cyclin B1-GFP G2/M fraction didn't seem to produce a major issue on the overall cyclin B1-GFP reporter profile and should be considered like an intrinsic background signal of the technique.

### 2.2.5.2 Standard TC retrieval protocol

The standard TC cultures cell retrieval was performed in parallel with the HF model retrieval/processing methodology. The general *standard TC retrieval protocol* was as follows:

*1.* The cell supernatant was removed and placed into a universal and the cells washed twice with saline buffer or PBS, the washes were pooled with the supernatant in the previous universal. The cells were then detached by standard TC Trypsin, re-suspended in medium (normally 10%McCoy's+25mM HEPES) and pooled together in the previous universal, it was always assumed that the analysed results corresponded to all the content (supernatant+ adherent cell component) of the well/dish.

2. The cell suspensions were centrifuged 5 min at 1000 rpm, the supernatant vacuum aspirated /discarded and the cells gently re-suspended in a volume of 20%McCoy's+25mM HEPES medium necessary to maintain proper cell density for flow cytometry. A minimum vol. of 0.25ml was used for cell counting using Z1

Coulter particle counter (Beckman Coulter) and a minimum vol. of 0.5ml was used for flow (all cells were kept at 4°C pending measurements).

## 2.3 Cell counting - Z1 Coulter counter

Cells were counted using Z1 Coulter particle counter with a single threshold size (Beckman Coulter, Fulton, CA, USA; see specification in Figure 2.4-c). Briefly, the threshold on the instrument was set to 8.7µm, meaning that all the particles with diameter above the threshold value were counted, 400 µl of each of the *retrieved cell suspension* sample (with or without ½ dilution) was added to 19.6 ml of the manufacturer isotonic solution in a Coulter pot and analysed on the instrument.

This instrument used the "Coulter principle", patented in 1953 by W. H. Coulter (Coulter 1953), to quantify cells or particles. An example of a typical Coulter counter general principle of operation is shown (Figure 2.4-a).

Briefly the set-up consists of one micro-channel that separate two chambers containing electrolyte solutions. Electrodes immersed in the electrolyte solution present in each chamber are used to drive an ionic current through the microchannel. When a particle flows through the microchannel, it results in the electrical resistance change of the liquid filling the micro-channel and thereby reduces the magnitude of the ionic current. The output of a Coulter counter is a matrix of current versus time (Figure 2.4-b) that contains a string of current pulses (Henriquez et al. 2004; Ito et al. 2003). The frequency of the pulses when a fixed sample volume of a particle suspension is driven through the channel and provides a count of the particle number and can be further related to the concentration. The pulse heights can be correlated with the size of the particles and limits can be set on the sizes of the particles to be counted, helping to prevent the counting of either very small or very large particles (Gibbins and Mahaut-Smith 1984; Herold and Rasooly 2009).

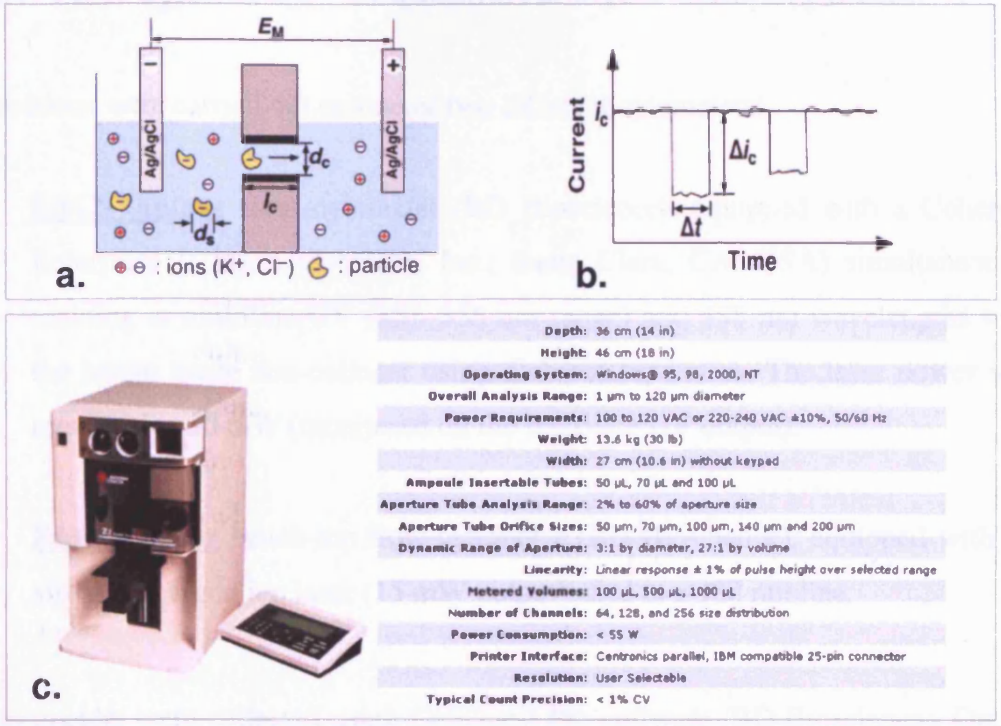


**Figure 2.4 – Coulter counter description. (a) Schematic with an example of the general electric field-driven Coulter counting principle**. The ($E_M$) electrode potential drives an (ic) ionic current in a solution containing ($K^+$) potassium and ($Cl^-$) chloride ions through a micro-channel of a given (dc) channel diameter and (lc) channel length. When a particle, with a given (ds) particle diameter, flow flows through the channel it changes the electrical conductance of the circuit measured as a current pulse ((adapted from (Henriquez et al. 2004; Ito et al. 2003)). **(b) Example of the Coulter counter data.** This consists of a series of (ic) ionic current pulses related with the presence of particles within the micro-channel. The (Δic) pulse height is proportional to the volume of electrolyte solution displaced by the particle and is related with particle size. The (ΔDt) pulse width corresponds to the particle transit time and can be used to determine the charge carried by the particle. The frequency of the current pulses when a fixed amount of sample volume is passes through the channel, provides a count of the particle number and can be related to the particle concentration (adapted from (Henriquez et al. 2004)). **(c) Z1 Coulter counter instrument photo with specifications table** (https://www.beckmancoulter.com/eCatalog/CatalogItemDetails.do?productId=13045 [2010]).

## 2.4 Flow cytometry

All flow cytometry acquisition of labelled or un-labelled cells were carried out with live cells Flow acquisition was performed immediately or as soon as possible following cell retrieval/processing protocols. Some measurements were performed on the FACSVantage system (BD Bioscience) with the supervision of Mrs Marie Wiltshire or Mrs Janet Fisher (School of Medicine, Cardiff University). Generally, most of the flow acquisition were performed on the bench-top FACSCalibur (BD Bioscience). The cytometers parameters and analysis procedures are presented next.

### 2.4.1 Flow cytometers – acquisition/analysis summary sheet

Acquisitions were carried out on one of two different cytometers:

- **FACSVantage** flow cytometer (BD Bioscience), equipped with a Coherent Enterprise II laser (Coherent, Inc., Santa Clara, CA, USA) simultaneously emitting at multiline UV (351–355 nm range) and 488 nm wavelengths with the beams made non-colinear using dichroic separators. The laser power was regulated at 30 mW (monitored on the multiline UV output).

- **FACSCalibur** bench-top flow cytometer (BD Bioscience), equipped with an air-cooled argon ion laser (15 mW output) used to a 488 nm line.

All parameters were collected using CellQuest Pro software (BD Bioscience). Optics used in both systems for the different probes are listed in Table 2.4, unless stated otherwise, all data was collected for 10,000 events. All flow data analysis was carried out using FlowJo v.7.5.5 (Tree Star, San Carlos, CA, USA) in Windows XP platform.

**Table 2.4: Flow cytometry set-up and optics used for acquisition.**

| | FACVantage | | FACSCalibur | |
|---|---|---|---|---|
| *Probe* | *Excitation (nm)* | *Parameter and emission filter (nm)* | *Excitation (nm)* | *Parameter and emission filter (nm)* |
| **Forward Scatter** | 488 | FSC | 488 | FSC, 488/10 |
| **Side Scatter** | | SSC | | SSC, 488/10 |
| **cyclin B1-GFP** | | FL1-H, 530/30 | | FL1-H, 530/30 |
| **PI** | | FL2-H, 585/42 | | FL2-H, 585/42 |
| **DRAQ5** | | FL3-A, 695 LP | | FL3-A, 650 LP |
| **QD705** | | FL3-H, 695 LP | | FL3-H, 650 LP |

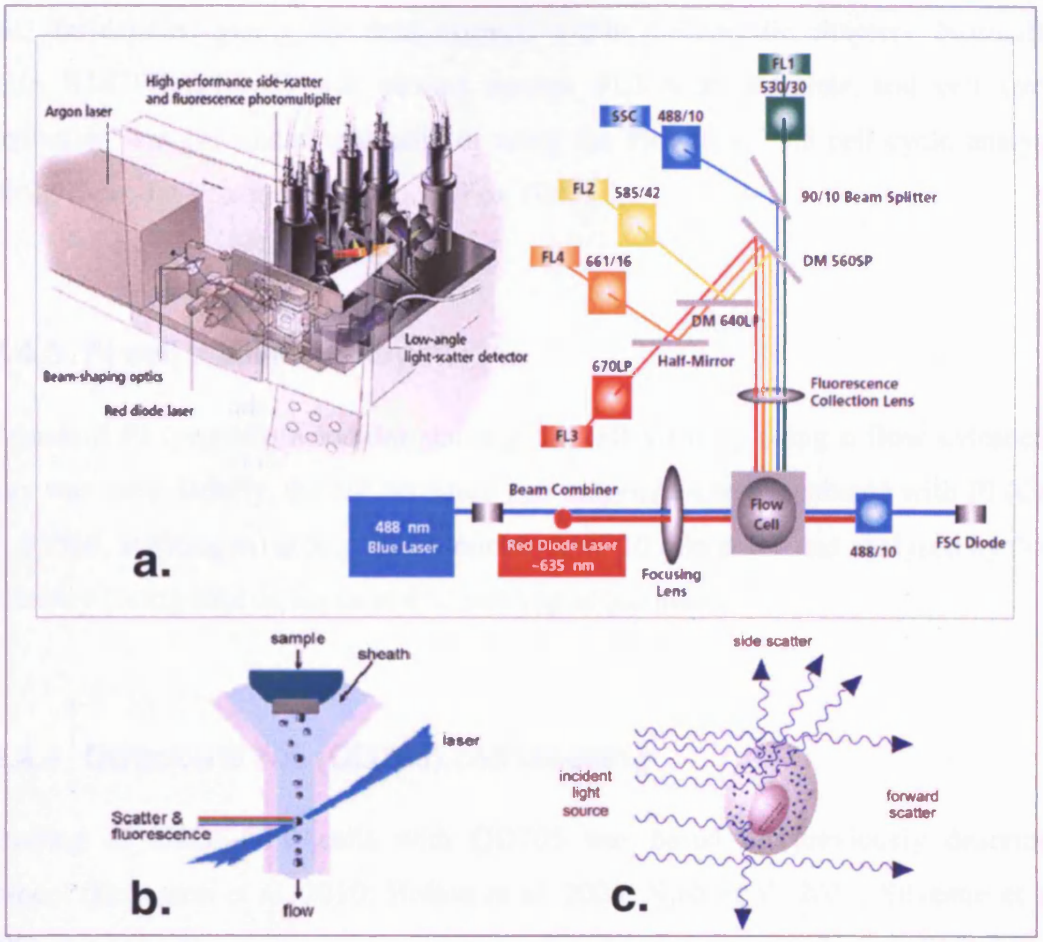


**Figure 2.5 – FACSCalibur instrument and flow cytometry basic principles.** (**a**) Inside the FACSCalibur cytometer with the schematic of optical set-up and specification (BD Bioscience) (adapted from (http://www.bdbiosciences.com/instruments/facscalibur/features/index.jsp [2010])); (**b**) basic configuration of a flow chamber (adapted from (Ormerod 2008)); (**c**) side and forward light scattering properties of a cell (adapted from (http://www.bd.com/videos/bdb/training_ITF/home.html [2010])).

### 2.4.2 Cell cycle (or DNA content versus cyclin B1-GFP)

Cell cycle or DNA measurements were adapted from preparation described previously (Smith et al. 2000; Smith et al. 2007b).

Briefly, cells after being retrieved and processed from the TC or HF models were transferred to a flow tube (minimum vol. 0.5 ml), 20μM DRAQ5 was added, gently mixed and held at RT at least 10 min before flow acquisition.

When applicable DNA content channels FL3-W (width) versus FL3-A (area) gating was used to eliminate duplets, death cells and debris, namely on DRAQ5 labelled

cells, the detailed gating are demonstrated within the specific chapters. Normally, cyclin B1-GFP (FL1-H) was plotted against FL3-A in dot-plots and cell cycle distribution was calculated manually or using the FlowJo v.7.5.5 cell cycle analysis built-in Dean-Jet-Fox model function (Fox 1980).

### 2.4.3 PI cell viability assay

A standard PI (propidium iodide) staining for cell viability using a flow cytometry assay was used. Briefly, the *HF retrieved cell suspension* was incubated with PI (Cat. No. P3566, InVitrogen) at 5µg/ml for minimum of 10 min at RT and analysed by flow cytometry (being kept on ice or at 4°C pending acquisition).

### 2.4.4 Qtracker® 705 (QD705) cell labelling

Labelling of U2OS-GFP cells with QD705 was based on previously described protocol (Errington et al. 2010; Holton et al. 2009; Njoh et al. 2007; Silvestre et al. 2009).

Adherent cells on standard culture plastics (or coverglass chambers for microscopy) were labelled with a 4nM concentration QD705 for 60 min using the Qtracker® 705 Cell Labelling Kit (Cat. No. Q25061MP, InVitrogen Life Sciences), following the manufacture guidelines. The volume of labelling solution used was selected to minimize the waste of QD705 whilst maintaining enough volume to cover the cells with minimal stress. Normally minimum volumes were as follows: T-75=4ml, T-25 =1ml, 6 well plate=0.75ml, 12 well plate and 2 well Nunc 1.5 coverglass chambers (Cat. No. 155379, Nunc/Lab-TekII)= 0.5ml. Briefly (e.g. for labelling one well of 6 well plate), 2µl of each of Qtracker® Reagent A and B were incubate for 5 minutes at RT in an eppendorf, 1 ml of fresh medium added, the mixture was vortexed for 30sec, original culture medium was removed, Qtracker® solution added to the cells and were incubated at 37°C for 60 min. After the incubation, the labelling solution was removed and the cells washed three times with medium, labelled QD705 cells were then cultured in full medium.

### 2.4.5 Flow acquisition of QD705 labelled cells

Labelled QD705 U2OS-GFP cells flow acquisition protocol was related to previously described (Brown et al. 2010a; Errington et al. 2010). Briefly, labelled cells after being retrieved and processed from the TC or HF models were transferred to a flow tube (minimum volume 0.5 ml) with fresh 10%McCoy's+25mM HEPES and as soon as possible (kept at 4°C if necessary) flow acquired. The initial flow analysis consisted of a forward (FSC) and side (SSC) scatter gating in order to eliminate most of the low fraction of small debris and death cell, further specific methodologies are described in Chapter 5.

## 2.5 DNA microarray (high-density oligonucleotide microarray)

A microarray analysis of HF–U2OS-GFP cell model after 5 days culture was performed and incorporated on a larger group array experiment. This included a control culture (CON) with cells growing in three standard 100 mm TC dishes and HF sets that were processed independently, within the same time frame. The chips used were high-density oligonucleotide microarray, also known as GeneChip®, made by Affymetrix Inc (Santa Clara, CA).

### 2.5.1 HF and control samples

*CON* (standard planar surface TC dish)

Four 100 mm TC treated polystyrene dishes (BD Falcon™, Cat.N.353003) (each dish growth surface area= 58.1 $cm^2$/dish), were seeded with 1.0 x $10^6$ U2OS-GFP cells/dish and incubated with 10% McCoy's under standard culture conditions for 3 days (72h), reaching a confluency of ~75% at day 3.

*HF model cell culture*

Three full length (34 cm) HFs were seeded with 1.2 x$10^6$ U2OS-GFP cell/ml (estimated ~2.5x$10^4$cell/$cm^2$) using the *HF cell loading protocol B* being heat sealed/cut into 4 cm length sections (approx. available adherent cell length of 3.6 cm,

area 1.13 $cm^2$). These 4 cm HFs were distributed into 6 TC 60mm dishes (two for each 34 cm HF) independent batches, with around 4 HF sections/dish in 6 ml 10%Mccoy's, in order to maximise diffusion and avoid any extra-fiber medium nutrient shortage effect They were then incubated for 5 days (120h) at 37°C under standard culture conditions.

### 2.5.2 Sample processing and TRIZOL treatment

The 3 TC CON cell dishes (t=3days), were washed with warm PBS, 1.5 ml TRIZOL (InVitrogen) reagent added per dish. After 10 min incubation cells were scraped from the dish surface using a sterile cell scarper and transferred as x2 750 µl aliquots to x2 Eppendorf CryoTube per dish and stored at -80C.

The HF culture (t=5days), were processed as previously described in point number 2 of the *HF retrieval protocol* (section 2.2.4) but without Trypsin detaching and discarding the "loose" HF cell component. Briefly, closed HF were washed in warm PBS, both ends cut and the "loose" cell component gently flushed with fresh media and discarded, the HFs were then further cut into ~2cm sections. All the HF sections corresponding to each batch were transferred to 3 well with 1.5 ml of TRIZOL in a 6 well plate and incubated for 15 min, shaking slightly. A sterile syringe with 1ml TRIZOL and a bended needle in an "L" shape was used to scrap the inside of the HF with the help of forceps. After, scraping the HF sections ~0.3 ml TRIZOL was flushed-out to empty any cells inside the needle into the well. The suspension was mixed well with P1000 tip, transferred like the CON samples as x2 750 µl aliquots to x2 Eppendorf cryotubes per HF batch and stored at -80°C.

### 2.5.3 Flow cytometry and cell counts

The remaining CON TC dish and 3 samples from each HF experimental batch of the cells submitted for microarray analysis were Z1-Coulter counted and DRAQ5 stained for FACS Vantage (Becton Dickinson) cell cycle and cyclin B1-GFP analysis by flow.

### 2.5.4 RNA extraction

Stored at -80°C cryotubes, TRIZOL treated samples were processed by Marie Wiltshire using a standard protocol for RNA extraction/isolation provided by CBS (Central Biotechnology Services) (http://medicine.cf.ac.uk/research/central-biotechnology-services/ [2008], School of Medicine, Cardiff). The RNA was then given to the CBS Cardiff Affymetrix GeneChip expression profiling service for RNA quality assessment and processing to run the chip array.

### 2.5.5 DNA microarray preparation and chip data acquisition

The microarray RNA processing sets and chip data acquisition were performed by the Affymetrix GeneChip expression profiling service CBS Cardiff, a summary and generic schematic is presented in Figure 2.6 . The used array chip was the Human genome_U133A_2.0 (HG_U133A_2.0), this is a single array with >22,000 probe sets representing 14,500 well-characterized human genes. The resulting gene data bioinformatics analysis, namely quality assessment, pre-processing, normalization, the differential expression and gene enrichment analysis is described within the specific methodology of Chapter 4.

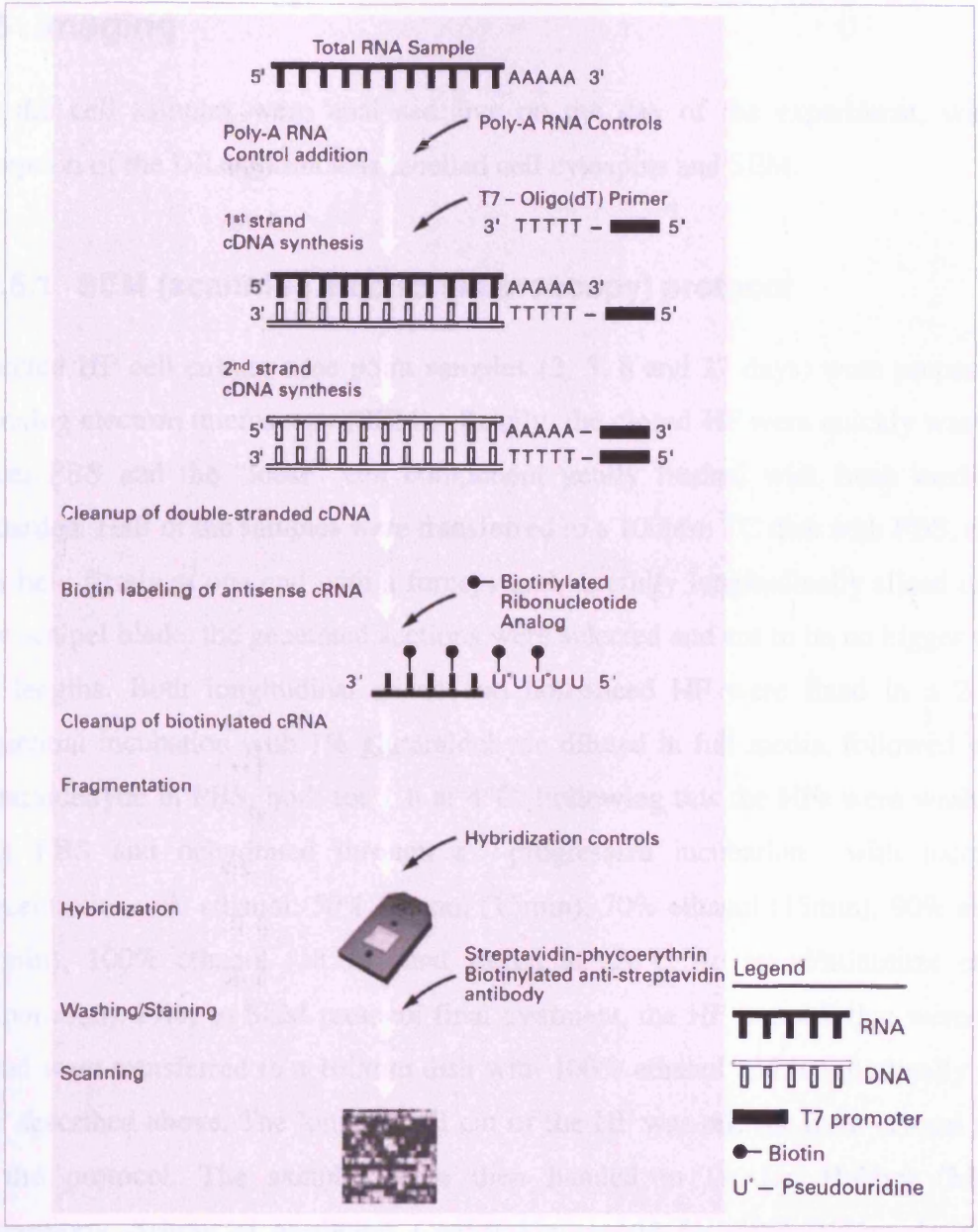


**Figure 2.6 – Schematic protocol chart of RNA samples preparation and processing for Affymetrix gene expression analysis.** Briefly, total RNA or mRNA is first reverse transcribed using a T7-Oligo(dT) Promoter Primer in the first-strand cDNA synthesis reaction. Following RNase H-mediated second-strand cDNA synthesis, the double-stranded cDNA is purified and serves as a template in the subsequent *in vitro* transcription reaction. This reaction is carried out in the presence of T7 RNA Polymerase and a biotinylated nucleotide analog/ribonucleotide mix for complementary RNA (cRNA) amplification and biotin labelling. The biotinylated cRNA targets are then cleaned up, fragmented, and hybridized to GeneChip expression arrays. After hybridization the arrays are washed, a crucial step, to remove unbound nucleic acid and labelled with fluorescent streptavidin–phycoerythrin conjugate (SAPE), which binds to the biotins incorporated during target amplification, with additional signal amplification process where biotinylated anti-streptavidin antibodies are bound to the initial SAPE molecules and then labelled with a second SAPE addition. Finally the array is scanned with the generations of a .CEL chip image which contained the raw hybridization signal intensities for each probe on the array (adapted from GeneChip® Expression Analysis Technical Manual: (http://media.affymetrix.com/support/downloads/manuals/expression_analysis_technical_manual.pdf) [2009]).

## 2.6 Imaging

All the cell samples were analysed live on the day of the experiment, with the exception of the DRAQ5 nucleus labelled cell cytospins and SEM.

### 2.6.1 SEM (scanning electron microscopy) protocol

Selected HF cell culture time point samples (2, 5, 8 and 27 days) were prepared for scanning electron microscopy (SEM). Briefly, the closed HF were quickly washed in warm PBS and the "loose" cell component gently flushed with fresh media and discarded. Half of the samples were transferred to a 100mm TC dish with PBS, the HF was held firmly at one end with a forceps and carefully longitudinally sliced using a new scalpel blade, the generated sections were selected and cut to be no bigger than 1 cm lengths. Both longitudinal sliced and non-sliced HF were fixed in a 2 stage sequential incubation with 1% glutaraldehyde diluted in full media, followed by 1% glutaraldehyde in PBS, both for 1 h at 4°C. Following this the HFs were washed x2 with PBS and dehydrated through a progressive incubation with increasing concentrations of ethanol: 50% ethanol (15min); 70% ethanol (15min); 90% ethanol (15min); 100% ethanol (1h x2) and stored at -20°C (to avoid/minimize ethanol evaporation). Prior to SEM protocol final treatment, the HF samples that weren't yet sliced were transferred to a 100mm dish with 100% ethanol and longitudinally sliced like described above. The longitudinal cut of the HF was one the most critical stages of the protocol. The samples were then handed to Dr Jan Hobbot (Medical Microscopy, School of Medicine, Cardiff University) for critical point drying and sputter gold coating service.

The samples mounted in SEM cylindrical sample steps were imaged on a Raith-50 EBL electron microscope (Raith GmbH, Germany) located in the clean room of the School of Physics and Astronomy, Cardiff University. The inability to adjust the tilt on the stage chamber to enhance the visualization of the HF lateral inner walls didn't presented any major issues to the acquisition. The acceleration voltage was set to 20kV with a spot size of 3.2. SEM images with progressive zooming were acquired to investigate the overall cell layer organization and any specify cell morphologic details.

### 2.6.2 Nikon upright confocal microscope summary sheet

This microscope imaging platform comprised of a Nikon Eclipse E600FN upright microscope with Bio-Rad Radiance 2100 Rainbow confocal system switchable to epi-fluorescence acquisition mode with brightfield (Figure 2.7). U2OS-GFP live cells labelled with QD705 were prepared using the set-up described in Supplementary Information 5.6-2, and imaged with the 40x 0.65NA objective, with the 488 nm laser and appropriate optics set-up (Figure 2.7-a).

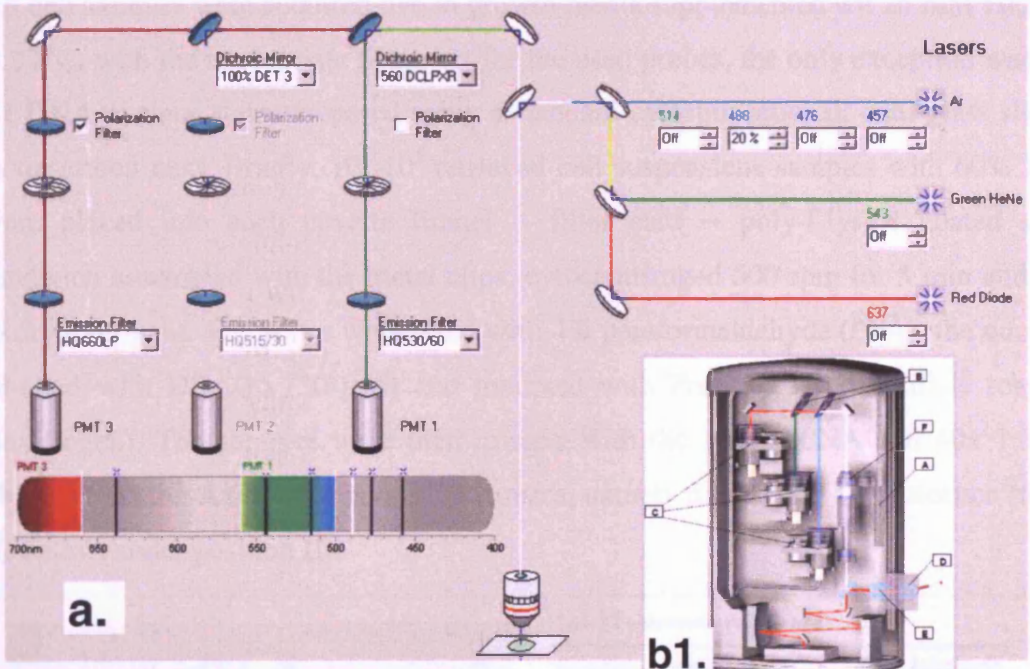


Table d – Nikon upright confocal lens used and respective parameters.

| Objective | Name | NA | Nikon code |
|---|---|---|---|
| 5x air | LU Plan | 0.15 | - |
| 40x air* | Plan Fluor ELWD | 0.60 | MRH48420 |
| 40x air | Achromat | 0.65 | MRP00402 |

ELWD = Extra Long Working Distance Lenses, *coverslip correction collar
(extra info: http://www.nikoninstruments.eu/ [2010].

d.

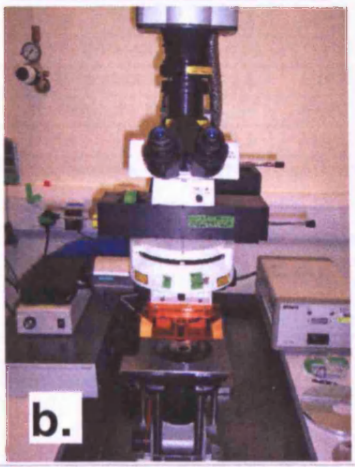


**Figure 2.7 – Nikon upright confocal laser scanning microscope system. (a)** Optical set-up for acquisition of eGFP (Em. Filter HQ530/60) and QD705 (Em. Filter HQ660LP) both excited at 488nm. **(b)** Picture of the Nikon Eclipse E600FN fixed stage upright with the **(b1)** Bio-Rad Radiance 2100 confocal scanning (again schematic of optical path). **(d)** Table of objective lenses used for imaging.

### 2.6.3 Axiovert inverted fluorescent microscope summary sheet

This microscope acquisition platform consisted of a Zeiss Axiovert S100TV inverted epi-fluorescent microscope, fitted with clear incubator case for live cell imaging and equipped in the bottom port with a Hamamatsu C4742-95 mono CCD camera. The system was later upgraded, being fitted in the available top port with the CRi Nuance FLEX multispectral liquid crystal tunable filter (LCTF) camera (Cambridge Research & Instrumentation, USA).

All cell samples were acquired live in growth media supplemented wit 25 mM HEPES at 37°C, with the appropriate filters set for the used probes, the only exception was the fix DNA nucleus stains prepared using a standard cytospin protocol onto glass slides, as described next. Briefly, $10^4$-$10^5$ retrieved cell suspensions samples with 60% FCS were placed into each cuvette funnel -- filter card -- poly-l-lysine coated slide sandwich assembled with the metal clips, cytocentrifuged 500 rpm for 5 min and left to dry overnight. The slides were fixed with 4% paraformaldehyde (PFA), the nucleus labelled with DRAQ5 (20 μM) and mounted with ProLong Gold antifade reagent (Invitrogen). The samples were then imaged with the 10x 0.50NA and 40x 1.3NA objective on the Axiovert mono CCD camera, namely for nucleus fluorescence (table b2 below, slider position II).

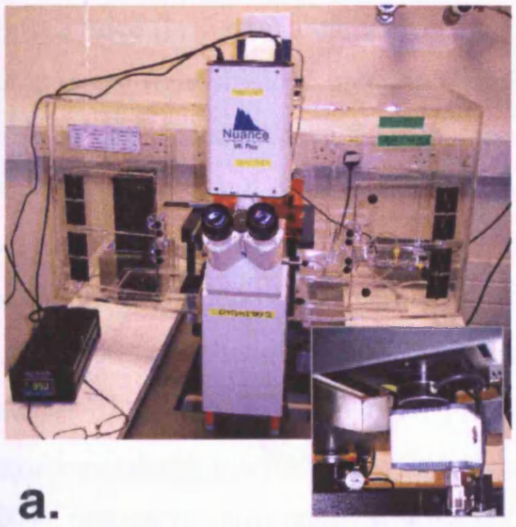


Table b1 – Microscope objective lens used.

| Objective | Name | NA | Zeiss code |
|---|---|---|---|
| 5x air | Plan-NeoFluar | 0.15 | 440320 |
| 10x air | Fluar | 0.5 | 440135 |
| 10x air | Plan-Apochromat (Ph1) | 0.45 | 1113-123 |
| 20x air | Plan-Apochromat (Ph2) | 0.6 | 440640 |
| 40x air* | Plan-Apochromat (Ph3) | 0.95 | 420661 |
| 40x oil | Fluar | 1.3 | 440256 |

(extra info: Zeiss - http://www.meditec.zeiss.de/ [2010]. *coverslip correction collar

Table b2 – Microscope filters set used.

| Filter Slider | position I (i.e. EGFP) | position II (i.e. DRAQ5) | position III (i.e. QD705) | position IV (i.e. spectral) |
|---|---|---|---|---|
| Exciter | 480/30 | 620/60 | 470/40x | 460/50x |
| Dichroic | 505dclp | 660lp | 500dcxr | 505dcxr |
| Emitter | 535/40 | 700/75 | 705/40m | HQ510lp |

(extra info: Chroma - http://www.chroma.com/ [2010].

b.

**Figure 2.8 – Axiovert inverted fluorescent microscope.** **(a)** Picture of the Zeiss Axiovert S100TV inverted fluorescent microscope with peripherals for live cell imaging and timelapse. The trinocular holds the CRi Nuance FLEX multispectral imaging head. Botton insert shows the location of the Hamamatsu C4742-95 mono CCD camera attached to the Keller port; **(b)** Tables describe the specification of the (b1) objective lenses and (b2) filters sets typically used for imaging in the current study.

### 2.6.4 Macro-imaging IVIS200 *in vivo* system - bioluminescence and fluorescence acquisition

The small animal live macro-imaging system [In Vivo Imaging System (IVIS) model 200 (Xenogen, now Caliper Life Sciences, Hopkinton, MA, USA)] allows non-invasive visualization and tracking of bioluminescence and fluorescence signal *in vitro* and *in vivo and* in real-time. The macro-imaging system was used in conjunction with the preliminary development of the biophotonic prototype described in *Chapter 6.* Acquisition and analysis was performed using the instrument Living Image® Software Version 2.50 (Xenogen – Living Image 2.50 Manual, 2004 (http://www.umgcc.org/research/xenogen_sw_manual.pdf [2008])). This instrument (Figure 2.9) comprises a highly sensitive charged coupled device (CCD) camera cryogenically cooled to -105°C to minimize system noise, capable of detecting very low levels of light, this is especially critical for bioluminescence. The instrument includes 12-position emission filter wheel and a 12-position excitation wheel (range of wavelengths from 400–950m) and a variety of bandpass optical filters with centred wavelengths in the range of 560 nm to 660 nm, all of these being tailored for specific fluorophore visualization (e.g., GFP, DsRed, Cy5.5, and ICG) and bioluminescence (luciferase activity). The IVIS 200 offers 5 magnifications with a field of view (FOV) of 26cm, 19.5cm, 13cm, 6.5cm, and 3.9cm. It has the capacity to monitor and image up to 5 mice (or 3 rats) simultaneously, and in addition imaging cell culture plates. It comprises a light-shielded imaging chamber with gas anaesthesia into which the host animals are placed. Above this chamber sits a macrolens (F/1) providing a good working distance and optimal light collection (~NA 0.5). This system is capable of detecting and quantifying the light emission from single cells *in vitro* and presents a maximum resolution of 60 microns (μm). The IVIS200 software allows for absolute quantification in photons/second/cm$^2$/steradian (p/sec/cm$^2$/sr) of both bioluminescence and fluorescence signal (Caliper Life Sciences, IVIS200 (http://www.caliperls.com/products/ivis-imaging-system-200-series.htm [2008]); Hardware manual, 2004 (http://www.umgcc.org/research/xenogen_hw_manual.pdf [2008]); Small Animal Imaging, Cornell University (http://www.brc.cornell.edu/brcinfo/?p=mifsai [2010]).

A schematic of optical-set up for both bioluminescence and fluorescence acquisition with corresponding advantages and disadvantage of each mode are showed in Figure

1.7. Briefly for bioluminescence acquisition the sample (or animal) is place in the chamber under anaesthesia, the 37°C heated stage moves up/down depending of the selected FOV to focus on the sample. A first image is acquired representing a short exposure of the sample illuminated by LED lights located in the top of the imaging chamber and displayed as a gray scale (black and white) "photographic" image to evaluate sample status and position. The second image is a longer exposure of the sample taken in darkness to record low level luciferase light emissions from inside the sample. For fluorescence acquisition the initial procedure is the same to acquire the photographic image. Then a 150 Watt quartz tungsten halogen lamp provides light for fluorescence excitation, the lamp output is delivered to the excitation filter wheel assembly through a fiber-optic bundle that splits into four separate bundles that deliver filtered light to four reflectors located on the ceiling of the IVIS chamber, providing a diffuse and relatively uniform excitation illumination of the 'sample'. The emission is filtered by a 60 mm diameter high quality filter selected thought the wheel assembly positioned directed before the camera. The excitation light may also causes the tissue to autofluoresce that may be detected by the camera interfering with the fluorophore actually signal readings (Xenogen- Living Image 2.50 Manual, 2004 (http://www.umgcc.org/research/xenogen_sw_manual.pdf [2008])).

The weak bioluminescence emitted light intensity, in relation to fluorescence, is more prone to absorbance and high scattering effects by the animal tissues, this distortion increases deeper in the tissue. This is aggravated by the fact that the firefly luciferin wavelength is limited to the green-yellow range (max. em. 562nm), that highly interacts with the tissues. The major advantage of bioluminescence in contrast to fluorescence, is that there is no inherent auto-bioluminescent background, making this technique highly sensitive and less prone to background fluctuations. But bioluminescence presents some additional limitations of its own, such the dependence of the generated imaging signal on the availability of ATP, $O_2$ and the luciferin substrate, which has to be administered exogenously (Choy et al. 2003; Contag and Bachmann 2002; Weissleder and Ntziachristos 2003). Also, although it is generally assumed that animals are characterized for not having natural background light emission, animal diet can be a source of background auto-luminescence that could interfere with specific bioluminescence acquisition (Zhang et al. 2008a).

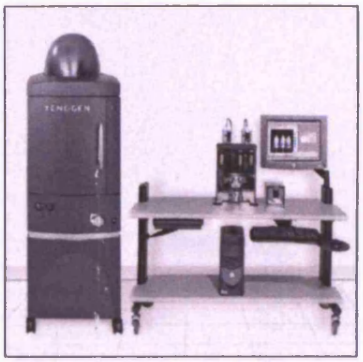

a.

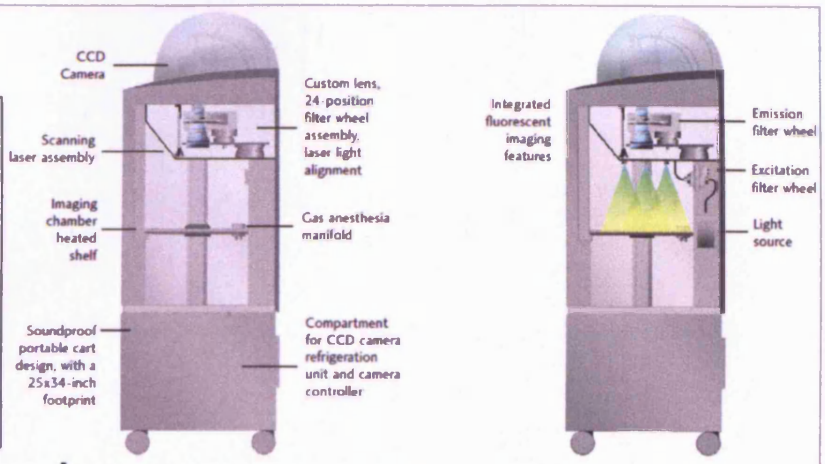


b.

IVIS® Imaging System 200 Series incorporates Xenogen standards for effective and humane animal handling, including an anesthesia manifold and heated animal shelf (up to 40° C) to help stabilize animal physiology and minimize testing variables.

**Standard filter sets:**

Fluorescence Filters

| Set | Name | Excitation (nm) | Emission (nm) | Background (nm) |
|---|---|---|---|---|
| 1 | GFP | 445–490 | 515–575 | 410–440 |
| 2 | DsRed | 500–550 | 575–650 | 460–490 |
| 3 | Cy5.5 | 615–665 | 695–770 | 580–610 |
| 4 | ICG | 710–760 | 810–875 | 665–695 |

Spectral Imaging Filters

| | | |
|---|---|---|
| 5 | 560 nm | 550–570 |
| 6 | 580 nm | 570–590 |
| 7 | 600 nm | 590–610 |
| 8 | 620 nm | 610–630 |
| 9 | 640 nm | 630–650 |
| 10 | 660 nm | 650–670 |

c.

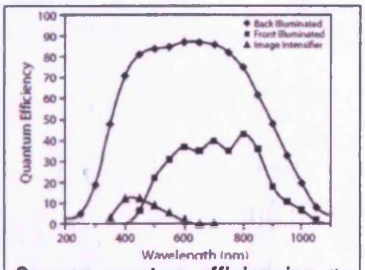


**Sensor quantum efficiencies,** the IVIS 200 uses a back illuminated CCD (top curve-diamonds).

e.

| Imaging Components | Specifications |
|---|---|
| Sensor | Back-thinned, back-illuminated Grade 1 CCD |
| CCD Operating Temperature | Nominal –105° C |
| Imaging Pixels | 2048 x 2048 |
| Minimum Resolution | 60 µm (at f/1) |
| Pixel Size | >13.5 µm square |
| CCD Size | 26 x 26 mm |
| Quantum Efficiency | >85% 500–700 nm; >50% 350-950 nm |
| Read Noise | <5 electrons RMS |
| Dark Current | <100 electrons/s/cm$^2$ |
| Minimum Detectable Radiance | <70 photons/s/sr/cm$^2$ |
| Lens | f/1–f/8, 1.5x, 2.5x, 5x, 7.5x, 10x magnifications |
| Fields of View | 3.9 x 3.9 cm to 26 x 26 cm (3.9, 6.5, 13, 19.5, 26 cm) |
| Scanning Laser | <1 mW power at 532 nm |
| Stage temperature | Ambient to 40° C |
| Imaging Chamber Dimensions | 51 cm x 51 cm x 66 cm (D x W x H) |
| Weight | <275 kg/600 lb |
| Noise | 55 dB < 500Hz |
| Power Requirements | 20 Amps for 120VAC or 10 Amps for 230VAC |

| Fluorescence Imaging Components | Specifications |
|---|---|
| Excitation Filter | 25 mm diameter 12-position (11-filter capacity) |
| Emission Filter | 60 mm diameter 24-position (22-filter capacity) |
| Background (autofluorescence and leakage) | <3 part in $10^6$ typical |
| Lamp | 150 W Quartz halogen 3250° Kelvin |
| Fluorescence Field of View | 6.5, 13, 19.5, 26 cm (fluorescence not available at 3.9 cm field of view) |

System Features: Heated stage up to 40° C; Gas anesthesia inlet and outlet ports; scanning laser for alignment and surface topography; High-performance acquisition computer; 20-inch, high-resolution flat screen monitor; Software-controlled focus, f-stop, field of view; Excitation/Emission filter wheel; Xenogen's Living Image® software provides image acquisition controls and image analysis.

d.

**Figure 2.9 – The In Vivo Imaging System (IVIS) model 200 instrument details** (Xenogen, now Caliper Life Sciences, Hopkinton, MA, USA). This system performs real-time quantification of bioluminescent/fluorescent markers *in vitro* and in live animals. **(a)** photo of the IVS200 and workstation desk; **(b)** Schematic of the instrument set-up and internal components (dimensions: 77x65x211cm (WxDxH); **(c)** table with imaging components specifications **(d)** table with standard available filters sets; **(e)** camera sensor efficiency response with wavelength; (adapted from: IVIS 200 Series (http://www.caliperls.com/products/ivis-imaging-system-200-series.htm [2008]); Summary Brochure, 2004 (http://www.umgcc.org/research/xenogen_intro.pdf [2007]); Hardware manual, 2004 http://www.umgcc.org/research/xenogen_hw_manual.pdf [2008]); Xenogen-Living Image 2.50 Manual, 2004 (http://www.umgcc.org/research/xenogen_sw_manual.pdf [2008]) ).

# CHAPTER 3

# HOLLOW FIBER *IN VITRO* U-2 OS CELL MODEL DEVELOPMENT/CHARACTERIZATION

Parts of this Chapter have been included or are related to the following publications:

**Silvestre**, O. F.; Holton, M. D.; Summers, H. D.; Smith, P. J.; Errington, R. J. In *Hollow fiber: a biophotonic implant for live cells*, Imaging, Manipulation, and Analysis of Biomolecules, Cells, and Tissues VII, San Jose, CA, USA, 2009; SPIE: San Jose, CA, USA, **2009**; pp 71820V-11.

**Smith**, P. J.; Marquez, N.; Wiltshire, M.; Chappell, S.; Njoh, K.; Campbell, L.; Khan, I. A.; Silvestre, O.; Errington, R. J., Mitotic bypass via an occult cell cycle phase following DNA topoisomerase II inhibition in p53 functional human tumor cells. *Cell Cycle* **2007b**, 6, (16), 2071-2081.

Print-out available on Appendix I

# 3 HOLLOW FIBER *IN VITRO* U-2 OS CELL MODEL DEVELOPMENT/CHARACTERIZATION ..... 81

# 3 HOLLOW FIBER *IN VITRO* U-2 OS CELL MODEL DEVELOPMENT/CHARACTERIZATION

## 3.1 Introduction

### 3.1.1 Hollow fiber characterization strategy

The strategy for the study and characterization of the HF model has been prompted by the approach followed by previous authors investigating other cell types within the hollow fiber (Bridges et al. 2006; Casciari et al. 1994; Hassan et al. 2001; Sadar et al. 2002; Suggitt et al. 2004; Temmink et al. 2007; Yamazoe and Iwata 2006). In the present investigation the U-2 OS cyclin B1-GFP cells growing in the hollow fiber (HF–U2OS-GFP model) was characterized at different time points both short term (2-8 days) and also long term (27 days) culture and characterised for: cell morphology and distribution by imaging (optical and SEM), cell size, cell viability and cell cycle distribution using flow cytometry. At all times the cells grown in the HF environment were evaluated against a standard tissue culture (TC) counterpart. The primary investigation was to assess the cell phenotype in terms of general morphology and proliferation features in both culture conditions. Importantly, to further characterise the HF–U2OS-GFP model, the cells were grown under control and drug perturbation conditions. Taxol or paclitaxel a highly cytotoxic anti-tumour drug targets microtubules; enhancing polymerization and causing cells to arrest in mitosis (Jordan et al. 1996; Schiff et al. 1979; Torres and Horwitz 1998); it represents a successful family of clinical agents against a number of cancers (Gascoigne and Taylor 2009). In this chapter, Taxol drug treatment, complemented by Colcemid validation assays, provides a standard drug model where cells change shape, change growth kinetics and cell cycle profile parameters which are easily evaluated in both the TC and HF conditions.

It is appropriate to note that the cells retrieved from the HF cultures were processed to account for both the "loose" component (HF_los) defined as the cell population which can be readily flushed out upon opening of the fiber; as well as the "adherent" component (HF_adh) which required trypsinization (see Chapter 2 for details). For analysis these components of each individual HF were treated either separately and

labelled as "HF_los" "HF_adh" respectively or all the HF content combined and labelled as "HF_all". Note that through-out the thesis, except when stated otherwise, the results represent the combined HF components content.

### 3.1.2 "in-fiber" cell growth assessment

The MTT assay is commonly used to test the effects of drug compounds on cell population growth and viability (Denizot and Lang 1986; Hamid et al. 2004; Mosmann 1983; Mueller et al. 2004) including previous HF investigations (Decker et al. 2004; Hollingshead et al. 1995a; Johnson et al. 2001; Morrell et al. 2006; Suggitt et al. 2004; Temmink et al. 2007). The MTT assay is essentially an indication of cell metabolic activity and therefore this is subject to limitations. There are several reports of agents that increase MTT reduction to formazan without increasing or being related to cell viability, this includes drug efflux inhibitors, genistein, ursolic acid, resveratrol and interferons (Bernhard et al. 2003; ElSaady et al. 1996; Pagliacci et al. 1993; Vellonen et al. 2004). Additionally, recent studies state that the MTT assay may be an under-estimate of cell number in high cell culture densities and because cells treated with drugs are usually compared with the results from untreated cells, it is likely that drug action may be over-estimated (Liu and Dalgleish 2009). Despite these reports, the MTT or tetrazolium based assays continue to be used for screening cell lines for the effectiveness of various drugs/compounds, many times without corroborating results using complementary assays (Sims and Plattner 2009).In addition the MTT assay normally requires the use of all the HF sample and the solubilisation of the formazan product inside the cells, making unviable other assays from the same HF. The MTT assay is not appropriate for single cell analysis. Instead the cell population growth was evaluated by removing the cells from the HF or the TC planar plastic substrate and undertaking a cell count (Z1 Coulter Counter (see section 2.3); a technique also previously applied to the HF (Casciari et al. 1994). In brief, this option allowed for multiple measurements of the cells retrieved from single HFs, i.e. cell viability and cell cycle while at the same time maximising the data output from a single HF ensuring sufficient sampling to determine fiber to fiber variations.

### 3.1.3 "in-fiber" cell morphology and organization

To determine cell-cell packing and morphology within the HF, scanning electron microscopy (SEM) was used. Other investigations have also employed this technique to evaluate cell organization inside HF bioreactor systems (Brayfield et al. 2008; Grek et al. 2009; Krasteva et al. 2002), and further (Bridges et al. 2006; Casciari et al. 1994) used TEM to evaluate high resolution features of cellular arrangement with the implant. The study by SEM was favoured in the present work over the methods used for morphological characterization of the implants by histological sections (Bridges et al. 2006; Casciari et al. 1994; Hassan et al. 2001; Sadar et al. 2002). Although, sections presented the advantage of allowing immunohistochemical staining, (i.e. for the identification of proliferative vs. apoptotic biomarkers) (Bridges et al. 2006), they are problematic in some aspects. It is difficult to produce intact sections, as the adherent cell layer detaches form the HF wall upon preparation, also the data corresponds only to a cross-sectional planar view of the HF. SEM would provide an overview of the organisation providing important insights for cell-cell and cell-substrate interactions; and inform the model system and future design of an integrated biophotonic approach.

### 3.1.4 Single cell analysis: cell viability, cell size, and cell cycle features

Alongside obtaining morphology/organization information, the population growth performance of HF encapsulated cells was characterized in detail using flow cytometry measurements of cell viability and cell cycle distribution and corresponding cyclin B1-GFP expression in the HF. The aim was to obtain a full profile of cell integrity, size and cell cycle traverse as well as the parameter inter-mitotic time (IMT) in this case using stathmokinetic analysis (Bhuyan and Groppi 1989; Stubblef.E and Klevecz 1965; Watson 1991). At the same time the study would inform on cell line phenotype differentiation and alteration promoted by the HF encapsulation compared to the standard TC planar surface culture.

This kind of investigation has been previously reported with Ewing's sarcoma family of tumours (Bridges et al. 2006), they detected considerable changes in terms of

cellular phenotypic behaviour within the HF. The normally adherent culture growing on standard flask surfaces formed aggregates and spheroids when encapsulated.

### 3.1.4.1 Challenging the HF with mitotic perturbing agent Taxol

Taxol has previously been used by Hassan et al. 2001 using the *in vitro* HF for the quantitative assessment of anti-tumour activity. More recently (Suggitt et al. 2004) performed a detail study of the drug pharmacodynamic effects, namely microtubule disruption and cell cycle G2/M block analysis, on *in vivo* HF A549 cells excised from Taxol treated mice. Taxol has also previously been used specifically in U-2 OS cells in standard tissue culture to block mitosis (Brito and Rieder 2009; Kelling et al. 2003; Lu et al. 2005b; Smith et al. 2007b; Zhu et al. 2005). In the current study a low drug concentration (5nM) was selected, as it represents a clinically relevant low-dose range (1–20 nM) drug (Huizing et al. 1993) Allman et al. 2003). It is at this dose level that Taxol induces more interesting cell responses mechanisms that lead to either cell death or survival (Gascoigne and Taylor 2009; Wang et al. 2000). Furthermore there is considerable previous knowledge of the effects of this low doses on the apoptotic responses of standard cell cultures (Allman et al. 2003) including specifically the U2OS-GFP cell line used in the present investigation (Smith et al. 2007b). The data obtained in the current study extends these investigations further to consider the biophotonic integration into the HF–U2OS-GFP model and the requirement for the HF assay to study the mechanism of drug action *in vivo* (Suggitt et al. 2004).

### 3.1.4.2 Colcemid for kinetic HF cell transverse analysis

Colcemid also targets the microtubules, but has a mechanism of action opposite to Taxol, Colcemid inhibits microtubule polymerization leading to prolonged mitotic arrest (Hastie 1991; Jordan and Wilson 2004; Rieder and Palazzo 1992; Sluder 1979). Colcemid causes a prolonged mitotic arrest with relative low cell toxicity, and in some cases reversible upon drug removal. This has made it a useful cytogenetic tool for cell cycle stathmokinetic calculations and synchronization (Darzynkiewicz et al. 1987; Puck and Steffen 1963; Stubblef.E and Klevecz 1965). In the classical example of a stathmokinetic method, a metaphase blocking agent allow the cells to continue progression through interphase and accumulate with 4n DNA content indicating

competency for cycle traverse to metaphase. Cells are sampled and analyzed by flow cytometry at defined time intervals to return the rate at which cells are entering (or accumulating) in mitosis (Bohmer 1982; Darzynkiewicz et al. 1987; Gray et al. 1987). This method can return an estimate of the total time required for population cell cycle traverse or the apparent time interval between cell mitoses, for the present work referred as inter-mitotic time (IMT). This technique depends on the persistence of arrested metaphases, however arrested metaphases do not, in fact, persist for long; therefore some estimates of the rate at which cells accumulate in rather than enter mitosis, based on a count of metaphases, may be therefore underestimated (Aherne and Challoner 1983). Some cell lines never escape the block and die after some days, but in some cases, a proportion of the cells within the prolonged mitotic arrested population escape the block (Davis et al. 2001; Kung et al. 1990; Rieder and Palazzo 1992; Sherwood et al. 1994b; Urbani et al. 1995).

In the current study colcemid was used to obtain kinetic cell cycle data, the action of this drug was studied in detail previously in U-2 OS cells (Matsusaka and Pines 2004). The antephase cell checkpoint has been shown to act at the end of interphase to delay cells from entering mitosis causing cells in prophase to return to G2 upon colcemid action. U-2 OS cells like other cell lines present a mutation in Chfr protein important in the regulation of the antephase checkpoint which leads to cells proceeding directly to mitosis without returning to interphase (Matsusaka and Pines 2004).

A wide range of Colcemid concentrations from: 20, 50, 70, 100 ng/ml (Kung et al. 1990; Li et al. 2005; Rieder and Maiato 2004; Sherwood et al. 1994b; Urbani et al. 1995) have been reported previously to ensure a mitotic block on different cell lines. Furthermore for U-2 OS a concentration of 15 uM (5.6 µg/ml) has been previously described (Matsusaka and Pines 2004). Stathmokinetic agents such as Colcemid exert undesirable effects manifesting as toxicity or perturbation of cell progression through other phases of the cell cycle besides mitosis. Following the strategy advised by Darzynkiewicz et al. 1987; Puck and Steffen 1963 to ensure that these effects are minimal, and that cells do not escape mitotic arrest, the "optimal" drug concentration was also determined prior to a full kinetic cell cycle traverse studies.

## 3.2 Specific chapter aims

The overall objective was to establish a reproducible *in vitro* human osteosarcoma (U-2 OS) cyclin B1-GFP hollow fiber encapsulation model (HF–U2OS-GFP model). Including characterisation of the response of the encapsulated cell population in the HF platform culture environment, under short (8-9 days) and long (27 days) term culture, in normal control and drug treatment conditions, specific aims included:

*1.* To determine the morphology/organization of the cells, and the consequences on cellular shape and size of cells growing in the HF;

*2.* To assess the biological behaviour, namely proliferation and growth features alongside cell viability and how these change in the hollow fiber (HF) culture compared to standard planar tissue cultures (TC);

*3.* To obtain dynamic parameters associated with cell cycle traverse and inter-mitotic time.

Taken all together this study provides insights of "life in a cylindrical hollow fiber" and the combined influences of this culture environment which also informs on the integration of the biophotonic components.

## 3.3 Specific methodology - HF–U2OS-GFP cell *in vitro* characterisation schema; culture duration, manipulation and analysis

The U-2 OS cyclin B1-GFP cells growing in the hollow fiber (HF–U2OS-GFP model) were prepared according to the protocol see chapter 2.1.1 – Figure 2.1 , and characterized first over short term incubation, around 8-9 days, that represented a common culture time, and also up to 27 days. This fits the general framework of previous HF studies for drug evaluation and other biological parameters (Bishai and Karakousis 2006; Bridges et al. 2006; Casciari et al. 1994; Decker et al. 2004; Hassan et al. 2001; Hollingshead et al. 1995a; Liu et al. 2004; Suggitt et al. 2004; Temmink et al. 2007).

The optimisation of the HF culture and cell retrieval protocols for the HF–U2OS-GFP derived cells has already been described in detail (chapter 2.2.4).

### 3.3.1 Short-term (8-9 days) HF–U2OS-GFP cell growth, morphology/ organization and cytometry single cell analysis

Hollow fibers of length 2 or 4 cm (chapter 2.1.1 – Figure 2.1) were loaded with U-2 OS cyclin B1-GFP cells (~1.0 x$10^6$ cells/ml) using the *HF cell loading protocol_A* (chapter 2.2.2.3) and cultured *in vitro* in independent experimental batches, with medium supplemented with 20% or 10% FCS. The encapsulated cells of the multiple experiments were retrieved (chapter 2.2.4) at different time points, typically 48h (2days), 72h (3days), 120h (5days), 144h (6days), 168h (7days), 192h (8days) and 216h (9days). Cell counts were performed using the Z1 Coulter counter accordingly, each corresponding to individual HFs cell content. Representative closed HFs after 48h (2 days), 120h (5 days) and 192h (8 days) culture time points were processed and imaged by SEM according to method previously described (chapter 2.6.1).

Cells growing in standard tissue culture (TC) on planar plastic surfaces consisted of two starting densities: First, a 6 well plate (area of one well = 9.6 $cm^2$), seeded 4 days prior to retrieval for flow cytometry analysis. This was performed in a way to have low confluency at the time of the drug addition (~50%CF=1.12 x$10^4$ cell/$cm^2$; ~65%CF=2.16 x$10^4$ cell/$cm^2$) or cell retrieval (~75%CF=3.65 x$10^4$ cells/$cm^2$). Second, a 12 well plate high confluency culture seeded in a parallel growth time-

course to the HF, for this the estimated cell/area seeding density by well was set to be similar to the HF starting cell density (estimated ~2.5 x$10^4$ cell/cm$^2$) with a high confluency (≥100%CF ~3.5 x$10^5$ cells/cm$^2$) at the time of retrieval. Note that the total surface area of one well (3.8 cm$^2$) was approximately equivalent to the combine area of three 4 cm length HF [3x 1.26 cm$^2$ total area (or 3x 1.13 cm$^2$ available HF adherent cell area)]. The general linear model statistic analysis of covariance (ANCOVA) was used to compare the 20% versus 10% FCS serum HF cell growth using the Minitab1.5 software (http://www.minitab.com [2010]) following the previously described (Currell and Dowman 2009; Guzzardi et al. 2009).

### 3.3.1.1 Taxol drug treatment perturbation

The HF–U2OS-GFP cells were exposed to Taxol treatment at different time points during culture. Taxol (5 nM) was added at 144h (day 6) and 168h (day 7) to the HF to give a 48h and 24h drug pre-treatment at 192h (8 days). Parallel standard TC cultures ( i.e. 6 and 12 well plate) were also exposed to 48h and 24h drug pre-treatment. Representative HFs of the 48h Taxol treatment were also prepared and imaged by SEM.

HF culture and the standard TC cells were all retrieved and processed at the same time (for the HF in some cases separated into adherent and loose component), stained with PI to detect dead cells or DRAQ5 to determine DNA content and run in the FACSCalibur bench-top flow cytometer (chapter 2.4). Additionally, parallel bright field snaps-shot and fluorescence microscopy of DRAQ5 nucleus stained cytospin of the retrieved cell suspensions were acquired (chapter 2.6.3).

The flow analysis protocol consisted of a FL3-W versus FL3-A channel for the DRAQ5 stained samples (Gate 1) and a forward and side scatter gate for the PI samples. Side versus forward scatter plus PI plots together with forward scatter, cyclin B1-GFP versus DNA content plots were constructed. Cell cycle phase histograms statistical data was calculated manually. An exemplar flow analysis procedure can be found in Supplementary Information 3.6-1.

### 3.3.1.2 Colcemid cell cycle kinetic analysis

A drug concentration optimization experiment was performed to establish the lowest concentration of Colcemid that is adequate to completely arrest cells in mitosis with minimal toxicity. The U-2 O S cyclin B1-GFP cells were cultured in standard 12 well plates and incubated during 24h with increasing drug concentrations: 1, 5, 20, 40, 60 and 100 ng/ml of Colcemid. The G1 emptying and G2/M accumulation, together with PI staining to determine the accumulation of a non-viable fraction, was evaluated by flow cytometry for each concentration. 60 ng/ml gave optimal outputs with stabilization of G1 emptying plus simultaneous G2/M accumulation and also a low PI positive fraction (data not shown).

HF–U2OS-GFP cell cultures were exposed to Colcemid treatments at different time points, to obtain cell cycle kinetic responses. Colcemid (60 ng/ml), was added at 72h (day 3) and 240h (day 10) to HF cultures to result in a 48, 24, 18, 12, 8 and 6 h exposure to the drug, plus the un-treated control (0h). Additional, parallel standard TC cultures were also assessed: 6 well plate low confluency (50%) culture and 12 well plate (equivalent starting cell density to the HF) with high confluency (>100%) culture.

HF and standard TC culture cells were retrieved and stained with DRAQ5 and run in the FACSVantage flow cytometer (chapter 2.4). Flow analysis was performed using similar gating to previously described for Taxol treatment (Supplementary Information 3.6-2) resulting in side scatter, forward scatter and cyclin B1-GFP versus DNA content dot-plots. Cell cycle phase histogram statistical data was obtained using the Dean-Jet-Fox model FlowJo v.7.5.5 function. These data were used to calculate the culture IMT by the equation in Supplementary Information 3.6-7.

## 3.3.2 Long-term (27days) HF–U2OS-GFP cell culture analysis

HF–U2OS-GFP cells were cultured in full medium for 27 days, with the media replaced at each 5 day intervals. At day 27 the HF cells were retrieved, separated in adherent and loose component, stained with PI and DRAQ5 accordingly and run in the FACSCalibur, representative HFs were also prepared and imaged by SEM. Flow cytometry analysis was performed similarly to described in the section 3.3.1.1.

## 3.4 Results and Discussion

### 3.4.1 Establishing a short-term (8-9 days) HF–U2OS model

A typical cell growth profile of the U-2 OS cyclin B1-GFP cells in the hollow fiber is presented in Figure 3.1 and compared to its TC tissue culture counterpart. The overall observation showed that these cells were able to grow in the HF, as demonstrated by the increased number of cells eight or nine days post-loading and retrieved from the HF. The rate of growth was influenced by a number of factors including HF length, fetal calf serum (FCS) concentration and initial seeding cell number. The latter factor was optimized at ~1.0 x$10^6$ cell/ml (estimate ~2.5 x$10^4$ cell/$cm^2$) confirming previous references (Zhang et al. 2004) for U-2 OS.

The tissue culture (TC) model represents a standard culture situation where cell growth on the planar plastic substrate of the 12 well plate in direct contact with the medium. The 12 well plate cell seeding concentration was set in order for the estimated starting cell number/area ($cm^2$) to be similar to that of the HF thus providing equivalent starting cell density. For reference, one 4 cm length HF with an available adherent cell length of ~1.6 cm and a surface area of 1.13 $cm^2$ represents approximately one third of the area of a single well on the plate.

The generated growth curve Figure 3.1-12well) presented a typical exponential growth of this cell culture, reaching saturation after 5 days. Increase, from 48 to 120 h (2-5days), where full confluency was reached before 96h (4 days), the cell number appeared to stabilized after around 120h (5 days) at ~3.5 x$10^5$ cells/$cm^2$ (calculated linear doubling time ~25h). This growth stabilization was most probably due to the typical limiting factors registered on highly confluency standard tissue cultures, such as cell to cell contact inhibition. For this specific assay, other factors such as limited nutrients in the cell medium were minimized with mid-term feeding (at four days).

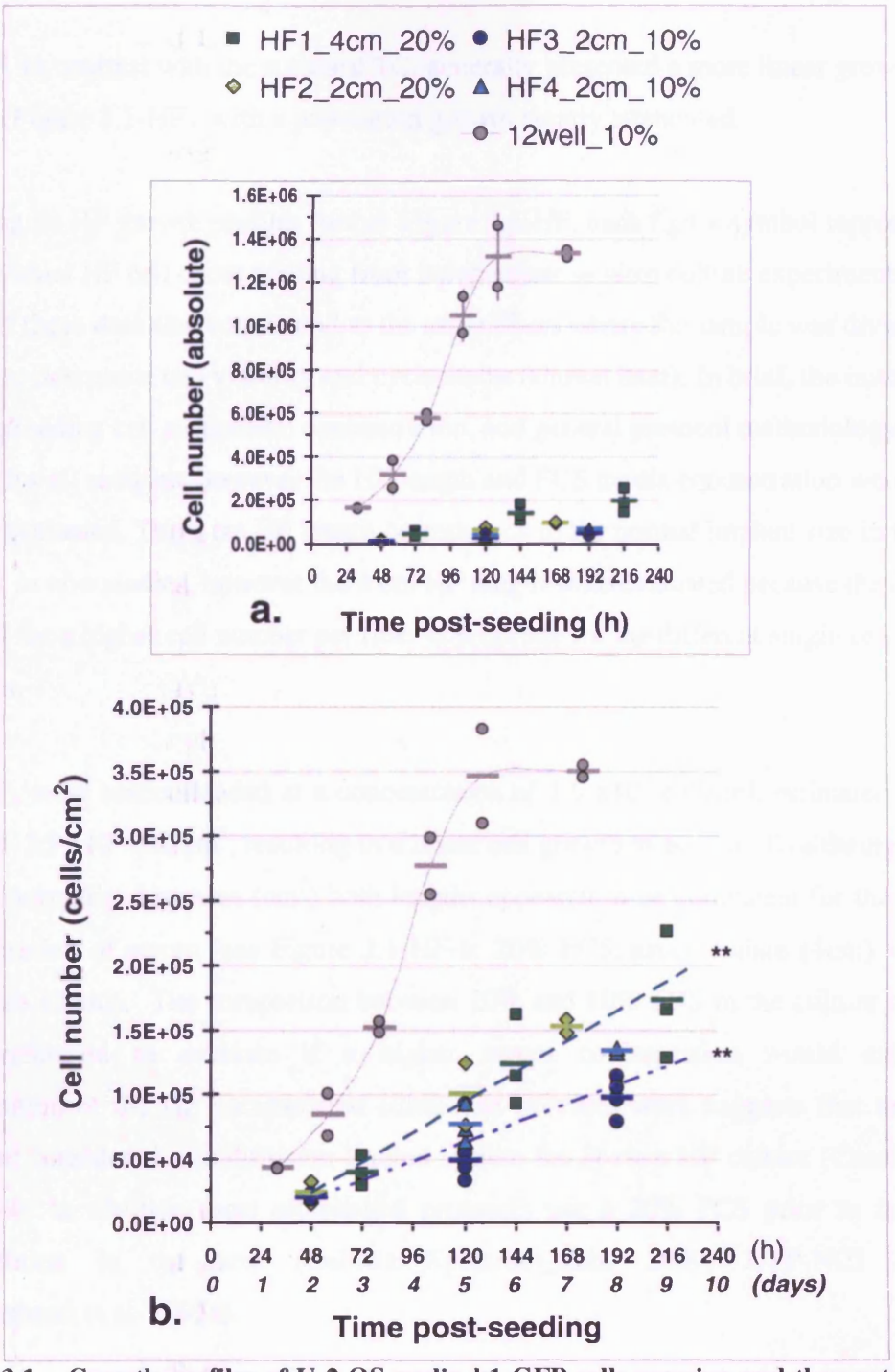


**Figure 3.1 – Growth profiles of U-2 OS cyclin b1-GFP cells growing and then retrieved from the well surface (TC) and in the hollow fiber (HF).** The profiles were obtained using cell counts. **(a)** Absolute cell number based on cells retrieved per well (grey) or per fiber (colour) and **(b)** normalized to surface area ($cm^2$) to demonstrate cell density. The HF cultures were exposed to 10% (green) and 20% (blue) fetal calf serum (FCS). For each time point the number of symbols represents an individual reading from an independent fiber or well, were the correspondent thick horizontal bar represent the mean value, the linear regression for the the two FCS concentrations groups (20% and 10%) are plotted like doted lines. ** Analysis of covariance (ANCOVA) was performed to compare the linear regression of 20% versus 10% FCS returned a p=0.024, meaning that these are significantly different for a p-value level of 0.05. *Note: [+]Estimate of growth area of the HF_2 cm, HF_4 cm and each 12well is 0.50, 1.13 and 3.8 $cm^2$ respectively. [++]Seeding density was estimated to be ≤2.5x10$^4$cell/$cm^2$.*

The HF, in contrast with the standard TC, generally presented a more linear growth profile (Figure 3.1-HF), with a population growth clearly attenuated.

Focusing on HF growth profiles further Figure 3.1-HF, each figure symbol represents an individual HF cell count reading from independent *in vitro* culture experiments. Some of these data also correspond to the same fibers where the sample was divided further to determine cell viability and cycle status (shown later). In brief, the initial seeding/loading cell suspension concentration, and general protocol methodology was similar for all samples; however the HF length and FCS media concentration were further evaluated. The 2 cm HF length corresponds to the normal implant size in the host for *in vivo* studies, however the 4 cm HF length were evaluated because they allowed for a higher cell number per fiber appropriate for the different single cell analyses.

The HFs were seeded/loaded at a concentration of 1.0 $x10^6$ cells/ml, estimated to be around ~2.5 $x10^4$ cell/$cm^2$, resulting in a linear cell growth in general. Evaluating fiber growth normalized by area ($cm^2$) both lengths appeared to be equivalent for the same concentration of serum (see Figure 3.1-HF-b: 20% FCS, green square (4cm) versus diamonds (2cm)). The comparison between 20% and 10% FCS in the culture media was performed to evaluate if a higher serum concentration would enhance proliferation of the HF encapsulated culture, as previous work suggests that the HF could be considered as a diffusion limited system for *in vitro* HF culture (Casciari et al. 1994). In addition most established protocols use a 20% FCS prior to *in vivo* implantation in the host (CellMax_Spectrum_Labs 2009; DTP-NCI 2009; Hollingshead et al. 1995a).

The analysis of the HF linear regression of each FCS serum concentrations (Figure 3.1-b) showed that 20% FCS (green) produced a slight higher proliferative rate compared to 10% FCS (blue). The analysis of covariance (ANCOVA) (Currell and Dowman 2009) between the 20% versus 10% FCS returned a p=0.024. So the null hypothesis that these FCS conditions lead to similar growth rates could be rejected for a p-value level of 0.05. This signifies that the calculated linear regressions for each of different FCS concentration are significantly different. The 20% FCS experiments

presented a standard deviation (SD) average value of ± 2.5 x$10^4$ cells/cm$^2$, a linear *m* slope value of 953 ($R^2$=0.84) and a mean doubling time ~46h calculated from the presented time points between 2 to 9 days. The 10% FCS experiments (only for 2cm length HFs) were slight more consistent, with the SD average value of ±1.0 x$10^4$ cells/cm$^2$, a linear *m* slope value of 624 ($R^2$=0.80) and a mean doubling time ~53h,

Overall, the HF–U2OS-GFP *in vitro* cell culture with 10% FCS in the media produced a predictable and reproducible cell growth with minimal variation between individual HFs and consistent linear cell growth and an overall mean population doubling of ~53h (2.2 days). Also, it is possible to infer some further insight for drug treatment perturbation experiments, namely that the first time-point for drug addition should be at around 96-144h (day 4-6). First, to obtain enough cells for the subsequent different analysis; and second, to maximize the perturbation effect (Suggitt et al. 2004).

#### 3.4.1.1 SEM of in-fiber cell organization/morphology

Removing cells from the hollow fiber throws away information relating to the spatial arrangement of the cells in the fiber. To gain the information regarding cell configuration and localization within the growing matrix inside the HF SEM imaging was conducted according to the methods previously described (chapter 2.6.1). The growth curves provided guidance on when to sample the HF and it was decided to assess organisation at 48h (day 2) (Figure 3.2-(a-d)), 120h (day 5) (Figure 3.2-(e-h)) and 192h (8 days) in culture. The progressive magnification in the SEM images sequence starts with a view from the top of almost the entire HF, with some parts still partially closed. It is possible to see that the longitudinal cut along the HF length provides details of the asymmetrical membrane fiber wall macro-pores and the cell layer attached to the inner wall surface. The subsequent images reveal with increasing magnification inside the fiber to gain a sense of cell organization and detail of the cell morphology at the fiber surface or/and in contact with other cells.

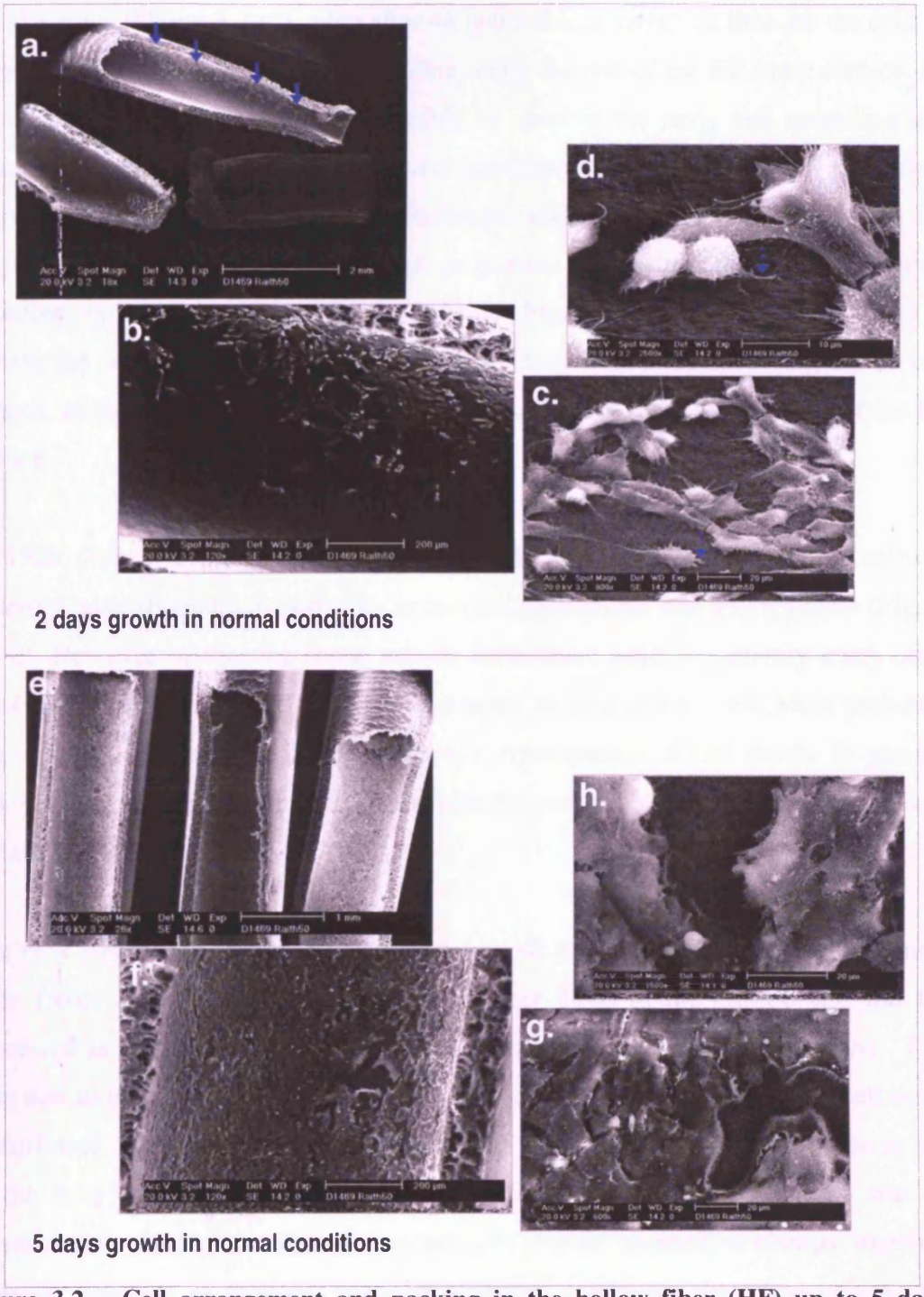


**Figure 3.2 – Cell arrangement and packing in the hollow fiber (HF) up to 5 days.** Scanning electron microscopy (SEM) images to show the adherent cell layer (HF_adh) located on the inside of the HF at different time points. **(a-d)** Longitudinally cut fiber to reveal the inner surface at 48h (2 days); with progressive zooming (bar represents 2000, 200, 20 and 10 µm respectively) and **(e-h)** after 120h (5 days); with progressive zooming (bar represents 1000, 200, 20 and 20 µm respectively). *Note: Solid arrows (a) represent early cell accumulation zone and dashed arrows (c,d) cell lamellipodia and filopodia cell extensions.*

After the initial loading into the HF the cells accumulate onto one side of the HF (presumably by gravity), hence resulting in a cellular 'stripe' 48h (2 day) in culture

(solid arrows (Figure 3.2-a)). Also after 48 hours this is sufficient time for the cells to recover, adapt and start spreading dividing along the rest of the HF inner surface. As illustrated in Figure 3.2-c it was possible to observe the early cell spreading and attachment with details of the membrane lamellipodia and filopodia cell extensions (Figure 3.2-d, dashed arrows) (Lauffenburger and Horwitz 1996), binding to the polymer fiber wall. Additionally, a high proportion of attached "rounded cells" were observed, typical of cells undergoing mitosis (Figure 3.2-d) After 120h (5days) of growth the cells spread across most of the HF inner wall, with increasing cell to cell contact, as the organized adherent layer, progressively covered the majority of the HF surface.

At 192h (8days) the cells completely coverered the inner wall forming a uniform adherent layer (Figure 3.3–(a-d)) the occasional mitotic cell was still apparent (Figure 3.3-d). However besides the round mitotic cells, there were consistently many other "globular" structures on the cell layer too small to be a mitotic cell. Most probably, these structures were cell debris perhaps a consequence of cell death. In general however, the adherent layer cellular organization was comparable to standard TC cell culture conditions.

The next step was to evaluate the impact on cell morphology after a 48h treatment with Taxol (5 nM). The drug was added after 144h in the culture and the HF processed as for the un-treated control conditions for SEM at the 192h (8 days). This drug acts to perturb the cell cycle, arresting the cells at mitosis followed by cell death (Schiff et al. 1979). In morphological terms the SEM images demonstrated the action of the drug on the HF adherent cell layer (Figure 3.3–(e-h)). First there was an accumulation of a high number of rounded cells (mitotic arrested) in clumps; together, with the presence of smaller "irregular globular" structures, described before, that probably correspond to trapped apoptotic cells (Figure 3.3 – g and h; solid arrows). Additionally, there was a total disruption of the adherent layer observed on the control, with most of the HF inner wall being denuded of adherent cells (Figure 3.3-f) Similar drug perturbation results where to some extend similar to previous reported U-2 OS cell appearance changes on standard tissue culture (Lu et al. 2005b), further confirmed on the present investigation by phase microscopy but the SEM revealed considerably more detail of the cell morphology.

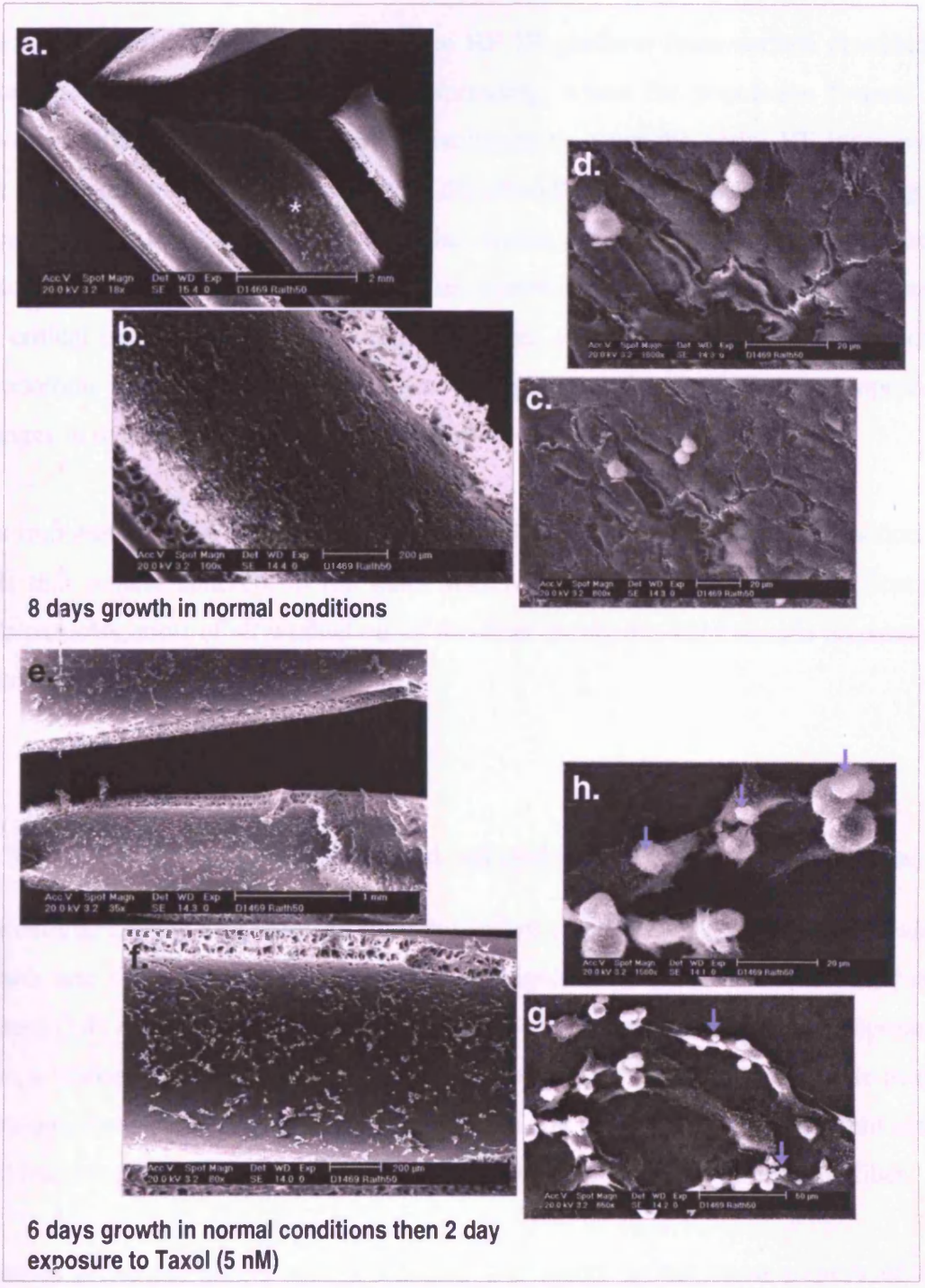


**Figure 3.3 – Cell arrangement and packing in the hollow fiber (HF) up to 8 days.** Scanning electron microscopy (SEM) images to show the adherent cell layer (HF_adh) located on the inside of the HF at different time points. **(a-d)** Longitudinally cut fiber to reveal the inner surface at 192h (8 days); with progressive zooming (bar represents 2000, 500, 200, 20 and 20 µm respectively) and **(e-h)** corresponding fibers with a 48h treatment with Taxol (5nM) after 6 days); with progressive zooming (bar represents 1000, 200, 50 and 20 µm respectively). *Important note: Market (*) HF cut section (a) doesn't represent an 8 days growth in normal conditions. Solid arrows (g) indicate small round "particles" probably debris or dead cells.*

Overall, the SEM results showed that the HF 3D platform inner surface provided a suitable substrate for cell growth and spreading, where the population formed an "epithelial like phenotype" uniformly distributed to cover the entire HF inner wall. The introduction of a drug such as Taxol disturbed this adherent layer transforming an organized "flat like" layer into an irregular chaotic distribution of cell clumps. These organizational differences, between the un-treated and drug-treated fibers, represent the critical features that could be exploited when considering the incorporation of a biophotonic components (e.g. changes in light absorbance/scattering properties, changes in dynamic cell cycle reporters) further discussed in Chapter 6.

It is important to note that the SEM results of the fiber only addresses the fraction of cells that remain adherent to the inner wall of the fiber and not the free floating cells/particles, most of all washed out of the fiber during the SEM sample preparation protocol.

#### 3.4.1.2 Cell viability, cell size and cell cycle of HF retrieved populations

The cellular content was retrieved from the hollow fiber after 192h (8 days) of *in vitro* growth and subjected to single cell analysis (Figure 3.4). The retrieved HF full cell content (HF_all), in some procedures was divided into two well-defined component: First, a "loose" component (HF_los) easily removed from the fiber by a simple media flush-out, immediately following the opening of the HF. Second, the adherent inner wall fraction (HF_adh), that required a trypsinization to be detached from the fiber.

A series of simple assays were conducted that report on the consequences of HF encapsulation on cell integrity, cell size, cell cycle content and DNA fragmentation. These measurements were additionally complemented by bright field/fluorescence microscopy acquisition. Together these provided a evaluation of the cell culture biological activity and the cell suspension phenotype.

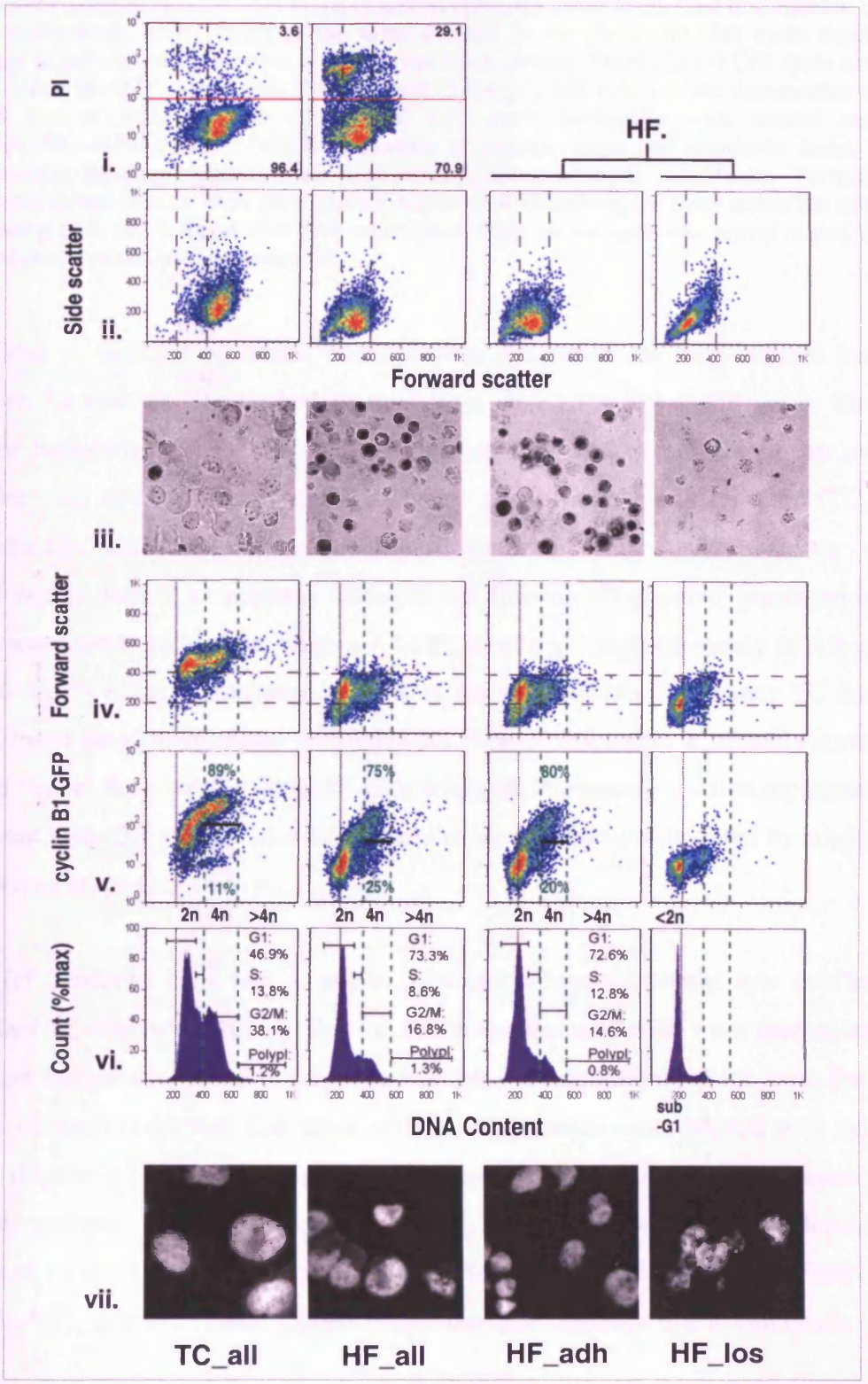


**Figure 3.4 – Flow and image cytometry analysis of cells retrieved from the hollow fiber (HF) after 192h (8 days) compared to standard tissue culture (TC).** Panels present the cell sample analysed versus the assay performed: ***Cell sample (4 columns):*** **1. TC_all** - All cells retrieved from a low confluency (~75%CF) 4 days standard tissue culture; **2. HF_all** - All cells isolated from the hollow fiber; **3. HF_adh** - Adherent component requiring trypsinization to remove cells (~85% all HF content); **4. HF_los** - Flushed out cell component, comprising the "loose" cellular material (~10% all HF content). ***Assay type (7 rows):*** **(i)** Identification of

damaged/dead cells using propidium iodide (PI)); **(ii)** Identification of cell size using forward and side scatter analysis; **(iii)** Demonstration of cell morphology using bright field transmission image (field dimensions: 128x128µm) of the same samples in the plots; **(iv)** Cell cycle dependent changes in cell size using forward scatter versus DNA content (DRAQ5); **(v)** Cell cycle analysis using cyclin B1-GFP plots versus DNA content (DRAQ5), line indicates the demarcation of the G2/M fraction with high/low signal; **(vi)** Cell cycle histograms with manual analysis (G1,S,G2/M,>4nPolyploidy); **(vii)** Identification of nucleus shape and chromatin status using fluorescence labelling (DRAQ5) of fixed cells (field dimensions: 64x64µm). Vertical and horizontal dotted lines on each panel provide a means for visualising the assay across the row thus comparing each cell fraction with each other. *Note: Data shown represents typical output, n=3x3 (independent experiments x individual HF).*

Cell size as depicted by scatter characteristics are shown for each cellular fraction (Figure 3.4-row ii). The dashed vertical lines depict the lower and upper forward scatter boundaries for the HF cellular fraction (HF_all), demonstrating an overall smaller cell size compared to the standard tissue culture counter part (TC_all). Importantly, the whole population participates in this marked scatter shift. Additionally there is an apparent damaged cell fraction (PI positive) presented in the HF encapsulated population (Figure 3.4-HF_all-row i). Approximately 29.1% of all events are PI positive compared to 3.6% in the standard low confluency TC derived cells. From the forward scatter properties the PI positive fraction is probably attributed to the 'loose' flush out fraction (HF_los), while the PI negative fraction represents the adherent layer (HF_adh). These flow analyses were further corroborated by brightfield transmission imaging (row iii).

The HF retrieved cells had a smaller diameter compared to the low confluency standard TC retrieved cells, and that the debris and damaged cells were predominantly (but not exclusively) found in the loose fraction. Further analysis of the loose fraction (final column) confirmed that these cellular components corresponded to a sub-G1 peak (Figure 3.4-HF_los-vi) and has a minimal retained GFP-derived fluorescence signal, probably because there is no cytosol left and/or the reporter molecule has diffused away. This is further confirmed by the nuclear labelling of cells (Figure 3.4-HF_los-vii), where the DNA appears fragmented and degraded due to cell death.

After an 8 day encapsulation the majority of the cells in the HF are represented by the adherent cell component and intact (PI negative) and able to report a cell cycle distribution (Figure 3.4-HF_adh). The reporter signal cyclin B1-GFP versus DNA content provided high resolution cell cycle distribution (chapter 1.6.1.2). The cyclin

B1-GFP signal gave a typical profile associated with the cell cycle in normal tissue culture conditions (Figure 3.4-TC-v). However this distribution became changed in cells growing in the HF (Figure 3.4-HF_adh-v). This distorted distribution reflects two possible effects which are not mutually exclusive. First the cell cycle distribution has altered in cells growing in the fiber; and second the cyclin B1-GFP reporter expression performance has been cell cycle independently perturbed and therefore altered as a result of growing in the hollow fiber. From the DNA content data alone it is clear that that the adherent layer of cells removed from the HF (Figure 3.4-HF_adh-vi) showed a dramatically different cell cycle distribution to its low confluency TC (Figure 3.4-TC_all-vi). The HF derived cells showed a frequency in G1 of 73.3% versus 46.9% for the TC derived cells, while the G2 fraction was of 38.1% and 14.6% respectively. The S-phase fraction remained similar (~14%) in each case as did the >4n polyploid fraction (~1%). The >4n fraction percentages were within the range previously reported in the TC culture of parental U2-OS cells (Pan et al. 2009). The above HF G1 redistribution frequency could be attributed to either a delay in G1 or quiescence (perhaps $G_0$) or a prolonged G1 traverse. This will be investigated further in the next sections.

To address the aspects of cell cycle status and the reporter performance, cyclin B1-GFP expression fluorescence outputs in relation to DNA content was analysed. The cells were identified accordingly to DNA content to be G1 or G2 and the corresponding cyclin B1-GFP mean fluorescence increase from G1 to G2 calculated with the respective standard deviation, including any low reporting fraction. This increase was of 89 (sd ±73) to 357 arbitrary (arb.) units (sd ±210) for the TC and 15 (sd ±16) to 125 units (sd ±96) respectively, showing that the reporter appeared to give a dynamic range output in both cases. It was evident that after eight days of growth in the HF removing these cells led to a low GFP reporting fraction (signal below 40-50 arb. units), 25-20% of the total G2/M population, which has previously discussed as a methodology issue (see chapter sections 2.2.4.1 and 2.2.5.1) and not a 'true' cell cycle related signal as there is not a persistent >4n sub-fraction.

The possible consequences of a hypoxic environment in the HF causing abnormalities in GFP-chromophore formation were also assessed (Vordermark et al. 2001) for the present reporter. U-2 OS cyclin B1-GFP cells were cultured in 1% oxygen levels and

compared to normoxic conditions and showed that both the cyclin B1-GFP expression levels and DNA content remained unchallenged in the hypoxic chambers (data not shown; personal communication Sally Chappell). So overall it seems that the cyclin B1 reporter remains intact and provides a high resolution readout together with DNA content to decipher cell cycle status and responses in the HF platform *in vitro*.

### 3.4.1.3 Perturbation of cell proliferation with Taxol

HF–U2OS-GFP *in vitro* cultures were incubated in the continuous presence of Taxol (5 nM) for 24h (added at 168h post-seeding) and 48h (added at 144h post-seeding), to determine the response of the cells in the hollow fiber. The retrieval procedure and sample processing was identical to above and provided parallel SEM samples. Again single cell analysis was undertaken to determine the extent of cell cycle perturbation and cell viability after a 24h and 48h Taxol exposure (Figure 3.5). The analysis confirmed that the HF loose component consisted of PI positive fraction (81.1%), representing mainly non-viable cells plus debris, while the HF adherent component is largely composed of viable PI negative cells (88.7%) (Figure 3.7-i). This did not vary much between the two doses of Taxol.

The scatter characteristics are shown for each cellular fraction (Figure 3.5-ii) after drug treatment. The HF cellular fraction, demonstrated an overall cell size (forward scatter), similar to untreated control HF conditions (Figure 3.4-ii). However, the greatest effect was to be found with TC derived cells treated with Taxol (Figure 3.5-TC_all-ii), where the forward scatter showed that cell size had decreased and that there was an increase and spread of cells with an increase in side scatter (cell internal complexity or granularity). This high granularity could be attributed to the increase in the density of small peripheral distributed vesicles/compartments in the cell due to the Taxol disruption action of the endocytic trafficking, previous reported (Sonee et al. 1998). The TC model response depicts the effect of U-2 OS cells treated with Taxol, with an accumulation of cells at G2/M, from 38.1% un-treated (Figure 3.4–vi) to 81.6% with 24h Taxol treatment (Figure 3.5–v, vi), this led almost a complete emptying of G1 (8% remaining) of the cell population after 24h.

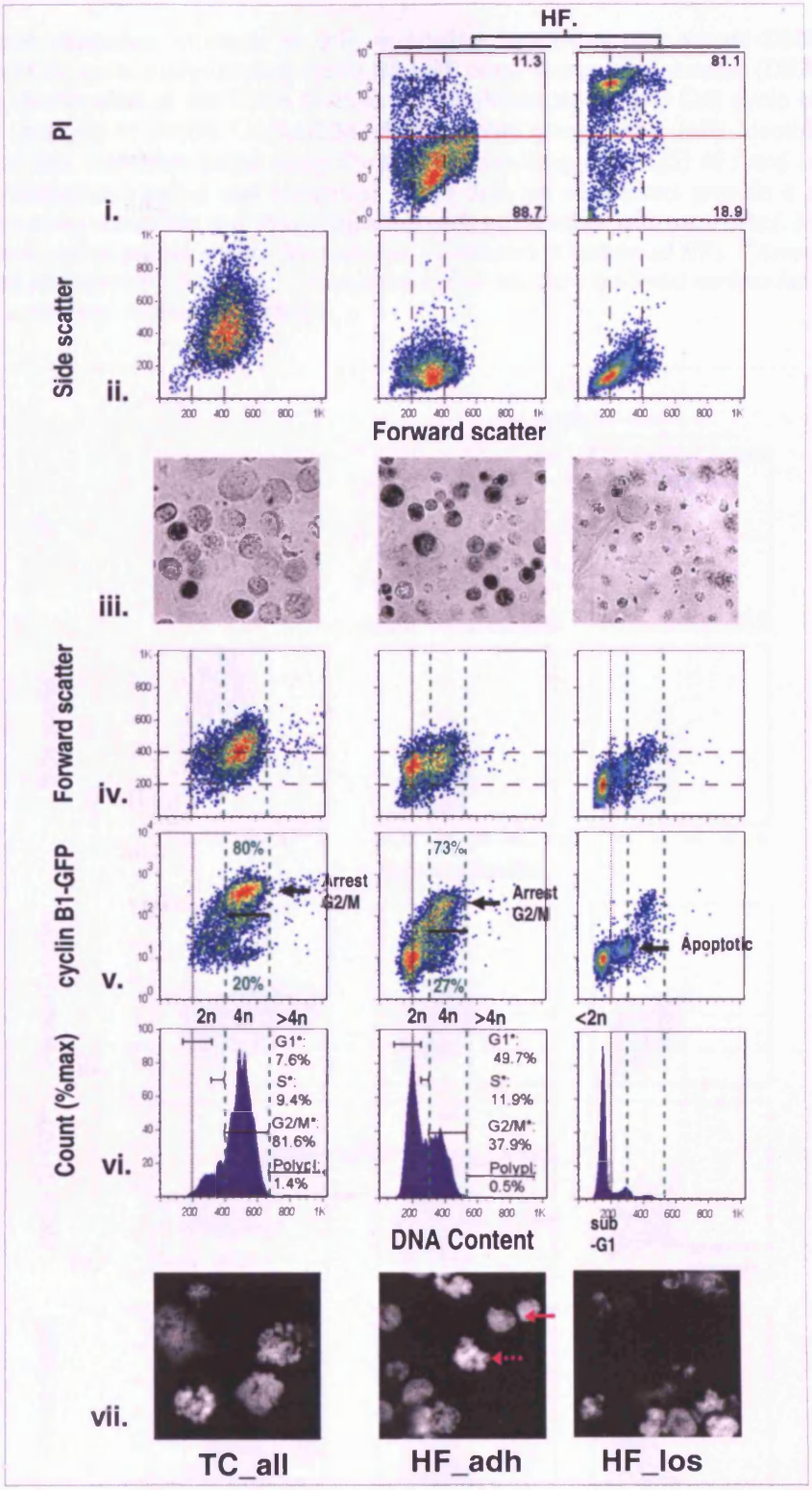


**Figure 3.5 – Flow and image cytometry analysis of cells retrieved from the hollow fiber (HF) after 7 days (control conditions) plus 1 day (24h) 5nM Taxol exposure (treatment) versus standard tissue culture (TC).** Panels present the cell sample analysed versus the assay performed: ***Cell sample (3 columns)*:** **1. TC_all** - All cells retrieved from a low confluency (~65%CF) 4 days standard tissue culture with 24h drug pre-treatment; **2. HF_adh** - Adherent component requiring trypsinization (~85% all HF content); **3. HF_los** "loose" flush out component (~14% all HF content). ***Assay type (7 rows)*:** **(i)** Identification of damaged/dead cells using propidium iodide (PI)); **(ii)** Cell size using forward and side scatter; **(iii)** Cell morphology using bright field transmission image (field dimensions: 128x128µm) of the same samples in the plots;

**(iv)** Cell cycle dependent changes in cell size using forward scatter versus DNA content (DRAQ5); **(v)** Cell cycle analysis using cyclin B1-GFP plots, versus DNA content (DRAQ5), line indicates the demarcation of the G2/M fraction with high/low signal; **(vi)** Cell cycle histograms with manual analysis to derive G1,S,G2/M,>4nPolyploidy percentages; **(vii)** Identification of nucleus shape and chromatin status using fluorescence labelling (DRAQ5) of fixed cells (field dimensions: 64x64µm).Vertical and horizontal dotted lines on each panel provide a means for visualising the assay across the row thus comparing each cell fraction with each other. *Note: +Data shown represent typical output, n=2x2 (independent experiments x individual HF). ++Arrows (row v) depict arrested and apoptotic fractions. +++Pink arrows (row vii) show a normal nucleus (solid) versus drug induced condensed chromatin (dashed).*

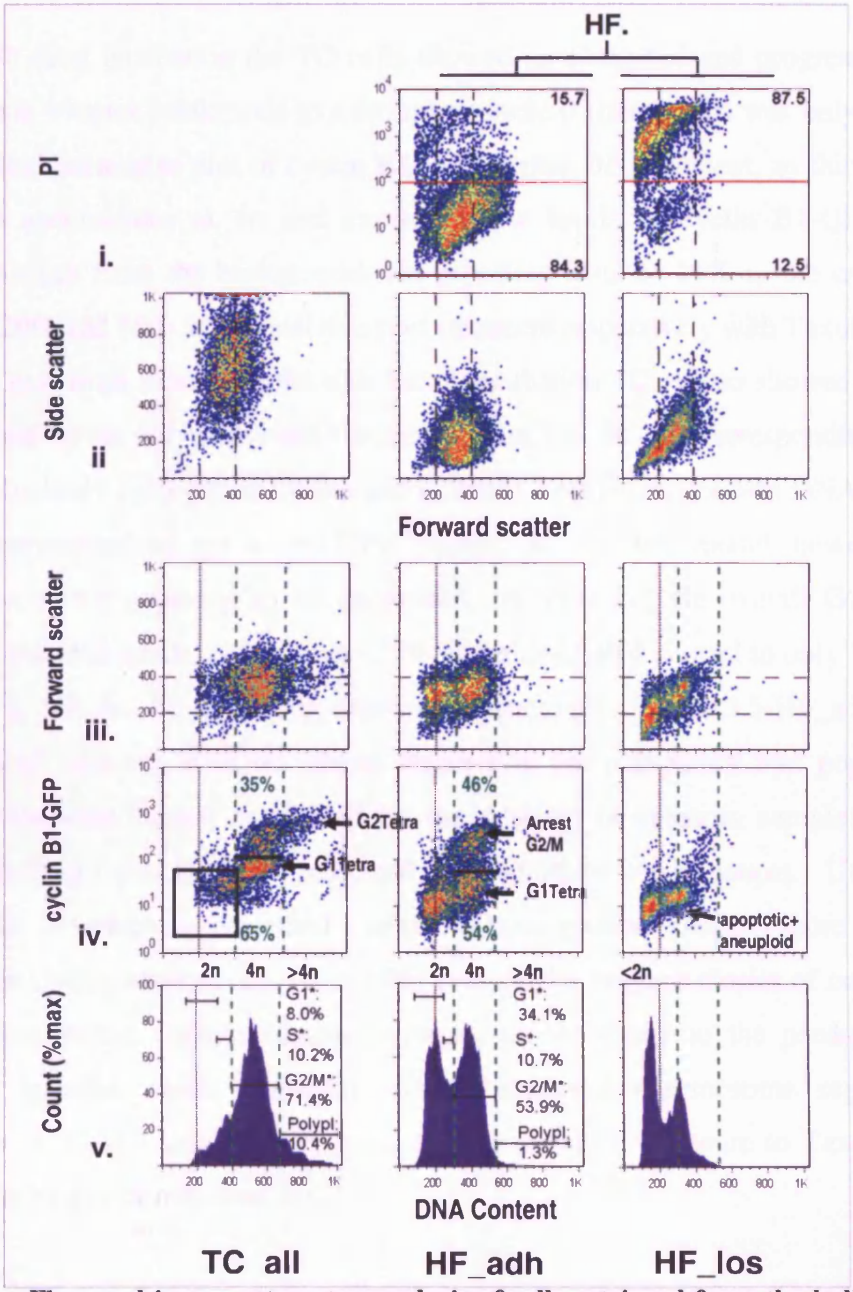


**Figure 3.6 – Flow and image cytometry analysis of cells retrieved from the hollow fiber (HF) after 7 days (control conditions) plus 2 days (48h) 5nM Taxol exposure (treatment) versus standard tissue culture (TC).** Panels present the cell sample analysed versus the assay performed: ***Cell sample (3 columns)*:** **1. TC_all** - All cells retrieved from a low confluency (50% CF) 4 days standard tissue culture with 48h drug pre-treatment; **2. HF_adh** - Adherent component

requiring trypsinization (~78% all HF content); **3. HF_los** "loose" flush out component (~22% all HF content). ***Assay type (5 rows):*** **(i)** Identification of damaged/dead cells using propidium iodide (PI)); **(ii)** Cell size using forward and side scatter; **(iii)** Cell cycle dependent changes in cell size using forward scatter versus DNA content (DRAQ5); **(iv)** Cell cycle analysis using cyclin B1-GFP plots, versus DNA content (DRAQ5), line indicates the demarcation of the G2/M fraction with high/low signal; **(v)** Cell cycle histograms with manual analysis to derive G1,S,G2/M,>4n Polyploidy percentages; Vertical and horizontal dotted lines on each panel provide a means for visualising the assay across the row thus comparing each cell fraction with each other. *Note: [+]Data shown represent typical output, n=2x2 (independent experiments x individual HF). [++]Arrows (row iv) depict arrested and apoptotic fractions. [+++]Box (row iv) highlights a low G1 fraction accumulation in TC versus HF.*

After a 48h drug incubation the TC cells showed an elongated and progressive exit from mitosis without cytokinesis to a tetraploid cycle (G1tetra), this was only evident from the dual parameter plot of cyclin B1-GFP versus DNA content, as this G1tetra population accumulates at 4n and expresses low levels of cyclin B1-GFP. This fraction changes from the background non reporting level of 11% in the un-treated control to 20% and 65% at 24h and 48h post treatment respectively with Taxol (Figure 3.6). The exit from mitosis in the 48h Taxol incubation TC is also showed with an 10% increase on the polyploidy cell fraction (Figure 3.6- TC-iv), corresponding to a S and G2 polyploidy cycle phase (Stetra and G2tetra), verified by the >4n DNA content and the correspondent cyclin B1-GFP profile. In the HF model however the perturbation affect appeared to be attenuated; for instance, the overall G2/M cell arrested population accumulated from ~17% in the un-treated control to only 38% and 54% after a 24h and 48 hour drug exposure respectively (Figure 3.5-HF_adh-v and Figure 3.6-HF_adh-iv), with no visible increase in the polyploidy >4n population. These results were further confirmed by the analysis of cytospin samples, where nuclear labelling (with DRAQ5) indicated morphological consequences. Un-treated control cells in interphase presented a spheroid homogeneous shape (Figure 3.5-vii - solid arrows) while arrested cells in mitosis presented a brighter cluster of condensed chromosomes in the nucleus (dashed arrows), probably due to the production of multipolar spindles which ultimately induces abnormal chromosome segregation (Kelling et al. 2003). Additionally even after 48 hours of exposure to Taxol in the 34% HF-derived cells remained in G1.

The HF_adh results at 48h Taxol treatment showed a high percentage (G1=34% + S= 10%) of <4n cells in relation to the standard TC culture (G1=8% + S=10%), also evident in cyclin B1-GFP plot results (Figure 3.6-TC-iv-square box). Furthermore, the HF_los component results showed besides the <2n sub-G1, a <4n PI positive non-

viable cell fraction (Figure 3.6-HF_los-iv). This fraction correspond to cells that did not exit mitosis and become apoptotic with progressive DNA degradation, plus probably cells that actually breached the Taxol block but divided unequally producing aneuploid daughter cells (Gascoigne and Taylor 2009) that later also become apoptotic. This might be also applicable to the HF_adh component <4n population, some cells may actually be apoptotic aneuploid but not yet stained by PI or even viable cells returning to the cell cycle. The above Taxol treatment perturbations seem to be observed also in the results of the high confluency equivalent 12 well plate (Supplementary Information 3.6-7). It therefore remained unclear at this point whether the above described HF response to the low Taxol dose was due to: i) the cells in the HF being arrested or delayed in G1, consistent with the growth curve analysis, effectively reducing the overall cell cycle response to the drug (i.e. accumulation in G2/M) together with cell death without exiting the mitotic block; or ii) alternatively, must not exclusively, the cells may attempt to exit mitosis and divide resulting in an aneuploid population, that could be either viable or progress to apoptosis. The following section with the Colcemid kinetic analysis addresses this problem.

Overall, the therapeutically relevant (5nM) Taxol response in the HF–U2OS-GFP model is attenuated and more complex than in low confluency standard TC. This may be consequence of an altered growth rate and cell cycle traverse hence reducing the effective Taxol response. In addition drug micro-pharmacokinetic factors might influence the effective concentration of Taxol in the fiber such that the single cells in the HF were exposed to lower levels of the drug as a result of reduced diffusion.

#### 3.4.1.4 Determination of cell cycle traverse kinetics of cells growing in the HF

In the present chapter Colcemid was employed to assess the cell cycle traverse properties of the U-2 OS cells growing in the hollow fiber, namely the rate of G1 emptying and accumulation in G2/M. This would provide an assessment of the cell cycle traverse of the HF culture compared to standard TC conditions. Colcemid was selected due to: First, it presents a less complex cell response compared to Taxol, at least in short/medium term cultures. Second, the maintenance of the mitotic block with the preservation of cell integrity (with low death and corresponding cell disintegration) for more prolonged time periods compared to Taxol.

HF–U2OS-GFP *in vitro* cell cultures were exposed to sequential Colcemid treatment at different time points, to obtain cell cycle kinetic response at an early stage HF culture (prior to 5 days) and in more established HF cultures (10 day). Colcemid (60 ng/ml), was added at 72h (day 3) and 240h (day 10) to HF cultures to result in different exposures times to the drug. Together with parallel standard TC, namely 6 well plate low confluency (50%) and 12 well plate with high confluency (>100%) equivalent culture, plus the un-treated control (0h). Display plots of the HF cell cycle kinetics obtained from dual parameter cyclin B1-GFP versus DNA content are showed in Figure 3.7 together with the DNA content histogram analysis (see Supplementary Information 3.6-4 to 3.6-6 for full experimental results). A graph analysis summarising the cyclin B1-GFP versus DNA content population frequency percentages evolution with Colcemid exposure time from all the sampled time series flow cytometry results is available in Supplementary Information 3.6-8.

The TC low confluency culture 18-24h Colcemid exposure demonstrated that practical all cells accumulate in G2/M (75-68.7%) with the virtual emptying of G1 (14.2-10.3%), clearly visible on the cyclin B1-GFP versus DNA content (Supplementary Information 3.6-6). By contrary the G1 frequency for 24h and 48h Colcemid exposure in the HF_5 days was 7.1% and 17.8% while for HF_12 days was of 23.1% and 17.8% respectively (Figure 3.7-ii). This confirms that the encapsulated cells in the HF are to some extend delayed in G1. Equally the cell cycle transverse empting of G1 promoted by Colcemid was clearly different from the Taxol treatment. The previous section histogram results showed that for 24h and 48h Taxol exposure G1 was 49.7% and 34.1% (only the adherent component) respectively. These values may indicate that in the Taxol treatment the cells had attempted to exit mitosis resulting in an aneuploid or viable division, which would eventually "contaminate" the G1 phase.

Parallel to the G2/M arrest, the cyclin B1-GFP signal progressively decreased in 4n cells with Colcemid exposure time (Figure 3.7-i). At 48h the low reporting fraction (below $10^2$ arb. units) was 41.5% in the HF_5 days against 31.5% in the HF_12 days. The cyclin B1-GFP slow degradation could be due to cell progressing to an apoptotic state, as previously observed for HeLa cells (Sherwood et al. 1994b; Urbani et al. 1995). The results showed also minimal C-mitosis exit to polyploidy after 48h drug treatment, overall the value was similar to all HF and standard TC conditions (5-9%).

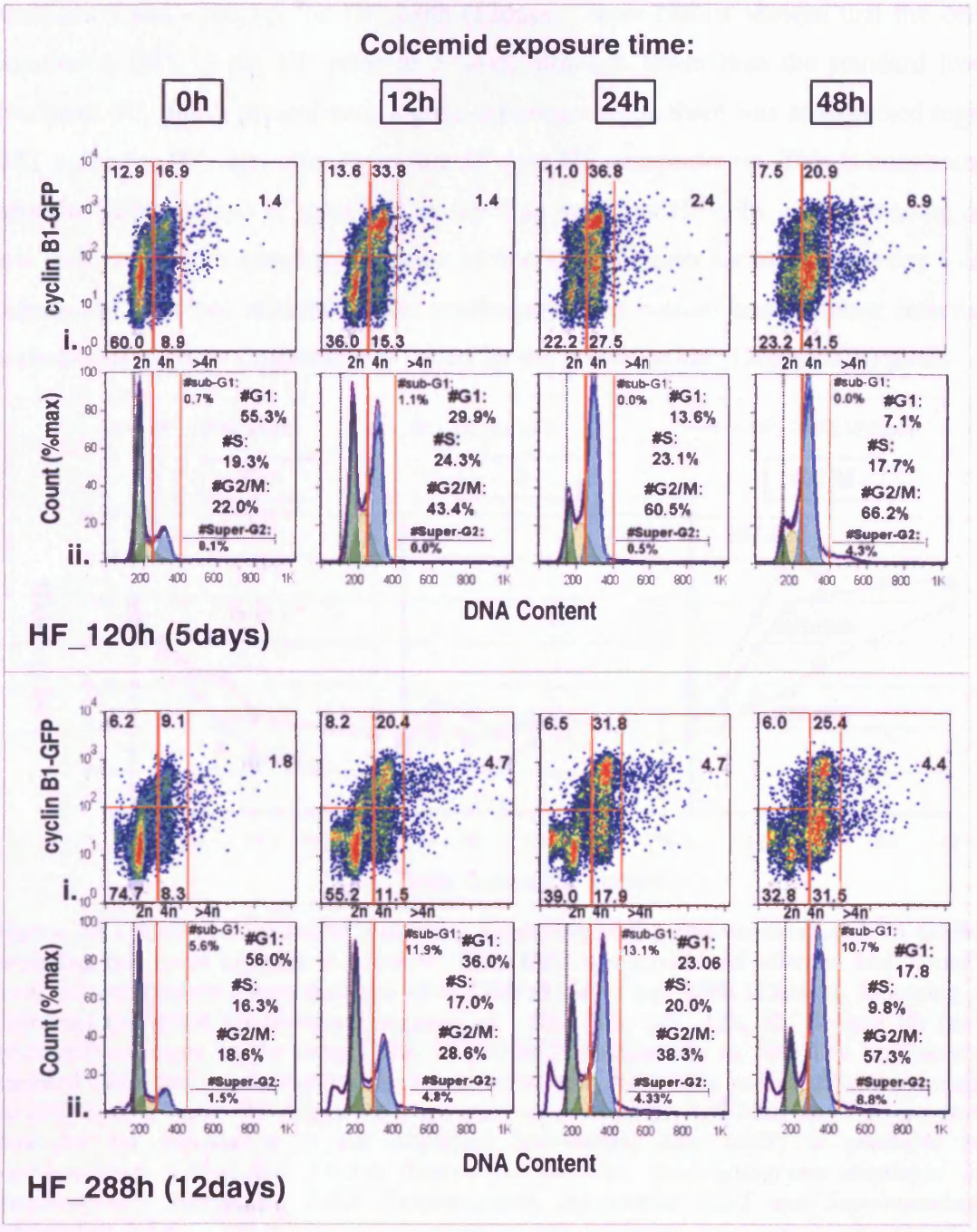


**Figure 3.7 – Cell cycle traverse analysis in cell populations growing in the hollow fiber (HF) between (a) 3-5 days and (b) 10-12 days.** All cells were analysed after **120h (5 days)** and **288h (12days)** following Colcemid (60ng/ml) pre-treatment regimen of 48h, 24h, 12h and 0h (no-treatment) exposure to the drug. The HF full population (combined adherent and "loose" flush out components) were analysed; **(i)** Dual parameter cell cycle analysis using cyclin B1-GFP versus DNA content (DRAQ5) and **(ii)** Cell cycle DNA content (DRAQ5) histograms. Cell cycle phase fitting statistical data (#) obtained using the Dean-Jet-Fox model with a RMS error average value of 16.3 (sd±3.9) for the presented fittings. *Note: [+]Orange lines segment the dot plots to show corresponding distribution (%) according to 2n, 4n and >4n (vertical) and high and low GFP fluorescence (horizontal).*

A summary of the cell cycle kinetic curves was plotted in Figure 3.8. The calculated inter-mitotic time (IMT) was ~24h for HF_120h (5days), ~20h for TC 50%

confluency and ~36h for the HF_288h (12days). These results showed that the cell population IMT in the HF prior to 5 days, although lower than the standard low confluent TC, didn't present such a great difference while there was an expected high IMT value for HF cells after more that 10 days HF encapsulation. This is consistent with the SEM analysis (Figure 3.2) at day 2 showed that HF cells were spreading at low confluency with reasonable amount of free HF wall inner surface and by day 5 of culture the cells had attained higher confluency. This culture time window interval corresponds to when Colcemid was added for the presented HF_120h (5days) plots.

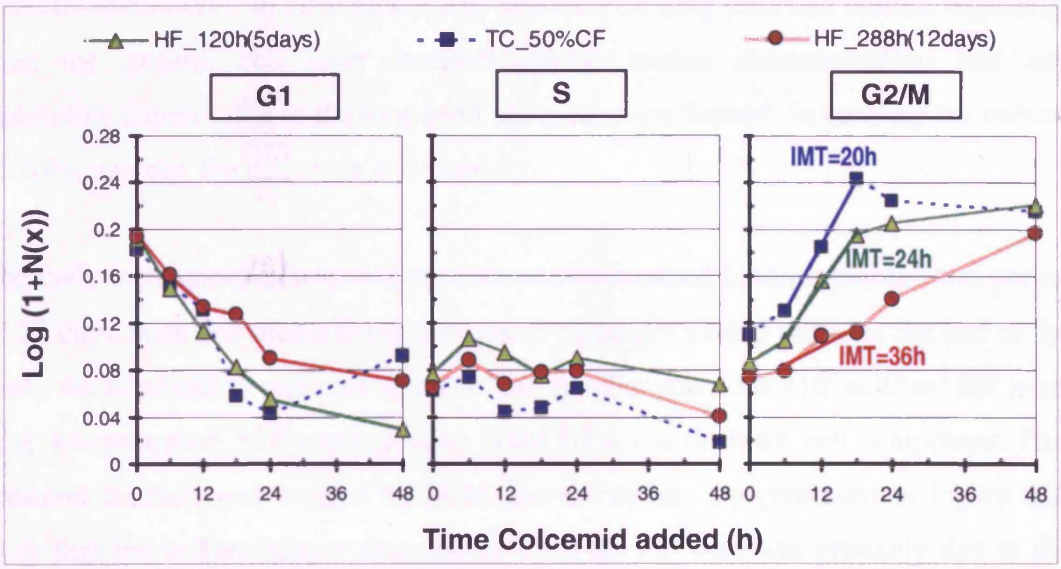


**Figure 3.8 – Cell cycle traverse summary, emptying of G1 and accumulation in G2/M depicting cell cycle kinetics.** All hollow fiber (**HF**) cells (combined adherent and "loose" flush out components) were analysed after **120h (5 days)** and **288h (12days),** following a Colcemid (60ng/ml) pre-treatment regimen of 48h, 24h, 18h, 12h, 8h, 6h and 0h (no-treatment) exposure to the drug. The **TC_50%CF** corresponds to 50% low confluency standard tissue culture with equivalent drug pre-treatment. *Note: ⁺The variable N(x) represents the cell fraction value (0.0-1.0) at the given cell cycle phase (G1, S, G2/M). Starting equation used for the calculation of the displayed inter-mitotic time (IMT) is available in Supplementary Information 3.6-7-b.⁺⁺Source for full flow plots/histograms displayed in Supplementary Information 3.6-4, Supplementary Information 3.6-5 and Supplementary Information 3.6-6.*

Overall, this section suggests that in comparsion to the low confluency standard TC, the HF–U2OS-GFP population, especially after 4-5 days in culture, presented a progressive decrease in the cell cycle traverse, with some cells exiting the cell cycle in G1. Further, this overall slower traverse does not explain totally the previous finding of Taxol-induced low G1 emptying and accumulation in G2/M. The findings support the proposal that Taxol (5 nM) treated cells may have attempted to exit

mitosis resulting in an aneuploid or viable division. Further confirmation could be obtained by tracking the progression of bromodeoxyuridine (BrdU) labelled cells through into the subsequent cell cycle under Taxol exposure (Rothaeusler and Baumgarth 2001; Terry and White 2001).

### 3.4.2 Long term (27days) HF–U2OS-GFP cell culture

The HF–U2OS-GFP *in vitro* model was assessed for long term cell culture regarding: First the general cell layer morphology/organization characterization and any distinctive features due to the long term encapsulation; Second, to measure the culture activity, namely, the cell cycle and viability.

The cells were encapsulated in 2 cm HFs and maintained *in vitro* culture for a period of 27 days, with cell media being periodically changed each 5 days. At the end of the assay the total cell or particles above 8.7μm number was ~3.6 x$10^5$ cell/$cm^2$ HF inner area, where approx 35% corresponded to the HF loose flush out cell component. This adherent fraction was imaged by SEM and the results are presented in Figure 3.9. Note that the cell multilayer detachment from the HF wall was probably due to the fixation/longitudinal cut or SEM protocol handling (Figure 3.9-a). The adherent cells grow inside the HF organized in a multilayer cell matrix with a thickness of roughly 20 μm (Figure 3.9-b1). Also, high amount of small "globular structures" on top of the cell layer are visible, probably cell debris or the remains of death cells (Figure 3.9-b2 and c2).

The 27 days HF cells were retrieved and analysed using flow cytometry, the full cellular content was allocated to two components, the "loose" component easily flushed out from the fiber and the adherent inner wall component, depicted in the above SEM. The representative flow cytometry profiles are presented in Figure 3.10. These plots showed that the HF_los component was constituted like expected mainly (56%) of PI positive cells (Figure 3.9-HF_los-row i). The fraction with low forward scatter and PI fluorescence just bellow $10^2$ arb. units may also represent cell debris where the nucleus was too fragmented.

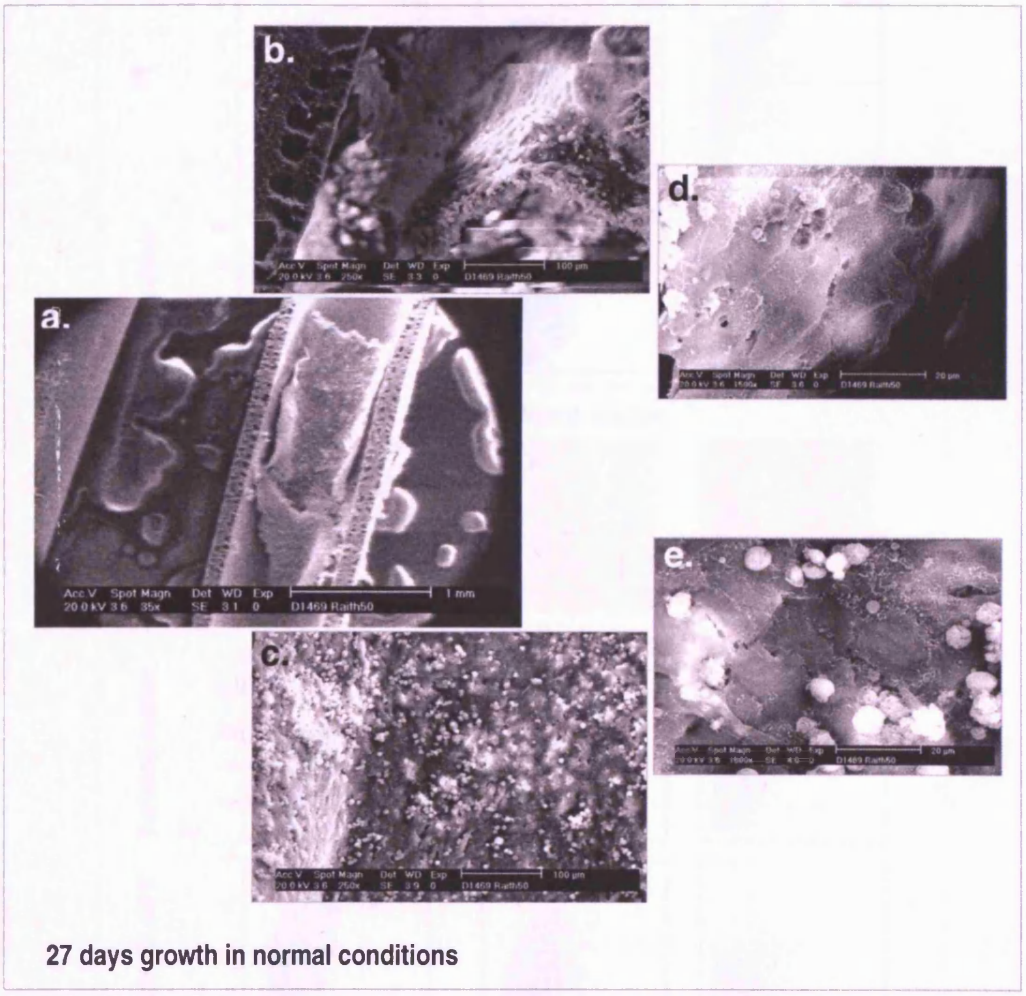


**Figure 3.9 – Cell arrangement and packing in the hollow fiber after 27 days.** Scanning electron microscopy (SEM) images to show the adherent cell layer (HF_adh) located on the inside of the hollow fiber. **(a-e)** Longitudinally cut fiber to reveal the inner surface at 27 days; with progressive zooming (bar represents 1000, 100, 100, 20 and 20 µm respectively). *Note: $^{+}$Cell multilayer detachment from the inner wall (a,b) with small round "particles" on top (c,e), probably debris or dead cells. $^{++}$Cells loaded at ~1.0 x10$^{6}$ cells/ml and fresh medium provided every 5 days.*

Importantly the cyclin B1-GFP expression profile and cell cycle obtained from DNA histograms for the HF_adh component after 27 days, presented on Figure 3.10 HF_adh - row v and vi, was similar to the HF 8 days culture (Figure 3.4). The 27 days cyclin B1-GFP reporter system presented a characteristic dynamic range for the HF, cyclin B1-GFP G1 to G2 mean fluorescence increase was of 22 (sd±36) to 184 arb. units (sd ±180) respectively, and a low reporting fraction of 33% of the G2/M population.

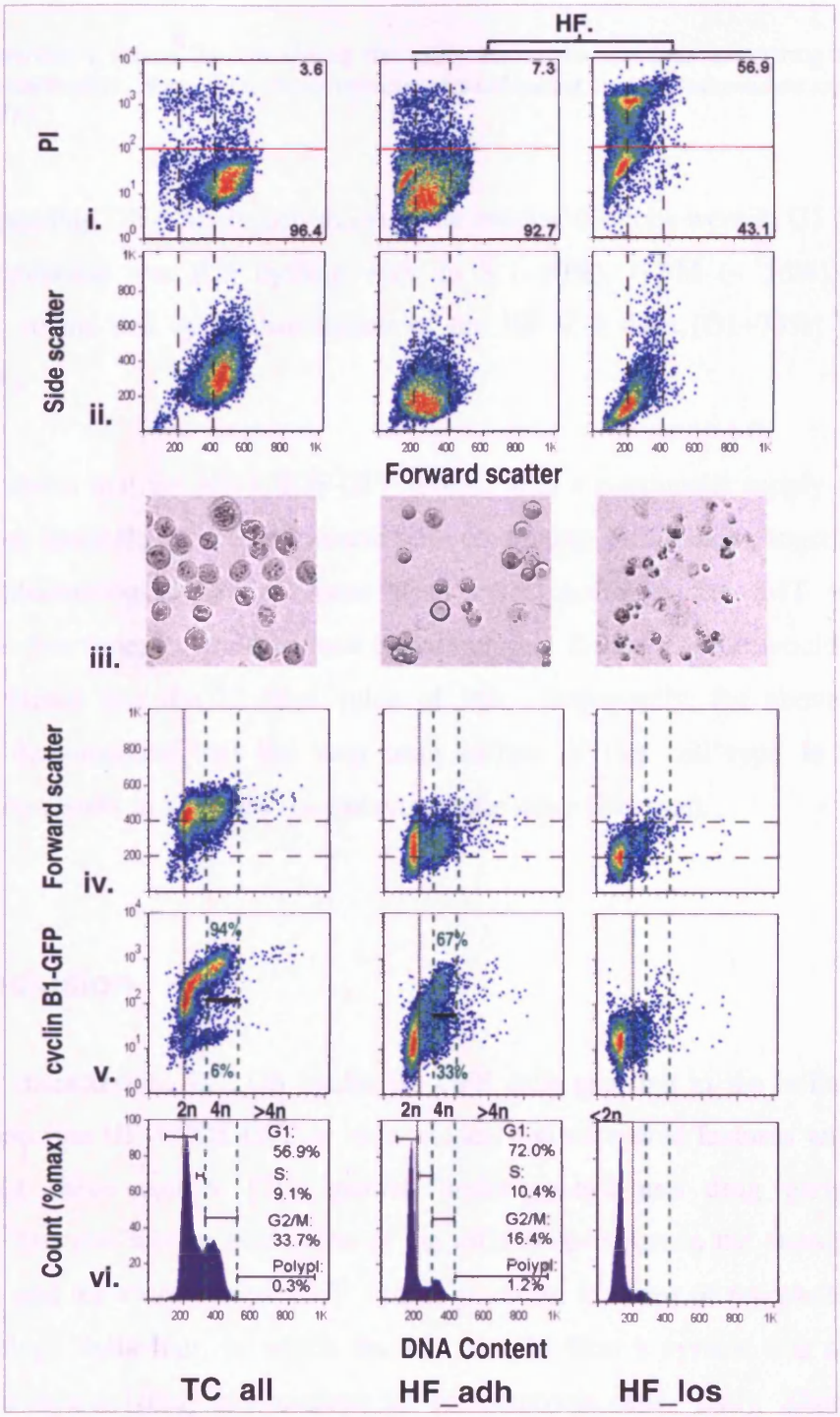


**Figure 3.10 – Flow and image cytometry analysis of cells retrieved from the hollow fiber (HF) after 27 days versus standard tissue culture (TC).** Panels present the cell sample analysed versus the assay performed: ***Cell sample (3 columns)*:** **1. TC_all** - All cells retrieved from a medium confluency (80%CF) standard tissue culture; **2. HF_adh** - Adherent component requiring trypsinization (~65% all HF content); **3. HF_los** "loose" flush out component (~35% all HF content). ***Assay type (6 rows)*:** **(i)** Identification of damaged/dead cells using propidium iodide (PI)); **(ii)** Cell size using forward and side scatter; **(iii)** Cell morphology using bright field transmission image (field dimensions: 128x128µm) of the same samples in the plots; **(iv)** Cell cycle dependent changes in cell size using forward scatter versus DNA content (DRAQ5); **(v)** Cell cycle analysis using cyclin B1-GFP plots, versus DNA content (DRAQ5), line indicates the demarcation of the G2/M fraction with high/low signal; **(vi)** Cell cycle histograms with manual analysis to derive G1,S,G2/M,>4nPolyploidy percentages; Vertical and horizontal dotted lines on

each panel provide a means for visualising the assay across the row thus comparing each cell fraction with each other. *Note: Data shown represent typical output, n=1x2 (independent experiments x individual HF).*

The corresponding DNA histogram showed that most of the cells were in G1 (~72%), and the population was still cycling with an S (~10%), G2/M (~ 16%) phases, comparable to the cell cycle distribution of the HF at 8 days (G1~73%; S~13%; G2/M~15%).

Overall, it seems that the HF–U2OS-GFP model, with a continuous supply of fresh nutrients, can maintain cell cycle traverse with continuous proliferation together with the accumulation/degradation of loose dead cells. Although the IMT was not measured at this time, it would be safe to assume that the IMT value would remain similar or higher that the 12 days value of 36h. Importantly, the above results apparently demonstrated that the long term culture of this cell type in the HF encapsulation results in a "stable" monolayer on the inner fiber wall.

## 3.5 Conclusion

This study characterised U-2 OS cyclin B1-GFP cells growing in the hollow fiber encapsulation [the HF–U2OS-GFP *in vitro* model] and compared features with those for standard tissue culture (TC) growth under control and drug perturbation conditions. The aim was an evaluation of the differences between the classic planar surface TC and the more complex HF culture platform in terms of morphology and cellular biology behaviour, to which the HF model offers a system that could be viewed as a suitable assay environment for osteosarcoma cells. Only Zhang et al. 2004 has previously described the culture of U-2 OS in the HF, both *in vitro* and also *in vivo*, but a major characterization has not been performed against its TC counterpart.

The HF–U2OS-GFP produced a predictable and reproducible consistent linear cell growth, with a mean population doubling of ~53h (2.2 days) over 8-9 days culture for 10% FCS serum content in the media. The HF cells presented a reduced cell growth

rate compared to the TC culture seeded to an equivalent starting cell density (~2.5 $x10^4$ cell/$cm^2$). This was vary apparent after 5 days when this TC culture reached maximum density with more than a 3 fold cell increase compared to the HF at the same time point. Several factors may contribute to this difference in overall growth rate between the HF and the TC cultures:

The first factor could arise at the initial seeding stage where an uneven cell distribution after seeding in the HF cells could accumulate and aggregate on one side of the HF compared to the even distribution achieved in TC. SEM observations, however reveals that the cells after 2-5 days actively spread and uniformly cover the entire HF inner wall (Figure 3.2) and the measured IMT at 4-5 days was only 4 hours longer than a low density TC culture.

The second factor cell attachment on the HF hydrophobic PVDF porous membrane and the TC hydrophilic polystyrene treated surface may differ providing effectively different plating efficiency. The TC polystyrene treated hydrophilic surface, has been developed to optimise cell attachment and growth of cell lines, representing the benchmark for planar TC cultures, namely for drug screening (NCI 60 panel)(Sharma et al. 2010). The porous PVDF potentially presents a non-ideal surface for adherent cell proliferation due to the membrane surface "topography" and material composition, namely its hydrophobic nature. However recent studies (Wlodkowic et al. 2009) have compared U-2 OS cell proliferation in a standard TC treated surface versus high hydrophobic polydimethylsiloxane (PDMS) surface in a planar 2D culture. No major difference was found between these surfaces relatively to U-2 OS cell growth, viability and cell cycle distribution up to a 5 days culture (Wlodkowic et al. 2009). Additionally, the observed U-2 OS cell morphology in the HF using SEM showed a normal anchorage-dependent monolayer, analogous to the TC standard, this is different to the cells on hydrophobic PDMS surfaces where the cells show a highly motile and polarised morphology (Errington et al.- unpublished). Therefore, evidence in this current work and that of others indicate that the cell growth differences between the HF and the TC can not be directly attributed to the hydrophobic nature *per se* of the surface. In addition U-2 OS clonogeniccapacity has not been shown to be attenuated by a PDMS hydrophobic surface (Errington et al unpublished results).

Further to this, previous studies by others (Klee et al. 2003; Rodrigues et al. 2008) have used PVDF as a biomaterial established for soft tissue applications looking at functionalised PVDF surfaces. These studies using primary human osteoblasts showed that surface activation of PVDF with plasma treatment and subsequent surface functionalisation indicated prolonged proliferation and survival after 8 days. However the studies provide informative insights into the biocompatibility of untreated PVDF surface (essentially representing the inner surface of the HF). Proliferation studies showed that midterm growth capacity was reduced 2-fold, but after 8 days all functionalised surfaces (including TC plastic) out performed untreated PVDF by at least 4-fold. In contrast to the Klee et al. 2003 studies the untreated hydrophobic surface of the hollow fiber inner wall however does show considerable topographic features in both the micro and nano range; it consists of 70-80 nm pores sporadically distributed (3-10 pores per $\mu m^2$ area) across a layered extruded PVDF with an appearance of "pits and crevasses" with less than 100 nm width (Figure 2.1-b), this probably provides sufficient cues for the U-2 OS cells to take on a normal adherent morphology (Figure 3.2-c,d), but perhaps does not provide sufficient receptor-mediated cues for signalling and good cell growth.

The final factor to address is the closed geometry of the HF cell culture platform where the cells are confined to growing on the inside of a semi-permeable tubular structure while the TC conditions provides an open planar surface. The cells in the TC grow in a planar surface on bottom of a well/dish in direct contact with media volume content. By contrast the cell in the HF is encapsulated in a closed tubular 3D geometry and grow attached to the inner membrane, where the total cell culture is limited by the geometric constraint of the close fiber. The semi-permeable porous membrane wall constitutes an artificial barrier that separates the tumour cells from their surroundings. This wall may inhibit the transport of very large molecules (i.e. above the 500kD molecular weight cut-off value), and may slow down the mass transfer of rapidly used low molecular weight molecules, such as oxygen and glucose, from the surrounding medium to the tumour cells (Casciari et al. 1994). Generally porous membranes and/or hollow fibers are characterized by the differential permeability of molecules between the HF lumen and the outside media, presenting diffusion coefficients dependent on the particle diameter and structure (Granicka et al. 2003). The manufacturing process influences the PVDF membrane pore structure and

permeability to molecules and gas (Atchariyawut et al. 2006; Wang et al. 1999). Although no concrete values are available to the specific PVDF hollow fiber used in the present study, other works with PVDF hollow fibers of higher pore size revealed an effect on reducing mass transfer including molecules such as bovine serum albumin (BSA) (Lu et al. 2005a). Furthermore the U-2 OS cells were grown *in vitro* inside the HF without agitation. So in general, compared to the TC where there is no membrane barrier, it may be possible to consider that in the HF due to the semi-permeable membrane barrier a gradient would be generated relatively to the diffusion of cell nutrients/waste between the HF lumen and the outside media. The consequences of growing in this configuration, where the cells retain a 2D phenotype but grow on a HF lumen will be further investigated using microarray analysis.

The SEM visualization showed that the HF inner surface provided a suitable substrate for cell growth and active spreading. The cells grew in the HF encapsulation forming an almost uniformly distributed adherent monolayer on the inner wall after 8 days (Figure 3.3). This is very different for example from Ewing's sarcoma tumours which also grow as adherent monolayers in TC but formed well-organised multi-cellular spheroids with a necrotic core in the HF (Bridges et al. 2006). Surprisingly, unlike other cell types (e.g. the SW620 colon carcinoma cell line) that form "solid" masses inside the HF when grown over fifteen days (Casciari et al. 1994), the U2OS-GFP cultures cells retained a monolayer or thin multi-layer sheet. Even after 27 days encapsulation the U2OS-GFP model did not progress to a high level multi-layer or aggregates organization that partially filled the HF lumen, which might be considered as "emulating" a solid tumour (Casciari et al. 1994).

In this study the encapsulated U-2 OS cells grown in both TC and HF conditions show a "strictly" anchorage dependent monolayer with a predominant hexagonal cell morphology when confluent. This U-2 OS morphology matches previously described *in vitro* conditions, and were similar to other osteosarcoma cells (i.e. SaOS-2 and 143B); U-2 OS cells have been shown to be the least capable of forming anchorage independent colonies (Dass et al. 2006). This low ability to grow in a cell mass or in a multilayer culture *in vitro* seems to have some translation to the behaviour of these cells *in vivo*. U-2 OS xenographs in general, were considered low tumorigenic in mice while grafting the cells subcutaneously (Ek et al. 2006; Manara et al. 2000) and non-

tumorigenic when orthotopically administered to the tibias (Dass et al. 2006), but present a high pulmonary metastatic ability rate following lateral tail vein injection (Manara et al. 2000).

The current study has shown that the cyclin B1-GFP reporter remains intact in the HF model and provides a detailed cell cycle readout together with DNA content to decipher cell cycle status and responses, providing information in cell cycle status. The HF–U2OS-GFP rate of cell cycle traverse is not constant through the culture period. The cell cycle traverse rate decreased between day 5 and day 12 by ~2 fold. The HF presented an IMT comparable to standard low confluency TC (20-25h), prior to 4-5 days. This progressively decrease and stabilized after this time point, with an IMT of ~37h at 11-12 days encapsulation. Cell cycle analysis showed a higher accumulation in G1(/G0) in the HF but the evidence for a permanently arrested or quiescent HF population was inconclusive. Serum starvation in tissue culture of a U-2 OS cell has been shown to cause quiescence (G0 accumulation) and provides a classic approach to synchronise the population (Zhang et al. 2003). However the Colcemid results although presented a minimum of 10% of the population always in G1(/G0) further assays are necessary to confirm if this population is truly quiescent. Furthermore although the proportions of non-viable cells continually increased inside the HF as the loose cell component sub-fraction. The HF still sustained a proliferative profile up to 27 days with a cell cycle distribution similar to 8 days culture. So it is true that the HF culture conditions or environment do not cause widespread serum starvation, even for long term culture up to 27 days.

The reduced cell growth rate and slower cell cycle traverse, plus the low cell size correlates with the observed densely pack tubular HF inner wall cell layer organization (SEM - Figure 3.3). In contrast to the high cell cycle traverse and bigger cells of the low confluency (50-75%) TC.

The SEM showed that the response to the clinical relevant low dose of Taxol (5 nM) resulted in a high perturbation of the HF inner wall uniform cell layer into an irregular mesh of cell clumps. Single cell analysis revealed more complex cell fates in the HF culture conditions. These included a higher cell death rate and also more cells routed to aneuploidy. Aneuploidy has been previously observed in standard TC with U-2 OS

cells using identical Taxol doses (Brito and Rieder 2009). However in the current study this outcome was less evident for the low density TC conditions, where most of the cells appeared to breach mitosis without undergoing division to a polyploidy state (G1tetra). Complementary assays, such as BrdU analysis of DNA replication patterns would provide further evidence for this subtle difference.

Therefore it appears that in response to Taxol, HF encapsulation enhances overall cytotoxicity, compared to low density TC conditions, where the cells appeared to not experience a catastrophic mitosis and therefore appear to be drug resistant. Although the more complex HF-Taxol drug response, with multitude of cell fates, is scientifically more pertinent for the study of the mechanisms and timing of cell death through the cell cycle that "mirrors" the clinical cases (Gascoigne and Taylor 2009). Furthermore, since the data represents an *in vitro* controlled response of the HF model with a clinical dose of Taxol, this result acts as a reference for cell activity *in vivo*. Following the initial proposal by Suggitt et al. 2004 this would allow the interrogation of the drug dynamic cell response mechanisms, using the HF as a transferable culture platform. An example for this line of approach was the recent work of (Wang et al. 2007) who investigated a biochemical cell therapeutic target in both *in vitro* TC and *in vivo* subcutaneous xenografts. A study that employed a small interfering RNA to down-regulate stathmin (Oncoprotein18), a signal transduction regulatory factor, to investigate the potential of this protein as a therapeutic target for human osteosarcomas with the combined use of taxanes.

The current Chapter confirms the difference in studying the cell proliferative activity and drug responses in the HF comparatively to the TC. The detailed biological assessment of the changes in the cell signalling response related with the shift from a standard planar TC to the HF culture platform would be invaluable to further understand this model. Chapter 4 starts to address this point, where gene profiling analysis informs on the wider molecular machinery differences between the HF model versus standard 2D TC.

## 3.6 Supplementary Information

**Supplementary Information 3.6-1:** A typical example of the flow cytometry analysis protocol. **(a)** HF control (un-treated) and **(b)** 24h Taxol drug pre-treatment.

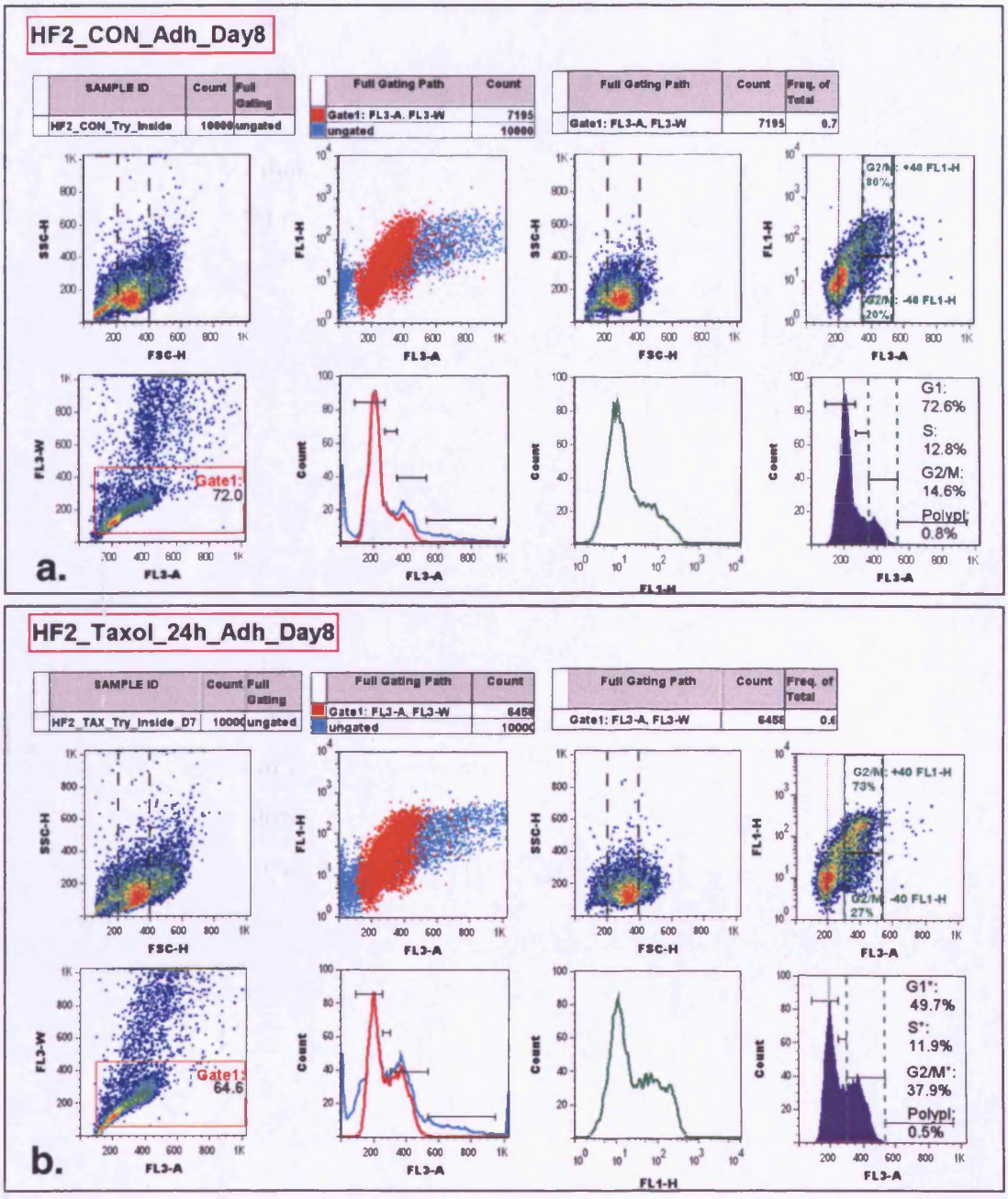


**Figure 3.11 – Example plot/histograms of the flow cytometry analysis protocol performed for the cells retrieved from the hollow fiber (HF2_CON_Adh_Day 8) versus a Taxol treated counterpart (HF2_Taxol_24h_Adh_Day 8). (a)** Hollow fiber (HF) control (un-treated) and **(b)** 24h Taxol drug pre-treatment. Gate 1 (red) based on DNA content (DRAQ5) channel FL3-W(width) versus FL3-A(area) therefore ungated (cyan). Gating was applied to all plots and cell cycle distribution was calculated manually (G1,S,G2/M,>4nPolyploidy) . Gate 1 population was used in the presented results accordingly, namely side (SSC-H) versus forward (FSC-H) scatter together with cyclin B1-GFP (FL1-H) versus DNA content (FL3-A) plots and cell cycle histograms were constructed. *Note: For all the PI (dead cell analysis) samples a "mirror" forward and side scatter gate of Gate1 for the corresponding samples was applied.*

**Supplementary Information 3.6-2:** A typical example of the flow cytometry analysis protocol. **(a)** HF control (un-treated) and **(b)** 24h exposure to Colcemid 60ng/ml.

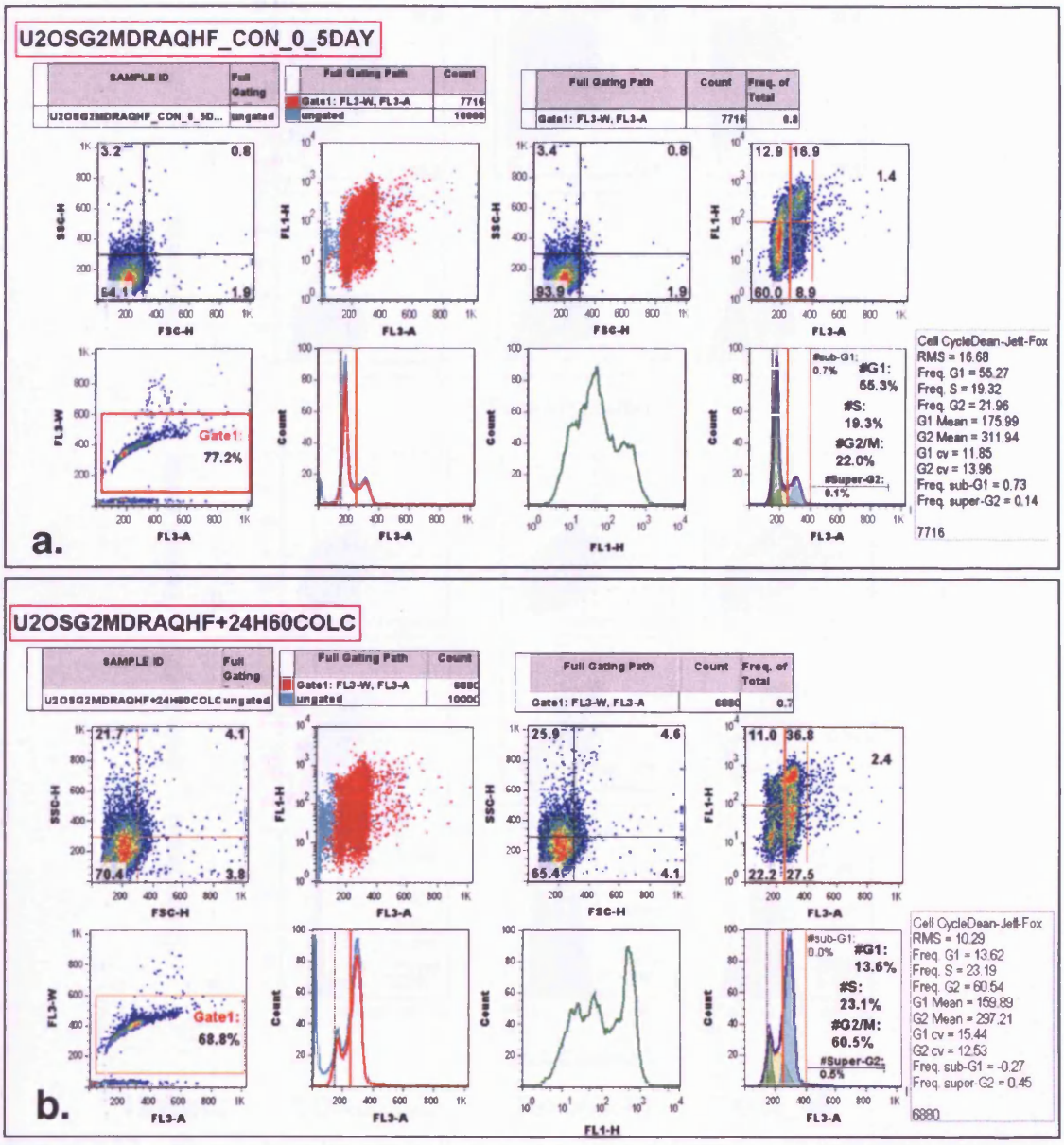


**Figure 3.12 – Example plot/histograms of the flow cytometry analysis protocol performed for the cells retrieved from the hollow fiber versus a Colcemid treated counterpart. (a)** Hollow fiber (HF) control (un-treated) and **(b)** 24h Colcemid (60ng/ml) drug pre-treatment. Gate 1 (red) based on DNA content (DRAQ5) channel FL3-W(width) versus FL3-A(area) therefore ungated (cyan). Gating was applied to all plots and cell cycle distribution was calculated using the Dean-Jet-Fox model (Fox 1980) FlowJo v.7.5.5 incorporated function with the RMS (root mean square) error for the presented fittings (G1,S,G2/M,>4nPolyploidy). Gate 1 population was used in the presented results accordingly, namely side (SSC-H) versus forward (FSC-H) scatter together with cyclin B1-GFP (FL1-H) versus DNA content (FL3-A) plots and cell cycle histograms were constructed. *Note: For all the PI (dead cell analysis) samples a "mirror" forward and side scatter gate of Gate1 for the corresponding samples was applied.*

**Supplementary Information 3.6-3:** 12 well plate high confluency (>100%CF) after 192h (8 days).

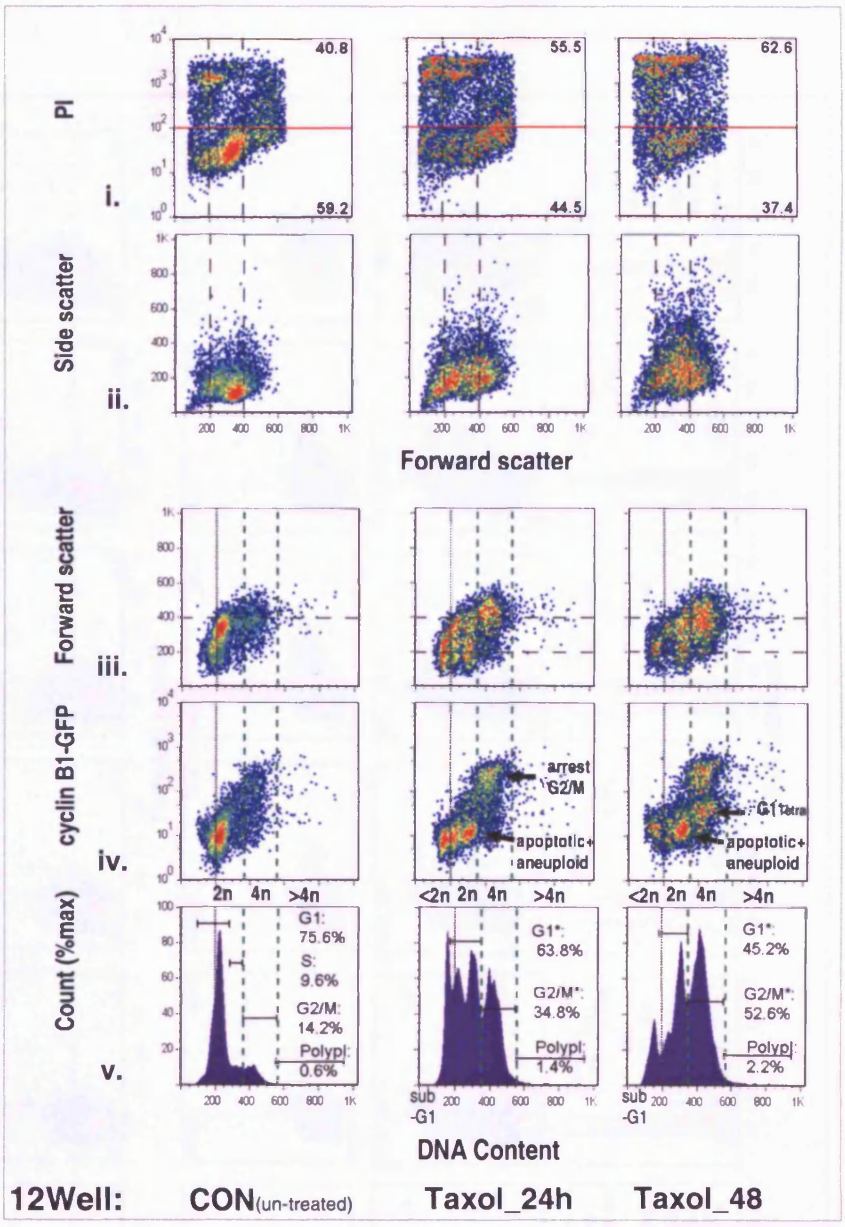


**Figure 3.13 – Flow cytometry analysis of cells retrieved from the 12 well plate standard tissue culture after 192h (8 days).** 12 well high confluency (>100%CF) standard tissue culture (TC) plate, with estimated cell/area seeding density by well set to be similar to the HF loading starting cell density (estimate ~2.5 x$10^4$ cell/$cm^2$). Taxol drug (5 nM) added at 144h (day 6) and 168h (day 7) to achieve a 48h and 24h pre-treatment respectively, all sample retrieved at 192h (day 8). Panels present the cell sample analysed versus the assay performed: ***Cell sample (3 columns):*** **1. CON** - All cells retrieved from an untreated control; **2. Taxol_24h** - 24h Taxol drug pre-treatment; **3. Taxol_48h** - 48h Taxol drug pre-treatment. ***Assay type (5 rows):*** **(i)** Identification of damaged/dead cells using propidium iodide (PI)); **(ii)** Cell size using forward and side scatter; **(iii)** Cell cycle dependent changes in cell size using forward scatter versus DNA content (DRAQ5); **(iv)** Cell cycle analysis using cyclin B1-GFP plots, versus DNA content (DRAQ5), line indicates the demarcation of the G2/M fraction with high/low signal; **(v)** Cell cycle histograms with manual analysis to derive G1,S,G2/M,>4n Polyploidy percentages; Vertical and horizontal dotted lines on each panel provide a means for visualising the assay across the row thus comparing each cell fraction with each other. *Note: [+]Data shown represent typical output, n=2xl (independent experiments x individual wells). [++]Arrows (row iv) depict arrested and apoptotic fractions.*

**Supplementary Information 3.6-4:** HF_122h(5days) Colcemid kinetic analysis.

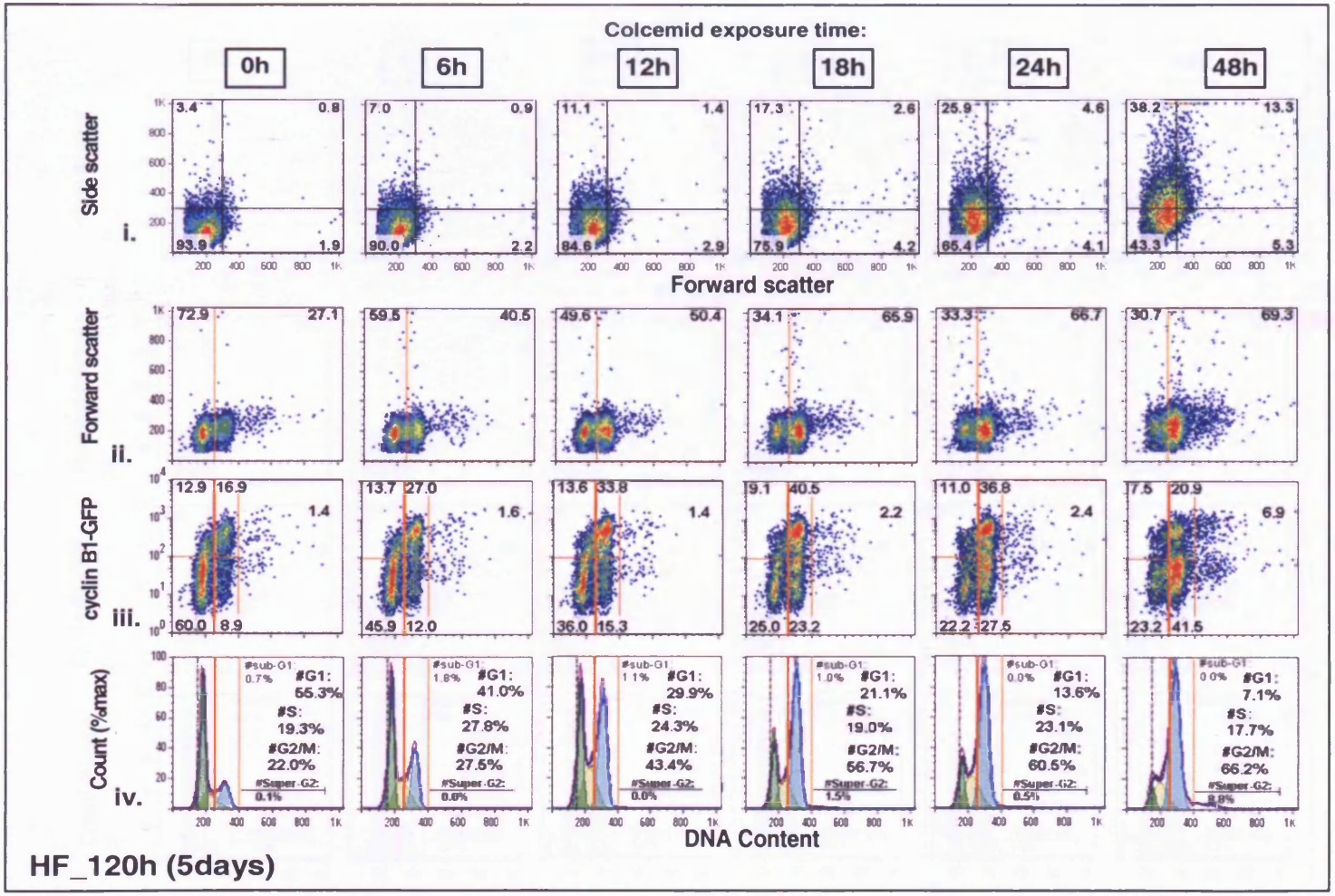


**Figure 3.14 – Flow cytometry Colcemid profiles at different time points to determine cell cycle kinetic analysis, from cells growing in the hollow fiber (HF) between 3-5 days.** All cell content (combined adherent and "loose" flush out components) were retrieved after **120h (5 days)** following Colcemid (60ng/ml) pre-treatment of 48, 24, 18, 12, 8, 6 and 0 h (no-treatment) exposure to the drug (columns). The cells were retrieved from all samples at the same time point (0h) after the different exposures. Assay type (rows): **(i)** side and forward scatter; **(ii)** forward scatter versus DNA content (DRAQ5); **(iii)** cyclin B1-GFP versus DNA content plots and **(iv)** cell cycle DNA content (DRAQ5) histograms. # cell cycle phase statistical data obtained using the Dean-Jet-Fox model with a RMS (root mean square) error average value of 13.2 (sd ±2.6) for the presented fittings.

**Supplementary Information 3.6-5:** HF_288h(12 days) Colcemid kinetic analysis.

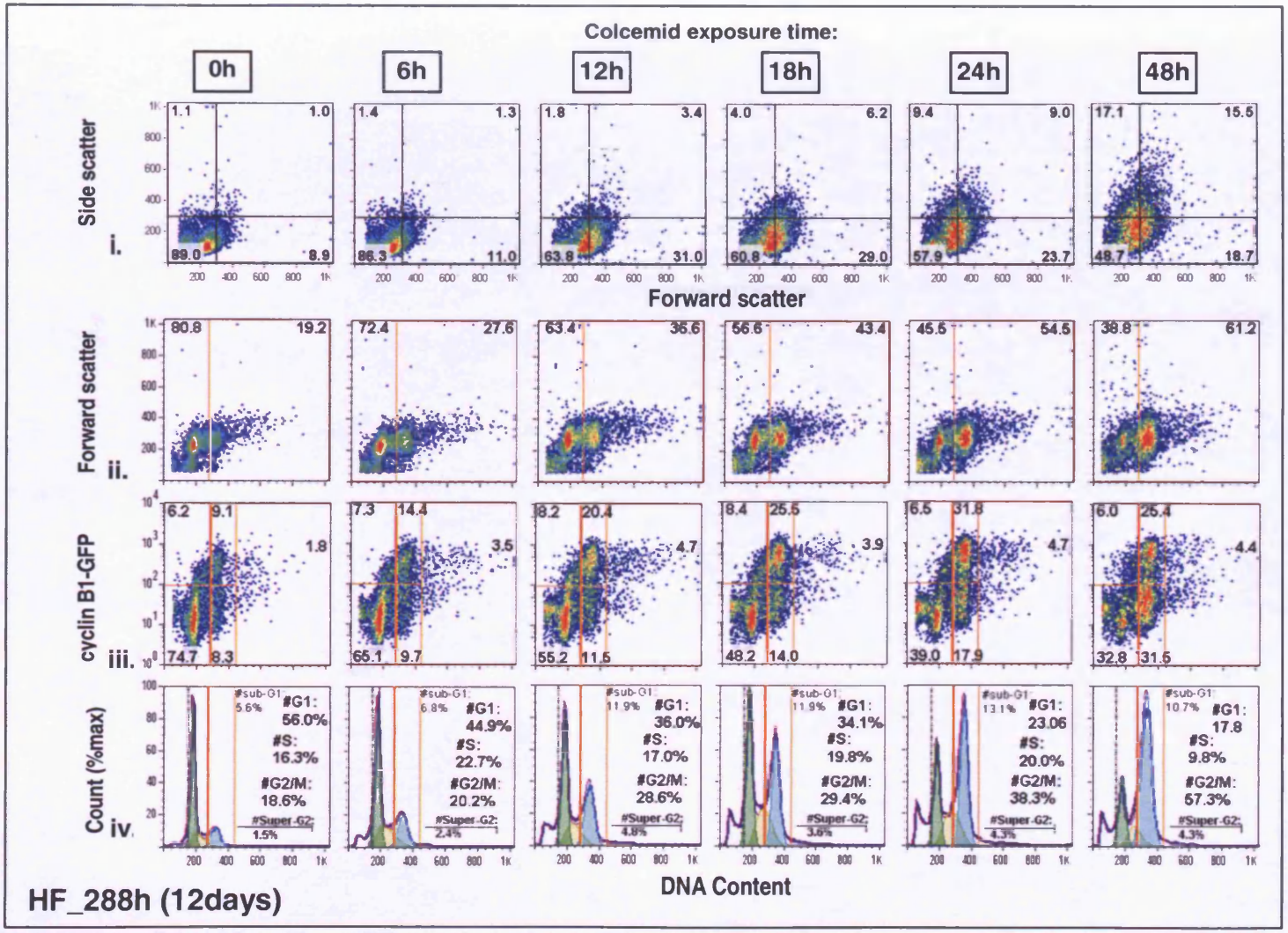


**Figure 3.15 – Flow cytometry Colcemid profiles at different time points to determine cell cycle kinetic analysis, from cells growing in the hollow fiber (HF) between 11-12days.** All cell content (combined adherent and "loose" flush out components) were retrieved after **288h (12days)** following Colcemid (60ng/ml) pre-treatment of 48, 24, 18, 12, 8, 6 and 0 h (no-treatment) exposure to the drug (columns). The cells were retrieved from all samples at the same time point (0h) after the different exposures. Assay type (rows): **(i)** side and forward scatter; **(ii)** forward scatter versus DNA content (DRAQ5); **(iii)** cyclin B1-GFP versus DNA content plots and **(iv)** cell cycle DNA content (DRAQ5) histograms. # Cell cycle phase statistical data obtained using the Dean-Jet-Fox model with a RMS (root mean square) error average value of 18.9 (sd ±1.8) for the presented fittings.

**Supplementary Information 3.6-6:** 6 well TC low confluency (50%CF) plate Colcemid kinetic analysis.

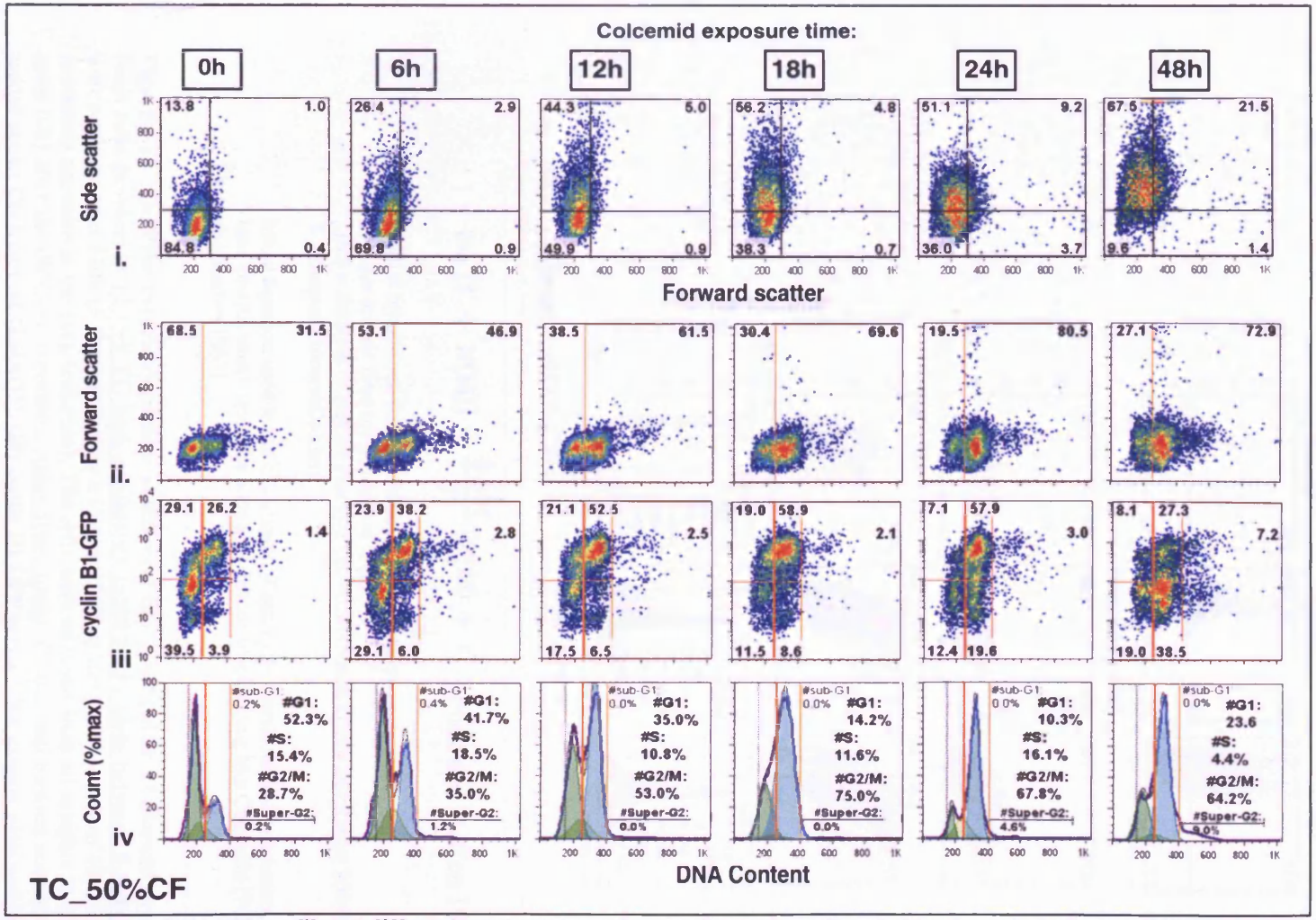


**Figure 3.16 – Flow cytometry Colcemid profiles at different pre-treatment times to determine cell cycle kinetic analysis, from cells growing in a 6 well TC low confluency (50%CF) plate between 3-5 days.** All cells were retrieved from a 6 well standard tissue culture plate (**TC**) after **120h (5 days)** following Colcemid (60ng/ml) pre-treatment of 48, 24, 18, 12, 6 and 0 h (no-treatment) exposure to the drug (columns). The cells were retrieved from all samples at the same time point (0h) after the different exposures. Assay type (4 rows): **(i)** side and forward scatter; **(ii)** forward scatter versus DNA content (DRAQ5); **(iii)** cyclin B1-GFP versus DNA content plots and **(iv)** cell cycle DNA content (DRAQ5) histograms. # Cell cycle phase statistical data obtained using the Dean-Jet-Fox model with a RMS (root mean square) error average value of 10.6 (sd ±3.0) for the presented fittings.

**Supplementary Information 3.6-7:** (**a**) 12 well TC high confluency (>100% culture) plate Colcemid kinetic analysis; (**b**) equation used for the calculation of the IMT.

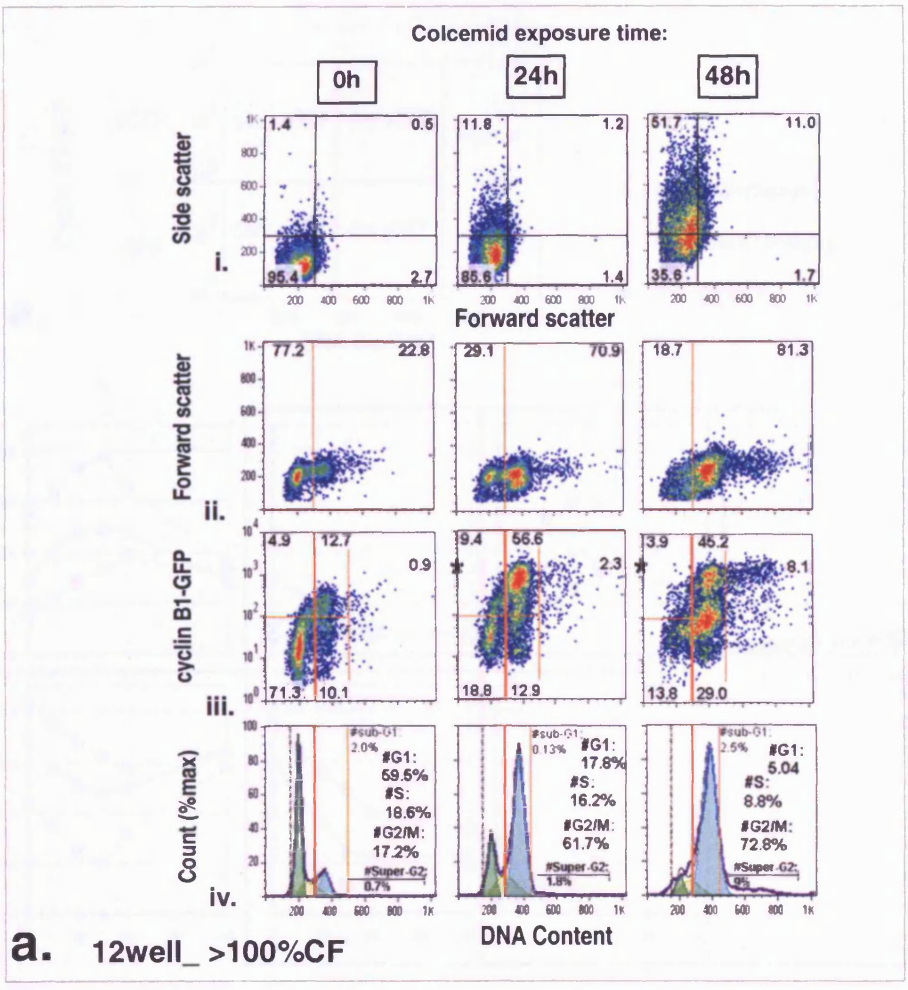


$$\log [1 + N(M)] = \frac{0.301}{T} [T(M) + t] \quad \text{(Puck and Steffen 1963)}$$

**N(M)** = mitotic cell fraction value of the population
**T=** inter mitotic time (or generation time)
**T(M)** = duration of mitosis (for U-2 OS ~0.5h (30min)(Brito and Rieder 2009)
**t** = time of Colcemid adding

Initial equation used in the calculation of cell cycle kinetic mitotic parameters, (i.e. inter-mitotic time) upon the adding of mitotic blocker drug like Colcemid (Puck and Steffen 1963).

**b.**

**Figure 3.17 – (a) Flow cytometry profiles at different time points after a Colcemid pre-treatment, from cells growing in 12 well TC high confluency (>100%CF) plate between 3-5 days.** All cells were retrieved after **120h (5 days)** following a Colcemid (60ng/ml) pre-treatment of 48, 24 and 0 h (no-treatment) exposure to the drug (columns). The cells were retrieved from all samples at the same time point (0h) after the different exposures. Assay type (rows): **(i)** side and forward scatter; **(ii)** forward scatter versus DNA content (DRAQ5); **(iii)** cyclin B1-GFP versus DNA content plots and **(iv)** cell cycle DNA content (DRAQ5) histograms. # cell cycle phase statistical data obtained using the Dean-Jet-Fox model with a RMS (root mean square) error average value of 10.9 (sd ±1.7) for the presented fittings. *Important Note: On the (*) market dot-plots (iii) the cyclin B1-GFP (FL2-H) channel voltage was modified in relation to the 0h Colcemid exposure.* **(b) Equation used for the calculation of the inter-mitotic time (IMT).**

**Supplementary Information 3.6-8:** Summary multi-graph of the cyclin B1-GFP versus DNA content population frequency evolution with Colcemid exposure time.

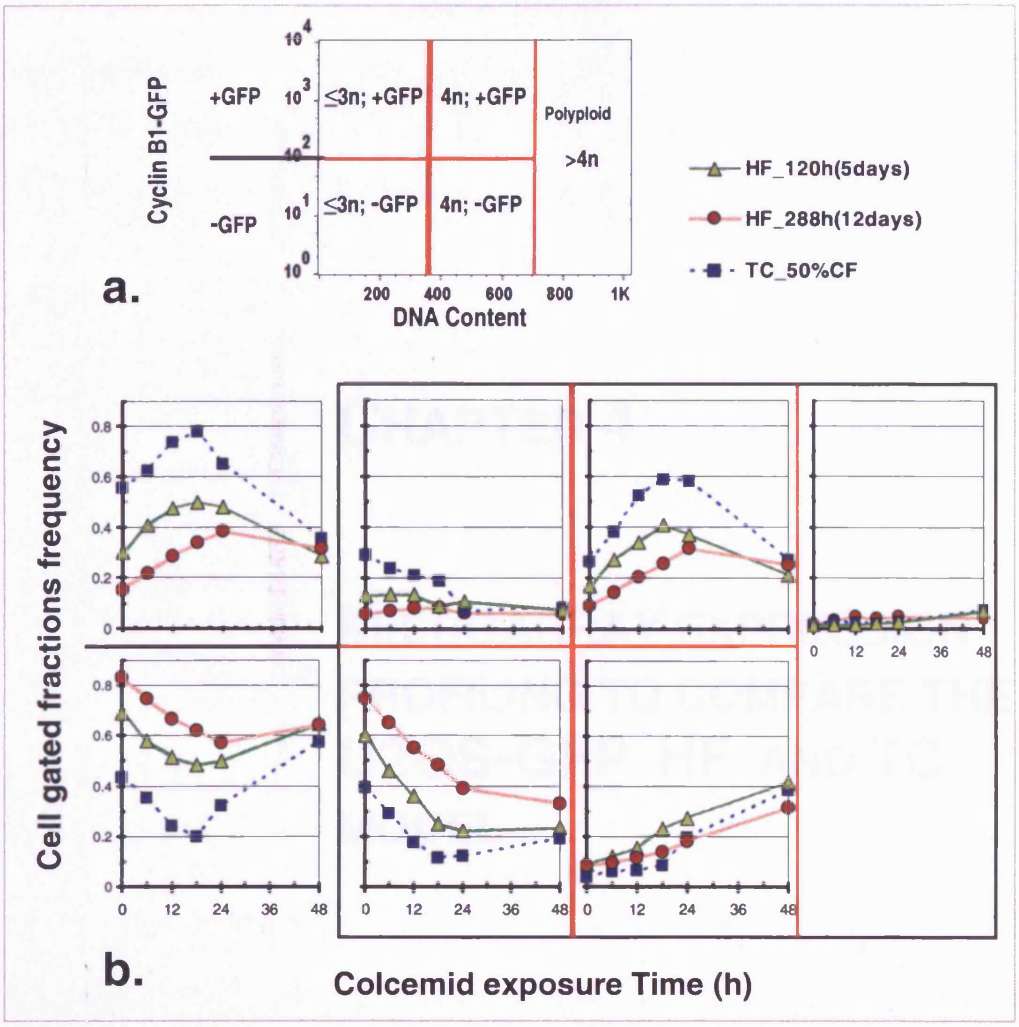


**Figure 3.18 – Cyclin B1-GFP versus DNA content population frequency evolution with Colcemid exposure time.** **(a)** Schematic dot plot segmentation representing the gates used for determining the cell fractions frequencies calculation, gates correspond to the flow cytometry cyclin B1-GFP versus DNA content (DRAQ5) for the Colcemid exposure time series analysis accordingly. (+GFP) fraction with cyclin B1-GFP above 100 arb. units or (-GFP) below 100 units; (≤3n), (4n) and (>4n) cellular ploidy. **(b)** Corresponding multi-graph of the gated fractions frequencies (y-axis) of the cell cultures: Hollow fiber (HF) all cells retrieved after 120h (5 days) and 288h (12days); (TC_50%CF) 6 well TC low confluency (50%CF) plate. Colcemid, 60ng/ml, was added to give a 48, 24, 18, 12, 8, 6 and 0 h pre-treatment to the drug (x-axis). *Note: Source for full flow plots/histograms displayed in Supplementary Information 3.6-4, Supplementary Information 3.6-5 and Supplementary Information 3.6-6 respectively.*

# CHAPTER 4

# MICROARRAY EXPRESSION PROFILING TO COMPARE THE U2OS-GFP HF AND TC MODEL

# 4 MICROARRAY EXPRESSION PROFILING TO COMPARE THE U2OS-GFP HF AND TC MODEL

## 4.1 Introduction

Studies have shown that cancer cells behave differently in 3D cell matrixes and that some of the model systems developed have greatly enhanced cancer research (Abbott 2003; Butcher et al. 2009; Hutmacher et al. 2010; Pampaloni et al. 2007; van Staveren et al. 2009; Weaver et al. 1997; Weigelt and Bissell 2008; Yamada and Cukierman 2007). The evaluation of gene expression patterns under the 3D micro-environment influence is vital for the ultimate understanding of the biological mechanisms involved. Systematic studies have confirmed alterations in the genetic expression patterns in 3D tumour models compared with 2D cultures (Feder-Mengus et al. 2008; Ghosh et al. 2005), enhanced through microarray bioinformatics analyses (Han et al. 2010; Harma et al. 2010).

Broad gene expression descriptions have been reported for chondrocytes (Dehne et al. 2010; Schulze-Tanzil 2009), osteoblasts (Boukhechba et al. 2009; Mastro and Vogler 2009) cell differentiation in 3D matrices, clinical osteosarcoma tumours in general (Bakhshi and Radhakrishnan 2010; Cleton-Jansen et al. 2009; Davicioni et al. 2008) and OS cell lines in 2D culture (Trougakos et al. 2010), including U-2 OS (Honorati et al. 2007; Luo et al. 2008; Monroe et al. 2005). Some studies tested U-2 OS in other 3D models, specifically in stirred bioreactors (Chen et al. 2003), soft-agar (Zucchini et al. 2008) and Matrigel invasion chambers (Xin et al. 2009) providing valuable insights, although they lacked a fully comprehensive integrated gene expression profiling evaluation. In terms of HF studies (Wang et al. 2006; Wang et al. 2008) the gene profiling of prostate cancer pathways for androgen independence, and gene expression analysis to characterize an *in vivo* HF LNCaP implant model.

By breaking down the tumour complexity into experimentally amenable distinct interactions, mechanistic biological studies with 3D models could ultimately help link different cell models *in vitro* and *in vivo* (Hutmacher 2010; Hutmacher et al. 2010; Pampaloni et al. 2007).

## 4.2 Specific chapter aims

A DNA microarray experiment was performed to compare the *in vitro* gene expression patterns of the Hollow Fiber U-2 OS cyclin B1-GFP adherent culture cell model (HF–U2OS-GFP) with a standard planar surface adherent tissue culture system (TC; also designated as CON). The main purpose of this gene expression profiling was:

*1.* To compare the HF encapsulated cell model with a standard TC. This is to provide insights on the impact of the HF enclosed tubular micro-environment including gene profiles associated with tumour growth, cell-cell packing and arrangement and then to evaluate if these match more closely *in vivo* tumours.

*2.* To evaluate, at the same time, integrated bioinformatics tools with a rational approach to the identification of biological features uniquely related to the HF cell culture model.

Thus the objective of the microarray analysis was to characterize the U2OS-GFP encapsulated cells in the HF and compare it to the TC counterpart to evaluate the overall *in vitro* gene expression differences and indentify patterns, thus establishing a gene expression "baseline" for the two assay formats. Thus the microarray analysis of the two culture conditions, the HF and the standard TC, was appropriated for this proposed objective and chapter aims.

The study aims was not to breakdown and determine the individual influences (i.e. such as topography surface and nutrient gradients). Although to systematically isolate and study all the interactions of the cells within the HF encapsulation specific parameters have to be considered, such as: i) the influence of the close tubular encapsulation, ii) porous membrane PVDF surface and iii) cell density increase with time. This would require for example to perform a comprehensive comparative study with an open planar surface porous membrane analogous to the HF inner wall or cells retrieved from open HF cultures for microarray analysis. This detailed analysis was deemed beyond the scope of the study. However it was possible to refer to this study and those performed by others to propose aspects of cell behaviour in the HF culture.

## 4.3 Specific methodology - DNA microarray (high-density oligonucleotide microarray)

A microarray analysis of U-2 OS cyclin B1-GFP (U2OS-GFP) cells in the HF encapsulated culture versus a standard TC was performed. The samples culture protocol and preparation for the microarrays were described in detail in chapter 2.5. Briefly, three independent HF–U2OS-GFP cell samples were compared against a control culture (CON) corresponding to three standard planar surface 100 mm TC dishes. The cells were processed directly on the growing surface with TRIZOL protocol, the RNA extracted, prepared and processed for Affymetrix gene expression analysis.

GeneChip® human genome_U133A_2.0 (HG_U133A_2.0) (Affymetrix; Santa Clara, CA) single arrays were used for the study comprising >22,000 probe sets representing 14,500 well-characterized human genes. The.CEL chip image which contained the raw hybridization signal intensities for each probe on the arrays were analysed and the procedure for quality assessment, pre-processing, normalization, differential expression and gene enrichment analysis is described in details in the following sections.

### 4.3.1 Data normalization and differential expression analysis

The analysis to obtain a differential expressed significant gene list was performed using the open source software framework BioConductor (Gentleman et al. 2004) (web: http://www.bioconductor.org/ [2010]) within the R environment Version 2.10.1 (R_DevelopmentCoreTeam 2009)(web: http://www.r-project.org/ [2010]).

The extracted significant gene list was further analysed by gene functional enrichment using a combination of free web software tools such as DAVID (Dennis et al. 2003); ConceptGen (Sartor et al. 2010); ClueGO (Bindea et al. 2009) a plug-in for Cytoscape (Shannon et al. 2003) with information derived from gene annotations/knowledge databases like: Gene Ontology (GO); KEGG pathways and NCBI - GEO experimental repository. A step-by-step summary flow diagram of all the processes used in the microarray analysis is shown in Figure 4.1.

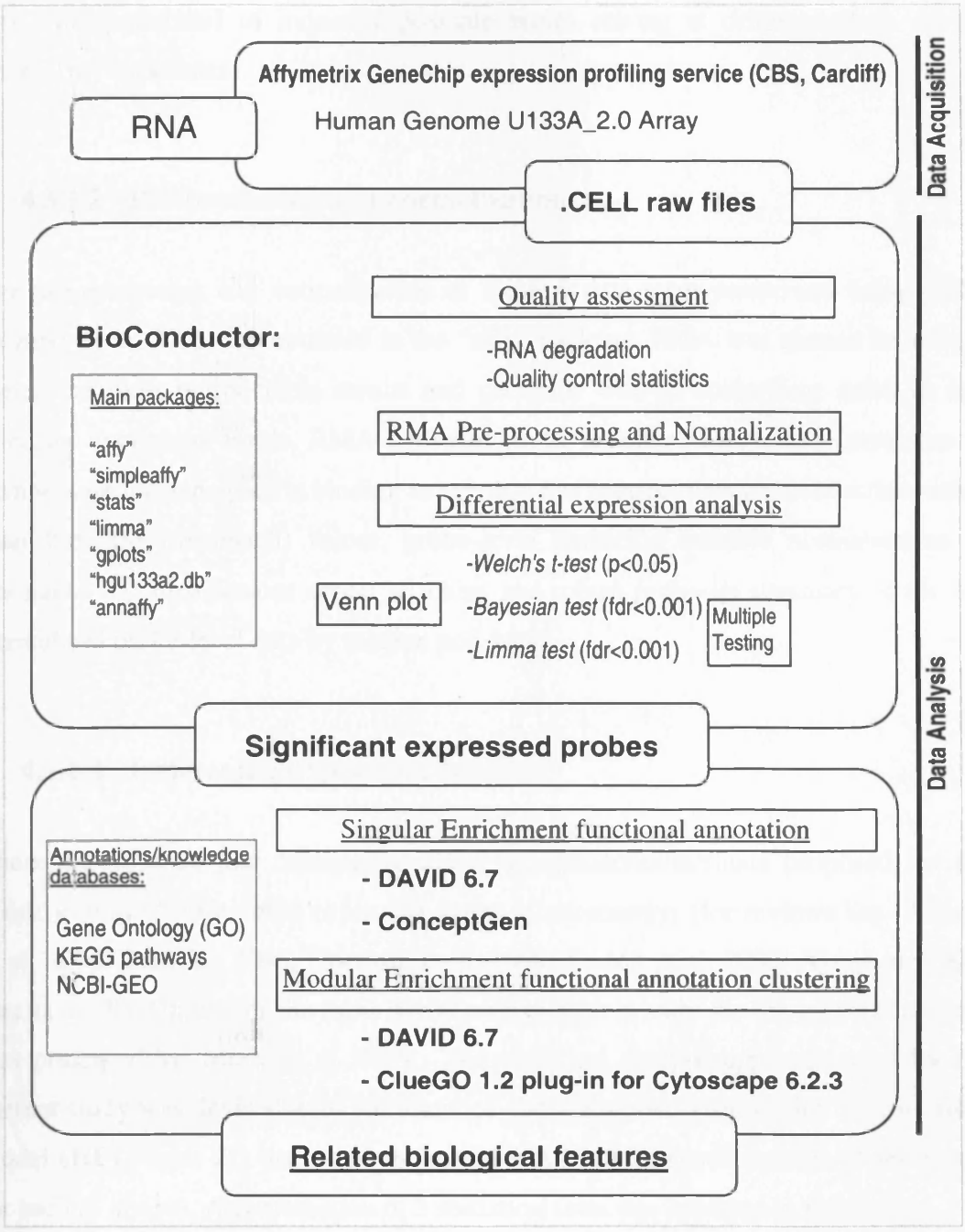


**Figure 4.1 – Workflow schematic of the microarray analysis.** All data analysis was performed using open-source software/tools (adapted from (Furon 2009)).

#### 4.3.1.1 Arrays quality assessment

Quality assessment for the array hybridization were performed using the Bioconductor. Raw array data files (.CEL) were analysed using the "affy"(Gautier et al. 2004) and "simpleaffy" (Wilson and Miller 2005) packages, for RNA degradation and quality control statistics, respectively (see Supplementary Information 4.6-1).

This was performed to indentify possible issues arising at different steps of the microarray experiment.

#### 4.3.1.2 Pre-processing and normalization

The pre-processing and normalization of the raw data were performed using RMA (Irizarry et al. 2003) incorporated in the "affy" package. RMA was choose because it yields the most reproducible results and performs well in controlling noise at low intensity expression levels. RMA performs probe specific background correction to compensate for non-specific binding using only PM (perfect match) distribution rather than PM-MM (mismatch) values, probe-level multichip quantile normalisation to normalise PM distributions across all chips and robust probe-set summary of the log normalised probe-level data by median polishing.

#### 4.3.1.3 Differential Expression Analysis

There are different and continually evolving approaches/methods proposed for the identification of differential expressed genes in microarrays (for reviews see (Allison et al. 2006; Breitling 2006; Dondrup et al. 2009; Dudoit et al. 2002; Xia et al. 2009; Zhu et al. 2008)); one of the most useful comparative studies for the present analysis was presented by Murie et al. 2009 . The statistical analysis approach used for the current study was devised with the intent of comparing two groups; the hollow fiber model (**HF**) versus 2D tissue culture model (**CON**) with small number of replicates for each (3 arrays). A combination of 3 statistical tests was assessed as follow:

*Welch's t-test* - A basic t-statistics method, representing an adaptation of Student's t-test, intended for use with two samples having possibly unequal variances, although this test present limitation for small samples size (replicates), it is useful like a "classical" approach. The probes were considerate significant for p-value $< 0.05$.

*Cyber-t* - Derived from the Bayesian probability introduced by Thomas Bayes (Barnard and Bayes 1958; Bayes and Price 1763), relies on the principle in which evidence or observations are used to update or to newly infer what is known about

underlying parameters or hypotheses. The Bayesian test probabilistic approach variant used in the present analysis was implemented by Baldi and Long 2001 in the Cyber-t package for microarray analysis.

*Limma test*- This represents a more advanced method that combines classical linear models with Bayesian inference (Smyth 2004; Smyth et al. 2005). The "limma" (Smyth 2009) (web: http://www.bioconductor.org/packages/release/bioc/html/limma.html [2010]) bioconductor package uses a linear model and empirical Bayes moderated t-test statistic (eBayes) in order to perform differential gene expression analysis. The main advantage of "limma" over classical t-tests is that for the estimation of variances and standard errors of a single gene, information is borrowed from other gene which stabilizes the analysis, this makes it particularly appropriate for small sample sizes, as is the case in this study.

*False discovery rate (FDR)* – The FDR of a statistical test was introduced by Benjamini and Hochberg 1995 , and is defined as the expected proportion of false positives among the declared significant results. This and several other derive multiple testing procedures reveal to be quite powerful to deal with type I error in high-throughput bioinformatics analysis (Allison et al. 2006) and because of its directly useful interpretation, FDR is a more convenient scale to work instead of the p-value scale (Pawitan et al. 2005). For example, if a collection of 1000 genes is declared differentially expressed with an fdr$\leq$0.01, it should be expect a maximum of 10 genes to be false positives. In the present work multiple testing procedure was performed on the Bayesian and "limma" p-values with step-up Benjamini & Hochberg FDR (Benjamini and Hochberg 1995) incorporated in the R "stats" package. The probes for this two test were considered significant for an adjusted p-value <0.01 (fdr < 0.01).

A Venn plot was produced incorporating the above tests outputs below the cut-off values, the resulted overlap probes in all 3 tests were considered the differential expressed probes between the two groups **HFvsCON.** The "limma" test was the most powerful method with all the returned significant probes incorporated in the other two tests and with more that 92% of probes in the final differential expressed list.

Although Fold Change (FC) provides usefully indications in the ranking of the probes, FC filtering presents always a degree of subjectivity related with the selection of the cut-off value (Allison et al. 2006; Murie et al. 2009). Post-statistical analysis FC filtering was not applied because all the above returned differential expressed probes had a log2(FC) above ±0.45 and were considered acceptable using the R function "treat"(McCarthy and Smyth 2009).

The Bioconductor R script files and code used in the arrays analysis is available in Supplementary Information 4.6-7–CD-Files. The statistical approach and the R script used for the analysis of the array samples was an adapted and highly modified version of a previous code generously provided by colleagues [personal communication by Victoria Griesdoorn, School of Medicine; expert advise by Dr Peter Giles, CBS (Central Biotechnology Services), School of Medicine, Cardiff University] (Burton et al. 2009).

### 4.3.2 Gene Enrichment Bioinformatics Analysis

After the generation of the differential expression gene list the most important and difficult part of the gene analysis workflow is to perform a meaningful correlation with specific underlying biological phenomena. The traditional "manual" analysis of gene-by-gene (e.g. top 20-50 genes) is extremely limited but represents a simple starting reference point for the analysis. The only way to realistically analyse a large genes list is to use bioinformatics software tools. The principal foundation of enrichment analysis is that if a biological process is abnormal in a given study, there would be several involved co-functioning related genes that should have a higher (enriched) potential to be selected as a relevant group. These tools map, in a systematic manner, the large number of genes from the user list to the associated biological annotation terms (e.g. GO terms, pathways) contained in knowledge databases, and then statistically examine the enrichment of gene members for each of the annotation terms by comparing the user gene list outcome to a control (or reference) background (Huang et al. 2009a; Khatri and Draghici 2005). High-throughput bioinformatics enrichment analysis tools started to appear from around 2002 and numbered 68 by 2008 (Huang et al. 2009a). These continue to grow

although some tools are more similar than others and the new arrivals are not necessarily more "powerful" than the more established ones (Huang et al. 2009a). The same could be said about the different statistical tests employed by these tools (Rivals et al. 2007). A typical workflow for gene enrichment analysis is shown in Figure 4.2.

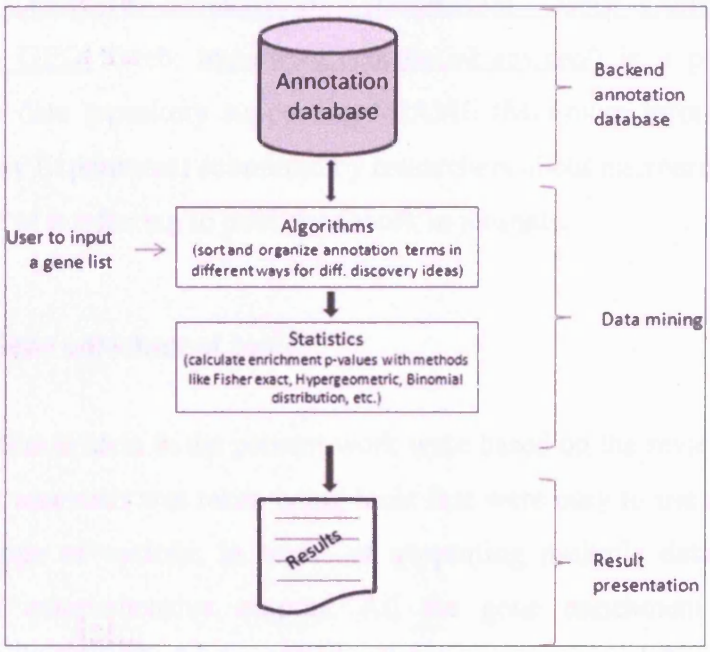


**Figure 4.2 – Typical workflow for gene enrichment analysis** (adapted from (Huang et al. 2009a)).

#### 4.3.2.1 Annotation databases

Gene ontologies are vocabularies that describe the known attributes or functions of a gene, each vocabulary entry is called a GO term witch represent a possible function associated to one or more genes. The database annotations or pathways selected for gene enrichment analysis considered the strengths and weakness of particular databases (Rhee et al. 2008). In the present work the following databases were used:

- Gene Ontology (GO) (web: http://www.geneontology.org/) (Ashburner et al. 2000). GO annotation comprises the assignment of GO terms to each gene or gene product, all of these were divided in three standard GO categories: biological process (BP), cellular component (CC) and molecular function (MF). Also the GO annotations are hierarchically organized into tree levels, from more general to more specific terms (i.e. level 1-20).

- Kyoto Encyclopedia of Genes and Genomes (KEGG) (web: http://www.genome.jp/kegg/) (Kanehisa and Goto 2000; Kanehisa et al. 2010), is a collection of manually drawn pathways maps representing knowledge on the molecular interactions and reactions networks for biological processes.
- National Center for Biotechnology Information - Gene Expression Omnibus (NCBI – GEO) (web: http://www.ncbi.nlm.nih.gov/geo/) is a public functional genomics data repository supporting MIAME (Minimum Information About a Microarray Experiment) submitted by researchers about microarray experimental data most of it referring to published work in journals.

#### 4.3.2.2 Gene enrichment tools

The tool selection criteria in the present work were based on the review by Huang et al. 2009a . An approach was taken using tools that were easy to use and presented a more wide range of options: in terms of supporting multiple databases and also production of comprehensive outputs. All the gene enrichment bioinformatics software tools used in this thesis analysis were open source and free, different tools output were compared and combined in certain instance of the analysis to better confirm and visualize a trend.

Overall these types of tools or analysis methodologies can be classified into three types: *Singular enrichment analysis (SEA), Modular enrichment analysis (MEA)* and Gene Set Enrichment Analysis (GSEA) (Mootha et al. 2003; Subramanian et al. 2005), with some tools belonging to more than one class (Huang et al. 2009a). The tools used in present analysis were as follows:

- *Singular enrichment analysis (SEA) – gene functional annotation*

Represents a traditional strategy where the user pre-selected gene list (i.e. differentially expressed, up/down-regulated) are iteratively tested for enrichment of each annotation term one-by-one in a linear mode grouping them into functional groups. SEA is simple and a very efficient way to extract the major biological meaning behind large gene lists, starting only from a list of gene names. The weakness of this approach is that output of terms can be very large, with the most highly

represented occurrences linked to common "general" annotations. Therefore, the data analysis focus and inter-relationships of relevant terms can be diluted. Representative tools include:

- DAVID 6.7 (Database for Annotation, Visualization and Integrated Discovery) (Huang et al. 2009b) (web: http://david.abcc.ncifcrf.gov/), mainly using the "Functional Annotation Chart" tool: Identifies enriched annotation terms associated with user's gene list, the statistical method is based on a modified Fisher Exact p-value the "EASE score", named from the DAVID creators original "Expression Analysis Systematic Explorer" software (Dennis et al. 2003). It supports multiple annotations databases with an informative help guide. However it is limited in terms of data output organization, handling and export.

- ConceptGen (http://conceptgen.ncibi.org/core/conceptGen/index.jsp) (Sartor et al. 2010) is a new tool. It uses the modified Fisher's exact test, similarly to the "EASE score" from DAVID and also supports multiple annotations databases. It has proved to be quite useful in terms of the gene ontology's visualization mapping tools and the main strength were in term of comparative analysis with NCBI-GEO experimental data. However the only apparent "problem" is that it offers a limited control on some of the analysis parameters and other options.

- Keyword literature gene mining tools: For literature mining the following web tools were used: (i) iHOP (http://www.ihop-net.org/UniPub/iHOP/) (Hoffmann and Valencia 2004); (ii) WikiGenes (http://www.wikigenes.org/); (iii) GoGENE (http://projects.biotec.tu-dresden.de/gogene/gogene/) (Plake et al. 2009).

***- Modular enrichment analysis (MEA) – gene groups functional clustering***

As above with SEA the input are a pre-selected gene name list and basically it explores annotations group by group rather than singular terms one by one generating functional annotation clusters of GO annotation. It analyses the gene functional annotation in a network context, bringing together a wide range of heterogeneous annotation contents from different databases. The drawback is that genes with low associated annotation would not be incorporated (Huang et al. 2009a).

The tools used for this type of analysis were:

- DAVID 6.7 mainly using the "Functional Annotation Clustering" tool (Huang et al. 2009b): Cluster the functional similar annotation terms associated with user's gene list into groups, it uses a Kappa statistics to calculated the strength of the association in the clusters and the relation with the user gene list returning a calculated Enrichment Score (ES) for each cluster. This ES ranks the biological significance the cluster in relation to the user's gene list. Basically is the geometric mean of all the enrichment p-values (EASE scores) for each of the cluster annotation terms, a minus log transformation is applied to the resulted relative geometric mean p-value. More attention should be given to clusters with scores $\geq 1.3$ (ES $=1.3$ is equivalent to non-log scale value = 0.05) however, clusters with lower scores could be potentially interesting (Huang et al. 2009b). Although it provides a list of functional enriched clusters, it is relatively poor in terms of visualization of the output results and to establish the relations between clusters.

- ClueGO 1.2 (web: http://www.ici.upmc.fr/cluego/cluegoDescription.shtml) (Bindea et al. 2009) a plug-in for Cytoscape 6.2.3 (http://www.cytoscape.org/index.php). Cytoscape (Shannon et al. 2003) represents a powerful bioinformatics software platform for visualizing molecular interaction networks and biological pathways and integrating these networks with annotations, gene expression profiles and other data. ClueGO is a recent plug-in developed for this platform, uses a two-sided hypergeometric test distribution equivalent to a classical Fisher's exact test statistic (Rivals et al. 2007) for singular functional annotations enrichment and kappa statistics in the modular enrichment to determine the association strength between the terms in the cluster. Briefly, the Kappa score shows the relationships between the functional terms based on their overlapping genes, being used to create the clusters groups and the network connections. This tool allows additional options in the analysis set-up parameters and is far more powerful in terms of easy visualization, selection and in "browsing" through the functional clusters and their network relations. However, it does not provide a wide selection of multiple annotation databases.

## 4.4 Results and Discussion

### 4.4.1 Gene expression of HF encapsulated cells in comparing to tissue culture monolayer

U2OS-GFP encapsulated in 4 cm HF and culture for 5 days was compared to a standard monolayer TC 2D control (CON) in a 100mm TC dish. Cell counts and flow cytometry of the samples submitted for microarray profiling provided some information about the overall cell culture status at the moment of the RNA "snap-shot". The calculated cell density in the HF was of ~1.2 x$10^5$ cell/$cm^2$ HF surface area while the 2D CON culture had a density of ~7.2 x$10^4$ cell/$cm^2$ 100mm TC dish area. The population cell cycle distribution was: Average 3 HF (G1=64%; S=13%; G2/M=23% (sd_max. ±2.2); CON TC dish (G1=53%; S=19%; G2/M=28%). From these results it was possible to verify that both cultures for the above parameters although not identical were to some extend similar.

The RNAs of three independent samples of each culture condition were extracted, processed and acquired on an Affymetrix HG_U133A_2.0 array chip (chapter 2.5). Statistical analysis of the chip data was performed to generate a differential expression gene list using a combination of three tests (section 4.3.1). Figure 4.3 depicts a brief analysis summary and the results of the statistical methodology used. The significant genes from *Welch's t-test* (p-value <0.05), *Cyber-t* (fdr<0.01) (Baldi and Long 2001) and *Limma test* (fdr<0.01) (Smyth 2004; Smyth et al. 2005) were compared and the resultant 632 overlap probe IDs common to all 3 tests were considered as the differential expression probes between the two sample conditions (HFvsCON) (Figure 4.3-d). Within all the 632 differentially expressed probes, around 4% had a fold change (FC) above 4 ($log_2$FC> ±2), 24% had a $log_2$(FC) between ±2 and ±1 and all probes had a $log_2$(FC)> ±0.45. The 632 probes represented, upon removal of the redundant probe sets, 507 unique differentially expressed gene list that were divided into two main clusters with 271 up and 236 down regulated genes for the HF–U2OS-GFP model culture (Figure 4.3-e). The top 20 FC up/down-regulated genes with some of the associated GO and KEGG functional annotations are presented on Table 4.4-1 and Table 4.4-2 respectively.

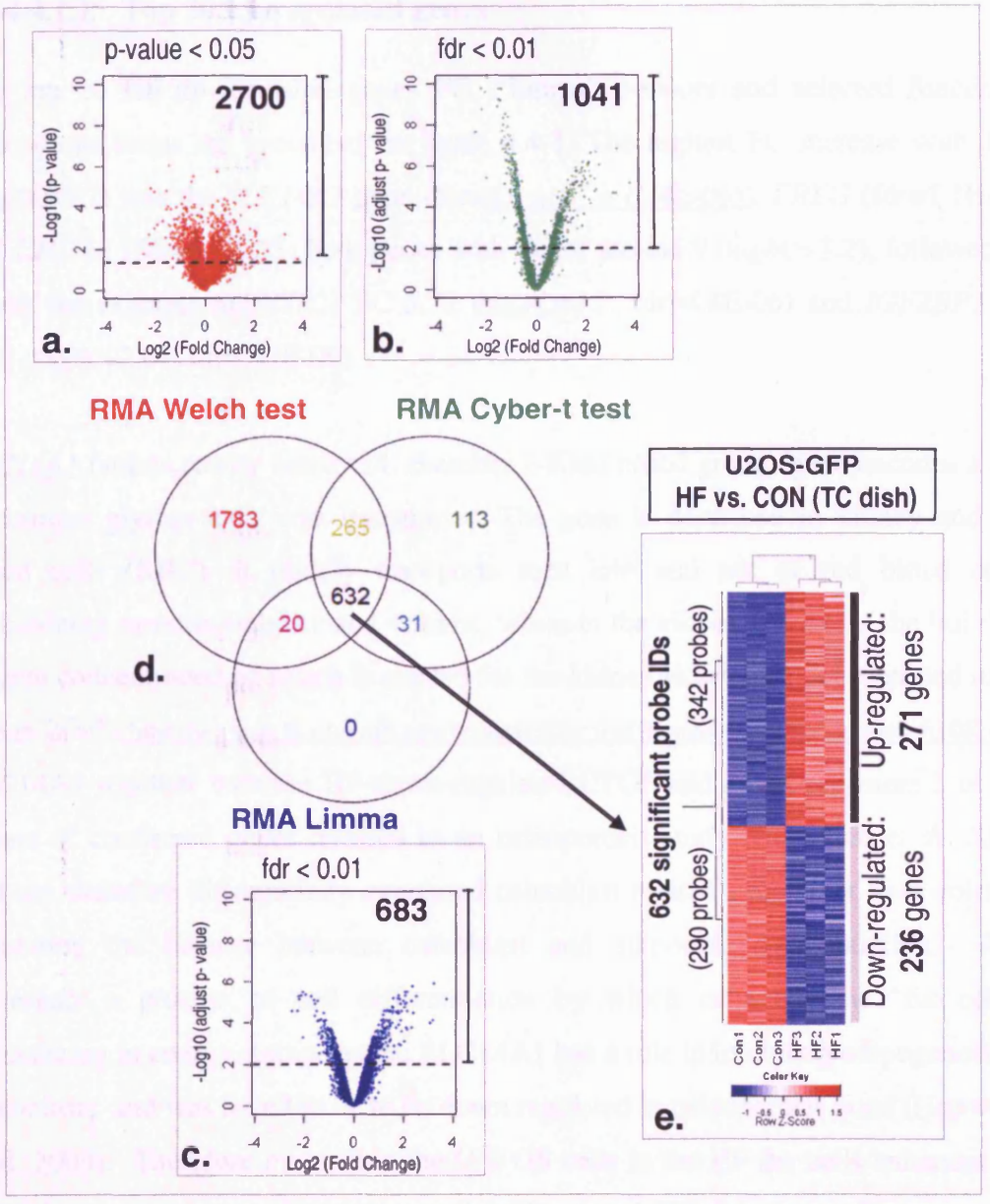


**Figure 4.3 – Differential expression analysis summary of the HF versus standard TC control U2OS-GFP microarray data.** Triplicate samples (**HF**) hollow fiber (5 days culture) and (**CON**) standard planar surface monolayer tissue culture (TC); Affymetrix array chips HG_U133A_2.0 with >22,000 probe sets representing 14,500 human genes, were RMA normalized (Irizarry et al. 2003) and statistically analysed. Volcano plots representing the Fold Change (log2) between the two groups HFvsCON against the p-value or adjusted p-value (-log10) for: (**a**) Welch's t-test, (**b**) Cyber-t (Baldi and Long 2001) and (**c**) Limma tests (Smyth 2004; Smyth et al. 2005); Cyber-t and "limma" p-values were adjusted by multiple testing procedure with step-up Benjamini & Hochberg FDR (Benjamini and Hochberg 1995). The probes were considered significant for a p-value <0.05 in the Welch's test and an adjusted p-value (fdr) <0.01 for the Cyber-t and "limma"; upper right value on each plots represents the number of significant probes below the cut-off value (dashed line). (**d**) Venn plot of the significant probes, the resulted 632 overlap probes common to all 3 tests were considered the differential expressed probes between the two sample conditions (HFvsCON). (**e**) Heat-map representing the two main clusters with around 271 up and 236 down regulated genes, in the heat-map, red indicates up-regulation and blue indicates down-regulation on the basis of gene wise standardized values (z-score, scale bar on the bottom).

### 4.4.1.1 Top 20 up-regulated genes

The top 20 HF up-regulated genes FC, "limma" p-values and selected functional annotations terms are presented on Table 4.4-1. The highest FC increase with 13.2 ($log_2$ FC=3.7) was the *SLC14A1* gene (fdr=$6.4 \times 10^{-6}$ = (6.4E-06)), *EREG* (fdr=1.1E-06) and *CHI3L1* (fdr=6.8E-05) both genes with FC of around 9 ($log_2$FC=3.2), followed by others for example *SOSTDC1* FC 5.72 ($log_2$FC=3.2; fdr=4.8E-06) and *IGF2BP3* FC 4.20 ($log_2$FC=2.07, fdr=2.9E-06).

*SLC14A1* (solute carrier family 14, member 1-Kidd blood group) gene encodes a cell membrane glycoprotein urea transporter. The gene is described in kidney and red blood cells (RBC). It rapidly transports urea into and out of red blood cells, maintaining osmotic stability and volume, while in the kidney it enables the build up of urea concentration of which is needed for the kidney to produce concentrated urine (Dean 2005)(http://www.ncbi.nlm.nih.gov/bookshelf/br.fcgi?book=rbcantigen&part=ch10Kidd). SLC14A1 together with the HF down-regulated CTGF and ADM represent 3 of a 5 subset of confirmed genes referred to an osteoporosis study (Hopwood et al. 2009) and are therefore differentially expressed osteoblast related genes that have roles in regulating the balance between osteoblast and adipocyte differentiation. This represents a process of cell differentiation by which cells become "fat cells", specializing in energy storage as fat. SLC14A1 has a role in inhibiting adipogenesis in osteoblasts, and was found to be to be down regulated in osteoporosis bone (Hopwood et al. 2009). Therefore by placing the U-2 OS cells in the HF the cells enhances the osteoblast expression profile while on the 2D control TC dish the profile was more close to an "adipocyte".

*EREG* (epiregulin) is an epidermal growth factor, part of the ErbB signaling pathway, it appears associated with cell proliferation in several tumour cells, including human colon cancer (Baba et al. 2000) and non–small cell lung cancer, where it is thought to be associated with their metastatic potential (Zhang et al. 2008b).

**Table 4.4-1: Top 20 HF up-regulated genes, fold change (FC), "limma" p-values and selected functional annotation.**

| Con HF | (Affymetrix ID) Gene Symbol EntrezGeneID | Gene Title | FC $log_2$(FC) | "limma" P-value FDR | GO Biological Process | GO Molecular Function | GO Cell Component | KEGG pathways |
|---|---|---|---|---|---|---|---|---|
| | (205856_at) **SLC14A1** 6563 | **solute carrier family 14 (urea transporter), member 1 (Kidd blood group)** | 13.18 **3.72** | 4.6E-09 **6.4E-06** | urea transport | transmembrane transporter activity, ubiquitin-ubiquitin ligase | PM | - |
| | (205767_at) **EREG** 2069 | **epiregulin** | 9.22 **3.20** | 5.2E-11 **1.1E-06** | negative/positive regulation of cell proliferation, angiogenesis | epidermal growth factor receptor binding | PM | 04012 |
| | (209395_at) **CHI3L1** 1116 | **chitinase 3-like 1 (cartilage glycoprotein-39)** | 9.04 **3.18** | 1.7E-07 **6.8E-05** | carbohydrate metabolish | sugar binding, catalytic activity | ER | - |
| | (213456_at) **SOSTDC1** 25928 | **sclerostin domain containing 1** | 5.72 **2.52** | 2.6E-09 **4.8E-06** | negative regulation bone morphogenetic protein (BMP) and Wnt receptor | protein binding | ER | - |
| | (206432_at) **HAS2** 3037 | **hyaluronan synthase 2** | 5.25 **2. 39** | 6.9E-08 **3.1E-05** | - | hyaluronan synthase activity, transferring glycosyl groups | PM | - |
| | (211596_s_at) **LRIG1** 26018 | **leucine-rich repeats and immunoglobulin-like domains 1** | 5.11 **2.35** | 1.5E-10 **1.7E-06** | - | protein binding | PM | - |
| | (214321_at) **NOV** 4856 | **nephroblastoma overexpressed gene** | 5.08 **2.34** | 7.9E-09 **8.2E-06** | regulation of cell growth | insulin-like growth factor binding | ER | - |
| | (202859_x_at) **IL8** 3576 | **interleukin 8** | 5.01 **2.32** | 6.3E-07 **1.6E-04** | angiogenesis, inflammatory response | chemokine activity, interleukin-8 receptor binding | ER | 05219; 04062; 04621; |
| | (217997_at) **PHLDA1** 22822 | **pleckstrin homology-like domain, family A, member 1** | 4.46 **2.16** | 3.9E-10 **2.9E-06** | FasL antigen biosynthetic process | protein binding | Cp, Nu | - |
| | (204337_at) **RGS4** 5999 | **regulator of G-protein signaling 4** | 4.43 **2.15** | 9.0E-07 **2.0E-04** | negative regulation of signal transduction, inactivation of MAPK activity | GTPase activator activity, calmodulin binding | - | - |
| | (210592_s_at) **SAT1** 6303 | **spermidine/spermine N1-acetyltransferase 1** | 4.41 **2.14** | 5.0E-08 **2.6E-05** | metabolic process | transferase activity, acyltransferase activity | Cp | 00330 |
| | (217757_at) **A2M** 2 | **alpha-2-macroglobulin** | 4.27 **2.10** | 6.5E-07 **1.7E-04** | negative regulation of complement activation, response to nutrient, | growth factor binding, interleukin-1 and 8 binding, lectin pathway | ER | 04610 |
| | (218501_at) **ARHGEF3** 50650 | **Rho guanine nucleotide exchange factor (GEF) 3** | 4.26 **2.09** | 2.0E-09 **4.4E-06** | Rho protein signal transduction, apoptosis | guanyl-nucleotide exchange factor activity | Cp | - |
| | (203820_s_at) **IGF2BP3** 10643 | **insulin-like growth factor 2 mRNA binding protein 3** | 4.20 **2.07** | 5.7E-10 **2.9E-06** | regulation of cytokine biosynthetic process | RNA binding, translation regulator activity | Cp, Nu | - |
| | (202291_s_at) **MGP** 4256 | **matrix Gla protein** | 4.12 **2.04** | 7.8E-06 **7.7E-04** | cartilage condensation | structural constituent of bone, calcium ion binding | ER | - |
| | (206843_at) **CRYBA4** 1413 | **crystallin, beta A4** | 4.09 **2.03** | 2.4E-08 **1.7E-05** | camera-type eye development | structural constituent of eye lens | ER | - |
| | (204919_at) **PRR4** 11272 | **proline rich 4 (lacrimal)** | 3.99 **2.00** | 8.1E-09 **8.2E-06** | visual perception | - | ER | - |
| | (204607_at) **HMGCS2** 3158 | **3-hydroxy-3-methylglutaryl-Coenzyme A synthase 2 (mitochondrial)** | 3.80 **1.93** | 4.4E-08 **2.6E-05** | cholesterol/isoprenoid biosynthetic process | hydroxymethylglutaryl-CoA synthase activity | MT | 00650; 03320; 00072; |
| | (209173_at) **AGR2** 10551 | **anterior gradient homolog 2 (Xenopus laevis)** | 3.79 **1.92** | 1.2E-06 **2.4E-04** | - | protein binding | ER, EpR | - |
| | (221911_at) **ETV1** 2115 | **ets variant 1** | 3.73 **1.90** | 1.3E-08 **1.2E-05** | transcription factor activity | transcription from RNA polymerase II promoter | Nu | - |
| | (206805_at) **SEMA3A** 10371 | **sema domain, immunoglobulin domain (Ig), short basic domain, secreted, (semaphorin)** | 3.67 **1.88** | 2.0E-07 **7.4E-05** | regulation of axon extension involved in axon guidance | receptor activity | ER | 04360 |

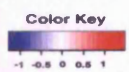


**Legend Cellular Component:**

**PM=** plasma membrane; **ER=** extracellular region; **Nu** =nucleus; **Cp** = cytoplasm; **EpR=** endoplasmic reticulum; **MT** = mitochondrial matrix

**Legend KEGG pathways:**

**04012**: ErbB signaling pathway; **05219**: Bladder cancer; **04062**: Chemokine signaling pathway; **04621**: NOD-like receptor signaling pathway; **04622**: RIG-I-like receptor signaling pathway; **04620**: Toll-like receptor signaling pathway; **00330**: Arginine and proline metabolism; **01100**: Metabolic pathways; **04610**: Complement and coagulation cascades; **00650**: Butanoate metabolism; **03320**: PPAR signaling pathway; **00072**: Synthesis and degradation of ketone bodies; **00900**: Terpenoid backbone biosynthesis; **00280**: Valine, leucine and isoleucine degradation; **04360**: Axon guidance

*CHI3L1* (chitinase 3-like 1), or the equivalent *GP39* (cartilage glycoprotein-39) or *YKL-40* is a highly studied secreted growth factor that is associated with different tissues, cancers and others diseases (Eurich et al. 2009). One function of CHI3L1 is to act as a cellular survival factor in response to an adverse environment, various types of physiological stress, such as inflammation, hypoxia, and nutrient deprivation may induce high expression of CHI3L1 (Junker et al. 2005). CHI3L1 is expressed and secreted during the course of inflammation disorders like hepatitis, asthma, rheumatoid arthritis, osteoarthritis (Recklies et al. 2005) and by several types of solid tumors including glioblastoma, colon cancer, breast cancer and malignant melanoma. The exact function of CHI3L1 in inflammation and cancer is still largely unknown, but CHI3L1 seems to play a role in the inflammatory processes and in promoting angiogenesis and remodeling of the extracellular matrix. Additionally, it also seems to be linked with the development of epithelial tumorigenesis presumably by the mitogen-activated protein (MAP) kinase and the protein kinase B signaling pathways (Eurich et al. 2009).

*SOSTDC1* (sclerostin domain containing 1) this encodes an N-glycosylated secreted protein that functions as a bone morphogenetic protein (BMP) antagonist. Specifically, it directly associates itself with BMPs, preventing them from binding to their receptors, thereby regulating BMP signalling during cellular proliferation, differentiation, and programmed cell death (NCBI-EntezGene; web: http://www.ncbi.nlm.nih.gov/gene/25928 [2010]). Some studies suggest an important role in kidney tumours with significant down-regulation in renal carcinomas versus normal. The restoration of SOSTDC1 in renal cell carcinoma cells profoundly suppressed cellular proliferation, presumably due to its effect in suppressing BMP7-induced signalling (Blish et al. 2008). In the HF–U2OS-GFP model this gene up-regulation could be interpreted as a "counter" regulation of cell proliferation. It is not exactly clear what would represent this BMP antagonism expression in U-2 OS cells. A previous study of the ability of osteosarcoma cell lines to induce new bone formation it was reported that U-2 OS cells, contrary to others osteosarcoma lines, despite expression of most of the normal BMPs, were unable induce bone formation (Anderson et al. 2002; Raval et al. 1996). U-2 OS cells may secrete BMPs inhibitory binding proteins, however it was found that this cell line expresses an inhibitory Smad

6 protein contrary to other osteosarcoma lines (Yu et al. 2004). So, there is a distinct probability that SOSTDC1 might represent a normal U-2 OS feature related with the low bone formation potential and is enhanced in the HF. It has also been suggested that the low U-2 OS bone differentiation potential seems to be associated with this cell line higher malignancy and metastasis capacity in relation to other osteosarcoma lines (Honorati et al. 2007).

*IL8* (interleukin 8; $log_2FC$=2.32; fdr=8.2E-06) a member of the CXC chemokine family. This chemokine is one of the major mediators of the inflammatory response, being is secreted by several cell types. It functions as a chemoattractant, and is also a potent angiogenic factor (NCBI-EntezGene: http://www.ncbi.nlm.nih.gov/gene/3576 ). The expression of this cytokine in U-2 OS cells, was previously shown by Nelissen et al. 2000 associated with the capacity of these cells to the stimulate hematopoietic bone marrow progenitor cells

*IGF2BP3* (insulin-like growth factor 2 mRNA binding protein 3); it is known that U-2 OS expresses insulin-like growth factor 1 and 2 receptors associated with the promotion of cell growth (Herzlieb et al. 2000; Raile et al. 1994). Related genes like *IGFBP7* (insulin-like growth factor binding protein 7: $log_2FC$= 1.19, fdr=3.06E-04) and *IGFBP5* (insulin-like growth factor binding protein 5: $log_2FC$=0.72, fdr=1.56E-03) were present on the HF up-regulated list. In particular, *IGF2BP3* gene/protein, which is also expressed during embryogenesis and on neonatal tissues, has been recently proposed to as a prognostic factor or a therapeutic target for clinical cases of osteosarcoma presenting a high potential for metastasis (Do et al. 2008).

Overall, the top 20 HF up-regulated genes relatively to the GO biological and molecular function most of the genes were connected with cell-cell signalling growth factors (protein/steroids) or associated gene pathways and receptors. Not surprising in the GO cellular component the majority of the genes were associated with the cell plasma membrane and extracellular region, but also some on the cytoplasm and nucleus. Other genes were more directly related with lipid metabolism (i.e. *SLC14A1*, HMGCS2) and a few related to cell matrix structural constituents (i.e. MGP, CRYBA4, PRR4). The over-expression of *CHI3L1* and also other genes like *EREG, IGF2BP3* and genes like *IL8* fits well with the more conditioned and stress

environment to which cells are subjected inside the HF, with higher cell density and lower nutrient access. These gene up-regulations may be interpreted as a response to increase cell proliferation/growth and also angiogenesis to enhance nutrient delivery, these genes together with other genes such as *SLC14A1* and *SOSTDC1* may also contribute to a low differentiation and more malignant cell phenotype.

#### 4.4.1.2 Top 20 down-regulated genes

The top 20 HF down-regulated genes are presented on Table 4.4-2. The highest down-regulation gene was *CYP24A1* ($log_2FC$=-2.48; fdr=2.6E-05). MATN2 ($log_2FC$=-2.6E-05; fdr=-2.27), SCG5 ($log_2FC$=-2.23; fdr=4.8E-06), *ANXA8* ($log_2FC$=-2.2; fdr=6.4E-06).

*CYP24A1* (cytochrome P450, family 24, subfamily A, polypeptide 1) this gene encodes a member of the cytochrome P450 superfamily of enzymes. This family of proteins are monooxygenases which catalyze many reactions involved in drug metabolism (Muindi et al. 2010) and synthesis of cholesterol, steroids and other lipids. This mitochondrial protein initiates the degradation of 1,25-dihydroxyvitamin D3, the physiologically active form of vitamin D3, by hydroxylation of the side chain, this enzyme plays a role in calcium homeostasis and the vitamin D endocrine system (NCBI-EntezGene: http://www.ncbi.nlm.nih.gov/gene/1591). This gene activity was reported in human primary osteoblasts and human osteoblastic cell lines and may be related with paracrine (near cell-cell signalling) pathways in promoting osteogenic (bone formation) response (Atkins et al. 2007).

Other genes in this list were calcium binding like CALB2 (calbindin 2) and *ANXA8* (annexin A8; $log_2FC$=-2.2; fdr=6.4E-06), the latter being necessary for cytoskeleton actin base endosome motility (Goebeler et al. 2008). Several cytoskeleton/actin directly related genes were present in this top 20 list, such as TAGLN, EPB41L3, KRT17 and *TPM1*.

**Table 4.4-2: Top 20 HF down-regulated genes, fold change (FC), "limma" p-values and selected functional annotation.**


| (Affymetrix ID) Gene Symbol EntrezGeneID | Gene Title | FC log2(FC) | "limma" P-value FDR | GO Biological Process | GO Molecular Function | GO Cell Component | KEGG pathways |
|---|---|---|---|---|---|---|---|
| (209283_at) **CRYAB** 1410 | **crystallin, alpha B** | 0.40 **-1.31** | 6.7E-07 **1.7E-04** | muscle contraction, protein homooligomerization | cytoskeletal protein binding, structural constituent of eye lens | Cp; PM | - |
| (205157_s_at) **KRT17** 3872 | **keratin 17** | 0.39 **-1.37** | 4.8E-05 **2.8E-03** | epidermis development | structural constituent of cytoskeleton | Cp; Nu | - |
| (211776_s_at) **EPB41L3** 23136 | **erythrocyte membrane protein band 4.1-like 3** | 0.38 **-1.40** | 1.9E-07 **7.1E-05** | cortical actin cytoskeleton organization | actin binding | Cp; Ck; PM | 4530 |
| (206116_s_at) **TPM1** 7168 | **tropomyosin 1 (alpha)** | 0.38 **-1.41** | 1.4E-05 **1.2E-03** | cytoskeleton organization, muscle contraction | actin binding, structural constituent cytoskeleton and muscle | Cp; Ck | 04260; 05414; 05410 |
| (206969_at) **KRT34** 3885 | **keratin 34** | 0.37 **-1.44** | 2.0E-06 **3.3E-04** | epidermis development | protein binding | Ck | - |
| (204298_s_at) **LOX** 4015 | **lysyl oxidase** | 0.36 **-1.45** | 8.1E-09 **8.2E-06** | protein modification process | copper ion binding | ER | - |
| (219529_at) **CLIC3** 9022 | **chloride intracellular channel 3** | 0.36 **-1.46** | 2.4E-07 **8.0E-05** | signal transduction, chloride transport | chloride channel activity | Cp; Nu | - |
| (209949_at) **NCF2** 4688 | **neutrophil cytosolic factor 2** | 0.35 **-1.52** | 3.7E-08 **2.5E-05** | cellular defense response, superoxide metabolic process | electron carrier activity | Cp; Nu | 4670 |
| (205547_s_at) **TAGLN** 6876 | **transgelin** | 0.34 **-1.56** | 1.4E-08 **1.2E-05** | muscle organ development | actin binding | Cp | - |
| (205428_s_at) **CALB2** 794 | **calbindin 2** | 0.34 **-1.56** | 9.5E-08 4.1E-05 | - | calcium ion binding | gap junction | - |
| (206268_at) **LEFTY1** 10637 | **left-right determination factor 1** | 0.33 **-1.60** | 6.6E-09 7.7E-06 | transforming growth factor beta receptor signaling pathway | cytokine activity | ER | 4350 |
| (213711_at) **KRT81** 3887 | **keratin 81** | 0.30 **-1.72** | 2.8E-09 **4.8E-06** | - | protein binding | Ck | - |
| (219014_at) **PLAC8** 51316 | **placenta-specific 8** | 0.26 **-1.96** | 1.2E-09 3.9E-06 | - | - | - | - |
| (205083_at) **AOX1** 316 | **aldehyde oxidase 1** | 0.24 **-2.03** | 6.8E-10 **2.9E-06** | inflammatory response, oxidation reduction | xanthine dehydrogenase activity | Cp | 00982; 00760; 00380; 00350; |
| (208690_s_at) **PDLIM1** 9124 | **PDZ and LIM domain 1** | 0.24 **-2.04** | 7.8E-10 2.9E-06 | response to oxidative stress | metal ion binding | Cp; Ck | - |
| (220232_at) **SCD5** 79966 | **stearoyl-CoA desaturase 5** | 0.24 **-2.05** | 4.0E-06 **5.0E-04** | oxidation reduction, fatty acid biosynthetic process | oxidoreductase activity, metal ion binding | EpR | 01040; 03320 |
| (205828) **MMP3_at** 4314 | **matrix metallopeptidase 3 (stromelysin 1, progelatinase)** | 0.23 **-2.14** | 1.6E-09 4.4E-06 | collagen catabolic process, response to cytokine stimulus | metalloendopeptidase activity | ER | - |
| (203074_at) **ANXA8** 653145 | **annexin A8/annexin A8-like 1/annexin A8-like 2** | 0.22 **-2.20** | 5.1E-09 6.4E-06 | calcium ion binding | calcium-dependent phospholipid binding | - | - |
| (203889_at) **SCG5** 6447 | **secretogranin V (7B2 protein)** | 0.21 **-2.23** | 2.4E-09 **4.8E-06** | peptide hormone processing | GTP binding, unfolded protein binding | ER | - |
| (202350_s_at) **MATN2** 4147 | **matrilin 2** | 0.21 **-2.27** | 4.7E-08 **2.6E-05** | - | proteinaceous extracellular matrix | ER | - |
| (206504_at) **CYP24A1** 1591 | **cytochrome P450, family 24, subfamily A, polypeptide 1** | 0.18 **-2.48** | 5.1E-08 **2.6E-05** | osteoblast differentiation, oxidation reduction, vitamin D receptor pathway | heme binding, oxidoreductase activity | MT | - |

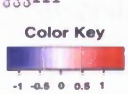


**Legend Cellular Component:**

**PM=** plasma membrane; **ER=** extracellular region; **Nu** =nucleus; **Cp** = cytoplasm; **Cy**= cytoskeleton; **EpR=** endoplasmic reticulum; **MT** = mitochondrial matrix

**Legend KEGG pathways:**

**4530:** Tight junction; **04260:** Cardiac muscle contraction; **05414**: Dilated cardiomyopathy; **05410**: Hypertrophic cardiomyopathy (HCM); **04670:** Leukocyte transendothelial migration **04350:** TGF-beta signaling pathway; **00982:** Drug metabolism - cytochrome P450; **00760:** Nicotinate and nicotinamide metabolism; **00380:** Tryptophan metabolism; **00350:** Tyrosine metabolism; **00280:** Valine, leucine and isoleucine degradation; **00750:** Vitamin B6 metabolism; **01040:** Biosynthesis of unsaturated fatty acids; **03320**: PPAR signaling pathway.

*TPM1* (tropomyosin 1 (alpha); $log_2FC$=-1.41; fdr=1.2E-03) is a member of the tropomyosin family a widely distributed actin-binding protein involved in the contractile system of muscles and the cytoskeleton of non-muscle cells. It also functions in association with the troponin complex to regulate the calcium-dependent interaction of actin and myosin during muscle contraction (NCBI-EntezGene: http://www.ncbi.nlm.nih.gov/gene/7168). Intracellular calcium concentration is responsible for the control of the cell's contractile system.

Overall, the top 20 HF down-regulated genes were, in general, involved in ion binding and cytoskeleton/actin, while for the cellular location the majority of the gene products were linked to cytoplasm and nucleus. This may reveal a trend related to changes in cell cytoskeleton organization, movement/migration.

### 4.4.2 Singular enrichment gene functional annotation

The previous top 20 gene lists may reveal some biological trends, but they are extremely limited in providing a sense of the overall gene expression (see section 4.3.2). The use of bioinformatics tools can provide an encompassing analysis of differentially expressed lists with large number of genes. However, the caveats for this approach are associated with the fact not all genes have known functions. Also the quality relative to the "proximity to the biological truth" of the singular or modular enrichment analysis generated by this bioinformatics tools is as good as the quality of the online knowledge sources from which the annotations are retrieved (Rhee et al. 2008).

A singular enrichment gene functional annotation analysis was performed using the web tool DAVID 6.7 "Functional Annotation Chart" (Huang et al. 2009b). Briefly, the HF up/down-regulated gene lists were statistically tested in relation to the GO (BP, MF and CC) DAVID cured databases and the KEGG pathways to determine the most represented functional terms with more associated single genes. The enriched functional terms for the HF up-regulated genes are presented on Figure 4.4-b, all the displayed terms had a p-value (ESA score) < 2.5E-04 and fdr < 0.25.

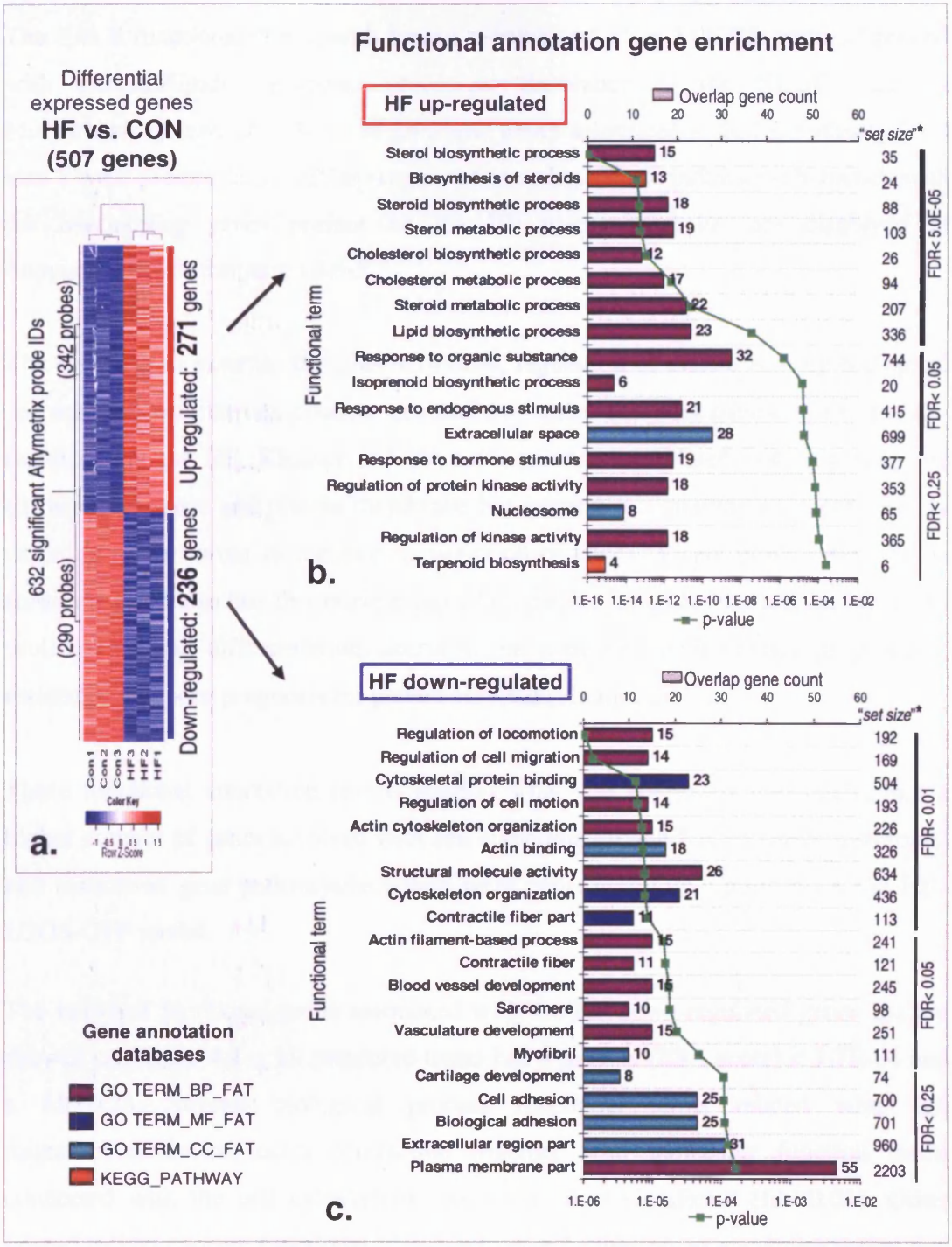


**Figure 4.4 – Singular enrichment gene functional annotation of HF versus CON.** U2OS-GFP hollow fiber model (**HF**) and standard tissue culture (**CON**) microarray analysis. **(a)** Heat-map representation of the HF up/down-regulated gene clusters. Histograms representing the top enriched functional terms for the: **(b)** 271 up-regulated gene list and **(c)** relatively to the 236 down-regulated list, with the overlapping number of genes relatively to each list, associated p-value (EASE score) <1.0E-4 and Benjamini & Hochberg FDR<0.25. Computed using the DAVID curate (GO) Gene Ontology; (BP) biological process, (CC) cellular component and (MF) molecular function database and KEGG pathway. For the used EASE threshold the number of genes from the lists represented in the analysis output were, 36% of HF up-regulated and 48% of HF down-regulated list. * "*set size*" represents the population hits, one of the background parameters used on the DAVID statistic, that could be interpreter like the total number of genes associated to a specific GO/KEGG functional term.

The first 8 functional terms, with lowest p-value and fdr < 5.0E-05, were all related with steroids/lipids metabolic processes. Relevance to the KEGG pathway *biosynthesis of steroids*, 13 out of 24 know genes associated with this pathway ("set size") were present in the HF up-regulated gene list. These pathway schematics with the overlapping genes present on the HF up-regulated list are displayed in Supplementary Information 4.6-3.

The response to external stimulus/hormones, regulation of kinase activity biological process, and cellular components extracellular space and nucleosome were also up-regulated on the HF. Kinases and steroid/hormones are related not only with the extracellular space and plasma membrane but interact in signalling cascades directly targeting nucleosomes to regulate transcription of genes (Vicent et al. 2006). Some studies suggest also that this nuclear signalling pathway, besides the regulation of cell proliferation and differentiation, seems to be correlated with tumour progression, resistance and poor prognosis for patient survival (Planque 2006).

These functional annotation results support what was suggested previously, that a higher number of genes involved with cell signalling growth factors (protein/steroids) and associated gene pathways/receptors were consistently up-regulated on the HF–U2OS-GFP model.

The enriched functional terms associated with the HF down-regulated genes list are showed on Figure 4.4-c, all presented terms had a p-value (ESA score) < 1.7E-04 and a fdr<0.25. Several biological process functional terms related with cell migration/movement, actin contraction together with molecular function terms connected with the cell cytoskeleton were the most significant (fdr<0.01). Other related cell component functional terms such as cell adhesion, extracellular region and plasma membrane were also enriched.

The above suggest that the model represented by cells growing on a 2D substrate showed cytoskeletal alterations that influence cell movement, cytoskeleton and adhesion patterns compared to the HF–U2OS-GFP model. One possible interpretation might be that the cells have an opportunity to take on a motile phenotype in the 2D TC configuration.

### 4.4.3 Modular enrichment functional clustering and network link

For an extended scrutiny, modular gene enrichment analysis provides an even stronger tool to improve the biological interpretation of large lists of genes. It allows the inclusion of a higher number of genes from the list to be included in the analysis, without overwhelming the interpretation of the output results and maintaining a minimum statistical significance. This bioinformatics tool explores annotations group by group, rather than singular terms one by one, grouping related/similar GO functional annotations into clusters. The other advantage is that it makes it possible to easily "visualize" the gene expression patterns within network context, connecting otherwise heterogeneous or initially non-related annotations.

The web tools DAVID 6.7 "Functional Annotation Clustering" (Huang et al. 2009b) and the Cytoscape 6.2.3 (Shannon et al. 2003) plug-in ClueGO1.2 (Bindea et al. 2009) were selected (see 4.3.2.2) to be used in the modular enrichment analysis of the HF vs CON differential expressed gene list. Although the output results (functional terms/clusters) from this two tools were not exactly identical for the same gene list, they were practically equivalent. The DAVID generated clusters ES summary and selected ClueGO 1.2 cluster network for the HF up-regulated list are presented in Figure 4.5 and for the HF down-regulated in Supplementary Information 4.6-2.

DAVID, an already extensively used and tested web tool (http://david.abcc.ncifcrf.gov/), provided a reference analysis. Also, DAVID Enrichment Score (ES) provided a useful summary parameter to characterize the clusters. ES ranks the significance of the cluster, based on the overall p-value (EASE scores) of the enriched functional terms (Huang et al. 2009b). For a highly simplified view: if ES= -log10 (geometric mean of the cluster terms p-values) then a mean value of 0.05 corresponds to an ES=1.3.

ClueGO1.2, the plug-in for Cytoscape 6.2.3, provides an intuitive and easy visualized networked representation of the analysis results. The GO/KEGG enriched terms were represented like nodes (circles), where the node size is approximately proportional to the term step-up Benjamini & Hochberg FDR value. The nodes were connected through lines (edges), which represent associations between the nodes related to

common genes. Nodes with same colour and with close interconnected edges, represent a distinctive cluster similar/related functional terms, where the common leading group term legend (bigger colour font) corresponds to the highest FDR significance. If a node present i.e. 2-3 dividing different colours it means that it has genes associated with distinct clusters. Similarly to DAVID, Kappa statistics was used to determine the association strength between the terms in the cluster or other neighbour clusters/nodes. Briefly, the Kappa scores rank the relationships between the functional terms based on their overlapping genes, being used to create the cluster groups and the network connections layout. The edge thickness is an approximately proportional kappa score between nodes. High kappa value leads to more isolated clusters while lower kappa would promote interconnection.

The highest ES score, with 7.18 was found for cluster 1 – *"sterol biosynthetic process"* (Figure 4.5-a) and the corresponding cluster network represented in Figure 4.5-b (light green nodes). This correlates perfectly with the associated functional terms being clearly dominant with low p-values in the previous singular gene enrichment (Figure 4.4-b). This combined cluster analysis provided not only an intuitive global view of the gene list terms, but an easy way to manage and identify any term/clusters. Browsing through the ClueGO cluster network, allowed the identification of several functional features. This was important in selecting term/clusters to further drill down to a biological relevance.

For example, cluster 9 "*primal sexual characteristics*" (ES=1.37), Figure 4.4-b pink node, refers to steroid receptors for androgen and estrogen controling cell proliferation, previously shown to play an important role in human osteosarcoma clinical tumours and cell lines (Dohi et al. 2008; Svoboda et al. 2010), more specifically the estrogen receptor in U-2 OS cells (Monroe et al. 2005).

A high value feature of ClueGO 1.2 was that it allowed a cluster network comparison analysis, used to compare the HF up versus down-regulated genes lists. For an enhanced visualization and "browsing" through the functional clusters and their network, the high definition generated full Cytoscape organic layout is available in Supplementary Information 4.6-4 – CD-PDF (note: zoom-in to 800% for more detail), with ~70% of HFvsCON differential expressed gene list represented on the

analysis. Some selected clusters for this comparison are presented in Figure 4.6. The functional network was generated using the same principles previously described, but this time the node colours red or blue represent HF up or down regulated genes respectively, where the colour gradient shows the up/down gene proportion associated to each term, equal proportions of the two gene list are represented in white.

For example, the cluster "*blood vessel development*" (Figure 4.6-d1) represents genes of both the HF up and down-regulated list, with almost equal proportion of genes within its functional term, translated in a white node colour. Specifically, the term *angiogenesis* has 7 genes HF up-regulated (EREG, FGF13, FN1, IL8, MMP2, NRP1, ROBO1) and 6 genes HF down-regulated (CDH13, CTGF, EPAS1, GNA13, HSPG2, THY1). This enhances the interpretation of this cluster or functional term, meaning that angiogenesis features are affected in the HFvsCON culture. On the other hand it allows also to select cluster/terms with clearly more up/down-regulated genes and easy indentify their genes names. Figure 4.5 Cluster 5- "*negative regulation of cell differentiation*" (ES= 1.81) and the close linked clusters/functional terms i.e. *cell development/morphogenesis, hemopoiesis,* were predominantly enriched with HF up-regulated genes with also genes from the HF down-regulated list (Figure 4.6-c1). For example, the specific functional term *negative regulation of developmental growth* (fdr= 8.9E-3) had only genes from the HF up-regulated list (NRP1, SEMA3A, SPP1), while the term *regulation of cell morphogenesis involved in differentiation* (fdr=6.2E-3) was more proportional (HF up-regulated genes: NRP1, SEMA3A, SPP1, ROBO1, TIAM1 and HF down-regulated genes: PTPRF, SKIL, THY1).

The above clusters related to low cell differentiation are consistent with two areas. First, the suggested model by Luo et al. 2008 which proposes that osteosarcoma malignancy may originate from a disruption in the bone marrow mesenchymal pluripotent cells differentiation pathway during osteogenic terminal differentiation. This leads the way for the occurrence of highly proliferative and low differentiated phenotype associated with osteosarcoma cell lines (including U-2 OS) and resistance to treatment. Second, focusing on the *SOSTDC1* (sclerostin domain containing 1) BMP inhibitor secreted protein gene. This gene is highly referenced in kidney tumours (Blish et al. 2008) and although apparently not yet associated with U-2 OS cells in the literature, may play a role in a non-differentiated phenotype. In other

words this gene may be related with low bone formation potential characteristic of the U-2 OS cell line, although these cells express most of the normal BMPs (Anderson et al. 2002; Yu et al. 2004), and has higher malignancy and metastasis capacity compared to other osteosarcoma lines (Honorati et al. 2007).

Overall, in the HF model the cell differentiation genetic signature is clearly altered and the cells seem to present a lower differentiation potential associated with higher malignancy.

A final remark to show of the effect of GO selection and analysis criteria parameters; *SOSTDC1* was not identified by the modal enriched DAVID 6.7 or ClueGO 1.2 using the present analysis criteria, this was due to the use of more restricted GO tree levels and significance/kappa threshold to avoid over-common functional terms/saturated networks. By using "DAVID_FAT" a more general DAVID curated GO database, *SOSTDC1* appeared associated with low significance functional terms such as *odontogenesis of dentine-containing tooth term* (p-value=0.027; fdr=37) and *pattern specification process*(p-value =0.29; fdr=99.7) that refers to the creation of defined areas within an organism to which cells respond and eventually are instructed to differentiate. This was included on the *"branching morphogenesis of a tube"* cluster. In the ClueGO 1.2 analysis, *SOSTDC1* was associated with the *Wnt receptor signalling pathway* functional term (fdr=0.1) with also FZD10, GPR177, LEF1, NDP, SOX4 of the HF up-regulated list and MITF of the HF down-regulated list. This last term did not group for kappa >0.4 threshold, but a kappa>0.35 incorporated this term.

The above points demonstrate that: i) the results for these two tools were widely equivalent, although the specific nuances in the computation of the database employed by each bioinformatics tool, especially for low statistical significance terms, appears to induce some variation; ii) that tools that employ adaptive mining analysis are indeed extremely powerful to manage/analyse the data in a manner otherwise un-practical in a manual approach, but a critical view and a minimal understanding of how these tools process the data is essential to ensure a meaning full biological interpretation and even new discoveries. Interesting clusters such as, *"camera type eye development"* (Figure 4.6-b3) and *"branching morphogenesis of a tube"* (Figure 4.6-c4) would be discussed further on the upcoming sections.

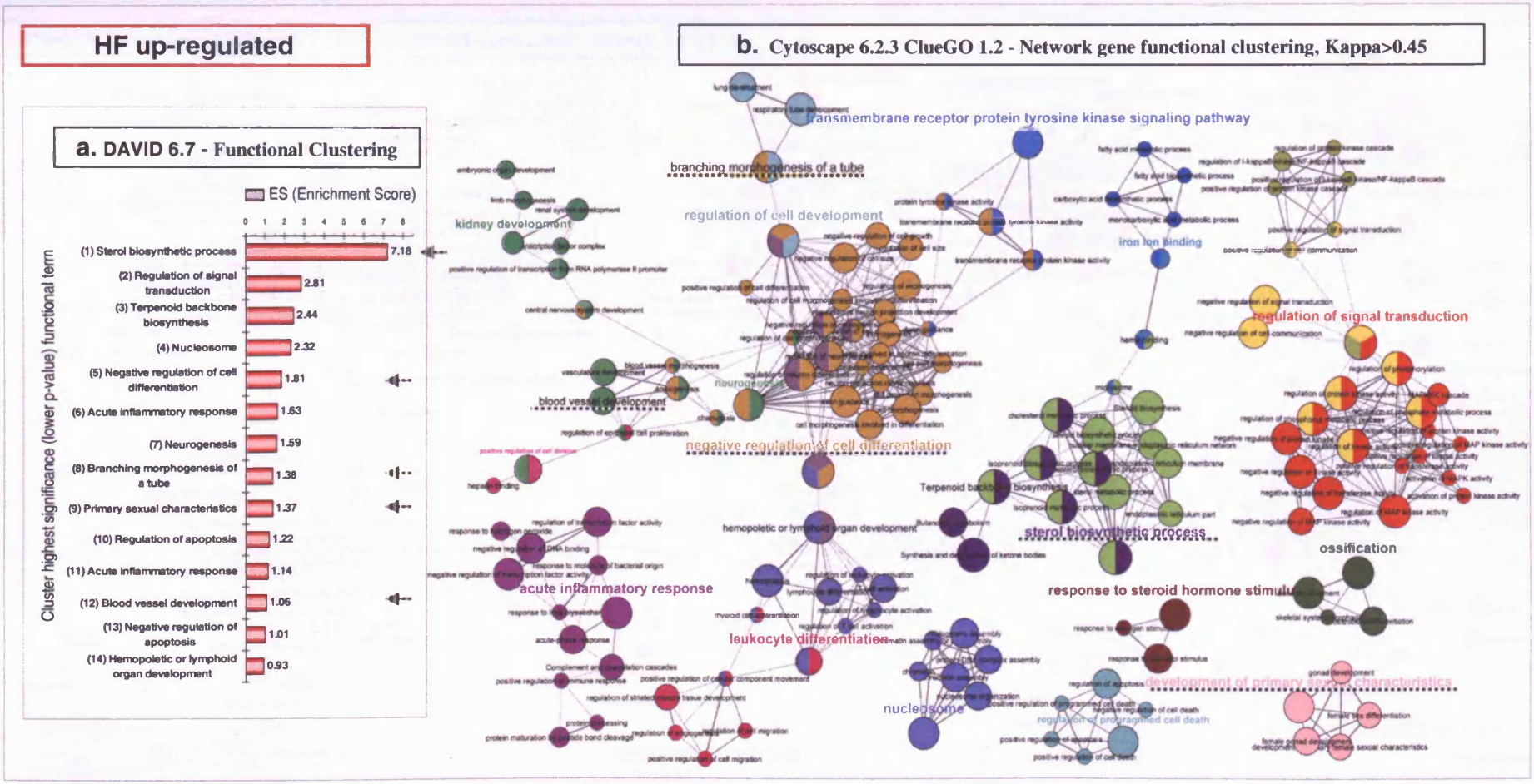


**Figure 4.5 – Modular enrichment analysis of the HF up-regulated gene list.** U2OS-GFP hollow fiber model (HF) versus standard tissue culture (CON) microarray analysis. **(a)** Summary histogram of DAVID 6.7 functional annotation clustering; databases "GO_TERM_(BP,CC and MF)_5" and KEGG (kappa>0.45 and ES>0.9). The value of the abscissa reflects the cluster enrichment score (ES), only the highest significance (lower p-value or fdr) functional annotation term of each cluster was presented. **(b)** Cytoscape 6.2.3 ClueGO 1.2 plug-in network gene clustering. Neighbour nodes with same colour and with close interconnected edges represent a distinctive cluster that may be connected to adjacent related terms or clusters, leading group term legend (bigger font) correspond to the highest FDR significance; *node size* ≈ proportional to the term FDR value (range from 3.6E-15 to 0.1); *edge thickness* ≈ proportional kappa score between nodes (kappa>0.4); Parameters: Databases KEGG and GO term restrictions tree level from 5-20 with min gene number and associated % =3; cluster: kappa>0.45; term grouping minimum initial size=3 with 50% for group merge. Output: ≤64% of the 271 HF up-regulated gene list represented in the analysis.

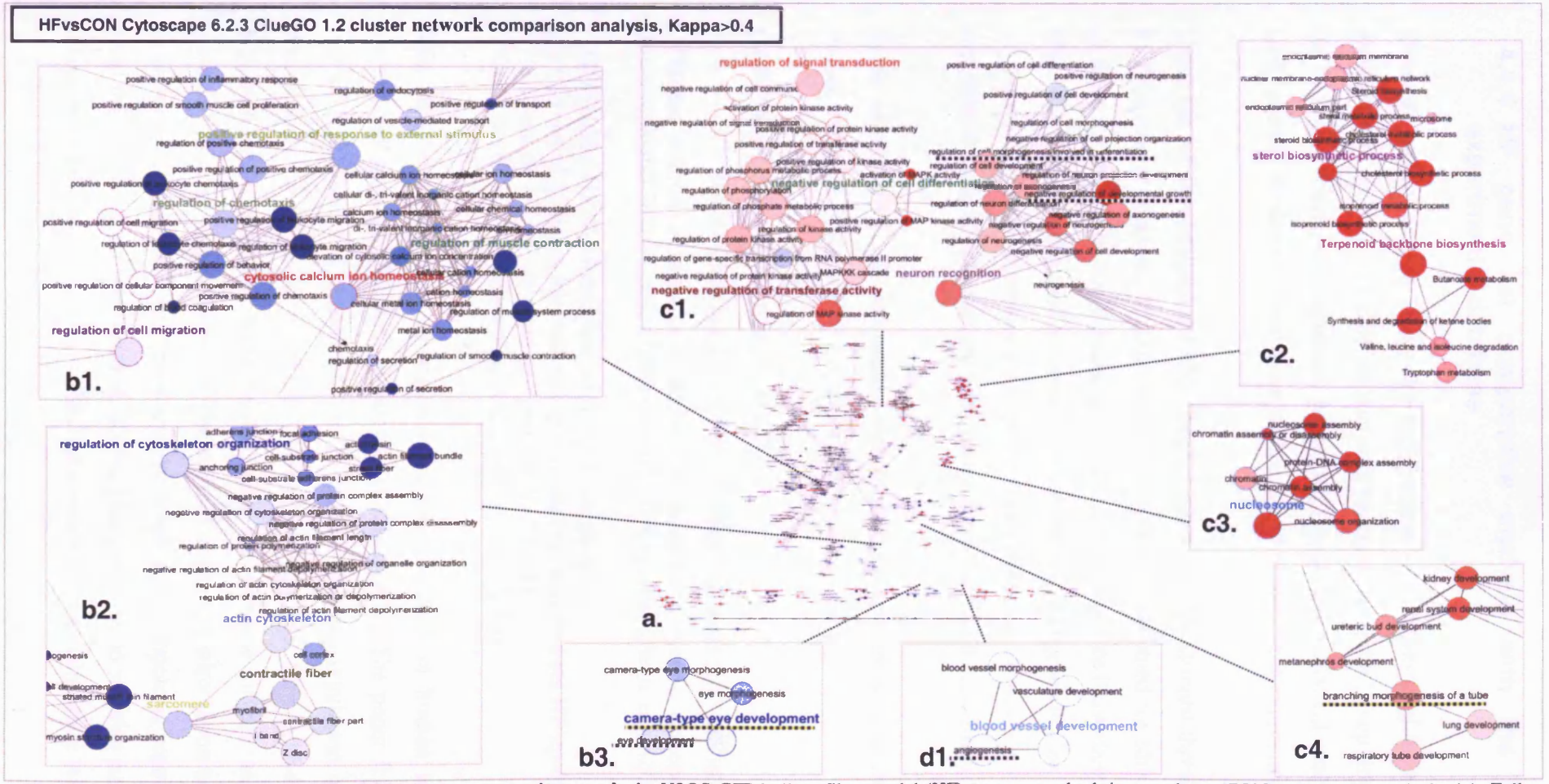


**Figure 4.6 – Functional network HFvsCON cluster comparison analysis.** U2OS-GFP hollow fiber model (HF) versus standard tissue culture (CON) microarray analysis. **(a)** Full network generated organic layout. Functional terms HF up/down regulated genes are shown in red/blue nodes, respectively; the colour gradient shows the up/down gene proportion associated to each term; equal proportions of the two clusters are represented in white; cluster leading group term legend (greater font) correspond to the highest FDR significance; *node size* ≈ proportional to the term FDR value (range from 2.4E-11 to 0.1); *edge thickness* ≈ proportional kappa score between nodes (kappa>0.4). Zoom-in example of clusters mainly enriched with: **(b)** HF down-regulated genes; **(c)** HF up-regulated genes; **(d)** equally proportional HF up/down genes. ClueGO 1.2 plug-in analysis criteria: Databases KEGG and GO tree level from 5-20 with min gene number and associated % =3; cluster kappa>0.4; term grouping minimum initial size=3 with 50% for group merge. Output: 70% of the 507 gene list represented in the analysis. PDF available in Supplementary Information 4.6-4 –CD-PDF.

### 4.4.4 HF gene list comparative analysis with the NCBI-GEO experimental database

ConceptGen (Sartor et al. 2010) web tool (section 4.3.2.2) was used for a comparative analysis with NCBI-GEO experimental data concepts using the HF up/down-regulated list to obtain overlapping common genes, with respective statistical analysis. NCBI-GEO permits the downloading of experiments and curated gene expression profiles.

Using the HF up-regulated list with the maximum possible strictest threshold allowed by the ConceptGen tool, 46 experiment concepts were obtained for fdr<1.0E-11. All of these with a size of 40-70 genes (of the 271 HF up-regulated) overlapping previous GEO database experimental concepts with around 300-900 genes in size. A summary of these results are presented in Supplementary Information 4.6-5 for the HF up-regulated list and Supplementary Information 4.6-6 for the HF down-regulated list.

Some examples of relevant highly significant ConceptGen experimental concepts related to the HF up-regulated list are described as follows:

***GDE10595-HS27+Monocytes_vs_HS27***

(NCBI-GEO: http://www.ncbi.nlm.nih.gov/geo/query/acc.cgi?acc=GSE10595)

"Human marrow stromal cells activate monocytes to secrete osteopontin, which down-regulates Notch1 gene expression in CD34(+) cells" (Iwata et al. 2004).

-GDE10595-HS27+Monocytes_vs_HS27Control-up:

- 14 out of 15 genes *biosynthesis of steroids* (top enriched set HF up-regulated list)
- 60 out of 271 HF up-regulated genes (fdr=5.1E-18)
- 50 out of 234 HF down-regulated genes (fdr=1.1 E-13)

This study reported genes up-regulated in the co-culture of human bone marrow stromal cell lines (HS27) with monocytes (CD14+ cells). The paper focused on the role of SSP1 (secreted phosphoprotein 1) in hematopoiesis regulation and this gene was equally up-regulated in the HF (SSP1: $\log_2$FC =1.25; fdr= 3.1E-04). The up-regulated genes/pathways were related with the increase of the segregation of steroids/cytokines in the co-culture. The stromal monocytes stimulation and vice-versa is believed to be related with monocyte/macrophage hemopoiesis regulation on the local microenvironment (Iwata et al. 2004). This comes as no surprise considering the discussion in the previous section that links osteosarcoma malignancy with disruption

of the differentiation pathway in bone marrow mesenchymal pluripotent cells (Luo et al. 2008). Additionally, this is probably also linked with the results of a previous study that revealed the capacity of U-2 OS cells in regulating and supporting the proliferation of hematopoietic progenitor cell *in vitro* (Nelissen et al. 2000), where IL8 was one of the cell growth factor up-regulated upon stimulation. The expression of this gene seemed to be related with immune recruitment/regulation and angiogenesis potentially linked with tumour invasion/metastasis features.

***GSE8702-LNCaP-AndrogenDeprived_***

(NCBI-GEO: http://www.ncbi.nlm.nih.gov/geo/query/acc.cgi?acc=GSE8702)

"Longitudinal analysis of androgen deprivation of prostate cancer cells identifies pathways to androgen independence" (D'Antonio et al. 2008).

-GSE8702-LNCaP-AndrogenDeprived-3_vs_contrl_up
- 44 genes out of 271 HF up-regulated genes (fdr=2.7E-7)

-GSE8702-LNCaP-AndrogenDeprived-11mon_vs_5mon_up
- 55 genes out of 271 HF up-regulated genes (fdr=5.1E-15)

These data sets are from a study that followed LNCaP prostate cancer cells gene expression during 12 months under androgen deprivation. The focus was on evaluating the cells phonotypical and genetically adaptive response to an androgen independence state that leads to long term cell growth and survival (D'Antonio et al. 2008). Most of the set overlapping genes with the HF up-regulated list are related with steroids/kinase metabolism, underling once more the importance of these pathways to long term tumour survival. This study comes in line also with the *in vivo* HF LNCaP implant model (Wang et al. 2006; Wang et al. 2008).

***GSE8772-Melanoma-KINK1-24h_vs_Control_***

(NCBI-GEO: http://www.ncbi.nlm.nih.gov/geo/query/acc.cgi?acc=GSE8772 )

"KINK-1, a novel small-molecule inhibitor of IKK beta, and the susceptibility of melanoma cells to antitumoral treatment" (Schon et al. 2008).

-GSE8772-Melanoma-KINK1-24h_vs_Control_down
- 58 genes out of 271 HF up-regulated genes (fdr=6.8E-17)

This study is related with KINK-1 (kinase inhibitor of nuclear factor-κB-1) a novel small molecule potent inhibitor of the the IκB kinase (IKK) complex associated to

chemotherapy resistance. In this study KINK-1 reduced the expression of NF-κB–dependent gene products that regulated proliferation, cytokine production, and anti-apoptotic response. This kinase inhibitor agent combined with "classical" anti-tumour drugs seemed to enhance melanoma cell metastases susceptibility to the chemotherapy in an *in vivo* melanoma model (Schon et al. 2008).

Overall, the HF up-regulated genes list was highly enriched in genes of the above NCBI-GEO concepts. Taking all together the HF up-regulated genes were more widely associated with proliferation, angiogenesis, immune regulation and resistance pathways related also with several other tumour types.

### 4.4.5 Identification of gene expression biomarkers directly related with the HF–U2OS-GFP model

• ***Interesting single gene - CRYBA4***

The top 20 *CRYBA4* ($log_2FC$ =2.03; fdr=1.7E-05) gene represents a potential candidate, for an "unusual" gene expressed in the HF–U2OS-GFP model. In relation to 569 GEO experimental concepts (using minimum cut-off threshold fdr=1) it only appears associates with two concepts as follows:

***GSE9916-PBMC-HeatShock_vs_Control_up***
(NCBI-GEO: http://www.ncbi.nlm.nih.gov/geo/query/acc.cgi )

This was related with human PBMC (peripheral blood mononuclear cells) up-regulated expression associated with heat shock stress.

***GSE11510-Placenta EPC_vs_CordBlood_up***
(NCBI-GEO: http://www.ncbi.nlm.nih.gov/geo/query/acc.cgi?acc=GSE11510 )

This study was connected with the taxonomy characterization of placenta cells. This gene was up-regulated in extra-embryonic mesodermal cells (EPC) that were shown to have a myogenic potential and regenerative capacity in skeletal muscle. This concept was also of significance with 56 out of 271 genes of the HF up-regulated list (fdr=4.3E-16).

*CRYBA4* (beta-A4-crystalline), crystallins are a family of long-lived, abundant structural proteins that are expressed in the vertebrate lens associated with the maintenance of the transparency and refractive index of the lens. These proteins are divided into different families (i.e. alpha, beta and gamma) with acid or basic groups. Beta-crystallins are the most heterogeneous, and form aggregates of different sizes and are able to self-associate to form dimers or to form heterodimers with other beta-crystallins (NCBI-EntezGene: http://www.ncbi.nlm.nih.gov/gene/8613 ). This gene in particular encodes a beta acidic group member (beta-A) that is part of a gene cluster with beta-B1, beta-B2, and beta-B3. CRYBB1 (crystallin, beta B1: $\log_2$FC =1.11; fdr= 1.4E-03) is also up-regulated in the HF.

Studies with this protein appear to address its function in epithelial lens eye cells or like cataract marker in case of mutations (Graw 2009), some other family members were reported in other tissues outside the lens ( i.e. alpha-B-crystallins), but beta-A4-crystalline did not seem to be referred (Andley 2007). One of the only references that even closely relates this gene/protein with tumours/cell lines, was related to its expression in HeLa, transfected with a *CRYBA4* expression construct and these cells were treated as a protein "secretion" vector system for protein-protein interactions (Liu and Liang 2007; Marin-Vinader et al. 2006). These studies deal with this protein family member's extracellular heteromer assembly interactions, and no concrete assessments on any biological implications of this protein in HeLa cells was performed. A study with, alpha-B-crystallins (alpha-basic–crystalline) encoded by CRYAB have demonstrated that this basal epithelial cell protein was expressed and associated with poor clinical outcome in invasive metastatic breast cancer (Sitterding et al. 2008). The relevance to osteosarcomas requires further investigation.

Importantly using 3D basement membrane cultures of MCF-10A cells on a Matrigel matrix layer, the cells organized in hollow spherical like clusters (Debnath et al. 2003), alpha-B-crystallin overexpression induced luminal filling and other neoplastic like phenotypic changes in mammary acini, increasing cell invasion *in vitro*, while silencing αB-crystallin by RNA interference inhibited these abnormalities (Moyano et al. 2006). In contrast, other works specifically with U-2 OS cells grown in soft agar

culture and *in vivo* (Zucchini et al. 2008) show that CRYAB is highly over-expressed and present in their corresponding FC gene list associated with low metastatic ability.

By contrast, in the present study CRYAB (alpha-B-crystallin) was also part of the HFvsCON differential expressed gene list, but listed in the top 20 HF down-regulated genes ($log_2FC$ =-1.31; fdr=1.7E-04), meaning that this was over-expressed on the standard 2D TC dish. This gene was part of the *"eye development"* functional term Figure 4.6-b3 (fdr=5.0E-1) and Supplementary Information 4.6-2 cluster 13 (ES=0.9), together with genes like COL5A1 , MITF, PTPRM, THY1, ZEB1 of the HF down-regulated list and CRYBA4, MAB21L1, SHROOM2 of the HF up-regulated list, curiously CRYBB1 did not appear to be associated.

*CRYBA4* (beta-A4-crystalline) was preferentially expressed by the U2OS-GFP cells associated with the more complex HF encapsulation micro-environment while CRYAB is associated with cell invasion capability in other 3D cultures. It is possible that *CRYBA4* is associated with this response in the HF–U2OS-GFP model. The exact impact requires further investigation but it seems that *CRYBA4* may represent a potential interesting biomarker.

• ***Interesting Cluster – "Branching morphogenesis of a tube"***

The HF up-regulated DAVID and ClueGO identified modular functional cluster *"branching morphogenesis of a tube"* showed on Figure 4.5 cluster 8 (ES= 1.34) and on the network comparison view Figure 4.6-c4 represents an "unexpected" feature; consistent with the consideration that the HF represents a "tubular" encapsulation system and according to the modular/network gene enrichment analysis the cluster presented a valid significance. Specifically related with the functional term *branching morphogenesis of a tube* (fdr=2.6E-1) the genes FGF13, FOXA2, MGP, NRP1, PBX1, SPRY2 were present on HF up-regulated list while GNA13, HOXD11 were part of the HF down-regulated list (Figure 4.6-c4).

## 4.5 Conclusion

The chapter aim was to compare and identify gene expression biological features associated with the HF model in relation to standard 2D TC and determine if this expression is closer to the complex features observed on other models and *in vivo* tumours. Several of the HF up-regulated signalling gene/pathways extensively discussed in the previous sections were all closely associated with metastatic, invasion, angiogenesis and proliferation on tumours/cell lines. Three issues have been investigated to attempt to link and understand the observed cells gene expression with the HF culture platform environment.

The first addresses the HF close encapsulation of cells which leads to a density constraint inside the tubular wall of the fiber; with a possible nutrient gradient between the extra-fiber space and the inner fiber core. The proposal is that cells inside the HF may be attempting to reach the extra-fiber nutrients rich medium. In a similar scenario, U-2 OS cells in the Matrigel invasion chamber/well, tend to move towards to the nutrient rich lower chamber (Han et al. 2008; Luu et al. 2005; Xin et al. 2009). The SEM analysis showed (Figure 3.2 and Figure 3.3) that the U-2 OS cells adopt a anchorage dependent organized monolayer on the HF inner wall, typical for this cell line (Dass et al. 2006). The U2OS-GFP cells exhibit an adherent morphology and importantly in the HF, it could be considered that the cells are in a type of apical–basal configuration (Affolter et al. 2003; Affolter et al. 2009). With the apical side facing the HF core interior giving access to a more conditioned and nutrient depleted medium while the basal side is attached to the HF inner-wall, with a nutrient rich medium in the out-wall. Additionally, as referred to in previous sections, the HF micro-environment also seemed to enhance a gene expression linked with a minimal osteoblast differentiation phenotype and *"branching morphogenesis of a tube"*. This phenotype has been associated with tumour angiogenesis and invasion (Carmeliet et al. 2009) and featured on other 3D models (Yamada and Cukierman 2007). Therefore the proposal is that the cell layer in the constrained HF tubular formation might be attempting to form a bud, trying to "breach through the wall barrier" toward the nutrients medium. This therefore represents an organisational and phenotypic distinction of U-2 OS cells encapsulated in the HF.

The second issue for discussion is that cells in the HF change their behaviour due to attachment to a PVDF porous wall surface. This surface, as previously discussed (chapter 3.5), presents a topography with pores (70-80nm) and also irregular "pits and crevasses" with less than 100 nm width, furthermore the surface is hydrophobic. This in contrast with the more smooth and hydrophilic polystyrene TC treated surface, fully optimized to enhance cell attachment. The gene expression analysis associated with standard TC presented an over-expression profile related to cell movement/migration, cytoskeleton and adhesion, overall the cells assume a more motile behaviour. A comparative study with the same U-2 OS cells growing on a PDMS hydrophobic surface (with no additional treatments or topographic features), and again compared to the TC surface, revealed significant up-regulation of GO clusters associated with adhesion and movement/migration (Errington et al. unpublished). Studies that analysed cell morphology and motile behaviour on PDMS surfaces confirmed changes in adhesion/motility (Tzvetkova-Chevolleau et al. 2008), thus supporting this results. However, these same GO clusters were down-regulated in the HF proposing that cell motility has been affected.

A recent study has shown that osteosarcoma derived cell lines, including U-2 OS, deform their nucleus in response to accentuated surface topography of a square pillar matrix [7, 7 and 4 μm (wide, spacing and height)] as they attempt to grow around and through the structures; this leads to an adaptation of the cytoskeleton such that actin filaments span the space between the pillars (Davidson et al. 2010). The HF inner wall topology provides a nanoscale topography that is irregular, so it could be assumed that it would have a minimum effect on the nucleus deformation and gross cytoskeletal consequences. However the current study reveals integrin expression differences. Integrins are receptors that mediate attachment between a cell and the surrounding tissue or surface, they also play a role in cell signalling and thereby define cellular shape, mobility, and regulate the cell cycle. Several authors (De Ruijter et al. 2001; Siebers et al. 2008; ter Brugge et al. 2002) studied the integrin expression of U-2 OS cells in irregular titanium or calcium phosphate coated surfaces of different roughness features, with more accentuated topography than the HF. The HFvsCON list presented genes associated with integrins, namely the up-regulated *ITGB8, ITGB5* and down-regulated *ITGB3, ITGA4*. Reports mention that *ITGB8* is expressed and may be related with control of human airway lung epithelial cell proliferation

(Fjellbirkeland et al. 2003) and *ITGB5* as been reported to be associated with metastatic cell migration and invasion behaviour

Finally, the third issue to address is that the differences in gene expression are complex and therefore a combination of multiple HF influences. It is interesting to note that the some of the HF highly enriched genes are related with extracellular structural and signalling molecules, such as steroid biosynthesis. These steroid molecules would have relatively greater affinity towards the PVDF hydrophobic wall where the cells are attached, becoming absorbed and with also possible relative low diffusion through the wall, enhanced by the fact that the HF cultures were not agitation. The absorption and diffusion limitations of steroid hormones on other types of hollow fibers composition (hydrophobic polypropylene) has been previously described on a test study with estrone (Chang et al. 2003). Additionally, the absorption of several other compounds and hormones were also reported in other types of planar membranes (Comerton et al. 2007). More concretely, the PVDF polymer in general is capable of binding proteins hydrophobically and thereby widely used in the Western immunoblotting for protein analysis (Pluskal et al. 1986). A recent *in vitro* study on PVDF planar membrane demonstrated a higher absorption of growth factors such as FGF7 in the membrane, both exogenously from the serum and endogenous produced by the cells compared to a polycarbonate (PC) control membrane. PVDF absorbed components from a cell culture model of the murine fetal submandibular gland has been shown to promote higher morphogenesis of the tissue (Yang et al. 2010). In the present study the TC treated surface would have a lower capacity compared to the PVDF wall to absorb macro-molecules. This together with an imposed HF gradient in and the porous wall surface features for cell attachment may explain the difference in gene expression. It is true that in the current study it is difficult to attribute the absorption of cellular factors to gene expression differences as this has not been validated. Furthermore, nucleosome associated GO clusters, highly up-regulated in the HF cultures, were also up-regulated in the PDMS cultures; but the genes related to steroid biosynthesis remained unique to the HF cultures.

An important outcome of this gene profiling chapter is to acknowledge that the analysis has required the capacity to undertake a comprehensive study with capabilities to "browse" through the large amounts of interconnected information.

Towards this goal the bioinformatics tools DAVID, ConceptGen but particularly Cytoscape ClueGO gene enrichment networks were the most versatile. This demonstrates the critical role of bioinformatics tools in providing a comprehensive gene enrichment and network analysis, highly enhancing the biological translation of the results (Hu et al. 2007; Lee and Tzou 2009). This is important at two levels: first that the mathematical algorithm advancements have allowed for the decoding and interconnecting of complex data. Second, and most pragmatic, is connected to the end-user hardware/software interface, where bioinformatics tools are required to easily analyse vast amounts of raw data (and ideally integrated with multi-modal sources). This is vital to highlight patterns and emergent features (Campbell et al. 2010; Chesler and Baker 2010; Hu et al. 2007). The capacity (or incapacity) to engage the end-user and its data with a "friendly" interface may represent one of the major general impairments holding back the progression of systems biology to the wider "wet laboratory" scientific community.

In summary, the HF up-regulated list was highly enriched in gene clusters associated with *"sterol biosynthetic process"* and *"nucleosome"* plus *"negative regulation of cell differentiation"* and *"branching morphogenesis of a tube"*. Furthermore some previously discussed genes represent good candidates to be further investigated in relation to the HF model indentified distinct features, namely: i) *SOSTDC1* previously connected to *pattern specification process* and included in the *"branching morphogenesis of a tube"* cluster and ii) *CRYBA4* expression represents a novel biomarker in tumours and again its expression could also be probably related with the HF cell culture. It will be of interest to explore the molecular consequences for differential-regulation of these select genes in the 3D micro-environment. *SOSTDC1* may be related with the U-2 OS differentiation, previous work showed that low differentiation potential in these cells is related with higher malignancy and metastasis (Honorati et al. 2007). *CRYBA4* is an external structural protein unknown in tumour cell lines, but a close family member CRYAB (top 20 FC list down-regulated in the HF) is widely associated with cell invasion and poor clinical outcome in metastatic breast cancer (Sitterding et al. 2008). By contrast in U-2 OS soft-agar 3D tissue culture and *in vivo,* CRYAB was highly expressed and seems to be associated with low metastatic ability (Zucchini et al. 2008). The U-2 OS cell population is subjected to different environmental constraints within the HF tubular encapsulation micro-

environment. These would mainly arise from limited space, close cell-cell proximity, the PVDF porous membrane wall topography and chemical composition (e.g. hydrophobicity) and the wall acting as a diffusion barrier producing a medium gradient. Thus promoting changes in the cell gene expression, which overall seems to bring the HF model closer to an *in vivo* "biological status" comparatively to a conventional planar tissue culture.

So far in the present study the cells were removed from the HF for analysis (i.e. SEM, cell counts, flow cytometry). Preliminary work has also been conducted to determine the options for tracking the cells using micro or macroscopic imaging directly inside the HF. However, the HF membrane optical (transmission and particularly auto-fluorescence) properties limit this option, as it is difficult to detect GFP expressing cells in the closed fiber (Silvestre et al. 2009) (see Appendix I-A for print-out). A far-red fluorescent protein alternative was considered (Shcherbo et al. 2007; Shu et al. 2009), but this represented the construction and optimization of a new cell transfected reporter system, also fluorescent proteins present low yield and photo-stability, compared to the potential of the new generation of nanoparticle probes (chapter 1.4.3). So since it was clear that the HF offers poor light transmission, hence Chapter 5 focuses on the benefits offered by highly quantum efficient, far-red quantum dots (QD) acting as in-fiber proliferative reporters.

## 4.6 Supplementary Information

### Supplementary Information 4.6-1: Arrays quality and normalization assessment

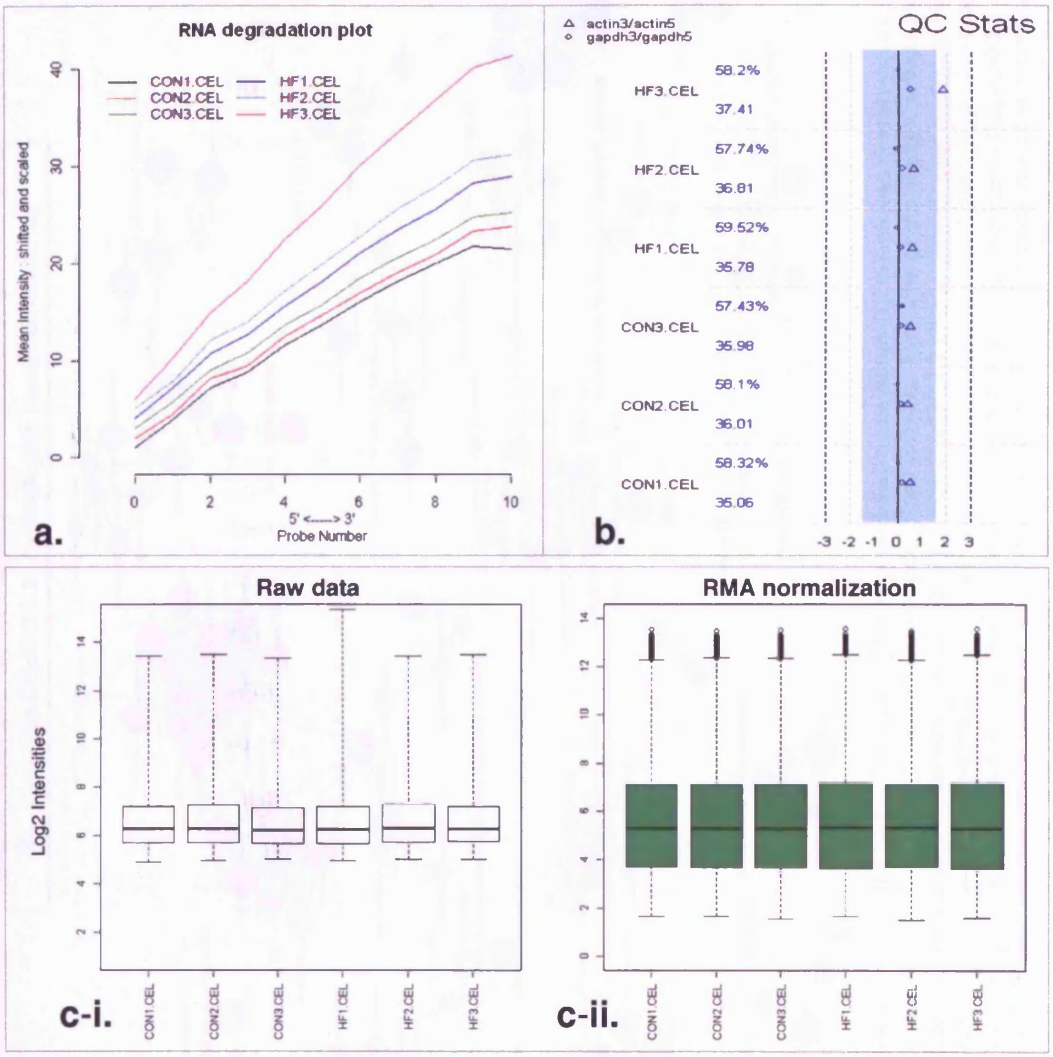


**Figure 4.7 – Array quality and normalization assessment.** U2OS-GFP hollow fiber model (HF) versus standard tissue culture (CON) microarray analysis. **(a) RNA degradation plot**; generated by the "affy" package, each line shows the mean expression from the 5' to the 3' end of the mRNA correspondent to an single chip and the slope of its trend indicates potential RNA degradation of the genetic material hybridized to the array chip (PM-probes only). The lines should present the lowest slope value and be as similar as possible. HF3 chip was the only that slightly deviated in this experiment, however, the deviation is not to extreme and it is acceptable. **(b) Quality control statistics**; (QC Stats) "simpleaffy" package generated quality control statistics, each array is represented by a separate row showing 5 metric parameters: Each row shows on the left hand side, the array sample, % present genes (upper number on each row), average background (lower number on each row), scale factor (bars with solid circles) and β-actin 3':5' ratios (open triangles) and GAPDH 3':5' ratios (open circles). The central vertical line corresponds to 0 fold change the dotted lines on either side correspond to up and down regulation (log2 scale). The scale factor is a measure of how mean intensities vary across the arrays. The blue bar represents the region in which all arrays have scale factors within, by default, three-fold of each other. Its position is found by calculating the mean scale factor for all chips and placing the center of the region such that the borders are -1.5 fold up or down from the mean value. The "simpleaffy" package documentation (Wilson and Miller 2005) and the Affymetrix guidelines (http://www.affymetrix.com) state that all the scaling factors or ratios should fall within the 3-fold region (1.25-fold for GADPH) and the background levels and % present genes need to be similar between chips, values considered within the acceptable range and colored blue, otherwise red. In short, everything in the figure should be blue, red highlights a problem. All the samples chip arrays had satisfactory values for all the tested metrics. **(c) Array data pre-processing and normalization. (c-i)** Un-normalized raw data. **(c-ii)** Expression summary generated using the RMA (Robust Multi-Array Average) pre-processing and normalization method (Irizarry et al. 2003) on the "simpleaffy" package.

**Supplementary Information 4.6-2: Modular enrichment analysis of the HF down-regulated gene list**

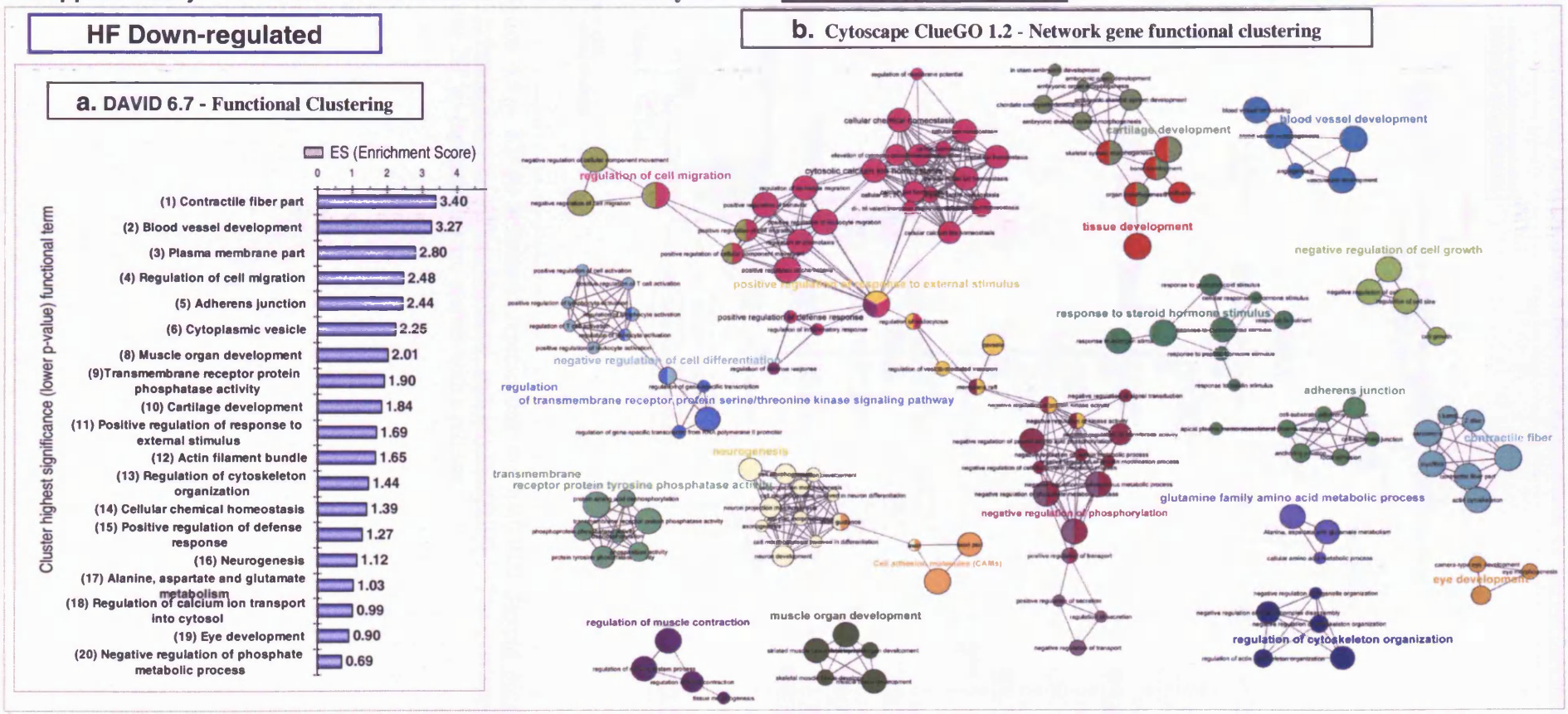


**Figure 4.8 – Modular enrichment analysis of the HF down-regulated gene list.** U2OS-GFP hollow fiber model (HF) versus standard tissue culture (CON) microarray analysis. **(a)** Summary histogram of DAVID 6.7 functional annotation clustering. Databases "GO_TERM_(BP,CC and MF)_5" and KEGG (kappa>0.5 and ES>0.9). The value of the abscissa reflects the cluster enrichment score (ES), only the highest significance (lower p-value or fdr) functional term of each cluster was presented. **(b)** Cytoscape ClueGO 1.2 plug-in network gene clustering. Neighbour nodes with same colour and with close interconnected edges represent a distinctive cluster that may be connected to adjacent terms or clusters, leading group term legend (bigger font) correspond to the highest FDR significance. *node size* ≈ proportional to the term FDR value (range from 3.6E-15 to 0.1); *edge thickness* ≈ proportional kappa score between groups (kappa>0.5); ClueGO 1.2 analysis criteria: Databases KEGG and GO term restrictions tree level from 5-20 with min gene number and associated % =3; cluster: kappa>0.4; term grouping min initial size=3 with 50% for group merge. Output: ≤67% of the 236 gene list represented in the analysis.

**Supplementary Information 4.6-3:** KEGG schematic of *Steroid biosynthesis* pathway.

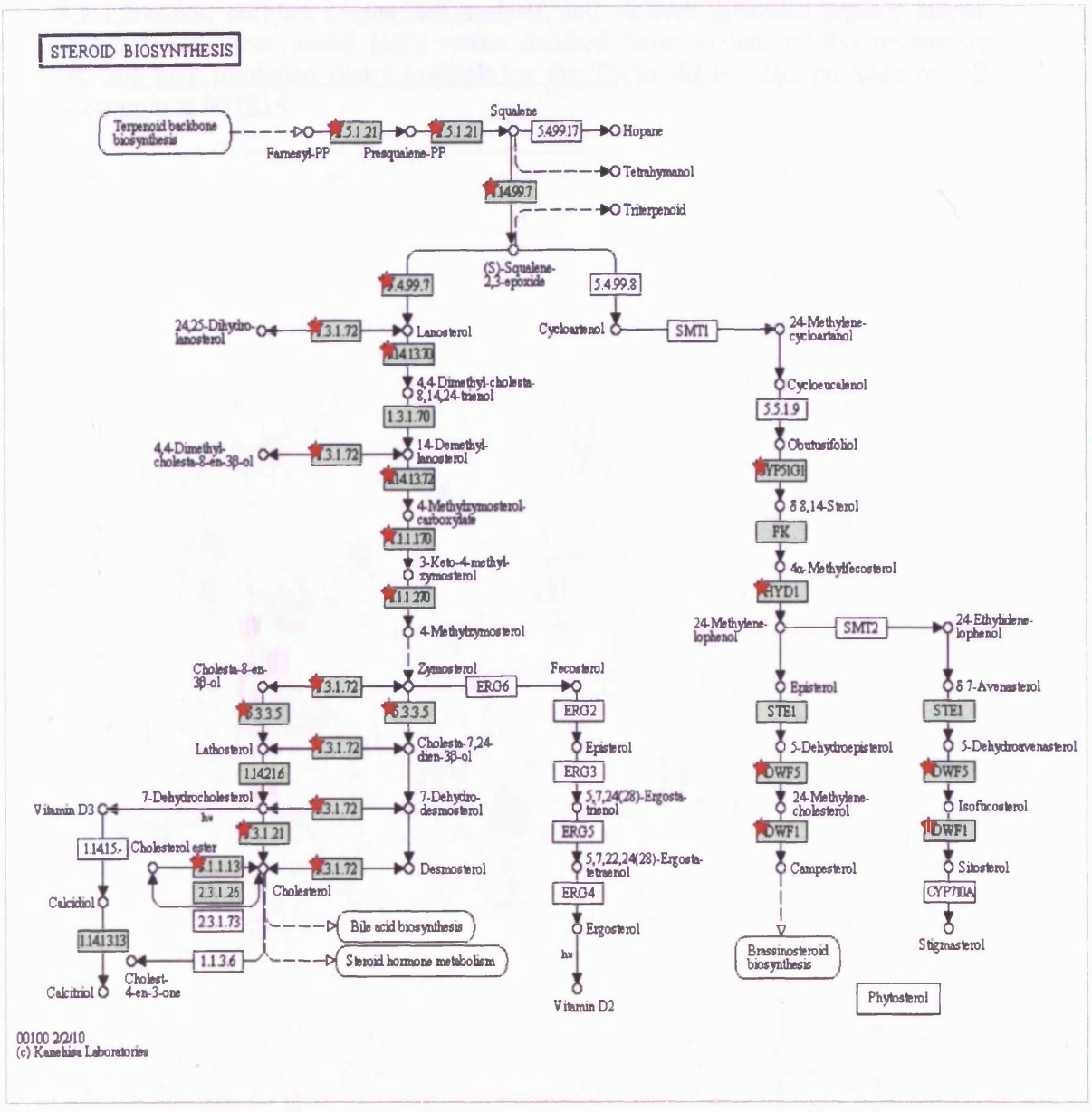


**Figure 4.9** – KEGG schematic representing the hsa00100 *Steroid biosynthesis* pathway (http://www.genome.jp/dbget-bin/show_pathway?hsa00100 ). The overlapping genes present on the HF up-regulated list are market with a red star.

**Supplementary Information 4.6-4:** Functional network HFvsCON Cytoscape 6.2.3 ClueGO 1.2 cluster network comparison analysis, full network generated organic layout. U2OS-GFP hollow fiber model (HF) versus standard tissue culture (CON) microarray analysis. See high resolution figure available on the Thesis digital copy on attached CD (please zoom-in to 800%)

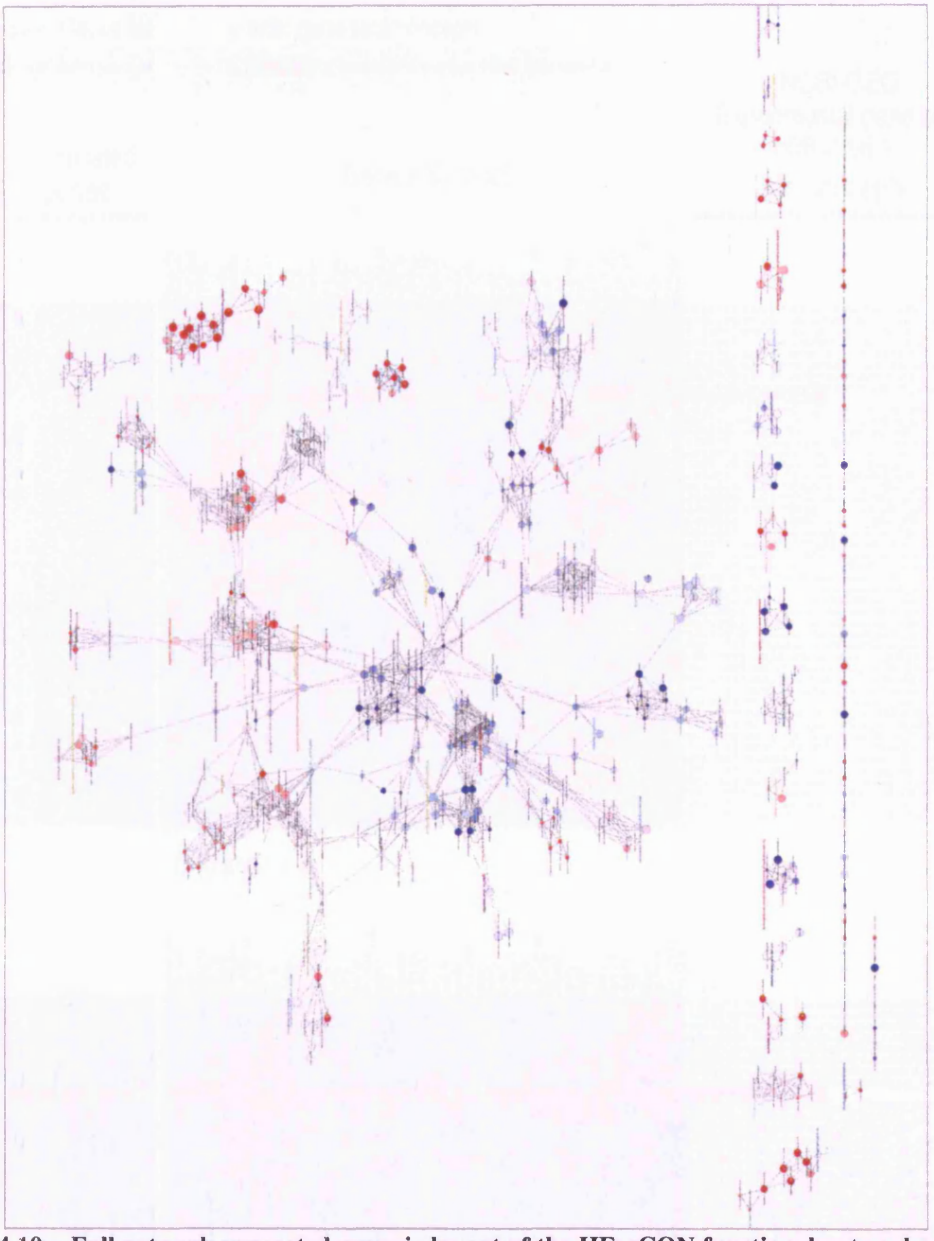

**Figure 4.10 – Full network generated organic layout of the HFvsCON functional network cluster comparison analysis.** Functional terms HF up/down regulated genes are shown in red/blue nodes, respectively; the colour gradient shows the up/down gene proportion associated to each term; equal proportions of the two clusters are represented in white. Clusters mainly enriched with: **(red)** HF up-regulated genes, **(blue)** HF down-regulated genes; **(white)** equally proportional HF up/down genes. Cluster leading group term legend (greater font) correspond to the highest FDR significance; node size ≈ proportional to the term FDR value (range from 2.4E-11 to 0.1); edge thickness ≈ proportional kappa score between nodes (kappa>0.4). ClueGO 1.2 plug-in analysis criteria: Databases KEGG and GO tree level from 5-20 with min gene number and associated % =3; cluster kappa>0.4; term grouping minimum initial size=3 with 50% for group merge. Output: 70% of the 507 gene list represented in the analysis. PDF single file also available on attached CD Supplementary Information 4.6-4 –CD-PDF (note: please zoom-in to 800%)

**Supplementary Information 4.6-5:** ConceptGen comparative analysis of the NCBI-GEO database concepts with the HF up-regulated gene list. For a FDR<1.0E-11, HF up-regulated list registers an average 40-70 genes overlap with the (300-900 genes size) Experimental NCBI-GEO database sets (http://conceptgen.ncibi.org/).

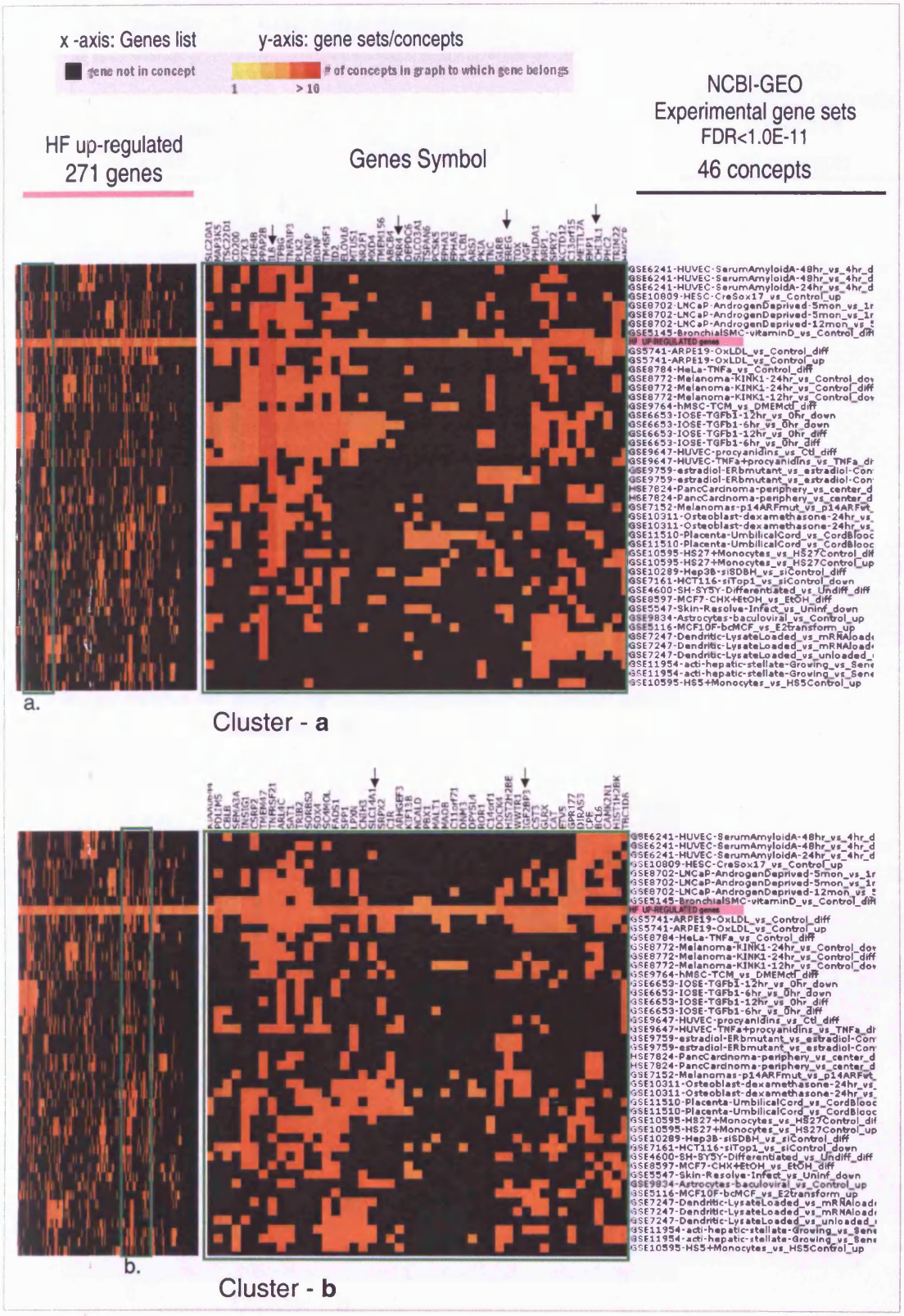

**Supplementary Information 4.6-6:** ConceptGen comparative analysis of the NCBI-GEO database concepts with the HF down-regulated gene list. For a FDR<2.2E-8, HF down-regulated list registers an average 40-70 genes overlap with the (~900 genes size) Experimental NCBI-GEO database sets (http://conceptgen.ncibi.org/).

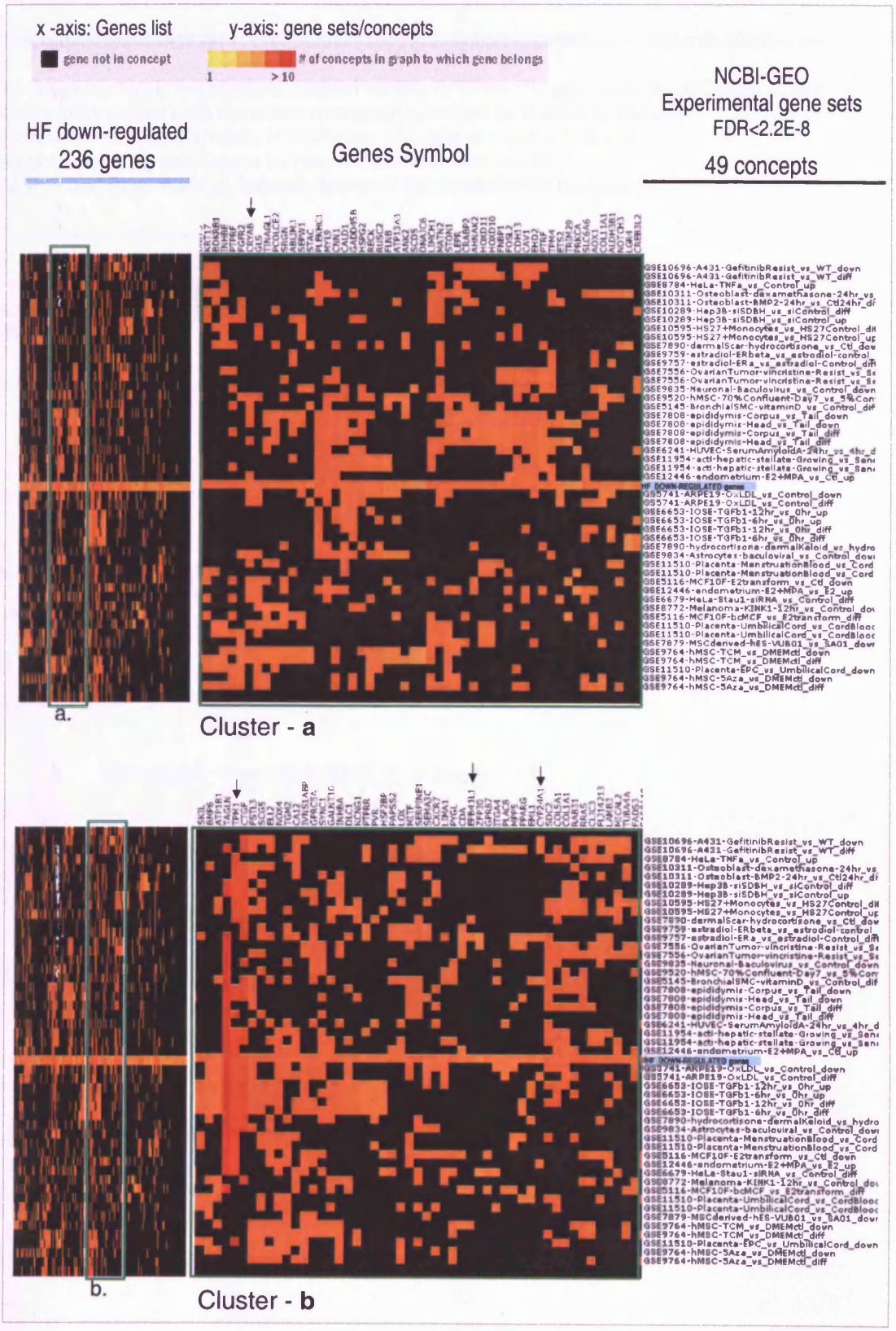

**Supplementary Information 4.6-7:** R script code used for the HFvsCON differential expression arrays analysis. U2OS-GFP hollow fiber model (HF) versus standard tissue culture (CON) microarray analysis.

```
"

############################################################~~~~~~[March-2010]~~~~~
#
#This Script is a highly modified and adapted version by Oscar Silvestre(silvestreor@Cardiff.ac.uk)
#(School of Medicine) from a previous code gently provided by Victoria Griesdoorn
#(GriesdoornV@cf.ac.uk)(School of Medicine) with help of expert advice and
# additional scripting and features by Peter Giles(GilesPJ@cf.ac.uk),
#(CBS(Central Biotechnology Services, School of Medicine,Cardiff University))
#
#-------------------------------------------------------------------------------
#
#R version 2.10.1 (2009-12-14)
#Copyright (C) 2009 The R Foundation for Statistical Computing
#ISBN 3-900051-07-0
#
#-------------------------------------------------------------------------------
#


... ... ...    "
```

Please consult in the folder "Supplementary Information 4.6-7–CD-Files" of the attached CD the following files:

- ..._ "HFvsCON_MicroArrayChip_R_Script.txt"
- ..._ "HFvsCON_MicroArrayChip_R_Script.R"
- ..._ "HFvsCON_MicroArrayChip_R_WorkSpace.RData"

# CHAPTER 5

# QUANTUM DOT DILUTION ASSAY FOR REMOTE TRACKING OF CELL PROLIFERATION IN THE HF–U2OS-GFP SYSTEM

Parts of this Chapter have been included or are related to the following publications:

**Errington**, R. J.; Brown, M. R.; Silvestre, O. F.; Njoh, K. L.; Chappell, S. C.; Khan, I. A.; Rees, P.; Wilks, S. P.; Smith, P. J.; Summers, H. D., Single cell nanoparticle tracking to model cell cycle dynamics and compartmental inheritance. *Cell Cycle* **2010,** 9, (1), 121-130.

**Brown**, M. R.; Summers, H. D.; Rees, P.; Chappell, S. C.; Silvestre, O. F.; Khan, I. A.; Smith, P. J.; Errington, R. J., Long-term time series analysis of quantum dot encoded cells by deconvolution of the autofluorescence signal. *Cytometry Part A* **2010a**, [Epub ahead of print].

**Holton**, M. D.; Silvestre, O. R.; Errington, R. J.; Smith, P. J.; Matthews, D. R.; Rees, P.; Summers, H. D., Stroboscopic fluorescence lifetime imaging. *Optics Express* **2009,** 17, (7), 5205-5216.

Print-out available on Appendix I

# 5 QUANTUM DOT DILUTION ASSAY FOR REMOTE TRACKING OF CELL PROLIFERATION IN THE HF–U2OS-GFP SYSTEM..... 176

# 5 QUANTUM DOT DILUTION ASSAY FOR REMOTE TRACKING OF CELL PROLIFERATION IN THE HF–U2OS-GFP SYSTEM

## 5.1 Introduction

The previous chapter has shown the overall growth and spatial arrangement of U-2 OS cells in the hollow fiber (HF), this was acquired alongside stathmokinetic analysis to show that cells grow slower in the HF environment and display delayed cell cycle traverse. There is a need however to develop an endpoint assay that gives a readout that represents an accumulated picture of proliferation history. Sub-fraction behaviour and possibly information on lineages – these could be called "dynamic endpoint assays". Therefore here a novel biophotonic approach was used where the *interpreter* component signal relates to intracellular nanoparticles dilution providing a method for tracking cell population proliferation in the encapsulated HF system. This is done by labelling cells with photonic quantum dots (QD) nanocrystals for a retrospective report on accumulated proliferative history.

This chapter addresses the use of nanocrystals (endosome targeted QDs) to track the proliferative features of a population growing in 2D tissue culture and the HF model. Since the aspiration is to also continuously monitor cell proliferation, lineage progression and cell division events we would consider the far-red QD signal to be the most compatible with the optical qualities of the HF-cell biomaterial.

### 5.1.1 Classical markers for cell proliferation tracking using organic fluorophores

As previously discussed, the capacity to monitor and track a live cell population perhaps labelled with a marker/reporter to determine a proliferative history and subsequently identify and sort sub-populations represents a major advantage in the study of cancer population dynamics and drug research.

Traditional techniques may allow only short term tracking (3-5 days) or are often destructive to the cells as they represent endpoint assays; most use labels that become incorporated into the cell, which may interfere with the normal physiological

behaviour of the cell. Ideally the marker/label should be persistent for successive cell divisions with minimal biological interference.

The focus of the present work is to develop a cell-based assay that gives a fluorescence readout that reflects the proliferative dynamics of the population ideally incorporating cell division kinetics and the lineage history. The fundamental principle is to label a cell with a stable fluorescent marker so that it acts as a conserved signal (photo-stable, non-metabolised and non-toxic) that becomes diluted upon each cell division and thus redistributes to each daughter cell.

Effectively as a result of each division event the total signal per cell becomes reduced. However the total signal in the population remains constant. Several such markers, see review by Parish 1999 , have been applied to track cells in this way with varying success depending on the cell type, namely PKH26 (Ashley et al. 1993) and SNARF-1 (Buckler and Vaughanjones 1990; Magg and Albert 2007). However, the most successful methodology using this principle has been carboxyfluorescein succinimidyl ester (CFSE) (Fulcher and Wong 1999; Lyons 1999; Parish 1999; Dumitriu et al. 2001; Putz et al. 2004). The dye–protein adducts that form in live cells are retained during mitosis; the label is inherited by daughter cells after cell division.

### 5.1.2 CFSE a widespread flow cytometry proliferation dye, assessing the advantages and limitations

(Weston and Parish 1990) initially described the use of a fluorescein based organic dye carboxyfluorescein succinimidyl ester (CFSE) (maximum ex.491 /em.518nm), for long term tracking in lymphocytes migration experiments. This was complemented by Lyons, 1994 that showed its use to track cell divisions, due to the fact that the dye is divided equally between daughter cells upon cell division, resulting in the sequential halving of mean fluorescence with each generation. When analyzed by flow cytometry, this sequential halving of fluorescence is visualized as distinct peaks and can be used to track division progression and to resolve multiple successive generations (Lyons 1999; Parish 1999).

Fluorescein diacetate and other derivatives, like carboxyfluorescein diacetate succinimidyl ester (CFDA-SE) the CFSE non-fluorescent form, can passively cross the cell plasma membrane where acetate groups are cleaved by intracellular esterases. As a result the dyes are 'locked' in the cell as they are membrane impermeable, in addition the former non-fluorescent permeable form becomes fluorescent after the reaction because of extended electron delocalization (Dumitriu et al. 2001). CFSE has a succinimidyl group, this highly activated carbonyl group can undergo a nucleophilic attack by amino groups of proteins, including cellular membrane, cytosolic, and nuclear membrane proteins forming a highly stable amide bond (Parish 1999). The dye, which is not associated with intracellular macromolecules, can escape the cell during the first hours of culture resulting in a drop of fluorescence intensity reaching a stable level within approximately 12 h (Lyons 1999). This technique when applied to non-dividing populations can detect labelled cells for considerable lengths of time, in early studies that was accomplish for up to 8 weeks (Weston and Parish 1990). However, in the case of proliferating cells were the dye is equally distributed between the daughter cells and therefore diluted out, CFSE is not detected beyond 8 to 10 divisions (Nordon et al. 1997; Lyons 1999; Lyons 2000) CFSE is primarily applied to lymphocytes studies and has advantages in its ability to stably label cells *in vitro* and *in vivo*, for migration or proliferation studies and analyses using fluorescence microscopy and/or flow cytometry, (Fulcher and Wong 1999; Lyons 1999; Parish 1999; Dumitriu et al. 2001; Putz et al. 2004).

However, CFSE has some disadvantages. Most of the successful applications of CFSE has been the use to track lymphatic cells, and although some reports refer to other cell types (Wang et al. 2005b), its does not have global application to all cell types, in epithelial and fibroblast systems (i.e. pre-adipocytes) (Hemmrich et al. 2006) it revealed long term toxicity and is only applicable for very limited tracking time periods. The dye is highly metabolised and therefore attenuates the stability of the readout (confirmed also in preliminary studies on U-2 OS) [personal communication Nuria Marquez]. CSFE is fluorescein-based and therefore produces a broad green emission and is highly pH sensitive (Rumphorst et al. 1994). Additionally cell auto-fluorescence has similar properties in this excitation/emission window (Baumgarth and Roederer 2000). The red dye PKH26 represents a sensible alternative (maximum ex.551/em.567nm), but also it is more difficult to get consistent uniform staining,

hence presenting a 'fuzzy' proliferation signal (Parish 1999). Additionally in more recent studies with peripheral blood mononuclear cells (PBMC) isolated from human patients the results seem to show that CFSE is toxic and substantially affects the expression of activation markers (Lastovicka et al. 2009). Also, CFSE like all organic dyes is more prone to metabolism by the cells and to photobleaching after frequent light exposure compared with other more recently introduced markers like quantum dots (Chan et al. 2002; Jaiswal et al. 2003; Resch-Genger et al. 2008).

### 5.1.3 QDs provide new opportunities for remote flow cytometry cell tracking of encapsulated cells

Quantum dots (QD) (see detailed description in chapter 1.4.3.4) composed of semiconductor materials, have been used in the encoding and the tracking of live heterogeneous cellular systems. Critical features such as signal persistence, biocompatibility, compartmentalization and bespoke targeting suggest that they are suitable for long term cellular tracking even through multiple cell divisions. Therefore the technical objective of the current investigation was to interlink nanoparticle tracking outputs in order to detect particles as they distribute within proliferating human tumour populations and so assess signal persistence over long time periods.

QDs have broad excitation spectra and narrow emission spectra they can be excited by one single wavelength and emit light of different wavelengths making them ideal probes for multiplex imaging (Gao et al. 2004; Michalet et al. 2005; Resch-Genger et al. 2008). (Bruchez et al. 1998; Chan and Nie 1998) were first to demonstrate that it is possible to label live cells with QD and detect these dots by microscopy. They chemically modified the QD exterior to make them water-soluble allowing also the covalent coupling of biomolecules. This has opened the door to the use of biocompatible QDs to tag biomolecules, for example antibodies, and also for use as a cell marker with delivery of QD via endocytic pathway (Chan et al. 2002; Chan and Nie 1998). Since this time extensive works have been published using imaging techniques for *in vitro* and *in vivo* identification and to track of live cells label with QDs (for reviews see (Biju et al. 2010; Gao et al. 2004; Ho and Leong 2010; Medintz et al. 2005; Michalet et al. 2005; Rogach and Ogris 2010)).

Specifically, more concrete examples refer their use to *in vitro* long term cell imaging by time-lapse (Jaiswal et al. 2003) and to spectral encoding of individual cells with unique mixtures of different QD that could have applications for the study of cell/cell interactions in mixed cell populations (Mattheakis et al. 2004). Applications include the *in vivo* tracking of metastatic tumour cell extravasation (Voura et al. 2004), mouse embryonic stem cells (Lin et al. 2007) and the tracking of human mesenchymal stem cells for quantitative *in vivo* three-dimensional fluorescence analysis (Rosen et al. 2007). These last two examples have specifically used the Qtracker® systems (Invitrogen) (see detailed description in chapter 1.4.3.5) which promoted the cellular internalisation and endosomal compartmentalisation of QDs through an 9-arginine peptide cell endocytosis mediator (Lagerholm et al. 2004).

Although a number of studies have been performed using QD for long term tagging and tracking of cells using, primarily, imaging techniques (as above), but not many studies exist with regards to using them in combination with flow cytometry measurements. This reveals a gap where multi-parameter analysis of cells containing QD has not really been exploited.

In this area it is possible to refer to some investigations where QDs reveal their superior fluorescent potential in comparison to traditional fluorophore dyes to be used in flow cytometry calibration beads (Gao and Nie 2004; Wu et al. 2007). Also the wide range of colours associated with broad excitation and narrow emission with low spectra overlap make them ideal for multi-colour flow cytometry. This was revealed to be of advantage in the characterization of complex phenotypic patterns of multiple antigen-specific T-cell populations using quantum dot–labelled antibodies and antigens (Chattopadhyay et al. 2006). Hoshino et al. 2004 was one of the first to use flow cytometric analysis along with imaging to trace mice T-cell lymphoma cells with QD internalized in the endosomes. The fluorescence of QDs held in the endosomes compartments could be detected by flow cytometry for up to a week *in vitro* and also in organ samples of animals previously injected with QD label cells. It is important to emphasise that all the above applications used the QD label only to indentify certain cell populations (i.e. tag) but not to use the signal output to interpret a cell division history (i.e. tag and track). This aspect exploits the stable or conserved signal in the

population, and the quantal nature of the QD signal distributed to subsequent daughter cells upon division. The distribution of the signal at different time points provides evidence of proliferation further granularity of information such as sub-population behaviour and inheritance of QD become features that define patterns of lineage behaviour underlying the population response. These parameters become essential in trying to understand the impact of the arrangement of cells in the HF and the microenvironment influences due to prolonged encapsulation, as well as the influence of a drug treatment/perturbation.

Recently, within the laboratory research group, initial studies were conducted with the U-2 OS cyclin B1-GFP (U2OS-GFP) cells labelled with CdTe/ZnS core-shell 705 nm emission QDs using the Qtracker® system (QD705) to track QD labelled endosomal compartment distribution dynamics through the daughter cells upon mitosis to obtain cell population division "history" by flow cytometry (Brown et al. 2007; Njoh et al. 2007; Summers et al. 2008).

## 5.2 Specific chapter aims

The overall aims for the current study was to build on the existing QD assay and validate its use for long-term studies on the Hollow Fiber U-2 OS cyclin B1-GFP model (HF–U2OS-GFP). Specifically there are three primary objectives:

*1.* To validate the QD studies already in place and determine the limitations and performance of the assay (e.g. dynamic range) for long-term tracking beyond 3 days and up to 8 days.

*2.* To determine QD tag and track analysis for determining the proliferation response of the osteosarcoma population under different growth pressures.

*3.* To optimise, evaluate and test the QD flow tracking technique for application to HF-encapsulation under normal and drug perturbation conditions, in an *in vitro* system.

A rationale behind these objectives is to also consider and accommodate future applicability for use *in vivo* by providing a benchmark *in vitro* assay.

## 5.3 Specific methodology - QD cell tracking by flow cytometry

Overall the experimental work of this Chapter can be grouped in two totally independent but similar experimental batches performed to study the tracking of QD labelled cell using single cell flow cytometry. Experiment 1 (Table 5.3-1), represented an initial study to optimize the protocol set-up, and acquisition procedure; including, temporal-sampling and minimal cell number for adequate flow analysis. This was followed, by a more intensive sampling Experiment 2 for improved time series analysis (Table 5.3-2).

Three experimental conditions were established for the long-term proliferative screen. Namely, two standard planar surface 2D adherent tissue culture (TC) with low confluency/density (6 well plate or 60mm culture dish (both seeded at a density of ~1.3 x$10^3$ cell/cm$^2$) (table pale green zone) and a high confluency/density 12 well plate (seeded density ~2.5 x$10^4$ cell/cm$^2$) (table purple zone). Plus the Hollow Fiber U-2 OS cyclin B1-GFP *in vitro* adherent culture model (HF–U2OS-GFP) (table orange zone), initial loading density estimated ~2.5 x$10^4$ cell/cm$^2$. Additionally, corresponding QD microscopy experiments were performed to show QD signal and distribution.

### 5.3.1 QD labelling of cells

All the experiments in this chapter were performed with U-2 OS cyclin B1-GFP (U2OS-GFP) cells (chapter 1.6.1.2) and the Qtracker® 705 kit (chapter 1.4.3.5). Cells were grown in 10% McCoy's to a confluency of approx 70-80% in standard TC conditions in T-75 flasks (table grey zone) on the day of the QD labelling. The day previous to QD label, half the flask cell media was replaced with fresh 20% McCoy's+25mM HEPES. The conditioned medium of the T-75 flash was retrieved and stored and the cells were QD label according to the Qtracker® 705 Cell Labelling Kit (Cat. No. Q25061MP, Invitrogen) (see chapter 2.4.4). Briefly, 3-4 ml volume of 4 nM QD in 10% Mccoy's+25mM HEPES was added to the T-75 and incubated for approx 60-80 min at 37°C. The cells were then washed and placed in the pre-conditioned medium with 25mM HEPES and returned to the flask for a further 24h at 37°C. Importantly time zero (0h) refers to the assay starting time when QDs were added to cells. Also the subsequent time-stamping refers to cells held in normal

growing conditions (i.e. 37°C), at appropriate points during the time course, cells were held at 4°C and during these short time periods the cells were not metabolically active and therefore held in a non-proliferative state.

**Table 5.3-1: Experiment 1: Summary chart of the experimental procedure.** Standard tissue culture(TC) with low confluency (6 well plate, growth area 9.6 $cm^2$ , seeding density ~1.3 x$10^3$ cell/$cm^2$) and high confluency (12 well plate, growth area 3.8$cm^2$, seeding density ~2.5 x$10^4$ cell/$cm^2$) conditions. Plus and the hollow fiber (HF) culture (2 cm length) *in vitro* growth (available adherent cell length of ~1.6 cm, area 0.50 $cm^2$, inner volume 12.6 µl, estimated loading density ~2.5 x$10^4$ cell/$cm^2$).

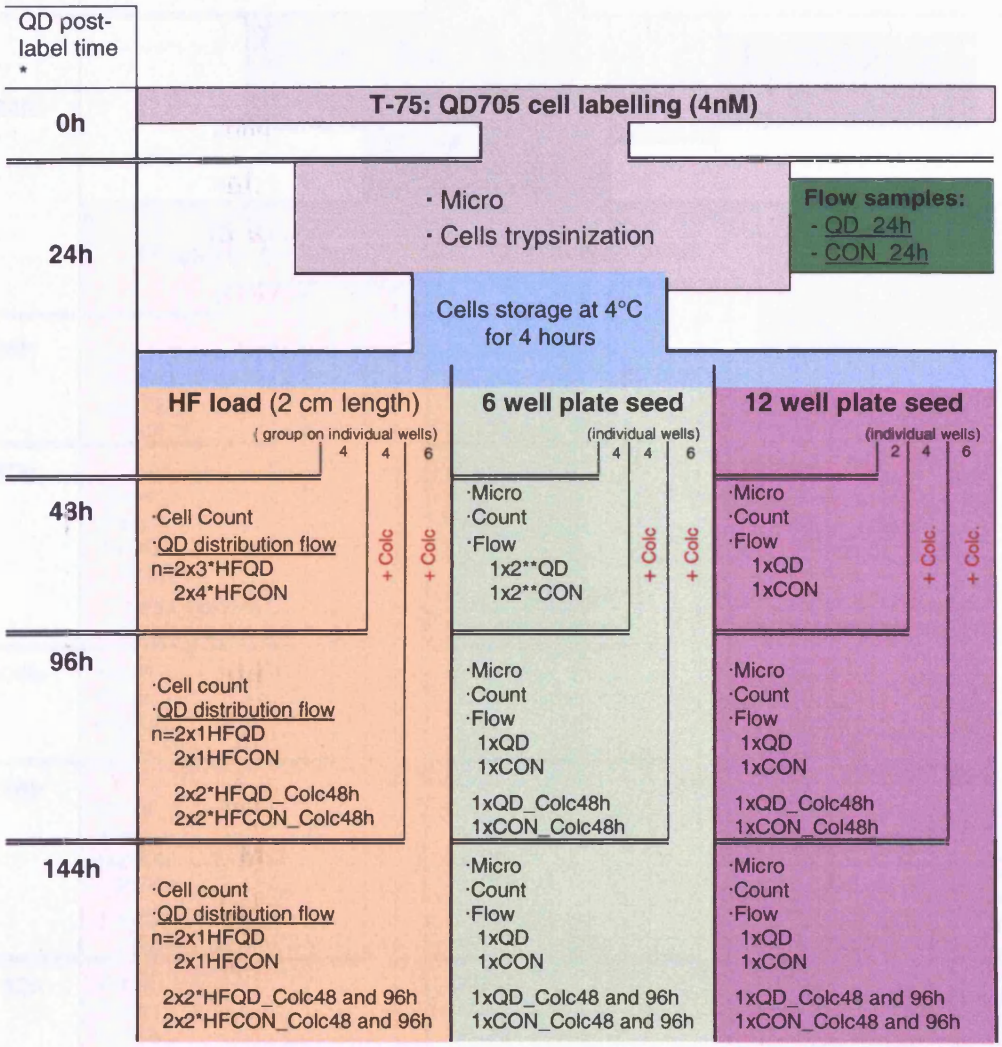


**Tables Legend:**

·**Micro** – Microscope acquisition, Ph2/QD705 epi-fluorescence 10x 0.45NA lens field (n>2);
·**Count** – Cell Count thought the Z1 Coulter Counter®;
·**Flow** – QD distribution FACSCalibur flow acquisition, live cells, main channels: cyclin B1-GFP (FL1), QD705, (FL3), forward and side scatter;
**+Colc** – Colcemid drug added to a final concentration of 60 ng/ml in the media;
**Colc…h** – Colcemid drug incubation time.

* samples not from individual HF, combine 2,3 or 4 HF (**or individual TC wells).
n= number of HF (or TC wells) acquired samples **x** when applicable the number of merged HF (or TC well)

**Table 5.3-2: Experiment_2. Summary chart of the experimental procedure.** Standard tissue culture (TC) with low confluency (60 mm dish, growth area 21.3 $cm^2$, seeding density ~1.3 x$10^3$ cell/$cm^2$) and high confluency (12 well plate, growth area 3.8 $cm^2$, seeding density ~2.5 x$10^4$ cell/$cm^2$) conditions. Plus and the hollow fiber (HF) culture (4 cm length) *in vitro* growth (available adherent cell length of ~3.6 cm, area 1.13 $cm^2$, inner volume 28.3 µl, estimated loading density ~2.5 x$10^4$ cell/$cm^2$). ***Note:** sampling at different time-points to Experiment_1.*

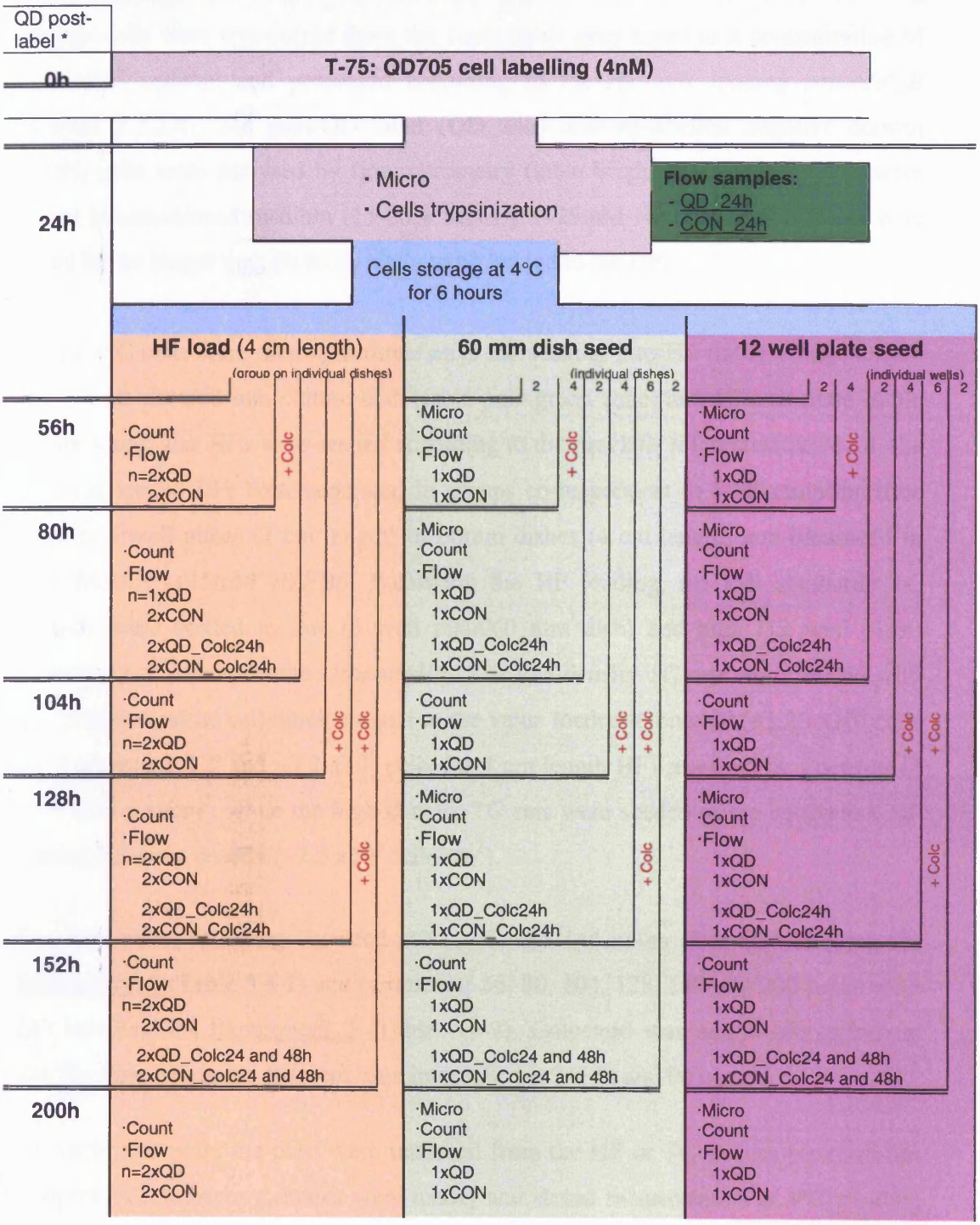


n= number of samples correspondent to individual HF (or TC wells) without any sample merge

### 5.3.2 Conventional TC versus *in vitro* HF model cell culture under normal proliferation and colcemid drug perturbation

After 24h post-QD labelling a sample field was phase/epi-fluorescence imaged to assess labelling, according to summarised in Table 5.3-1 and Table 5.3-2. Following this the cells were trypsinized from the flask (table grey zone) to a concentration of ~1.0 x$10^6$ cells/ml and processed according to the *HF cell loading protocol_B* (chapter 2.2.2.4). 24h post-QD label (QD_24h) and un-labelled negative control (CON) cells were analysed by flow cytometry (table bright green zone). Cells were stored in conditioned medium (15-20% McCoy's+25mM HEPES) at 4°C (table blue zone) for no longer than 6h total, ready to be loaded to the HF.

Stored 4°C cells were then split three ways for seeding into HF (table orange zone); into 6 well plate/60 mm culture dish (table pale green zone) and 12 well plate (table purple zone). The HFs were seeded according to the previous referenced protocol, the resulting loaded HFs were separated in groups correspondent to each sampling time point in 6 well plates (2 cm length) or 60mm dishes (4 cm length) and incubated in 10% McCoy's+25mM HEPES. Following the HF loading, the cell standards TC samples were seeded to low (6 well plate/60 mm dish) and high (12 well plate) confluency or density in the same media. The low density TC sets were seeded with the estimated initial cell number equal to the value loaded to one HF (~1.26 x$10^4$ cells for 2 cm length HF and ~3.2 x$10^4$ cells for 4 cm length HF) resulting in a density of ~1.3 x$10^3$ cell/cm$^2$, while the high density TC sets were seeded to the equivalent HF starting cell/area density (~2.5 x$10^4$ cells/cm$^2$).

The time series sampling occurred at 48, 96, and 144 hours after QD labelling for Experiment_1 (Table 5.3-1) and sampled at 56, 80, 104, 128, 152 and 200 hours after QD labelling for Experiment_2 (Table 5.3-2). Colcemid was added (60 ng/ml) at specific time points for different time intervals, i.e. 24, 48 and 96 hours.

For each time point the cells were retrieved from the HF or TC culture plates/dishes (sometimes microscopy checks were made) and stored in suspension at 4°C pending measurements. Except where indicated, every one of the analysed sample corresponds to an individual HF or well/dish, each sample was sub-divided and measured (live)

using flow cytometry and in most cases a cell count was conducted. The number of microscope fields, fibers or wells/dish sampled at each time point for each QD label or negative control samples is indicated (n =1,2,3...) in the table.

### 5.3.3 Flow cytometry to determine QD dilution

All samples were run through a FACSCalibur flow cytometer (Becton Dickinson) (chapter 2.4). Initially the flow cytometer PMT detector voltages and other settings were adjusted by running the un-labelled control and the post-24h QD labelled samples to capture all cells in the plots/histograms accordingly for optimal output. After this initial adjustment, all the settings were maintained the same for every remaining samples for each experiment. Calibration beads (Cat. No. K0110, FluoroSpheres 6-Peak Beads, DakoCytomation and Cat. No. 349502PE, Calibrite Beads, BD Bioscience) were run on each time point to evaluate the instrument "hardware" stability. During each experiment 1 and 2 the bead standards showed equivalent performance every time.

Experiment_1 (Table 5.3-1) performed to optimize the experimental protocol set-up and acquisition procedure. These results informed about protocol parameters, important to maximize the output of the QD reporting cell population. Namely flow cytometer calibration and sampling intervals, that were applied in Experiment_2. For example, in the flow Experiment_2 it was decided that it would be best to sample with shorter interval, up to 24h to improve temporal resolution (hence sampling cell cycle traverse in the fiber from 0.9 to 1.4 on time after seeding). With regards to raising the number of QD label compartments per cell by increasing the Qtracker® kit label, it was decided to maintain the previous protocols values of 4 nM QD cell incubation for ~1h at 37°C, this presumably reduces label toxicity effects and means that it is possible to compare and relate the data with previous investigations. These decisions formed the basis for Experiment_2 (Table 5.3-2).

Flow analysis was executed using FlowJo v.7.5.5 in Windows XP platform and mean fluorescence intensity values exported to Excel 2003 for further analysis. The flow analysis protocol consists of a forward and side scatter gate (Gate1) in order to

eliminate most of the low fraction of small debris and dead cells. So, except when stipulated otherwise, all the following presented flow results were derived from this Gate1. A second gate (Gate2) was also used determine the positively labelled QD cells (FL3) above auto-fluorescence (<10 arb. units). Exemplar flow analysis procedure can be consulted as follows: Experiment_1-Supplementary Information 5.6-3 and Experiment_2-Supplementary Information 5.6-4. The entire full raw and gated plots of all the flow analysis used in this chapter can be found on the attached CD accordingly: Experiment_1-Supplementary Information 5.6-3 – CD-A3 and Experiment_2-Supplementary Information 5.6-4 – CD-A3.

### 5.3.4 QD live cell tracking by microscopy (confocal time-lapse, epi-fluorescence and phase)

The QD compartment distributions inside the cells were imaged for selected samples prior to being processed for flow cytometry. Phase and QD705 epi-fluorescence 10x 0.45NA lens fields were acquired using the Axiovert wide field microscope (chapter 2.6.3).

Confocal laser scanning time-lapse microscopy was also performed on QD labelled U2OS-GFP cells (chapter 2.6.2). Two channel, x,y,z stacks were acquired corresponding to cyclin B1-GFP and QD705, therefore each frame in the final time sequences corresponds to a merged Z stack (12 planes x 2.40μm) sampled every 4 min. The need to image live cells labelled with QDs and cultivated on glass 1.5 coverslips using an upright microscopy configuration led to the design/build of a "silicone chamber set-up" (see Supplementary Information 5.6-2). Cell image analysis was performed using MetaMroph v7.6 and ImageJ v1.42 software in Windows XP platform.

## 5.4 Results and Discussion

The QD cell labelling technique used in this investigation is based on the delivery of QDs to the endocytic cell compartments pathway, using the QD705 and on tracking the distribution of the QD signal from cell to cell using flow cytometry. The simplicity of the assay has been previously reported (Brown et al. 2007; Njoh et al. 2007; Summers et al. 2008), where a population of QD labelled cells under standard cell culture was sampled at 24, 48 and 72 hours post-QD label by flow cytometry demonstrating a progressive signal decrease, apparently due to the cell QD (endosome) compartment partitioning/segregating QDs to each daughter cell. In this chapter this initial study was expanded to incorporate an extended 8 days, hence challenging concepts of dynamic range and sensitivity as the signal dilutes to auto-fluorescent background levels. Then further to place the same QD labelled cells onto a 2D TC substrate and in the HF model.

### 5.4.1 QD cell to cell dilution tracked by microscopy

Initially it was necessary to confirm that the QD intrinsic signal would remain stable – and not influenced by cellular internalization with time. In addition it was necessary to demonstrate that the QD fluorescence decrease per cell was related with the QD partition through the daughter cells upon cell division. A live single cell confocal laser scanning time-lapse microscopy method was selected to illustrate the QD partitioning of labelled U2OS-GFP cells traversing through G2 and mitosis. Upon the initiation of mitosis the cell became rounded and the QD fluorescence coalesced in the cell (Figure 5.1–35min), during anaphase (Figure 5.1–50min) the QD endosomal compartments became redistributed to each daughter through an asymmetrically partition (Errington et al. 2010). This clearly demonstrated the concept of using QD labelled endosomal compartments to report the consequence of cell division – namely signal attenuation per cellular unit.

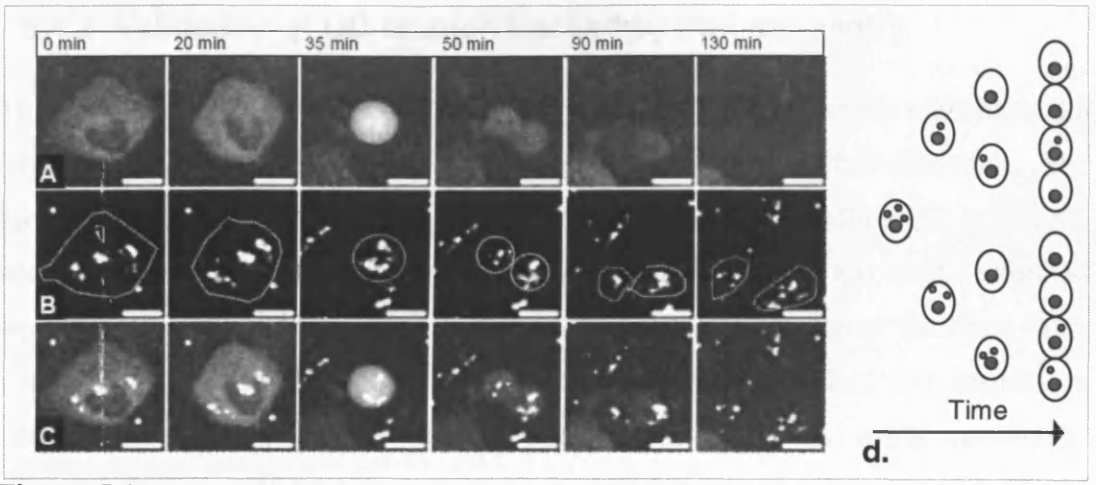


**Figure 5.1 – Time-lapse sequence of a single U2OS-GFP cell undergoing mitosis and Single cell tracking of the QD compartment as the cell divides.** Image sequence of the QD705 compartments typical partition through the daughter cells upon division. (**a**) Cyclin B1-GFP expression levels change as the cell progress from G2 (flat cell) to mitosis (round cell) and through mitosis followed by the reporter switch-off as the cell divides; (**b**) Corresponding QD705 sequence demonstrating the localisation and segregation of label compartments upon division, cell limits (punctuate signal); (**c**) Merge image. Size bar = 10µm (Errington et al. 2010). Full field size video availably on attached CD: Supplementary Information 5.6-2 –CD-Video. (**d**) Representative schematic of the QD compartment distribution through the daughter cells.

To observe the overall partition effect over time; a standard 6 well plate cell culture labelled with QDs (according to the protocol) was sampled at different time points post-QD label. For each time point before the cells were processed for flow cytometry, widefield microscopy phase and fluorescence images were acquired (Supplementary Information 5.6-1). These images were analysed with the QD cell compartments size and average fluorescence measured to detect basic signal variation with time. General observation of the example image fields in Figure 5.17 showed an increase in cell number, this is further validated by the cell growth data based on cell counts (Figure 5.2). At the same time there was a corresponding decrease in the QD number of compartments per cell, so much so that at 144 hours most of the cells showed no detectable QD signal. Equally the average fluorescence intensity of each QDs compartments itself, also showed a stabilization (Figure 5.17). Overall, the QD individual compartmental mean fluorescence was stable for the depicted conditions and therefore does contribute overall population fluorescence signal with time. This confirms that the QD cell population signal variation is indeed due to daughter to daughter cell partition upon cell division. This ultimately represents the concept to be exploited in this chapter, illustrated in the simple diagram of Figure 5.1-d.

### 5.4.2 Validation of QD dilution tracked by flow cytometry

This section demonstrated the QD cell compartment dilution tracking technique; the first stage is to validate the direct relation with the cell growth/proliferation. The second stage is to assess the technique possible limitations in handling QD label cells and in tracking the dilution long-term. The initial reported assay has been performed over 3 days post-QD label from parallel cell samples QD labelled at the same time, without trypsinization and posterior re-seeding of the QD labelled cell suspension (Brown et al. 2007; Njoh et al. 2007; Summers et al. 2008). The initial question to address is how the assay holds up in terms of dynamic range and sensitivity for 5 and up to 8 days. Finally, the investigation focus was to transpose this technique to the HF model and derive growth and cell cycle dynamics of this HF system. A standard cell culture seeded to a low confluency has provided the conventional 2D TC condition, where exponential cell growth was observed for populations both QD-labelled and empty un-labelled control populations over 6 days post QD-labelling (Figure 5.2).

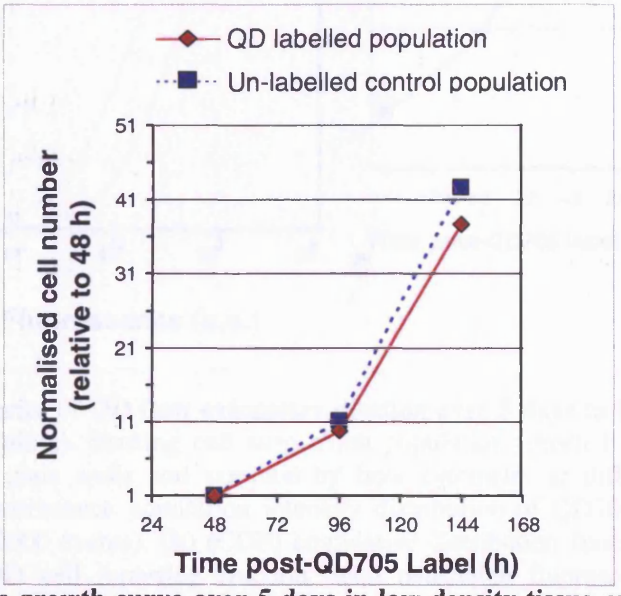


**Figure 5.2 – Relative growth curve over 5 days in low density tissue culture (6 well TC plate).** Cells seeded at 24h post-QD label prior to counting at later time-points. Cell number derived from Z1 Coulter counts starting at 48h. Normalised change in cell number, relatively to the 48h initial value, of QD705 labelled and the un-labelled U2OS-GFP cell samples retrieved from the 6 well TC plate Experiment 1 regime (see Table 5.3-1 for details).

The trypsinization retrieval protocol of the QD labeled cells, after a 24h QD stabilization period, followed by seeding of the obtained cell suspension produced a minimal influence on the cell proliferation capacity compared to the un-labelled counterpart; this was confirmed by flow cytometry results (see Supplementary Information 5.6-3–CD-A3).

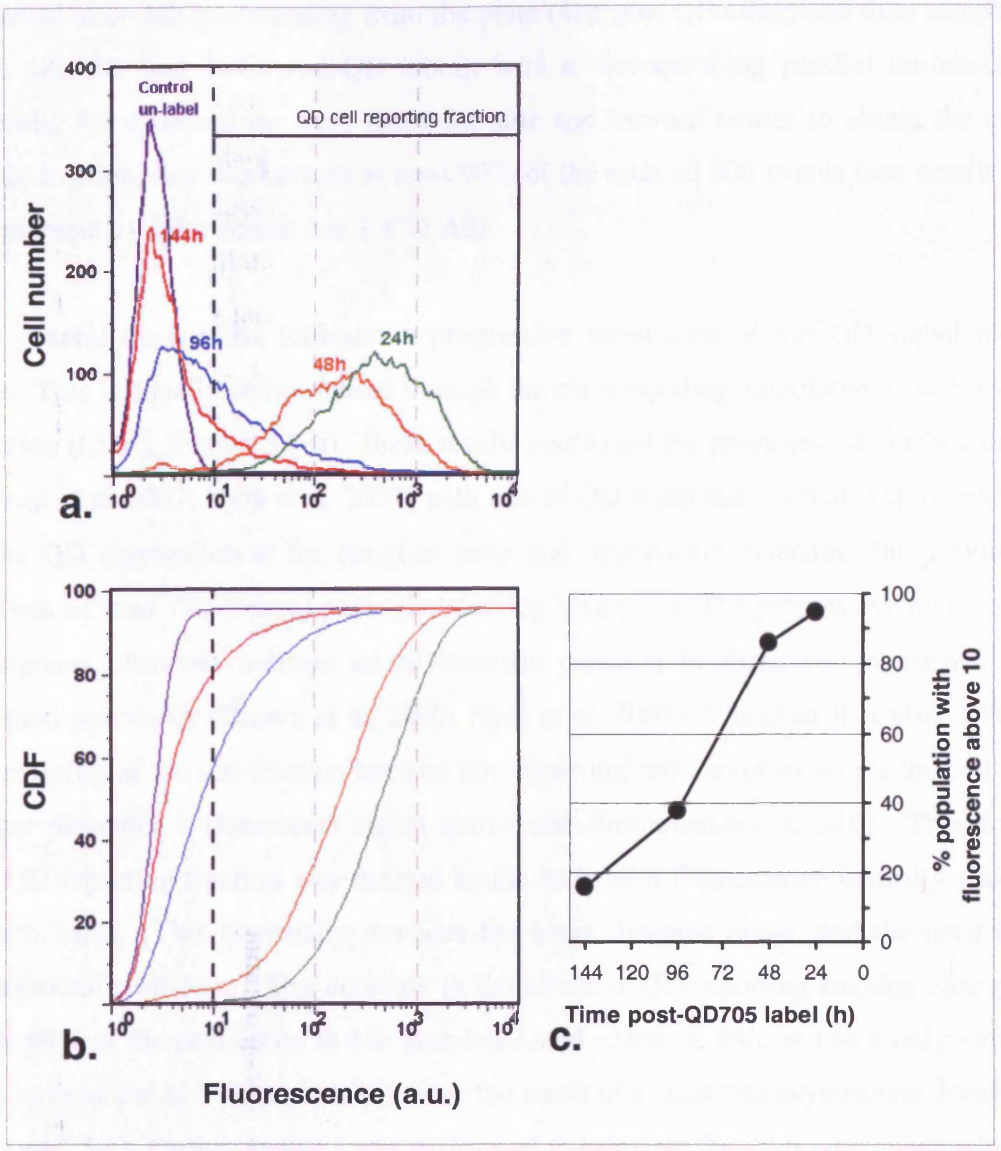


**Figure 5.3 – Time series of QD flow cytometry dilution over 5 days in low density tissue culture (6 well TC plate).** Starting cell suspension population (green line - 24h post-QD label) seeded in the plate wells and sampled by flow cytometry at different time-points. Experiment 1 **(a)** fluorescence population intensity distribution of QD705 labelled U2OS-GFP cells (approx 10000 events). **(b)** (CDF) cumulative distribution function; **(c)** Decrease percentage of the QD cell reporting fraction, with detectable fluorescence above auto-fluorescence (designated as >10 arb. units depicted by the vertical dotted line). Cell populations colour code: (green line) 24h, (orange) 48h, (blue) 96h, (red) 144h post-QD labelling; (purple) control un-labelled cell auto-fluorescence background signal.

The corresponding population QD time-series flow cytometry distributions were plotted together in the same graph (Figure 5.3-a.) giving up an overview of the QD705 label U2OS-GFP cell population progression. The initial 24h post-QD label green distribution corresponded to the initial QD-labelling cell suspension population reading before seeding into the multi-well TC 2D dish/plate or in the HF. Cells were

retrieved after 24h post-seeding from the plate (48h post-QD label) and then sampled each 48h (96 and 144h post-QD label), with a corresponding parallel un-labelled controls. All distributions were gated for side and forward scatter to obtain the cell viable fraction, that represented at least 90% of the total 10 000 events (see details in Supplementary Information 5.6-3–CD-A3).

The general observation indicates a progressive attenuation of the QD signal over time. This is equally demonstrated through the corresponding cumulative distribution function (CDF), (Figure 5.3-b). These results confirmed the previously described data (Brown et al. 2007; Njoh et al. 2007) with loss of QD fluorescent signal with time due to the QD segregation to the daughter cells and importantly extending the previous analysis beyond 72h (3days) post-QD labelling time point. The progressive elongated histograms observed indicate an asymmetric partition of these compartments, as reported previously (Brown et al. 2007; Njoh et al. 2007). It is clear that after 144 h the majority of the sub-fraction became non-reporting cells; in other words the cell no longer presented a fluorescent signal above auto-fluorescence (i.e. >10). Therefore the QD reporting fraction was defined as the cells with fluorescence intensity above 10 arb. units. This essentially provides the assay dynamic range, and the need for background correction. The decrease in the effective QD reporting fraction changed from 86% of the population at 48h post-label, and ~38% at 96h; at 144 h only ~16% was represented and these probably were the result of a sustained asymmetric division (Figure 5.3-c). Further analysis was performed to calculate the arithmetic mean which represents the population average QD fluorescence (Figure 5.4-a) (note: fluorescence was measured on a logarithmic scale, therefore both the log and linear outputs were represented). The mean value decreased with time as expected, with a greater decrease from 24 to 48h and 48 to 96h (Figure 5.4-b).

To validate the decrease in mean QD fluorescence calculated from the flow cytometry histograms a corresponding calculation was made where a calculated mean fluorescent signal was derived using the cell Coulter counts. This was calculated by dividing the 48h integral fluorescence value by the cell number assuming the relative increase from Figure 5.2 with approx 9 000 starting number of cells. Co-plotting of the two graphs Figure 5.4 showed a close match between the flow cytometry population measured

data and the calculated mean derived from the cell counts values. The calculated mean deviation was always lower than 3 units in relation to the flow statistics value.

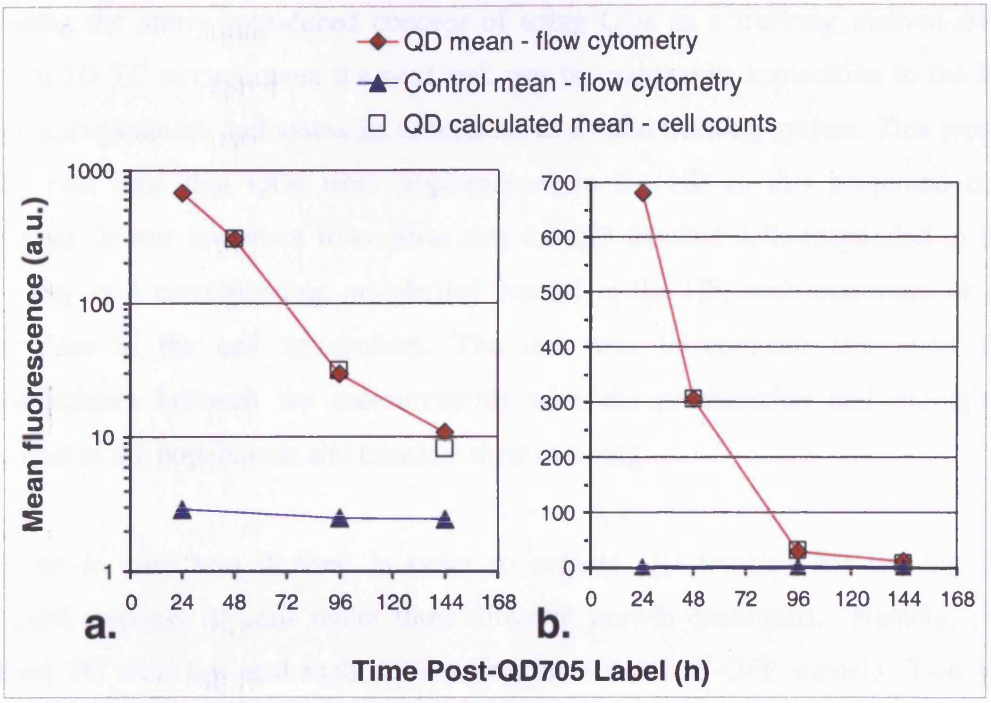


**Figure 5.4 – Arithmetic mean of QD cell fluorescence flow cytometry distribution at different time points in a low density tissue culture (6 well TC plate).** Y-axis **(a)** log scale; **(b)** linear scale. Experiment 1 **(red diamonds)** QD705 labelled U2OS-GFP population mean fluorescence intensity values obtained from the flow cytometry histograms of Figure 5.3. **(blue triangles)** un-labelled control cells. Additional co-plotted with the calculated mean fluorescence (markers with no background) from corresponding cell growth Z1 Coulter counts. Calculated mean was executed dividing the integral flow cytometry fluorescence value corresponding to 48h by the cell number based on the relative increase of Figure 5.2 assuming an initial cell number of 9000, following the equation: QD_calculated_mean_fluorescence_from_cell_counts_$\alpha$_h = [flow_cytometry_integral_fluorescence_48h / (9000 x normalised_cell_number_Figure 5.2_$\alpha$h)], where $\alpha$ h = 48, 96, 144 h.

Long-term QD tracking using flow cytometry revealed some limitations, associated with the accumulation of non-assay reporting cells. However, it was possible to establish a close correspondence between the flow cytometry measured population mean fluorescence signal progression and the cell number increase. This means that with this technique, using only the cell-QD fluorescence measurements, it is possible to estimate the associated population cell growth. Never-the-less the real advantage of this method is beyond just establishing a cell growth curve, but supplying an insight about cell heterogeneity within the population and division dynamics including possibly a lineage history.

### 5.4.3 Incorporating the QD assay into the HF model

Following the above introduced concept of using QDs as a tracking method on a standard 2D TC environment, the next task was to evaluate its application to the HF model encapsulation and assess its robustness as a valid tracking system. This would be the first time that QDs were implemented in the HF so this presented new challenges. It was important to confirm that the QD labelled cells responded in the same way as a corresponding un-labelled control in the HF, with minimum or no interference to the cell metabolism. The task was to compare and chart the correspondence between the measurements with the proliferation and biological behaviour of the populations and translate their meaning.

A screen *in vitro* was devised in order to explore QD tracking for sensing the biological response of cells under three different growth conditions. Namely, two standard TC with low and high density and the HF–U2OS-GFP model. Two HF lengths were used: 2 cm length with available adherent cell length of ~1.6 cm, area 0.50 $cm^2$; and 4 cm length with available adherent cell length of ~3.6 cm, area 1.13 $cm^2$; both loaded with an estimated cell density ~2.5 $x10^4$ cell/$cm^2$. The low density TC corresponded to a 6 well plate (area 9.6 $cm^2$) or 60mm culture dish (area 21.3 $cm^2$), both seeded at a density of ~1.3 $x10^3$ cell/$cm^2$, while the high density TC was a 12 well (area 3.8 $cm^2$) plate seeded at a ~2.5 $x10^4$ cell/$cm^2$ and was equivalent to the HF starting cells/area density.

While the minimal cell influence of the QD labelling on standard tissue cultures; the same dilution behaviour might be expected in the HF. However, to confirm this, dual-parameter forward and side scatter plots of QD labelled and un-labelled cells retrieved from HF were analysed. The mean scatter values and corresponding standard deviations were extracted for each time point (Figure 5.5), overall (Figure 5.5-b) there is no major detectable difference between the labelled and un-labelled cells with regards to their cell scatter properties.

The growth curves derived from cell counts (Figure 5.6) showed a close correspondence between the QD labelled and un-labelled population, with the exception of the 128 and 200h samples of the 60 mm cell culture dish growth.

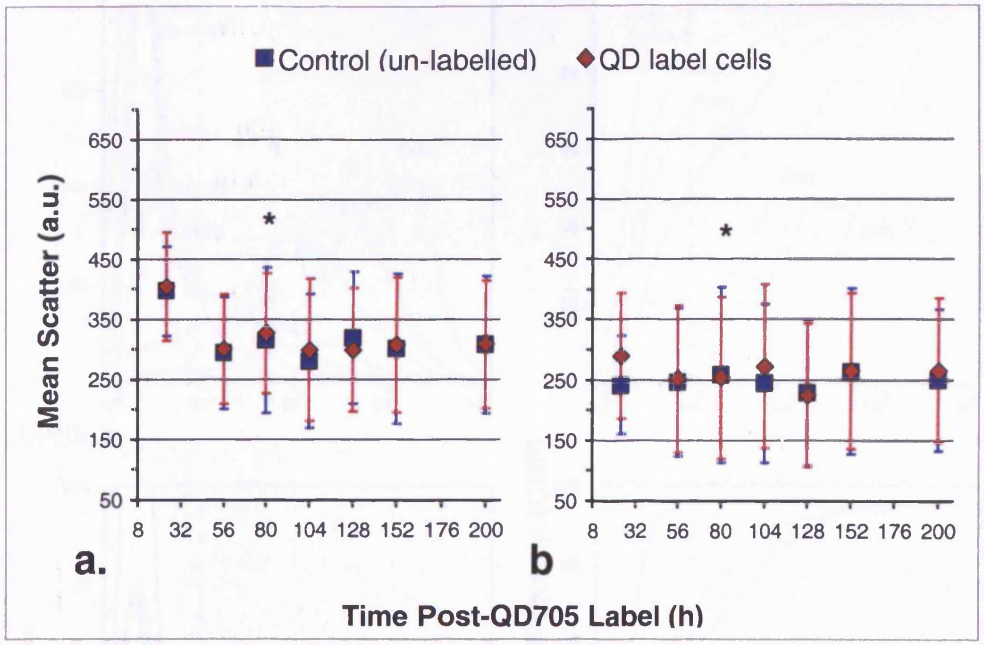


**Figure 5.5 – Analysis of cell size and granularity in the HF.** Experiment 2 mean values of (**a**) forward and (**b**) side scatter flow cytometry population distribution of the HF–U2OS-GFP over time; (**red diamonds**) QD705 labelled cells and (**blue squares**) un-labelled control. Each set was seeded from the 24h cell population and from this point the values are the average of two 4cm length HFs for each set, *except when indicated. Error bars correspond to flow histogram standard deviation (SD).

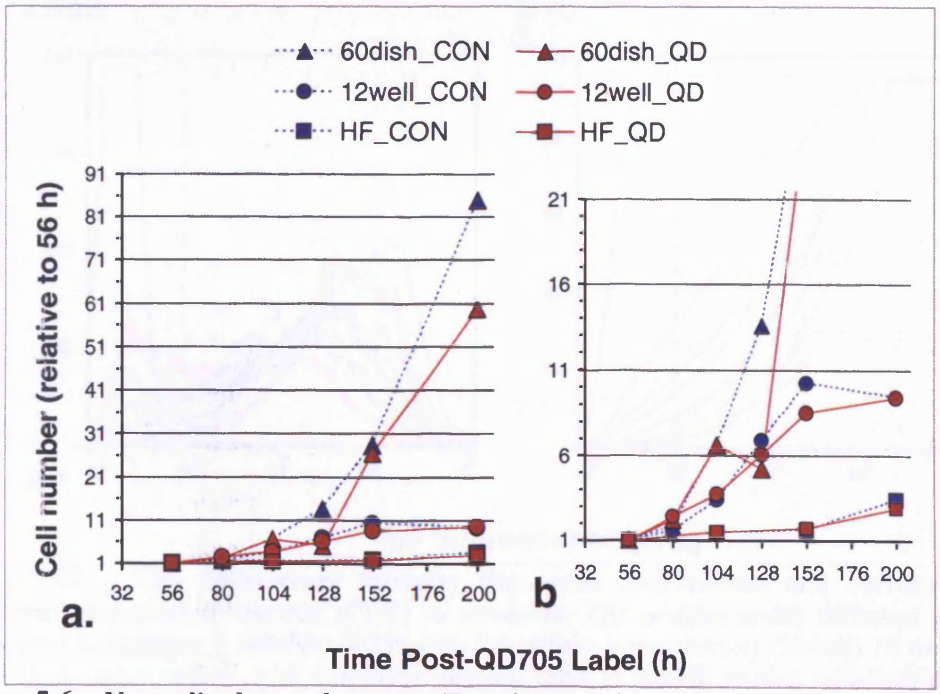


**Figure 5.6 – Normalised growth curves.** Experiment 2 (**a**) Growth curves from cell counts of the U2OS-GFP cells labelled with (**QD - red**, solid lines) QD705 labelled cells and (**CON - blue**, dotted lines) un-labelled control, over time under different growth conditions: (**60dish**) 60 mm dish low density tissue culture; (**12well**) 12 well plate high density tissue culture, with equivalent seeding value to the HF starting cells/area density; (**HF**) hollow fiber cell encapsulation *in vitro* growth. (**b**) zoomed area to show low growth rates.

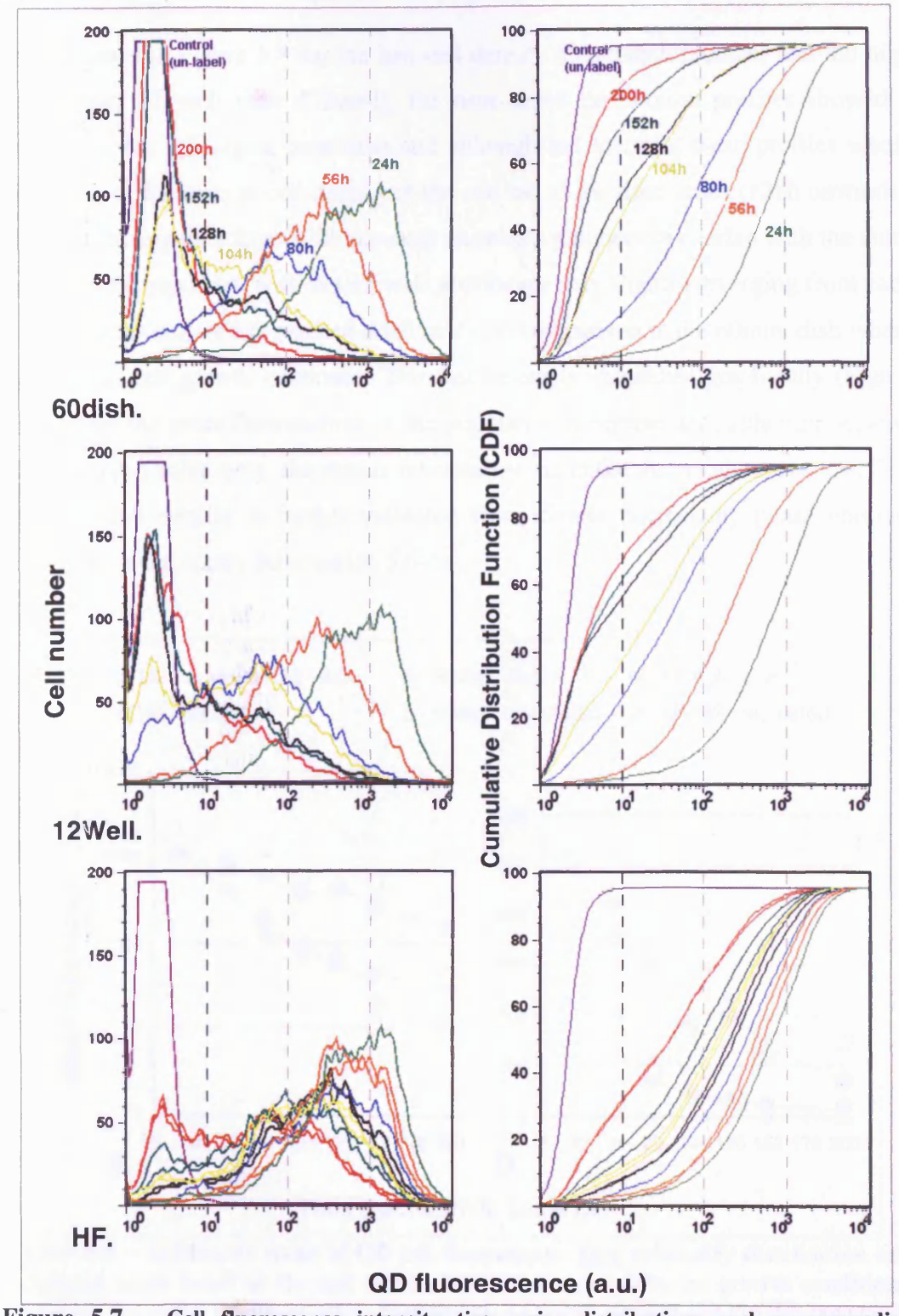


**Figure 5.7 – Cell fluorescence intensity time-series distributions and corresponding cumulative distribution function (CDF) to screen for QD profiles under different growth conditions:** Experiment_2 (**60dish**) 60mm dish low density tissue culture; (**12well**) 12 well plate high density tissue culture, with equivalent seeding value to the HF starting cells/area density; (**HF**) hollow fiber cell model *in vitro* growth. All samples were seeded with the same starting QD705 labelled U2OS-GFP cell population with the flow cytometry distribution (green line) 24h post-QD labelling and sample at different time points. Resultant cell populations distribution are colour coded: (orange) 56h, (blue) 80h, (yellow) 104h, (black) 128h, (dark green) 152h and (red) 200h post-QD labelling; (purple) control un-labelled cells. *Note: two parallel individual HF samples, except for 80h were analysed.*

As illustrated in Figure 5.7 for the low cell density 60mm dish (60dish) and the high cell density 12 well plate (12well), the time-series distribution profiles showed a dilution of the QD signal over time and although not identical these profiles would reflect the differences in cell density at the end tail of the time series (128h onwards). The three time points from 128h onwards showed a progressive overlap with the auto-fluorescent component, with the 12 well population only slightly diverging from each other, but this culture has reached confluency, in comparison to the 60mm dish where exponential cell growth continues. This can be easily visualized graphically (Figure 5.8), where the mean fluorescence of the population is represented, although because this is a mean value only, the details revealed by the entire distributions are lost. The effect of cell density is further validated from simple microscopy phase contrast images (Supplementary Information 5.6-6).

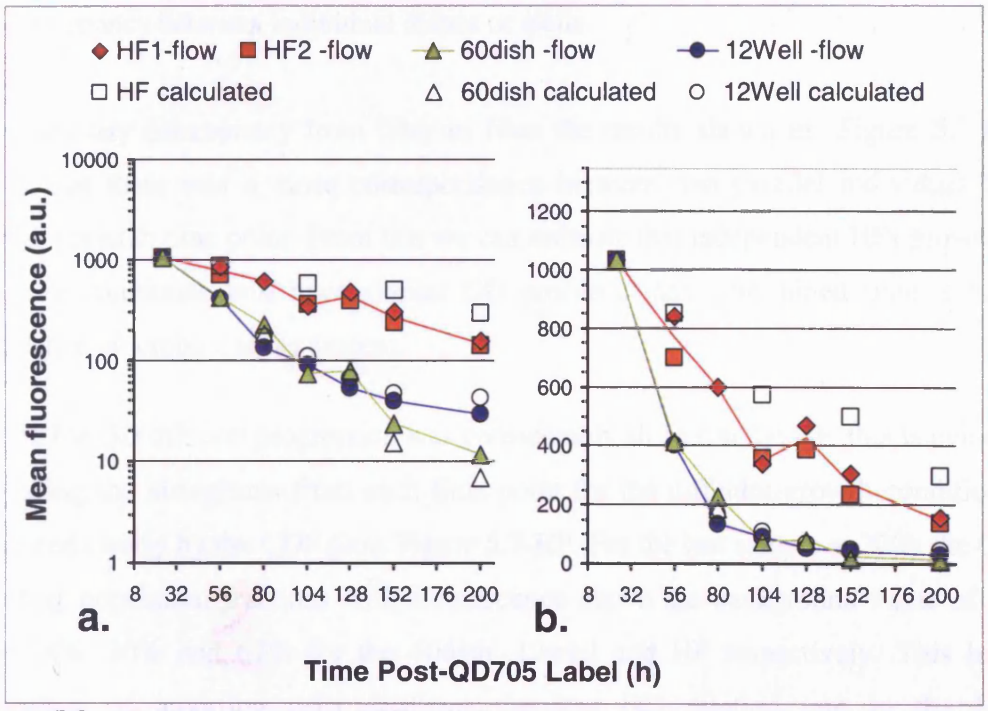


**Figure 5.8 – Arithmetic mean of QD cell fluorescence flow cytometry distribution and calculated mean based on the cell counts, over time under different growth conditions.** Y-axis (**a**) log scale; (**b**) linear scale. Experiment 2 QD705 labelled U2OS-GFP population mean fluorescence intensity values obtained from the flow cytometry histograms of Figure 5.7. (**60dish**) 60mm dish low density tissue culture; (**12well**) 12 well plate high density tissue culture, with equivalent seeding value to the HF starting cells/area density; (**HF_1 and 2**) HF cell encapsulation *in vitro* growth, values of two parallel individual HFs. Co-plotted with the calculated mean (markers with no background) performed dividing the 56h integral fluorescence value by the cell number based on the relative increase (Figure 5.6), with 9000 cells as a starting number, following the equation: QD_calculated_mean_fluorescence_from_cell_counts_$x$_h = [flow_cytometry_integral_fluorescence_56h / (9000 x normalised_cell_number_Figure 5.6_$x$h)], where $x$ h = 56, 80, 104, 128, 152 and 200 h.

As in the previous section a mean fluorescence based on the cell number increase was calculated to observe the overall correspondence between the QD measured data and the cell growth obtained from the cell counts. As observed in Figure 5.8 overall there was a correspondence between the measured and calculated values for the standard TC (60dish and 12well) and closer but not completely matching in all points for the HF. However, it should be noted that, first, the estimation is based on a perfect situation. Second, in the particular case of the HF due to the usual low cell number/volume and necessary dilutions of the HF samples in relations to the standard tissues cultures controls, the cell number is more prone to error and under-estimation. These results represented a simple way to monitor the differences of the proliferation progression of the same starting population, subjected to different conditions and growth pressures. The standard TC data, due to assay restrictions, presented the limitation of missing a duplicate sample for the same time point in order to evaluate any discrepancy between individual dishes or wells.

To assess any discrepancy from fiber to fiber the results shown in Figure 5.7-HF shows that there was a close correspondence between two parallel individual HF profiles for each time point. From this we can estimate that independent HFs grown in the same conditions will have similar QD profile at any determined time, giving confidence of a robust assay system.

Second the QD dilution progression was considerably slower in the HF, this is evident comparing the histograms from each time point for the different growth conditions, illustrated clearly by the CDF plots Figure 5.7-HF. For the last sample at 200h the QD reporting population fractions with fluorescence above the background value of 10 were 14%, 30% and 67% for the 60dish, 12well and HF respectively. This high percentage of reporting cells confirms the low QD dilution rate in the HF. Furthermore, the low cell proliferation results of the HF were supported by the cell counts curve (Figure 5.6). The HF low growth rate was previously discussed in chapter 3.4.1 where independent assays demonstrated slower cell cycle traverse and longer IMTs in the HF encapsulation, corroborating the observed HF QD tracking results. For example, the mean fluorescence (Figure 5.8-b) of the HF presented the typical "closer to linearity" progression, with average "m" slope of -6 from 24 to

128h, while the standard TC had a sharper (average slope of -12 from 24 to 104h) "closer to exponential" progression.

Importantly the QD profile provides extra interrogating sensitivity, not accomplished by the traditional absolute cell growth based on counts or even stathmokinetic approach. It presents a comparative snapshot from where it is possible to extract "dynamic" inferences about the entire cell population, such as: i) Proliferation de-synchronizations, evident by the observation of the HF histogram profiles (Figure 5.7-HF), where the 104h sample (yellow line) presented a slightly higher progression in relation to the following time point at 128h (black line), confirmed by the mean fluorescence curve (Figure 5.8), and the opposite was expected. ii) Indentify specific high or low proliferative cell fractions, this can be denoted by analysing the profile of the last HF time point at 200h (Figure 5.7-HF - red line). The 33% non-reporting fraction with fluorescence bellow 10 arb. units represents a population with higher probability of had undergone successive divisions with corresponding QD partition events. Contrary to the residual ~3% fraction at the other end with fluorescence above $10^3$ arb. units, presenting a high fluorescence and denoting lower probability of QD partition events.

### 5.4.4 Colcemid drug treatment evaluation using the QD proliferation tracking

The effect of a drug perturbation and the related cell behaviour with QDs incorporated into the HF encapsulation system is addressed here. It is important to demonstrate the potential application and advantages of the QD readouts applied to the HF to monitor cell activity and the response to the treatment with anti-cancer drugs, with the prospect of being in the future transposed to an *in vivo* pharmacokinetic assay in host animals.

A model drug assay using the agent Colcemid (chapter 3.4.1.4), was devised to compare the behaviour of the drug treated QD cell populations in relation to the normal drug un-treated QD populations as part of Experiment_1 [the Experiment_2 Colcemid results are not shown here (see Supplementary Information 5.6-4–CD-A3)]. Colcemid (60 ng/ml) was added at the 48h post-QD label time point and cells sampled after a further 48h or 96h drug incubation time, with parallel un-treated and un-

labelled controls (for details see Table 5.3-1). All the presented drug treatment flow cytometry results should correspond mainly to viable or still relatively intact cell fraction, whose value were most of the time above 80% and never lower than 70% of the total 10 000 events for all the samples.

Figure 5.9 presents an overview of the population mean fluorescence intensities calculated from the time-series flow cytometry histogram profiles - indicating a progressive signal decrease due to QD compartment dilution in the un-treated samples (solid lines). After Colcemid addition, at 48h post-QD label, the HF as well as the standard TC conditions (6W and 12W) registered a stabilization of the population fluorescence mean signal. This was most probably due to the cell population being arrested at mitosis and therefore no consequential partition of the QD compartments through the daughter cells, resulting in a plateau fluorescence signal mean value ~170 arb. units (log(170) = 2.2). Overall this was validated by corresponding growth curves derived by cell counts (Supplementary Information 5.6-7). Despite the clear stabilisation of the QD signal (i.e. a block of QD dilution) additional features became apparent (Figure 5.9), as follows.

First, the population mean fluorescence signal increased in the un-labelled CON cells (small violet squares), representing an auto-fluorescence increase with Colcemid, in other words the fluorescence baseline in drug treated cells is now different from the un-treated counterpart. After a 96h incubation with Colcemid the auto-fluorescence component showed a mean fluorescence value 4 times greater than the un-treated cells, a change of ~0.4 to 1 (log(2.6 and 10 arb. units) respectively This can be further corroborated when viewing the actual profiles (Figure 5.10-c) where there was an profile shift of the drug cell populations above 10 units, directly proportional to the drug incubation time. Although, the cell's natural auto-fluorescence increase should be taken in consideration, this effect seems of relatively low importance for the presented non-reporting background HF Colcemid profile shift, having only considerable implication in cell samples with highly diluted QD compartments (see further exemplification in Supplementary Information 5.6-8).

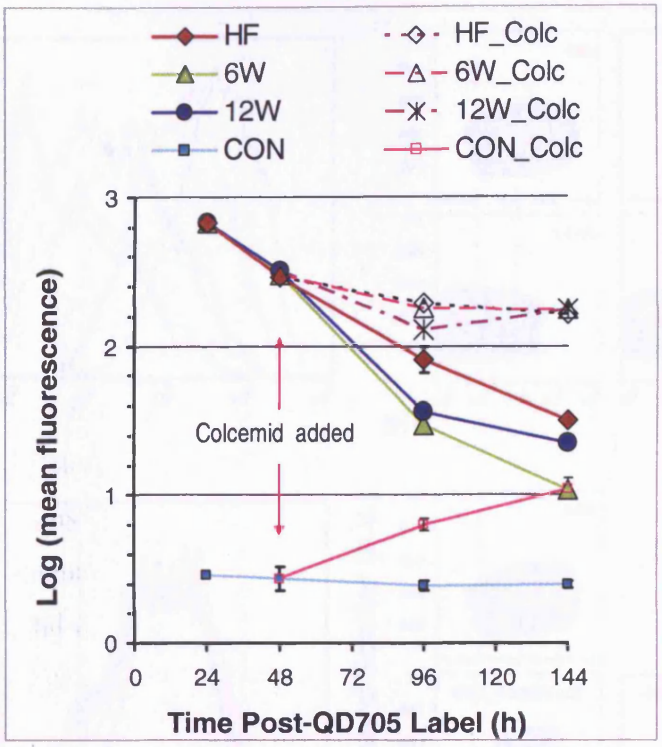


**Figure 5.9 – Blocking of mitosis consequences on the QD cell arithmetic mean fluorescence intensity.** Population mean fluorescence intensity values obtained from the flow cytometry histograms statistic of Supplementary Information 5.6-7 and Supplementary Information 5.6-3–CD-A3. Experiment_1 QD705 label U2OS-GFP cells over time, under different growth conditions: (**6W**) 6 well plate low density tissue culture; (**12W**) 12 well plate high density tissue culture, with equivalent seeding value to the HF starting cells/area density; (**HF**) HF cell encapsulation *in vitro* growth, average of two parallel individual HFs; (**CON**) un-labelled no QD control cells, average of all different growth conditions (HF+6W+12W) samples for the different time points. All samples were seeded with the same starting cell population (labelled or un-labelled accordingly) at 24h post-QD label and sample at different time points. Drug treatment (Colc) Colcemid 60 ng/ml added at 48h. Error bars: 0.434 x (SD/mean fluorescence).

Second, there was a decrease of the population mean fluorescence value for all the QD Colcemid treated samples when compared to the 48h post-QD label value when the drug was added, i.e. the mean fluorescence changed from ~2.5 to 2.2 (log(293 to 170 arb. units) respectively) more or less similarly for all drug treated samples. This was due to an accumulated fraction in the profile histogram below 30-40 units like that seen for the HF in Figure 5.10-bi. Therefore just from the profile it might seem that this cell fraction was able to continue to divide despite the drug. But, previous studies have shown that U-2 OS cells immediately started accumulating into mitosis without delay upon addition of Colcemid (Matsusaka and Pines 2004). Chapter 3 results confirm this and suggest that for long term incubation with Colcemid (i.e. 48h) only a minimal percentage (7-9%) of cells apparently exit mitosis, but within a 4n state continuing to >4n polyploidy without dividing and partitioning the QDs.

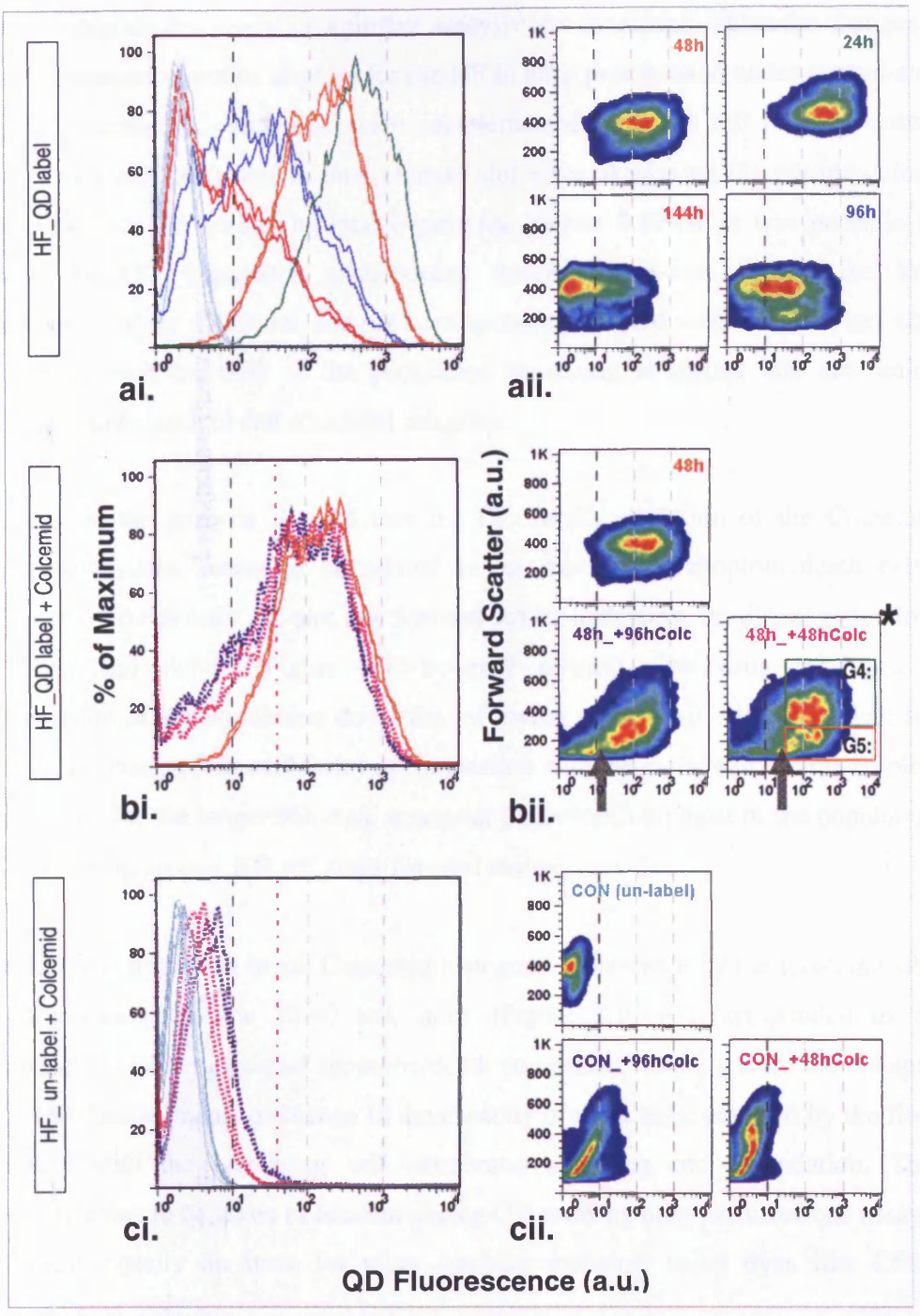


**Figure 5.10 – Colcemid perturbation on the QD cell tracking system in the HF. (i)** Fluorescence intensity time-series of flow cytometry population distribution histograms and correspondent **(ii)** example density dot-plot of the Experiment_1 QD705 label U2OS-GFP cells of the (HF) hollow fiber model HF–U2OS-GFP *in vitro* culture. **(a)** normal un-treated QD cell proliferation; drug treatment perturbation both on **(b)** QD cells and **(c)** (CON) un-label control no QD cells. All samples seeded from the same flask cell population (green line) 24h post-QD label; HF retrieved cell populations (orange) 48h, (blue) 96h, (red) 144h post-QD label, (light blue) control un-label cells. All histogram values represent two parallel individual HF for all time points, except the 24h. Drug perturbation (**Colc**) Colcemid 60 ng/ml added at 48h, samples time point (+48h_Colc) 96h of what 48h with drug and (+96h_Colc) 144h of what 96h with drug incubation. *Gated sub-population (G4 and G5) to be analysed in Figure 5.11.

Indeed, to explain this deviation a further analysis was conducted, where the changes in QD fluorescence profile channel for the HF *in vitro* proliferation under normal and the drug perturbation conditions, were complemented using the cell forward scatter (related with cell size), within dual channel dot plots. Analysing the pseudo-colour density plot for the normal un-treated samples (Figure 5.10-aii) it was possible to observe the QD population proliferation though the x-axis toward the low fluorescence values with time, and the corresponding forward scatter related cell size distribution, with the bulk of the population remaining at around 400 arb. units, denoting maintenance of cell structural integrity.

Furthermore, the analysis showed that the QD profile deviation of the Colcemid treated populations seems to be related to an increase of apoptotic/death cells, confirmed by the density dot-plot low forward scatter indicating, i.e. disintegrated low cell sizes and debris (Figure 5.10-bii–gray arrows). The drug produced a fragmentation of the population down the y-forward scatter axis, clearly evident for 48h drug incubation (48h+48hColc) in comparison with the initial 48h un-treated plot. Furthermore, for the longer 96h drug treatment (48h+96hColc) most of the population shifted closer to around 200 arb. units forward scatter.

Overall, the cell fraction in the Colcemid histogram represented by the left-hand side with fluorescence below 30-40 arb. units (Figure 5.10-bi) corresponded to an increasing QD label low signal apoptotic/death population, resulting from the collapse of the QD compartments or change in the capacity of these to be detected by the flow cytometry with the increasing cell membrane shrinking and degradation. This represents a fact to be taken in account during QD tracking drug perturbations assays, but this is equally an issue for other tracking protocols using dyes like CFSE (Hawkins et al. 2007).

Importantly because the measurements were acquired by flow cytometry, it is possible to selectively gate, analyse or sort any cell fraction or any other desirable sub-population. For example, it is possible to exploit the QD single cell information together with forward scatter from the Colcemid treatment in a dual channel mode to isolate and track the different sub-responses in the population derived from the drug perturbation Figure 5.10-bii. The 48h Colcemid incubation (48h+48hColc) was gated

into two fractions, (G4) high and (G5) low forward scatter sub-populations and analysed independently Figure 5.11. The plots showed that the G4 high forward scatter sub-population for the selected threshold mark had high cyclin B1-GFP (88%) and side scatter (89%) (Figure 5.11-i and ii); in comparison to the G5 sub-population (with 21% and 25% respectively). This confirms the G5 sub-population cell death progression maintains a fairly similar histogram profile to the G4 intact cell sub-population (Figure 5.11-iii).

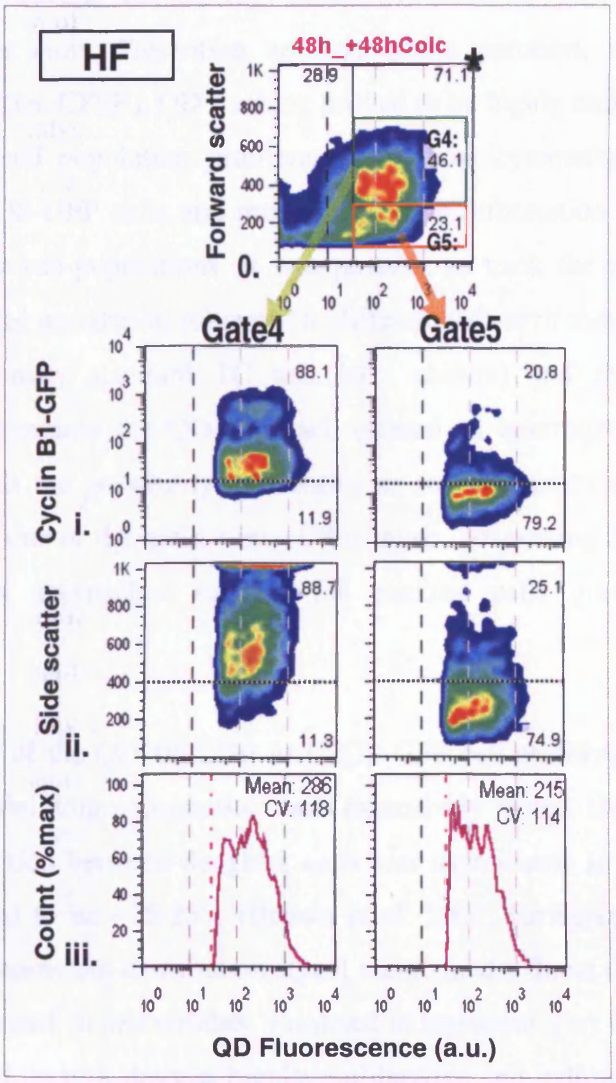


**Figure 5.11 – Mitotic arrested QD label cell sub-fraction analysis.** (**0**) Density dot-plot of the Experiment_1 QD705 label U2OS-GFP cells, (HF) hollow fiber model HF–U2OS-GFP *in vitro* growth corresponding to 48h post-QD label cell after 48h incubation with Colcemid (48h+48h_Colc), *dot-plot transposed from Figure 5.10. (**G4**) high and (**G5**) low forward scatter gated sub-population analysed separated with QD cell fluorescence versus (**i**) Cyclin B1-GFP, (**ii**) Side scatter plots and (**iii**) counts histograms.

## 5.5 Conclusion

The labelled QD cell endosomal compartment partitioning between daughter cells upon cell division has provided a stable cell fluorescence method for tracking live cells in different culture systems. This technique was validated and further developed beyond the previous studies (Brown et al. 2007; Njoh et al. 2007; Summers et al. 2008) for longer tracking time periods in different culture systems and conditions. Specifically this technique was optimized and positively applied to the HF *in vitro* encapsulation with several methodology details evaluated and new findings, fulfilling the stated chapter aims. Presenting an asymmetric partition, relatively to other classical methods (i.e. CFSE), QD tracking proved to be highly maintained and robust enough to track cell population proliferation by flow cytometry up to 8 days in osteosarcoma U2OS-GFP cells and provided relative information about the division history of specific sub-populations. It was possible to track the progression of one original QD labelled population subjected to different cell environment conditions (i.e. low and high density standard TC and HF culture) and also a model drug perturbation. In summary the QD approach offered an interrogation technique and output signal, with the possibility to identify or sort any fraction of interest. This speaks directly to one of the main aims of this thesis, concerning the development of new biophotonics approaches suitable for tracking cells growing in different environments.

The sustainability of the QD705 label in U2OS-GFP cell proliferation under normal and Colcemid model drug perturbations was extensively mined. Even though the QD compartment partition between daughter cells was asymmetric in the U-2 OS cells, previous calculated to be ~75:25% (Brown et al. 2007; Errington et al. 2010), the decrease in QD fluorescent distribution signal maintained a direct correlation with the corresponding increase in cell number, validated independently by Coulter cell counts. This was achieved up to 8 days in highly proliferative cell cultures (i.e. low density 2D cultures), where the QD signal is highly redistributed through the tumour population with a progressively reduced QD reporting fraction detectable above the auto-fluorescence background.

A recent study has used this type of QD output signal to derive a computer-based simulation model of standard TC and further global parameters of proliferative patterns (i.e. IMT, proliferative fraction %, QD partition ratio), at both the single cell level and was able to identify whole population cell cycle routing, with no a-priori knowledge of the population proliferation potential (Errington et al. 2010) (for print-out see Appendix I-C). Briefly this computer simulation mathematical model assumes that cells were randomly distributed within the cell cycle period. As the time variable was incremented a Monte Carlo algorithm was applied to determine whether or not a given cell divided within the time window using a random sampling of the Gaussian profile for the inter-mitotic time distribution. On division it was assume the total number of QD in each daughter cell was equal to the number of dots in the parent cell. The QD fraction allocated to each daughter cell was again chosen at random from the Gaussian distribution of partition ratios. At a set time a fluorescent histogram was calculated by determining the number of QD in each cell, this histogram was then compared directly with experimental data. Genetic algorithms were used to select and modify the variable parameters (mean and standard deviation) that describe the Gaussian distributions with "evolutionary fitness" being determined by comparison of the modelled histograms with flow data. This in order to achieve a favourable fit of the theoretically calculated QD distributions with that measured experimentally (Brown et al. 2007; Errington et al. 2010).

This analytical and modelling tool enhances the *biophotonic interpreter* component of the system to generate useful data even with perturbations or low levels of QD cell signal. Recent investigations (Brown et al. 2010a) (for print-out see Appendix I-D) have addressed this by addressing the impact of the auto-fluorescence background. This was performed by adapting the previous discussed mathematical model incorporating the cell auto-fluorescence background signal in the cell total fluorescence signal. Thus enabling the segregation of both the QD and auto-fluorescence signals in order to increase the tracking capabilities in population where the QD signal becomes highly redistributed or diluted over-time (Brown et al. 2010a). Similar developments at this modelling level could also be investigated to account for alterations of auto-fluorescence increase due to the drug treatment and even the QD death/apoptotic cell signal collapse, enhancing data translation and interpretation.

Furthermore, the current study shows that the QD tracking approach seems inherently independent of the culture system used (i.e. standard TC and HF model), this provides a basis for its further application in different culture systems.

Addressing now specifically the application of the QD tracking for the HF–U2OS-GFP model HF culture platform, in this thesis it was demonstrated for the first time that it was possible to encapsulate QD labelled cells and place them into the 'bounded' HF; then culture the cells *in vitro* in this HF system for up to 8 day following the population under normal proliferation or subjected to drug perturbation, and then retrieve the cells from the HF for analysis or other assays. The 'bounded' aspect of the HF is critical in undertaking this QD assay since monitoring the dilution of the conserved QD signal cannot be contaminated with other cells not originally part of the loaded population. This approach also demonstrated the potential of the cell QD tracking in the HF culture platform for a drug cell response assay. By identifying the general action of the drug, translated into a stabilisation of the QD fluorescence. This could be enhanced with extra-channels such as forward scatter (or other channels and even additional probes), to further segment signal. Furthermore, general technique issues were identified, Colcemid treatment led to an increase in cell auto-fluorescence with a shift of the assay dynamic range. Another parallel fact was the QD labelled cells progressive signal collapse, proportional to the drug incubation time, probably due to cell death.

To deal with the progressive loss of reporting cells due to eventual QD signal dilution below the background it might be possible to increase the QD label at the start. However, this has implications of nanotoxicity and therefore may disturb the proliferative system. To address the QD death/apoptotic cell signal collapse interference during drug treatment, the addition of another probe (i.e. Annexin V (Vermes et al. 1995)) to identify these cells would be an advantage, allowing the selective gating of this fraction and also providing additional multi-channel information for the analysis.

Obtaining a proliferation signal output using image acquisition from inside the present HF platform is indeed challenging (Silvestre et al. 2009) (for print-out see Appendix I-A). Preliminary studies have been undertaken to assess the feasibility of fluorescence

macro-imaging techniques (Figure 5.12). The conclusions from these studies suggest that imaging QD label cells in the HF although possible is difficult. The macro-imaging approach (with the ViSen system) showed a HF signal from encapsulated QD705 labelled cells, the signal was low and difficult to detect particularly if the fibers were implanted into animals. This is due to the fact that the cells effectively carry low levels of signal tissue volume compared to a tail injected QD animal study (personal communication Marcus Salmon, 2010, ViSen: http://www.visenmedical.com/). Furthermore the feature of attenuated signal over time is evident even in the bounded system where total signal is maintained but as it is dispersed it becomes undetectable as predominantly the cells after 144 hours will not contain significant QD signal. The whole population response (i.e. signal per unit fiber) matches the single cell flow cytometry analysis (section 5.4.4), and therefore shows only some potential short-term. However it is unclear if after the HF subcutaneous implantation into animals a sufficient signal would still be detected.

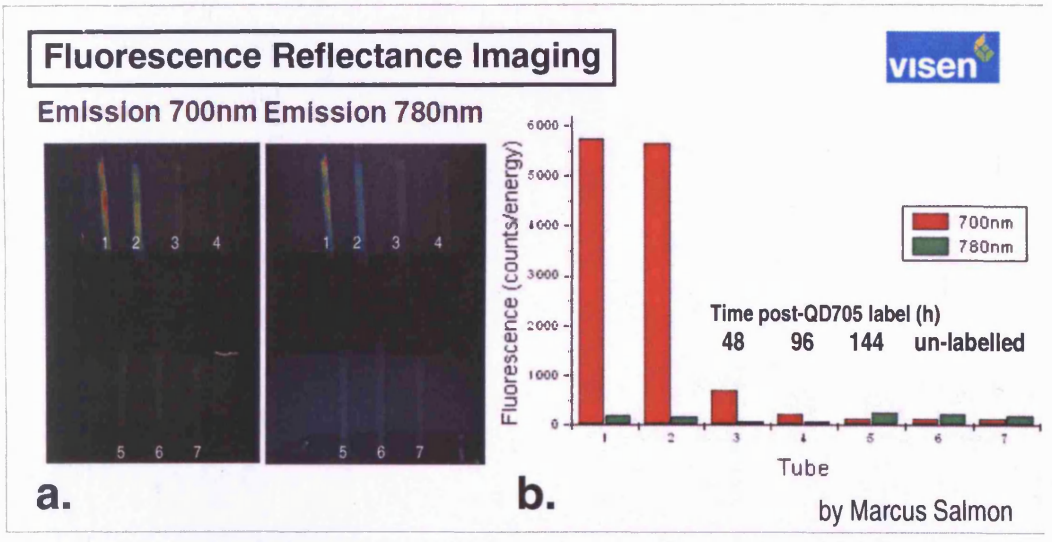


**Figure 5.12 – Hollow fiber encapsulated cells macro-optical imaging.** (**a**) Fluorescent images of ~1 cm length close HFs. (**b**) Correspondent mean fluorescence of the HF samples. The samples were acquired on the ViSen (Fluorescence Molecular Tomography) FMT2500 quantitative animal imaging system, whose principles are described in detail elsewhere (Graves et al. 2005). Acquisition kindly undertaken by Marcus Salmon (ViSen Medical Inc., Bedford, USA). HF fixed samples contents as follows: HF with 15 µm fluorescent 1.0 x$10^6$ beads/ml (ex645/em680nm) in (**1**) suspended in water and (**2**) suspended in a 2% alginate gel. HF seed with culture cells labelled with QD705 post-label time (**3**) 48h, (**4**) 96h and (**5**)144h; control (**6**) 144h un-label cells and (**7**) empty HF; parallel samples from flow cytometry Experiment_1 (section 5.4.4).

In summary, the QD cell tracking approach described in this chapter represents an embedded biophotonic system where the *sensor* (i.e. QD nanoparticles) is integrated directly in the cell. The *interpreter* component of this system provides insights into cell heterogeneity within the population, retrospective division history including the potential to retrieve cell cycle and lineage information, enhancing the systems inherent potential to detect the origins of drug resistant sub-fractions. Importantly this is a fully transferable approach and could be applied to both the TC and HF culture. Further the work with the HF *in vitro* culture platform also suggests the feasibility of QD cell tracking in a HF *in vivo* animal implant; where the 'bounded' HF implant again provides the means to seed and retrieve the QD interpreter component independently from the host.

## 5.6 Supplementary Information

**Supplementary Information 5.6-1: Example fields of QD cell to cell dilution analysed by microscopy and flow cytometry from Experiment_1**

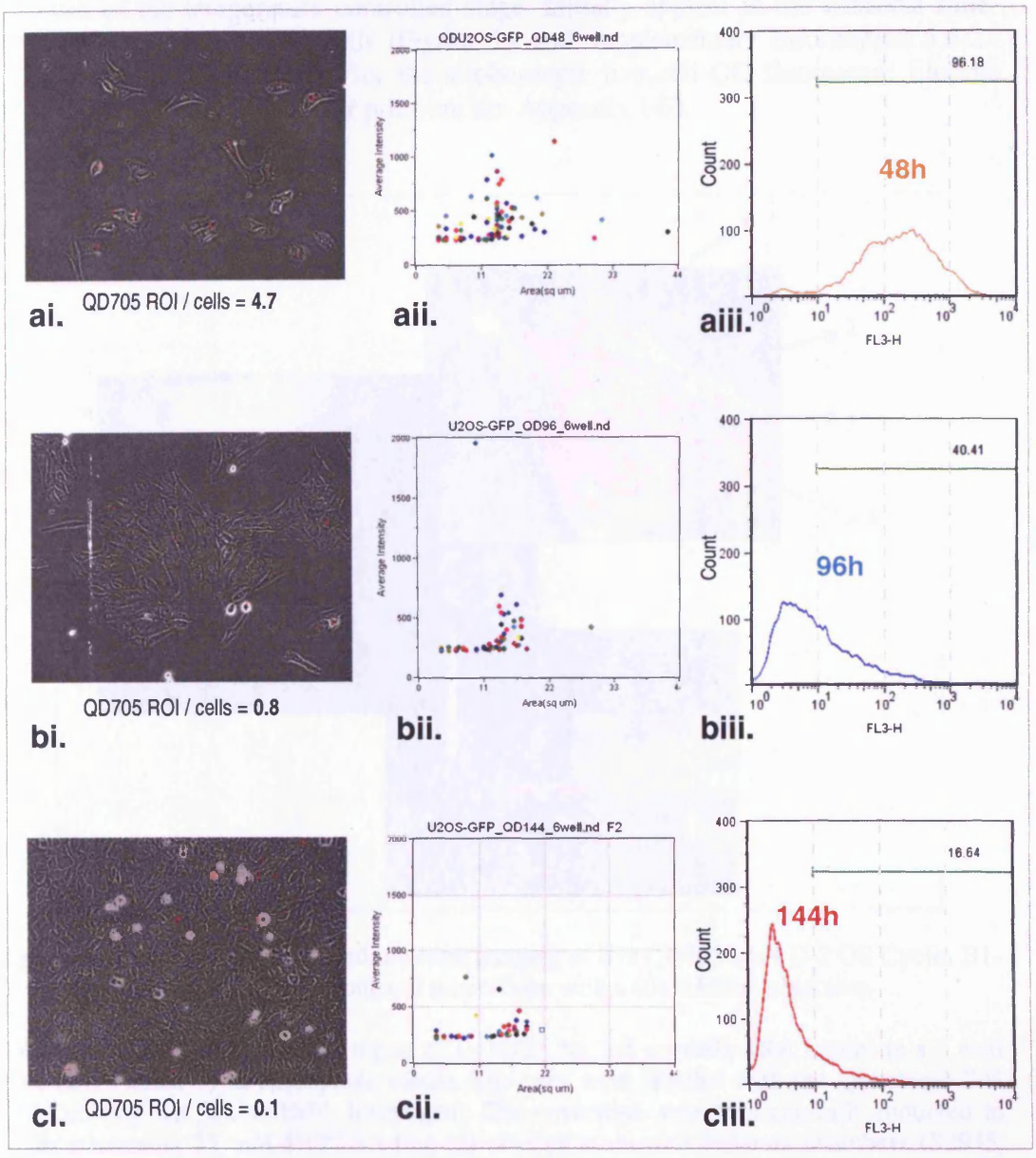


**Figure 5.13 – QD cell compartments evolution post-labelling time inside the cells on 6 well plate culture.** **(a)** 48, **(b)** 96 and **(c)** 144 h post QD label. **(i)** merge phase and QD705 epi-fluorescence, Axiovert microscope mono CCD 10x 0.45NA lens example fields (874x665µm) with the approx ratio between the QD705 compartments (ROI) region of interest by the number of cells in the field; **(ii)** graph of the average intensity versus the area of the QD705 ROI; and **(iii)** correspondent FACSCalibur QD705 fluorescence (FL3-H) profile histograms. *Note: In the average intensity versus the area graphs column (ii), the fluorescence background signal threshold was set at ~250 arb. units, corresponding to the bottom 6% of the dynamic range (12 bits rage 0-4092 units).*

**Supplementary Information 5.6-2: Nikon upright confocal live cell acquisition set-up**

The design and development of a short/medium term silicone chamber set-up, that allow the imaging of coverslip attached cells in an aqueous media for an upright microscope configuration, was performed by the author in partnership with Mark Holton (School of Physics and Astronomy), who was more concretely responsible by the built of the temperature controlled stage. Initially applied in the confocal time-lapse tracking of QD label cells (Figure 5.1 and Supplementary Information 5.6-2–CD-Video), later was critical for the stroboscopic live cell QD fluorescent lifetime studies (Holton et al. 2009) (for print-out see Appendix I-E).

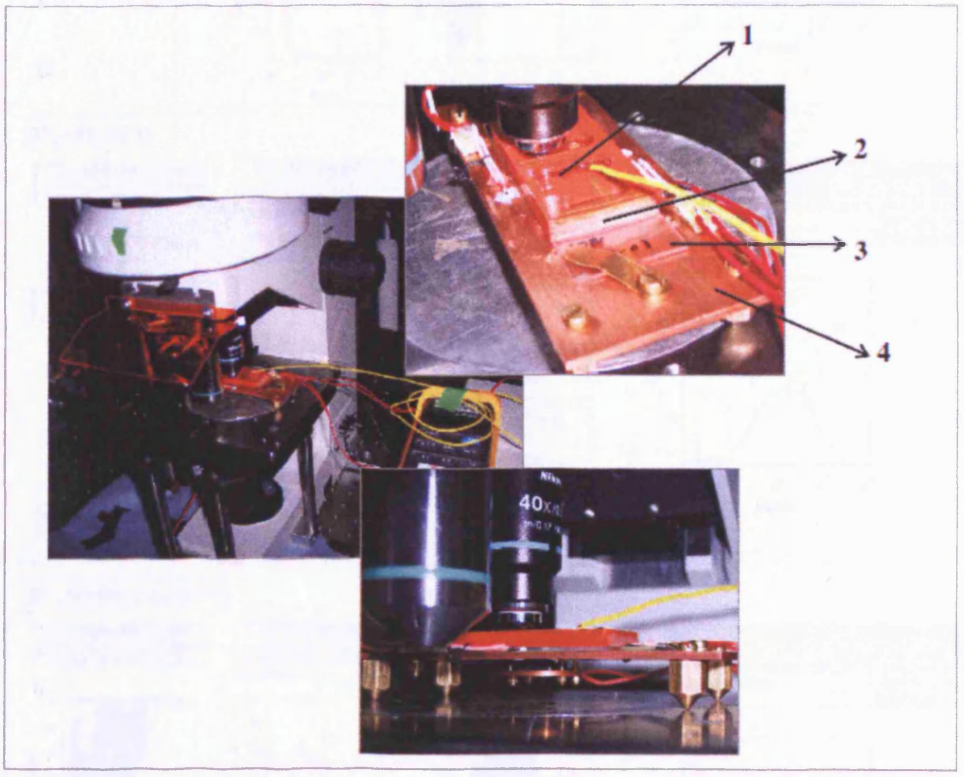


**Figure 5.14** – Set-up for short/medium term imaging of live QD705 label U-2 OS Cyclin B1-GFP cells on the Nikon upright confocal microscope with a 40x 0.65NA objective.

Cells were seeded and grown on top of a (**1**) 24x24 No. 1.5 coverslip (RA Lamb) in a 6 well plate (BD Falcon™) in appropriate media. The cells were labelled with the Qtracker® 705 Cell Labeling Kit (Q25061MP, Invitrogen). The coverslips were then carefully mounted in media containing 25 mM HEPES using (**2**) silicone multi-well isolators chambers (S2935, Sigma) on a (**3**) glass slide and placed on top of a (**4**) temperature controlled stage. For that, part of the middle section of the 8 chamber silicone isolators was cut away and 2 or 3 were stack on top of the glass slide, this was performed to increase media volume on the chambers. Afterwards, under aseptic conditions, media was placed on the chambers and the coverslip with the live cells gently placed inverted on the top. A pipette tip was used to "press to seal" the coverslip to the silicone avoiding air bubbles, excess media was removed with a tissue. Finally, all set was sealed with nail polish and placed on an "in-house" build temperature controlled stage. All the set-up was previous calibrated to maintain the cell media at a temperature of approx 36°C. The set-up can also be used to image i.e. fix cells in PBS buffer.

**Supplementary Information 5.6-3: Example of the analysis protocol for Experiment_1**

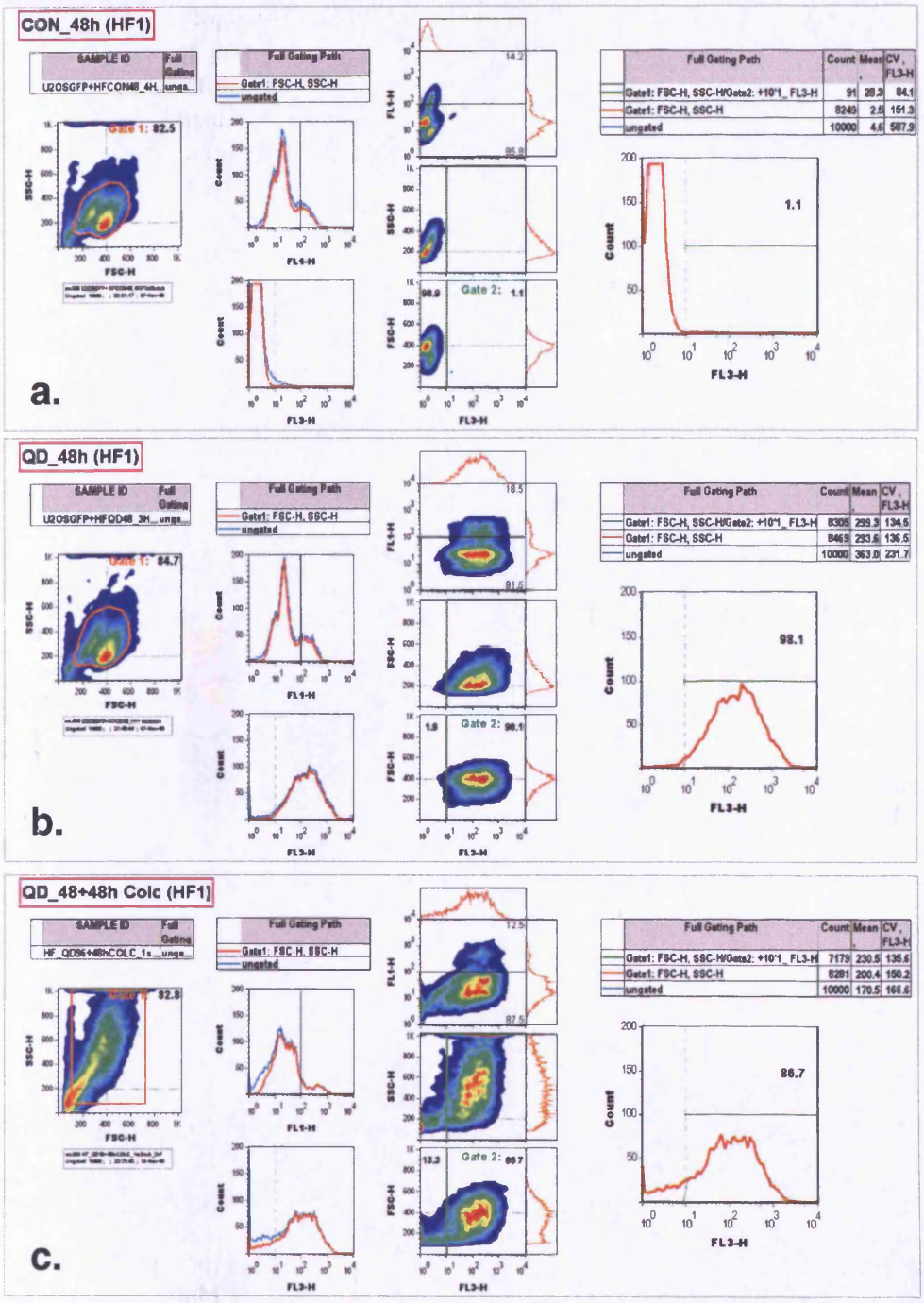


**Figure 5.15 – Example plot/histograms of the analysis protocol performed for the QD705 flow Experiment_1**. Samples retrieved from the HF (**a**) un-label control; (**b**) post-48h QD label; (**c**) after (48+48h Colc) 96h of which the last 48h incubated with 60 ng/ml colcemid drug. Channels: (FSC) forward and (SSC) side scatter: (FL1) Cyclin B1-GFP and (FL3) QD705 fluorescence. Raw data sets were (Gate1-orange line) forward and side scatter gated to eliminate the low fraction of small debris and death cell, all the reported results derived from this gated population. A second informative gate (Gate2-green line) was placed to report about the population fraction above the normal un-label control auto-fluorescence background with fluorescence higher than 10 arb. units. The complete compilation of all the raw and analysed flow results sets are displayed in Supplementary Information 5.6-3–CD-A3.

**Supplementary Information 5.6-4: Example of the analysis protocol for Experiment_2**

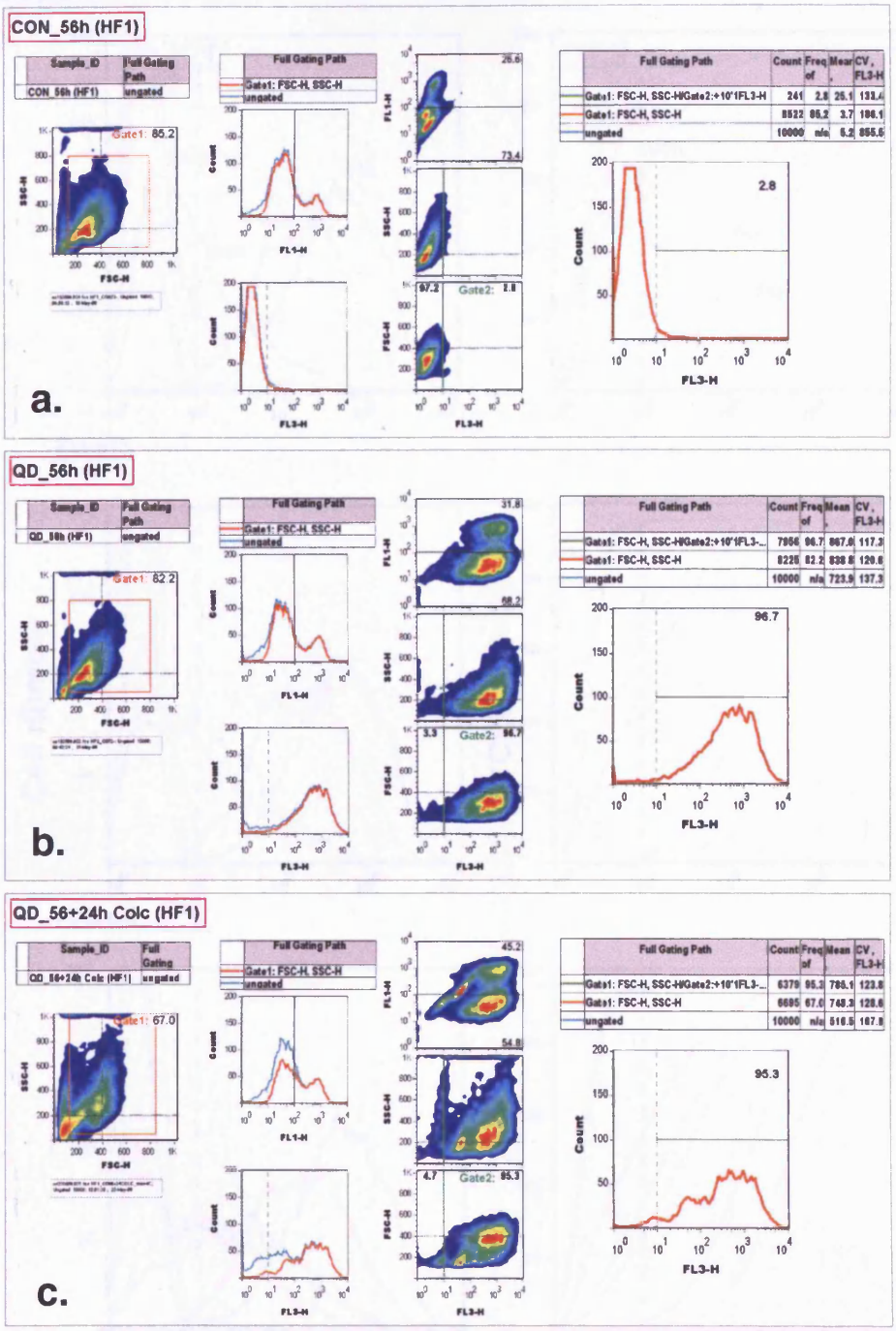


**Figure 5.16 – Example plot/histograms of the flow analysis protocol performed for QD705 flow Experiment_2.** Samples retrieved from the HF (**a**) un-label control; (**b**) post-56h QD label; (**c**) after (56+24h Colc) 80h of which the last 24h incubated with 60 ng/ml colcemid drug. Channels: (FSC) forward and (SSC) side scatter: (FL1) Cyclin B1-GFP and (FL3) QD705 fluorescence. Raw data sets were (Gate1-orange line) forward and side scatter gated to eliminate the low fraction of small debris and death cell, all the reported results derived from this gated population. A second informative gate (Gate2-green line) was also performed to report about the population fraction above the normal un-label control auto-fluorescence background with fluorescence higher than 10 arb. units. The complete compilation of all the raw and analysed flow results sets are displayed in Supplementary Information 5.6-4–CD-A3.

**Supplementary Information 5.6-5: Fluorescence intensity histogram profiles of Experiment 1**

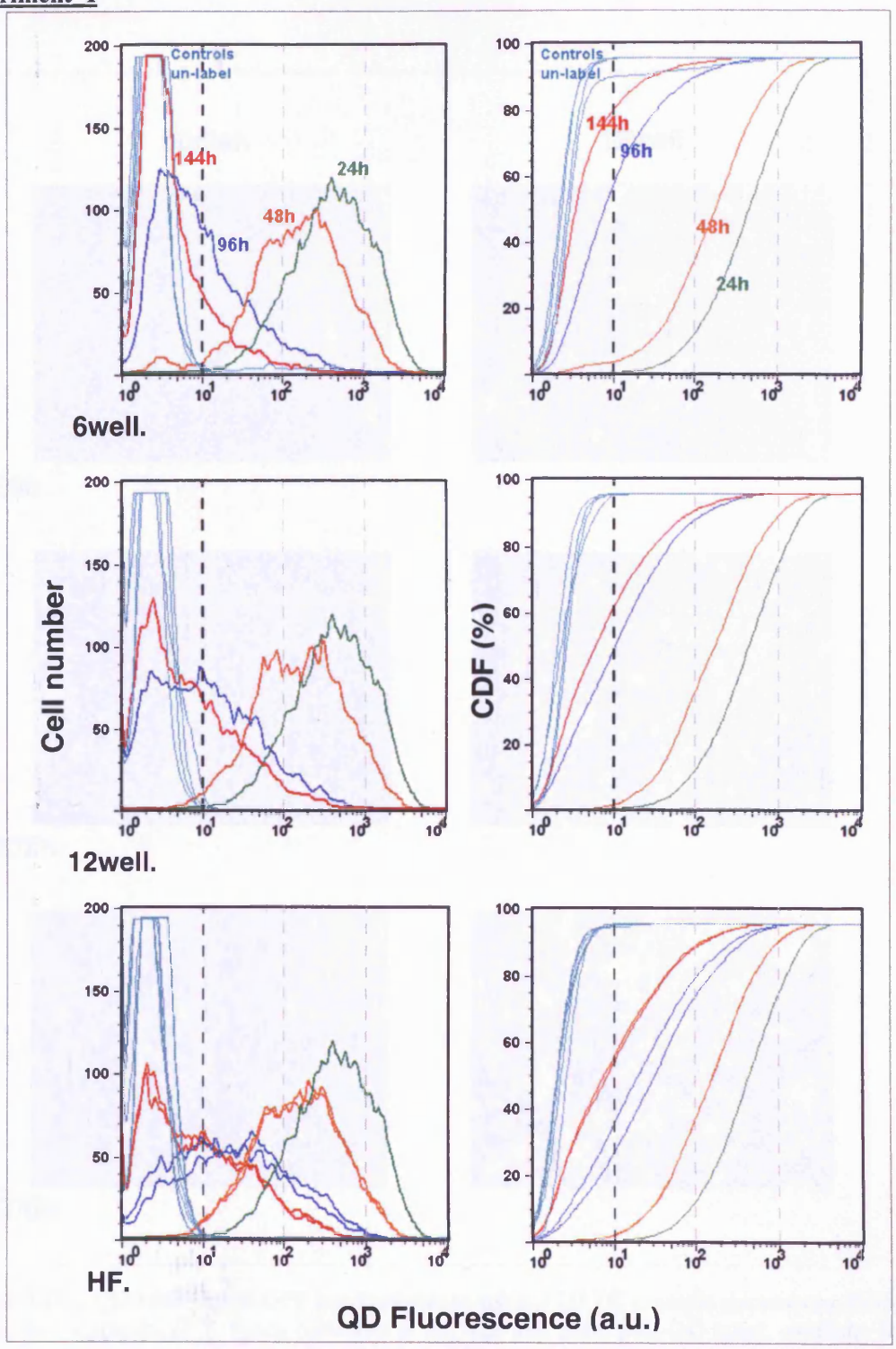


**Figure 5.17** – Fluorescence intensity flow histograms and correspondent cumulative distribution function (CDF) of the Experiment 1 QD705 label U2OS-GFP cells over time under different growth conditions: (**6well**) 6 well plate; (**12well**) 12 well plate; (**HF**) HF cell encapsulation *in vitro* culture, average of two parallel individual HFs. All samples seeded with the same cell population (green line) 24h post-QD labelling; cell populations (orange) 48h, (blue) 94h, (red) 144h post-QD labelling; (light blue) control un-label cells.

**Supplementary Information 5.6-6: Microscope fields of the standard TC of Experiment_2**

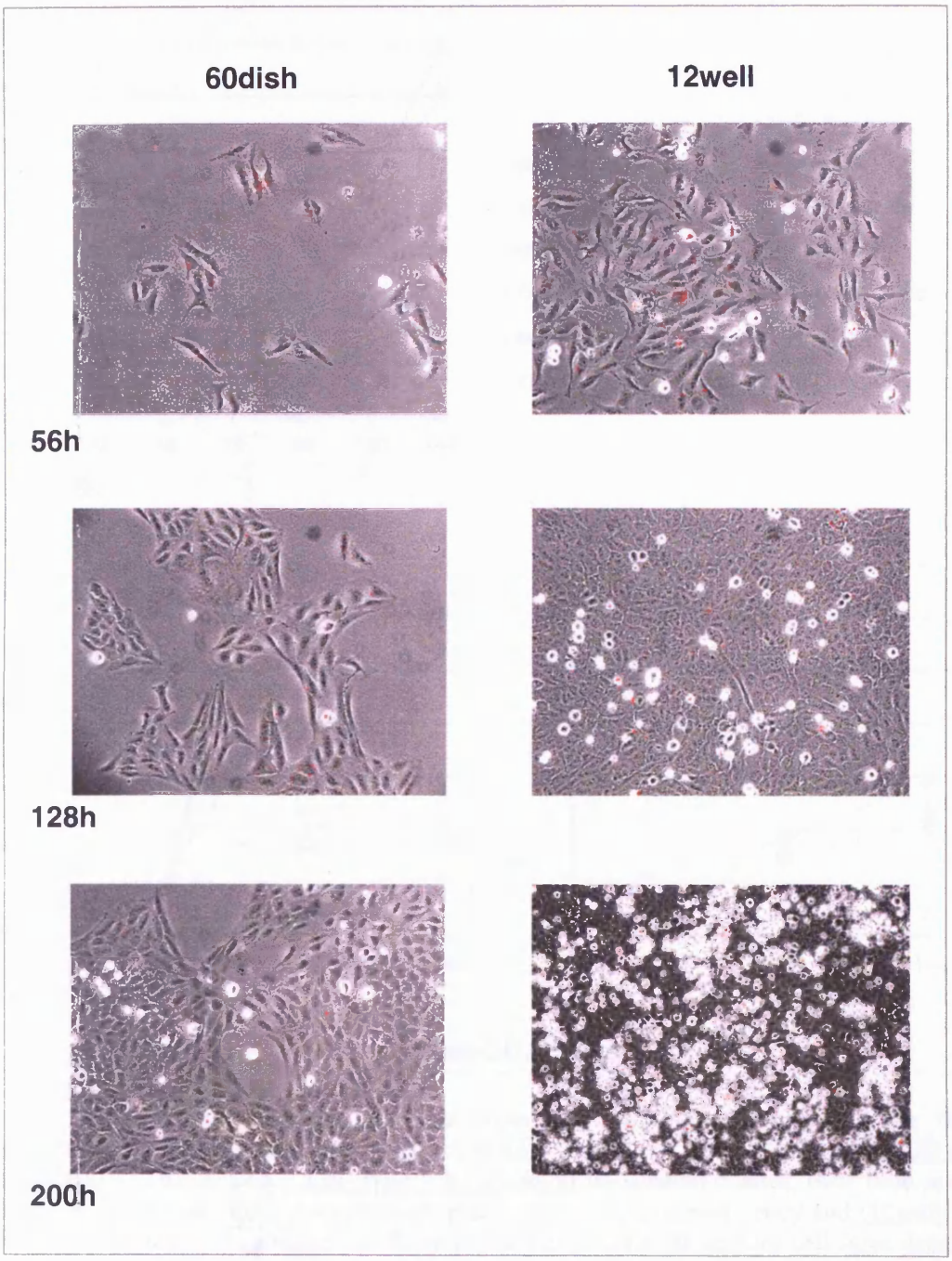


**Figure 5.18** – QD label U2OS-GFP standard planar surface 2D TC example microscope fields of the flow Experiment_2, fields collected at 56, 128 and 200h post-QD label. (**60dish**) 60 mm cell culture dish seed to low density; (**12well**) 12 well plate seed to a higher density, equivalent to the HF starting cells/area density. Merge phase and QD705 epi-fluorescence Axiovert mono CCD 10x 0.45NA lens example fields, 874x665µm.

**Supplementary Information 5.6-7: Growth curves obtained from cell counts for Experiment_1**

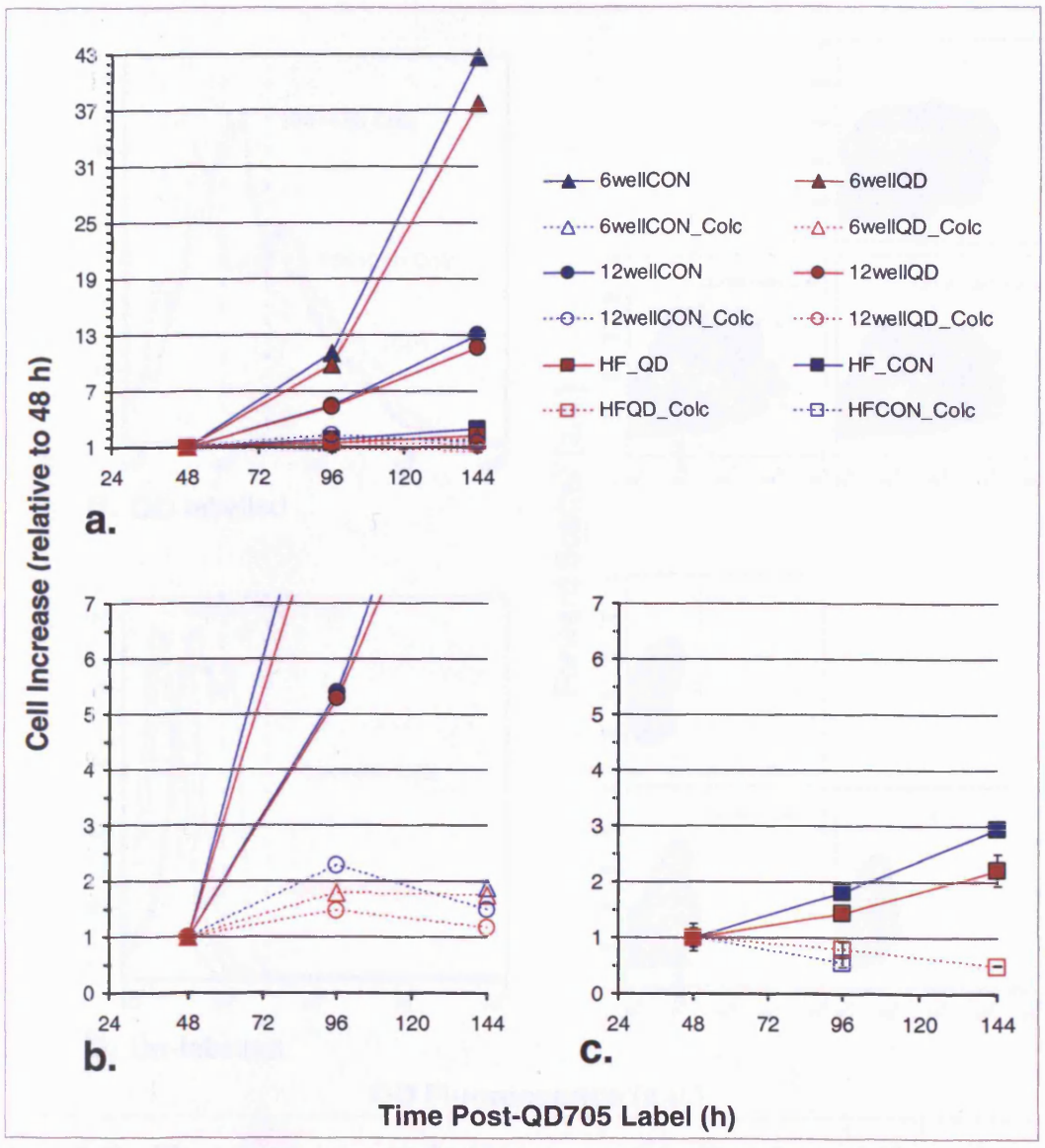


**Figure 5.19 – Growth curves obtained from cell Z1 Coulter counts of the flow Experiment_1.** **(a)** Complete growth curves graph; U2OS-GFP labelled cells with (QD-red solid markers) QD705 and (CON- blue solid markers) un-labelled control, over time under different growth conditions: (6well) 6 well plate cell seed to low confluency and (12well) 12 well plate culture seed to a higher confluency, equivalent to the HF starting cells/area density; (HF) hollow fiber cell encapsulation *in vitro* growth. Drug treatment (Colc - markers with no background) Colcemid 60 ng/ml added at 48h. Zoom-in graph detail of the low Y-axis values for the **(b)** 6 and 12 well plate and **(c)** HF.

**Supplementary Information 5.6-8: Details of the 60mm dish culture analysis for Experiment_2**

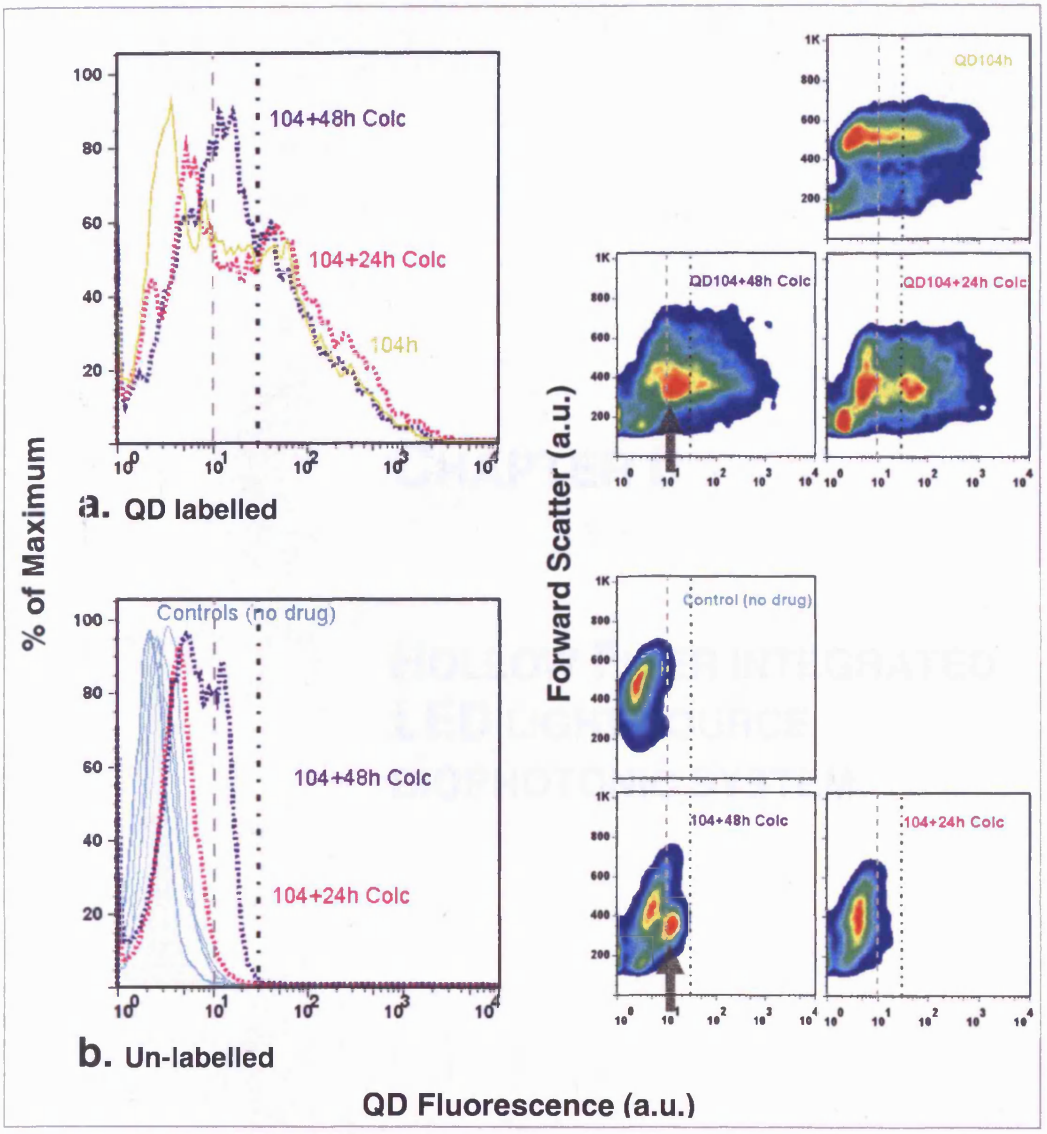


**Figure 5.20 – Fluorescence intensity flow histograms of the Experiment_2 60 mm dish standard TC.** Drug perturbation on **(a)** QD705 label and **(b)** un-label negative control U2OS-GFP cell populations. (Colc) Colcemid drug (60ng/ml) added at 104h post-QD labelling with a 24 and 48h incubation.

The (b) un-label auto-fluorescence background signal profile shifted form 10 fluorescence arb. units in the un-treated population (pale blue solid profiles) to 30-40 units in the colcemid treated (light and dark violet doted). This was similarly emulated by the correspondent (a) highly diluted QD label cell population (yellow solid) with the fluorescent profile shift, directly proportional to Colcemid incubation time. Note the sub-population pointed by the gray arrow auto-fluorescence.

# CHAPTER 6

# HOLLOW FIBER INTEGRATED LED LIGHT SOURCE BIOPHOTONIC SYSTEM

Parts of this Chapter have been included or are related to the following publication:

**Silvestre**, O. F.; Holton, M. D.; Summers, H. D.; Smith, P. J.; Errington, R. J. In *Hollow fiber: a biophotonic implant for live cells*, Imaging, Manipulation, and Analysis of Biomolecules, Cells, and Tissues VII, San Jose, CA, USA, 2009; SPIE: San Jose, CA, USA, **2009**; pp 71820V-11.

Print-out available on Appendix I

# 6 HOLLOW FIBER INTEGRATED LED LIGHT SOURCE BIOPHOTONIC SYSTEM ..... 221

# 6 HOLLOW FIBER INTEGRATED LED LIGHT SOURCE BIOPHOTONIC SYSTEM

## 6.1 Introduction

The use of QDs as an in-fiber biophotonic sensing nanoparticle for cell proliferation tracking (Chapter 5), necessitated the retrieval of cells from the HF followed by a flow cytometry analysis. This therefore represents an end-point assay due to mandatory tissue disaggregation with the loss of spatial information ruling out repetitive sampling "time-lapse" measurements. However, through a retrospective analysis of time-series acquisition it was possible to infer the proliferative features of the cell population. The present chapter represents a preliminary study heading towards the end goal of developing biophotonic micro-devices, comprising a light source and a detector integrated in the HF to report encapsulated cell population "real-time" behaviour (i.e. cell proliferation, cell death and cell clustering). The focus here is on assessing the interaction of encapsulated particles/cells with an in-fiber side coupled light source, namely in terms of optical properties (light attenuation and fluorescence) and what is the best way to detect this output.

Some relevant literature biophotonic/optical imaging micro-devices and implantable micro electronics are considered below. Followed by a short introduction describing some relevant light interactions with biological material (matrix/cells and particules).

### 6.1.1 Biophotonic optical devices

Biophotonic/optical imaging micro-devices, such as lab-on-a-chip, use a variety of optical components in combination with microfluidics (Schulze et al. 2009; Velasco-Garcia 2009). The optical/biophotonic components could be "off-chip" as part of a macro-scale optical instrument or "on-chip" integrated onto the chip itself.

The "off-chip" set-up incorporates the chip apparatus placed on an epi-fluorescence microscope with charge coupled devices (CCD) as detectors or within a confocal configuration with photomultiplier tube (PMT) detectors (Craighead 2006). Another

example is the use of an optical fiber to deliver and collect light together with LEDs (light-emitting diode) light sources. LEDs are one of the most effective light sources available and require only low power driving circuits. These advantages, combined with their very compact dimensions, suggest that they are suitable for integration onto micro-devices. For example they have been used in the design of LED-induced detection devices set-ups, where the LED excitation and emission light is guided through the optical fiber to and from the sample to a detector, to measure absorbance (Malcik et al. 2005) and fluorescence (Miyaki et al. 2005). The advantages of the above "off-chip" optics approach are, besides the possibility of using already pre-developed systems, very low levels of background signal that can be combined with very sensitive photon acquisition techniques and robust instrumentation based on PMT and CCD devices which in turn, results in good detection capability (Kuswandi et al. 2007).

The "on-chip" approach integrates optical components and possibly microfluidic onto a single platform to integrate all functionality onto a single device. This requires increased integration of not only fluidic elements, but also electrical or other types of elements (Balslev et al. 2006; Kuswandi et al. 2007).

The described micro-devices and even other macro-instruments (i.e. flow cytometry), when applied to cell/tissue analysis, represent systems where the cells are "exposed to a biological–unfriendly" environment and sometimes subjected to stressful measurement regime, basically in these devices the cells are analysed totally detached from their normal growth media. To mitigate this disadvantage and make use of the full potential of these technologies, the long term end goal of the approach initiated on this Chapter is to "bring" the device/instrumentation to the cells or tissue biological environment, namely inside living hosts. This raises up several other challenges, for example in terms of the micro-device hardware. Although this would not be investigated directly in the present work, there are already several micro-devices developed to study biological responses *in vivo* or probe the inside of subjects, for use in medical human diagnostics/ therapeutically or research applications (Puers and Ieee 2006; Receveur et al. 2007; Sauer et al. 2005). Namely medical diagnostic endoscopy capsules (Glukhovsky 2003; Iddan et al. 2000; Kfouri et al. 2008; Wang et al. 2005a; Xin et al. 2010); Given Imaging, Israel, http://www.givenimaging.com/ [2009]; RF System

Lab, Japan, www.rfsystemlab.com [2010]), other types of wireless implantable micro-devices used in animal research (Cong et al. 2009; Cong et al. 2008), including radio frequency identification (RFID) tags (Lewejohann et al. 2009; Paulson 2007; Rao et al. 2005; Troyk 1999); http://www.trovan.com/ [2010]; www.verichipcorp.com [2009]; http://www.hitachi-eu.com/mu/Products/Mu%20Chip.htm [2010]) some with biophotonic component (Mandecki et al. 2006); http://www.pharmaseq.com/pages/rfid.html [2010]).

### 6.1.2 Biological matter (particles/cells) versus light interactions

In the general introduction (chapter 1.4.2) a brief overview of the light interactions with biological material has been described. The light can be *transmitted, reflected, refracted, scattered and absorbed* by the target *subject* biological material. In this section the focus is absorbance and scattering interactions.

Both absorption and scattering contribute to light attenuation in a direct measurement of transmitted light which have independent origins (Cheong et al. 1990; Hayat 2008; Tuchin 2007).

Most of the cell components and molecules absorb in the ultra-violet (UV) wavelength range. Proteins are an important component, amino acids absorb at wavelengths shorter than 240 nm, other amino acids including phenylalanine, tyrosine and tryptophan absorb at wavelengths longer than 240 nm but well below the visible region of the light spectrum. Proteins also contain chromophores which provide strong absorption bands; examples include the heme group (in hemoglobin) as well as the *cis*-retinal (in case of retinal proteins). The absorption peaks for hemoglobin are around 280 nm, 420 nm, 540 nm and 580 nm. Aside from proteins, other cellular components also absorb light. Purines and pyrimidines, the basic components of DNA and RNA absorb light ranging from 230-300 nm and carbohydrates have absorption coefficients below 230 nm (Mthunzi 2010). Water, a major cell constituent has no absorption bands or peaks from UV to NIR, it starts weakly absorbing light above 1,300 nm with more pronounced peaks at $\geq$ 2,900 nm and very strong absorption at 10,000 nm (Hale and Querry 1973).

Importantly in cells and tissue, especially for wavelengths from visible to NIR, elastic scattering is by far the most prevalent form of light interaction with biological tissue (Boustany et al. 2010). Cell light scattering is essentially due to the presence of interphases or refractive index discontinuities at the microscopic level. For visible and NIR light, scattering is believed to be originated mostly from cells nuclei and sub-cellular organelles. The scattering properties are affected by both the size and density of these scattering centres, so their assessment can provide information on the structure of cell and tissue, and in particularly, on the local density of cellular nuclei and organelles (Hayat 2008; Tuchin 2007).

The absorbance of a molecular agent at a given wavelength dissolved in a transparent solvent sample varies linearly with both the agent concentration (C) and the sample optical distance (d) through which the light passes, this relationship can be represented by the Beer-Lambert law:

$$A = \varepsilon C d \qquad \textbf{Equation 6-1}$$

This law can be applied to other samples, in a simple way the transmittance (T) of a collimated beam of light that passes through a cell or tissue sample of thickness d [$cm^{-1}$] is represented by:

$$T = I / Io = e^{-\mu t d} \qquad \textbf{Equation 6-2}$$

Or represented in terms tissue light absorbance (A),

$$A = -\ln (I_0 / I) = -\ln (T) = \mu_t d \qquad \textbf{Equation 6-3}$$

with the total attenuation coefficient ($\mu_t$) given by,

$$\mu_t = (\mu_a + \mu_s) \qquad \textbf{Equation 6-4}$$

Following the mentioned above, the absorption coefficient in the visible and NIR light propagation through in biological tissues is greatly overwhelmed by scattering ($\mu_s >>$

$\mu_a$). In this situation of scattering-dominated light transport the reduced scattering coefficient ($\mu_s'$), obtained with the incorporation of anisotropy factor (g), is a useful parameter to describe this light diffusion regime (Tuchin 2007; Wax and Backman 2010; Yavari 2006).

$$\mu_s' = \mu_s (1-g) \qquad \textbf{Equation 6-5}$$

where:

A = absorbance [dimensionless]
T = transmittance [dimensionless]
$\varepsilon$ = molar extinction coefficient of the agent at a given wavelength [L $mol^{-1}$ $cm^{-1}$]
C = concentration of the agent [mol $L^{-1}$]
d = optical distance or thickness of medium through which light passes [cm]
Io = intensity of light source or of the incident light [$mW/cm^2$]
I = intensity of the light after passing through the medium optical path [$mW/cm^2$]
$\mu_t$ = total attenuation coefficient [$cm^{-1}$]
$\mu_a$ = absorption coefficient [$cm^{-1}$]
$\mu_s$ = scattering coefficient [$cm^{-1}$]
g = anisotropy [dimensionless]
$\mu_s'$ = reduced scattering coefficient [$cm^{-1}$]

The above described principles and the calculation performed later on in this Chapter but represents a highly simplistic overall view of the light propagation in biological tissues, considering the complexity of these phenomena, summarized elsewhere (Jacques and Pogue 2008; Ntziachristos 2010; van Rossum and Nieuwenhuizen 1999; Wax and Backman 2010).

## 6.2 Aims

In the present chapter the overall aim was to develop and assess a design for integrating simple biophotonic components for an in-fiber biophotonic innovative light delivery/detection onto the HF platform. The interaction of HF encapsulated particles/fix cells with a side coupled light source, in terms of fluorescence and light attenuation, was tested with the following technical approaches:

*1.* Prototype_A: To design and evaluate a prototype that considers the detection of HF encapsulated 15 µm fluorescent beads using a LED light delivery through a coupled optical fiber to one side of the HF embedded within a semi-solid "phantom", with signal acquisition through an external detection device offered by a commercially available animal macro-imaging system.

*2.* Prototype_B: To produce and test a system, where optical fibers were used to deliver light to one end of the HF and conduct the transmitted light from the other end to a detector. This prototype was used to evaluate the light attenuation of the HF loaded with fixed U-2 OS cells under different LED wavelengths.

## 6.3 Specific methodology

Two simple HF integrated biophotonic prototypes were designed, fabricated in-house from basic components and characterized in non-live cells or non-biological proof of principle studies.

### 6.3.1 HF agarose gel phantom Prototype_A model system

This prototype system (Silvestre et al. 2009) was developed to assess the effect of a direct optical fiber LED excitation from one end of the HF placed inside a semi-solid gel phantom within the IVIS200 imaging system. This commercial instrument was specially developed and commonly used for small live animal research, consisting on macro-imaging system based on a reflectance optical set-up and CCD detector (chapter 2.6.4).

The biophotonicic model prototype system (Figure 6.1) was constructed using a 650nm LED like a light source, the light was delivered using a 1mm outer diameter plastic optical fiber plugged to the HF and fitted with the help off Tygon tube inside a black weighing boat filled with a 1% agarose gel to simulate an ideal transparent "phantom".

The model prototype system was tested using HF encapsulated red 15 µm polystyrene fluorescent beads (ex.645/em.680nm) (Cat. No. F-8843, Invitrogen) homogeneous suspended and distributed in alginate gel matrix. The 15 µm fluorescent beads were added to 2% alginate to a concentration of 5.0 x$10^5$ beads/ml, the mixture was injected in the HF submersed in a 3.5% $CaCl_2$ solution, and left to polymerize for 20 min followed by heat sealing one or both ends of the HF, controls with alginate only were also prepared. Tygon tube loaded with the same alginate + 15 µm beads and heat sealed was also used; this represented a secondary control (results not showed), because the Tygon tube has the same inner diameter of the HF and is totally transparent, so it was possible to have a clear view of the beads inside.

The prototype set-up was placed inside the IVIS200 animal imaging system to study and compare the fluorescent emission and light attenuation (absorbance/scattering) of

the HF alginate 15 μm beads matrix under LED optical fiber side light excitation versus the standard instrument top excitation illumination.

### 6.3.2 HF Prototype_B model system

The schematics set-up and specification of the *in vitro* model system are presented in Figure 6.2. Briefly, the system consisted of exchangeable LEDs of several wavelengths powered by an adjustable constant current source (set to 20 mA) connected to AC/DC voltage converter plug. The light was delivered using a 1mm outer diameter plastic optical fiber to the approx 2 cm length HF on the bottom of a 60 mm TC dish with 10 ml of water.

The transmission properties through the HF were tested using a range of different LED wavelength (361, 400, 450, 490, 572, 650 and 760 nm) with only water inside the HF (control blank signal) and after loading the HF in medium with 50 μl of 4.1 $x10^6$ cells/ml fixed U-2 OS cells with 4% PFA. Light that is transmitted along the HF was collected at the far end by an optical fibre connected to an amplified silicon photo-detector, being then translated to voltage and the signal displayed on the multimeter. The cells inside the HF induced changes in the light transmission properties of the HF (due to absorbance and scattering), and so the collected signal can potentially be used to infer the state of the cellular constituents within the encapsulated growth chamber.

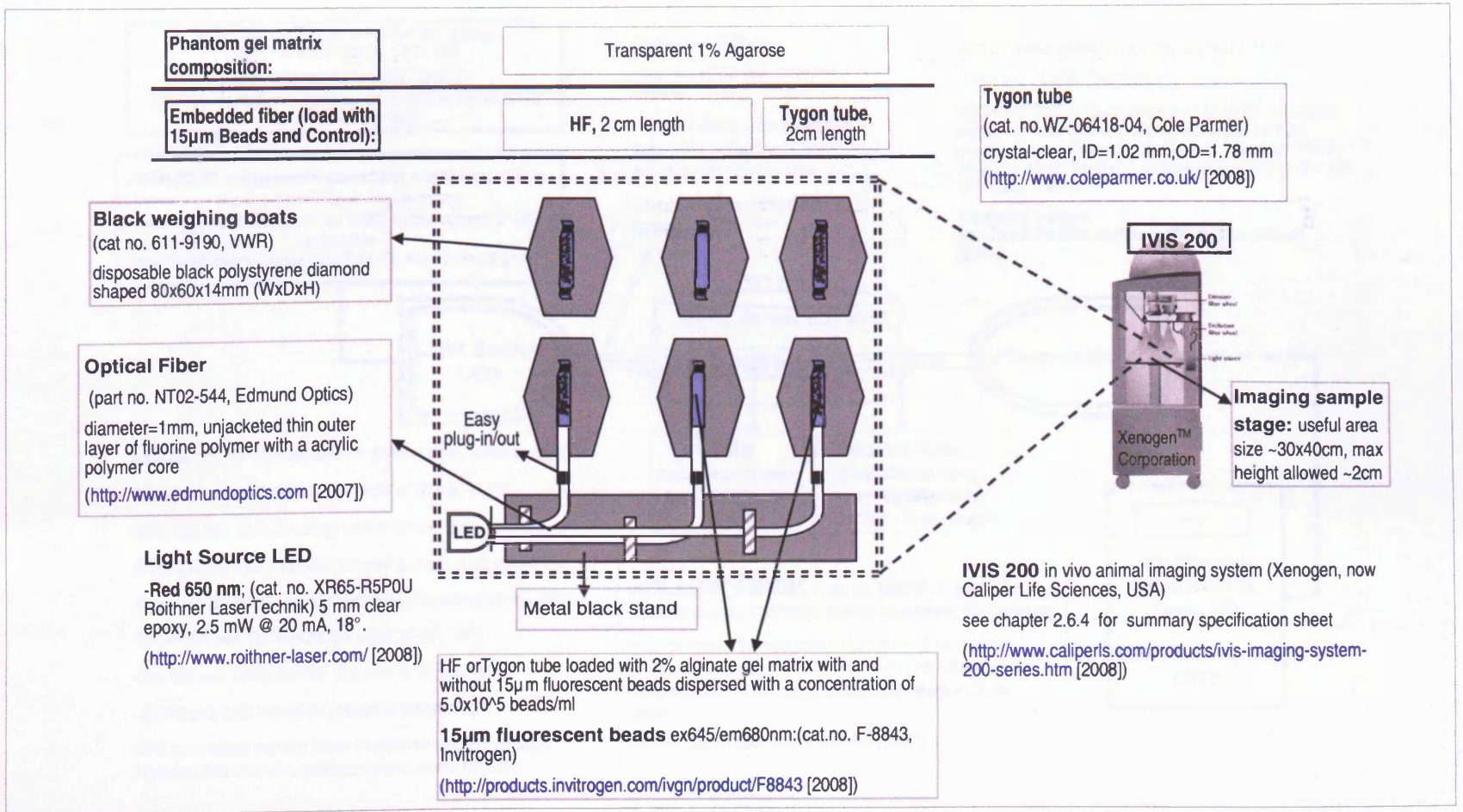


**Figure 6.1** – Schematic set-up and components specification of the IVIS200 HF gel phantom Prototype_A model system.

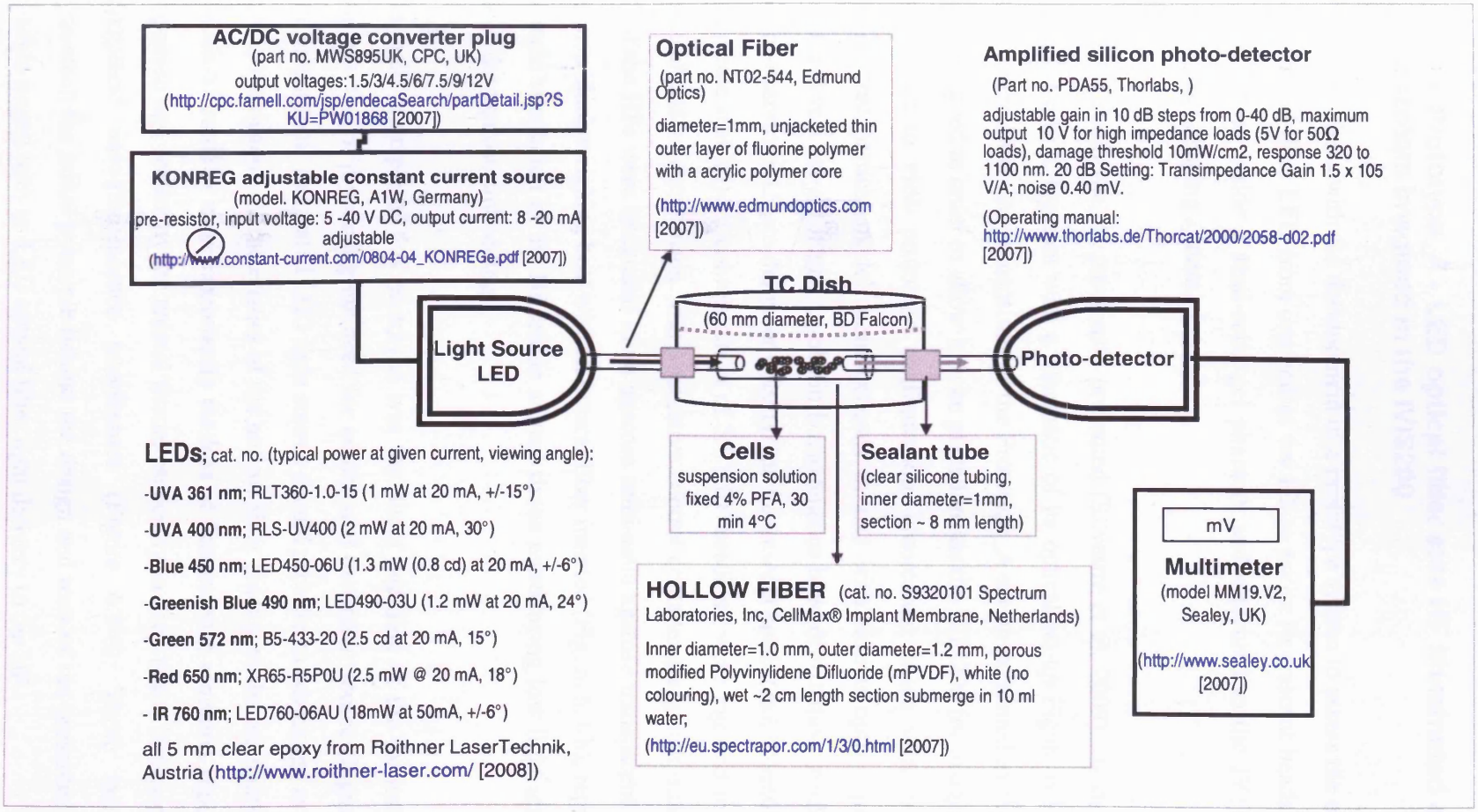


**Figure 6.2 –** Schematic set-up and components specification of the HF Prototype_B model system.

## 6.4 Results and Discussion

### 6.4.1 HF Prototype_A - LED optical fiber side HF illuminated agarose phantom imagined in the IVIS200

This section deals with the development of a prototype system to assess the effect of a direct optical fiber LED from one end of the HF to excite fluorescent beads. The HF was embedded inside a semi-solid gel phantom and measured in the IVIS200 live small animal imaging system.

A view of Prototype_A, previously presented (Silvestre et al. 2009), is depicted in Figure 6.3-a to c, together with a schematic of its optical set-up Figure 6.3-d and e. The characteristics and dimensions of the Prototype_A set-up presented in Figure 6.3-a was designed in order to allow it to be placed inside the IVIS200 for imaging signal outputs and to view prototype configuration. Fluorescent beads were used as a uniform test particle model, homogeneous in size with similar optical properties, embedded in a sol-gel matrix to obtain homogeneous bead distribution inside the HF lumen. Therefore, 15 μm diameter polystyrene fluorescent beads (ex645/em680nm) in an alginate matrix to a concentration of 5.0 $x10^5$ beads/ml were injected in the HFs and analysed in comparison with a negative control containing alginate matrix only. All of the HFs were integrated in an agarose semi-solid agarose transparent phantom within a black weighing boat with an optical fiber inserted (Figure 6.3-b), representing a simple simulation of the HF inside animal tissue reproducing low light attenuation due to the agarose embedding.

The main principle of this prototype was the direct coupling of the excitation light source to the HF bypassing the need for an external excitation source (Figure 6.3-e). This biophotonic integrated LED *light source* should provide an advantage as it avoids the relative opaque characteristics of the hollow fiber leading to the attenuation of the excitation source or more importantly the loss of fluorescence emission signal due to absorption and scatter by the animal tissue, especially in deep tissue imaging, and the background auto-fluorescence interference (Figure 6.3-d). These last factors represented the initial principle behind the design and tests of the presented proof of principle model with an LED optical fiber light delivery to the HF.

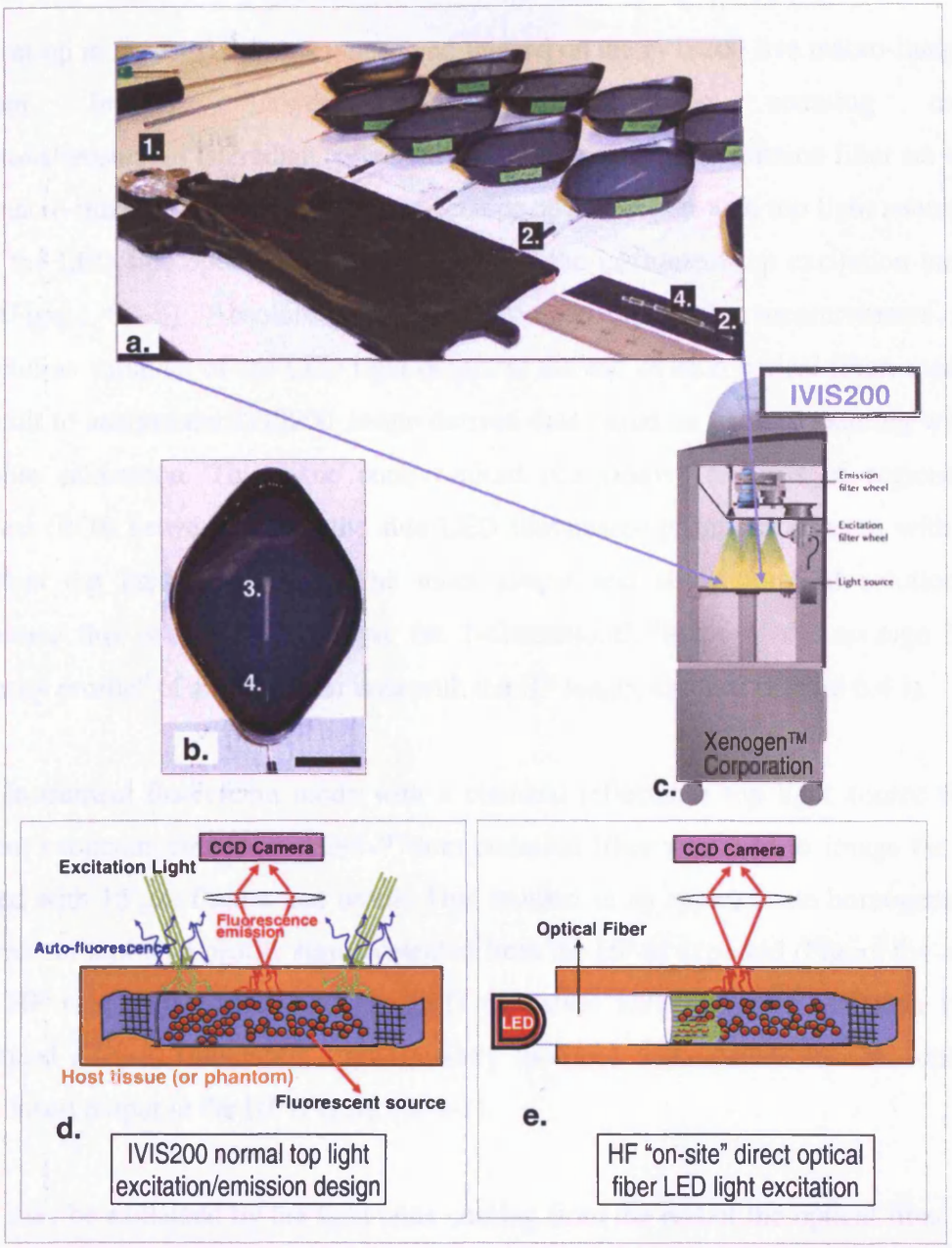


**Figure 6.3 – HF Prototype_A set-up and operation design.** **(a)** HF with directly coupled optical fiber LED excitation set up. (1) 650nm LED is the light source, the light is conducted through an (2) 1mm diameter optical fiber to the HF inside the phantom, providing direct illumination from one side of the HF. Detail of the optical fiber phantom insert, the (3) HF is connected to the end of the optical fiber fitted with a (4) Tygon tube to help support the insert glued to the black weighing boat. This set-up with up to three phantoms with the optical fiber insert at one side of the HF (bottom column) and three control phantoms without the insert (top column), was placed inside the IVIS 200 imaging sample stage (useful area size ~30x40cm, max height objects allowed ~2cm) (Silvestre et al. 2009). **(b)** Detail of the transparent phantom made of 1% agarose gel in the black weighing boat (~80x60x14mm WxDxH at top widest points). Scale bar 20 mm. **(c)** IVIS 200 macro imaging system diagram (adapted from: Xenogen now Caliper Life Sciences, http://www.caliperls.com/products/ivis-imaging-system-200-series.htm [2008]). Schematic of the HF optical set-up with CCD detector; **(d)** "epi-fluorescence like" acquisition with the instrument top light source and **(e)** LED light excitation from one side of the HF delivered through an optical fiber.

The set-up in Figure 6.3-a was placed and imaged on the IVIS200 live macro-imaging system. Images were acquired in photon counting mode (photons/second/cm$^2$/steradian (p/sec/cm$^2$/sr) using appropriate emission filter set with the macro-imaging system classical reflectance optical set-up with top light source or with the LED side optical fiber excitation, with the instrument top excitation turned off (Figure 6.4-ii). Absolute quantitative comparison of the measurements was difficult as variation of the LED light output at the end of each optical fiber, made it difficult to analyse the IVIS200 image-derived data based on photon counting with a suitable calibration. This issue compromised comparative analysis of regions of interest (ROI) between any of the side LED illuminated phantoms or even with the classical top light excitation. The more simple and straightforward solution to overcome this issue was to analyse the 1-dimensional "shape of the average light intensity profile" of a rectangular area with the HF length distance (Figure 6.4-i).

The instrument fluorescent mode with a classical reflectance top light source 615–665nm excitation filter and a 695–770nm emission filter was used to image the HF loaded with 15 µm fluorescent beads. This resulted in an approximate homogeneous fluorescent emission profile signal detected from the HF as expected (Figure 6.4-a-1). The HF side optical fiber 650 nm LED excitation with the same emission filter produced a lower fluorescent signal, mainly localized immediately near the optical fiber insert output in the HF (Figure 6.4-b-1).

This may be explained by the light cone coming from the end of the optical fiber that would be uneven along the HF length preferentially exciting the HF zone closer to the optical fiber. Also it was possible that the beads in the HF would attenuate the light transmission, with a consequence of uneven illumination of the beads along the HF. Both control HFs with only matrix (no beads) showed only background noise registered in the 1-dimensional profile (Figure 6.4-a and b-2). The HF 15 µm fluorescent beads light attenuation was evaluated by examining the LED 650 nm excitation light pattern emerging from the optical fiber using 575–650nm emission filter, in other words the "transmitted light" from the fiber (Figure 6.4-c), because the emission filter included the LED excitation wavelength. This confirmed that indeed the light output pattern was not uniform in the HF.

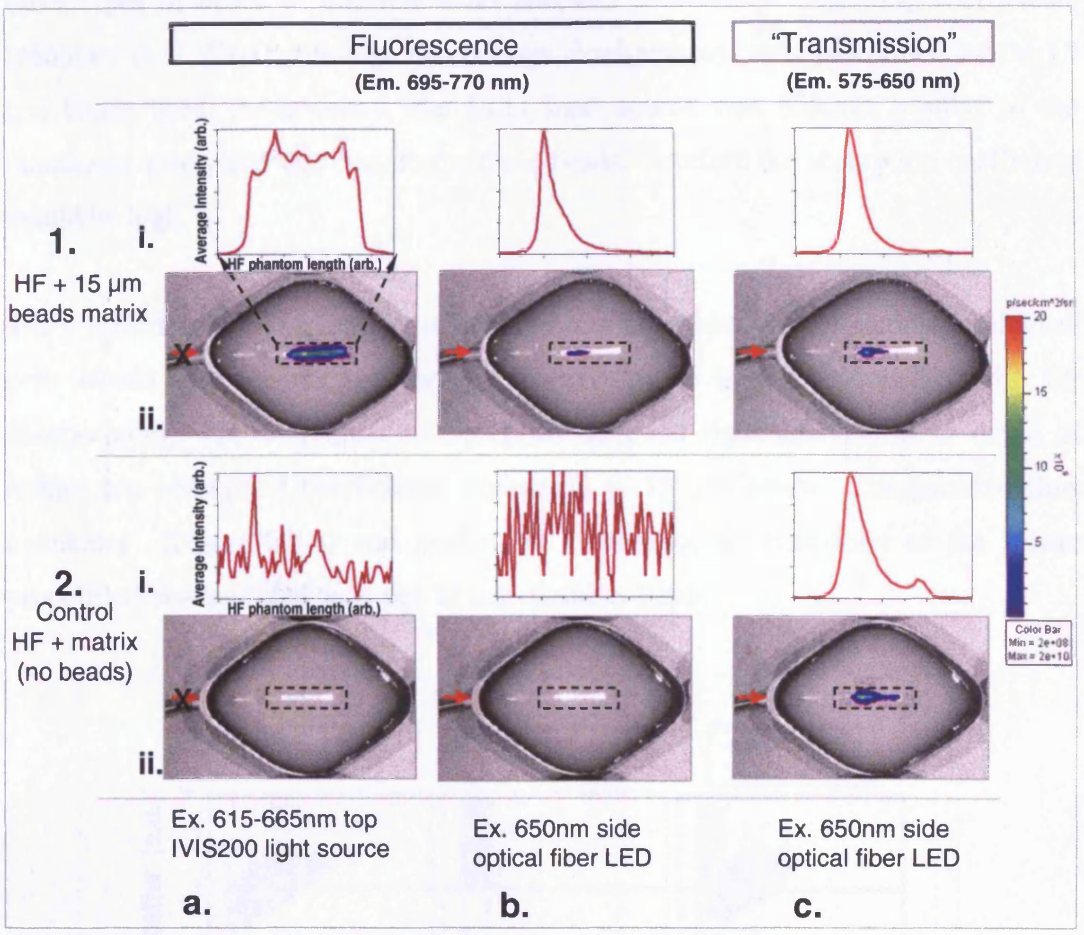


**Figure 6.4 – HF Prototype_A proof of principle device demonstrating the HF placed in a transparent agarose phantom and imaged on the IVIS200 system.** (**row 1**) HF loaded with 5.0 x$10^5$ beads/ml of 15 µm fluorescent beads ex645/em680 nm suspended in 2% alginate matrix and (**row 2**) control HF loaded with only 2% alginate matrix, both embedded on a 1% agarose phantom. (**sub-row ii**) Phantoms photon count images (p/sec/cm$^2$/sr) using the following light sources: (**Column a**) external excitation top source of the IVIS200 at low power and the (**column b and c**) 650 nm directly side coupled optical fiber LED only. (**Column a and b**) fluorescence images collected with the instrument 615–665nm filter and (**column c**) transmitted light image collected with 575–650 nm filter. (**sub-row i**) HF images derived linescan area graph (dashed rectangle) of the average light intensity versus the embedded HF length distance with arb. units. Phantom black weighing boat dimensions ~80x60x14mm WxDxH at top widest points.

The control HF with no beads (Figure 6.4-c-2) presented a better distributed signal along the HF in relation to the HF with 15 µm beads (Figure 6.4-c-1), this was apparent in the 1-dimensional profile. The control presented a peak near the optical fiber light output side, with approximately 12% of this peak light intensity reaching the opposite site of the HF (Figure 6.4-c-2-i). By contrast in the HF with 15 µm beads there was complete attenuation with no light reaching the end of the HF (Figure 6.4-c-1-i). The possible explanation is that the beads loaded in the HF absorbed and scattered light in comparison to the control (without beads). Previous studies with

other types of beads of different sizes revealed considerable scattering coefficients (Mourant et al. 2001), although no concrete measurements were performed for the 15 µm beads used. Additionally, the LED light source was 650 nm similar to the maximum absorption wavelength for these beads, therefore the absorption coefficient would be high.

The critical factor is that the 15 µm beads represent an ideal model particle; biological cells would have different properties relative to the light attenuation in the HF encapsulation. The individual cell presents different light attenuation in terms of scatter and absorption coefficients in relation to 15 µm beads. Comparative flow cytometry (Figure 6.5-a) was performed to produce an evaluation of the scatter properties between fixed cells and 15 µm diameter beads.

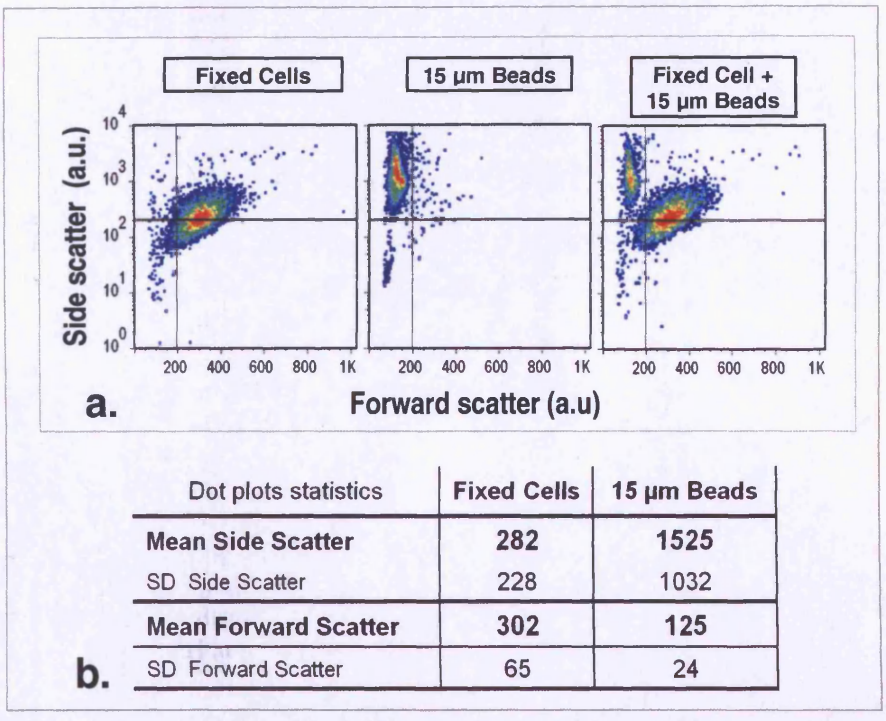


| Dot plots statistics | Fixed Cells | 15 µm Beads |
|---|---|---|
| **Mean Side Scatter** | **282** | **1525** |
| SD Side Scatter | 228 | 1032 |
| **Mean Forward Scatter** | **302** | **125** |
| SD Forward Scatter | 65 | 24 |

b.

**Figure 6.5 – Side and forward scatter analysis of fixed cells versus 15 µm diameter beads.** Flow cytometry measurement (FACSVantage) of fix U-2 OS cells (4% PFA) and 15 µm diameter polystyrene fluorescent beads (ex645/em680nm). **(a)** Dot plots of individual and a merge sample. **(b)** Table with the cell population measured plots statistics: mean and standard deviation (SD).

As shown in table of Figure 6.5-b, the 15 µm presented a 5 fold increase in mean side scatter and a 2 fold decrease in forward scatter compared to the fixed cells. This mean that overall the 15 µm beads would present a higher scatter coefficient in relation the

fixed cells. These results demonstrate the importance of evaluating the light attenuation of HF loaded with cells, described in more detail in the following section.

### 6.4.2 HF Prototype_B model system

The Prototype_B system set-up is presented in Figure 6.6.

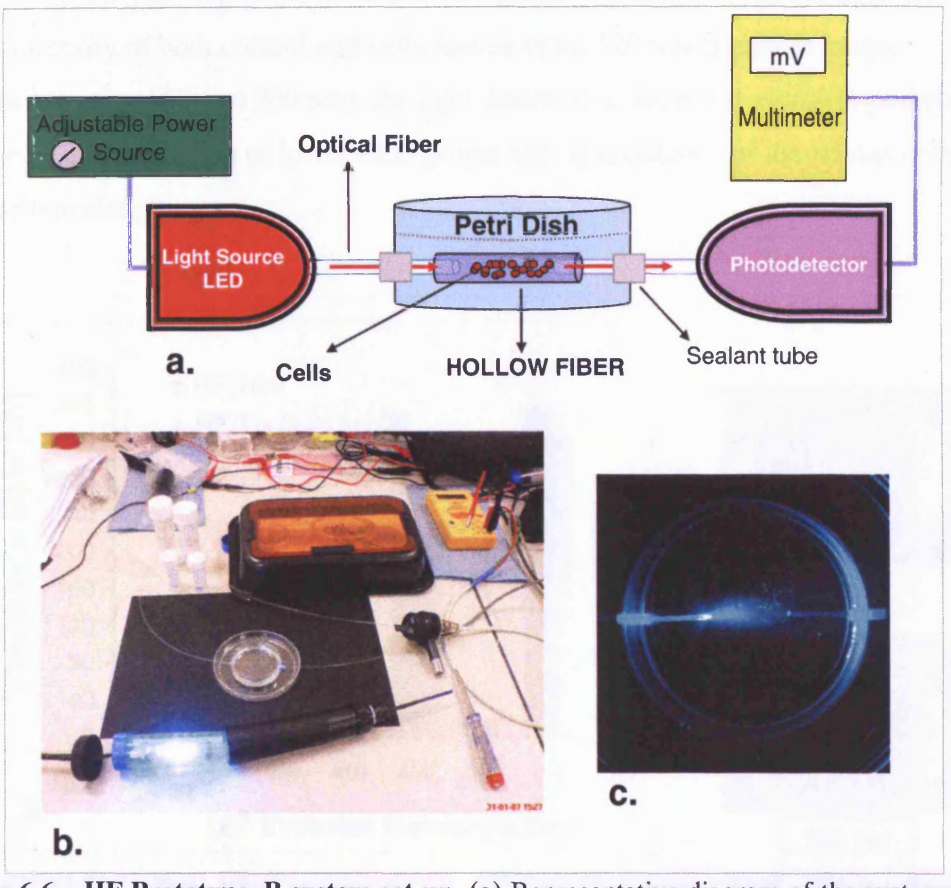


**Figure 6.6 – HF Prototype_B system set up.** (**a**) Representative diagram of the systems set-up. Light source an LED (Light Emitting Diode), was powered by an adjustable constant current source (set to 20 mA) connected to AC/DC voltage converter plug. The light was delivered using a multimode optical fibre to the HF on the bottom of a TC 60 mm Petri dish with 10 ml of water. The "cells" inside the HF induced changes in the transmission properties of the light (due to absorbance/scattering), that was conducted and collected at the other end by the optical fibre connected to the photodetector (amplified silicon detector), being translated to voltage and the signal displayed on the multimeter. (**b**) Picture of the actual Prototype_B system set up with the 490 nm LED. (**c**) Detail picture of the TC dish without the HF, were is possible to observe the viewing angle of light cone coming from the optical fiber. Full components specifications available on Figure 6.2.

The light source was an LED where the light was delivered using an optical fiber coupled to a 2 cm length HF section (with 1.6 cm available length) in a TC dish in solution and the transmitted light collected at the other end of the HF via another

optical fiber to the amplified photo-detector, where it was translated to voltage and the signal displayed on a multi-meter. The transmission properties through the HF system were tested using a range of different LED wavelengths (361, 400, 450, 490, 572 and 760 nm) with only water inside the HF (control blank signal) and after loading the HF with 2.05 x$10^5$ fixed cells (equivalent to 4.1 x$10^5$ cell/cm$^2$; 1.63 x$10^7$ cell/ml), corresponding to the maximum U-2 OS cell number obtained for a 2 cm length HF (chapter 3.4.2). The results are presented in Figure 6.7, the overall photo-detector signal intensity of both control and cells loaded in the HF was higher at longer wavelengths (i.e. 650 and 760 nm), the light detection at short wavelengths probably represents a combination of lower LED power and/or sensitivity of the silicon detector at these wavelengths.

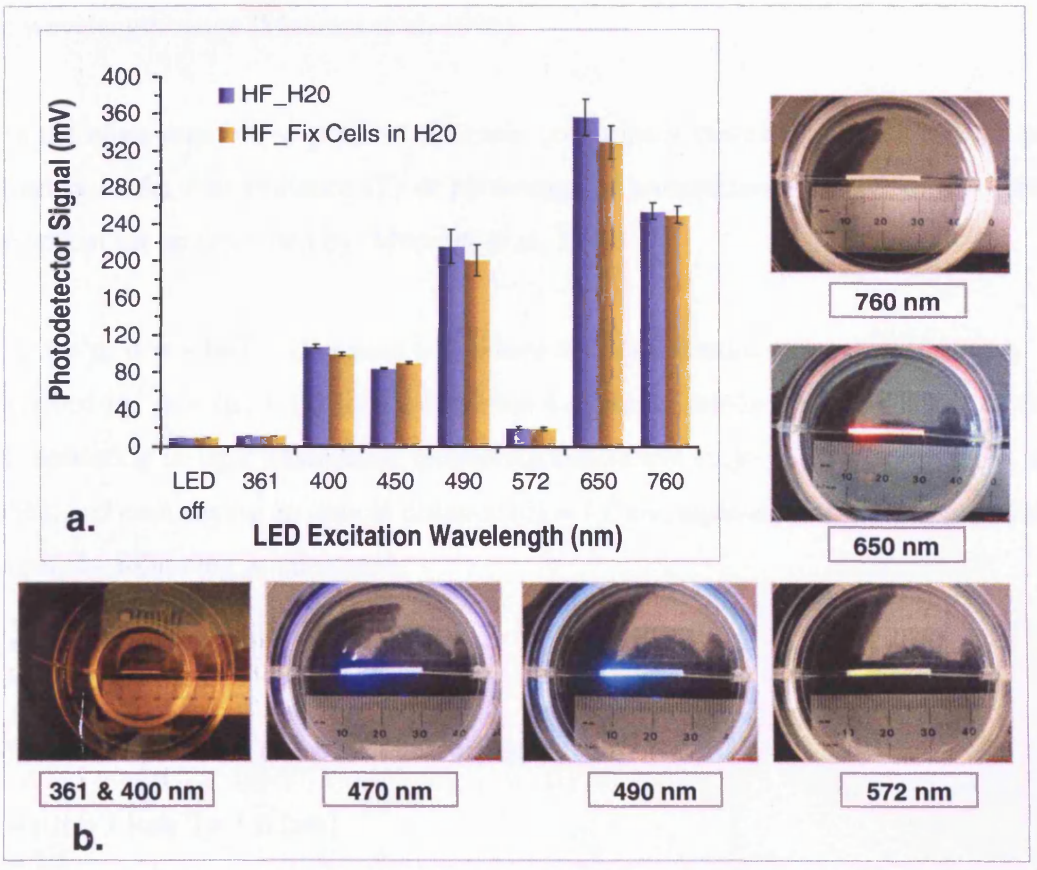


**Figure 6.7 – HF Prototype_B proof of principle demonstration.** **(a)** Light signal (mV) of different LED wavelengths transmitted through the HF with water (control blank) against a load of 2.05 x$10^5$ cells in the 2cm HF (equivalent to 4.1 x$10^5$ cell/cm$^2$; 1.63 x$10^7$ cell/ml), error bar ±standard deviation, number of non-consecutive measurements n=3. **(b)** Actual pictures of the HF Prototype_B set-up with the different LED incorporated. LED input current = 20mA; multimeter amplified gain =20dB.

Overall as shown in Figure 6.7 there were no relative changes in light transmission (or attenuation) at each wavelength between the HF with water or fixed cells. Simple parameters including scattering coefficients have been previously described for suspensions of cells or multicellular spheroids and also beads (Hargrave et al. 1996; Mourant et al. 1997a; Mourant et al. 1996; Mourant et al. 1997b; Mourant et al. 2001).

A previous study (Mourant et al. 1996), using a different optical set-up to Prototype_B, characterized a cell suspension ($4.6x10^7$ cells/ml) of EMT6 mouse mammary carcinoma, kept under constant agitation, between 350-850nm. The cell suspension produced a low cell absorption coefficient ($\mu_a$) from 480 nm, with only a slight peak at around 400 nm, probable due to cytochrome absorption. But the measured scattering coefficient ($\mu_s$) returned a relatively stable value of 1 $cm^{-1}$ across the wavelength range (Mourant et al. 1996).

It is therefore possible to perform a simple preliminary calculation to estimative the absorbance (A), transmittance (T) or percentage of transmittance (%T) changes from the optical set up described by Mourant et al. 1996 .

For, $A= \mu_t d = - \ln(T)$ (Equation 6-3) where the total attenuation coefficient ($\mu_t$) is described by, $\mu_t = (\mu_a + \mu_s)$ [$cm^{-1}$] (Equation 6-4), consideration only the effect of the cell scattering in light attenuation (scattering coefficient ($\mu_s$)= 1 $cm^{-1}$ (Mourant et al. 1996)) and considering an optical distance (d) = 1.6 cm, equivalent to the HF available length, the following is calculated:

$\mu_t = 1\ cm^{-1}$
$d = 1.6$ cm

Where the absorbance (A) and transmittance (T) are:

$A = \mu_t l = 1\ [cm^{-1}] \times 1.6$ [cm]
**A = 1.6**

$A = - \ln(T)$
$T = e^{-1.6} = 0.202$
**%T = 20%**

The EMT6 cell line, while different, is also an epithelial adherent cell line like the U-2 OS. The above preliminary estimates provide some parameters to perform a simple extrapolation of the cells light attenuation. The calculation suggest that for a similar set-up described by Mourant et al. 1996 the cell suspension concentration of $4.6x10^7$ cells/ml would produced considerable light attenuation with a percentage of transmittance (%T) of 20%. The EMT6 cell concentration normalized for the 2 cm HF ($5.64 \times 10^5$ cell/2cmHF; $4.6x10^7$ cells/ml) was approximately three time more than that used for the U-2 OS ($2.05 \times 10^5$ cell/2cmHF; $1.63 \times 10^7$ cell/ml) in Prototype_B, so it could be extrapolated that the %T for this last concentration should be of around 60%.

The Prototype_B optical set-up, light source and detector was quite different form the used by (Mourant et al. 1996), not to mention the basic design and possible sensitivity issues. This considering the above preliminary calculation apparently don't explain the clearly lack of light attenuation observed on Figure 6.7. Also although the measurement were performed immediately after the cell loading probable the suspension cell would had settled down on the HF bottom even before the measurements started because there was no agitation. This last was most probable the main reason why there was no significant change in the signal between the HF with water and fixed cells. Importantly, the estimated cell volume occupied by the $2.05 \times 10^5$ settled down cells in the HF represents only ~4% of the available HF lumen volume, this was extrapolated considering the following:

Tubular 2 cm HF (1.6 cm) length with 1.0 mm diameter presents,

Vol. = $1.26 \times 10^{10}$ $\mu m^3$ (12.6µl)
Surface area = $5.0 \times 10^7$ $\mu m^2$ ($0.5 cm^2$)

A cell like a perfect sphere with 15 µm diameter presents,

Vol. = $1.8 \times 10^3$ $\mu m^3$
Cross-sectional area of cell = 178 $\mu m^2$

Therefore in the lumen of a 2 cm HF (1.6 cm) length with 1.0 mm diameter in theory is possible to accommodate:

Total in the lumen vol.: ~ 7 million cells ($7.0 \times 10^6$ cell/2cmHF)
Attached to the inner wall area: ~ 280,000 cells ($2.8 \times 10^5$)

Overall, in the HF Prototype_B cell experiment (Figure 6.7) a total of ~2.05 x$10^5$ cells (4.1 x$10^5$ cell/cm$^2$ inner wall) were added to the 2 cm HF, close to the above maximum calculated value of 2.8 x$10^5$ cells that can be theoretical attached to the wall of a 2 cm HF in a "monolayer". This represents only ~4% of the available HF lumen volume. Based on Chapter 3 results this value was also not so different from the maximum stabilizing cell number reached by the HF–U2OS-GFP model, the intrinsic biological reasons for this were already extensively discussed (see chapter 3.5). Briefly, the culture of U-2 OS cells in the HF grow as an adherent layer on the inner wall and would not fill a most of the lumen. This means that for optical set-up described in Prototype_B for the U-2 OS cell line it would be difficult to obtain considerable changes in transmittance because most of the HF lumen light path would be free from cells, even if agitation was applied to the culture system.

An alternative to overcome the above limitation of Prototype_B with incorporated *in vitro* U-2 OS culture, would be the use of a contrast agent to enhance the HF lumen light attenuation (i.e. increase $\mu_a$ to overcome limited value of $\mu_s$). This might be achieved with the use of alamarBlue™ (Invitrogen), a cell viability quantification assay (Page et al. 1993). Briefly, alamarBlue is based on the resazurin dye (Twigg 1945), this compound oxidized form (abs $_{max}$ = 600 nm) is virtually non-fluorescent and cell permeable. During the assay is converted in the mitochondria of viable cells to a resorufin reduced form (abs$_{max}$ = 570nm), that is additionally fluorescent (ex = 530–560 nm ; em$_{max}$ = 590 nm). The reduced form is equally cell permeable and diffuses to the external medium enabling not only by measuring absorbance spectrophotometrically but fluorescence measurements (alamarBlue_manual 2008; O'Brien et al. 2000; Voytik-Harbin et al. 1998).

For spectrophotometric or colorimetric quantification of the absorbance there is considerable overlap in the absorption spectra of the oxidized and reduced forms of alamarBlue. When there is no region in which just one component absorbs, it is still possible to determine the two substances by making measurements of two wavelengths at 570 (or 540 nm) and 600 nm, where the reduced and oxidized forms absorb maximally, respectively. The plate reader is first blanked on a well containing medium only at the two wavelengths. The absorbance of the medium without cells

plus alamarBlue and the absorbance of the medium with cells containing alamarBlue is read at the two chosen wavelengths (alamarBlue_manual 2008). In monitoring alamarBlue reduction spectrophotometrically, reduction is expressed as a percentage (% Reduced).

Considering the following molar extinction coefficients [L $mol^{-1}$ $cm^{-1}$]:

alamarBlue at 600 nm
$\varepsilon_{ox}$ =117.216 ; $\varepsilon_{red}$ = 14.652

alamarBlue at 570 nm
$\varepsilon_{ox}$ = 80.586 ; $\varepsilon_{red}$ = 155.677

alamarBlue at 540 nm
$\varepsilon_{ox}$ =47.619 ; $\varepsilon_{red}$ = 104.395

with,

$$A\lambda 1 = C_{RED}(\varepsilon_{RED})\lambda 1 + C_{OX}(\varepsilon_{OX})\lambda 1 \qquad \textbf{Equation 6-6}$$

$$A\lambda 2 = C_{RED}(\varepsilon_{RED})\lambda_2 + C_{OX}(\varepsilon_{OX})\lambda_2 \qquad \textbf{Equation 6-7}$$

The calculation of % Reduced is as follows:

$$\textbf{\% Reduced} = \frac{(\varepsilon_{ox}\,\lambda_2)(A\,\lambda_1) - (\varepsilon_{ox}\,\lambda_1)(A\,\lambda_2)}{(\varepsilon_{red}\,\lambda_1)(A'\,\lambda_2) - (\varepsilon_{red}\,\lambda_2)(A'\,\lambda_1)} \qquad \textbf{Equation 6-8}$$

where,

$C_{RED}$ = concentration of reduced form alamarBlue
$C_{OX}$ = oxidized form of alamarBlue
$\varepsilon_{OX}$ = molar extinction coefficient of alamarBlue oxidized form
$\varepsilon_{RED}$ = molar extinction coefficient of alamarBlue reduced form
A = absorbance of test wells
A' = absorbance of negative control well (media + alamarBlue but no cells)
$\lambda 1$ = 570nm (540nm may also be used)
$\lambda 2$ = 600nm (630nm may also be used)

A preliminary experiment was performed on a planar TC well culture of U2OS-GFP cells to measure the light attenuation (most due to absorption) of the alamarBlue reduced form (570 or 540 nm) in presence of viable cell against the control with no cells. AlamarBlue (10% vol/vol) was added to 1.0 ml cell medium (optical distance= ~0.27 cm) on a 12 well plate with ~1.0 x$10^5$ cells (2.6 x$10^4$ cell/$cm^2$, a value close to

the HF estimated seeding density), incubated at 37°C (to allow reduction or conversion by the cell) during 14h and the absorbance measured on a PolarStar Optima microplate reader. This experiment returned a absorbance at 540 nm and 600 nm of 0.526 (%T= 59%) and 0.349 (%T= 75%), respectively, for the cell sample. While for the control with no cells the absorbance at 540 nm and 600 nm was of 0.348 (%T= 71%) and 0.572 (%T= 56%), respectively. This translated using Equation 6-8 in a % reduction = 83%. These results revealed that for a optical distance of ~0.27 cm at 540nm the alamarBlue reduced form only in the cell medium volume produced a decrease in transmittance of around 12% comparatively to the control with no cells.

Furthermore taking in account the above data a simple calculation could be performed to extrapolate the light attenuation of only the alamarBlue reduced form (considering also no interference from alamarBlue oxidized form) on a optical distance of 1.6 cm. Considering, $A = \varepsilon_{RED} C_{RED} d$ (Equation 6-1) and that the $C_{RED}= 1.87 \times 10^{-2}$ [mol $L^{-1}$], the absorbance (A) and transmittance (T) are:

For 540 nm,

$A = 104.395$ [L $mol^{-1}$ $cm^{-1}$] x $1.87 \times 10^{-2}$ [mol $L^{-1}$] x 1.6 cm

**A= 3.12**

$T= e^{-3.12} = 0.044$

**%T = 4.4%**

For 570 nm,

$A = 155.677$ [L $mol^{-1}$ $cm^{-1}$] x $1.87 \times 10^{-2}$ [mol $L^{-1}$] x 1.6 cm

**A= 4.65**

$T= e^{-4.65} = 0.01$

**%T = 1.0%**

This preliminary calculation suggest that, for similar experimental acquisition conditions to the described above the alamarBlue reduced form produces a %T of 4.4% and 1.0% using a wavelength of 540 and 570 nm respectively for a optical distance of 1.6 cm, a distance equivalent to the HF Prototype_B available light path length.

Additionally the alamarBlue was also tested for cell fluorescent quantification of 1cm useful length HF encapsulated U2OS-GFP cell culture placed on a 12 well plate. This experiment confirmed that the alamarBlue oxidized and reduced form was able to diffuse in and out of the HF for cell conversion and that it was possible to estimate HF cell number from ~2.0 $x10^4$ to 1.0 $x10^5$ cell/$cm^2$ based on the quantification of the alamarBlue reduced form in the medium using the PolarStar Optima microplate reader. Furthermore, similar results were observed in other works that used alamarBlue to quantify standard tissue culture cells in plate wells, returning a considerable light absorbance value proportional to cell number and/or incubation time (Voytik-Harbin et al. 1998). Also alamarBlue as been used in HF bioreactors cell culture systems (Gloeckner et al. 2001).

Overall, the above results seem to suggest that alamarBlue applied to Prototype_B may indeed produce detectable light attenuation when using the 572 nm LED. Furthermore the addition of a 600 nm LED would be also advantageous to better calculate cell concentrations.

## 6.5 Conclusion

Two simple HF biophotonic proofs of principle devices were developed and tested to address the aim of integrating new light delivery and detection functionality into the HF encapsulation platform. Both prototypes revealed issues and the need for considerable further improvements, but also generated progressive knowledge and "hands on" experience representing a step closer to a truly integrated micro-device.

Prototype_A with a direct optical fiber LED coupled-light excitation to one side of the HF embedded in a gel phantom was designed and tested using the animal macro-imaging system with HF encapsulated 15 µm beads red fluorescent beads. In fluorescent mode this LED side-excitation method proved that it was possible to excite the in-fiber encapsulated beads. Furthermore in a "transmission" mode the LED imaged light profile along HF with the 15 µm beads was completely attenuated in relation to control with no beads, where ~12% of the imaged peak light intensity reached the HF end.

Additionally, Prototype_A proof of principle LED side excitation presented some issues concerning the non-uniformity fluorescence excitation of the beads. Nevertheless, the fluorescent mode could reveal itself valuable for deep tissue imaging, where normally the external light source would be attenuated, particulary for blue-green (450-520) excited fluorophores. Importantly, the "transmission" mode could be advantageous, because it would allow the quantification of particles or cells inside the HF based on the attenuation profile along the HF. This last could be potentially advantageous, first because it would not require any fluorescent probe being label free. Second the transmitted LED light would be higher than any generated fluorescent signal.

The tested transparent phantom represents a best case scenario; in a host animal the percentage of light would be subjected to attenuation and interference by the host tissue (chapter 1.5.4.2). These last interference depend on various factors such as: animal fur colour (the best option are nude or shaved animals), location and deepness of the implant in the animal tissue. A visual comparison of the above transparent phantom model images with typical subcutaneous HF implant in nude animals reveals

medium to low light scatter dispersion, considering previous works with bioluminescence in the IVIS200 system (Zhang et al. 2007; Zhang et al. 2004). But, even in extreme cases with the HF deep in the animal with light interference from tissue, it is reasonable to assume that the measured 1-dimensional light intensity profile at the surface of the animal could be traced back/reconstructed through tomography mathematical models to the HF point of origin. Thus reflecting any differences in the particle or cell content inside the HF lumen.

Prototype_B used optical fibers to conduct light from an LED light source to and from the HF to detector, this to evaluate the light attenuation of HF loaded with fix cells under different LED wavelengths. The described Prototype_B set-up proved to be unviable to be used with the U-2 OS cells without any additional extra labelling (i.e. alamarBlue). The same may be not the case for other cells lines. This set-up would have greater potential with cell lines (suspension or adherent) that fill completely or in great extend the HF lumen volume, thus producing light attenuation mostly due to cell scattering. For example, suspension cultures, such as the SUD-4 (human B cell lymphoma cell line) would actively growth and "fill-up" all the HF lumen, the same for SW620 (Casciari et al. 1994). Also pigmented cells such as melanoma could be good model candidates (Fu et al. 2008). Or even the adherent multi-layer osteosarcoma SaOS-2 (Dass et al. 2006). Furthermore, the addition of an anti-cancer drug, such as Taxol or Colcemid would enhance the light attenuation due to cell scatter increase and could potentially be used to detect drug action. Cell scatter changes, namely side scatter, due to drug action was previously discussed for Taxol in the flow cytometry results analysis (chapter 3.4.1.3) and also evident for Colcemid (Supplementary Information 3.6-4 to Supplementary Information 3.6-6).

Additionally, derived designs from Prototype_B could have potential advantageous applications in HF bioreactors culture systems (chapter 1.3.2). Though, further work will be required to address some practical issues. A hypothetical concept derived from the Prototype_B design with a LED light source and an array of detectors at both ends of the HFs bundle/cartridge could provide valuable measurement, namely of cell mass/density with time. This could be usefully considering that one of the limitation of the HF bioreactors is that the quantification of the biomass inside the bioreactor is difficult (Jain and Kumar 2008). Normally, this is achieved by measuring metabolic

parameters as indicators for cell growth, e.g. consumption of glucose and generation of lactate (Gloeckner et al. 2001). As cell proliferation and viability are crucial factors indicating the success of the cultivation procedure, these parameters should be regularly monitored during cultivation especially in commercially HF bioreactors for the production of highly valuable pharmaceutical biomolecules. Therefore, the integration of a simple cheap and reliable biophotonic component to monitor these parameters in the bioreactor set-up could represent an important contribution for the system operation.

In summary, both the prototypes reveal the potential of an integrated LED light source in the HF. For fluorescence, this would be useful to a direct in-fiber excitation of i.e. QD705 nanoparticles labelled cells with blue or green light bypassing the animal tissue light attenuation effects. Furthermore, a "transmission" mode or the detection of the light attenuation in the HF optical path through macro-imaging or with an optical fiber plugged to a detector, may provide the potential in quantifying increases in HF cell density, providing the HF lumen is completely filled with cell mass.

# CHAPTER 7

# GENERAL DISCUSSION AND FUTURE DIRECTIONS

# 7 GENERAL DISCUSSION AND FUTURE DIRECTIONS ..... 249

# 7 GENERAL DISCUSSION AND FUTURE DIRECTIONS

## 7.1 Highlights and conclusions

### 7.1.1 Insight, innovation and integration

There is an increasing realization that cellular responses to potential therapeutic agents require cells to be situated in a topographic context that can be well-defined and thus enables better discovery of new targets and associated agents (Griffith and Swartz 2006; Hutmacher et al. 2010; Weigelt and Bissell 2008). At the same time the ability to perform comprehensive mechanistic experimental biological studies using progressive 3D cellular models could ultimately help bridge the gap between conventional 2D cell culture methods and *in vivo* animal models (Abbott 2003; Hutmacher 2010; Pampaloni et al. 2007; Yamada and Cukierman 2007). In this thesis a significant advancement is presented in the embedding of biophotonic capability directly in the already established hollow fiber (HF) encapsulation platform, both at the micro and nano-scale level (see outlook schematic Figure 7.1). This biophotonic engineering concepts are still compatible with the HF remit of providing a bounded assay system (Hollingshead et al. 1995a; Wang et al. 2008; Zhang et al. 2008a), but further provides the opportunities for obtaining dynamic cell-based readouts. Pragmatically this offers possibilities for high-through-put drug screening and for the purpose of undertaking an integrative systems biology approach with cytometry based acquisition (Gerstner et al. 2009; Nolan and Yang 2007; Smith et al. 2007a; Smith et al. 2009; Tarnok et al. 2010; Wilson et al. 2006), which will be termed in this thesis more appropriately as "systems cytometry" (as pursued by the Cardiff–Swansea Systems Cytometry group, 2010). The highlight of the current study is that the human osteosarcoma U-2 OS hollow fiber model system (HF–U2OS-GFP) enables the manipulation of cells at biologically relevant scales; as well as the control of a culture environment with incorporated biophotonic assessment of function with cellular resolution (Figure 7.1).

***The thesis presents four specific high-lights (see Figure 7.1):***

• The *in vitro* HF–U2OS-GFP human osteosarcoma cell encapsulated model was comprehensively characterized, at the genomic level and single cell level providing insights on life in the HF. The U-2 OS cells retained an adherent dependent phenotype in the HF, however cell growth rate was attenuated and sensitivity to microtubule disrupting agents altered.

• Adaption to the HF encapsulation environment has led to an altered genetic signature where the cells present a lower differentiation potential associated with higher malignancy.

• Single cell encoding with quantum dots as live cell optical probes has been developed for the remote tracking of cell cycle and proliferative outputs of U-2 OS cells in the HF; hence demonstrating the potential of embedding the biophotonic nanoparticle sensors directly into cells. This provides future opportunities for cell-barcoding and *in vivo* applications.

• Finally, the study leads to a discussion and proposal of a multi-modal "systems cytometry" approach with the use of intracellular embedded nanoparticles to generate experimental data suitable to parameterise and calibrate tumour cells development.

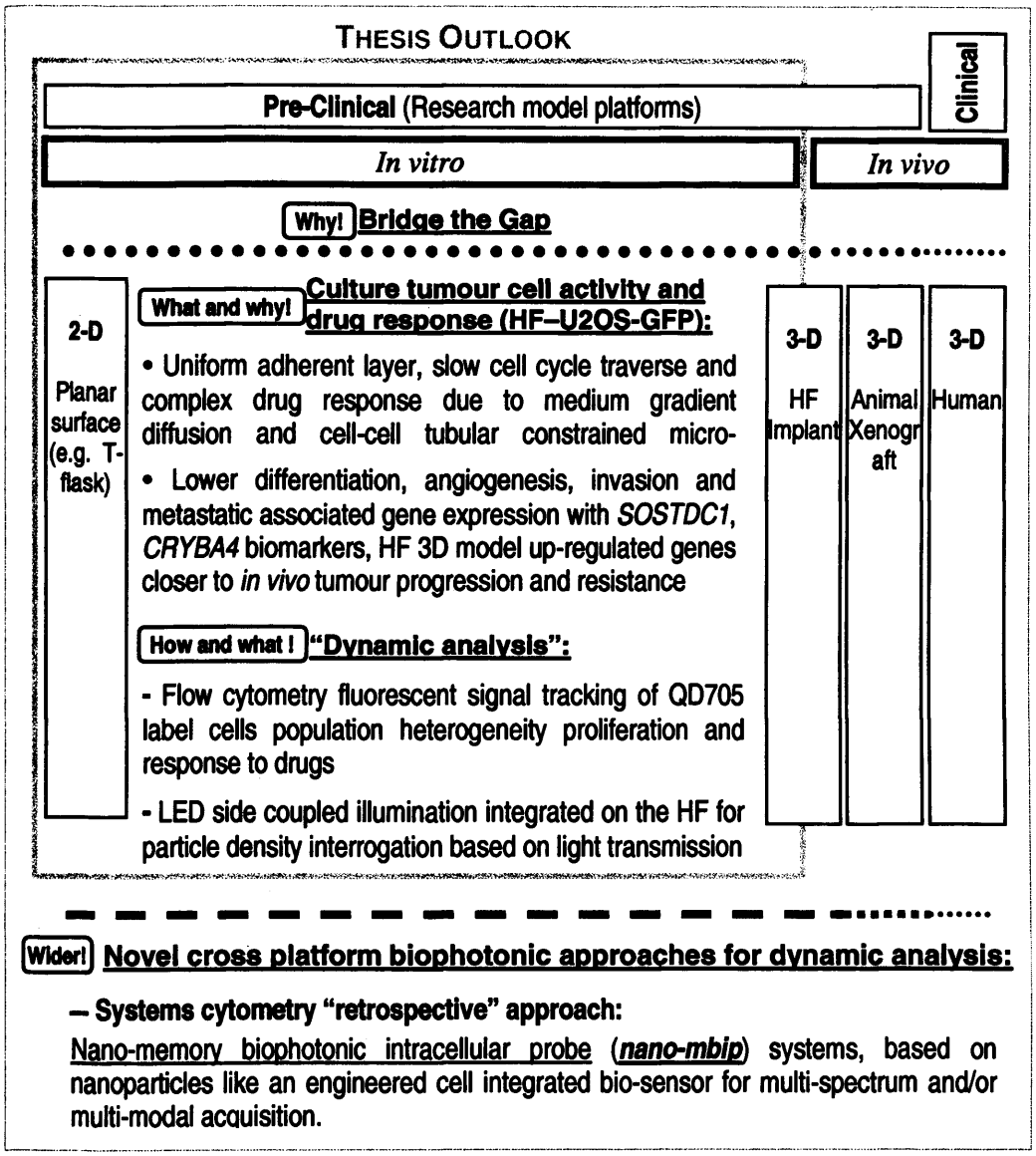


**Figure 7.1** – Outlook schematic to bring together the thesis conclusions and further propose hollow fiber biophotonic future research directions and a new vision for dynamic analysis.

### 7.1.2 U2OS-GFP tumour cell model – HF versus TC culture

***Aim i*** *- To establish and study the in vitro U-2 OS cyclin B1 GFP human osteosarcoma HF encapsulated model (HF–U2OS-GFP) parallel to the standard tissue culture (TC). Characterize and compare both of these model culture systems in relation to tumour cell morphology and biological behaviour, under normal proliferation and drug perturbation conditions, namely the action of Taxol and Colcemid (Chapter 3).*

To meet ***Aim i*** U-2 OS cyclin B1-GFP (U2OS-GFP) human osteosarcoma tumour cells were fully characterized *in vitro* in the HF culture and compared to standard tissue culture; here cell morphology and arrangement was evaluated together with the assessment of proliferative features and drug response. The U2OS-GFP cells grew in the HF encapsulation forming a uniformly distributed adherent layer to the tubular inner wall. The cells retained an anchorage dependent monolayer morphology on the wall of the HF (Dass et al. 2006) and did not progress to higher level multi-layer or aggregate organization. The U2OS-GFP cells showed exponential growth and cell cycle traverse that was slower compared to standard tissue culture, but still sustained a proliferative profile up to 27 days after seeding into the HF.

The cyclin B1-GFP reporter performance was assessed and showed to continue to provide cell cycle status in the HF model both at short and long term *in vitro* culture on normal and under drug treatment conditions. The HF culture promoted complex drug response to a clinical relevant dose of Taxol, confirmed by stathmokinetic Colcemid studies; this included a higher cell death rate and aneuploidy accumulation, where cells exit mitosis by division and later become apoptotic or survive further cycles. This was similar to previous reports for U-2 OS (Brito and Rieder 2009), but cell death was less evident in the low density standard TC results, where most of the cells appear to exit mitosis without undergoing division to a >4n polyploidy state.

Several factors may contribute to differences in U-2 OS culture behaviour in HF compared to TC: i) the initial restricted cell seeding post-loading in the HF; ii) A HF PVDF porous surface for cell attachment; iii) A gradient through the semi-permeable wall and the generated overall encapsulation niche. This supports the importance of taking into consideration the detailed arrangement of cell-cell and cell-surface interactions and access of agents in the HF. A further level of complexity is that characterized by active reciprocal communications between the tumours cells and host

normal cells in the adjacent tissue environment (Bissell and Radisky 2001; Debnath and Brugge 2005; Griffith and Swartz 2006), which can be addressed once the HF are placed *in vivo*.

***Aim ii*** *- To perform gene expression profiling of the HF versus standard TC culture, interconnected with a "systems biology level" bioinformatics analysis, to ultimately evaluate the HF culture environment effect on the U-2 OS cells (Chapter 4).*

To meet ***Aim ii*** a microarray gene expression study of the HF versus TC culture was undertaken including a comprehensive bioinformatics gene differential, enrichment and network analysis that provided access and greatly enhanced the biological interpretation of the gene expression data. Overall the profiling of U2OS-GFP cells cultured *in vitro* in the HF platform, compared to standard tissue culture, presented features closely associated with a lower differentiated phenotype, metastatic, invasion, angiogenesis and proliferation. This could correlate with the multiple factors/constraints in the HF tubular encapsulation environment, namely: limited space, close cell-cell proximity and the effect of a PVDF porous membrane and hydrophobic substrate. Biomarkers, which appear to be unique to the HF culture, were indentified, such as *SOSTDC1* and *CRYBA4*. Further, in general in the HF culture genes associated with cell motility and the cytoskeleton were clearly down-regulated, while presenting enhanced number of up-regulated *"sterol biosynthetic process"* associated genes. Kinases and steroid/hormones have been shown to be correlated with tumour progression, resistance and poor prognosis for patient survival (Planque 2006). Additionally, specific studies confirmed that steroid hormones and receptors expression play an important role in bone remodelling and control of U-2 OS cell proliferation (Monroe et al. 2005; Salvatori et al. 2009; Stossi et al. 2004), other osteosarcoma cell lines and interestingly in human osteosarcoma clinical tumours (Dohi et al. 2008; Svoboda et al. 2010).

In conclusion, it is clear that there is a consequence of encapsulation which alters the biological status of the U-2 OS cells. The proposal suggested by the thesis results is that these changes brings the U-2 OS cell model closer to an "*in vivo* respresentation", similar to that observed with other developed models (Birgersdotter et al. 2005; Feder-Mengus et al. 2008; Weigelt and Bissell 2008; Yamada and Cukierman 2007); hence making the HF model highly attractive for cancer research. However at the same time

the HF 3D architecture presents challenges in the interrogation and linking of the pre-clinical culture platforms. This provides a further rationale for developing HF biophotonic cell assays that are suitable for or transferable between both *in vitro* and *in vivo* manipulation (Figure 7.1), following a trend of other cellular models (Hutmacher et al. 2010; Moreau et al. 2007; Pampaloni et al. 2007), and enabling the design of cross platform mechanistic experiments.

### 7.1.3 Systems cytometry - flow approach

***Aim iii*** *- To explore and validate a cross platform flow cytometry approach, tracking the consequences of introducing a nanoparticle presenting a conserved fluorescent signal, into a proliferative system. Thus providing quantitative generational information about the cell population in both the standard TC and the HF culture (Chapter 5).*

To meet ***Aim iii*** a systems cytometry approach was applied using flow cytometry time series analysis. The limitations of this approach are that all HF spatial information is lost however the benefits mean that that a large number of cells were analysed accounting for cell heterogeneity and providing good statistically meaningful distributions over time. Importantly HF allowed for sufficient cell numbers early after seeding into the fiber lumen and QD nanoparticle labelled cell manipulation maintaining viability. The tracking of labelled QD705 cells located in the endosomal compartment and subsequently partitioning between daughter cells upon cell division has proved to be a powerful tool. Providing a division history from generation to generation and with the potential to model cell cycle and derived lineage parameters, with vast analytical advantages (Khan et al. 2007). Importantly this approach might identify and segment different sub-population behaviour such as quiescent or drug resistant fractions. Other factors demonstrate the current limitations of the study: i) the loss of cells from the assay as they became non-reporting thus restricting the effective assay dynamic range; ii) drug treatments promoted auto-fluorescence thus effecting background signal and iii) the QD signal collapse due to damaged or dead cells.

The immediate next stage is to incorporate the above added complexity in to the already established computer-based simulation model already applied to simulate 2D tumour cells (Errington et al. 2010; Rees et al. 2010), accounting for changes in background fluorescence. The objective would be to derive global cell cycle parameters and partitioning indices from the QD fluorescence distribution profiles

from the HF culture platform. These would provide insights in the lineage features and patterns and the consequences of encapsulation.

In conclusion, this section of the thesis intends to represent a biophotonic principle where the *sensor* component (i.e. nanoparticle) is directly embedded into the tumour population. Since by its very nature the nanoparticle signal is both conserved and quantal in the bounded HF (and not contaminated from other cells) this approach is highly transferable between an *in vitro* and *in vivo* context and truly cross platform. The next phase in this application therefore is to implement an HF *in vivo* animal implant study (see outlook schematic Figure 7.1) where the requirement for bridging the pre-clinical assay systems would be met. Furthermore, the idea would be to understand the QD internalization, associated endosomal trafficking and asymmetrical partition cell biological mechanisms to further deliver and target engineered nanoparticles to different cellular compartments or even specific pathways (Delehanty et al. 2010; Delehanty et al. 2009).

### 7.1.4 Systems cytometry - imaging approach

The QD flow cytometry tracking has provided clear advantages in single cell high-throughput analysis by retrospective decoding of biological features comparing the fluorescent population distributions at a given time with the initial QD post-label profiles. But this technique presents limitations intrinsic to any flow cytometry assay. In short it isn't a "true" dynamic assay where the same population or cell is followed over time but a time series represented by cross-sectional analysis. In other words, the disaggregation of the tissue results in the loss of spatial information ruling out repetitive measurements of the same sample with time. The solution to overcome this limitation consists of incorporating an imaging approach to add real-time spatial/temporal information to the above QD cell tracking technique and thus supply multi-modal data for the computer model analysis.

Both the cyclin B1-GFP protein reporter [(Silvestre et al. 2009) (for print-out see Appendix I-A)] and QD705 fluorescence signal (chapter 5.5) was difficult to detect inside the HF due to wall auto-fluorescence and opacity. A preliminary optical coherence tomography (OCT) study was undertaken in collaboration with Christoph

Kasseck (Ruhr-Universität Bochum, German). The results revealed virtually no apparent detectable difference between an empty HF control versus a HF cultured *in vitro* for 17 days. The future for using OCT for single cell tracking in the HF could be possible through the use of contrast agents such as PEG coated gold nanoshells, (Agrawal et al. 2006; Kah et al. 2009; Leung 2008; Loo et al. 2004) providing the nanoparticle features currently exploited with QDs.

Overall there is a need for a biocompatible equivalent of the present HF implant platform in all aspects except with better optical properties and including a porous membrane (related to (Yamazoe and Iwata 2006) fibers) and perhaps engineered to offer light waveguide performance (Pone et al. 2006). This would be ideal to enhance optical imaging capability inside the HF, but this option presents drawbacks. There would be a requirement for optimization, and a need for establishing and licensing a new implant platform for animal applications. Although a transparent HF would alleviate some of the issues and improve the optical imaging for the HF *in vitro* culture, the general issues (e.g. signal to noise signal, absorbance scattering and auto-fluorescent interferences) for the interrogation of 3D systems or live animal deep-tissue would remain (Pampaloni et al. 2007). Therefore in this thesis a direction was proposed where the current PVDF HF was retained and biophotonic components were directly placed or integrated in the HF. The objective was to enhance signal/noise output and overcome the limitations of deep-tissue imaging.

### 7.1.5 Integration of biophotonic components in the HF

*Aim_iv - To develop and assess the design of a hollow fiber format with embedded illumination for detecting particle and/or cell density (Chapter 6).*

To meet *Aim_iv* two prototype systems were designed, built and evaluated as a proof-of-concept. Prototype_A consisted of an optical fiber LED coupled-light excitation to one end of the HF loaded with 15 μm red fluorescent beads imaged using an animal macro-imaging system (IVIS200). The LED light along the HF length was attenuated by the beads and it was possible to retrieve a fluorescent signal from the beads in the immediate proximity of the HF coupled light source zone. Prototype_B incorporated optical fibers to input light from a LED light source and then from the HF to the detector. This configuration was used to evaluate the light attenuation of HF loaded

with fixed cells under different wavelengths. However, it became clear that this format is not tenable to monitor U-2 OS HF cultures as the cells growth like a attached monolayer to the fiber wall leaving a HF lumen empty, thus not providing sufficient light attenuation.

In conclusion, further development of these prototypes for the U-2 OS would be suitable only for *in vitro* cultures with the use of additional contrast agents a problem similarly encountered by the OCT approach, the suggestion would be a probe such as. alamarBlue. However other sarcoma models could be more compatible with Prototype B as the tumour mass might fill the HF lumen (e.g. SaOS-2) (Dass et al. 2006).

## 7.2 Future directions and proposed concepts

Future direction of the studies emerge that are inspired from the thesis and the requirement for a systems approach that enables assay transferability from 2D to 3D culture platforms and *in vitro* to *in vivo*.

### 7.2.1 Nano-memory biophotonic intracellular probe (*nano-mbip*) systems concepts

This section deals with the conceptual expansion of systems cytometry approaches, the proposal is to explore the potential of nanoparticle intracellular biophotonic *sensors* to report the cellular system's inherent complexity and underlying functional relationships. The paradigm shift here would be in engineering terms not to only consider the nanoparticles as a classic incorporated bio-*sensor* but as the *interpreter* component encoding a retrospective or "memory" on single cell history. The rational for the proposed *nano-memory biophotonic intracellular probe* (*nano-mbip*) approach would be based on multi-spectrum and/or multi-modal acquisition.

Recent studies have incorporated silica chip on cells (Fernandez-Rosas et al. 2010; Gomez-Martinez et al. 2010). This line of work is still progressing, the "chunks of silica" are probably far too big to be incorporated in all intracellular environments, plus the main challenge is to make these chips functional and capable of retrieving any biological information; the potential is infinite, considering the ongoing quest in silicon photonics computing (Krishnamoorthy et al. 2009; Leuthold et al. 2010).

This section proposes a starting point for a more simple *nano-mbip* systems approach. The previous QD flow cytometry tracking (Chapter 5) represents an extremely simple example of how by analysing the "mono-channel" QD705 compartments signal partition is possible to retrospectively infer about the history of several biological features (i.e. cell proliferation heterogeneity). This concept could be considered as encoding with a "memory capacity" to output chronological data about previous biological events "stored" in the QD labelled cell system. The way forward is to explore this more comprehensively for the nanoparticle-cell system dynamics and applying innovative *interpreter* analysis (e.g. mathematical algorithms). Furthermore nanoparticle high-content multi-channel/spectra data acquisition would potentially expand this concept to high levels.

#### 7.2.1.1 Proposed systems cytometry: *nano-mbip* concept 1

The QD705 when added to biological media revealed an un-expected far more complex biophotonic response with time when analysed in detail (Holton et al. 2009) (for print-out see Appendix I-E) the life-time florescence altered over time post QD-labelling, providing a suggestion of a nanoparticle that could act as a sensor. In other words apparently the bioprocessing of the nanoparticles in the endosome pathway changed the fluorescent lifetime properties, indicating that the environment or length spent in this environment influences this property of the QD. This was further expanded using a simple approach of QD photo-activation and spectral acquisition (Figure 7.2). The preliminary results show that there is a correspondence between the exposure time of QD705 with biological media and their photo-activation profile (Figure 7.2-b) and they also become blue emission shifted (Figure 7.2-c). Importantly this demonstrated that by using the same colour and type of QD it is possible to estimate "the time" of particulate delivery and uptake into each individual cell of the QD compartments. Although is unclear at this point the exact mechanisms it is probably due to oxidation and the accumulation of surface imperfections at the surface (Lee and Osborne 2009; Mancini et al. 2008; Zhang et al. 2006a). The photo-activation or spectra "optical patterns" could provide a tag that reflects and accumulated "memory output" (i.e. exposure of QD to the biological system).

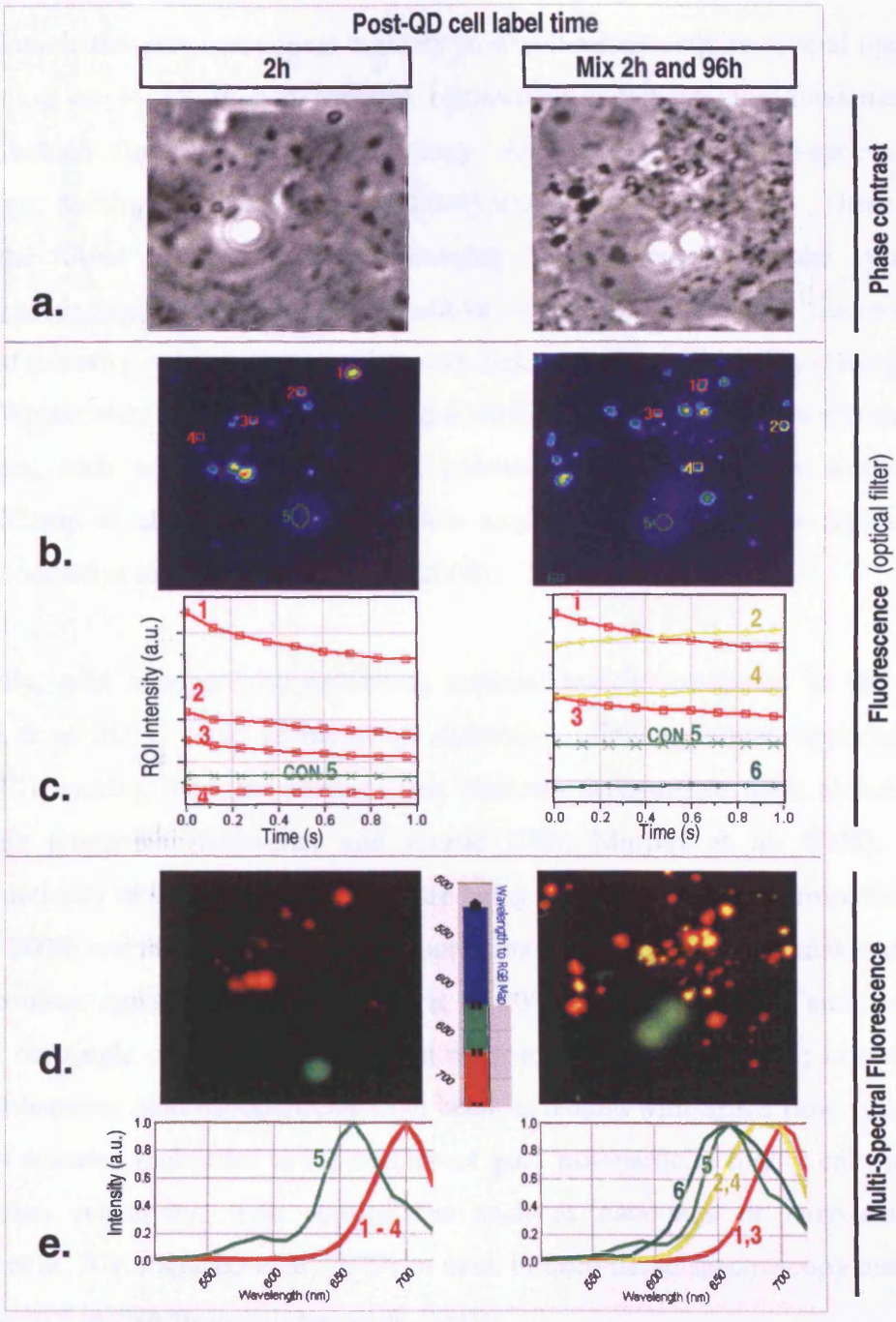


**Figure 7.2 –Typical photo-activation and spectral shift of QD705 on live U-2 OS cells.** High density standard tissue cultured (coverglass chambers) with live cells labelled with QD705, for all cell samples QD705 cell contact for 1.5h followed by the QD wash and removal. Post-QD label sets (columns): Total time after the first adding of QD705 to the cells: 2h and mix of 2h + 96h. Acquisition type and selected ROI graph (rows): (**a**) phase-contrast image. (**b**) Epi-fluorescent image (intensity pseudo-colours) and (**c**) corresponding photo-activation profile of selected regions of interest (ROI) average intensity with time (0-1s). (**d**) spectral image (note: modified RGB wavelength to enhance visualization – see legend key), (**e**) corresponding normalized spectra of selected ROI. Acquired using the Axiovert microscope (chapter 2.6.3) with 20x 0.6NA lens on normal epi-fluorescence and spectral mode. Note: multiple acquisition of the same field was performed during an interval of 4-5 min (Focus–Ph2–2minRest–Spectra(2s)-2minRest–Photo-activation(1s)) so cell QD compartment movements occurred. **(CON 5)** Control reference control 6µm red beads em.633/ex.660. Fields size 52x52µm.

The biophotonic *detector* component capacity to simultaneous acquire several optical channels (i.e. up to 18 in conventional cytometers) represents the fundamental principle behind flow cytometry technology. Also the recent multi-spectra or spectroscopic developments (Wilson et al. 2006) remain largely untapped. These last include; the fusion between flow and imaging (i.e. Amnis commercial system, http://www.amnis.com/ [2010]), providing cellular image resolution with fluorescent spectra and intensity interrogation together with high-throughput versatility (George et al. 2006; Wojakowski et al. 2009). Other signal modes include Raman flow cytometry technologies, such as label-free multiplex *coherent anti-Stokes Raman scattering* (CARS) (Camp et al. 2009) or nanoparticle *surface-enhanced Raman scattering* (SERS) (Goddard et al. 2010; Watson et al. 2008).

Additionally, gold nanoparticles exhibiting minimal toxicity compared to the QD (Lewinski et al. 2008) could represent an alternative, allowing human applications (Shan 2010), making them the perfect cross platform nanoparticle, with associated biophotonic properties (Boisselier and Astruc 2009; Murphy et al. 2008). For example, optically tunable gold nanoshells are being tested for tumour thermoablation (Lal et al. 2008) and though they are non-fluorescent their high scattering makes them an ideal contrast agent for OCT (Agrawal et al. 2006; Kah et al. 2009), and can be tracked at the single cell level by dark field microscopy (Jain et al. 2006; Loo et al. 2005). Furthermore gold nanoparticles have been exploited with SERS flow systems to identify encoded molecules at the surface of gold nanoparticles highly enhancing the detection sensitivity, with applications such as nano-tags or nano-sensors (Goddard et al. 2010; Kneipp et al. 2010) or even in deep-tissue spectroscopy tumour interrogation of *in vivo* animals (Qian et al. 2008).

In summary, all the above would represent the basis for a proposed *nano-memory biophotonic intracellular probe* (*nano-mbip*) compatible with high-throughput detection technologies. The "memory capacity" in these probes would be imprinted (or self-assembled) on the nanoparticle(s) with different "optical patterns". This would be created chronological depending on the cell intracellular environment or other parameters (Torchilin 2009). This can be conceived similarly to the work of (Jamshidi et al. 2009; Liu and Tang 2010) where the nanoparticles would represent the structure where by a "permanent pattern" would be created with time. The biophotonic *detector*

mentioned above and more importantly the *interpretor* component would be amenable to developing predictive mathematical models linking cellular level and molecular level information.

#### 7.2.1.2 Proposed image systems cytometry: *nano-mbip* concept 2 – multi-modal imaging with *mbip* nanoparticles

The above proposed *nano-mbip* so far still has the disadvantage that cell position or organization is lost with tissue disaggregation for flow cytometry analysis. However the advances in OCT acquisition together with other techniques, namely magnetic resonance imaging (MRI), together with nanoparticle probes that may allow a multi-modal imaging approach (Kim et al. 2009; Li et al. 2010), predict a future where biologists could incorporate image analysis of tumours. Single nanoparticles can be tracked using real-time MRI, recent studies point its potential use in live tissues with engineered nanoparticles, specifically QD-iron oxide+silica (Koole et al. 2009) and gold nanoshell-iron oxide-NIR fluorophore (Bardhan et al. 2009). This potentially would allow the detection of nanoparticles/cells in deep-tissue, and to identify and locate different encoded sub-groups and finally enable a traditional dynamic time point acquisition, where the "memory" nanoparticle component would conceptually in the future be capable of filling the gap between the different data time points. This by itself is pertinent for *in vivo* dynamic imaging, but would also be invaluable together with optical imaging to strength the *nano-mbip* analytical approach.

In conclusion, the presented systems cytometry embedded biophotonic engineering concepts would provide a step change to current systems biology approaches. Meeting the data acquisition needs of a "middle-out" approach where the single cell acts as the minimal interrogation unit (Brenner et al. 2001) but has connectivity to higher (e.g. "HF tumour") and lower levels (e.g. molecular) of structural and functional integration. This would potentially be achieved with the high resolution features of the system being monitored at the single cell level using *nano-mbip* sensors based nanotechnology (Kim et al. 2009; Lee et al. 2009). The integrated multi-modal biophotonic approach would ultimately bridge the gap between pre-clinical research platforms, enabling simultaneous kinetic monitoring of a tumour system *in vitro* and possibly *in vivo.*

# REFERENCES:

# REFERENCES:

Abbott, A. 2003. Cell culture: Biology's new dimension. *Nature* 424(6951), pp. 870-872.

Affolter, M. et al. 2003. Tube or not tube: Remodeling epithelial tissues by branching morphogenesis. *Developmental Cell* 4(1), pp. 11-18.

Affolter, M. et al. 2009. Tissue remodelling through branching morphogenesis. *Nature Reviews Molecular Cell Biology* 10(12), pp. 831-842.

Agrawal, A. et al. 2006. Quantitative evaluation of optical coherence tomography signal enhancement with gold nanoshells. *Journal of Biomedical Optics* 11(4), p. 8.

Aherne, W. A. and Challoner, D. 1983. A REAPPRAISAL OF THE STATHMOKINETIC TECHNIQUE .2. METAPHASE DEGENERATION AND ITS CORRECTION. *Virchows Archiv B-Cell Pathology Including Molecular Pathology* 42(1), pp. 111-118.

alamarBlue_manual. 2008. *alamarBlue user manual* [Online]. Invitrogen. Available at: http://tools.invitrogen.com/content/sfs/manuals/PI-DAL1025-1100_TI%20alamarBlue%20Rev%201.1.pdf [Accessed: 2010].

Alivisatos, A. P. 1996. Semiconductor clusters, nanocrystals, and quantum dots. *Science* 271(5251), pp. 933-937.

Alley, M. C. et al. 1991. MORPHOMETRIC AND COLORIMETRIC ANALYSES OF HUMAN TUMOR-CELL LINE GROWTH AND DRUG SENSITIVITY IN SOFT AGAR CULTURE. *Cancer Research* 51(4), pp. 1247-1256.

Alley, M. C. et al. 1988. FEASIBILITY OF DRUG SCREENING WITH PANELS OF HUMAN-TUMOR CELL-LINES USING A MICROCULTURE TETRAZOLIUM ASSAY. *Cancer Research* 48(3), pp. 589-601.

Allison, D. B. et al. 2006. Microarray data analysis: from disarray to consolidation and consensus. *Nature Reviews Genetics* 7(1), pp. 55-65.

Allman, R. et al. 2003. Delayed expression of apoptosis in human lymphoma cells undergoing low-dose taxol-induced mitotic stress. *British Journal of Cancer* 88(10), pp. 1649-1658.

Anderson, H. C. et al. 2002. Selective synthesis of bone morphogenetic, proteins-1,-3,-4 and bone sialoprotein may be important for osteoinduction by Saos-2 cells. *Journal of Bone and Mineral Metabolism* 20(2), pp. 73-82.

Andley, U. P. 2007. Crystallins in the eye: Function and pathology. *Progress in Retinal and Eye Research* 26(1), pp. 78-98.

Arnal, I. and Wade, R. H. 1995. HOW DOES TAXOL STABILIZE MICROTUBULES. *Current Biology* 5(8), pp. 900-908.

Ashburner, M. et al. 2000. Gene Ontology: tool for the unification of biology. *Nature Genetics* 25(1), pp. 25-29.

ATCC_HTB-96. 2010. *U-2 OS human osteosarcoma cell line* [Online]. American Type Culture Collection Available at: http://www.atcc.org/ATCCAdvancedCatalogSearch/ProductDetails/tabid/452/Default.aspx?ATCCNum=HTB-96&Template=cellBiology [Accessed: 2010].

Atchariyawut, S. et al. 2006. Effect of membrane structure on mass-transfer in the membrane gas-liquid contacting process using microporous PVDF hollow fibers. *Journal of Membrane Science* 285(1-2), pp. 272-281.

Ateya, D. A. et al. 2008. The good, the bad, and the tiny: a review of microflow cytometry. *Analytical and Bioanalytical Chemistry* 391(5), pp. 1485-1498.

Atkins, G. J. et al. 2007. Metabolism of vitamin D-3 in human osteoblasts: Evidence for autocrine and paracrine activities of 1 alpha,25-dihydroxyvitamin D-3. *Bone* 40(6), pp. 1517-1528.

Baba, I. et al. 2000. Involvement of deregulated epiregulin expression in tumorigenesis in vivo through activated Ki-Ras signaling pathway in human colon cancer cells. *Cancer Research* 60(24), pp. 6886-6889.

Bakhshi, S. and Radhakrishnan, V. 2010. Prognostic markers in osteosarcoma. *Expert Review of Anticancer Therapy* 10(2), pp. 271-287.

Baldi, P. and Long, A. D. 2001. A Bayesian framework for the analysis of microarray expression data: regularized t-test and statistical inferences of gene changes. *Bioinformatics* 17(6), pp. 509-519.

Ballou, B. et al. 2005. Fluorescence imaging of tumors in vivo. *Current Medicinal Chemistry* 12(7), pp. 795-805.

Balslev, S. et al. 2006. Lab-on-a-chip with integrated optical transducers. *Lab on a Chip* 6(2), pp. 213-217.

Bardhan, R. et al. 2009. Nanoshells with Targeted Simultaneous Enhancement of Magnetic and Optical Imaging and Photothermal Therapeutic Response. *Advanced Functional Materials* 19(24), pp. 3901-3909.

Barnard, G. A. and Bayes, T. 1958. Studies in the History of Probability and Statistics: IX. Thomas Bayes's Essay Towards Solving a Problem in the Doctrine of Chances. *Biometrika* 45(3/4), pp. 293-315.

Bayes, M. and Price, M. 1763. An Essay towards Solving a Problem in the Doctrine of Chances. By the Late Rev. Mr. Bayes, F. R. S. Communicated by Mr. Price, in a Letter to John Canton, A. M. F. R. S. *Philosophical Transactions* 53, pp. 370-418.

BD-Matrigel™InvasionChamber. 2010. *BD BioCoat™ Matrigel™ Invasion Chambers* [Online]. Available at: http://www.bdbiosciences.ca/discovery_labware/products/display_product.php?keyID=202 [Accessed: 2010].

Benjamini, Y. and Hochberg, Y. 1995. CONTROLLING THE FALSE DISCOVERY RATE - A PRACTICAL AND POWERFUL APPROACH TO MULTIPLE TESTING. *Journal of the Royal Statistical Society Series B-Methodological* 57(1), pp. 289-300.

Bernhard, D. et al. 2003. Enhanced MTT-reducing activity under growth inhibition by resveratrol in CEM-C7H2 lymphocytic leukemia cells. *Cancer Letters* 195(2), pp. 193-199.

Berridge, M. V. and Tan, A. S. 1993. CHARACTERIZATION OF THE CELLULAR REDUCTION OF 3-(4,5-DIMETHYLTHIAZOL-2-YL)-2,5-DIPHENYLTETRAZOLIUM BROMIDE (MTT) - SUBCELLULAR-LOCALIZATION, SUBSTRATE DEPENDENCE, AND INVOLVEMENT OF MITOCHONDRIAL ELECTRON-TRANSPORT IN MTT REDUCTION. *Archives of Biochemistry and Biophysics* 303(2), pp. 474-482.

Bhuyan, B. K. and Groppi, V. E. 1989. CELL-CYCLE SPECIFIC INHIBITORS. *Pharmacology & Therapeutics* 42(3), pp. 307-348.

Biju, V. et al. 2010. Bioconjugated quantum dots for cancer research: Present status, prospects and remaining issues. *Biotechnology Advances* 28(2), pp. 199-213.

Bindea, G. et al. 2009. ClueGO: a Cytoscape plug-in to decipher functionally grouped gene ontology and pathway annotation networks. *Bioinformatics* 25(8), pp. 1091-1093.

Birgersdotter, A. et al. 2005. Gene expression perturbation in vitro - A growing case for three-dimensional (3D) culture systems. *Seminars in Cancer Biology* 15(5), pp. 405-412.

Bishai, W. R. and Karakousis, P. C. 2006. Hollow fiber technique for in vivo study of cell populations.

Bissell, M. J. and Radisky, D. 2001. Putting tumours in context. *Nature Reviews Cancer* 1(1), pp. 46-54.

Blish, K. R. et al. 2008. A human bone morphogenetic protein antagonist is down-regulated in renal cancer. *Molecular Biology of the Cell* 19(2), pp. 457-464.

Bohmer, R. M. 1982. FLOW-CYTOMETRY AND CELL-PROLIFERATION KINETICS. *Progress in Histochemistry and Cytochemistry* 14(4), pp. 1-65.

Boisselier, E. and Astruc, D. 2009. Gold nanoparticles in nanomedicine: preparations, imaging, diagnostics, therapies and toxicity. *Chemical Society Reviews* 38(6), pp. 1759-1782.

Boukhechba, F. et al. 2009. Human Primary Osteocyte Differentiation in a 3D Culture System. *Journal of Bone and Mineral Research* 24(11), pp. 1927-1935.

Boustany, N. N. et al. 2010. Microscopic Imaging and Spectroscopy with Scattered Light.*Annual Review of Biomedical Engineering, Vol 12*. Vol. 12. Palo Alto: Annual Reviews, pp. 285-314.

Boyden, S. 1962. CHEMOTACTIC EFFECT OF MIXTURES OF ANTIBODY AND ANTIGEN ON POLYMORPHONUCLEAR LEUCOCYTES. *Journal of Experimental Medicine* 115(3), pp. 453-&.

Brayfield, C. A. et al. 2008. Excimer laser channel creation in polyethersulfone hollow fibers for compartmentalized in vitro neuronal cell culture scaffolds. *Acta Biomaterialia* 4(2), pp. 244-255.

Breitling, R. 2006. Biological microarray interpretation: The rules of engagement. *Biochimica Et Biophysica Acta-Gene Structure and Expression* 1759(7), pp. 319-327.

Brenner, S. et al. 2001. Complexity in Biological Information Processing. In: Bock, G. and Goode, J. eds. *Novartis Foundation Symposium: Complexity in Biological Information Processing* Vol. 239. Chichester: John Wiley & Sons, Ltd, pp. 150-159.

Bridges, E. M. et al. 2006. The hollow fiber assay for drug responsiveness in the Ewing's sarcoma family of tumors. *The Journal of Pediatrics* 149(1), pp. 103-111.

Brito, D. A. and Rieder, C. L. 2009. The Ability to Survive Mitosis in the Presence of Microtubule Poisons Differs Significantly Between Human Nontransformed (RPE-1) and Cancer (U2OS, HeLa) Cells. *Cell Motility and the Cytoskeleton* 66(8), pp. 437-447.

Brown, J. Q. et al. 2009. Advances in quantitative UV-visible spectroscopy for clinical and pre-clinical application in cancer. *Current Opinion in Biotechnology* 20(1), pp. 119-131.

Brown, M. R. et al. eds. 2007. *Computational simulation of optical tracking of cell populations using quantum dot fluorophores.* International Conference on Computational Methods in Systems Biology. Edinburgh, SCOTLAND, Sep 20-21. Springer-Verlag Berlin.

Brown, M. R. et al. 2010a. Long-term time series analysis of quantum dot encoded cells by deconvolution of the autofluorescence signal. *Cytometry Part A*, p. [Epub ahead of print].

Brown, M. R. et al. 2010b. Flow-Based Cytometric Analysis of Cell Cycle via Simulated Cell Populations. *Plos Computational Biology* 6(4), p. 10.

Brown, S. C. et al. 2010c. Nanoparticle Characterization for Cancer Nanotechnology and Other Biological Applications. Vol. 624. pp. 39-65.

Bruchez, M. et al. 1998. Semiconductor nanocrystals as fluorescent biological labels. *Science* 281(5385), pp. 2013-2016.

Bullen, A. 2008. Microscopic imaging techniques for drug discovery. *Nature Reviews Drug Discovery* 7(1), pp. 54-67.

Buono, C. et al. 2009. Fluorescent pegylated nanoparticles demonstrate fluid-phase pinocytosis by macrophages in mouse atherosclerotic lesions. *Journal of Clinical Investigation* 119(5), pp. 1373-1381.

Burdett, E. et al. 2010. Engineering Tumors: A Tissue Engineering Perspective in Cancer Biology. *Tissue Engineering Part B-Reviews* 16(3), pp. 351-359.

Burton, D. G. A. et al. 2009. Microarray analysis of senescent vascular smooth muscle cells: A link to atherosclerosis and vascular calcification. *Experimental Gerontology* 44(10), pp. 659-665.

Butcher, D. T. et al. 2009. A tense situation: forcing tumour progression. *Nature Reviews Cancer* 9(2), pp. 108-122.

Camp, C. H. et al. 2009. Multiplex coherent anti-Stokes Raman scattering (MCARS) for chemically sensitive, label-free flow cytometry. *Optics Express* 17(25), pp. 22879-22889.

Campbell, S. J. et al. 2010. Visualizing the drug target landscape. *Drug Discovery Today* 15(1-2), pp. 3-15.

Carmeliet, P. et al. 2009. Branching morphogenesis and antiangiogenesis candidates: tip cells lead the way. *Nature Reviews Clinical Oncology* 6(6), pp. 315-326.

Casciari, J. J. et al. 1994. Growth and Chemotherapeutic Response of Cells in a Hollow-Fiber in-Vitro Solid Tumor-Model. *Journal of the National Cancer Institute* 86(24), pp. 1846-1852.

CellMax_Spectrum_Labs. 2009. *CellMax® Implant Membrane - Spectrum Product Instruction Manual* [Online]. Spectrum Laboratories, Inc. Available at: http://eu.spectrapor.com/lit/CellmaxImplantInstr.pdf [Accessed: 2010].

Chalfie, M. et al. 1994. GREEN FLUORESCENT PROTEIN AS A MARKER FOR GENE-EXPRESSION. *Science* 263(5148), pp. 802-805.

Chan, W. C. W. et al. 2002. Luminescent quantum dots for multiplexed biological detection and imaging. *Current Opinion in Biotechnology* 13(1), pp. 40-46.

Chan, W. C. W. and Nie, S. M. 1998. Quantum dot bioconjugates for ultrasensitive nonisotopic detection. *Science* 281(5385), pp. 2016-2018.

Chang, S. et al. 2003. Adsorption of the endocrine-active compound estrone on microfiltration hollow fiber membranes. *Environmental Science & Technology* 37(14), pp. 3158-3163.

Chappell, M. J. et al. 2008. A coupled drug kinetics-cell cycle model to analyse the response of human cells to intervention by topotecan. *Computer Methods and Programs in Biomedicine* 89(2), pp. 169-178.

Chattopadhyay, P. K. et al. 2006. Quantum dot semiconductor nanocrystals for immunophenotyping by polychromatic flow cytometry. *Nature Medicine* 12(8), pp. 972-977.

Chen, C. N. et al. 2003. Effects of three-dimensional culturing on osteosarcoma cells grown in a fibrous matrix: Analyses of cell morphology, cell cycle, and apoptosis. *Biotechnology Progress* 19(5), pp. 1574-1582.

Chen, G. and Palmer, A. F. 2009. Hemoglobin-Based Oxygen Carrier and Convection Enhanced Oxygen Transport in a Hollow Fiber Bioreactor. *Biotechnology and Bioengineering* 102(6), pp. 1603-1612.

Chen, J. G. and Horwitz, S. B. 2002. Differential mitotic responses to microtubule-stabilizing and -destabilizing drugs. *Cancer Research* 62(7), pp. 1935-1938.

Cheng, G. et al. 2009. Micro-Environmental Mechanical Stress Controls Tumor Spheroid Size and Morphology by Suppressing Proliferation and Inducing Apoptosis in Cancer Cells. *PLoS One* 4(2), p. 11.

Cheong, W. F. et al. 1990. A REVIEW OF THE OPTICAL-PROPERTIES OF BIOLOGICAL TISSUES. *Ieee Journal of Quantum Electronics* 26(12), pp. 2166-2185.

Chesler, E. J. and Baker, E. J. 2010. The importance of open-source integrative genomics to drug discovery. *Current Opinion in Drug Discovery & Development* 13(3), pp. 310-316.

Chiu, W. L. et al. 1996. Engineered GFP as a vital reporter in plants. *Current Biology* 6(3), pp. 325-330.

Chong, E. Z. et al. 2007. Development of FRET-Based assays in the Far-Red using CdTe quantum dots. *Journal of Biomedicine and Biotechnology*, p. 7.

Choy, G. et al. 2003. Comparison of noninvasive fluorescent and bioluminescent small animal optical imaging. *Biotechniques* 35(5), pp. 1022-+.

Cleton-Jansen, A. M. et al. 2009. Profiling of high-grade central osteosarcoma and its putative progenitor cells identifies tumourigenic pathways. *British Journal of Cancer* 101(11), pp. 1909-1918.

Clute, P. and Pines, J. 1999. Temporal and spatial control of cyclin B1 destruction in metaphase. *Nature Cell Biology* 1(2), pp. 82-87.

Comerton, A. M. et al. 2007. Membrane adsorption of endocrine disrupting compounds and pharmaceutically active compounds. *Journal of Membrane Science* 303(1-2), pp. 267-277.

Cong, P. et al. 2009. A Wireless and Batteryless 10-Bit Implantable Blood Pressure Sensing Microsystem With Adaptive RF Powering for Real-Time Laboratory Mice Monitoring. *Ieee Journal of Solid-State Circuits* 44(12), pp. 3631-3644.

Cong, P. et al. 2008. *Wireless Less-Invasive Blood Pressure Sensing Microsystem for Small Laboratory Animal In Vivo Real-Time Monitoring*. New York: Ieee, pp. 80-86.

Contag, C. H. and Bachmann, M. H. 2002. Advances in vivo bioluminescence imaging of gene expression. *Annual Review of Biomedical Engineering* 4, pp. 235-260.

Cormack, B. P. et al. 1996. FACS-optimized mutants of the green fluorescent protein (GFP). *Gene* 173(1), pp. 33-38.

Cosgrove, B. D. et al. 2008. Fusing Tissue Engineering and Systems Biology Toward Fulfilling Their Promise. *Cellular and Molecular Bioengineering* 1(1), pp. 33-41.

Coulter, W. H. 1953. Means for counting particles suspended in a fluid.United States: Coulter, Wallace H.

Craighead, H. 2006. Future lab-on-a-chip technologies for interrogating individual molecules. *Nature* 442(7101), pp. 387-393.

Cucullo, L. et al. 2008. Immortalized human brain endothelial cells and flow-based vascular modeling: a marriage of convenience for rational neurovascular studies. *Journal of Cerebral Blood Flow and Metabolism* 28(2), pp. 312-328.

Currell, G. and Dowman, A. 2009. *Essential mathematics and statistics for science.* Chichester, West Sussex; Hoboken, NJ: Wiley-Blackwell.

D'Antonio, J. M. et al. 2008. Longitudinal analysis of androgen deprivation of prostate cancer cells identifies pathways to androgen independence. *Prostate* 68(7), pp. 698-714.

Darzynkiewicz, Z. et al. 1994. ASSAYS OF CELL VIABILITY - DISCRIMINATION OF CELLS DYING BY APOPTOSIS.*Methods in Cell Biology, Vol 41*. Vol. 41. San Diego: Academic Press Inc, pp. 15-38.

Darzynkiewicz, Z. et al. 1987. Assay of Cell Cycle Kinetics by Multivariate Flow Cytometry Using the Principle of Stathmokinesis. pp. 291-336.

Dass, C. R. et al. 2006. A novel orthotopic murine model provides insights into cellular and molecular characteristics contributing to human osteosarcoma. *Clinical & Experimental Metastasis* 23(7-8), pp. 367-380.

Dass, C. R. et al. 2007. Human xenograft osteosarcoma models with spontaneous metastasis in mice: clinical relevance and applicability for drug testing. *Journal of Cancer Research and Clinical Oncology* 133(3), pp. 193-198.

Davicioni, E. et al. 2008. Diagnostic and Prognostic Sarcoma Signatures. *Molecular Diagnosis & Therapy* 12(6), pp. 359-374.

Davidson, P. M. et al. 2010. Topographically induced self-deformation of the nuclei of cells: dependence on cell type and proposed mechanisms. *Journal of Materials Science-Materials in Medicine* 21(3), pp. 939-946.

Davis, P. K. et al. 2001. Biological methods for cell-cycle synchronization of mammalian cells. *Biotechniques* 30(6), pp. 1322-+.

De Bartolo, L. et al. 2009. Human hepatocyte functions in a crossed hollow fiber membrane bioreactor. *Biomaterials* 30(13), pp. 2531-2543.

De Ruijter, J. E. et al. 2001. Analysis of integrin expression in U2OS cells cultured on various calcium phosphate ceramic substrates. *Tissue Engineering* 7(3), pp. 279-289.

Dean, L. 2005. *Chapter 10 The Kidd blood group - Blood Groups and Red Cell Antigens* [Online]. NCBI. Available at: http://www.ncbi.nlm.nih.gov/bookshelf/br.fcgi?book=rbcantigen&part=ch10Kidd [Accessed: 2010].

Debnath, J. and Brugge, J. S. 2005. Modelling glandular epithelial cancers in three-dimensional cultures. *Nature Reviews Cancer* 5(9), pp. 675-688.

Debnath, J. et al. 2003. Morphogenesis and oncogenesis of MCF-10A mammary epithelial acini grown in three-dimensional basement membrane cultures. *Methods* 30(3), pp. 256-268.

Decker, S. et al. 2004. The hollow fibre model in cancer drug screening: the NCI experience. *European Journal of Cancer* 40(6), pp. 821-826.

Dehne, T. et al. 2010. Gene expression profiling of primary human articular chondrocytes in high-density micromasses reveals patterns of recovery, maintenance, re- and dedifferentiation. *Gene* 462(1-2), pp. 8-17.

Delehanty, J. B. et al. 2010. Delivering quantum dot-peptide bioconjugates to the cellular cytosol: escaping from the endolysosomal system. *Integrative Biology* 2(5-6), pp. 265-277.

Delehanty, J. B. et al. 2009. Delivering quantum dots into cells: strategies, progress and remaining issues. *Analytical and Bioanalytical Chemistry* 393(4), pp. 1091-1105.

Denizot, F. and Lang, R. 1986. RAPID COLORIMETRIC ASSAY FOR CELL-GROWTH AND SURVIVAL - MODIFICATIONS TO THE TETRAZOLIUM DYE PROCEDURE GIVING IMPROVED SENSITIVITY AND RELIABILITY. *Journal of Immunological Methods* 89(2), pp. 271-277.

Dennis, G. et al. 2003. DAVID: Database for annotation, visualization, and integrated discovery. *Genome Biology* 4(9), p. 11.

Do, S. I. et al. 2008. Expression of Insulin-Like Growth Factor-II mRNA Binding Protein 3 (IMP3) in Osteosarcoma. *Oncology Research* 17(6), pp. 269-272.

Dohi, O. et al. 2008. Sex steroid receptors expression and hormone-induced cell proliferation in human osteosarcoma. *Cancer Science* 99(3), pp. 518-523.

Dondrup, M. et al. 2009. An evaluation framework for statistical tests on microarray data. *Journal of Biotechnology* 140(1-2), pp. 18-26.

Dothager, R. S. et al. 2009. Advances in bioluminescence imaging of live animal models. *Current Opinion in Biotechnology* 20(1), pp. 45-53.

DTP-NCI. 2009. *Hollow Fiber Assay Protocols for Tumor Cell Lines* [Online]. Biological Testing Branch, DTP, DCTDC, NCI. Available at: http://dtp.nci.nih.gov/branches/btb/pdf/cancer_protocol_hollow_fiber.pdf [Accessed: 2009].

Dudoit, S. et al. 2002. Statistical methods for identifying differentially expressed genes in replicated cDNA microarray experiments. *Statistica Sinica* 12(1), pp. 111-139.

Eigsti, O. J. and Dustin, P. 1955. *Colchicine in agriculture, medicine, biology, and chemistry [by] O. J. Eigsti [and] Pierre Dustin, Jr.* Ames: Iowa State College Press.

Ek, E. T. H. et al. 2006. Commonly used mouse models of osteosarcoma. *Critical Reviews in Oncology Hematology* 60(1), pp. 1-8.

ElSaady, D. et al. 1996. MCF-7 cell cycle arrested at G1 through ursolic acid, and increased reduction of tetrazolium salts. *Anticancer Research* 16(1), pp. 481-486.

Errington, R. J. et al. 2010. Single cell nanoparticle tracking to model cell cycle dynamics and compartmental inheritance. *Cell Cycle* 9(1), pp. 121-130.

Eurich, K. et al. 2009. Potential role of chitinase 3-like-1 in inflammation-associated carcinogenic changes of epithelial cells. *World Journal of Gastroenterology* 15(42), pp. 5249-5259.

Feder-Mengus, C. et al. 2008. New dimensions in tumor immunology: what does 3D culture reveal? *Trends in Molecular Medicine* 14(8), pp. 333-340.

Fernandez-Rosas, E. et al. 2010. Internalization and cytotoxicity analysis of silicon-based microparticles in macrophages and embryos. *Biomedical Microdevices* 12(3), pp. 371-379.

Fischbach, C. et al. 2007. Engineering tumors with 3D scaffolds. *Nature Methods* 4(10), pp. 855-860.

Fischer, U. M. et al. 2009. Pulmonary Passage is a Major Obstacle for Intravenous Stem Cell Delivery: The Pulmonary First-Pass Effect. *Stem Cells and Development* 18(5), pp. 683-691.

Fjellbirkeland, L. et al. 2003. Integrin alpha v beta 8-mediated activation of transforming growth factor-beta inhibits human airway epithelial proliferation in intact bronchial tissue. *American Journal of Pathology* 163(2), pp. 533-542.

Florenes, V. A. et al. 1994. MDM2 GENE AMPLIFICATION AND TRANSCRIPT LEVELS IN HUMAN SARCOMAS - RELATIONSHIP TO TP53 GENE STATUS. *Journal of the National Cancer Institute* 86(17), pp. 1297-1302.

Fotos, J. S. et al. 2006. Automated time-lapse microscopy and high-resolution tracking of cell migration. *Cytotechnology* 51(1), pp. 7-19.

Fox, M. H. 1980. A MODEL FOR THE COMPUTER-ANALYSIS OF SYNCHRONOUS DNA DISTRIBUTIONS OBTAINED BY FLOW-CYTOMETRY. *Cytometry* 1(1), pp. 71-77.

Frasco, M. F. and Chaniotakis, N. 2010. Bioconjugated quantum dots as fluorescent probes for bioanalytical applications. *Analytical and Bioanalytical Chemistry* 396(1), pp. 229-240.

Fu, D. et al. 2008. Probing skin pigmentation changes with transient absorption imaging of eumelanin and pheomelanin. *Journal of Biomedical Optics* 13(5), p. 7.

Furon, E. 2009. *Phenotypic plasticity is demonstrated in small cell lung cancer.* Cardiff University.

Galanzha, E. I. et al. 2008. In vivo multispectral, multiparameter, photoacoustic lymph flow cytometry with natural cell focusing, label-free detection and multicolor nanoparticle probes. *Cytometry Part A* 73A(10), pp. 884-894.

Gao, J. H. and Xu, B. 2009. Applications of nanomaterials inside cells. *Nano Today* 4(1), pp. 37-51.

Gao, X. H. et al. 2004. In vivo cancer targeting and imaging with semiconductor quantum dots. *Nature Biotechnology* 22(8), pp. 969-976.

Gao, X. H. and Nie, S. M. 2004. Quantum dot-encoded mesoporous beads with high brightness and uniformity: Rapid readout using flow cytometry. *Analytical Chemistry* 76(8), pp. 2406-2410.

Gascoigne, K. E. and Taylor, S. S. 2009. How do anti-mitotic drugs kill cancer cells? *Journal of Cell Science* 122(15), pp. 2579-2585.

Gautier, L. et al. 2004. affy - analysis of Affymetrix GeneChip data at the probe level. *Bioinformatics* 20(3), pp. 307-315.

GE_Healthcare. 2003. *G2M Cell Cycle Phase Marker Assay User Manual* [Online]. GE Healthcare Life Sciences (formerly Amersham Biosciences) Available at: http://www4.gelifesciences.com/aptrix/upp00919.nsf/Content/0D387E3C4C6D4FFFC1257628001D05DD/$file/25-8010-50UM.pdf [Accessed: December 2009].

Geiger, B. et al. 2001. Transmembrane extracellular matrix-cytoskeleton crosstalk. *Nature Reviews Molecular Cell Biology* 2(11), pp. 793-805.

Gentleman, R. C. et al. 2004. Bioconductor: open software development for computational biology and bioinformatics. *Genome Biology* 5(10), p. 16.

George, T. C. et al. 2006. Quantitative measurement of nuclear translocation events using similarity analysis of multispectral cellular images obtained in flow. *Journal of Immunological Methods* 311(1-2), pp. 117-129.

Gerstner, A. O. H. et al. 2009. Clinical applications of slide-based cytometry - an update. *Journal of Biophotonics* 2(8-9), pp. 463-469.

Ghosh, S. et al. 2005. Three-dimensional culture of melanoma cells profoundly affects gene expression profile: A high density oligonucleotide array study. *Journal of Cellular Physiology* 204(2), pp. 522-531.

Gibbins, J. M. and Mahaut-Smith, M. P. 1984. Methods in molecular biology. *Methods in molecular biology.*, pp. 80,81.

Giepmans, B. N. G. et al. 2006. Review - The fluorescent toolbox for assessing protein location and function. *Science* 312(5771), pp. 217-224.

Gloeckner, H. et al. 2001. Monitoring of cell viability and cell growth in a hollow-fiber bioreactor by use of the dye Alamar Blue (TM). *Journal of Immunological Methods* 252(1-2), pp. 131-138.

Glukhovsky, A. 2003. Wireless capsule endoscopy. *Sensor Review* 23(2), pp. 128 - 133.

Godara, P. et al. 2008. Design of bioreactors for mesenchymal stem cell tissue engineering. *Journal of Chemical Technology and Biotechnology* 83(4), pp. 408-420.

Goddard, G. et al. 2010. High-Resolution Spectral Analysis of Individual SERS-Active Nanoparticles in Flow. *Journal of the American Chemical Society* 132(17), pp. 6081-6090.

Goebeler, V. et al. 2008. Annexin A8 Regulates Late Endosome Organization and Function. *Molecular Biology of the Cell* 19(12), pp. 5267-5278.

Gomez-Martinez, R. et al. 2010. Intracellular Silicon Chips in Living Cells. *Small* 6(4), pp. 499-502.

Gorelik, E. et al. 1987. Microencapsulated Tumor Assay - New Short-Term Assay for Invivo Evaluation of the Effects of Anticancer Drugs on Human-Tumor Cell-Lines. *Cancer Research* 47(21), pp. 5739-5747.

GPCR-MolecularDevices. 2010. *Transfluor Assay Technology-GPCR Assays* [Online]. Molecular Devices-Danaher Corporation. Available at: http://www.moleculardevices.com/pages/reagents/transfluor.html [Accessed: 2010].

Granicka, L. H. et al. 2003. Polypropylene hollow fiber for cells isolation: Methods for evaluation of diffusive transport and quality of cells encapsulation. *Artificial Cells Blood Substitutes and Immobilization Biotechnology* 31(3), pp. 249-262.

Graves, E. E. et al. 2005. Validation of in vivo fluorochrome concentrations measured using fluorescence molecular tomography. *Journal of Biomedical Optics* 10(4), p. 10.

Graw, J. 2009. Genetics of crystallins: Cataract and beyond. *Experimental Eye Research* 88(2), pp. 173-189.

Gray, J. W. et al. 1987. Flow Cytokinetics. pp. 93-137.

Grek, C. L. et al. 2009. CHARACTERIZATION OF ALVEOLAR EPITHELIAL CELLS CULTURED IN SEMIPERMEABLE HOLLOW FIBERS. *Experimental Lung Research* 35(2), pp. 155-174.

Griffith, L. G. and Swartz, M. A. 2006. Capturing complex 3D tissue physiology in vitro. *Nature Reviews Molecular Cell Biology* 7(3), pp. 211-224.

Guzzardi, M. A. et al. 2009. Study of the Crosstalk Between Hepatocytes and Endothelial Cells Using a Novel Multicompartmental Bioreactor: A Comparison Between Connected Cultures and Cocultures. *Tissue Engineering Part A* 15(11), pp. 3635-3644.

Haas, J. et al. 1996. Codon usage limitation in the expression of HIV-1 envelope glycoprotein. *Current Biology* 6(3), pp. 315-324.

Hale, G. M. and Querry, M. R. 1973. OPTICAL-CONSTANTS OF WATER IN 200-NM TO 200-MUM WAVELENGTH REGION. *Applied Optics* 12(3), pp. 555-563.

Hamid, R. et al. 2004. Comparison of alamar blue and MTT assays for high through-put screening. *Toxicology in Vitro* 18(5), pp. 703-710.

Han, I. et al. 2008. Expression of macrophage migration inhibitory factor relates to survival in high-grade osteosarcoma. *Clinical Orthopaedics and Related Research* 466(9), pp. 2107-2113.

Han, J. et al. 2010. Molecular Predictors of 3D Morphogenesis by Breast Cancer Cell Lines in 3D Culture. *Plos Computational Biology* 6(2), p. 12.

Hargrave, P. et al. 1996. Optical properties of multicellular tumour spheroids. *Physics in Medicine and Biology* 41(6), pp. 1067-1072.

Harma, V. et al. 2010. A Comprehensive Panel of Three-Dimensional Models for Studies of Prostate Cancer Growth, Invasion and Drug Responses. *PLoS One* 5(5), p. 17.

Hassan, S. B. et al. 2001. A hollow fiber model for in vitro studies of cytotoxic compounds: activity of the cyanoguanidine CHS 828. *Anti-Cancer Drugs* 12(1), pp. 33-42.

Hastie, S. B. 1991. INTERACTIONS OF COLCHICINE WITH TUBULIN. *Pharmacology & Therapeutics* 51(3), pp. 377-401.

Hawkins, E. D. et al. 2007. Measuring lymphocyte proliferation, survival and differentiation using CFSE time-series data. *Nature Protocols* 2(9), pp. 2057-2067.

Hayat, M. A. 2008. *Lung and breast carcinomas.* Amsterdam; Boston: Elsevier, Academic Press.

Heindryckx, F. et al. 2009. Experimental mouse models for hepatocellular carcinoma research. *International Journal of Experimental Pathology* 90(4), pp. 367-386.

Hemmrich, K. et al. 2006. Applicability of the dyes CFSE, CM-Dil and PKH26 for tracking of human preadipocytes to evaluate adipose tissue engineering. *Cells Tissues Organs* 184(3-4), pp. 117-127.

Henriquez, R. R. et al. 2004. The resurgence of Coulter counting for analyzing nanoscale objects. *Analyst* 129(6), pp. 478-482.

Herold, K. E. and Rasooly, A. 2009. *Lab on a chip technology.* Norfolk, UK: Caister Academic Press.

Herzlieb, N. et al. 2000. Insulin-like growth factor-I inhibits the progression of human U-2OS osteosarcoma cells towards programmed cell death through interaction with the IGF-I receptor. *Cellular and Molecular Biology* 46(1), pp. 71-77.

Ho, Y. P. and Leong, K. W. 2010. Quantum dot-based theranostics. *Nanoscale* 2(1), pp. 60-68.

Hoffman, R. M. 2002. Green fluorescent protein imaging of tumour growth, metastasis, and angiogenesis in mouse models. *Lancet Oncology* 3(9), pp. 546-556.

Hoffmann, R. and Valencia, A. 2004. A gene network for navigating the literature. *Nature Genetics* 36(7), pp. 664-664.

Hollingshead, M. G. et al. 1995a. In vivo cultivation of tumor cells in hollow fibers. *Life Sciences* 57(2), pp. 131-141.

Hollingshead, M. G. et al. 2004. A potential role for imaging technology in anticancer efficacy evaluations. *European Journal of Cancer* 40(6), pp. 890-898.

Hollingshead, M. G. et al. 2005. The Hollow Fiber Assay in Cancer Efficacy Testing in the Developmental Therapeutics Program at the National Cancer Institute. pp. 351-354.

Hollingshead, M. G. et al. 1995b. In-Vivo Drug Screening Applications of Hiv-Infected Cells Cultivated within Hollow Fibers in 2 Physiological Compartments of Mice. *Antiviral Research* 28(3), pp. 265-279.

Holton, M. D. et al. 2009. Stroboscopic fluorescence lifetime imaging. *Optics Express* 17(7), pp. 5205-5216.

Hong, J. et al. 2009. Micro- and nanofluidic systems for high-throughput biological screening. *Drug Discovery Today* 14(3-4), pp. 134-146.

Honorati, M. C. et al. 2007. Possible prognostic role of IL-17R in osteosarcoma. *Journal of Cancer Research and Clinical Oncology* 133(12), pp. 1017-1021.

Hopwood, B. et al. 2009. Gene expression profile of the bone microenvironment in human fragility fracture bone. *Bone* 44(1), pp. 87-101.

Hoshino, A. et al. 2004. Applications of T-lymphoma labeled with fluorescent quantum dots to cell tracing markers in mouse body. *Biochemical and Biophysical Research Communications* 314(1), pp. 46-53.

Hu, P. Z. et al. 2007. Computational prediction of cancer-gene function. *Nature Reviews Cancer* 7(1), pp. 23-34.

Huang, D. W. et al. 2009a. Bioinformatics enrichment tools: paths toward the comprehensive functional analysis of large gene lists. *Nucleic Acids Research* 37(1), pp. 1-13.

Huang, D. W. et al. 2009b. Systematic and integrative analysis of large gene lists using DAVID bioinformatics resources. *Nature Protocols* 4(1), pp. 44-57.

Hutmacher, D. W. 2010. Biomaterials offer cancer research the third dimension. *Nature Materials* 9(2), pp. 90-93.

Hutmacher, D. W. et al. 2010. Can tissue engineering concepts advance tumor biology research? *Trends in Biotechnology* 28(3), pp. 125-133.

Iddan, G. et al. 2000. Wireless capsule endoscopy. *Nature* 405(6785), pp. 417-417.

Irizarry, R. A. et al. 2003. Exploration, normalization, and summaries of high density oligonucleotide array probe level data. *Biostatistics* 4(2), pp. 249-264.

Ito, T. et al. 2003. Simultaneous determination of the size and surface charge of individual nanoparticles using a carbon nanotube-based coulter counter. *Analytical Chemistry* 75(10), pp. 2399-2406.

Iwata, M. et al. 2004. Human marrow stromal cells activate monocytes to secrete osteopontin, which down-regulates Notch1 gene expression in CD34(+) cells. *Blood* 103(12), pp. 4496-4502.

Jacques, S. L. and Pogue, B. W. 2008. Tutorial on diffuse light transport. *Journal of Biomedical Optics* 13(4), p. 19.

Jain, E. and Kumar, A. 2008. Upstream processes in antibody production: Evaluation of critical parameters. *Biotechnology Advances* 26(1), pp. 46-72.

Jain, P. K. et al. 2006. Calculated absorption and scattering properties of gold nanoparticles of different size, shape, and composition: Applications in biological imaging and biomedicine. *Journal of Physical Chemistry B* 110(14), pp. 7238-7248.

Jaiswal, J. K. et al. 2003. Long-term multiple color imaging of live cells using quantum dot bioconjugates. *Nature Biotechnology* 21(1), pp. 47-51.

Jaiswal, J. K. and Simon, S. M. 2004. Potentials and pitfalls of fluorescent quantum dots for biological imaging. *Trends in Cell Biology* 14(9), pp. 497-504.

Jamshidi, A. et al. 2009. NanoPen: Dynamic, Low-Power, and Light-Actuated Patterning of Nanoparticles. *Nano Letters* 9(8), pp. 2921-2925.

Jha, M. N. et al. 1994. CELL-CYCLE ARREST BY COLCEMID DIFFERS IN HUMAN NORMAL AND TUMOR-CELLS. *Cancer Research* 54(18), pp. 5011-5015.

Johnson, J. I. et al. 2001. Relationships between drug activity in NCI preclinical in vitro and in vivo models and early clinical trials. *British Journal of Cancer* 84(10), pp. 1424-1431.

Jonsson, E. et al. 2000. Determination of drug effect on tumour cells, host animal toxicity and drug pharmacokinetics in a hollow-fibre model in rats. *Cancer Chemotherapy and Pharmacology* 46(6), pp. 493-500.

Jordan, M. A. et al. 1993. MECHANISM OF MITOTIC BLOCK AND INHIBITION OF CELL-PROLIFERATION BY TAXOL AT LOW CONCENTRATIONS. *Proceedings of the National Academy of Sciences of the United States of America* 90(20), pp. 9552-9556.

Jordan, M. A. et al. 1996. Mitotic block induced in HeLa cells by low concentrations of paclitaxel (Taxol) results in abnormal mitotic exit and apoptotic cell death. *Cancer Research* 56(4), pp. 816-825.

Jordan, M. A. and Wilson, L. 2004. Microtubules as a target for anticancer drugs. *Nature Reviews Cancer* 4(4), pp. 253-265.

Junker, N. et al. 2005. Regulation of YKL-40 expression during genotoxic or microenvironmental stress in human glioblastoma cells. *Cancer Science* 96(3), pp. 183-190.

Kah, J. C. Y. et al. 2009. Control of optical contrast using gold nanoshells for optical coherence tomography imaging of mouse xenograft tumor model in vivo. *Journal of Biomedical Optics* 14(5), p. 13.

Kalbfuss, B. et al. 2007. Harvesting and concentration of human influenza A virus produced in serum-free mammalian cell culture for the production of vaccines. *Biotechnology and Bioengineering* 97(1), pp. 73-85.

Kanehisa, M. and Goto, S. 2000. KEGG: Kyoto Encyclopedia of Genes and Genomes. *Nucleic Acids Research* 28(1), pp. 27-30.

Kanehisa, M. et al. 2010. KEGG for representation and analysis of molecular networks involving diseases and drugs. *Nucl. Acids Res.* 38(suppl_1), pp. D355-360.

Kelling, J. et al. 2003. Suppression of centromere dynamics by Taxol (R) in living osteosarcoma cells. *Cancer Research* 63(11), pp. 2794-2801.

Kfouri, M. et al. 2008. Toward a miniaturized wireless fluorescence-based diagnostic Imaging system. *Ieee Journal of Selected Topics in Quantum Electronics* 14(1), pp. 226-234.

Khalil, I. G. and Hill, C. 2005. Systems biology for cancer. *Current Opinion in Oncology* 17(1), pp. 44-48.

Khan, I. A. et al. 2007. ProgeniDB - A novel cell lineage database for generation associated phenotypic behavior in cell-based assays. *Cell Cycle* 6(7), pp. 868-874.

Khatri, P. and Draghici, S. 2005. Ontological analysis of gene expression data: current tools, limitations, and open problems. *Bioinformatics* 21(18), pp. 3587-3595.

Kherlopian, A. R. et al. 2008. A review of imaging techniques for systems biology. *BMC Systems Biology* 2, p. 18.

Kim, J. et al. 2009. Multifunctional nanostructured materials for multimodal imaging, and simultaneous imaging and therapy. *Chemical Society Reviews* 38(2), pp. 372-390.

Klee, D. et al. 2003. Surface modification of poly(vinylidenefluoride) to improve the osteoblast adhesion. *Biomaterials* 24(21), pp. 3663-3670.

Kneipp, J. et al. 2010. Novel optical nanosensors for probing and imaging live cells. *Nanomedicine-Nanotechnology Biology and Medicine* 6(2), pp. 214-226.

Kobayashi, H. et al. 2010. New Strategies for Fluorescent Probe Design in Medical Diagnostic Imaging. *Chemical Reviews* 110(5), pp. 2620-2640.

Koole, R. et al. 2009. Magnetic quantum dots for multimodal imaging. *Wiley Interdisciplinary Reviews-Nanomedicine and Nanobiotechnology* 1(5), pp. 475-491.

Krasteva, N. et al. 2002. Membranes for biohybrid liver support systems - investigations on hepatocyte attachment, morphology and growth. *Biomaterials* 23(12), pp. 2467-2478.

Krishnamoorthy, A. V. et al. 2009. Computer Systems Based on Silicon Photonic Interconnects. *Proceedings of the Ieee* 97(7), pp. 1337-1361.

Kung, A. L. et al. 1990. CELL LINE-SPECIFIC DIFFERENCES IN THE CONTROL OF CELL-CYCLE PROGRESSION IN THE ABSENCE OF MITOSIS. *Proceedings of the National Academy of Sciences of the United States of America* 87(24), pp. 9553-9557.

Kuswandi, B. et al. 2007. Optical sensing systems for microfluidic devices: A review. *Analytica Chimica Acta* 601(2), pp. 141-155.

Lagerholm, B. C. et al. 2004. Multicolor coding of cells with cationic peptide coated quantum dots. *Nano Letters* 4(10), pp. 2019-2022.

Lal, S. et al. 2008. Nanoshell-Enabled Photothermal Cancer Therapy: Impending Clinical Impact. *Accounts of Chemical Research* 41(12), pp. 1842-1851.

Lamers, C. H. J. et al. 1999. Large-scale production of natural cytokines during activation and expansion of human T lymphocytes in hollow fiber bioreactor cultures. *Journal of Immunotherapy* 22(4), pp. 299-307.

Lanza, R. P. et al. 1991. XENOTRANSPLANTATION OF CANINE, BOVINE, AND PORCINE ISLETS IN DIABETIC RATS WITHOUT IMMUNOSUPPRESSION. *Proceedings of the National Academy of Sciences of the United States of America* 88(24), pp. 11100-11104.

Lastovicka, J. et al. 2009. Assessment of lymphocyte proliferation: CFSE kills dividing cells and modulates expression of activation markers. *Cellular Immunology* 256(1-2), pp. 79-85.

Lauffenburger, D. A. and Horwitz, A. F. 1996. Cell migration: A physically integrated molecular process. *Cell* 84(3), pp. 359-369.

Leblond, F. et al. 2010. Pre-clinical whole-body fluorescence imaging: Review of instruments, methods and applications. *Journal of Photochemistry and Photobiology B-Biology* 98(1), pp. 77-94.

Lee, J. et al. 2008. Three-dimensional cell culture matrices: State of the art. *Tissue Engineering Part B-Reviews* 14(1), pp. 61-86.

Lee, S. F. and Osborne, M. A. 2009. Brightening, Blinking, Bluing and Bleaching in the Life of a Quantum Dot: Friend or Foe? *Chemphyschem* 10(13), pp. 2174-2191.

Lee, W. P. and Tzou, W. S. 2009. Computational methods for discovering gene networks from expression data. *Briefings in Bioinformatics* 10(4), pp. 408-423.

Lee, Y. E. K. et al. 2009. Nanoparticle PEBBLE Sensors in Live Cells and In Vivo. *Annual Review of Analytical Chemistry* 2, pp. 57-76.

Leung, K. 2008. *Gold-polyethylene glycol nanoshells [Au-PEG-nanoshells]* [Online]. Molecular Imaging and Contrast Agent Database (MICAD), Bethesda (MD): National Library of Medicine (US). Available at: http://www.ncbi.nlm.nih.gov/bookshelf/br.fcgi?book=micad&part=PEG-gold-NP [Accessed: 2010 NCBI; 2004-2008].

Leuthold, J. et al. 2010. Nonlinear silicon photonics. *Nature Photonics* 4(8), pp. 535-544.

Lewejohann, L. et al. 2009. Behavioral phenotyping of a murine model of Alzheimer's disease in a seminaturalistic environment using RFID tracking. *Behavior Research Methods* 41(3), pp. 850-856.

Lewinski, N. et al. 2008. Cytotoxicity of nanoparticles. *Small* 4(1), pp. 26-49.

Li, H. et al. 2005. Colcemid inhibits the rejoining of the nucleotide excision repair of UVC-induced DNA damages in Chinese hamster ovary cells. *Mutation Research-Genetic Toxicology and Environmental Mutagenesis* 588(2), pp. 118-128.

Li, S. C. et al. 2010. A Biological Global Positioning System: Considerations for Tracking Stem Cell Behaviors in the Whole Body. *Stem Cell Reviews and Reports* 6(2), pp. 317-333.

Lin, S. et al. 2007. Quantum dot imaging for embryonic stem cells. *Bmc Biotechnology* 7, p. 10.

Lind, M. et al. 1996. Bone morphogenetic protein-2 but not bone morphogenetic protein-4 and -6 stimulates chemotactic migration of human osteoblasts, human marrow osteoblasts, and U2-OS cells. *Bone* 18(1), pp. 53-57.

Liu, B. F. and Liang, J. J. N. 2007. Protein-protein interactions among human lens acidic and basic beta-crystallins. *Febs Letters* 581(21), pp. 3936-3942.

Liu, D. et al. 2004. TESTING CELL CYCLE REGULATION EFFECT OF A COMPOUND USING A HOLLOW FIBRE CELL IMPLANT.

Liu, S. Q. and Tang, Z. Y. 2010. Nanoparticle assemblies for biological and chemical sensing. *Journal of Materials Chemistry* 20(1), pp. 24-35.

Liu, W. M. and Dalgleish, A. G. 2009. MTT assays can underestimate cell numbers. *Cancer Chemotherapy and Pharmacology* 64(4), pp. 861-862.

Liu, Y. B. et al. 1997. Mechanism of cellular 3-(4,5-dimethylthiazol-2-yl)-2,5-diphenyltetrazolium bromide (MTT) reduction. *Journal of Neurochemistry* 69(2), pp. 581-593.

Loo, C. et al. 2005. Gold nanoshell bioconjugates for molecular imaging in living cells. *Optics Letters* 30(9), pp. 1012-1014.

Loo, C. et al. 2004. Nanoshell-enabled photonics-based imaging and therapy of cancer. *Technology in Cancer Research & Treatment* 3(1), pp. 33-40.

Lu, H. F. et al. 2005a. Galactosylated poly(vinylidene difluoride) hollow fiber bioreactor for hepatocyte culture. *Tissue Engineering* 11(11-12), pp. 1667-1677.

Lu, K. H. et al. 2005b. Paclitaxel induces apoptosis via caspase-3 activation in human osteogenic sarcoma cells (U-2 OS). *Journal of Orthopaedic Research* 23(5), pp. 988-994.

Lugli, E. et al. 2010. Data Analysis in Flow Cytometry: The Future Just Started. *Cytometry Part A* 77A(7), pp. 705-713.

Luo, X. J. et al. 2008. Osteogenic BMPs promote tumor growth of human osteosarcomas that harbor differentiation defects. *Laboratory Investigation* 88(12), pp. 1264-1277.

Luu, H. H. et al. 2005. Increased expression of S100A6 is associated with decreased metastasis and inhibition of cell migration and anchorage independent growth in human osteosarcoma. *Cancer Letters* 229(1), pp. 135-148.

Lyons, A. B. 1999. Divided we stand: Tracking cell proliferation with carboxyfluorescein diacetate succinimidyl ester. *Immunology and Cell Biology* 77(6), pp. 509-515.

Machleidt, T. et al. 2009. Multiplexing of Pathway-Specific beta-Lactamase Reporter Gene Assays by Optical Coding With Qtracker (R) Nanocrystals. *Journal of Biomolecular Screening* 14(7), pp. 845-852.

Malcik, N. et al. 2005. The performance of a microchip-based fiber optic detection technique for the determination of Ca2+ ions in urine. *Sensors and Actuators B-Chemical* 107(1), pp. 24-31.

Manara, M. C. et al. 2000. Reversal of malignant phenotype in human osteosarcoma cells transduced with the alkaline phosphatase gene. *Bone* 26(3), pp. 215-220.

Mancini, M. C. et al. 2008. Oxidative quenching and degradation of polymer-encapsulated quantum dots: New insights into the long-term fate and toxicity of nanocrystals in vivo. *Journal of the American Chemical Society* 130(33), pp. 10836-+.

Mandecki, W. et al. 2006. Microtransponders, the miniature RFID electronic chips, as platforms for cell growth in cytotoxicity assays. *Cytometry Part A* 69A(11), pp. 1097-1105.

Marin-Vinader, L. et al. 2006. In vivo heteromer formation. Expression of soluble beta A4-crystallin requires coexpression of a heteromeric partner. *Febs Journal* 273(14), pp. 3172-3182.

Martin, Y. and Vermette, P. 2005. Bioreactors for tissue mass culture: Design, characterization, and recent advances. *Biomaterials* 26(35), pp. 7481-7503.

Mastro, A. M. and Vogler, E. A. 2009. A Three-Dimensional Osteogenic Tissue Model for the Study of Metastatic Tumor Cell Interactions with Bone. *Cancer Research* 69(10), pp. 4097-4100.

Matsusaka, T. and Pines, J. 2004. Chfr acts with the p38 stress kinases to block entry to mitosis in mammalian cells. *Journal of Cell Biology* 166(4), pp. 507-516.

Mattheakis, L. C. et al. 2004. Optical coding of mammalian cells using semiconductor quantum dots. *Analytical Biochemistry* 327(2), pp. 200-208.

McCarthy, D. J. and Smyth, G. K. 2009. Testing significance relative to a fold-change threshold is a TREAT. *Bioinformatics* 25(6), pp. 765-771.

McGrogan, B. T. et al. 2008. Taxanes, microtubules and chemoresistant breast cancer. *Biochimica Et Biophysica Acta-Reviews on Cancer* 1785(2), pp. 96-132.

Medintz, I. L. et al. 2005. Quantum dot bioconjugates for imaging, labelling and sensing. *Nature Materials* 4(6), pp. 435-446.

Megason, S. G. and Fraser, S. E. 2007. Imaging in systems biology. *Cell* 130(5), pp. 784-795.

Michalet, X. et al. 2005. Quantum dots for live cells, in vivo imaging, and diagnostics. *Science* 307(5709), pp. 538-544.

Mittag, A. and Tarnok, A. 2009. Basics of standardization and calibration in cytometry - a review. *Journal of Biophotonics* 2(8-9), pp. 470-481.

Miyaki, K. et al. 2005. Fabrication of an integrated PDMS microchip incorporating an LED-induced fluorescence device. *Analytical and Bioanalytical Chemistry* 382(3), pp. 810-816.

Molinaro, M. 2010. *Introduction to Biophotonics-Lecture Talk.*

Monroe, D. G. et al. 2005. Estrogen receptor alpha and beta heterodimers exert unique effects on estrogen- and tamoxifen-dependent gene expression in human U2OS osteosarcoma cells. *Molecular Endocrinology* 19(6), pp. 1555-1568.

Mootha, V. K. et al. 2003. PGC-1 alpha-responsive genes involved in oxidative phosphorylation are coordinately downregulated in human diabetes. *Nature Genetics* 34(3), pp. 267-273.

Moreau, J. E. et al. 2007. Tissue-engineered bone serves as a target for metastasis of human breast cancer in a mouse model. *Cancer Research* 67(21), pp. 10304-10308.

Morgan, D. O. 2006. *The cell cycle : principles of control.* London: New Science Press ; Oxford : Oxford University Press [distributor], pp. xxvii, 297 p.

Morrell, A. et al. 2006. Evaluation of indenoisoquinoline topoisomerase I inhibitors using a hollow fiber assay. *Bioorganic & Medicinal Chemistry Letters* 16(16), pp. 4395-4399.

Mosmann, T. 1983. RAPID COLORIMETRIC ASSAY FOR CELLULAR GROWTH AND SURVIVAL - APPLICATION TO PROLIFERATION AND CYTO-TOXICITY ASSAYS. *Journal of Immunological Methods* 65(1-2), pp. 55-63.

Mourant, J. R. et al. 1997a. Measuring absorption coefficients in small volumes of highly scattering media: source-detector separations for which path lengths do not depend on scattering properties. *Appl. Opt.* 36(22), pp. 5655-5661.

Mourant, J. R. et al. 1996. Measurements of scattering and absorption in mammalian cell suspensions. In: Alfano, R.R. and Katzir, A. eds. *Advances in Laser and Light Spectroscopy to Diagnose Cancer and Other Diseases Iii: Optical Biopsy, Proceedings.* Vol. 2679. Bellingham: Spie - Int Soc Optical Engineering, pp. 79-84.

Mourant, J. R. et al. 1997b. Predictions and measurements of scattering and absorption over broad wavelength ranges in tissue phantoms. *Applied Optics* 36(4), pp. 949-957.

Mourant, J. R. et al. 2001. Quantification of tissue properties in small volumes. In: Chance, B. et al. eds. *Optical Tomography and Spectroscopy of Tissue Iv.* Vol. 2. Bellingham: Spie-Int Soc Optical Engineering, pp. 276-281.

Moyano, J. V. et al. 2006. alpha B-crystallin is a novel oncoprotein that predicts poor clinical outcome in breast cancer. *Journal of Clinical Investigation* 116(1), pp. 261-270.

Mthunzi, P. 2010. *Optical sorting and photo-transfection of mammalian cells.* University of St Andrews.

Mueller, H. et al. 2004. Comparison of the usefulness of the MTT, ATP, and calcein assays to predict the potency of cytotoxic agents in various human cancer cell lines. *Journal of Biomolecular Screening* 9(6), pp. 506-515.

Muindi, J. R. et al. 2010. CYP24A1 Inhibition Enhances the Antitumor Activity of Calcitriol. *Endocrinology* 151(9), pp. 4301-4312.

Muller-Taubenberger, A. and Anderson, K. I. 2007. Recent advances using green and red fluorescent protein variants. *Applied Microbiology and Biotechnology* 77(1), pp. 1-12.

Murasawa, S. et al. 2005. Niche-dependent translineage commitment of endothelial progenitor cells, not cell fusion in general, into myocardial lineage cells. *Arteriosclerosis Thrombosis and Vascular Biology* 25(7), pp. 1388-1394.

Murie, C. et al. 2009. Comparison of small n statistical tests of differential expression applied to microarrays. *Bmc Bioinformatics* 10, p. 18.

Murphy, C. J. et al. 2008. Gold Nanoparticles in Biology: Beyond Toxicity to Cellular Imaging. *Accounts of Chemical Research* 41(12), pp. 1721-1730.

Nasevicius, A. and Ekker, S. C. 2000. Effective targeted gene 'knockdown' in zebrafish. *Nature Genetics* 26(2), pp. 216-220.

Nelissen, J. et al. 2000. Molecular analysis of the hematopoiesis supporting osteoblastic cell line U2-OS. *Experimental Hematology* 28(4), pp. 422-432.

Niforou, K. N. et al. 2008. The Proteome Profile of the Human Osteosarcoma U2OS Cell Line. *Cancer Genomics - Proteomics* 5(1), pp. 63-77.

Njoh, K. et al. eds. 2007. *Live cell tracking on an optical biochip platform. - art. no. 64410X.* Conference on Imaging, Manipulation, and Analysis of Biomolecules, Cells, and Tissues V. San Jose, CA, Jan 22-24. Spie-Int Soc Optical Engineering.

Nolan, J. P. and Yang, L. 2007. The flow of cytometry into systems biology. *Briefings in Functional Genomics & Proteomics* 6(2), pp. 81-90.

Ntziachristos, V. 2006. FLUORESCENCE MOLECULAR IMAGING. *Annual Review of Biomedical Engineering* 8(1), pp. 1-33.

Ntziachristos, V. 2010. Going deeper than microscopy: the optical imaging frontier in biology. *Nature Methods* 7(8), pp. 603-614.

Ntziachristos, V. et al. 2005. Looking and listening to light: the evolution of whole-body photonic imaging. *Nature Biotechnology* 23(3), pp. 313-320.

O'Brien, J. et al. 2000. Investigation of the Alamar Blue (resazurin) fluorescent dye for the assessment of mammalian cell cytotoxicity. *European Journal of Biochemistry* 267(17), pp. 5421-5426.

O'Neill, K. et al. 2010. Bioluminescent imaging: a critical tool in pre-clinical oncology research. *Journal of Pathology* 220(3), pp. 317-327.

Oakley, R. H. et al. 2002. The cellular distribution of fluorescently labeled arrestins provides a robust, sensitive, and universal assay for screening G protein-coupled receptors. *Assay and Drug Development Technologies* 1(1), pp. 21-30.

Okabe, M. et al. 1997. 'Green mice' as a source of ubiquitous green cells. *Febs Letters* 407(3), pp. 313-319.

Ormerod, M. G. 2008. *Flow Cytometry- a basic introduction* [Online]. Available at: http://flowbook.denovosoftware.com/Flow_Book/Chapter_2%3a_The_Flow_Cytometer [Accessed: 2010].

Page, B. et al. 1993. A NEW FLUOROMETRIC ASSAY FOR CYTOTOXICITY MEASUREMENTS IN-VITRO. *International Journal of Oncology* 3(3), pp. 473-476.

Pagliacci, M. C. et al. 1993. GENISTEIN INHIBITS TUMOR-CELL GROWTH IN-VITRO BUT ENHANCES MITOCHONDRIAL REDUCTION OF TETRAZOLIUM SALTS - A FURTHER PITFALL IN THE USE OF THE MTT ASSAY FOR EVALUATING CELL-GROWTH AND SURVIVAL. *European Journal of Cancer* 29A(11), pp. 1573-1577.

Pampaloni, F. et al. 2007. The third dimension bridges the gap between cell culture and live tissue. *Nature Reviews Molecular Cell Biology* 8(10), pp. 839-845.

Pan, S. H. et al. 2009. Epstein-Barr virus nuclear antigen 2 disrupts mitotic checkpoint and causes chromosomal instability. *Carcinogenesis* 30(2), pp. 366-375.

Parak, W. J. et al. 2005. Labelling of cells with quantum dots. *Nanotechnology* 16(2), pp. R9-R25.

Parish, C. R. 1999. Fluorescent dyes for lymphocyte migration and proliferation studies. *Immunology and Cell Biology* 77(6), pp. 499-508.

Paruthiyil, S. et al. 2009. Drug and Cell Type-Specific Regulation of Genes with Different Classes of Estrogen Receptor beta-Selective Agonists. *PLoS One* 4(7), p. 14.

Paulson, L. D. 2007. Hitachi researchers develop powder-sized RFID chips. *Computer* 40(5), pp. 23-23.

Pautke, C. et al. 2004. Characterization of osteosarcoma cell lines MG-63, Saos-2 and U-2OS in comparison to human osteoblasts. *Anticancer Research* 24(6), pp. 3743-3748.

Pawitan, Y. et al. 2005. False discovery rate, sensitivity and sample size for microarray studies. *Bioinformatics* 21(13), pp. 3017-3024.

Peng, H. C. 2008. Bioimage informatics: a new area of engineering biology. *Bioinformatics* 24(17), pp. 1827-1836.

Plake, C. et al. 2009. GoGene: gene annotation in the fast lane. *Nucleic Acids Research* 37, pp. W300-W304.

Planque, N. 2006. Nuclear trafficking of secreted factors and cell-surface receptors: new pathways to regulate cell proliferation and differentiation, and involvement in cancers. *Cell Communication and Signaling* 4(1), p. 7.

Pluskal, M. G. et al. 1986. IMMOBILON PVDF TRANSFER MEMBRANE - A NEW MEMBRANE SUBSTRATE FOR WESTERN BLOTTING OF PROTEINS. *Biotechniques* 4(3), pp. 272-283.

Pone, E. et al. 2006. Drawing of the hollow all-polymer Bragg fibers. *Optics Express* 14(13), pp. 5838-5852.

Ponten, J. and Saksela, E. 1967. 2 ESTABLISHED IN VITRO CELL LINES FROM HUMAN MESENCHYMAL TUMOURS. *International Journal of Cancer* 2(5), pp. 434-&.

Popp, J. and Strehle, M. 2006. *Biophotonics : visions for better health care.* Weinheim; Chichester: Wiley-VCH ; John Wiley, distributor].

Prasad, P. N. 2004. *Introduction to Biophotonics.* Hoboken, NJ: Wiley-Interscience.

Prasher, D. C. et al. 1992. PRIMARY STRUCTURE OF THE AEQUOREA-VICTORIA GREEN-FLUORESCENT PROTEIN. *Gene* 111(2), pp. 229-233.

Provenzano, P. P. et al. 2009. Shining new light on 3D cell motility and the metastatic process. *Trends in Cell Biology* 19(11), pp. 638-648.

Puck, T. T. and Steffen, J. 1963. LIFE CYCLE ANALYSIS OF MAMMALIAN CELLS .1. A METHOD FOR LOCALIZING METABOLIC EVENTS WITHIN LIFE CYCLE, AND ITS APPLICATION TO ACTION OF COLCEMIDE AND SUBLETHAL DOSES OF X-IRRADIATION. *Biophysical Journal* 3(5), pp. 379-&.

Puers, R. and Ieee 2006. *Sensors and sensorsystems for in vivo monitoring.* New York: Ieee, pp. 6135-6142.

Qian, X. M. et al. 2008. In vivo tumor targeting and spectroscopic detection with surface-enhanced Raman nanoparticle tags. *Nature Biotechnology* 26(1), pp. 83-90.

R_DevelopmentCoreTeam. 2009. *A Language and Environment for Statistical Computing* [Online]. Vienna, Austria: R Foundation for Statistical Computing. Available at: http://www.R-project.org [Accessed: 2010].

Raile, K. et al. 1994. HUMAN OSTEOSARCOMA (U-2 OS) CELLS EXPRESS BOTH INSULIN-LIKE GROWTH-FACTOR-I (IGF-I) RECEPTORS AND INSULIN-LIKE GROWTH FACTOR-II MANNOSE-6-PHOSPHATE (IGF-II/MGP) RECEPTORS AND SYNTHESIZE IGF-II - AUTOCRINE GROWTH-STIMULATION BY IGF-II VIA THE IGF-I RECEPTOR. *Journal of Cellular Physiology* 159(3), pp. 531-541.

Rao, J. H. et al. 2007. Fluorescence imaging in vivo: recent advances. *Current Opinion in Biotechnology* 18(1), pp. 17-25.

Rao, K. V. S. et al. 2005. Antenna design for UHF RFID tags: A review and a practical application. *Ieee Transactions on Antennas and Propagation* 53(12), pp. 3870-3876.

Raval, P. et al. 1996. Expression of bone morphogenetic proteins by osteoinductive and non-osteoinductive human osteosarcoma cells. *Journal of Dental Research* 75(7), pp. 1518-1523.

Receveur, R. A. M. et al. 2007. Microsystem technologies for implantable applications. *Journal of Micromechanics and Microengineering* 17(5), pp. R50-R80.

Recklies, A. D. et al. 2005. Inflammatory cytokines induce production of CHI3L1 by articular chondrocytes. *Journal of Biological Chemistry* 280(50), pp. 41213-41221.

Rees, P. et al. 2010. A transfer function approach to measuring cell inheritance. *submitted to: BMC Systems Biology.*

Resch-Genger, U. et al. 2008. Quantum dots versus organic dyes as fluorescent labels. *Nature Methods* 5(9), pp. 763-775.

Rhee, S. Y. et al. 2008. Use and misuse of the gene ontology annotations. *Nature Reviews Genetics* 9(7), pp. 509-515.

Rieder, C. L. and Maiato, H. 2004. Stuck in division or passing through: What happens when cells cannot satisfy the spindle assembly checkpoint. *Developmental Cell* 7(5), pp. 637-651.

Rieder, C. L. and Palazzo, R. E. 1992. COLCEMID AND THE MITOTIC-CYCLE. *Journal of Cell Science* 102, pp. 387-392.

Rivals, I. et al. 2007. Enrichment or depletion of a GO category within a class of genes: which test? *Bioinformatics* 23(4), pp. 401-407.

Robertson, F. M. et al. 2010. Imaging and Analysis of 3D Tumor Spheroids Enriched for a Cancer Stem Cell Phenotype. *Journal of Biomolecular Screening.*

Rodrigues, M. T. et al. 2008. beta-PVDF Membranes Induce Cellular Proliferation and Differentiation in Static and Dynamic Conditions. In: Marques, A.T. et al. eds. *Advanced Materials Forum Iv.* Vol. 587-588. Stafa-Zurich: Trans Tech Publications Ltd, pp. 72-76.

Rogach, A. L. and Ogris, M. 2010. Near-infrared-emitting semiconductor quantum dots for tumor imaging and targeting. *Current Opinion in Molecular Therapeutics* 12(3), pp. 331-339.

Rosen, A. B. et al. 2007. Finding fluorescent needles in the cardiac haystack: Tracking human mesenchymal stem cells labeled with quantum dots for quantitative in vivo three-dimensional fluorescence analysis. *Stem Cells* 25(8), pp. 2128-2138.

Rothaeusler, K. and Baumgarth, N. 2001. *Assessment of Cell Proliferation by 5-Bromodeoxyuridine (BrdU) Labeling for Multicolor Flow Cytometry.* John Wiley & Sons, Inc.

Rowinsky, E. K. et al. 1990. TAXOL - A NOVEL INVESTIGATIONAL ANTIMICROTUBULE AGENT. *Journal of the National Cancer Institute* 82(15), pp. 1247-1259.

Ruei-Zhen, L. and Hwan-You, C. 2008. Recent advances in three-dimensional multicellular spheroid culture for biomedical research. *Biotechnology Journal* 3(9-10), pp. 1172-1184.

Rumphorst, A. et al. 1994. Optical determination of pH on surfaces using immobilized Fluorescent dyes. *Journal of Fluorescence* 4(1), pp. 45-48.

Russell, P. 2003. Photonic crystal fibers. *Science* 299(5605), pp. 358-362.

Sadar, M. D. et al. 2002. Characterization of a new in vivo hollow fiber model for the study of progression of prostate cancer to androgen independence. *Molecular Cancer Therapeutics* 1(8), pp. 629-637.

Sahai, E. 2007. Illuminating the metastatic process. *Nature Reviews Cancer* 7(10), pp. 737-749.

Salvatori, L. et al. 2009. Down-Regulation of Epidermal Growth Factor Receptor Induced by Estrogens and Phytoestrogens Promotes the Differentiation of U2OS Human Osteosarcoma Cells. *Journal of Cellular Physiology* 220(1), pp. 35-44.

Sartor, M. A. et al. 2010. ConceptGen: a gene set enrichment and gene set relation mapping tool. *Bioinformatics* 26(4), pp. 456-463.

Sauer, C. et al. 2005. Power harvesting and telemetry in CMOS for implanted devices. *Ieee Transactions on Circuits and Systems I-Regular Papers* 52(12), pp. 2605-2613.

Schäfer-Korting, M. et al. 2010. Nanoparticle Technologies for Cancer Therapy.*Drug Delivery*. Vol. 197. Springer Berlin Heidelberg, pp. 55-86.

Scheinberg, D. A. et al. 2010. Conscripts of the infinite armada: systemic cancer therapy using nanomaterials. *Nature Reviews Clinical Oncology* 7(5), pp. 266-276.

Schiff, P. B. et al. 1979. PROMOTION OF MICROTUBULE ASSEMBLY INVITRO BY TAXOL. *Nature* 277(5698), pp. 665-667.

Schiff, P. B. and Horwitz, S. B. 1980. TAXOL STABILIZES MICROTUBULES IN MOUSE FIBROBLAST CELLS. *Proceedings of the National Academy of Sciences of the United States of America-Biological Sciences* 77(3), pp. 1561-1565.

Schmelzer, E. et al. 2010. Three-Dimensional Perfusion Bioreactor Culture Supports Differentiation of Human Fetal Liver Cells. *Tissue Engineering Part A* 16(6), pp. 2007-2016.

Schon, M. et al. 2008. KINK-1, a novel small-molecule inhibitor of IKK beta, and the susceptibility of melanoma cells to antitumoral treatment. *Journal of the National Cancer Institute* 100(12), pp. 862-875.

Schulze-Tanzil, G. 2009. Activation and dedifferentiation of chondrocytes: Implications in cartilage injury and repair. *Annals of Anatomy-Anatomischer Anzeiger* 191(4), pp. 325-338.

Schulze, H. et al. 2009. Multiplexed optical pathogen detection with lab-on-a-chip devices. *Journal of Biophotonics* 2(4), pp. 199-211.

Shan, L. 2010. *Polyethylene glycol–coated (PEG5000) gold nanoparticles* [Online]. Molecular Imaging and Contrast Agent Database (MICAD), Bethesda (MD): National Library of Medicine (US). Available at: http://www.ncbi.nlm.nih.gov/bookshelf/br.fcgi?book=micad&part=PEG-gold-NP#PEG-gold-NP.REF.1 [Accessed: 2010 NCBI; 2004-2010].

Shaner, N. C. et al. 2005. A guide to choosing fluorescent proteins. *Nature Methods* 2(12), pp. 905-909.

Shannon, P. et al. 2003. Cytoscape: A software environment for integrated models of biomolecular interaction networks. *Genome Research* 13(11), pp. 2498-2504.

Shapiro, H. M. 2004. Excitation and emission spectra of common dyes. *Curr Protoc Cytom* Chapter 1, p. Unit 1 19.

Sharma, S. V. et al. 2010. Cell line-based platforms to evaluate the therapeutic efficacy of candidate anticancer agents. *Nature Reviews Cancer* 10(4), pp. 241-253.

Shcherbo, D. et al. 2007. Bright far-red fluorescent protein for whole-body imaging. *Nature Methods* 4(9), pp. 741-746.

Sherwood, S. W. et al. 1994a. CYCLIN B1 EXPRESSION IN HELA S3 CELLS STUDIED BY FLOW-CYTOMETRY. *Experimental Cell Research* 211(2), pp. 275-281.

Sherwood, S. W. et al. 1994b. INDUCTION OF APOPTOSIS BY THE ANTITUBULIN DRUG COLCEMID - RELATIONSHIP OF MITOTIC CHECKPOINT CONTROL TO THE INDUCTION OF APOPTOSIS IN HELA S3 CELLS. *Experimental Cell Research* 215(2), pp. 373-379.

Shu, X. K. et al. 2009. Mammalian Expression of Infrared Fluorescent Proteins Engineered from a Bacterial Phytochrome. *Science* 324(5928), pp. 804-807.

Siebers, M. C. et al. 2008. The behavior of osteoblast-like cells on various substrates with functional blocking of integrin-beta 1 and integrin-beta 3. *Journal of Materials Science-Materials in Medicine* 19(2), pp. 861-868.

Sihn, C. R. et al. 2005. Sec13 induces genomic instability in U2OS cells. *Experimental and Molecular Medicine* 37(3), pp. 255-260.

Silvestre, O. F. et al. eds. 2009. *Hollow fiber: a biophotonic implant for live cells.* Imaging, Manipulation, and Analysis of Biomolecules, Cells, and Tissues VII. San Jose, CA, USA. SPIE.

Sims, J. T. and Plattner, R. 2009. MTT assays cannot be utilized to study the effects of STI571/Gleevec on the viability of solid tumor cell lines. *Cancer Chemotherapy and Pharmacology* 64(3), pp. 629-633.

Sitterding, S. M. et al. 2008. alpha B-crystallin: A novel marker of invasive basal-like and metaplastic breast carcinomas. *Annals of Diagnostic Pathology* 12(1), pp. 33-40.

Sklar, L. A. et al. 2007. Flow cytometry for drug discovery, receptor pharmacology and high-throughput screening. *Current Opinion in Pharmacology* 7(5), pp. 527-534.

Sluder, G. 1979. ROLE OF SPINDLE MICROTUBULES IN THE CONTROL OF CELL-CYCLE TIMING. *Journal of Cell Biology* 80(3), pp. 674-691.

Smith, P. J. et al. 2000. Characteristics of a novel deep red/infrared fluorescent cell-permeant DNA probe, DRAQ5, in intact human cells analyzed by flow cytometry, confocal and multiphoton microscopy. *Cytometry* 40(4), pp. 280-291.

Smith, P. J. et al. 2007a. Cytomics and drug development. *Cytometry Part A* 71A(6), pp. 349-351.

Smith, P. J. et al. 2009. Cytomics and cellular informatics - coping with asymmetry and heterogeneity in biological systems. *Drug Discovery Today* 14(5-6), pp. 271-277.

Smith, P. J. et al. 2007b. Mitotic bypass via an occult cell cycle phase following DNA topoisomerase II inhibition in p53 functional human tumor cells. *Cell Cycle* 6(16), pp. 2071-2081.

Smith, P. J. et al. 2002. DNA damage-induced Zn2+ (i) transients: correlation with cell cycle arrest and apoptosis in lymphoma cells. *American Journal of Physiology-Cell Physiology* 283(2), pp. C609-C622.

Smith, P. J. et al. 1999. A novel cell permeant and far red-fluorescing DNA probe, DRAQ5, for blood cell discrimination by flow cytometry. *Journal of Immunological Methods* 229(1-2), pp. 131-139.

Smyth, G. 2004. Linear models and empirical bayes methods for assessing differential expression in microarray experiments. *Statistical applications in genetics and molecular biology* 3(1).

Smyth, G. 2009. *limma: Linear Models for Microarray Data (BioC 2.5 limma package)* [Online]. Available at: http://www.bioconductor.org/packages/release/bioc/html/limma.html [Accessed: 2010

Smyth, G. K. et al. 2005. Limma: linear models for microarray data.*Bioinformatics and Computational Biology Solutions using R and Bioconductor.* Springer, New York, pp. 397-420.

Snow, C. 2004. Flow cytometer electronics. *Cytometry Part A* 57A(2), pp. 63-69.

Soncin, S. et al. 2009. A practical approach for the validation of sterility, endotoxin and potency testing of bone marrow mononucleated cells used in cardiac regeneration in compliance with good manufacturing practice. *Journal of Translational Medicine* 7, p. 9.

Sonee, M. et al. 1998. Taxol inhibits endosomal-lysosomal membrane trafficking at two distinct steps in CV-1 cells. *American Journal of Physiology-Cell Physiology* 275(6), pp. C1630-C1639.

Souza, G. R. et al. 2010. Three-dimensional tissue culture based on magnetic cell levitation. *Nature Nanotechnology* 5(4), pp. 291-296.

Spectrum_Labs. 2010. *Pore Size Chart* [Online]. Spectrum Laboratories, Inc. Available at: http://eu.spectrapor.com/cell/PoreSize.html [Accessed: 2010].

Stossi, F. et al. 2004. Transcriptional profiling of estrogen-regulated gene expression via estrogen receptor (ER) alpha orER beta in human osteosarcoma cells: Distinct and common target genes for these receptors. *Endocrinology* 145(7), pp. 3473-3486.

Stubblef.E and Klevecz, R. 1965. SYNCHRONIZATION OF CHINESE HAMSTER CELLS BY REVERSAL OF COLCEMID INHIBITION. *Experimental Cell Research* 40(3), pp. 660-&.

Subramanian, A. et al. 2005. Gene set enrichment analysis: A knowledge-based approach for interpreting genome-wide expression profiles. *Proceedings of the National Academy of Sciences of the United States of America* 102(43), pp. 15545-15550.

Suggitt, M. and Bibby, M. C. 2005. 50 years of preclinical anticancer drug screening: Empirical to target-driven approaches. *Clinical Cancer Research* 11(3), pp. 971-981.

Suggitt, M. et al. 2004. Characterization of the hollow fiber assay for the determination of microtubule disruption in vivo. *Clinical Cancer Research* 10(19), pp. 6677-6685.

Summers, H. D. et al. eds. 2008. *Cell-population tracking using quantum dots in flow cytometry - art. no. 68650L.* Conference on Nanoscale Imaging, Sensing, and Actuation for Biomedical Applications V. San Jose, CA, Jan 21-23. Spie-Int Soc Optical Engineering.

Sun, T. et al. 2006. Culture of skin cells in 3D rather than 2D improves their ability to survive exposure to cytotoxic agents. *Journal of Biotechnology* 122(3), pp. 372-381.

Svoboda, M. et al. 2010. Steroid hormone metabolizing enzymes in benign and malignant human bone tumors. *Expert Opinion on Drug Metabolism & Toxicology* 6(4), pp. 427-437.

Taggart, B. R. et al. 2004. HIV hollow fiber SCID model for antiviral therapy comparison with SCID/hu model. *Antiviral Research* 63(1), pp. 1-6.

Tarnok, A. et al. 2010. Potential of a Cytomics Top-Down Strategy for Drug Discovery. *Current Medicinal Chemistry* 17(16), pp. 1719-1729.

Taylor, E. W. 1965. MECHANISM OF COLCHICINE INHIBITION OF MITOSIS .I. KINETICS OF INHIBITION AND BINDING OF H3-COLCHICINE. *Journal of Cell Biology* 25(1P2), pp. 145-&.

Temmink, O. H. et al. 2007. The hollow fibre assay as a model for in vivo pharmacodynamics of fluoropyrimidines in colon cancer cells. *British Journal of Cancer* 96(1), pp. 61-66.

ter Brugge, P. J. et al. 2002. Initial interaction of U2OS cells with noncoated and calcium phosphate coated titanium substrates. *Journal of Biomedical Materials Research* 61(3), pp. 399-407.

Terry, N. H. A. and White, R. A. 2001. Cell cycle kinetics estimated by analysis of bromodeoxyuridine incorporation.*Methods in Cell Biology, Vol 63*. Vol. 63. San Diego: Academic Press Inc, pp. 355-374.

Thanos, C. G. et al. 2010. Microencapsulated Choroid Plexus Epithelial Cell Transplants for Repair of the Brain.*Therapeutic Applications of Cell Microencapsulation*. Vol. 670. Berlin: Springer-Verlag Berlin, pp. 80-91.

Thomas, N. 2003. Lighting the circle of life: fluorescent sensors for covert surveillance of the cell cycle. *Cell cycle (Georgetown, Tex.)* 2(6), pp. 545-549.

Thomas, N. et al. 2005. Characterization and gene expression profiling of a stable cell line expressing a cell cycle GFP sensor. *Cell Cycle* 4(1), pp. 191-195.

Torchilin, V. 2009. Multifunctional and stimuli-sensitive pharmaceutical nanocarriers. *European Journal of Pharmaceutics and Biopharmaceutics* 71(3), pp. 431-444.

Torres, K. and Horwitz, S. B. 1998. Mechanisms of taxol-induced cell death are concentration dependent. *Cancer Research* 58(16), pp. 3620-3626.

Trougakos, I. P. et al. 2010. Genome-wide transcriptome profile of the human osteosarcoma Sa OS and U-2 OS cell lines. *Cancer Genetics and Cytogenetics* 196(2), pp. 109-118.

Troyk, P. R. 1999. Injectable electronic identification, monitoring, and stimulation systems. *Annual Review of Biomedical Engineering* 1, pp. 177-209.

Tsien, R. Y. 1998. The green fluorescent protein. *Annual Review of Biochemistry* 67, pp. 509-544.

Tuchin, V. V. 2007. *Tissue optics : light scattering methods and instruments for medical diagnosis*. Bellingham, Wash.: SPIE Press.

Tuchin, V. V. et al. 2009. Towards in vivo flow cytometry. *Journal of Biophotonics* 2(8-9), pp. 457-458.

Twigg, R. S. 1945. OXIDATION-REDUCTION ASPECTS OF RESAZURIN. *Nature* 155(3935), pp. 401-402.

Tzvetkova-Chevolleau, T. et al. 2008. The motility of normal and cancer cells in response to the combined influence of the substrate rigidity and anisotropic microstructure. *Biomaterials* 29(10), pp. 1541-1551.

Uchiyama, S. et al. 2004. Protein composition of human metaphase chromosomes analyzed by two-dimensional electrophoreses. *Cytogenetic and Genome Research* 107(1-2), pp. 49-54.

Ulbricht, M. 2006. Advanced functional polymer membranes. *Polymer* 47(7), pp. 2217-2262.

Uludag, H. et al. 2000. Technology of mammalian cell encapsulation. *Advanced Drug Delivery Reviews* 42(1-2), pp. 29-64.

Urbani, L. et al. 1995. DISSOCIATION OF NUCLEAR AND CYTOPLASMIC CELL-CYCLE PROGRESSION BY DRUGS EMPLOYED IN CELL SYNCHRONIZATION. *Experimental Cell Research* 219(1), pp. 159-168.

van Rossum, M. C. W. and Nieuwenhuizen, T. M. 1999. Multiple scattering of classical waves: microscopy, mesoscopy, and diffusion. *Reviews of Modern Physics* 71(1), pp. 313-371.

van Staveren, W. C. G. et al. 2009. Human cancer cell lines: Experimental models for cancer cells in situ? For cancer stem cells? *Biochimica Et Biophysica Acta-Reviews on Cancer* 1795(2), pp. 92-103.

Velasco-Garcia, M. N. 2009. Optical biosensors for probing at the cellular level: A review of recent progress and future prospects. *Seminars in Cell & Developmental Biology* 20(1), pp. 27-33.

Vellonen, K. S. et al. 2004. Substrates and inhibitors of efflux proteins interfere with the MTT assay in cells and may lead to underestimation of drug toxicity. *European Journal of Pharmaceutical Sciences* 23(2), pp. 181-188.

Vermes, I. et al. 1995. A NOVEL ASSAY FOR APOPTOSIS - FLOW CYTOMETRIC DETECTION OF PHOSPHATIDYLSERINE EXPRESSION ON EARLY APOPTOTIC CELLS USING FLUORESCEIN-LABELED ANNEXIN-V. *Journal of Immunological Methods* 184(1), pp. 39-51.

Vicent, G. P. et al. 2006. Induction of progesterone target genes requires activation of Erk and Msk kinases and phosphorylation of histone H3. *Molecular Cell* 24(3), pp. 367-381.

Vollmers, C. et al. 2008. A High-Throughput Assay for siRNA-Based Circadian Screens in Human U2OS Cells. *PLoS One* 3(10), p. 6.

Vordermark, D. et al. 2001. Green fluorescent protein is a suitable reporter of tumor hypoxia despite an oxygen requirement for chromophore formation. *Neoplasia* 3(6), pp. 527-534.

Voura, E. B. et al. 2004. Tracking metastatic tumor cell extravasation with quantum dot nanocrystals and fluorescence emission-scanning microscopy. *Nature Medicine* 10(9), pp. 993-998.

Voytik-Harbin, S. L. et al. 1998. Application and evaluation of the alamarBlue assay for cell growth and survival of fibroblasts. *In Vitro Cellular & Developmental Biology-Animal* 34(3), pp. 239-246.

Wagnieres, G. A. et al. 1998. In vivo fluorescence spectroscopy and imaging for oncological applications. *Photochemistry and Photobiology* 68(5), pp. 603-632.

Walker, J. M. et al. 2001. In Vitro Invasion Assay Using Matrigel®.*Metastasis Research Protocols*. Vol. 58. Humana Press, pp. 61-70.

Wang, D. L. et al. 1999. Preparation and characterization of polyvinylidene fluoride (PVDF) hollow fiber membranes. *Journal of Membrane Science* 163(2), pp. 211-220.

Wang, G. et al. 2006. Identification of genes targeted by the androgen and PKA signaling pathways in prostate cancer cells. *Oncogene* 25(55), pp. 7311-7323.

Wang, G. et al. 2008. Crosstalk between the Androgen Receptor and beta-Catenin in Castrate-Resistant Prostate Cancer. *Cancer Research* 68(23), pp. 9918-9927.

Wang, L. M. et al. 2005a. Wireless spectroscopic compact photonic explorer for diagnostic optical imaging. *Biomedical Microdevices* 7(2), pp. 111-115.

Wang, R. et al. 2007. Inhibiting proliferation and enhancing chemosensitivity to taxanes in osteosarcoma cells by RNA interference-mediated downregulation of Stathmin expression. *Molecular Medicine* 13(11-12), pp. 567-575.

Wang, T. H. et al. 2000. Paclitaxel-induced cell death - Where the cell cycle and apoptosis come together. *Cancer* 88(11), pp. 2619-2628.

Wang, X. Q. et al. 2005b. Carboxyfluorescein diacetate succinimidyl ester fluorescent dye for cell Labeling. *Acta Biochimica Et Biophysica Sinica* 37(6), pp. 379-385.

Wani, M. C. et al. 1971. PLANT ANTITUMOR AGENTS .6. ISOLATION AND STRUCTURE OF TAXOL, A NOVEL ANTILEUKEMIC AND ANTITUMOR AGENT FROM TAXUS-BREVIFOLIA. *Journal of the American Chemical Society* 93(9), pp. 2325-&.

Watson, D. A. et al. 2008. A flow cytometer for the measurement of Raman spectra. *Cytometry Part A* 73A(2), pp. 119-128.

Watson, D. A. et al. 2009. Spectral Measurements of Large Particles by Flow Cytometry. *Cytometry Part A* 75A(5), pp. 460-464.

Watson, J. V. 1991. *Introduction to flow cytometry.* Cambridge: Cambridge University Press, p. 443p.

Watson, P. 2009. LIVE CELL IMAGING FOR TARGET AND DRUG DISCOVERY. *Drug News & Perspectives* 22(2), pp. 69-79.

Wax, A. and Backman, V. 2010. *Biomedical applications of light scattering.* New York: McGraw-Hill.

Weaver, V. M. et al. 2002. beta 4 integrin-dependent formation of polarized three-dimensional architecture confers resistance to apoptosis in normal and malignant mammary epithelium. *Cancer Cell* 2(3), pp. 205-216.

Weaver, V. M. et al. 1997. Reversion of the malignant phenotype of human breast cells in three-dimensional culture and in vivo by integrin blocking antibodies. *Journal of Cell Biology* 137(1), pp. 231-245.

Weigelt, B. and Bissell, M. J. 2008. Unraveling the microenvironmental influences on the normal mammary gland and breast cancer. *Seminars in Cancer Biology* 18(5), pp. 311-321.

Weissleder, R. and Ntziachristos, V. 2003. Shedding light onto live molecular targets. *Nature Medicine* 9(1), pp. 123-128.

Weissleder, R. and Pittet, M. J. 2008. Imaging in the era of molecular oncology. *Nature* 452(7187), pp. 580-589.

Welsh, D. K. and Kay, S. A. 2005. Bioluminescence imaging in living organisms. *Current Opinion in Biotechnology* 16(1), pp. 73-78.

Westmuckett, A. D. et al. 2000. Fluid flow induces upregulation of synthesis and release of tissue factor pathway inhibitor in vitro. *Arteriosclerosis Thrombosis and Vascular Biology* 20(11), pp. 2474-2482.

Weston, S. A. and Parish, C. R. 1990. NEW FLUORESCENT DYES FOR LYMPHOCYTE MIGRATION STUDIES - ANALYSIS BY FLOW-CYTOMETRY AND FLUORESCENCE MICROSCOPY. *Journal of Immunological Methods* 133(1), pp. 87-97.

White, N. S. and Errington, R. J. 2005. Fluorescence techniques for drug delivery research: theory and practice. *Advanced Drug Delivery Reviews* 57(1), pp. 17-42.

Wilson, C. L. and Miller, C. J. 2005. Simpleaffy: a BioConductor package for Affymetrix Quality Control and data analysis. *Bioinformatics* 21(18), pp. 3683-3685.

Wilson, R. et al. 2006. Encoded microcarriers for high-throughput multiplexed detection. *Angewandte Chemie-International Edition* 45(37), pp. 6104-6117.

Wilson, T. and Hastings, J. W. 1998. Bioluminescence. *Annual Review of Cell and Developmental Biology* 14, pp. 197-230.

Wlodkowic, D. et al. 2009. Biological Implications of Polymeric Microdevices for Live Cell Assays. *Analytical Chemistry* 81(23), pp. 9828-9833.

Wojakowski, W. et al. 2009. Mobilization of Bone Marrow-Derived Oct-4(+) SSEA-4(+) Very Small Embryonic-Like Stem Cells in Patients With Acute Myocardial Infarction. *Journal of the American College of Cardiology* 53(1), pp. 1-9.

Workman, V. L. et al. 2007. Microfluidic chip-based synthesis of alginate microspheres for encapsulation of immortalized human cells. *Biomicrofluidics* 1(1), p. 9.

Wu, Y. et al. 2007. The development of quantum dot calibration beads and quantitative multicolor bioassays in flow cytometry and microscopy. *Analytical Biochemistry* 364(2), pp. 180-192.

Xia, X. Q. et al. 2009. WebArrayDB: cross-platform microarray data analysis and public data repository. *Bioinformatics* 25(18), pp. 2425-2429.

Xin, W. H. et al. 2010. Study of a wireless power transmission system for an active capsule endoscope. *International Journal of Medical Robotics and Computer Assisted Surgery* 6(1), pp. 113-122.

Xin, Z. F. et al. 2009. Risedronate inhibits human osteosarcoma cell invasion. *Journal of Experimental & Clinical Cancer Research* 28, p. 8.

Xing, Y. et al. 2009. Semiconductor Quantum Dots for Biosensing and In Vivo Imaging. *Ieee Transactions on Nanobioscience* 8(1), pp. 4-12.

Yamada, K. M. and Cukierman, E. 2007. Modeling tissue morphogenesis and cancer in 3D. *Cell* 130(4), pp. 601-610.

Yamazoe, H. and Iwata, H. 2006. Efficient generation of dopaminergic neurons from mouse embryonic stem cells enclosed in hollow fibers. *Biomaterials* 27(28), pp. 4871-4880.

Yang, K. et al. 2009. Effect of Peptide-Conjugated Near-Infrared Fluorescent Quantum Dots (NIRF-QDs) on the Invasion and Metastasis of Human Tongue Squamous Cell Carcinoma Cell Line Tca8113 in Vitro. *International Journal of Molecular Sciences* 10(10), pp. 4418-4427.

Yang, T. L. et al. 2010. Biomaterial mediated epithelial-mesenchymal interaction of salivary tissue under serum free condition. *Biomaterials* 31(2), pp. 288-295.

Yao, H. Q. et al. 2007. Quantum dot/bioluminescence resonance energy transfer based highly sensitive detection of proteases. *Angewandte Chemie-International Edition* 46(23), pp. 4346-4349.

Yavari, N. 2006. *Optical spectroscopy for tissue diagnostics and treatment control.* University of Bergen.

Ye, H. et al. 2007. Studies on the use of hollow fibre membrane bioreactors for tissue generation by using rat bone marrow fibroblastic cells and a composite scaffold. *Journal of Materials Science-Materials in Medicine* 18(4), pp. 641-648.

Yong, K. T. et al. 2009. Multifunctional nanoparticles as biocompatible targeted probes for human cancer diagnosis and therapy. *Journal of Materials Chemistry* 19(27), pp. 4655-4672.

Yu, Y. et al. 2004. Differential expression of osteogenic factors associated with osteoinductivity of human osteosarcoma cell lines. *Journal of Biomedical Materials Research Part A* 70A(1), pp. 122-128.

Zhang, G. H. et al. 1996. An enhanced green fluorescent protein allows sensitive detection of gene transfer in mammalian cells. *Biochemical and Biophysical Research Communications* 227(3), pp. 707-711.

Zhang, G. J. et al. 2007. Optical Imaging of tumor cells in hollow fibers: Evaluation of the antitumor activities of anticancer drugs and target validation. *Neoplasia* 9(8), pp. 652-661.

Zhang, G. J. et al. 2008a. Bioluminescence imaging of hollow fibers in living animals: its application in monitoring molecular pathways. *Nature Protocols* 3(5), pp. 891-899.

Zhang, G. J. and Kaelin, W. G. 2005. Bioluminescent imaging of ubiquitin ligase activity: Measuring cdk2 activity in vivo through changes in p27 turnover.*Ubiquitin and Protein Degradation, Pt B.* Vol. 399. San Diego: ELSEVIER ACADEMIC PRESS INC, pp. 530-+.

Zhang, G. J. et al. 2004. Bioluminescent imaging of Cdk2 inhibition in vivo. *Nature Medicine* 10(6), pp. 643-648.

Zhang, J. et al. 2008b. Intratumoral Epiregulin Is a Marker of Advanced Disease in Non-Small Cell Lung Cancer Patients and Confers Invasive Properties on EGFR-Mutant Cells. *Cancer Prevention Research* 1(3), pp. 201-207.

Zhang, Y. et al. 2006a. Time-dependent photoluminescence blue shift of the quantum dots in living cells: Effect of oxidation by singlet oxygen. *Journal of the American Chemical Society* 128(41), pp. 13396-13401.

Zhang, Y. et al. 2006b. HaloTag protein-mediated site-specific conjugation of bioluminescent proteins to quantum dots. *Angewandte Chemie-International Edition* 45(30), pp. 4936-4940.

Zhang, Y. W. et al. 2003. A novel route for connexin 43 to inhibit cell proliferation: Negative regulation of S-Phase kinase-associated protein (Skp 2). *Cancer Research* 63(7), pp. 1623-1630.

Zhu, J. J. et al. 2005. The tumor suppressor p33(ING1b) enhances taxol-induced apoptosis by p53-dependent pathway in human osteosarcoma U2OS cells. *Cancer Biology & Therapy* 4(1), pp. 39-47.

Zhu, Y. R. et al. 2008. EzArray: A web-based highly automated Affymetrix expression array data management and analysis system. *Bmc Bioinformatics* 9, p. 10.

Zimmer, M. 2002. Green fluorescent protein (GFP): Applications, structure, and related photophysical behavior. *Chemical Reviews* 102(3), pp. 759-781.

Zucchini, C. et al. 2008. Apoptotic genes as potential markers of metastatic phenotype in human osteosarcoma cell lines. *International Journal of Oncology* 32(1), pp. 17-31.

# Appendix I

# List of Thesis related publications

## APPENDIX I: LIST OF THESIS RELATED PUBLICATIONS

# Appendix I-A

(Silvestre et al. 2009)

**Silvestre**, O. F.; Holton, M. D.; Summers, H. D.; Smith, P. J.; Errington, R. J. In *Hollow fiber: a biophotonic implant for live cells*, Imaging, Manipulation, and Analysis of Biomolecules, Cells, and Tissues VII, San Jose, CA, USA, 2009; SPIE: San Jose, CA, USA, **2009**; pp 71820V-11.

# Hollow fiber: a biophotonic implant for live cells

Oscar F. Silvestre*[a], Mark D. Holton[b], Huw D. Summers[b], Paul J. Smith [a], Rachel J. Errington [a]
[a]School of Medicine, Heath Park, Cardiff University, Cardiff, CF14 4XN, UK;
[b]Multi-disciplinary Nanotechnology Centre, Swansea University, Swansea, SA2 8PP, UK.

## ABSTRACT

The technical objective of this study has been to design, build and validate biocompatible hollow fiber implants based on fluorescence with integrated biophotonics components to enable in fiber kinetic cell based assays. A human osteosarcoma *in vitro* cell model fiber system has been established with validation studies to determine in fiber cell growth, cell cycle analysis and organization in normal and drug treated conditions. The rationale for implant development have focused on developing benchmark concepts in standard monolayer tissue culture followed by the development of *in vitro* hollow fiber designs; encompassing imaging with and without integrated biophotonics. Furthermore the effect of introducing targetable biosensors into the encapsulated tumor implant such as quantum dots for informing new detection readouts and possible implant designs have been evaluated. A preliminary micro/macro imaging approach has been undertaken, that could provide a mean to track distinct morphological changes in cells growing in a 3D matrix within the fiber which affect the light scattering properties of the implant. Parallel engineering studies have showed the influence of the optical properties of the fiber polymer wall in all imaging modes. Taken all together, we show the basic foundation and the opportunities for multi-modal imaging within an *in vitro* implant format.

**Keywords:** hollow fiber implant, multi-modal imaging, nanoparticles, quantum dots

## 1. INTRODUCTION

Several *in vitro* and *in vivo* tumour models are used in screening programmes to determine the potential of anticancer agents. Since 1990, the National Cancer Institute (NCI) has an *in vitro* screening programme of a 60 cell line panel to define novel anticancer agents. Widely used test systems include human tumor cells grown in culture or grown as xenografts in murine hosts. As a testament to the importance of currently used xenograft modes, no currently accepted anticancer compound has failed in xenograft testing [1]. Although xenograft approaches have proved to generate highly valuable parameters and descriptors, and recent chemoinformatics analysis offers an effective means to identify compound classes with superior efficacy and reduced toxicity; however xenograft studies and trials are accompanied by limitations like high costs associated with large-scale screening, time, and implications on the number of animals required [2-4]. Therefore further evaluation on *in vivo* model systems was the required [2]. To address this problem, Hollingshead *et al.* [4] have developed the Hollow Fiber Assay (HFA). This *in vivo* assay involves the growth of tumor cells within biocompatible polyvinylidene fluoride (PVDF) hollow fibers (HF) implants (Fig. 1), permeable to substances with a molecular weight <500 000 Da, surgically implanted in mice at the intraperitoneal or/and subcutaneous sites. The mice are treated with test compound, fibers excised and analyzed for cell viability/proliferation. The compounds identified as active are subsequent tested using xenograft models [2-4].

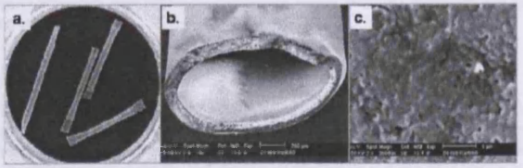


Fig. 1. Empty hollow fiber (HF). (a) Close ~20 mm HF heat sealed at both ends in a 35 mm diameter plate well. SEM images (b) cross-section, inner diameter 1.0 mm, outer diameter 1.2 mm; (c) detail of the porous on the outer wall surface.

* silvestreor@cardiff.ac.uk; phone +44 (0)29 206 87301; fax +44 (0)29 206 87343;





Please verify that (1) all pages are present, (2) all figures are acceptable, (3) all fonts and special characters are correct, and (4) all text and figures fit within the margin lines shown on this review document. Return to your MySPIE ToDo list and approve or disapprove this submission.

The HFA provides a rapid, *in vivo* routinely applied drug screening approach based currently on cell viability and cell counts. However the hollow fiber (HF) also offers the potential to deliver and retrieve non-contaminated tumor cells from the fiber accessible to a wide range of cellular analyses [5, 6], in simple terms the HF offers the ability to "emulate" a tumor system, but importantly also provides a transferable system between *in vitro* and *in vivo* drug screening. Though currently it lacks the high-throughput spectrum of *in vitro* techniques, in part, because is necessary to retrieve the encapsulated cells from inside the fiber and the host. However, the advent of advanced imaging technologies offers new opportunities that allow non invasive kinetic *in vivo* readouts measurements. The studies of Hollingshead *et al.* [7] and Zhang *et al.* [8] with bioluminescence luciferase reporters are some of the few that have used HFA in conjunction with imaging. Luminescence imaging presents some advantages compared to fluorescence since excitation light is not required and the absence of autofluorescence emission from surrounding tissue. However, luminescence has limitations, as the emitted light will be scattered and absorbed by the tissue [7].

The main objective of this study is to develop non-evasive and real time imaging approaches to evaluate drug responses of cells encapsulated inside the HF without having to remove them from the host. The hypothesis is that this can be measured by using a range of reporters, in conjugation with new in fiber biophotonic innovative delivery/detection light features based on fluorescence, absorbance and light scattering. The outcome of such an approach is to increase the data throughput (spatial and temporal parameters) from the HF encapsulation. In addition the aim is to address the need for an *in vitro* and *in vivo* transferable system hence bridging the gaps in pre-clinical screening.

## 2. METHODOLOGY

The cell work was performed using the human osteosarcoma cell line, U-2 OS (ATCC HTB-96) stably transfected with cyclin B1-EGFP, a G2M cell cycle phase marker (GE Healthcare, UK). The cells were cultured under G418 (1000ug/ml) selection in McCoys 5A modified medium (Sigma) supplemented with 10 % foetal calf serum, 2mM glutamine, 100 units/ml penicillin and 100 µg/ml streptomycin at 37°C and 5 % $CO_2$.

### 2.1 HF cell seeding and growth characterization

The HF seeding was primarily based on the protocols from Hollingshead *et al.* [4] and Suggitt *et al.* [6] with some in-house adaptation. Briefly, the HF (S932010, Cellmax® Implant Membranes, Spectrum Europe BV, NL) supplied dry, length approx. 340 mm, were pre-wetted with 70% ethanol for minimum 48h and washed with sterile water. The cells were harvested by standard trypsinisation, resuspended at a density of approx 1.0-1.5 x$10^6$ cells/ml and injected into the HF using cold medium supplemented with 25 mM HEPES to stabilizes the pH and to minimize cell stress. Following this, the loaded HF was immediately heat-sealed and cut in to section of 20 or 40 mm. The resultant cell seeded HF sections were washed to remove any cells external to the fiber and incubated into tissue culture dishes or plates in growth medium. The prediction is that the cells will attach to the fiber inner wall, grow and divide as an encapsulated system.

At different time points after seeding (day 2, 5 and 8) the HF and cells inside were analyzed to determine cell growth, cell spatial organization inside the HF and finally cell cycle characteristics using flow cytometry under control conditions and post 24h treatment with the microtubule stabilizing drug Taxol, causing cells to stall and arrest in mitosis.

The samples were prepared for scanning electron microscopy (SEM) by fixation with 2% glutaraldehyde in phosphate buffer saline (PBS), pH 7.4 and dehydrated with graded concentrations of ethanol. The HF were than carefully cut longitudinally using a scalpel and the resultant sections were critical point dried and sputter coated with gold. Samples were analyzed with a Raith-50 EBL (Raith GmbH, Germany).

For flow cytometry analysis the HF were flushed, cut in approx. 2 mm sections and placed in trypsin to promote the detachment of the cells adherent to the HF inner wall, after centrifugation the cells were run live on a Becton Dickinson FACSCalibur for cell cycle analysis using DRAQ5 [8] for DNA content together with the cyclin B1-GFP reporter.

### 2.2 Imaging of GFP cells inside the HF and fiber emission spectra

In order to determine the potential for imaging GFP fluorescent cells inside the HF, different concentration ($5.0x10^5$ cells/ml, $2.0x10^6$ cells/ml and $5.3x10^6$ cells/ml) of U-2 OS cyclin B1-GFP cells were seeded in to HF as described above and imaged live using the IVIS200 *in vivo* animal imaging system (Xenogen, now Caliper Life Sciences, USA).

The emission fluorescence spectra of the HF was determined with a luminescence spectrometer Perkin-Elmer LS50B.

### 2.3 Imaging of QD label cells within the HF

Fluorescent nanoparticles CdTe/ZnS quantum dots emission 705 nm (QD705) were used to label the cells in order to evaluate their detection potential within the HF. Cells were labelled with commercially available targeted nanocrystals using the Qtracker® 705 Cell Labeling Kit (Q25061MP, Invitrogen) at 4 nM, briefly the QD labeling solution was added to the cells and incubated for 1 hour at 37°C before washing twice with full growth medium.

The above protocol was used to label adherent cells on previously seeded and longitudinally cut open HF on day 5, after the labeling with QD705 the sections were incubated for 24h. For imaging the HF cut sections were mounted in medium supplemented with 25 mM HEPES using silicone multi-well perfusion chamber (Z379131, Sigma) on a 24 x 40mm No 1.5 coverslip, sealed with clear nail polish and imaging live on an upright confocal laser scanning microscope (Nikon Eclipse E600FN, Bio-Rad Radiance 2100 Rainbow) with an 5x 0.15 NA objective.

Cells on T-25 plates were also labelled with QD705, incubated for 24h, trypsinized and seeded in to a HF. These closed HFs were placed on black well plates in 25 mM HEPES medium and imaging live on the IVIS200 animal imaging system and on an inverted fluorescence microscope (Axiovert S100TV, Zeiss) with an 5x 0.15NA lens, equipped with a Nuance FLEX multispectral camera (Cambridge Research & Instrumentation, USA), in order to evaluate the potential to macro/micro imaging QD705 label cells inside a close HF.

### 2.4 HF direct optical fiber LED excitation model system

To assess the effect of direct optical fiber LED excitation from one end of the HF, a basic model system was constructed and tested using encapsulated red 15 µm fluorescent beads (ex645/em680nm) (F-8843, Invitrogen) suspended in alginate gel.

The 15 µm fluorescent beads were added to a 2% alginate to a concentration of $5.0x10^5$ beads/ml, the mixture was injected in the HF submersed in a 3.5% $CaCl_2$ solution, and polymerized for 20 min followed by heat sealing one or both ends of the HF, controls with alginate only were also prepared. The roughly uniformly distribution of 15 µm beads HF encapsulated matrix was also analyzed by confocal laser scanning microscopy on a Nikon TE300 Inverted, Bio-Rad Radiance2000MP with a 10x 0.45NA objective, to evaluate scattering and optical penetration through the HF wall.

The biophotonicic model system was constructed using a 650nm LED (XR65-R5P0U, Roithner LaserTechnik) like a light source, the light was delivered using a 1mm outer diameter plastic optical fiber (NT02-544, Edmund Optics) to the HF fitted with the help off Tygon tube (WZ-06418-04, Cole Parme) inside a black holder "phantom" made of a gel matrix of 1% agarose (Fig. 9). The system was placed inside IVIS200 animal imaging system to study and compare the fluorescent emission and scattering/absorbance of the HF alginate 15 µm beads matrix under LED light excitation versus the standard instrument illumination.

## 3. RESULTS

The first and most important step was to fully characterize the selected U-2 OS cyclin B1-GFP model in relation to in fiber cell growth, cell-cell and cell-substrate organization inside the HF and further to determine the consequences on cell cycle state.

### 3.1 HF cell growth characterization (SEM, FACS)

The seeding density at a concentration of 1.0-1.5 $x10^6$ cells/ml provided exponential growth of the in fiber U-2 OS culture during the first 8 days of the assay. The growth in fiber was initially assessed visually by analyzing the SEM images of the longitudinally cut HF, 2 days after seeding (Fig. 2.a) it was possible to verify the seeding positions of the cells after injection in the HF and subsequent attachment and growth along the HF inner wall.





Please verify that (1) all pages are present, (2) all figures are acceptable, (3) all fonts and special characters are correct, and (4) all text and figures fit within the margin lines shown on this review document. Return to your MySPIE ToDo list and approve or disapprove this submission.

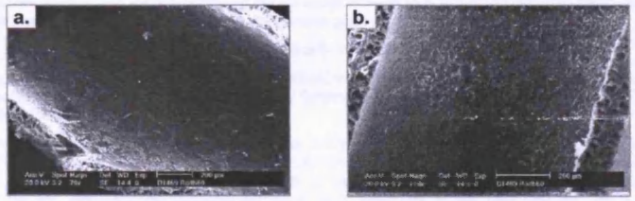


Fig. 2. SEM images of longitudinally cut open HF. (a) 2 days and (b) 5 days after seeding at a density of $1.0x10^6$ cells/ml (U-2 OS cyclin B1-GFP).

Figure 2.b showed that after 5 days the cells spread across all the inner wall growing as an adherent layer. Observing the morphology and spread of the cell monolayer (Fig 3.a) after 8 days showed that the cells completely cover the HF inner wall, this actually alleviated the initial suspicions that the cells would only accumulate in clonal islands were initial contact and spread on the HF was made. This indicated that the HF surface provided a suitable substrate for cell growth and spreading.; note the presence of round shaped cells that corresponded to mitotic cells. The status of the monolayer was further characterized using flow cytometry (Fig. 3.b and 3.c); the cells appeared to be actively cycling with a slight accumulation in G1 compared to normal tissue culture conditions of U-2 OS cells, however the results provided validation of an actively dividing cell population with a sub-population of around 20% in the G2/M phase (Fig. 3.c).

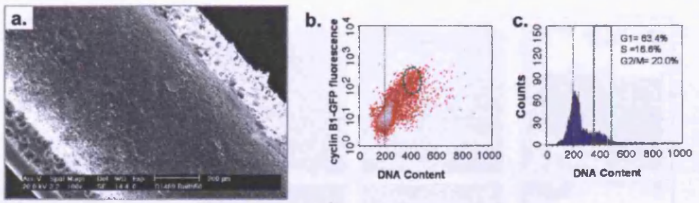


Fig. 3. Cells, seeded at $1.0x10^6$ cells/ml of U-2 OS cyclin B1-GFP, after 8 days in the HF. (a) SEM images of longitudinally cut open HF; Flow cytometry live cell cycle profiling, (b) cyclin B1-GFP fluorescence versus DRAQ5 DNA content (c) DNA histogram to determine compartmental localization of cells through the cell cycle.

The influence of a 24h pre-treatment with the anti-cancer drug (Taxol) is show in Figure 4; this drug acts to perturb the cell cycle, arresting the cells at mitosis (G2/M) followed by cell death. The action of the drug was first confirmed by SEM (Fig. 4.a) where there was high number of rounded cells in mitosis. Confirmed also by the flow cytometry analysis with an increase of the cyclin B1-GFP fluorescence population (Fig. 4.b) compared to control conditions (Fig 3 b.) with no drug treatment, this was further analysed using the cell cycle histogram which indicated a decrease of the G1 population to around 42% and an increase to 41% of the G2/M cells (Fig. 4.c). The characterization of the in fiber cell behavior and organization under normal and drug perturbation conditions was an important step; not only in evaluating the cellular system encapsulated inside the HF but also provided the basic information leading to the incorporation of the imaging and biophotonic components.

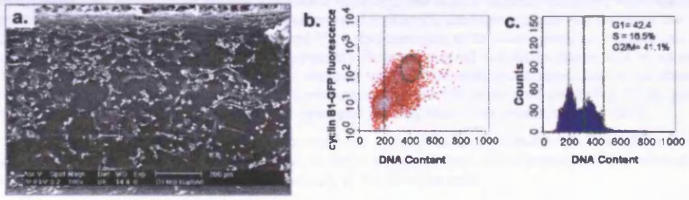


Fig. 4. Cells, $1.0x10^6$ cells/ml of U-2 OS cyclin B1-GFP, 8 days after being seeded in to the HF, with 24 h drug pre-treatment (5 nM Taxol). (a) SEM images of longitudinally cut open HF; Flow cytometry live cell cycle profile, (b) cyclin B1-GFP fluorescence versus DRAQ5 DNA content and (c) DRAQ5 cell cycle DNA histogram.

### 3.2 Optical limitations of the PDVF HF wall

The U-2 OS cyclin B1-GFP cell line was selected to be used as an in fiber cellular model system engineered with a fluorescent GFP cell cycle reporter; with the prospect of imaging and detecting GFP fluorescence of cells encapsulated inside the HF. Therefore further characterization was required to determine the optical properties of the fiber material and dealing with the collective consequences of the PDVF HF wall having autofluorescent, highly reflecting and also highly scattering features, providing low optical penetration and aberrated imaging conditions.

#### 3.2.1 Autofluorescence problems

Different concentrations of live U-2 OS cyclin B1-GFP cells encapsulated in the HF were imaged using the IVIS200 imaging system, together with empty control HF (Fig. 5 a,b,c) there was no obvious difference between the HF loaded with cells and the empty control counterpart (shorter HF). The signal detected appeared to be only background fluorescence from the HFs. In order to confirm the above results HF empty samples were analyzed for their emission spectra under different excitation wavelengths (Fig. 5.d). The typical GFP excitation wavelength of 488 nm corresponded to a high fluorescent emission signal from the HF that interfered with the GFP emission window, this confirms why in Figure 5 a,b,c all the fibers appeared to be fluorescent at these wavelengths.

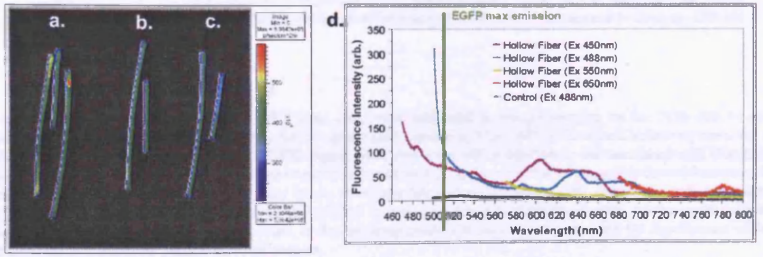


Fig. 5. Fluorescent image, 65x65mm, of HF seeded with live U-2 OS cyclin B1-GFP cells (a) $5.0x10^5$ cells/ml, (b) $2.0x10^6$ cells/ml and (c) $5.3x10^6$ cells/ml, shorter HF correspond to empty controls with no cells. Acquired using a IVIS 200 *in vivo* imaging system using the instrument standard GFP fluorescent filter set, ex445-490/em515-575nm. (d) fluorescence emission spectra of the HF excited at different wavelengths, acquired using a luminescence spectrophotometer Perkin-Elmer LS50B.



Please verify that (1) all pages are present, (2) all figures are acceptable, (3) all fonts and special characters are correct, and (4) all text and figures fit within the margin lines shown on this review document. Return to your MySPIE ToDo list and approve or disapprove this submission.

A formal spectral analysis using high wavelength excitation such as 550 nm and 650 nm showed that the HF material would emit less background signal, confirming the advantage of exciting in the red. This also corresponds to the fact that the far-red/near infrared zone of tissue highest transmission gives minimal autofluorescence [10].

#### 3.2.2 Imaging of QD label cells within longitudinally cut open HP

Following the results discussed in the previous subsection, where the use of far-red/near infrared fluorescent revealed to be potentially advantageous for in fiber cell imaging, fluorescent nanoparticle QD705 were used to label cells using the Qtracker® 705 Cell Labeling Kit.

This study was performed to undertake a preliminary analysis before the encapsulation of QD705 labelled cells in a closed HF. Allowing, first, the visualization of the QD705 labelled cell behavior on the fiber material with a better degree of control and access over the sample. Second, we tested the concept to image the same zone from "inside" and "outside" the HF, evaluating the detected cell signal from either side of the fiber (Fig. 6). The results from this investigation is shown in Figure 6 (Fig. 6.1 top row) and corresponds to a HF section approached from the open top where apparently it is possible to detect the high cyclin B1-GFP fluorescence corresponding to G2/mitotic cells above the HF autofluorescence (Fig. 6.1.a left column). The QD705 signal was also easily detected (Fig. 6.1.b). However, imaging the cells from below the fiber demonstrated to be profoundly difficulty (Fig. 6.2 bottom row), the results showed that under the same imaging settings used and with the 5x 0.15NA lens it was difficult to visualize any structure and even detect the QD705 florescent signal though the HF wall (Fig. 6.2.b), this was also impaired due to using an objective lens with a low NA. The positive aspect was that the protocols used to image the live cell HF preparations provided a potential low resolution alternative to the use of SEM to determine the cell organization of the adherent cells to the PDVF HF wall substrate. Live cells imaging growing and dividing on this substrate are now in progress. In future assays it would be possible to simply cut open longitudinally, mounted fibers and image fixed or live preparations (for short periods), providing validation and spatial organization studies similar to those performed in cell-based screening studies.

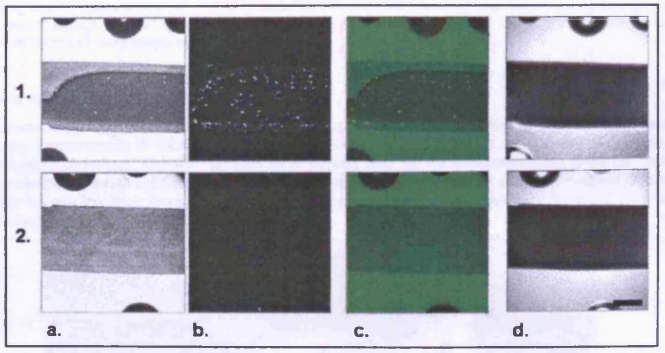


Fig. 6. Confocal images of longitudinal cut open HF with adherent live U-2 OS cyclin B1-GFP cells labelled with QD705, 5x objective lens. HF z projection image from the (row 1) open top and (row 2) from the HF bottom. Laser excitation 488 nm and emission images acquired with (column a) HQ530/60 and (column b) HQ660LP emission filters with the resultant (column c) merge (column d) transmission image. Scale bar 500 µm.

#### 3.2.3 Optical penetration and imaging depth

Following the results in the previous subsection it was then necessary to establish a benchmark system to evaluate the true limitations of the HF. We used fluorescent beads as a test model system embedded in an alginate matrix and placed inside the HF. Therefore, HFs were injected with a 15 µm fluorescent bead mix (ex645/em680nm) in an alginate matrix and confocal laser scanning microscopy was used to collect bead signal at different z depths. Figure 7.1 represents the

control views, where the beads inside the alginate matrix were detected at all z depths. However, when analyzing the same alginate/beads matrix through the PDVF HF wall material a dramatic decrease in signal was demonstrated. In order to detect any bead fluorescent signal from the enclosed HF it was necessary to increase overall laser power and open the iris aperature to 10 mm (Fig 7.2.b and 7.2.c), these pragmatic changes revealed that the excitation was being attenuated and that by opening the confocal aperature the highly scattered emitted light could be detected. Also it was observed that the highest amount of fluorescence emission signal emanated from the HF outer wall level (Fig 7.2.b), penetrating further into the HF led to both a decrease in detected signal and blurring (decreased resolution) (Fig 7.2.c).

The results show that it was possible to detect the fluorescence signal from encapsulated beads in the HF, although due to the higher scattering of the HF wall it was difficult to obtain any significant optical penetration or resolve with detail any fluorescent structures. The best focal point corresponds to the HF outer wall.

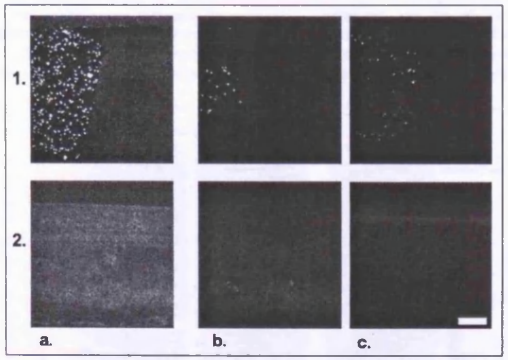


Fig. 7. Confocal laser scanning microscopy , using 10x objective lens, of (row1) 15 µm fluorescent beads ex645/em680nm in alginate matrix extruded from the end of a HF; laser 488nm 30% power, iris 2 mm and laser 637nm 40% power, iris 1mm. (row 2) Closed HF section filled with the same 15 µm beads matrix, laser 488nm 30% power, iris 4 mm and laser 637nm 70% power, iris 10mm. (column a) Projection of all z planes from the "green channel" HQ500LP+HQ530SP emission filter; HQ660LP confocal fluorescent image of the z section (column b) ~0-20 µm and (column c) ~230-250 µm inside the HF. Scale bar 250 µm.

### 3.3 Macro and micro imaging of closed HF

Closed HFs post-24h loaded with live QD705 label cells were subjected to macro imaging on the IVIS 200 *in vivo* system in black plate wells. Figure 8.a shows that using the GFP excitation filter (445-490nm) and collecting emission at 695-770nm, it was possible to detect the QD705 signal from inside the HF in relation to the non-label cells (Fig.8.b). This confirmed, in line with previous discussed results (subsection 3.2.1), the potential of using this far-red biosensor to label cells and detected fluorescent signal from inside an encapsulated tumor implant model. Although, with the current assay parameters the signal to noise ratio of the QD705 is low, and for consideration *in vivo*, further work will be required to improve fluorescent read-outs. Also, in this imaging mode it is important to consider the significance of the concentration of fluorescent particle per unit volume.

The QD705 live cell label HFs were also analyzed by widefield multispectral fluorescent microscopy, in Figure 8.d where it was possible to enhance the effective numerical aperature of the system and to also observe spectral emission profiles of the HF, with the detailed spectra of the a HF background zone emission of the wall and of a QD705 zone (Fig. 8.e). The QD705 fluorescence intensity was moderately above the background in the 700 nm window. The HQ700LP filter image confirms the QD705 signal (Fig. 8.f). Note that the cells were seeded for only 24 hours previously, so they would still be all accumulated on one of the side of the HF.



Please verify that (1) all pages are present, (2) all figures are acceptable, (3) all fonts and special characters are correct, and (4) all text and figures fit within the margin lines shown on this review document. Return to your MySPIE ToDo list and approve or disapprove this submission.

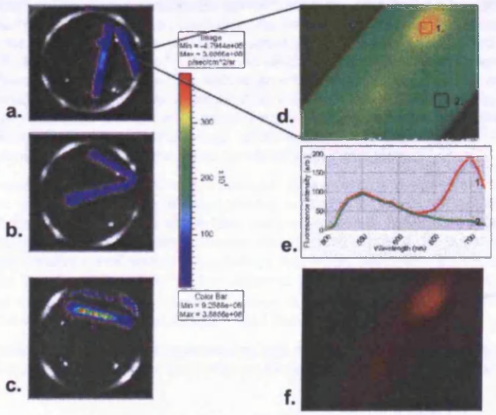


Fig. 8. Closed HFs load with live U-2 OS cyclin B1-GFP cells labelled with QD705. IVIS 200 macro imaging, on a 15.5mm diameter plate well, of (a) cells labelled with QD705, (b) empty cells and (c) $5.0x10^5$ 15µm, ex645/em680nm, beads control / ml, using excitation at 445-490nm and collecting emission at 695-770nm. (d) Multispectral widefield image of the same HF load with QD705 label cells, excitation D480/30x, emission HQ515LP and (e) corresponding spectrally un-mixed analysis to remove the fiber autofluorescence (f) fluorescent HQ700LP image, focused plane at the HF bottom outer wall; both images are 1.7x1.3mm.

### 3.4 HF direct optical fiber LED excitation model system

The results from the previous section demonstrated that although it is possibly to detect the QD705 signal from inside a closed HF, any improvements in increasing the signal to noise ratio, particularly in combination with macro imaging, would be of a great advantage. Therefore the concept of directly coupling the excitation source to the HF bypassing the need for an exterior excitation light should provide an advantage as it avoids all the attenuation effects revealed above. Therefore this became the drive behind the design and tests of a proof of concept model with optical fiber delivery of LED light to the HF (Fig. 9).

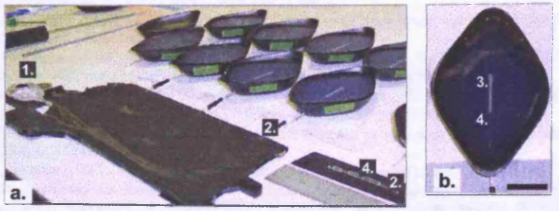


Fig. 9. (a) HF with directly coupled optical fiber LED excitation set up. (1) 650nm LED is the light source, the light is conducted through an (2) 1mm diameter optical fiber to the HF inside the phantom, providing direct illumination from one side of the HF. (b) Detail of the phantom made of 1% agarose gel in a black holder (~80x58mm at top widest points), the (3) HF is connected to the end of the optical fiber fitted with a (4) Tygon tube to help support the insert. Scale bar 20 mm.

The set up in Figure 9 was placed and tested on the IVIS200 *in vivo* imaging system. The instrument 615-665 nm excitation filter source was used to image the HF loaded with 15 µm fluorescent beads (Fig 10.1.a) in the agarose phantom, as before the bead signal was detected. The corresponding fluorescent HF direct optical fiber LED excitation mode produced by comparing with the instrument excitation, low signal mainly localize immediately after the optical fiber insert in the HF (Fig 10.1.b). This may be explained by the light cone coming from the end of the optical fiber that would preferentially excite that zone and that the beads inside the HF were not uniformly excited.

This lead to an evaluation of the 650 nm excitation light pattern coming out from the optical fiber using 575-650 nm emission filter (Fig 10.c) (in other words the transmitted light from the fiber), confirming that indeed the light pattern coming from the optical fiber was not uniform and as a result of the HF side excitation, but also revealed some surprising potential advantages. The "background"/transmitted light signal coming from the HF was inversely related to the previous fluorescent signal. The control HF with no beads (Fig 10.2.c) presented higher signal in relation to the HF with beads (Fig 10.1.c). Beads loaded in the HF highly absorb in the signal in comparison to the control, were there are no beads, generating visible difference between the particulate loaded HF and the un-loaded HF. This differential absorbance or perhaps scatter signal could provide a means for quantifying increases in cell mass/growth inside the 3D HF matrix or/and track morphological cell changes that would alter their absorbance/scatter properties. Also the HF LED side excitation under certain parameters could provide additional advantages over exterior light excitation.

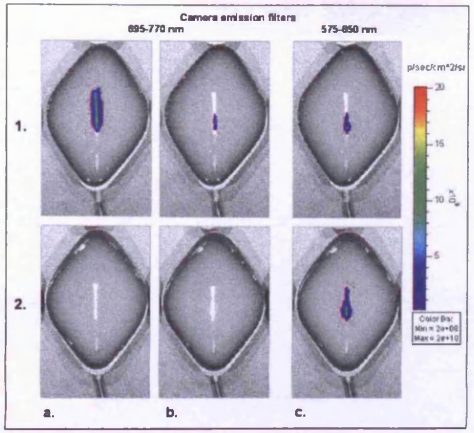


Fig. 10. HF inserted into 1% agarose gel phantoms for macro imaging in the IVIS200 imaging system. (row 1) HF loaded with $5.0x10^5$ beads/ml of 15 µm fluorescent beads ex645/em680 nm in a 2% alginate matrix and (row 2) control HF loaded with only 2% alginate matrix. Fluorescence images using external excitation source (column a) the IVIS200 instrument 615-665nm filter with low power; (column b and c) 650 nm directly coupled optical fiber LED excitation only; The images of column (c) correspond to transmitted light collected by the instrument 575-650 nm filter using the 650 nm LED excitation source. Phantom black holder ~80x58mm at top widest points.

## 4. CONCLUSIONS

The U-2 OS cyclin B1-GFP cells provided a suitable *in vitro* HF adherent cell model, cells seeded into the fiber completely covered the HF inner wall after 5-8 days; this indicated that the HF surface provided a suitable substrate for cell growth and spreading, furthermore the cells appeared to undergo normal cell cycle kinetics, making the model system suitable to test anti-cancer drugs that effect cell cycle traverse and checkpoint induction (e.g. Taxol).



Please verify that (1) all pages are present, (2) all figures are acceptable, (3) all fonts and special characters are correct, and (4) all text and figures fit within the margin lines shown on this review document. Return to your MySPIE ToDo list and approve or disapprove this submission.

The HF polymer material wall presented considerable optical limitations, related with a broadband HF autofluorescence that interfered with the GFP emission window, confirming the far-red/near infrared is the spectral window of choice for imaging cells within the HF implant. It was possible to detect the fluorescence signal of red beads and even QD705 encapsulated in the HF, although it proved to be difficult to obtain any significant optical penetration due to attenuation of illumination and fluorescence signal alike. The next stage will be to assess access to the cellular information using polycarbonate transparent "viewing" windows in combination with multi-photon laser scanning microscopy. The macro imaging of HF encapsulated QD705 labelled cells provided whole fiber integrated readouts suitable for QD biosensors in cells, this is very relevant for tracking the endosomal uptake and delivery of QD sensors [11]. Furthermore widefield spectral imaging and analysis also provided the means for added spatial resolution.

A model device that enabled direct optical fiber LED coupled-light excitation to one side of the HF was designed and tested using the macro imaging system with HF encapsulated red beads. In fluorescent mode this LED side-excitation method proved that it was possible to excite the in fiber encapsulated beads, further improvements will be required to ensure even illumination throughout the fiber. However the approach revealed the potential for a highly sensitive transmitted light device sensitive to cell density and cell shape (live versus apoptotic cells) throughout the 3D HF matrix. This concept could be tested and would be further enhanced by the incorporation of colorimetric probes such as alamarBlue® designed to provide a rapid and sensitive measure of cell proliferation and cytotoxicity in various cell lines. It is simple to use as the indicator dye is water soluble [12] and therefore HF compatible.

The HF provides considerable challenges for implementing high content screening applications, however with the direct coupling of biophotonic components we have shown that kinetic readouts from such implants will be achievable.

## ACKNOWLEDGEMENTS

The authors would like to acknowledge the elements of the group, namely: Sally Chappell, Janet Fisher, Marie Wiltshire, Kerenza Njoh, Imtiaz Khan and Emilene Furon. Also, Nick White (School Optometry) for the advice on the confocal, Jan Hobot (School Medicine) and Gareth Edwards (School of Physics, Cardiff University) for the initial help with the SEM and Steve Shnyder (University of Bradford) for the feedback on the HF seeding protocol. All authors would also like to acknowledge the PhD funding support from Cardiff University under the Richard Whipp Interdisciplinary Studentship Scheme and the Research Councils UK Basic Technology Research Programme (GR/S23483).

## REFERENCES

[1] Wallqvist, A., Huang, R., and Covell, D.G., "Chemoinformatic Analysis of NCI Preclinical Tumor Data: Evaluating Compound Efficacy from Mouse Xenograft Data, NCI-60 Screening Data, and Compound Descriptors," Journal of Chemical Information and Modeling 47(4), 1414-1427 (2007).

[2] Suggitt, M. and Bibby, M.C. , "50 years of preclinical anticancer drug screening: Empirical to target-driven approaches," Clinical Cancer Research 11(3), 971-981 (2005).

[3] Decker, S., Hollingshead, M., Bonomi, C. A., Carter, J. P. and Sausville, E. A., "The hollow fibre model in cancer drug screening: the NCI experience," European Journal of Cancer 40(6), 821-826 (2004).

[4] Hollingshead, M.G., Alley, M.C., Camalier, R.F., Abbott, B.J., Mayo, J.G., Malspeis, L. and Grever, M.R., "In vivo cultivation of tumor cells in hollow fibers," Life Sciences 57(2),131-141 (1995).

[5] Bishai, W.R. and Karakousis, P.C., "Hollow fiber technique for in vivo study of cell populations," United States Patent Application 20060182685, (2006).

[6] Suggitt, M., Swainel, D.J., Pettit, G.R. and Bibby, M.C., "Characterization of the hollow fiber assay for the determination of microtubule disruption in vivo," Clinical Cancer Research 10(19) 6677-6685(2004).

[7] Hollingshead, M.G., Bonomi, C.A., Borgel, S.D., Carter, J.P., Shoemaker R., Melillo, G. and Sausville E.A., "A potential role for imaging technology in anticancer efficacy evaluations," European Journal of Cancer 40(6), 890-898 (2004).

[8] Zhang, G. J., Safran, M., Wei, W., Sorensen, E., Lassota, P., Zhelev, N., Neuberg, D. S., Shapiro, G. and Kaelin, W. G., Jr., "Bioluminescent imaging of Cdk2 inhibition in vivo," Nature Medicine 10(6), 643-648 (2004).

[9] Smith, P.J., Blunt, N., Wiltshire, M., Hoy, T., Teesdale-Spittle, P., Craven, M.R., Watson, J.V., Amos, W.B., Errington, R.J. and Patterson, L.H., "Characteristics of a novel deep red/infrared fluorescent cell-permeant DNA probe, DRAQ5, in intact human cells analyzed by flow cytometry, confocal and multiphoton microscopy," Cytometry 40(4),280-91 (2000).

[10] Weissleder, R., Ntziachristos, V., "Shedding light onto live molecular targets," Nature Medicine 9(1),123-128 (2003).

[11] Nakase, I., Niwa, M., Takeuchi, T., Sonomura, K., Kawabata, N., Koike, Y., Takehashi, M., Tanaka, S., Ueda, K., Simpson, J.C., Jones, A.T., Sugiura, Y. and Futaki, S., "Cellular uptake of arginine-rich peptides: roles for macropinocytosis and actin rearrangement," Molecular therapy 10(6),1011-22 (2004).

[12] de Fries, R. and Mitsuhashi, M., "Quantification of mitogen induced human lymphocyte proliferation: comparison of alamarBlue assay to 3H-thymidine incorporation assay," Journal of Clinical Laboratory Analysis 9(2), 89-95(1995).

# Appendix I-B

(Smith et al. 2007b)

**Smith**, P. J.; Marquez, N.; Wiltshire, M.; Chappell, S.; Njoh, K.; Campbell, L.; Khan, I. A.; Silvestre, O.; Errington, R. J., Mitotic bypass via an occult cell cycle phase following DNA topoisomerase II inhibition in p53 functional human tumor cells. *Cell Cycle* **2007b,** 6, (16), 2071-2081.

Report

# Mitotic Bypass Via An Occult Cell Cycle Phase Following DNA Topoisomerase II Inhibition in p53 Functional Human Tumor Cells

Paul J. Smith[1,†,*]
Nuria Marquez[1,A]
Marie Wiltshire[1]
Sally Chappell[1]
Kerenza Njoh[1]
Lee Campbell[1]
Imtiaz A. Khan[3]
Oscar Silvestre[2]
Rachel J. Errington[2,†]

[1]Departments of Pathology, [2]Medical Biochemistry and Immunology and the [3]Biostatistics and Bioinformatics Unit; University of Wales College of Medicine; Heath Park, Cardiff UK

[A]Cardiff School of Biosciences; Life Sciences Building; Museum Avenue, Cardiff UK

[†]These authors contributed equally to this work.

*Correspondence to: Paul J. Smith; Cardiff University; School of Medicine; Department of Pathology; Cardiff CF14 4XN UK; Tel.: 44.0.29207.42730; Email: smithpj2@cf.ac.uk

Original manuscript submitted: 05/30/07
Revised manuscript submitted: 06/16/07
Manuscript accepted: 06/16/07

Previously published online as a Cell Cycle E-publication:
http://www.landesbioscience.com/journals/cc/article/4585

KEY WORDS

mitosis, endocycle, chromosomal instability, TP53, DNA topoisomerase II, ICRF-193, cyclin B1, decatenation checkpoint

ABBREVIATIONS

| | |
|---|---|
| CIN | chromosomal instability |
| DC | decatenation checkpoint |
| MSC | mitotic spindle checkpoint |

ACKNOWLEDGEMENTS

See page 2080.

## ABSTRACT

Cell cycle checkpoints guard against the inappropriate commitment to critical cell events such as mitosis. The bisdioxopiperazine ICRF-193, a catalytic inhibitor of DNA topoisomerase II, causes a reversible stalling of the exit of cells from $G_2$ at the decatenation checkpoint (DC) and can generate tetraploidy via the compromising of chromosome segregation and mitotic failure. We have addressed an alternative origin—endocycle entry—for the tetraploidisation step in ICRF-193 exposed cells. Here we show that DC-proficient p53-functional tumor cells can undergo a transition to tetraploidy and subsequent aneuploidy via an initial bypass of mitosis and the mitotic spindle checkpoint. DC-deficient SV40-tranformed cells move exclusively through mitosis to tetraploidy. In p53-functional tumor cells, escape through mitosis is enhanced by dominant negative p53 co-expression. The mitotic bypass transition phase (termed $G_2^{endo}$) disconnects cyclin B1 degradation from nuclear envelope breakdown and allows cells to evade the action of Taxol. $G_2^{endo}$ constitutes a novel and alternative cell cycle phase—lasting some 8 h—with distinct molecular motifs at its boundaries for $G_2$ exit and subsequent entry into a delayed $G_1$ tetraploid state. The results challenge the paradigm that checkpoint breaching leads directly to abnormal ploidy states via mitosis alone. We further propose that the induction of bypass could: facilitate the covert development of tetraploidy in p53 functional cancers, lead to a misinterpretation of phase allocation during cell cycle arrest and contribute to tumor cell drug resistance.

## INTRODUCTION

Changes in chromosomal quota are common in cancer.[1] Attention has focused on events in mitosis and the nondisjunction of chromosomes yielding tetraploidy and aneuploidy[2] with mounting evidence that a doubling of DNA content (tetraploidy) is a critical initial step. Tetraploidy can arise from readily observable mitotic transition abnormalities triggered by mitotic machinery/chromosomal defects, endocycle entry in S phase or $G_2$ or indeed rare cell fusions. The dynamic balance between the different routes to tetraploidy is neither clearly understood nor readily observable.[2-5] We have focused on the decision conflict for progression to tetraploidy faced by human cancer cells presented with chromatin anomalies that mimic naturally occurring errors—catenated DNA molecules. If committed to mitosis, such unresolved topologically intertwined DNA replication products are capable of preventing chromosome segregation.[6,7]

The current view is that unresolved intertwined DNA replication products are normally sensed and potentially resolved at a pre-mitotic decatenation checkpoint (DC) in the $G_2$ stage of cell cycle in human cells[8-12] and at a $G_2$/M checkpoint in budding yeast.[6] Conceptually these checkpoints halt cycle progression until decatenation is completed by the resolving enzyme DNA topoisomerase II. The current paradigm is that unresolved errors and checkpoint breaching lead to tetraploidy due to a failure of chromosomal segregation and cytokinesis although the endoreduplication potential is under-explored.[12,13] The human DC imposes a delay on the progression from $G_2$ into mitosis until decatenation is complete. Catalytic inhibitors of topoisomerase IIα, such as the bisdioxopiperazines ICRF -187, and ICRF -193[13] inhibit the ATPase activity of the enzyme and stabilize it in the form of a "closed clamp". Initially it was thought that such agents can induce catenation stress without DNA damage[8] and it has been suggested that the ATR -dependent inhibition of polo-like kinase 1 (Plk1) activity may be one of the mechanisms to regulate cyclin B1 phosphorylation and sustain nuclear exclusion to maintain the decatenation checkpoint response.[14] The catenation block to mitotic progression requires BRCA1 and appears to be enforced by ATR -dependent signalling.[9,15] Recent evidence has also





suggested a potential involvement of Chk1 in the $G_2$/M checkpoint response induced by ICRF-193 highlighting the need to assess the genomic stress sequelae of the inhibition of decatenation.[16] Although p53 function does not appear to be required to trigger the decatenation checkpoint, it is possible that escape from checkpoint arrest could have different outcomes for abnormal ploidy generation according to p53 status.

Here we examined the exclusivity of a mitotic route to tetraploidy using the bisdioxopiperazine ICRF-193, a catalytic inhibitor of DNA topoisomerase II, to suppress decatenation[11] and to activate any DC function[10] in human cells detectable by a reversible stalling of exit from $G_2$.[12] We have studied the consequences of decatenation inhibition in terms of $G_2$ exit to tetraploidy (Fig. 1A shows the concept diagram) in a range of human cells with a focus on DC resolution and associated stress signaling in the human p53-functional U-2 OS osteosarcoma cell line.[17] Using single cell tracking approaches we show that decatenation checkpoint-deficient cells move exclusively through mitosis to tetraploidy, triggered by events in S phase, while decatenation checkpoint -proficient p53-functional U-2 OS tumor cells favour a transition which avoids mitosis. We show that the mitotic bypass transition phase has unique features and constitutes a distinct cell cycle phase with implications for the interpretation of elongated $G_2$ arrests.

## MATERIALS AND METHODS

**Cell lines and drug treatments.** Culture conditions and transfection constructs for the cell lines and strains have been described previously. The SV40-transformed MRC-5 fibroblast cell line (MRC5CVI) has been described previously;[18] U-2 OS (ATCC HTB-96) cells were transfected with $G_2$M Cell Cycle Phase Marker (GE Healthcare, UK), yielding stably transfected U-2 OS cyclin B1-eGFP cells;[19] K1E7neo (control; p53 wt) and the stable transfectant Scx (expressing dominant negative mutant p53;[20,21]) were kindly supplied by Prof D Wynford Thomas, Cardiff, UK. Human primary lung fibroblasts (MRC-5; ATCC) and hTERT MRC-5 (kindly supplied by Prof. D Kipling, Cardiff UK) have been described previously.[22] ICRF -193 [bis(2,6 -dioxopiperazine)], a kind gift from Dr. A.M. Creighton (ICRF, London, UK) was prepared in DMSO at 2 mg/ml and used at a peak concentration of 2 μg/ml (equivalent to 7.2 μM). Colcemid (GIBCO-BRL Life Technologies) was used at 60 ng/ml. Taxol® was kindly supplied by Dr T Maughan (Velindre NHS Trust, UK).

**Cell cycle and immuno-detection of γH2AX, er -RPA, $p53^{ser-15}$, $ATM^{ser-1981}$, cyclin B1.** Single parameter DNA measurements were made using the preparation and analysis methods described previously.[23,24] Dual parameter protein/DNA measurements were performed using the method described previously[24] using primary antibody preparations against phospho -γH2AX$^{ser139}$ (Cell Signaling, USA; #2577) replication protein A (RPA; epitope p34 subunit) (Oncogene, USA, #NA18) p53 (Oncogene, USA, monoclonal (ab-6), clone D0-1), phosph-$p53^{ser-15}$ (Cell Signaling, USA; #9284), phosphor-$ATM^{ser-1981}$ (Upstate, USA clone10H11E12, mouse monoclonal), cyclin B1 (BD Pharmingen, mouse monoclonal, #554179). Followed by secondary antibody detection using, either Alexa Fluor 488-conjugated anti-rabbit IgG secondary antibody or Alexa Fluor 488-conjugated anti-mouse IgG secondary antibody (Invitrogen, USA). In brief, for immuno-fluorescence U-2 OS cells were grown on glass coverslips for at least 24 h prior to drug treatment. Following treatment cells were then fixed with 1% paraformaldehyde in PBS for 15 min at 4°C and permeablised by flooding coverslips with 2 ml of 80% ethanol in PBS for 2 h at -20°C. Cells were washed twice with PBS and then blocked overnight at 4°C in blocking buffer (PBS supplemented with 5% BSA). For example histone γH2AX$^{ser139}$ immunostaining, cells were incubated with 1:500 (PBS/0.6% BSA) of rabbit anti -Ser139 phosphorylated histone H2AX antibody for 2 h at room temperature. Cells were then labelled with the secondary Alexa Fluor 488 -conjugated anti-rabbit IgG and incubated in the dark for 1hr. DRAQ5™ (20 μM Biostatus Ltd., UK) was used as a marker of DNA content.[24] Coverslips were then mounted onto slides using Prolong Gold mountant (Invitrogen, USA).

For flow cytometric analysis, six well plates were set up and cells cultured for at least 24 h prior to drug treatment. Following treatment, media was decanted and kept for inclusion of apoptotic populations, cells were then trypsinised, and pelletted. For histone H2AX, resuspended cells were fixed and permeabilized as for above immunofluoresence method and incubated with primary antibody 1:100 (PBS/0.6% BSA) 1h. Cells were then labelled with Alexa Fluor 488 -conjugated anti-rabbit IgG secondary antibody and incubated in the dark for 1 h. Cells were washed and resuspended in PBS and DRAQ5™ (20 μM) was used as a marker of DNA content. Cells were run on a FACS Vantage (Becton Dickinson). For RPA, resuspended cells were fixed and permeabilized as above, blocked overnight in PBS/5%BSA and incubated with mouse anti -RPA 1:200 (PBS/0.6% BSA) for 1hr. Cells were then labelled with Alexa Fluor 488-conjugated anti-mouse IgG secondary antibody (Invitrogen) and incubated in the dark for 1 h. Cells were washed and resuspended in PBS. DRAQ5™ (20 μM) was used as a marker of DNA content. Cells were run on FACS Vantage (Becton Dickinson).

**Sequential detection of cyclin B1 and $p21^{CDKN1A}$.** Cells were plated onto Matek gridded coverslips, and cyclin B1 expression recorded together with grid coordinates and then fixed in 4% paraformaldehyde/PBS for 15 min at room temperature for immunolabelling. Quenched in 100mM glycine for 10 minutes and permeabilized with 0.2% triton/PBS 20 minutes at RT. The cells were blocked overnight in 10% FCS/PBS at 4°C, followed by mouse anti -$p21^{Waf1Cip1}$ (Pharmingen Cat No. 554228) in 0.6%BSA/PBS and detected using anti -mouse Alexa 488 (Invitrogen, USA).

**Confocal laser scanning microscopy of nuclear structure.** U-2 OS cells were seeded into eight well Nunc coverglass chambers (Labtek Inc) and treated with 2 μg/ml ICRF-193. Media containing 10 μM DRAQ5 (Biostatus Ltd, Shepshed, UK) was added to each well and the cells incubated at 37°C for 10 minutes prior to imaging. A single optical slice dual channel (Cyclin B1-GFP (488 nm excitation; 535 ± 20 nm emission, DRAQ5 (647 nm excitation; 680 ± 15 nm) emission image was acquired using a confocal laser scanning microscope (CLSM) (BioRad Microsciences Ltd, Hemel Hempsted, UK) equipped with a krypton/argon ion laser and attached to a Zeiss Axiovert 135 using a 40x, 1.3 NA oil immersion plan apochromat lens).

**Timelapse microscopy: tracking mitotic delivery and outcome.** Immediately post-treatment culture dishes were placed onto a time-lapse instrument designed to capture transmission-phase images from multi-well plates. An Axiovert 100 microscope (Carl Zeiss, Welwyn Garden City, UK), was fitted with an incubator to maintain 37°C/5% $CO_2$ (Solent Scientific, Portsmouth, UK) and images captured using an ORCA-ER CCD camera (Hamamatsu, Reading, UK). Illumination was controlled by a shutter in front of

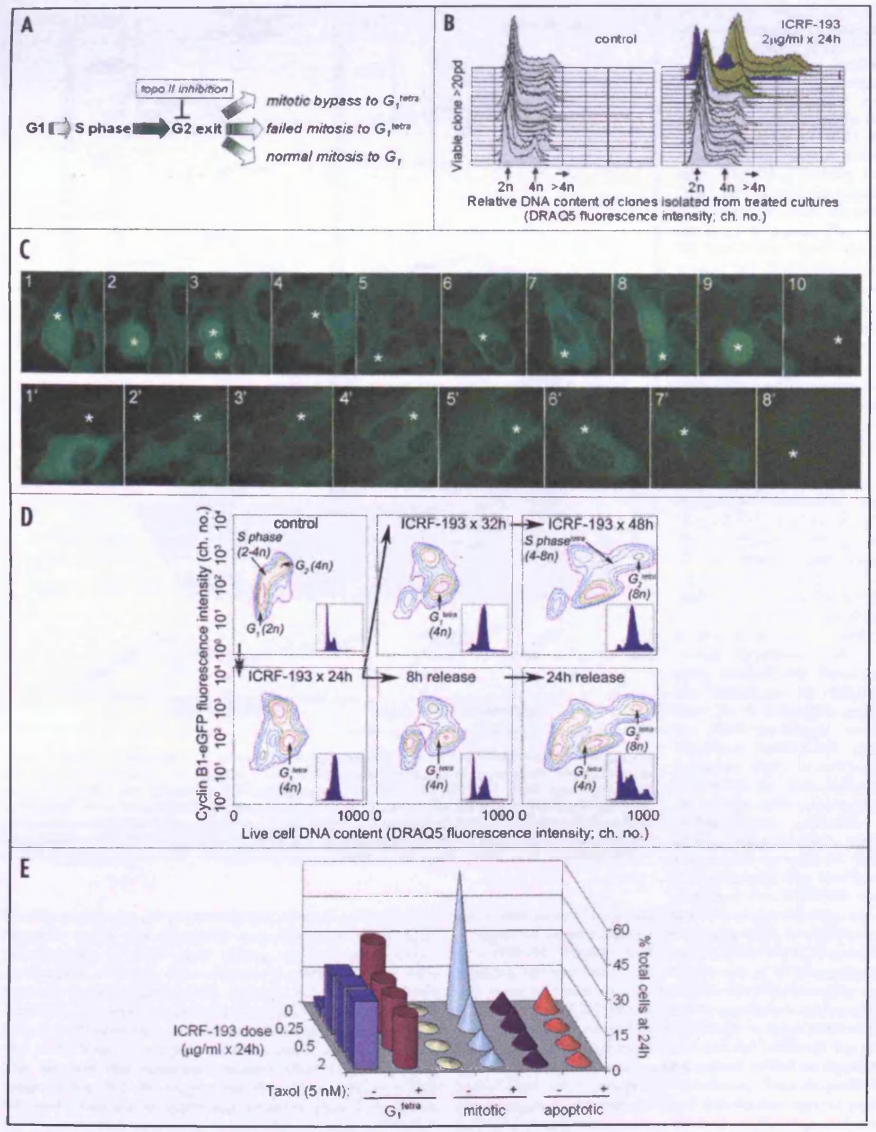






Figure 1, see page e3. ICRF-193-induced abnormal ploidy following endocycle entry via evasion of mitosis and recovery from tetraploidy arrest in U-2 OS cells. (A) Schema for the breaching of $G_2$ decatenation checkpoint (DC) delay and $G_2$ exit. (B) DNA content distributions[24] for proliferating clones randomly isolated from control cultures (left panel) or cultures originally exposed to ICRF-193 for 24 h (right panel). Both increased and reduced levels of parental cell DNA contents are apparent in clones arising from ICRF-193 exposed cultures. (C) Timelapse imaging[25] of changes in cyclin B1-eGFP reporter expression during cell cycle progression to mitosis in control cells (upper sequence) or into mitotic bypass (up to 70% events; lower sequence) in the presence of 2 μg/ml ICRF-193. No evidence of a commitment to mitosis before cyclin B1 switch-off (lower sequence). See typical video sequences in supplementary data. (D) Typical changes in cyclin B1-GFP reporter expression and DNA content determined by flow cytometry of live cells.[24] Contour plots include the corresponding DNA distribution profiles as insets for U-2 OS control cultures, treated with 2 μg/ml ICRF-193 or upon release into fresh medium. (E) Flow cytometry (mean data given as bars & cylindrical columns) shows that the appearance of cells in $G_1^{tetra}$ during ICRF -193 treatment is not prevented by Taxol®. Direct observation of cytocentrifuge samples (cone symbols) shows that ICRF-193 causes a significant inhibition ($p < 0.05$) of mitotic capture but no enhanced cell loss through apoptosis (sd < 3% for n > 3 experiments).

the transmission lamp, and an x,y positioning stage with separate z-focus (Prior Scientific, Cambridge, UK) controlled multi-field acquisition. Image capture was controlled by AQM 2000 software (Kinetic Imaging Ltd). All images were collected with a 10x (PH1) apochromat objective lens providing a field size of 500 x 500 μm. Sequences were captured over 24 hours, every 10 minutes, and for three fields per treatment regime.

The analysis of the images was performed with the integrated AQM 2000 software package (Kinetic Imaging Ltd, Nottingham, UK). Each cell in the field was tracked individually and the time to mitosis, duration of mitosis, and other key cellular events detected by morphology were recorded. The classification of the event was determined according to key outcomes: a successful mitosis to two daughter cells, a tripolar or quadripolar division, a mitosis with cell re-fusion (i.e., furrow regression), mitosis followed by no cytokinesis (polyploidy) event or cell death. The duration of the mitotic/polyploid event was also extracted. The multitag time-lapse event curves were processed appropriately and visualized in graphical plots as previously described.[25,26]

**Time-laspe microscopy: tracking eGFP-cyclin B1 profiles.** The principles have been described previously.[19] Briefly, culture dishes were placed onto a time-lapse instrument designed to capture transmission-phase images from multi-well plates. High resolution fluorescence cell tracking was performed with cells seeded into eight well Nunc coverglass chambers and collected with a 40x, 0.90 NA air objective lens suitable for multi-well timelapse microscopy. Immediately post -addition the cultured dishes were placed on to the time -lapse instrument in dual channel capture mode designed to obtain bright -field phase images and GFP fluorescence (480/25 nm excitation and 525/30 nm emission). Fluorescence tracking on a single cell basis was achieved in Lucida (KI Ltd). The levels of cyclin B1 reporter fluorescence were recorded in the cytoplasm from a region of interest drawn in an area adjacent to the nucleus. The movement of the cell was compensated for during the time course. The intensity readout was background subtracted only for display and visualisation purposes. To quantify the profile responses the traces were normalised against basal levels of cyclin B1.

**Live cell flow cytometry and cell cloning.** Cells were trypsinised from the substrate and resuspended to a final concentration of $2 \times 10^5$ cells per ml in full culture medium supplemented with 10 mM HEPES and allowed to equilibrate at 37°C prior to the addition of 20 μM DRAQ5. The resulting preparations were analysed using a Becton-Dickinson FACSCalibur flow cytometer with a single excitation (488 nm) and dual emission FL1 (515–540 nm) to detect GFP expression and FL2 (580LP) to detect DRAQ5 labelling. The cell cycle results were extracted according to the algorithm described by Watson et al.[23] To obtain clones sublines unstained cells were plated at low density in 24-well dishes and examined for single colony growth prior to transfer to culture flasks for ≥20 population doublings.

## RESULTS

**ICRF-193 induced tetraploidy in U-2 OS Cells.** Our initial studies revealed that human p53-functional U-2 OS osteosarcoma cells can survive such growth delay imposed by ICRF-193 and yield clonal lineages (>20 population doublings [pd]) that frequently express aneuploid DNA profiles (Fig. 1B). To resolve the early origins of ICRF-193-induced tetraploidy[13] (Fig. 1A), we studied ICRF-193-induced delay in U-2 OS cells, stably transfected with a cyclin B1-eGFP reporter construct,[19,27] allowing us to track the reporter destruction to basal levels upon transition to a $G_1$-like early tetraploid state (i.e., $G_1^{tetra}$) without disturbing cyclin dynamics[28] (Fig. 1C, upper sequence). We could distinguish $G_2$ (4n DNA content) exit to a normal cycle $G_1$ (2n DNA content) from exit to tetraploidy ($G_1^{tetra}$ with 4n DNA content) and progression into S $phase^{tetra}$ (>4n DNA content) by co-mapping reporter expression with live cell DNA content[24] (Fig. 1D) using flow cytometry. ICRF-193 caused cells to accumulate with both a 4n DNA content and a reduced cyclin B1-eGFP $G_1^{tetra}$ signature (Fig. 1D). No cells traversed the 2n to 4n cell cycle without significantly elevating cyclin B1-eGFP expression. Drug removal resulted in enhanced progression from $G_1^{tetra}$ into S $phase^{tetra}$ and eventually an 8n state, revealing an ICRF-193-maintained delay operating in $G_1^{tetra}$ cells. In parallel, cells released from the high cyclin B1-eGFP fraction in $G_2$ (DC checkpoint delayed) exit to a normal $G_1$ compartment. The results suggest that movement to $G_1^{tetra}$ is post-delay and therefore post-catenation resolution.

**Routing to ICRF-193-induced tetraploidy avoids the mitotic spindle checkpoint in U-2 OS Cells.** The 'absence of segregation mitosis' model[13] for $G_2$ exit from the DC predicts that the additional presence of a mitotic spindle checkpoint (MSC) activator (e.g., Taxol®) should trap cells in M as they breach the DC,[29] thereby verifying a mitotic routing to either tetraploidy or an escape to a normal cycle (Fig. 1A). Testing this model we found that after 24 h exposure to Taxol® alone, U-2 OS cells become trapped into mitosis (Fig. 1E), with some breaching of the MSC to $G_1^{tetra}$. However, after co-exposure with ICRF-193 for 24 h, flow cytometry revealed a persistent accumulation of cells into $G_1^{tetra}$ (Fig. 1E) despite severe dose-responsive depression of mitotic capture or no additive apoptotic cell death (Fig. 1E) as determined by direct observation of cytocentrifuge preparations. We propose that in catenation-stressed U-2 OS cells, escape to tetraploidy is primarily via an endocycle route that bypasses mitosis.

**Cytoplasmic cyclin B1-eGFP signal destruction associated with endocycle entry.** To verify this suspected and normally unnoticed mitotic bypass route, we tracked[30] cyclin B1 eGFP expression in individual U-2 OS cells during exposure to 2 μg/ml ICRF-193 (i.e., 7 μM; Fig. 1 upper sequence shows control cells; lower sequence shows ICRF-193-treated cells). We consistently observed that

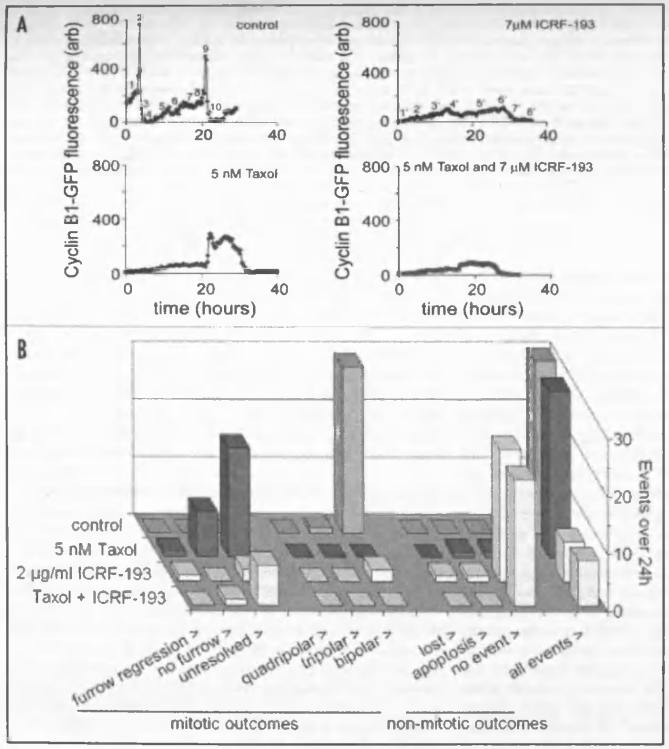


Figure 2. Evasion of intra-mitotic checkpoints in ICRF-193-treated U-2 OS cells. (A) Typical traces from single cells showing relative changes in cytoplasmic cyclin B1-eGFP expression for regions of interest coded in Figure 1C for an untreated (control; upper left panel) U-2 OS cell or treated with 2 μg/ml ICRF-193 (i.e., 7 μM; upper right panel), 5 nM Taxol® (lower left panel) or a combination of agents (lower right panel). Absolute levels of fluorescence cannot be compared directly between different cells due to cell-to-cell variation in reporter expression. (B) Cumulative frequencies for different event outcomes, as indicated, monitored by time -lapse imaging[25] over a maximum period of 24 h for control, Taxol®, ICRF -193 and combination -treated cultures (typical results for 30 progenitor cells).

50–75% of cells showed an extended and elevated cyclin B1-eGFP expression profile that proceeded to a destruction of the cytoplasmic cyclin B1-eGFP signal without any intervening nuclear translocation or mitotic event apparent in control cells (see video sequences in supplementary data). Typically, ICRF-193-treated cells delayed in $G_2$ ~3-times longer than untreated controls (i.e., a DC delay period) while the reporter destruction phase took on average ~8.3 ± 2.2 hours to complete before reaching basal $G_1^{tetra}$ levels (Fig. 2A; note that numerical indicators relate to corresponding images in Fig. 1C). We suggest that these features define a bone fide intervening 'gap' or 'gap-to-gap transition' phase (termed here $G_2^{endo}$) rather than an interface between $G_2$ (4n) and $G_1^{tetra}$ (4n).

To test MSC bypass we tracked reporter expression in individual cells in the presence of Taxol® and found that an elevated signal was maintained during an elongated mitosis with destruction upon breaching to tetraploidy (Fig. 2A). The co-presence of ICRF-193 caused bypass without mitotic entry (Fig. 2A). Tracking individual cells allowed the mapping of cumulative event outcomes for a 24 h period (Fig. 2B). We found that Taxol® did not prevent the ICRF-193-induced increase in the frequency of cells apparently showing no event (Fig. 2B) or mitotic bypass (Fig. 2A), while in the presence of Taxol® alone resulted in the expected capture in compromised mitoses (Fig. 2B; with extended mitotic cyclin profiles as in Fig. 2A) primarily resolving as tetraploidy via a furrow failure (Fig. 2B).

**Loss of mitotic bypass in decatenation-checkpoint deficient SV40-transformed cells.** We hypothesized that the loss of DC sensing would disallow bypassing and remove a decision conflict for $G_2$ exit. To test this we used long-term established SV40-transformed MRC-5 human fibroblasts,[31] likely to show minimal DC function.[32] We focused on the transition from $G_2$ to polyploidy profiles for SV40-transformed normal fibroblasts (MRC5CVI) under catenation stress. To analyse the traverse of cell cycle landmarks we initially used a conventional stathmokinetic approach in which passage through mitosis was blocked by colcemid. Using flow cytometry, (Fig. 3A–C), we confirmed that ICRF-193 treatment could accumulate 4n and >4n DNA content cells (Fig. 3A).

Figure 3A shows the extensive emptying of $G_1$ in response to a 24 h ICRF-193 exposure confirming the lack of any $G_1$/S arrest. $G_1$ emptying was matched by the accumulation of SV40-transformed cells in the 4n fraction (nominally $G_2$/M) this effect becoming saturated at 1 μg/ml ICRF-193. Preliminary experiments confirmed the rapid saturation of the ability of ICRF-193 to target DNA topoisomerase II at approximately 1 μg/ml and also confirmed that even high ICRF-193 concentrations (2–4 μg/ml) yielded no significant level of direct DNA cleavage (data not shown). Thus the profile for topoisomerase II inhibition correlated with the dose response profile for its pharmacodynamic action at the level of cell cycle perturbation.





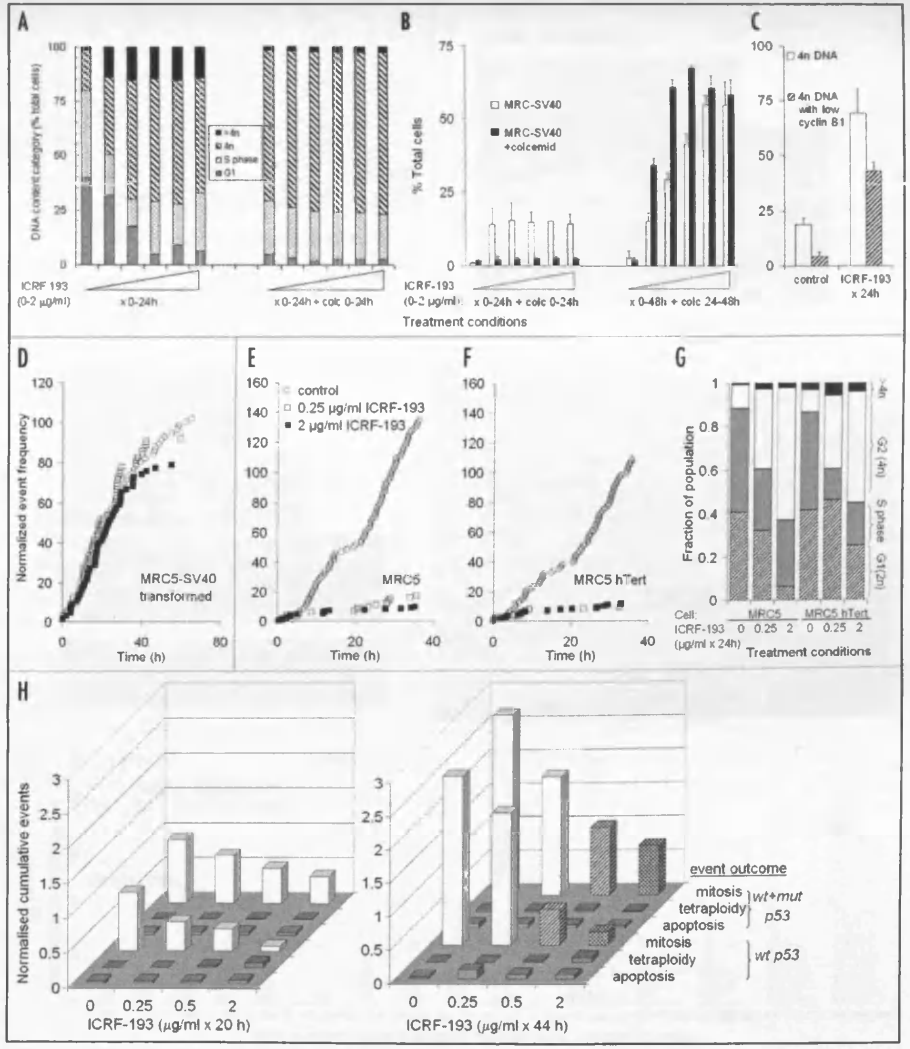


Figure 3. For legend, see page e7.

In the presence of colcemid, control cultures of both cell lines showed a >65% accumulation in the 4n fraction and complete emptying of $G_1$. Thus low doses of ICRF-193 permit leakage of cells into normal $G_1$ through mitosis while higher doses close down this route. Figure 3B shows the ICRF-193-induced dose-dependent progression of cells to polyploidy over a 24 or 48 h incubation period. Concentrations

Figure 3. Decatenation checkpoint deficiency and routing through mitosis. (A) Dose -dependent changes in cell cycle distribution of SV40-transformed MRC5 fibroblasts (MRC5CV1 cell line[31]) for a 24 h exposure period to 0, 0.125, 0.25, 0.5, 1 and 2 μg/ml ICRF-193 with and without the continuous presence of colcemid. Data are mean results for three experiments and show that ICRF-193-induced progression beyond $G_1^{tetra}$ is blocked by the initial presence of colcemid although cells are efficiently captured with 4n DNA content. (B) Commitment of MRC5-SV40 fibroblasts cells to ICRF-193-induced progression beyond $G_1^{tetra}$ to polyploidy (>4n), as a % total cells, is insensitive to colcemid if addition is delayed for 24 h after the commencement of ICRF-193 at the concentrations indicated in Figure 2A. Data are mean values (± sd) for 3–5 experiments. (C) Flow cytometric analysis of cyclin B1 expression[24] in ICRF-193-treated MRC5-SV40 fibroblasts with 4n DNA content. Columns: open: all 4n cells; shaded: 4n cells with low cyclin B1; Data are means of 3 experiments (± sd). (D) Integrated event outcomes, tracked by timelapse imaging, over a 20 or 44 h treatment period with ICRF-193 for K1E7 cells expressing functional wt p53 or co-expression of dominant negative p53mut. Data are normalised to the initial number of cells in an analysis field (n = 3 experiments). Increasing doses of ICRF-193 reduce normal mitotic commitment to basal levels in K1E7$^{wtp53}$ without diversion through mitosis to $G_1^{tetra}$. K1E7$^{wtp53+mutp53}$ cells show significantly ($p < 0.05$; shaded columns) greater attempts at mitosis with normal cytokinesis outcomes. (E–G) Cumulative event curves (1st cycle only) for MRC5 -SV40 transformed cells (E), MRC5 primary cells (F), MRC5 hTERT expressing cells (G). Symbols: •, control; ▫, Δ, continuous exposure to 0.25 or 2 μg/ml ICRF-193 respectively. Combined events comprise mitotic commitment events and low levels (≤10%) of apoptosis. (H) ICRF-193-induced accumulation of MRC5 (primary and hTERT) cells with 4n DNA content.

of >0.125 μg/ml ICRF-193 were active at inducing approximately 20% cells to progress to the >4n fraction over the first 24 h of drug treatment. There was a significant increase in the number of cells progressing to >4n fraction over the 24–48 h incubation period. Progression was initially blocked completely by the presence of colcemid while progression during the 24–48 h exposure period was colcemid-insensitive. The increased frequency of cells with 4n DNA content at 24 h but with low levels of cyclin B1 (Fig. 3C; detected by immunofluorescence) indicated that many cells had already resolved any putative delay and had actively entered a $G_1^{tetra}$ state via mitosis.

Time-lapse analyses of events for MRC5CV1 cells excluded any cell fusion events and provided definitive evidence of the lack of a DC (Fig. 3D; and data not shown). This contrasts with the clear stalling of commitment to mitosis observed with the corresponding primary MRC-5 cell strain (Fig. 3E) or an hTERT-immortalized counterpart with extended in vitro lifespan[22] (Fig. 3F). MRC-5 and MRC-5 hTERT cells showed and an increased frequency of 4n DNA content cells but highly restricted penetrance through to >4n DNA content at 24h; Fig. 3G). Overall, the findings show that any mitotic bypass is minimal in DC-deficient SV40 transformed cells. Primary cells massively restrict commitment to mitosis or indeed any breaching to S phase$^{tetra}$ in the presence of ICRF-193.

**Moderation of p53 function maintains a higher mitotic commitment in ICRF-193 treated K1E7 cells.** Overlapping p53-dependent and -independent pathways generally enforce $G_2$ arrest in response to DNA damage and chromatin anomalies.[33] However, to-date there is no clear evidence for any dependence of the DC on p53 function.[10,34] We hypothesised that low levels of genomic stress sensing and signal transduction, induced by ICRF-193-compromised decatenation,[34] are involved in the bypass-versus-mitosis $G_2$ exit decision. We tested the impact of moderating p53 function on the post-DC routing decision. Human thyroid carcinoma K1E7 cells[20] express wild-type p53 and when exposed to ICRF -193 over a 48h period show significant ($p \leq 0.05$) accumulation of tetraploid cells with >4n DNA content (0.82 ± 0.26 and 37.10 ± 2.17% total cells for control and 2 μg/ml ICRF-193 treatments respectively; n=3). This accumulation of cells with >4n DNA content, cannot be accounted for by the very limited supply via tetraploidy outcome mitotic events tracked using time-lapse imaging (Fig. 3H)—highly suggestive of a mitotic bypass. Expressing dominant negative p53$^{mut}$ in the K1E7 p53 functional background,[20] effecting an extensive but incomplete abrogation of p53 function (data not shown) significantly increased ($p < 0.05$) resistance to the inhibition of mitotic attempts at higher ICRF-193 doses and for extended exposures (Fig. 3H). We found that mitotic attempts were primarily resolved as normal cytokinesis outcomes with low levels of tetraploidy events (Fig. 3H). This argues against p53$^{mut}$ compromising DC checkpoint integrity per se, since the prediction would be that a premature commitment to mitosis would be revealed as tetraploid mitotic outcomes—as observed for SV40—transformed fibroblasts. Thus, $G_2$ exit routing is a post-checkpoint decision with moderation of p53 function enhancing mitotic commitment.

**Genomic stress signalling in ICRF-193-treated U-2 OS Cells undergoing $G_2$ exit.** Pursuit of bypass may be accompanied by stress signals, perhaps insufficient to sustain an overt DNA damage checkpoint arrest, but sufficient to confound and negatively regulate cyclin-cdk dynamics.[35] We examined potential sensors of DNA damage or stalled replication forks in U-2 OS cells. H2AX phosphorylation was markedly elevated, as previously reported,[36] suggesting a degree of sustained double strand break formation (Fig. 4A). Prominent γH2AX-positive nuclear foci were found in all cell cycle stages regardless of eventual routing (Fig. 4B). Minor escape through mitosis yielded elongated foci at the ends of failed furrows, suggesting chromatin structures under tensile stress (Fig. 4B) and a possible reflection of furrow-induced DNA damage.[2] The formation of extraction-resistant replication protein A (er-RPA) in S phase[36] was not changed indicating little disturbance of replicon dynamics during catenane generation[7] (Fig. 4A). We next profiled p53 by flow cytometry (Fig. 4A) and consistently observed moderate increases (>2-fold; confirmed by fluorescence microscopy; data not shown) in nuclear p53 levels and phosphorylations at p53$^{ser-15}$. Highest levels of p53$^{ser-15}$ phosphorylation were found in cells with enlarged nuclei (≥4n) and therefore bypass candidates (data not shown). Phosphorylation of the ATM signal transducer (ATM$^{ser-1981}$; Fig. 4A) at nuclear foci (Fig. 4C) also pointed to a late cell cycle stress signalling response irrespective of mitotic commitment.

Significantly increased (>2 -fold) p21$^{CDKN1A}$ expression, consistent with ATM/p53 stress signal transduction,[33] was evident in U-2 OS cells at the 4n/>4n interface (Fig. 4D). Using imaging of reporter expression in live cells, followed by fixation and immunofluorescence analysis for nuclear p21$^{CDKN1A}$ expression, we could map this dramatic increase to cells that had already bypassed to $G_1^{tetra}$ (lost the cyclin B1 eGFP signal by cytoplasmic destruction) rather than cells holding in late $G_2$ delay (Fig. 4E). High-speed sorting and gene expression analyses could resolve whether or not p21$^{CDKN1A}$ gene expression is actually instigated in $G_2$ proper and the delay in appearance of significantly increased protein levels only realised in $G_1^{tetra}$. Irrespective, it is reasonable to suggest that this intra -$G_1^{tetra}$ p21$^{CDKN1A}$ spike would constitute a strong and actively maintained inhibition of Cdk2-cyclin complexes[33] in $G_1^{tetra}$. This $G_1^{tetra}$ arrest is sustained by the presence of ICRF-193 perhaps via maintenance of the triggering chromatin anomalies. The loss of this putative arrest





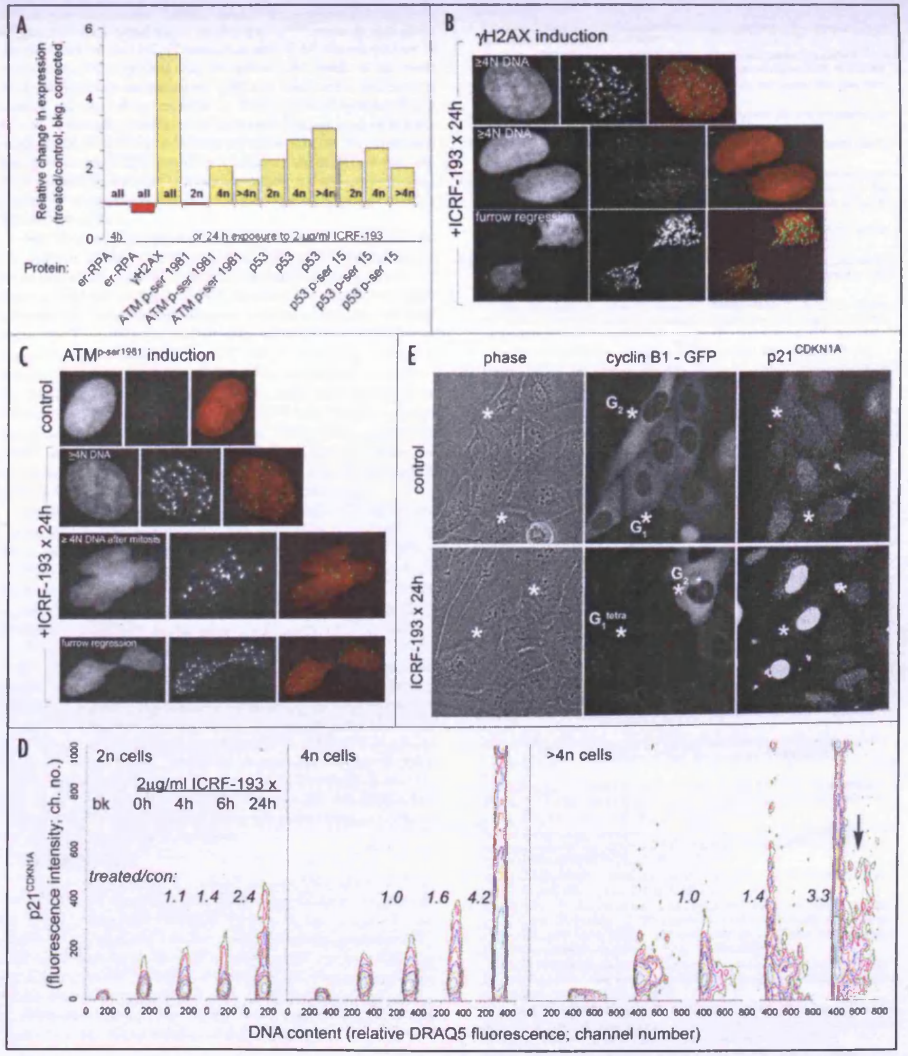


Figure 4. For legend, see page e9.

Figure 4. Endocycle routing and genomic stress signalling in $G_2$ with induction of $p21^{CDKN1A}$ upon $G_1^{tetra}$ entry. Panel a) Flow cytometric profiles of DNA damage sensing and signal transduction protein expression in defined cell cycle compartments of U -2 OS cells. Data are mean corrected values relative to controls. Panels b &c) γH2AX DNA -associated foci (panel b) and ATM $^{ser1981}$ foci (panel c) induced by ICRF -193 exposure. Fields left to right are DNA (DRAQ5), protein immunofluorescence (Alexa -488) and merged images respectively. Panel d) Contour plots of $p21^{CDKN1A}$ expression in U -2 OS cells as a function of cell cycle position and exposure period to ICRF -193 (2 μg/ml) analysed by flow cytometry. Treated/control values show $p21^{CDKN1A}$ enhancement at the 4n/ > 4n interface. Panel e) Comparison of $p21^{CDKN1A}$ expression in U -2 OS cells fixed after analysis of live cell cyclin B1 -eGFP expression. Fields show marked cells for control or 24 h exposure to ICRF -193 (2 μg/ml). Elevated $p21^{CDKN1A}$ expression occurs in cells that have undergone reporter destruction [i.e., entered $G_1^{tetra}$] to levels, equivalent to those found in $G_1$ control cells, but not in cells that maintain high levels of cyclin B1 -eGFP expression [i.e., delayed in $G_2$].

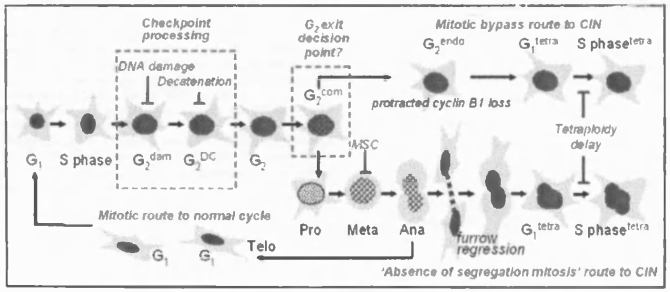


Figure 5. Proposed scheme for the origins of abnormal ploidy and the early steps towards chromosomal instability (CIN) via $G_2$ exit routes through mitosis and by mitotic bypass.

signal is apparent in cells breaking through to S $phase^{tetra}$ (Fig. 4D, arrowed > 4n fraction).

## DISCUSSION

The results highlight a previously hidden phase of the cell cycle—$G_2^{endo}$—in cells undergoing endocycle traverse. Our findings suggest that for mitotic bypass to occur in the presence of ICRF-193, treated cells need to experience a transient DC delay. It appears unlikely that mitotic bypass into $G_1^{tetra}$ by ICRF-193-treated U-2 OS cells is merely an expression of an enforced $G_2$ delay per se or overt DNA damage since preliminary screens of the U-2 OS systems expressing the cyclin B1-eGFP reporter (Smith PJ, Errington RJ, unpublished data) show that: (1) $G_1^{tetra}$ accumulation was detectable although greatly reduced (≤5%) for exposure to the DNA -damaging topoisomerase II inhibitor VP -16, (2) $G_1^{tetra}$ accumulation was not detectable for exposure to the DNA cross-linking agent cis-Pt, and (3) $G_1^{tetra}$ accumulation did not occur in the presence of ICRF-193 if cells were pre-treated with the DNA damaging and $G_2$-arresting agent topotecan.

Direct observations using time -lapse imaging to track the earliest appearance of compromised mitotic outcomes during a continuous exposure of MRC5CV1 cells to ICRF-193, maps catenation generation to S phase (>8h before first mitotic mis-segregation event; data not shown). This supports the view that in these SV40-transformed cells decatenation, in the absence of ICRF-193, appears to be completed by $G_2$. Indeed, efficient decatenation may permit cells to dispense with DC function under non-selective conditions. Under continuous ICRF-193 treatment, cells in S phase would develop catentation-related anomalies and 'commit' cells to mitotic catastrophe since they lack an opportunity in $G_2$ to intercept non-completion events.

In cells showing a pre-mitotic stall in the presence of ICRF-193, commitment to future bypass may also occur in S phase irrespective of downstream DC activation—an issue that could be resolved by checkpoint reversal studies. We present a proposed scheme to collate our views in which cells breaching DC restraint reach a decision fork for $G_2$ exit via mitosis or the bypass phase $G_2^{endo}$ (Fig. 5), with both routes able to deliver cells to a $G_1^{tetra}$ arrest. Our studies with the K1E7 cell system suggest that p53 function may partly define the propensity to resist the drive through mitosis under catenation stress—potentially increasing opportunities for endocycle entry via bypass. The question arises as to whether there is a commitment stage that marks irreversible endocycle entry in S phase or $G_2$. In preliminary experiments we have observed that cells holding in $G_2$ proper show a partial and transient condensation of chromatin prior to the cyclin B1 reporter signal loss (data not shown), suggestive of a possible early prophase -like commitment stage (suggested in Fig. 5 scheme as $G_2^{com}$) without mitotic follow-through—an aspect of bypass that may share features with antephase and requires further study. Understanding the molecular motifs of $G_2^{com}$ may provide new targets for shunting cancer cells through mitotic catastrophe rather than an occult route to abnormal ploidy via bypass.

The $G_1^{tetra}$ arrest of cells escaping $G_2$ via bypass appears distinct from any putative sensing of tetraploidy that requires a mitotic routing[37] or the impact of a prolonged mitosis sensed by p53.[38] There also appears to be a parallel here with the intra-$G_1$, but potentially DNA-damage independent, arrest associated with centrosome disruption, which requires p38 phosphorylation of $p53^{ser-33}$ for $p21^{CDKN1A}$ induction.[33,39] The impact of bypass on centrosome dynamics and the convergence of the pathways are unknown. $G_1^{tetra}$ delay may represent several influences such as the need to re-align the regulators for S phase commitment following the slow destruction of cyclin B1 in the absence of a mitosis coordinated and





APC-driven destruction. Further, there is the potential for low levels of genomic stress signalling to reinforce a $G_1^{tetra}$ arrest process given our observations on γH2AX induction and ATM phosporylation. A recent study has suggested that phosphor-Chk1 levels, at the lower limits of detection are associated with and likely to be sufficient to cause a cell cycle delay response to ICRF-193-highlighting that it cannot be formally excluded that catenated chromosomes experience other kinds of aberrant structures or distortions in the chromatin that give rise to γH2AX positivity in delayed nuclei.[16] However, our study underlines the need to assess functional cell cycle position with respect to endocycle entry to place the cellular responses to such lesions into context.

The "absence-of-chromosome-segregation mitosis" model[10,13] for the action of catalytic inhibitors of topoisomerase II does not appear to be universally applicable and may primarily relate to certain cell types or cells with compromised DC function. We suggest that under sustained and extensive decatenation inhibition and late cell cycle stress signalling, p53 dysfunction may enhance the probability of escape through mitosis after any DC delay—separating checkpoint function from post-checkpoint routing. The results have implications for the functional description of the DC itself, since the bypass of mitosis via $G_2^{endo}$ and the subsequent $G_1^{tetra}$ delay may be misconstrued as an extended pre-mitotic delay. Others have suggested a model of genetic instability whereby an attenuated DC promotes abnormal mitoses.[32] Here we show that tetraploidy can be attained with an operating checkpoint but via a non-mitotic route.

In this alternative cancer cell cycle defined here, $G_2^{endo}$ avoids the trauma of a mitosis attempting to deal with errors in decatenation but at the expense of generating tetraploid and transient resistance to MSC-targeting anticancer drugs. Low levels of naturally generated decatenation errors, or indeed other inducing events,[40] occurring in early tumor populations could trigger this occult routing to tetraploidy in addition to the more visible routes of chromosomal nondisjunction or tetraploidization by furrow-regression.[1,2] $G_2^{endo}$ entry would have to be 'programmed out' of some cell lineages, such as stem cells,[10] that may rely on mitotic catastrophe to eliminate abnormal daughters. The accrual of hidden tetraploidisation events, in a background of replication errors such as incomplete decatenation, in early tumor cell populations could be perceived as another driver for chromosomal instability. A potential linkage between mitotic bypass and p53 status is worthy of further study since transient drug resistance and facilitated chromosomal instability could compromise the effectiveness of cancer treatment strategies aimed at the regaining of partial p53 function.

**Acknowledgements**

The work was supported by research grants to P.J.S. and R.J.E. from the UK Research Councils' Basic Technology Research Programme, the Biotechnology and Biological Sciences Research Council, and the AICR. We thank GE Healthcare (Amersham Biosciences Plc) for making available the cyclin GFP expressing cells, and David Kipling and Chris Jones for the MRC 5 hTERT cells). We are grateful for helpful discussions and advice from J. Pines and Z. Darzynkiewicz, D. Wynford Thomas, Alan Clarke. We thank Paolo Ubezio and Simon Reed for critical readings of the manuscript.

**Note**

Supplemental materials can be found at:
www.landesbioscience.com/supplement/smithCC6-16sup.pdf
www.landesbioscience.com/supplement/smithCC6-16movie1.avi
www.landesbioscience.com/supplement/smithCC6-16movie2.avi

**References**

1 Sieber OM, Heinimann K, Tomlinson IPM. Genomic instability - The engine of tumorigenesis? Nat Rev Cancer 2003; 3:701-8.
2 Shi Q, King RW. Chromosome nondisjunction yields tetraploid rather than aneuploid cells in human cell lines. Nature 2005; 437:1038-44. [Comment in: Nature 2006; 442:E9-10].
3 Bharadwaj R, Yu H. The spindle checkpoint, aneuploidy, and cancer. Oncogene 2004; 23:2016-27.
4 Grafi G. Cell cycle regulation of DNA replication: The endoreduplication perspective. Exp Cell Res 1998; 244:372-8.
5 Erenpreisa J, Cragg MS. Mitotic death: A mechanism of survival? A review. Cancer Cell Int 2001; 1.
6 Andrews CA, Vas AC, Meier B, Gimenez-Abian JF, Diaz-Martinez LA, Green J, Erickson SL, Vanderwaal KE, Hsu WS, Clarke DJ. A mitotic topoisomerase II checkpoint in budding yeast is required for genome stability but acts independently of Pds1/securin. Genes Dev 2006; 20:1162-74.
7 Germe T, Hyrien O. Topoisomerase II-DNA complexes trapped by ICRF-193 perturb chromatin structure. EMBO Rep 2005; 6:729-35.
8 Downes CS, Clarke DJ, Mullinger AM, Gimenez-Abian JF, Creighton AM, Johnson RT. A topoisomerase II-dependent $G_2$ cycle checkpoint in mammalian cells. Nature 1994; 372:467-70.
9 Deming PB, Cistulli CA, Zhao H, Graves PR, Piwnica-Worms H, Paules RS, Downes CS, Kaufmann WK. The human decatenation checkpoint. Proc Natl Acad Sci USA 2001; 98:12044-9.
10 Damelin M, Bestor TH. The decatenation checkpoint. Br J Cancer 2007; 96:201-205.
11 Ishida R, Hamatake M, Wasserman RA, Nitiss JL, Wang JC, Andoh T. DNA topoisomerase II is the molecular target of bisdioxopiperazine derivatives ICRF-159 and ICRF-193 in *Saccharomyces cerevisiae*. Cancer Res 1995; 55:2299-303.
12 Pastor N, Jose Flores M, Dominguez I, Mateos S, Cortes F. High yield of endoreduplication induced by ICRF-193: A topoisomerase II catalytic inhibitor. Mutat Res 2002; 516:113-20.
13 Ishida R, Sato M, Narita T, Utsumi KR, Nishimoto T, Morita T, Nagata H, Andoh T. Inhibition of DNA topoisomerase II by ICRF-193 induces polyploidization by uncoupling chromosome dynamics from other cell cycle events. J Cell Biol 1994; 126:1341-51.
14 Deming PB, Flores KG, Downes CS, Paules RS, Kaufmann WK. ATR enforces the topoisomerase II-dependent $G_2$ checkpoint through inhibition of Plk1 kinase. Journal of Biological Chemistry 2002; 277:36832-8.
15 Franchitto A, Oshima J, Pichierri P. The $G_2$-phase decatenation checkpoint is defective in Werner syndrome cells. Cancer Research 2003; 63:3289-95.
16 Robinson HMR, Bradie-Thoresen S, Brown R, Gillespie DAF. Chk1 is required for $G_2$/M checkpoint response induced by the catalytic topoisomerase II inhibitor ICRF-193. Cell Cycle 2007; 6:1265-7.
17 Campbell KJ, Chapman NR, Perkins ND. UV stimulation induces nuclear factor B (NF-B) DNA-binding activity but not transcriptional activation. Biochem Soc Trans 2001; 29:688-91.
18 Falk SJ, Smith PJ. DNA damaging and cell cycle effects of the topoisomerase I poison camptothecin in irradiated human cells. Int J Radiat Biol 1992; 61:749-57.
19 Thomas N, Kenrick M, Giesler T, Kiser G, Tinkler H, Stubbs S. Characterization and gene expression profiling of a stable cell line expressing a cell cycle GFP sensor. Cell Cycle 2005; 4:191-5.
20 Wyllie FS, Haughton MF, Rowson JM, Wynford-Thomas D. Human thyroid cancer cells as a source of iso-genic, iso-phenotypic cell lines with or without functional p53. Br J Cancer 1999; 79:1111-20.
21 Jones CJ, Soley A, Skinner JW, Gupta J, Haughton MF, Wyllie FS, Schlumberger M, Bacchetti S, Wynford-Thomas D. Dissociation of telomere dynamics from telomerase activity in human thyroid cancer cells. Exp Cell Res 1998; 240:333-9.
22 McSharry BP, Jones CJ, Skinner JW, Kipling D, Wilkinson GW. Human telomerase reverse transcriptase-immortalized MRC-5 and HCA2 human fibroblasts are fully permissive for human cytomegalovirus. J Gen Virol 2001; 82:855-63.
23 Watson JV, Chambers SH, Smith PJ. A pragmatic approach to the analysis of DNA histograms with a definable $G_1$ peak. Cytometry 1987; 8:1-8.
24 Smith PJ, Blunt N, Wiltshire M, Hoy T, Teesdale-Spittle P, Craven MR, Watson JV, Amos WB, Errington RJ, Patterson LH. Characteristics of a novel deep red/infrared fluorescent cell-permeant DNA probe. DRAQ5, in intact human cells analyzed by flow cytometry, confocal and multiphoton microscopy. Cytometry 2000; 40:280-91.
25 Marquez N, Chappell SC, Sansom OJ, Clarke AR, Court J, Errington RJ, Smith PJ. Single cell tracking reveals that Msh2 is a key component of an early-acting DNA damage-activated $G_2$ checkpoint. Oncogene 2003; 22:7642-8.
26 Errington RJ, Marquez N, Chappell SC, Wiltshire M, Smith PJ. Time-lapse microscopy approaches to track cell cycle progression at the single-cell. In: Robinson JP, ed. Current Protocols in Cytometry. Wiley Interscience, 2006. (ISBN: 978-0-471-16131-8).
27 Clute P, Pines J. Temporal and spatial control of cyclin B1 destruction in metaphase. Nat Cell Biol 1999; 1:82-7.
28 Thomas N, Kenrick M, Giesler T, Kiser G, Tinkler H, Stubbs S. Characterization and gene expression profiling of a stable cell line expressing a cell cycle GFP sensor. Cell Cycle 2005; 4:191-5.
29 Allman R, Errington RJ, Smith PJ. Delayed expression of apoptosis in human lymphoma cells undergoing low-dose taxol-induced mitotic stress. Brit J Can 2003; 88:1649-58.

30 Meraner N, Chappell SC, Sansam CJ, Clarke AR, Thomble-Spinde R, Errington RJ, Smith PJ. Microtubule stress modifies intra-nuclear location of Mah2 in mouse embryonic fibroblasts. Cell Cycle 2004; 3:662-71.

31 Smith PJ, Makinson TA. Cellular consequences of overproduction of DNA topoisomerase II in an ataxia-telangiectasia cell line. Cancer Res 1989; 49:1118-24.

32 Kaufmann WK, Campbell CB, Simpson DA, Deming PB, Filatov L, Galloway DA, Zhao XJ, Creighton AM, Downes CS. Degradation of ATM-independent decatenation checkpoint function in human cells is secondary to inactivation of p53 and correlated with chromosomal destabilization. Cell Cycle 2002; 1:210-9.

33 Taylor WR, Stark GR. Regulation of the $G_2$/M transition by p53. Oncogene 2001; 20:1803-15.

34 Park I, Avraham HK. Cell cycle-dependent DNA damage signaling induced by ICRF-193 involves ATM, ATR, CHK2, and BRCA1. Experimental Cell Research 2006; 312:1996-2008.

35 Tyson JJ. Monitoring p53's pulse. Nat Genet 2004; 36:113-4.

36 Liu JS, Kuo SR, Melendy T. DNA damage-induced RPA focalization is independent of gamma-H2AX and RPA hyper-phosphorylation. J Cell Biochem 2006; 99:1452-62.

37 Uetake Y, Sluder G. Cell cycle progression after cleavage failure: Mammalian somatic cells do not possess a "tetraploidy checkpoint". J Cell Biol 2004; 165:609-15.

38 Blagosklonny MV. Prolonged mitosis versus tetraploid checkpoint: How p53 measures the duration of mitosis. Cell Cycle 2006; 5:971-5.

39 Mikule K, Delaval B, Kaldis P, Jurcyzk A, Hergert P, Doxsey SD. Loss of centrosome integrity induces p38-p53-p21-dependent $G_1$-S arrest. Nature Cell Biology 2007; 9:160-70.

40 Cortes F, Mateos S, Pastor N, Domynguez I. Toward a comprehensive model for induced endoreduplication. Life Sciences 2004; 76:121-35.

# Appendix I-C

(Errington et al. 2010)

**Errington**, R. J.; Brown, M. R.; Silvestre, O. F.; Njoh, K. L.; Chappell, S. C.; Khan, I. A.; Rees, P.; Wilks, S. P.; Smith, P. J.; Summers, H. D., Single cell nanoparticle tracking to model cell cycle dynamics and compartmental inheritance. *Cell Cycle* **2010,** 9, (1), 121-130.

Cell Cycle Vol. 9, Issue 1, January 1, 2010; © 2010 Landes Bioscience

# Single cell nanoparticle tracking to model cell cycle dynamics and compartmental inheritance

Rachel J. Errington,[1,*] Martyn R. Brown,[2,†] Oscar F. Silvestre,[1] Kerenza L. Njoh,[1] Sally C. Chappell,[1] Imtiaz A. Khan,[1] Paul Rees,[2] Steve P. Wilks,[2] Paul J. Smith[1] and Huw D. Summers[2]

[1]School of Medicine; Cardiff University; Cardiff, UK; [2]Multi-disciplinary Nanotechnology Centre; Swansea University; Swansea, UK

[†]These authors contributed equally to this work.

Key words: cell proliferation, cell lineage encoding, nanocrystal quantum dots, cell cycle, flow cytometry

**Single cell encoding with quantum dots as live cell optical tracers for deriving proliferation parameters has been developed using modelling to investigate cell cycle and proliferative outputs of human osteosarcoma cells undergoing mitotic bypass and endocycle routing. A computer-based simulation of the evolving cell population provides information on the dilution and segregation of nanoparticle dose cell by cell division and allows quantitative assessment of patterns of division, at both single cell and including whole population level cell cycle routing, with no a priori knowledge of the population proliferation potential. The output therefore provides a unique mitotic distribution function that represents a convolution of cell cycle kinetics (cell division) and the partitioning coefficient for the labelled cell compartment (daughter-daughter inheritance or lineage asymmetry). The current study has shown that the cellular quantum dot fluorescence reduced over time as the particles were diluted by the process of cell division and had the properties of a non-random highly asymmetric event. Asymmetric nanoparticle segregation in the endosomal compartment has major implications on cell-fate determining signaling pathways and could lead to an understanding of the origins of unique proliferation and drug-resistance characteristics within a tumour cell lineage.**



## Introduction

A central theme in cell biology is to seek and understand the origin and nature of innate and induced heterogeneity at the cell population level. The cell cycle, with its highly conserved features, is the fundamental driver for the temporal control of growth and proliferation in humans—while abnormal control and modulation of the cell cycle are characteristic of cancer cells particularly in response to therapy.[1] Cellular heterogeneity is a confounding factor in the analysis of cell population dynamics and is apparent in physiological, pathological and therapeutic situations. Acquiring and synthesising multi-parameter data from individual cells into predictive mathematical models—a systems approach, can address the disassembly of such underlying biological complexity. The core challenges are to ensure that acquisition platforms discern cellular or behavioral identity and that the analytical and modeling approaches act as integrating principles and provide tangible parameter outputs for both validation and discovery.

To meet the demands of both systematic and generic data format generation, flow cytometry analysis has provided an essential tool for cell cycle studies and represents a multi-parameter data source ideal for further interrogation via computational modeling. Here we describe an application of inorganic fluorescent-contrast nanoparticle agents, in this case quantum dots (Qdots) composed of semiconductor materials, and their use in the encoding and the tracking of live heterogeneous cellular systems. Critical features such as signal persistence, biocompatibility, compartmentalization and bespoke targeting suggest that they are suitable for long term cellular tracking even through multiple cell divisions.[2] The technical objective of the current investigation was to interlink nanoparticle tracking outputs in order to detect particles as they distribute within proliferating human tumour populations and so assess signal persistence. The scientific aim was to establish an integrated approach to reveal the extent of cellular bifurcation within a population (i.e., cell division and lineages), potentially providing profiles of drug resistance, clonality and ploidy changes in complex tumour populations. Furthermore, we have addressed for patterns of Qdot partitioning or cellular compartment inheritance between daughter-to-daughter at cell division. To achieve this a genetic algorithm was used to computationally determine, given experimental data input, a unique 'mitotic distribution function' which represents a convolution of cell proliferation kinetics (cell division) and the partitioning coefficient for the labelled cell compartment (lineage asymmetry).

Traditional approaches used for determining cell proliferation require knowledge of population size or the behaviour of a cellular marker diluted on a cell-to-cell basis. The latter approach can utilise samples of populations and a frequently used chemical marker is based on an organic fluorophore CFSE (carboxy-fluorescein diacetate succinimidyl ester). CSFE diffuses freely into cells where intracellular esterases cleave the acetate groups converting it to a fluorescent, membrane impermeable dye that is retained within the cytoplasm of the cell.[3,4] During each round of subsequent cell division, partitioning of the dye is essentially equal.[5] Cells can be analysed by flow cytometry to determine the intensity distribution of the fluorophore signal within the cell population and thereby quantify the extent of proliferation.[6,7] This systematic measure of attenuated fluorescence intensity provides a robust quantitative indicator of cell generation and has allowed detailed modelling of cell populations.[7] However for CFSE, fluorescence intensity declines rapidly over the first 48 hours but then stabilises in the absence of cell division due to catabolism making to difficult to determine a short term proliferative index.[8] Although the CFSE approach has been successfully used with lymphatic cell types it does not have global applicability, and it also limits the spectral channels available for multi-encoding, for instance substantial overlap of fluorescein into longer wavelength channels makes compensation for CFSE cross-talk challenging.[9] We have therefore considered the use of Qdots a broadband excitor with emission properties that can be continuously tuned thus providing flexibility when undertaking multi-colour labelling of cells.[10-13] The advantages of using Qdots in the place of traditional organic fluorophores have been widely reported.[2,14] Firstly, they are photostable allowing long-term labelling of live cell populations.[15,16] Secondly, Qdots present major advantages over conventional organic fluorophores as they are chemically stable and are not metabolised by the cell. Therefore not only is the fluorescent signal very much brighter than an organic fluorophore but also remains unperturbed by intra-cellular bio-chemical reactions.[17,18] Finally when linked with ligands such as antibodies, peptides or small molecules, Qdots can be used to target specific cellular or molecular compartments.[19] It is the stability and persistence of the Qdot signal within cells over multiple generations that offer an approach for cellular lineage encoding and tracking.

We have exploited this tracking capability to detect proliferative sub-fractions and alternative cell routing within human osteosarcoma cell populations (U-2 OS cell line) treated with bisdioxopiperazine ICRF-193, a catalytic inhibitor of topoisomerase II which blocks the ability of the enzyme to resolve inter-linked DNA replication products without inducing overt damage.[20] The decatenation of chromosomal replication products is vital for the completing of segregation and hence normal division.[21] This agent causes a pre-mitotic delay, at an ATR-dependent "decatenation checkpoint", effected through cyclin B1 phosphorylation and a sustained nuclear exclusion of cyclin B1.[22] We have previously shown that in p53-functional ICRF-193-treated cells can enter an endocycle and undergo a transition to tetraploidy that bypasses mitosis and the mitotic spindle checkpoint.[23] Thus, decatenation inhibition provides a means of removing some or all division events while retaining viability and abnormal cell cycle progression. To address the complex proliferation patterns in this heterogeneous system we have used the far-red Qtracker® 705 (Qtracker705) system which enables cellular internalisation and endosomal compartmentalisation of CdTe/ZnS core-shell Qdots using arginine-rich peptides.[24] The loading of Qdots via endocytosis has been shown to be an effective delivery method for cell labelling;[17] and Qdot fluorescence has been used for cell identification via multi-colour labelling.[25,26] Here, we report on the first use of Qdots to provide quantitative information on cell proliferative features such as cell division and endosome inheritance supported by computation of mitotic distribution function.

## Results

**Uptake and patterning of quantum dots in tumour cells.** Initially, the delivery and stabilisation of the Qdot signal in interphase cells was assessed. U-2 OS cells growing on gridded coverslips were pulse loaded with Qdots (4 nM Qtracker705 for 1 hour). After 5 hours of further equilibration the cells exhibited primarily plasma membrane-diffuse and punctuate fluorescence signal (Fig. 1A). 24 hours later the same cells exhibited intracellular (perinuclear) punctuate localisation of fluorescence signal (Fig. 1B). Single cell fluorescent microscopy was carried out to determine whether the cell cycle position affected the loading of Qtracker705 into cells as previous vehicle delivery systems have shown preferential loading. U-2 OS cells expressing the cyclin B1-GFP reporter were loaded with Qdots (Fig. 1C).

Timelapse microscopy experiments were carried out to determine whether the endosome targeted Qdots had any perturbing effect on the U-2 OS population. By conducting single cell analysis rather than whole population cell counting we were able to detect small and transient perturbations of cell growth and relate this to cell cycle induced stress responses. A mitotic event curve was derived from measuring cumulative time to mitosis of individual cells, each contributing to a kinetic overview of the population response U-2 OS ATCC cells were loaded with a single concentration of Qdots (4 nM), cell growth was determined via transmission timelapse microscopy for a period of 48 hours.[10] Image analysis provided the ability to extract the time-to-event curves that demonstrated the dynamics of event delivery in quantum dot loaded and control conditions. Targeted endosome labelling with Qdots showed no acute effects on the ability of the cells to traverse the cell cycle and deliver to mitosis (**Suppl. data A**). The carrier alone showed a slight perturbation (between 7 to 14 hours) with a subsequent recovery over the remaining 10 hours. In control conditions all of the mitotic events during the course of the sequence led to successful cell division (i.e., two daughters). We conclude that there is a minimal perturbation to the cell cycle associated with specific near-infrared quantum dots via the endosomal pathway.

**Multi-generation tracking.** Tracking of the population via the Qdot fluorescence was carried out at 24 h intervals after an initial 24 h period to allow for stabilisation of the signal following Qdot uptake; in particular the trafficking of the Qdots to internal compartments (endosomal vesicles). To obtain quantitative analyses statistically relevant numbers were required and so flow cytometry was used to measure Qdot fluorescence in sample sets of 10,000 cells. A typical set of histograms is shown in **Figure 2A**, these data have been gated to ensure sampling of only healthy cells. The endosomal targeting of the Qdots produced a large

*Correspondence to: Rachel J. Errington; Email: erringtonrj@cf.ac.uk
Submitted: 07/02/09; Revised: 08/04/09; Accepted: 10/05/09
Previously published online: www.landesbioscience.com/journals/cc/article/10246

dynamic range in the dot fluorescence per cell and hence the acquisition using a logarithmic detection scale.

As the assay progressed the histograms shifted down on the x-axis and broadened leading to a reduced peak cell count. The loss of fluorescence signal was expected as the nanoparticle density per cell became diluted by partitioning upon cell division. In normal growth conditions U-2 OS cells divide every 20.5 ± 4 hours (**Fig. 2C**) thus for a steady state distribution of cell position within the cell cycle we expected 97% of cells to have divided within a 24 hour period. Therefore if the dot partitioning between daughter cells is symmetrical, conforming to a ~50:50 split, then the distribution should shift to half the x-axis value with an unchanged peak cell count (all histograms having the same sample number of 10,000). The broadening of the distribution therefore indicated that dot partitioning was asymmetric through the endosomal pathway. To quantify the distributions we used two statistical measures; the arithmetic mean ( $\bar{x}$ ) and the co-efficient of variation ( $CV = \sigma/\bar{x}$ ). When using logarithmic scale distributions the geometric mean is usually preferred. We have choosen the arithmetic mean as this gives a measurement that is physically meaningful—namely the average Qdot fluorescence per cell. The values of $\bar{x}$, normalised to the 24 hour value, and the CVs are plotted in **Figure 2B**. The mean should halve in each 24 h period as Qdots become diluted between daughter cell pairs. The solid line in **Figure 2** showed an exact halving and the measured fluorescence signal was within ~10% of this thus confirming that the dots do provide a persistent and stable optical tracking signal. The CV doubled between 24 and 72 hours due to the asymmetric division of the Qdots (for symmetric partitioning $\bar{x}$ and σ halve upon division i.e., CV would be constant). These simple, statistical descriptors of the fluorescence histograms provide detailed outputs, validating the integrity of the tracking signal and providing an insight to the mechanics of the dot dilution by the growing cell population.

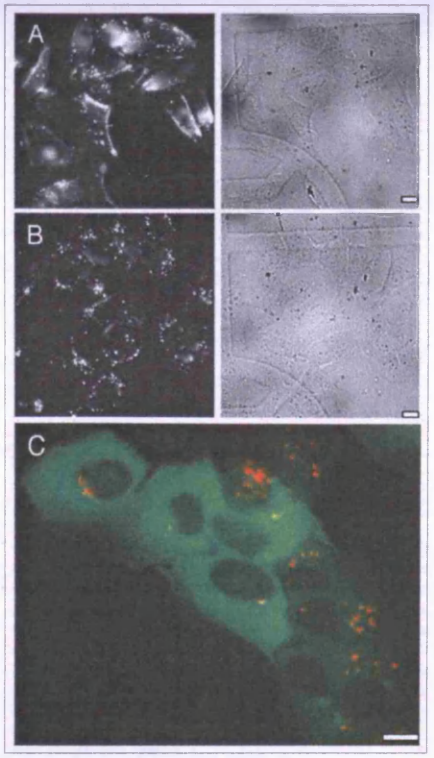


**Figure 1.** Uptake, patterning and impact of QTracker705 loading in human osteosarcoma cells (U-2 OS). (A) U-2 OS cells exposed to QTracker705 (4 nM for 1 hour), 5 h post-labelling; (B) identical coverslip area as (A) 24 h post-labelling cells (C) QTracker705 intracellular localisation (red) in cells expressing cyclin B1-GFP (green) to indicate cell cycle position 24 hours post-labelling.

**Computational modelling of Qdot dilution by cell division.** To obtain a quantitative analysis of cell cycle perturbation computational data analysis was performed, based on a stochastic model of cell mitosis within a large population.[27] The purpose was to simulate the evolution of the fluorescence histogram and so provide a more detailed analysis of quantum dot partitioning during mitosis and quantitative prediction of the proliferation dynamics. The Qdot fluorescence data, taken at 24 hours, was used as an input set for this computational analysis, the output of which was subsequently compared to data at later time points. The computational approach treated cell proliferation as a discrete process, tracking cell division events and the associated Qdot dilution in the daughter cells. The evolution of the fluorescence distribution was determined by the influence of the population and division dynamics: the time from mitosis-to-mitosis or intermitotic time (IMT) drives the time dependency of the fluorescence reduction whilst the asymmetric particle partitioning determines the extent of the distribution broadening. The independence of these processes allows a unique fit to the data requiring no a-priori knowledge of the population proliferation parameters. The simulation was therefore determined by the variables of IMT and partition ratio that are modeled as Gaussian functions defined by a mean and standard deviation. The Gaussian form was adopted for mathematical expediency allowing some cell-to-cell variation in the parameter values and implies no physical significance beyond this. Indeed the computational approach as a whole sought to provide predictive modeling of the changing data, the detail of the biological process driving this change was not specified. The model assumed that cells were randomly distributed within the cell cycle period. As the time variable was incremented a Monte Carlo algorithm was applied to determine whether or not a given cell divided within the time window using a random sampling of the Gaussian profile for the inter-mitotic time distribution. On division we assume that the number of quantum dots was conserved i.e., the total number of Qdots in each daughter cell was equal to the number of dots in the parent cell and that the fluorescence efficiency remains constant. The fraction of Qdots within a dividing cell allocated to each daughter cell was again chosen at random from the Gaussian distribution of partition ratios. At the set 'measurement' time a fluorescent histogram was calculated by determining the number of dots in each cell, this histogram was then compared directly with experimental data. Genetic algorithms were used to select and modify the variable parameters (mean and standard deviation) that describe the Gaussian distributions with 'evolutionary fitness' being determined by comparison of the modeled histograms with flow data.[15] The computational analysis follows the evolution of the fluorescence intensity distribution in an increasing cell population and did not consider cell death. Because the experimental data was gated to acquire information for healthy cells the modeling procedure was unaffected by cell apoptosis, i.e., the experiment and the model only consider the viable cell population. The modelled histogram at 48 hours, computed from the 24 hour data was compared to the experimentally determined distribution at 48 hours (**Fig. 3**), black and red distribution respectively. This fit was achieved with an asymmetric fluorescence partitioning of 74:26% with a standard deviation of 6% and an IMT of 22 ± 4 hours. The two data sets were virtually indistinguishable and so this substantiated the evidence of asymmetric dot dilution and indicated that there was some stochastic variation about the mean.

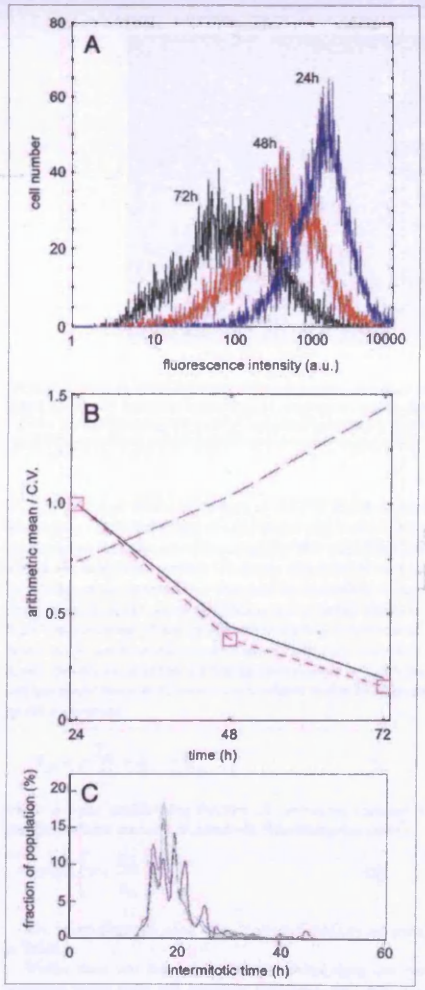


**Figure 2.** (A) QTracker705 fluorescence intensity histograms taken at 24 hour intervals post-labelling; (B) Statistics from the histograms: arithmetic mean (red line) and coefficient of variation (blue line). The solid black line represents the expected mean due to halving of the dot density per cell every 20.5 hours. (C) Distribution of intermitotic time (IMT) over three generations taken from lineage tracking of U-2 OS cells. The mean IMT from generation 1 to 3 was 21.20 h (green), 20.01 h (blue) and 20.26 h (black) respectively.

To further corroborate the asymmetric partitioning a transformed version of the 24 hour data set was obtained for which the fluorescence per cell has been scaled to half the measured value. This corresponds to an exact and equal halving of the Qdots between daughter cells and was in obvious disagreement with the data measured at 48 hours (**Fig. 3**, light blue distribution). Confocal microscopy was performed to track and validate Qdot partitioning during cell cycle traverse through $G_2$ and mitosis. Upon the initiation of mitosis the cell became rounded and the Qdot fluorescence coalesced in the cell [(**Fig. 4** (35 min)), during anaphase (50 min)] the available endosomal organelles became redistributed to each daughter again asymmetrically (130 min). Therefore taken altogether the impact of labelling the endosomal pathway with Qdots showed that this approach would differentiate a non-dividing from a proliferating population.

**Cell cycle routing through mitotic bypass.** The distinct pharmacodynamic response of U-2 OS cells to ICRF-193 (23) provided a biological model system in which to test the concept that the total Qdot signal from cells treated with a proliferation blocking drug should not change. A schematic (**Fig. 5F**) offers a simple description of the differential routing in the cell cycle. A normal untreated population should show a predicted decrease in signal as the same quanta of fluorescence become reassigned to daughters of sequential generations. We undertook a 'pulse chase' experiment in which cells were labelled with Qdots and then treated with ICRF-193 for 24 hours post-loading (**Fig. 5**).

The cell cycle routing of cells treated with ICRF-193 was established using flow cytometric analysis of U-2 OS cells expressing cyclin B1-GFP to confirm mitotic bypass and the driving of cells into tetraploidy. In control conditions U-2 OS cells divide (+m) and remain in normal cycle (representing the proliferative fraction). With ICRF-193 treatment the U-2 OS cells continue to cycle but bypass mitosis (-m) to enter a polyploid cycle (p) (representing the non-proliferative fraction). Flow cytometry analysis of living U-2 OS cells expressing cyclin B1-GFP and labelled with DRAQ5 (DNA content) provided a means for dissecting out the routing of cell in normal and polyploidy cycles. After 24 h in control conditions all cells were engaged in normal cell cycle (**Fig. 5A**).

Cyclin B1-GFP levels were approximately 10-fold increased in $G_2$ compared to cells in $G_1$. Following a 24 h continuous treatment with ICRF-193 (2 ug/ml) cells had DNA content of 4n, 65% expressed high cyclin B1-GFP and 30% expressed low cyclin B1-GFP (blue ($G_2$) versus pink (G1p)) (**Fig. 5B**). After 48 h continuous treatment of cells with ICRF-193, the cells further accumulated into into G1p (**Fig. 5C**). After 72 hours all cells were in the polyploidy cycle (yellow (G1p)). However for the population subjected to a 24 h continuous treatment with ICRF-193 followed by a wash and chase for 18 h in normal conditions, cells occupy both the normal and polyploidy cycle (**Fig. 5D**). This has occurred because ICRF-193 is a reversible topoisomerase II blocker and removal of this agent enabled the population of cells captured in $G_2$ after 24 hours in ICRF-193 to be routed normally. Hence after 18 hours of wash and chase approximately 49% of the population was found in $G_1$ and S of the normal cell cycle. While removal of the inhibitor allowed for enhanced traverse of the polyploid fraction (39%), a detectable fraction (3%) was even found in G2p compared to the 48 hour continuous treatment counterpart (**Fig. 5E**). The Qdot fluorescence signal (obtained at 24 and 48 hour time points) was then used to obtain a quantitative measure of the fraction of the cell population that proceeded through mitosis during the 18 hour wash and chase period (24–42 hours). The results were compared to the standard fluorescence techniques using nuclear stains and cell cycle reporters to analyse the state of sub-populations within $G_1$ and $G_2$ phases and hence classify the dividing and non-dividing fractions (**Fig. 6**). The dot fluorescence clearly informs on the dynamics of the interaction of the drug with the cell population showing minimal change between 24 and 48 hours as cell division was minimised thus preventing dot dilution (blue and red traces). In the sample subjected to a wash out at 24 hours the fluorescence signal attenuated and broadened indicating that progression through mitosis had been re-initiated (black trace) although comparison with the control sample (at 48 hour green trace) a net reduction in cell proliferation had occurred.

**Modelling quantum dot encoding and cell cycle routing.** Using the modelling procedure described above we were able to fit all three distributions shown in **Figure 6** and compute the proliferative fraction of cells in each scenario. **Figure 7** shows the computed and experimental distributions 48 hours into the assay and corresponding parameter values predicted by the fits (**Table 1**). The predicted proportion of 61% of cells dividing

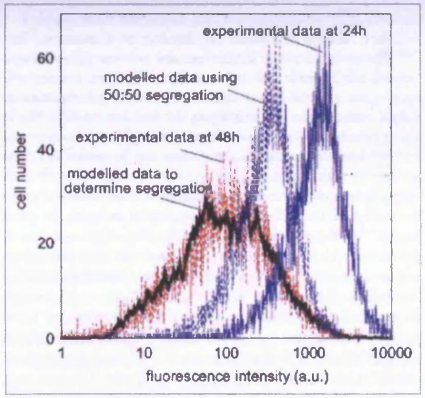


**Figure 3.** Modelled intensity partitioning of QTracker705 upon cell division. Computed (black) and experimentally measured (red trace) QTracker705 fluorescence histograms 72 hours post labelling. The modelled fit has a peak probability of partitioning ratio of 74:26% with a 6% standard deviation.

within the 'wash-out' sample was in good agreement with that obtained from the experimental analysis of the $G_2$ arrest via GFP cell cycle and DRAQ nuclear markers.[10] It is likely that a small sub-population of cells do breach the ICRF-193 decatenation checkpoint and proceed to mitosis and hence leads to a reduction of both the mean fluorescence signal and the small increase in the CV between the continuous drug treatment at 24 and 48 hours. The margins of error quoted in **Table 1** are obtained from the distribution of results produced by the stochastic variation encoded in the model as evidenced over a thousand independent runs.

The computational model used probabilistic algorithms to mimic the stochastic nature of the cell cycle and cell division processes. Within a 24 h measurement period it tracked the subfractions of non-proliferating cells and first and second generation daughter cells with only an assumption of persistence of overall Qdot fluorescence signal. Whilst this approach provided a robust and accurate analysis of cell cycle dynamics it required bespoke computer coding and so becomes limited in its availability and application to the wider scientific community. We therefore adopted an approach of minimal assumptions and maximum model accuracy as a benchmark and progressively simplify our approach to provide a guide to the generic applicability of Qdot-enabled cell tracking using data analysis rather than computational modelling.

The requirement of a computational approach stems from the stochastic modelling of cell division. This can be avoided by an appropriate choice of measurement interval close to the intermitotic time which allowed for the assumption that all cells undergo a single division between measurement points. For example the



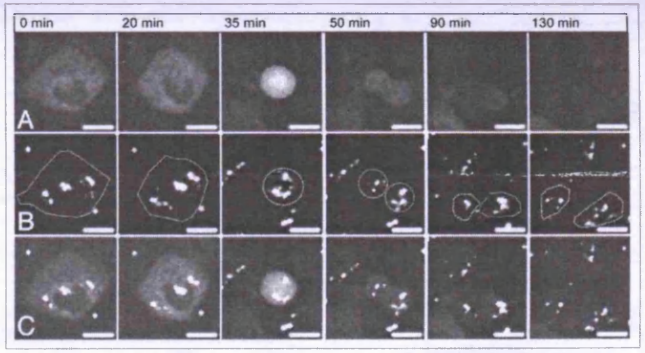


**Figure 4.** Tracking QTracker705 partitioning through the cell cycle in single cells. Timelapse sequence of a single U-2 OS cell undergoing mitosis. (A) Cyclin B1-GFP expression levels change as cells progress from $G_2$ (flat cell) to M (round cell) and through mitosis followed by switch-off as the cell divides; (B) Corresponding QTracker705 sequence demonstrating the localisation and segregation of signal upon division; (C) dual channel merge cyclin B1-GFP) signal (diffuse) and QTracker705 (punctuate signal). Bar = 10 μm.

U-2 OS cells used in this study have an IMT of 20.5 ± 4 hours which gives a 97% probability of cell division within the 24 hour measurement interval and <1% probability of a second division within the same time period. Obviously this required a-priori knowledge of the intermitotic time and its variability. Once a single division of the whole population was assumed an immediate quantification of the proliferating fraction was obtained, based on the arithmetical mean of the fluorescence histogram. A cell division event halves the average fluorescence intensity per cell and so the mean at 48 hours can be related to that at 24 hours by the expression:

$$\bar{x}_{48} = a\frac{\bar{x}_{24}}{2} + (1-a)\bar{x}_{24} \quad (1)$$

where $a$ is the proliferating fraction. Re-arranging equation 1 provides a direct measure of $a$ from the flow histogram mean:

$$a = 2.\left(1 - \frac{\bar{x}_{48}}{\bar{x}_{24}}\right) \quad (2)$$

The values obtained using these numerical analyses are given in **Table 1**.

Whilst there was some discrepancy between these and the predicted values from full computer simulation they still provide a reasonable estimate of the proliferating fraction albeit with a greater degree of uncertainty. This type of numerical analysis could of course be done using cell counts rather than a fluorescence signal. However by using the flow cytometry based approach the analysis was based on measurement of 10,000 cells rather than a few hundred and so the margin of error was reduced and the detail of the proliferating process can be viewed in the evolving intensity distributions e.g., in **Figure 6** the re-establishment of mitosis following removal of the ICRF-193 was graphically displayed in the movement of the distribution along the x-axis and the suggestion of two separate, proliferative and non-proliferative, sub-populations within the flow histogram. Thus the analysis was not 'blind' to the driving process as was the case for simple cell counting procedures. Measures based on cell counts are also affected by the rate of cell death (an unknown) whereas the flow analysis was independent of this because it is based on the measurement of Qdot fluorescence reduction in the healthy cell population.

## Discussion

Engineered nanoparticles are increasingly providing advantages for the building of robust cell-based bioassays combining exceptional photo- and chemically stability with other unique properties.[28] The potential for nanoparticle use in drug discovery, bioengineering and therapeutics has been reviewed previously.[29] We showed that the growth dynamics of cells loaded with peptide-targeted 705 nm emitting quantum dots was not adversely affected. The Qdots therefore provided a non-invasive encoding system for profiling global proliferative events in tumour populations and tracking cell cycle routing. The use of stochastic, Monte Carlo simulations linked to experimental flow cytometry data provided an analysis technique capable of providing quantitative assessment of the proliferation kinetics based on the evolving Qdot fluorescence distribution across the cell population. The computational data analysis approach required no a-priori knowledge of the cell division process relying solely on the evolution of the measured data sets to provide a unique prediction of the population dynamics. The inorganic quantum dots provided

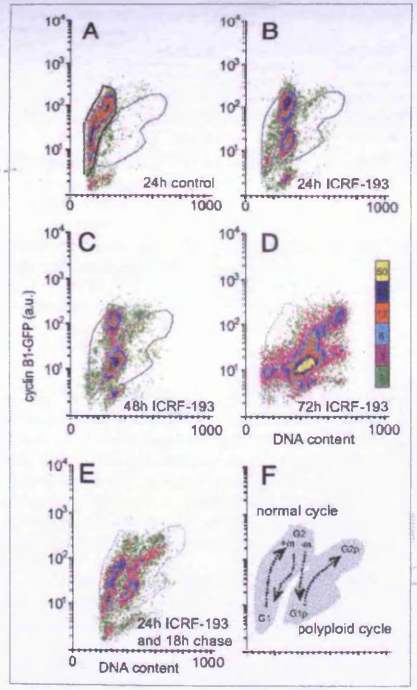


**Figure 5.** Normal cell cycle and endocycle routing of human osteosarcoma cells treated with ICRF-193. Colour dot plots from flow cytometry bivariate analysis of cyclin B1 expression versus DNA content for different treatment regimens. (A) 24 h control; (B) Post-24 h continuous treatment with ICRF-193; (C) 48 h continuous treatment of cells with ICRF-193 (2 ug/ml) (D) 72 h continuous treatment of cells with ICRF-193 (2 ug/ml), (E) 24 hour continuous treatment with ICRF-193 followed by a wash step and chase for 18 h in normal conditions. (F) Schematic to depict normal and endocycle cell routing. First outline shape represents normal (2n to 4n cycle). Second outline shape represents polyploidy (4n to 8n cycle). Colour LUT = % of peak height.

a fluorescent identifier of cell generation and therefore position within a cell lineage that was derived by a combination of different core factors including (1) the intrinsic cellular uptake mechanism and processing to a single compartment via endocytosis, (2) long term Qdot signal stability in an acidic cellular compartment and (3) partitioning properties equivalent from generation to generation. They represent therefore a marker with global applicability with the potential to provide accurate determination of pharmacodynamic response in drug screens or quantitative analysis of tumour cell lineage in both in vivo and in vitro tissue samples.

Previous work has shown that the partitioning of endosomes and lysosomes is an ordered, yet stochastic, process, and that organelle copy number was maintained by the daughter cells.[30,31] Our current studies have shown that the cellular Qdot fluorescence reduced over time as the dots were diluted by the process of cell division and had the properties of a non-random highly asymmetric event. Furthermore this was a highly predictive property. The impact of this asymmetric inheritance on proliferation and cell cycle survival capacity under various forms of stress is yet to be determined. Molecular functional and structural asymmetry for daughter inheritance at cell division has been observed in adult stem cells and perhaps early tumour formation.[32] Recent studies with hematopoietic stem cells have associated a direct link between asymmetric segregation of endosomal proteins and the determination of cell-fate such as self-renewal versus differentiation.[33] Asymmetry may act to impose proliferation advantages or disadvantages acting to widen Darwinian fitness while limiting the divisional potential of a given lineage. Cell division requires tight control of spindle orientation and therefore division is influenced by cytoskeletal perturbations.[34] Nanoparticle compartmentalization in endsomes are effectively 'artificial aggresomes' with implications for nanotoxicology modeling and the development of scalable methods for cell tracking and profiling—a process driven by advances in chemistry and photophysics. There are several precedents of this view including 'aggresomes' of misfolded proteins located at the microtubule (MT) organizing centre as cages with various cellular structures (e.g., mitochondria).[35] Therefore the overall challenge is to dissect the impact and operation of asymmetric division and the inter-relationships of cells as lineages develop and perhaps collapse as part of a pharmacodynamic response. In the future it will be important to assess the extent of co-segregation of cellular structural elements, obtained by targeting of multi-spectral nanoparticles, capable of providing readouts of cell cycle progression and lineage asymmetry suitable for deconvolution and mathematical modelling analysis.

## Materials and Methods

**Cell culture.** U-2 OS (ATCC HTB-96) cells were transfected with the $G_2$M Cell Cycle Phase Marker (GE Healthcare, UK), yielding stable expression of U-2 OS cyclin B1-eGFP cells.[36] The culture was maintained under G418 selection in McCoy's 5a medium supplemented with 10% foetal calf serum (FCS), 1 mM glutamine, and antibiotics and incubated at 37°C in an atmosphere of 5% $CO_2$ in air. For imaging experiments, cells were grown at a density of 1 x $10^6$ cells $ml^{-1}$ as a monolayer in either coverglass bottomed chambers (Nunc, 2 Well Lab-Tek II, Fisher Scientific); glass bottomed (24 multi-well Sensoplate, Greiner Bio-one); or plastic tissue culture plates (6 multi-well, BD Falcon); or onto glass coverslips with silica cell location grids (Carl Zeiss, Welwyn Gardn City, UK) for 24 h prior to imaging. All cell concentrations were determined using a Coulter Particle Counter (Beckman Coulter, High Wycombe, UK).

**Reagent preparation and treatments.** Cells were loaded with commercially available targeted nanocrystals using the Qtracker® 705 (QTracker705) Cell Labelling Kit (4 nM) (Invitrogen



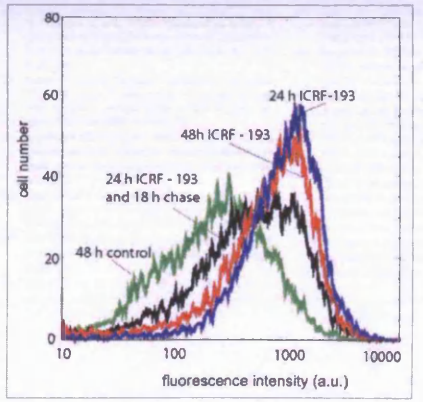


**Figure 6.** QTracker705 fluorescence intensity histograms for U-2 OS cells treated with ICRF-193; drug treated cells measured at 24 hours (blue line), at 48 hours (green line) and cells measured at 48 hours following wash out of the drug 24 hours earlier (red line).

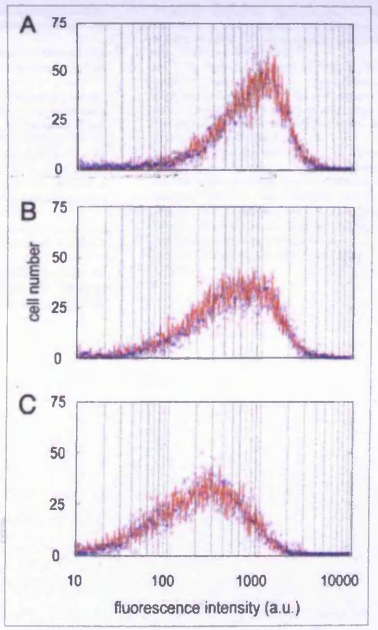


**Figure 7.** QTracker705 fluorescence intensity histograms at 48 hours post loading for U-2 OS cells (A) continuously treated with ICRF-193 (division blocked); (B) 24 hour continuous treatment with ICRF-193 followed by a wash step and chase for 18 h (block and release) and (C) control with no drug treatment (normal cell division). The blue squares represent the experimental data, the solid red lines are the modelled histograms.

(Q25061MP). The reagents in the Qtracker® 705 Cell Labelling Kit use a custom targeting peptide (9-arginine peptide) to deliver near-infrared-fluorescent nanocrystals into the cytoplasm of live cells via the endosomal pathway.[17] Briefly, Qtracker reagent A and B were premixed and then incubated for 5 mins at room temperature. 1 ml of fresh full growth media was added to the tube and vortexed for 30 seconds. This labelling solution was then added to each well of the cells and incubated for 1 hour at 37°C after which they were washed twice with fresh media. Subsequently 24 (48 and 72) hours later, labelled cells were then analysed either by flow cytometry, fluorescent microscopy, confocal microscopy or timelapse microscopy. Sham treated control cells were loaded only with Qtracker reagent B (carrier) solution. ICRF-193 [bis(2,6-dioxopiperazine)], a kind gift from Dr. A.M. Creighton (ICRF, London, UK) was prepared in DMSO at 2 mg/ml and used at a peak concentration of 2 µg/ml (equivalent to 7.2 µM).[23] DRAQ5™ (20 µM Biostatus Ltd., UK) was used as a marker of DNA content.[37]

**Microscopy (transmission, fluorescence and timelapse).** For phase timelapse microscopy, a 6 well plastic tissue culture plate was seeded with U-2 OS ATCC cells and loaded with either: 0, 4 nM or sham (carrier only) QTracker705 nanocrystals and then placed onto a microscope stage with an incorporated incubator. The instrument comprised a Zeiss Axiovert 100 microscope (Zeiss, Welwyn Garden City, UK) fitted with a temperature regulating incubator system and $CO_2$ supply (Solent Scientific, Portsmouth, UK). The motorised xy microscope stage was from Prior Scientific and the phase transmission images (x10 objective lens) were captured every 10 min over 24 h (144 frames per field) or 120 h (720 frames per field) using an Orca I ER charge-coupled device camera (Hammamatsu, Welwyn Garden City, UK). The camera, stage (xy) and focus (z) were PC controlled via AQM 2000 software (Kinetic Imaging, Wirral, UK). For single well timelapse fluorescence microscopy, one well of a 24 well glass bottomed plate was seeded with U-2 OS ATCC cells in phenol free media and loaded with 4 nM targeted QTracker705 nanocrystals, as described above, and captured with a x40 0.9 NA objective lens every 5 min over 48 h. Tiff-format Images (512 x 512 pixels) were played back for analysis as movies using MetaMorph software (Molecular Devices Corporation, PA, USA). The timelapse image sequences were manually analysed by counting the start and end numbers of cells, and by recording the time and nature of mitotic or death events during the observation period.[38,39]

**Confocal laser scanning microscopy radiance CLSM (BioRad Ltd.) timelapse.** Was performed to track dual labelled U-2 OS cells through mitosis: Cyclin B1-GFP (488 nm ex/540–35 nm

**Table 1. Cell proliferation parameters derived from model simulation and experimental analysis**

| | Control | Mitotic bypass [ICRF-193 continuous] | Mitotic bypass and chase [ICRF-193 plus wash] |
|---|---|---|---|
| IMT (h) | 22 ± 4 | 21 ± 4 | 21.5 ± 4 |
| Partitioning fraction (%) | 72 ± 2 | 68 ± 5 | 76 ± 4 |
| Proliferative fraction [from Monte Carlo simulation] | 98 ± 2 | 8 ± 2 | 61 ± 5 |
| Proliferative fraction (%) [from direct numerical analysis] | 92 | 36 | 73 |
| Proliferative fraction (%) [from experimental analysis] | 97.2 | N/A | 65 |

em) and Qtracker705 (488 nm ex/680–20 nm em); x,y,z,t optical sections (using x40, 0.75 NA air lens) were collected every 5 mins for 2 hours. Single cell dual channel snap-shot images were obtained for high resolution details of localization and cell cycle cyclin B1-GFP expression (using x40 1.3 NA oil lens). Cell locate grids were used to follow uptake and redistribution of QTracker705 signal (over the initial 0–24 hours); dual channel phase transmission and red fluorescence (647/20 nm ex/660/30 nm em).

**Time series flow cytometry of QTracker705 distribution.** U-2 OS cyclin B1-GFP cells were seeded into fifteen 25 $cm^2$ cell culture flasks and incubated at 37°C and 5% $CO_2$ for 24 hours prior to the experiment. For each of the 3 days of the experiment, 5 samples were prepared: a control sample, a sham treated sample, and 4 nM Qtracker705 for one hour in media; a sample loaded with 2 µg/ml ICRF-193 only and a sample loaded with both Qtracker® 705 (4 nM) and ICRF-193 (2 µg/ml). The flasks were then incubated at 37°C and 5% $CO_2$ 24 hours prior to flow cytometric analysis. U-2 OS cyclin B1-GFP cell monolayers were detached from the plates using trypsin and cells re-suspended in complete medium. To determine the cell population distribution of Q-dot®705 fluorescence intensity a FACScan *flow cytometer was used* (Becton Dickinson Inc., Cowley, UK) which was equipped with an aircooled argon ion laser (with 488 nm output only). CELLQuest software (Becton Dickinson Immunocytometry Systems) was used for signal acquisition. The optics for the analysis of Qtracker 705 excited by the 488 nm beam comprised reflection at a short pass 560 nm filter and a long pass 650 nm filter. Forward and side scattered light was collected for 10,000 cells and were analysed to exclude any cell debris. Data were expressed as mean fluorescence intensity (FI) values. Instrument response for the fluorescence signal collection was calibrated using Dako FluoroSpheres (DakoCytomation) which comprise a mixture of 5 bead populations having different fluorescent intensities, and one non-fluorescent bead population. A parallel time-series analysis was undertaken in full culture medium supplemented with 10 mM HEPES prior to the addition of 20 µM DRAQ5. The resulting preparations were analysed with a single excitation (488 nm) and dual emission FL1 (515–540 nm) to detect GFP expression and FL2 (580LP) to detect DRAQ5 labelling.


## Acknowledgements

The authors acknowledge grant support from the Research Councils UK Basic Technology Research Programme (GR/S23483) and the Biotechnology and Biological Sciences Research Council (75/E19292). We also thank D.R. Matthews and M. Wiltshire for their contribution to this work.


## Note

Supplementary materials can be found at:
www.landesbioscience.com/supplement/ErringtonCC9-1-Sup.pdf

## References


1. Massagué J. $G_1$ cell cycle control and cancer. Nature 2004; 432:298-306.
2. Resch-Genger U, Grabolle M, Cavaliere-Jaricot S, Nitschke R, Nann T. Quantum dots versus organic dyes as fluorescent labels. Nature Methods 2008; 5:76-775.
3. Dumitriu IE, Mohr W, Kolowos W, Kern P, Kalden JR, Herrmann M. Carboxyfluorescein diacetate succinimidyl ester-labeled apoptotic and necrotic as well as detergent-treated cells can be traced in composite cell samples. Anal Bioch 2001; 299:247-52.
4. Hasbold J, Hodgkin PD. Flow cytometric cell division tracking using nuclei. Cytometry 2000; 40:230-7.
5. Lyons AB, Parish CR. Determination of lymphocyte division by flow cytometry. JIM 1994; 171:131-7.
6. Lyons AB, Hasbold J, Hodgkin PD. Flow cytometric analysis of cell division history using dilution of CFSE, a stably integrated fluorescent probe. Meth in Cell Biol 2001; 63:375-98.
7. Bernard S, Pujo-Menjouet L, Mackey MC. Analysis of cell kinetics using a cell division marker: Mathematical modeling of experimental data. Biophys J 2003; 84:3414-24.
8. Lee JH, Hodgkin PD, Lyons AB. B cell differentiation and isotype switching is related to division cycle number. J Exp Med 1996; 184:277-81.
9. Baumgarth N, Roederer M. A practical approach to multicolor flow cytometry for immunophenotyping. J Immunol Meth 2000; 243:77-97.
10. Alivisatos AP. Semiconductor clusters, nanocrystals and quantum dots. Science 1996; 271:933-7.
11. Pinaud F, Michalet X, Bentolila LA, Tsay JM, Doose S, Li JJ, et al. Advances in fluorescence imaging with quantum dot bio-probes. Biomaterials 2006; 27:1679-87.
12. Hines MA, Guyot-Sionnest P. Synthesis and characterization of strongly luminescing ZnS-Capped CdSe nanocrystals. J Phys Chem 1996; 100:468-71.
13. Dabbousi BO, Rodriguez-Viejo J, Mikulec FV, Heine JR, Mattoussi H, Ober R, et al. (CdSe)ZnS core-shell quantum dots: synthesis and characterization of a size series of highly luminescent nanocrystallites. J Phys Chem 1997; 101:9463-75.
14. Jyoti K, Sanford MS. Potentials and pitfalls of fluorescent quantum dots for biological imaging. Trends in Cell Biol 2005; 14:497-504.
15. Parak WJ, Pellegrino T, Plank C. Labelling of cells with quantum dots. Nanotech 2005; 16:9-25.
16. Hoshino A, Hanaki K, Suzuki K, *Yamamoto K.* Applications of T-lymphoma labeled with fluorescent quantum dots to cell tracing markers in mouse body. Biochem and Biophys Res Comm 2004; 314:46-53.
17. Hanaki K, Momo A, Oku T, Komoto A, Maenosono S, Yamaguchi Y, Yamamoto K. Semiconductor quantum dot/albumin complex is a long-life and highly photostable endosome marker. Biochem and Biophys Res Comm 2003; 302:496-501.
18. Jaiswal JK, Mattoussi H, Mauro JM, Simon SM. Long-term multiple color imaging of live cells using quantum dot bioconjugates. Nature Biotech 2002; 21:47-51.
19. Matheakis LC, Dias JM, Choi YJ, Gong J, Bruchez MP, Liu J, et al. Optical coding of mammalian cells using semiconductor quantum dots. Anal Biochem 2004; 327:200-8.
20. Clarke DJ, Johnson RT, Downes CS. Topoisomerase II inhibition prevents anaphase chromatid segregation in mammalian cells independently of the generation of DNA strand breaks. J Cell Sci 1993; 105:563-9.
21. Ishida R, Sato M, Narita T, Utsumi KR, Nishimoto T, Morita T, et al. *Inhibition of DNA topoisomerase II* by ICRF-193 induces polyploidization by uncoupling chromosome dynamics from other cell cycle events. J Cell Biol 1994; 126:1341-51.
22. Deming PB, Cistulli C, Zhao H, Graves PR, Piwnica-Worms H, Paules R, et al. The human decatenation checkpoint. PNAS 2001; 98:12044-9.
23. Smith PJ, Marquez N, Wiltshire M, Chappell S, Njoh K, Campbell L, et al. Mitotic bypass via an occult cell cycle phase following DNA topoisomerase II inhibition in p53 functional human tumor cells. Cell Cycle 2007; 6:2071-81.
24. Nakase I, Niwa M, Takeuchi T, Sonomura K, Kawabata N, Koike Y, et al. Cellular uptake of arginine-rich peptides: roles for macropinocytosis and actin rearrangement. Mol Ther 2004; 10:1011-22.
25. Lagerholm BC, Wang M, Ernst LA, Ly DH, Liu H, Bruchez MP, et al. Multicolor coding of cells with cationic peptide coated quantum dots. Nano Lett 2004; 4:2019-22.
26. Gao X, Cui Y, Levenson R, Chung L, Nie S. In vivo cancer targeting and imaging with semiconductor quantum dots. Nat Biotech 2004; 22:969-76.
27. Vose MD. The Simple Genetic Algorithm: Foundations and Theory. 1st edn. Cambridge Mass.; London: MIT Press 1999.
28. Zhang H, Yee D, Wang C. Quantum dots for cancer diagnosis and therapy: biological and clinical perspectives. Nanomed 2008; 3:83-91.
29. Oulton M. Quantum dots and other nanoparticles: what can they offer to drug discovery? Drug Discov Today 2004; 9:1065-71.
30. Bergeland T, Widerberg J, Bakke O, Nordeng TW. Mitotic partitioning of endosomes and lysosomes. Curr Biol 2001; 11:644-51.
31. Dunster K, Toh BH, Sentry JW. Early endosomes, late endosomes and lysosomes display distinct partitioning strategies of inheritance with similarities to Golgi-derived membranes. Eur J Cell Biol 2002; 81:117-24.
32. Wodarz A, Gonzalez C. Connecting cancer to the asymmetric division of stem cells. Cell 2006; 124:1121-3.
33. Giebel B, Beckmann J. Asymmetric cell divisions of human hematopoietic stem and progenitor cells meet endosomes. Cell Cycle 2007; 6:2201-4.
34. Yamashita YM, Fuller MT. Asymmetric centrosome behavior and the mechanisms of stem cell division. J Cell Biol 2008; 180:261-6.
35. Rieu NP, Milward K, Lee T, Adams M, Askham MJ, Morrison EE. Trapping of normal EB1 ligands in aggresomes formed by an EB1 deletion mutant. BMC Cell Biol 2005; 6:17.
36. Thomas N, Kenrick M, Gloster T, Kiser G, Tibbler H, Stubbs S. Characterization and gene expression profiling of a stable cell line expressing a cell cycle GFP sensor. Cell Cycle 2005; 4:191-5.
37. Smith PJ, Blunt N, Wiltshire M, Hoy T, Teesdale-Spittle P, Craven MR, et al. Characteristics of a novel deep red/infrared fluorescent cell-permeant DNA probe, DRAQ5, in intact human cells analyzed by flow cytometry, confocal and multiphoton microscopy. Cytometry 2000; 40:280-91.
38. Marquez N, Chappell SC, Sansom OJ, Clarke AR, Teesdale-Spittle P, Errington RJ, et al. Microtubule stress modifies intra-nuclear location of Msh2 in mouse embryonic fibroblasts. Cell Cycle 2003; 3:662-71.
39. Marquez N, Chappell SC, Sansom OJ, Clarke AR, Court J, Errington RJ, et al. Single cell tracking reveals that Msh2 is a key component of an early-acting DNA damage-activated $G_2$ checkpoint. Oncogene 2003; 22:7642-8.

# Appendix I-D

(Brown et al. 2010a)

**Brown**, M. R.; Summers, H. D.; Rees, P.; Chappell, S. C.; Silvestre, O. F.; Khan, I. A.; Smith, P. J.; Errington, R. J., Long-term time series analysis of quantum dot encoded cells by deconvolution of the autofluorescence signal. *Cytometry Part A* **2010a**, [Epub ahead of print].

Cytometry
PART A

# Long-Term Time Series Analysis of Quantum Dot Encoded Cells By Deconvolution of the Autofluorescence Signal

M. Rowan Brown,[1]* Huw D. Summers,[2] Paul Rees,[2] Sally C. Chappell,[1] Oscar F. Silvestre,[1] Imtiaz A. Khan,[1] Paul J. Smith,[3] Rachel J. Errington[1]

[1]Department of Infection, Immunity and Biochemistry, School of Medicine, Cardiff University, Heath Park, Cardiff CF14 4XN, United Kingdom

[2]Multidisciplinary Nanotechnology Centre, School of Engineering, Swansea University, Swansea SA2 8PP, United Kingdom

[3]Department of Pathology, School of Medicine, Cardiff University, Heath Park, Cardiff CF14 4XN, United Kingdom

Received 22 April 2010; Revision Received 3 June 2010; Accepted 7 June 2010

Additional Supporting Information may be found in the online version of this article.

Grant sponsor: EPSRC; Grant number: EP/G037841/1

*Correspondence to: M. Rowan Brown, Department of Infection, Immunity and Biochemistry, Tenovus Building, School of Medicine, Cardiff University, Heath Park, Cardiff CF14 4XN, United Kingdom

Email: brownmr@cardiff.ac.uk

Published online 8 July 2010 in Wiley Online Library (wileyonlinelibrary.com)

DOI: 10.1002/cyto.a.20936



## Abstract

The monitoring of cells labeled with quantum dot endosome-targeted markers in a highly proliferative population provides a quantitative approach to determine the redistribution of quantum dot signal as cells divide over generations. We demonstrate that the use of time-series flow cytometry in conjunction with a stochastic numerical simulation to provide a means to describe the proliferative features and quantum dot inheritance over multiple generations of a human tumor population. However, the core challenge for long-term tracking where the original quantum dot fluorescence signal over time becomes redistributed across a greater cell number requires accountability of background fluorescence in the simulation. By including an autofluorescence component, we are able to continue even when this signal predominates (i.e., >80% of the total signal) and obtain valid readouts of the proliferative system. We determine the robustness of the technique by tracking a human osteosarcoma cell population over 8 days and discuss the accuracy and certainty of the model parameters obtained. This systems biology approach provides insight into both cell heterogeneity and division dynamics within the population and furthermore informs on the lineage history of its members. © 2010 International Society for Advancement of Cytometry

## Key terms

flow cytometry; cell-cycle; quantum dot; nano-toxicity; systems biology; proliferation; *in-silico* modeling

FLOW cytometry is an essential tool for the study of the cell cycle by the measurement of the fluorescence properties of large cell populations (1–6). Using appropriate fluorescent markers, various elements of the cell-cycle or proliferation processes concealed within the population can be elucidated. To gain a deeper understanding of cell-cycle, its perturbation and potential clonogenic expansion within large cell populations over extended periods (>1 week) requires fluorescent labeling of individuals with stable, high intensity, and biologically compatible and adaptable markers. One candidate that meets these stringent criteria is the semiconductor colloidal quantum dot. The inorganic nature of these nanoparticles provides longevity to the fluorescence signal that is brighter than organic fluorophores and is unperturbed by intracellular biochemical reactions (7,8). Furthermore, their physical and chemical properties can be transformed to yield specific emission wavelengths and preferential binding to particular cellular compartments respectively. In addition, quantum dots are chemically stable and do not metabolize, facilitating their uptake by the cell and allowing passage to endosomic compartments, which through mitosis provide a means for daughter cells to inherit a diluted nanoparticle load (7).

Previously, we have tracked the inheritance of QTracker® 705 nm quantum dots (Qdot705) that have been compartmentalized within the endosomes of human osteosarcoma cells (U-2 OS cells) (9–11). A combination flow cytometry fluorescent measurements and a stochastic cell-cycle model determined the U-2 OS population inheritance properties. In a preceding publication (10), we have drawn a detailed comparison between cellular labeling with nanoparticles and that of the organic fluorophore Carboxy-fluorescein diacetate succinimidyl ester (CFSE). This study found cellular labeling via Qdot705's to be the most robust tool when proliferative features of a U-2 OS population is inferred from intracellular compartmentalization and segregation. Additionally, the inherent stability of the Qdot705's provides a means to initialize parameters within stochastic cell-cycle model, whereas the continual redistribution of signal of the CFSE signal for periods <48 h may be subject to fluctuations (12) (and unpublished results) and thus would not be suitable. Typically, two temporally distinct flow cytometry measurements are conducted; the first initializes the stochastic cell-cycle model, the second is used as a template to which the stochastic cell-cycle model attempts to emulate. Using a suitable evolutionary algorithm, important cell-cycle parameters are optimized to maximize the correlation of the fluorescence histograms generated numerically, to that measured experimentally. These initial investigations, measured the redistribution of Qdot705 fluorescent intensity, over a 2-day period, corresponds to approximately two cell-cycle durations for the unperturbed U-2 OS cell line (dilution due to two mitotic events). Even after two mitotic events, the quantum dot signal per cell was significantly above the intrinsic autofluorescence signal (9–11), produced primarily by intracellular chromaphores such as NADH, riboflavins, and flavin coenzymes (13). Therefore, for this small time-frame the actual measured total fluorescence signal can be attributed to the quantum dot component only. Pragmatically, the total measured signal also includes a signal due to noise, which represents the statistical variations in both quantum dot and autofluorescence signals (14). In this study, we are measuring the fluorescence of between 1 and $2.5 \times 10^4$ cells, which naturally minimizes the effect of noise, however, we will comment later on the effect this would have in the analysis of our data.

There are, however, a host of applications which require the long-term tracking (i.e., days to weeks) of proliferating cell populations, such as, assessment of drug pulse-chase perturbations on cell cycle and tumor growth, also nanotoxicity studies, where highly asymmetric partitioning of cell located nanoparticles rapidly results in a low signal. In these cases, the successive dilution of the quantum dots by partitioning over multiple mitosis events means that the quantum dot signal will eventually be reduced to the level of the autofluorescence signal and becomes indistinguishable from it using current measurement techniques. To recover the quantum dot signal from the total measured signal, we developed an *in-silico* cell population that has an associated stochastic cell-cycle. Previously, the evolution or redistribution of quantum dot signal through mitosis was solely considered (9–11). Here, we present an updated stochastic cell-cycle model that actually uses the autofluorescent signal to boost numerical fitting to measured data and allow important population parameters, such as intermitotic time to be predicted. The stochastic cell-cycle model integrates (i) an autofluorescence component to the total signal predicted and (ii) a long-tailed distribution that accurately describes the range of intermitotic times across an unperturbed U-2 OS population. The autofluorescence component for each cell is derived from the measurement of a control U-2 OS population, where the autofluorescence is measured in the absence of quantum dots. As the autofluorescence signal per cell remains constant, with respect to time, we are able to deconvolve this signal from the time dependent quantum dot signal by comparison with experimental flow measurements over extended periods (up to 8 days).

## Materials and Methods

### Cell Culture

U-2 OS (ATCC HTB-96) cells were maintained in McCoy's 5a medium (Sigma M8403) supplemented with 10% foetal calf serum (FCS), 1mM glutamine, and antibiotics and incubated at 37°C in an atmosphere of 5% $CO_2$ in air. For Qdot loading preparation, cells were grown at a density of $1 \times 10^4$ cells/ml as a monolayer in 25 $cm^2$ cell culture flasks and incubated at 37°C and 5% $CO_2$ for 24 h prior to the Qdot loading phase. All cell concentrations were determined using a Coulter Particle Counter (Beckman Coulter, High Wycombe, UK).

### Reagent Preparation and Treatments

Cells were loaded with commercially available targeted nanocrystals using the Qtracker® 705 Cell Labeling Kit (4 nM) (Invitrogen (Q25061MP). The reagents in the Qtracker® 705 Cell Labeling Kit use a custom targeting peptide (9-arginine peptide) to deliver near-infrared-fluorescent nanocrystals into the cytoplasm of live cells via the endosomal pathway. Briefly, Qtracker® reagent A and B were premixed and then incubated for 5 min at room temperature. Fresh full growth media (1.5 ml) was added to the tube and vortexed for 30 s. This labeling solution was then added to each flask of cells and incubated for 1 h at 37°C after which they were washed twice with fresh warm media. Subsequently 2, 4, and 8 days post-labeling cells were then analysed by flow cytometry. Sham (carrier only) treated control cells were loaded only with Qtracker® reagent B solution and this provided the distribution of autofluorescence in a population. In previous studies (10), we have used time-lapse microscopy to track culture growth and have shown that at these doses (4 nM for 1 h) that the culture remains unperturbed.

### Time Series Flow Cytometry Acquisition of QTracker705 Fluorescence Distribution

For each day of the experiment post-Qtracker® 705 load, two samples were prepared: a sham treated sample and a Qdot705 loaded sample (4 nM of Qdot705 for 1 h in media). On the appropriate day (2,4,8), U-2 OS cell monolayers were detached from the plates using trypsin and cells resuspended in complete medium. To determine the cell population distribution of Qtracker® 705 fluorescence intensity, a FACSCalibur

flow cytometer was used (Becton Dickinson Inc., Cowley, UK), which was equipped with an air-cooled argon ion laser (with 488 nm output) and controlled with CELLQuest software (Becton Dickinson Immunocytometry Systems) used for signal acquisition. The optics for the analysis of Qtracker® 705 excited by the 488 nm beam comprised reflection at a short pass 560 nm filter (scatter) and a long pass 670 nm filter to detect Qtracker 705 emission. Data was collected for 25,000 events. Instrument response for the fluorescence signal collection was monitored and calibrated using Dako FluoroSpheres (DakoCytomation K0110), which comprise a mixture of five-bead populations having different fluorescent intensities, and one non-fluorescent bead population.

### Time-Series Data Analysis and Modeling of the QTracker705 Distribution

Our approach to extracting cell-cycle system parameters relies on fitting the intensity profile of an experimental flow data set, $S^E_{total}(t_1)$, measured at a time $t_1$, to that of produced by an *in-silico* virtual population, $S^V_{total}(t_1)$. The virtual population is initialized at time $t_0$ ($t_1 > t_0$) to a further flow data set, $S^E_{total}(t_0)$, the virtual population, $S^V_{total}(t_0)$, is then evolved from its state at $t_0$ to $t_1$ by means of a stochastic cell-cycle model (9–11). Important ensemble parameters, within the cell-cycle model, are iteratively refined by an evolutionary algorithm [15], to maximize correlation between $S^V_{total}(t_1)$ and $S^E_{total}(t_1)$. Details of the stochastic cell-cycle model used to evolve the initial Qdot705 intensity profile are given in the manuscripts Supplementary Information. Further information regarding the evolutionary strategy used to minimize cell-cycle parameters are given in references (9–11).

However, to facilitate a long-term tracking capability, the stochastic cell-cycle model used previously (9–11) is updated to include (i) the intensity profile due to autofluorescence ($S_{auto}$) and (ii) a temporal distribution that better describes the range of inter-mitotic times (IMTs) experimentally observed across the U-2 OS population. The former refinement accounts for the fact that intensity due to Qdot705 ($S_{qdot}$) is continuously being redistributed throughout the growing cellular population as time passes. As a result, $S_{qdot}$ will ultimately be indistinguishable from $S_{auto}$ at some later time. By accounting for $S_{auto}$ at the initialization stage, when $S_{auto}$ and $S_{qdot}$ are distinct, provides a means to separately evolve both signals within each cell and permit signal deconvolution at later times to infer the extent of each signal. The second modification is included to reflect the outcome of extensive time-lapse studies of the IMT distributions across a U-2 OS population. These investigations revealed that IMT temporal distribution is intrinsically long-tailed (10) over multiple generations, as a result, we use the Gumbol distribution in place of the symmetric Gaussian distribution when assigning chronological placement of each member of the *in-silico* population. Explicit details of these two additional features to the stochastic cell-cycle model are given in the associated Supplementary Information for this manuscript.

This version of the stochastic cell-cycle model has five fitting parameters; the mean inter-mitotic time, $\mu_{IMT}$, a parameter describing its width, $\sigma_{IMT}$, the partitioning ratio of the quantum dots between daughters, $\mu_{DPR}$, and its associated standard deviation, $\sigma_{DPR}$. The final optimization parameter is effectively a calibration multiplier, which has the ability to adjust the position of the peak value of the autofluorescent component of the total signal. This parameter is required because acquisition of the control fluorescent data and that of the combined quantum dot and autofluorescent data are measured at two separate and distinct times. Subsequently, the positions of the peak values of the measured histograms do not necessarily fall in the same channel the latter optimization parameter adjusts the data for this outcome. What is important, is the shape of the autofluorescent distribution, not its magnitude i.e., *x*-axis on intensity histogram.

## Results

### Monitoring Long-Term Cell Proliferation Dynamics Using Qdot705 Reporting

As in previous studies, the general principle is demonstrated by a progressive attenuation of the Qdot705 signal over time, this is displayed in the form of density-scatter plot in Figures 1a–1c, corresponding to 2, 4, and 8 days post-quantum dot labeling of the cells. The density range scales from black (low density) to red (high density). It is clearly, evident that the fluorescent intensity of the total signal measured reduces by three orders of magnitude during this period. In addition, there is an attenuation of the forward scatter signal (FCS intensity) throughout this period. This loss is mirrored in the control population (i.e., no Qdot705 present), and is therefore attributed to the reduction of cell size due to stress caused by nutrient deficiency and increased cell density in the 2D culture over the extended period.

Typically, density-scatter information is displayed as cumulative distribution function (CDF), as shown in Figure 1d, where the blue, green and red curves are the CDF's of the $S^E_{total}$ at 2, 4, and 8 days post-quantum dot labeling. Also, indicated on this figure is the autofluorescent CDF (black curve) measured from the control population together with the median lines of the four CDF's (i.e., 50% of the total fluorescent intensity measured). It is evident from this figure, that the CDF of total signal 8 days post-labeling, $S^E_{total}(8)$, deviates marginally from the measured autofluorescent CDF, this is exemplified by comparison of the median values of 4.8 and 3.7 arbitrary intensity units.

The model imports the data sets $S^E_{total}$ (2) and $S^E_{auto}$ (2) for *in-silico* initialization and the data sets $S^E_{total}$ (4) and $S^E_{total}$ (8) for comparison to that computationally generated. Figure 1e, displays these data sets in histogram form; blue, green, red and black histograms refer to the 2, 4, and 8 day total intensities along with the autofluorescence respectively. The dotted black line in this figure, illustrates the upper limit to the dynamic range associated with the autofluorescent signal of the control sample; below this fluorescent intensity (i.e., $S^E_{total} < 10$) the total measured signal cannot be distinguished from the autofluorescent. The format of this figure clearly displays the reduction of total intensity as the Qdot705 signal is redistributed over time and highlights the consequential





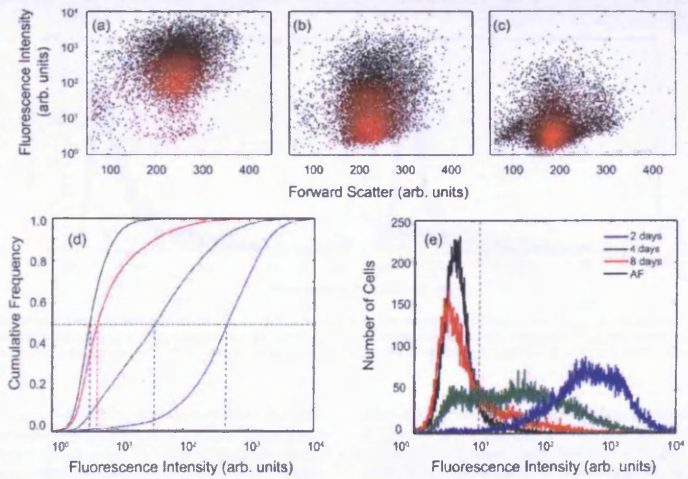


**Figure 1.** Long-term time series flow cytometry analysis demonstrating the Qdot705 signal attenuation or dilution over 2, 4, and 8 days post-labeling, in a human osteosarcoma cell (U-2 OS) population. (**a–c**) Density-scatter plots displaying Qdot705 fluorescence versus forward scatter. (**d**) Qdot705 fluorescence intensity cumulative frequency distributions for 2, 4, and 8 days post-labeling (blue, green, and red curves respectively), black curve shows the autofluorescent signal; dashed lines indicate the median values of Qdot705 at the respective times. (**e**) Qdot705 fluorescence intensity histograms ($2.5 \times 10^4$ cells), the intrinsic auto-fluorescence from the control sample is shown in black. Signal below the dashed line refers to the fraction where the autofluorescent signal $S_{auto}$ dominates.

encroachment of the 4 and 8-day total signal into the autofluorescent regime. The decrease in the effective reporting fraction, (i.e., $S^E_{total} > 10$) has changed from 98% at the experiment initialization (2 day post-quantum dot loading) to ~74% at 4 days and only ~27% at 8 days.

This compartmentalization is not to be confused with the error in binning at low intensity values; the log-linear amplification used for the signal detection ensured equal binning across the entire intensity range. Figure 1e illustrates this point, highlighting the dynamic range of intensities for this particular cellular system. The detector log-amplifier allows the first intensity signal (2 days post-labeling) to be compressed over the intensity range $10^3$–$10^4$ permitting the detection of the range of fluorescent signal (4 and 8 days post-labeling) that have shifted significantly in relation on the same log scale with equal weighting. As discussed earlier, the decrease in subsequent measurements is a consequence of Qdot705 dilution, due to continuing cell division occurring over the increased temporal period considered. Thus, as $S^E_{total}$ decreases with time $S^E_{auto}$ become more significant in comparison, complicating the deconvolution of information associated solely with $S^E_{qdot}$. Hence, long-term Qdot705 tracking using flow cytometry reveals some limitations, associated with the accrual of nonassay reporting cells. Never the less the real advantage of this method is beyond just establishing a cell growth curve, but providing an insight into cell heterogeneity within the population and division dynamics including possibly a sequential cell cycle and lineage history.

### Model to Derive System Parameters for Division Dynamics

Figures 2a and 2c displays the experimentally determined total fluorescence intensity histograms (grey curves) generated by randomly sampling $10^4$ Qdot705 labeled U-2 OS cells after 4 and 8 days post-labeling. Also, displayed on these plots, are the total fluorescence intensity histograms generated by $10^4$ randomly sampled *in-silico* cells (red circles). Figure 2a displays the resulting histogram of the virtual population being initialized 2 days post-Qdot705 then evolved to 4 days post-labeling, $S^V_{qdot}$ (2 → 4), i.e., 2 day simulation period. Similarly, Figure 2c displays the resulting histogram of the virtual population being initialized 4 days post-Qdot705 then evolved to 8 days post-labeling, $S^V_{qdot}$ (4 → 8), i.e., 4 day simulation period. Comparison of the experimental fluorescent intensity histograms with that generated from the *in-silico* populations reveal almost identical distributions (Figs. 2a and 2c) with coefficient of determination of 0.99 in both cases. This coefficient is deduced by comparing smoothed versions of the experimental and computational histograms. We use a simple moving average smoothing algorithm that spans over 10 con-

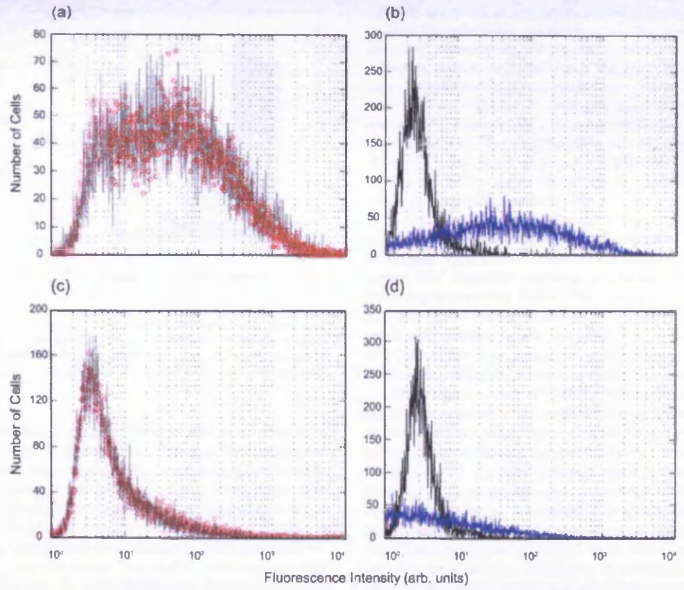


**Figure 2.** Modeled intensity distribution evolving from 2 to 8 days postlabeling. (**a**) Fluorescence intensity histograms of $10^4$ cells from the Qdot705 labeled U-2 OS cells after 4 days (solid grey line), $S^V_{\text{total}}$ (4), together with the *in-silico* population, $S^V_{\text{total}}$ (4) (circled red). (**b**) The $S^V_{\text{qdot}}$ (2 → 4)(blue) and the autofluorescence $S^V_{\text{auto}}$ (4) (black) only components of the total fluorescent intensity. (**c**) Fluorescence intensity histograms of $10^4$ cells from the Qdot705-labeled U-2 OS cells after 8 days, $S^V_{\text{total}}$ (8) (experiment grey solid line, *in-silico* population, $S^V_{\text{total}}$ (8) (circled red). (**d**) The $S^V_{\text{qdot}}$ (4 → 8) (blue) and the autofluorescence $S^V_{\text{auto}}$ (8) (black) only components of the total fluorescent intensity. [Color figure can be viewed in the online issue, which is available at wileyonlinelibrary.com.]

secutive points of the data. As discussed above, the population wise parameters describing the stochastic cell-cycle model are optimized, by the differential evolution algorithm, to maximize the magnitude of the coefficient of determination, the values of optimization parameters are displayed in Table 1, where they have been averaged over 1,000 independent optimization trials. In both cases, (2 → 4 and 4 → 8 days) we have consistent mean inter-mitotic times ($\mu_{\text{IMT}}$) of the bifurcating population and mean partitioning ratios ($\mu_{\text{DPR}}$), which describe quantum dot inheritance of daughter cells. There is slight variation in the three other optimization parameters of both time-courses, i.e., there is a reduction in the mean values of the standard deviations associated with the aforementioned optimization parameters and an increase of the calibration parameter, which effectively positions the autofluorescent component of the total signal bestowed to the *in-silico* population. However, some variation is expected due to different inherent variability due to measurement and that due to differing simulation periods.

In addition, due to the way in which the *in-silico* population is initialized, the numerical technique permits access to both fluorescent components at any time throughout the *in-silico* experiment. Figures 2b and 2d above, display both the intrinsic autofluorescent signal and that associated with the Qdot705 fluorescence as the black and blue histograms respectively, for the two differing time-courses. Thus, even though from an experimental point-of-view, a large fraction of the $S^V_{\text{qdot}}$, for both time-series is embedded within the dynamic range of the autofluorescence and is traditionally, labeled non-

**Table 1.** System parameters of the U-2 OS population tracked at a 2 day (2 → 4, 4 → 8 and 2 → 8 days)

| TIME INTERVAL (DAYS) | $\mu_{\text{IMT}}$ (H) | $\sigma_{\text{IMT}}$ (H) | $\mu_{\text{DPR}}$ (%) | $\sigma_{\text{DPR}}$ (%) | CALIBRATION |
|---|---|---|---|---|---|
| 2 → 4 | 22 | 8.5 | 83:17 | 6.8 | 0.57 |
| 4 → 8 | 24 | 6.6 | 82:18 | 4.2 | 0.70 |
| 2 → 8 | 23 | 6.9 | 84:16 | 4.5 | 0.71 |





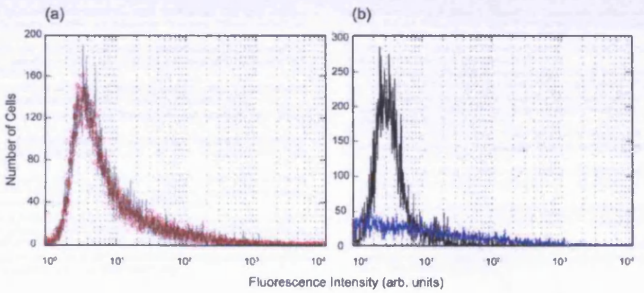


**Figure 3.** (**a**) Fluorescence intensity histograms of $10^4$ cells from the Qdot705 labeled U-2 OS cells after $S^E_{\text{total}}$ (8) (experiment grey solid line *in-silico* population, $S^V_{\text{total}}$ (2 → 8) (circled red). (**b**) The $S^V_{\text{qdot}}$ (2 → 8) (blue) and the autofluorescence $S^V_{\text{auto}}$ (8) (black) only components of the total fluorescent intensity. [Color figure can be viewed in the online issue, which is available at wileyonlinelibrary.com.]

reporting, here it can still be distinguished from the background and subsequently used. As expected the high quantum dot density tail ($x$-axis range: $10^2$–$10^4$) of this graph exactly matches that of the combined signal as the autofluorescence does not contribute due to constraints set experimentally (i.e., gain limited).

To further, demonstrate the validity of the numerical model and its applicability to infer population parameters in the long-term. We conduct a similar *in-silico* experiment, where the population is initialized by that measured at two days post-quantum dot loading, and evolved to 8 days post-quantum dot loading, $S^V_{\text{qdot}}$ (2 → 8) where the autofluorescence clearly dominates the flow-fluorescence intensity histogram. Figure 3a displays the experimentally measured and an example of that numerically derived fluorescent intensity histograms (solid grey line and red circles respectively). Again, we take an average, of the stochastic cell-cycle model parameters, over 1,000 trials, where in each case we achieve a coefficient of determination of $> 0.99$; results are displayed in Table 1. It is evident that all optimization parameters agree favorably with that predicted when the *in-silico* population is evolved over the shorter periods, validating and providing confidence in the long-term simulation. After 8 days, the predominant signal is the nonreporting autofluorescence signal (Fig. 3b) however the long-tail fluorescence signal is segmented providing reportable parameters.

Figure 4 displays the distribution of the two main optimization parameters, namely, the inter-mitotic time and quantum dot-partitioning ratio of the *in-silico* daughter cells. It was found that the stochastic cell-cycle model and its subsequent minimization are most sensitive to the magnitude of these parameters. Figure 4, displays the distribution of these parameters resulting, from the numerical experiment where, 1,000 runs of the optimization procedure were completed, this

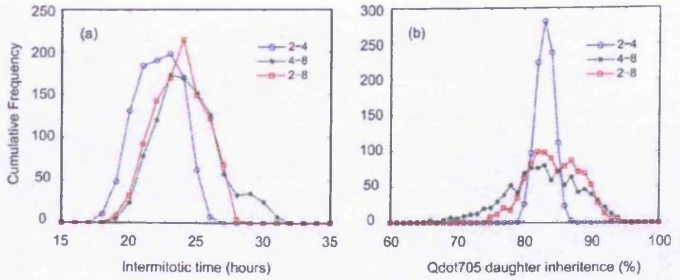


**Figure 4.** Distribution of the model optimization parameters. (**a**) Inter-mitotic time; (**b**) Qdot705 segregation. [Color figure can be viewed in the online issue, which is available at wileyonlinelibrary.com.]

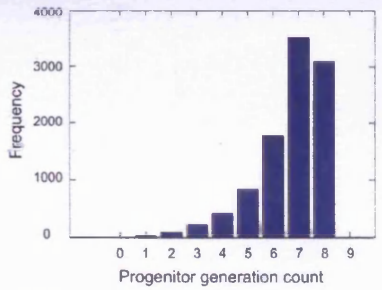


**Figure 5.** A histogram detailing the distribution of the number generations an original *in-silico* cell experiences in the simulation to generate subsequent progeny (taken from a random sample of $10^4$ virtual cells for the simulation 2→8 days.) [Color figure can be viewed in the online issue, which is available at wileyonlinelibrary.com.]

was performed for the three different time-series depicted in Figures 2 and 3. It is evident from Figure 4a that the spread of inter-mitotic time increases as the temporal range of the simulation is increased, however, the position of the mean value does not deviate substantially, reflecting the tabulated values of 22, 24, and 23 for the three time-courses. This behavior is even more pronounced when considering the quantum dot inheritance ratio, the shorter time period, predicts a very tight distribution over the 1,000 experiments, this distribution fills out as the simulation period is increased, but retains almost exact mean values. The broadening of these distributions is a penalty of both the innate variability of the measured data sets, i.e., variation in quantum dot loaded population that is introduced by experimental acquisition and that associated with the numerical stochastic nature of the cell-cycle model, which randomly assigns cell mitosis and subsequent quantum dot redistribution. However, despite these traits the *in-silico* population robustly predicts both consistent and experimentally verified asymmetric quantum dot inheritance and population-wise inter-mitotic times.

## Discussion

We have demonstrated the use of flow cytometry to track the inheritance of colloidal QTracker705 markers located within the endosomes of U-2 OS cells over 8 days. This is achieved by simulating the cell population using a stochastic model of the cell-cycle and subsequent mitosis events together with an evolutionary algorithm that optimizes important ensemble parameters. The quantum dots are partitioned at cell division between the progeny, the fraction allocated to each daughter cell, together with their inter-mitotic times are optimized, to maximize correlation, between a fluorescent histogram generated numerically to that measured experimentally.

Our future studies, will address the pattern of endosome segregation across different cell types; the redistribution of the QDot705 labeled compartments throughout a lineage depends on both the subcellular processing of the nanoparticles and the actual context of the cell division event itself. Therefore, we would predict variability across different cell types and their environment. However, preliminary results show that other cell lines (e.g. MCF-7; A549) growing on a 2D substrate also exhibit, nanoparticle asymmetric inheritance patterns (data not shown). The fundamental impact and consequences of endosome asymmetry may be the requirement for driving cell fate and differentiation for example in neurosensory cells via the Notch signaling pathway (16).

Long-term Qdot705 tracking of the fluorescence signal in a tumor system presents some technical limitations as the signal becomes attenuated to levels not detected above autofluorescence this essentially represents the accrual of an ever-increasing nonreporting fraction. However, because the quantum dot signal is conserved over time the remaining fluorescence redistribution, in this case after 8 days, representing only 20% of the entire population, gives a leading edge from which we can interpret and predict proliferation features.

Previously, a variety of mathematical models have been developed to correct for cell autofluorescence. These methods use numerical or a combination of numerical and experimental techniques to estimate the true fluorescence signal from a combination of the total measured signal and that corresponding to the autofluorescence. For example Corsetti et al. (17) use mathematical deconvolution to deduce cell fluorescence, Watson (18) uses cumulative frequency subtractions to infer labeled and unlabeled fractions of the total measured signal. This work has been built upon by Lampariello (19,20) whose mathematical methods use ratios of the cumulative distributions and negative control histograms together with an iterative numerical routine that locate the proportion of labeled cells by continual refinement of a specific distribution that reflects the background/control attributes. Our approach uses an *in-silico* simulation rather than data analysis techniques, to separate the autofluorescence and quantum dot signal derived from the flow measurements. The real advantage of this approach goes beyond just establishing a growth curve for a given population, but provides an insight into cell heterogeneity within the population and division dynamics including possibly a sequential cell cycle and lineage history (Fig. 5). For example, we can predict from the model simulation that atypical *in-silico* cell will undergo seven generations of cell division over 6 days. Importantly this approach maintains accuracy in the simulation predictions despite seven successive dilutions of the marker during mitosis events, which reduces the fluorescent signal below the autofluorescence level.

## Literature Cited

1. Wang H, Huang S. Mixture-model classification in DNA content analysis. Cytometry Part A 2007;71A:716–723.
2. Perry MBA, Lehman JM. Activities of SV40 T antigen necessary for the induction of tetraploid DNA content in permissive CV-1 cells. Cytometry 1998;31:251–259.
3. Darzynkiewicz Z, Gong J, Juan G, Ardelt B, Traganos F. Cytometry of cyclin proteins. Cytometry 1996;25:1–13.
4. Carbonari M, Mancaniello D, Tedesco T, Fiorilli M. Flow acetone-staining technique: A highly efficient procedure for the simultaneous analysis of DNA content, cell morphology, and immunophenotype by flow cytometry. Cytometry Part A 2008;73A:168–174.





5. Rabinovitch P. Practical Considerations for DNA Content and Cell Cycle Analysis. Clinical Flow Cytometry: Principles and Application. Baltimore: Williams and Wilkins; 1993.
6. Darzynkiewicz Z. The Cell Cycle: Application of Flow Cytometry in Studies of Cell Reproduction. Clinical Flow Cytometry: Principles and Application. Baltimore: Williams and Wilkins; 1993.
7. Resch-Genger U, Grabolle M, Cavaliere-Jaricot S, Nitschke R, Nann T. Quantum dots versus organic dyes as fluorescent labels. Nat Methods 2008;5:763–775.
8. Alivisatos AP. Semiconductor clusters: Nanocrystals, and quantum dots. Science 1996;271:933–937.
9. Summers HD, Errington RJ, Smith PJ, Chappell S, Rees P, Brown MR, Leary JF. Cell-population tracking using quantum dots in flow cytometry. SPIE Proc 2008;6865:68650I.
10. Errington RJ, Brown MR, Silvestre O, Njoh K, Chappell SC, Khan I, Rees P, Wilks S, Smith PJ, Summers HD. Single cell nanoparticle tracking to model cell cycle dynamics and compartmental inheritance. Cell Cycle 2010;9:121–130.
11. Brown M, Rees P, Wilks S, Summers H, Errington R, Njoh K, Chappell S, Smith P, Leary J. Computational simulation of optical tracking of cell populations using quantum dot fluorophores. Comput Methods Syst Biol 2007;LNBI 4695:96–105.
12. Hodgkin PD, Lee JH, Lyons AB. B cell differentiation and isotype switching is related to division cycle number. J Exp Med 1996;184:277–281.
13. Chance B, Cohen P, Jobsis F, Schoener B. Intracellular oxidation-reduction states in vivo: The microfluorometry of pyridine nucleotide gives a continuous measurement of the oxidation state. Science 1962;137:499–508.
14. White NS, Errington RJ. Fluorescence techniques for drug delivery research: Theory and practice. Adv Drug Deliv Rev 2005;57:17–42.
15. Storn R, Price K. Differential evolution. A simple and efficient heuristic for global optimization over continuous spaces. Journal of Global Optimization 1997;11(4):341–359.
16. Kaji K, Shigeo H. Dynamic intracellular distribution of Notch during activation and asymmetric cell division revealed by functional fluorescent fusion proteins. Genes Genes to Cells 2010;15(7):749–759.
17. Corsetti JP, Sotirchos SV, Cox C, Cowles JW, Leary JF, Blumburg N. Correction of cellular autofluorescence in flow cytometry by mathematical modeling of cellular fluorescence. Cytometry 1988;9:539–547.
18. Watson JV. Proof without prejudice revisited: Immunofluorescence histogram analysis using cumulative frequency subtraction plus ratio analysis of means. Cytometry 2001;44:53–68.
19. Lampariello F, Antonella A. Complete mathematical modeling method for the analysis of immunofluorescence distributions composed of negative and weakly positive cells. Cytometry 1998;32:241–254.
20. Lampariello F. Ratio analysis of cumulatives for labeled cell quantification from immunofluorescence histograms derived from cells expressing low antigen levels. Cytometry Part A 2009;75A:665–674.

# Appendix I-E

(Holton et al. 2009)

**Holton**, M. D.; Silvestre, O. R.; Errington, R. J.; Smith, P. J.; Matthews, D. R.; Rees, P.; Summers, H. D., Stroboscopic fluorescence lifetime imaging. *Optics Express* **2009,** 17, (7), 5205-5216.

# Stroboscopic fluorescence lifetime imaging

**Mark D. Holton,[1] Oscar R. Silvestre,[2] Rachel J. Errington,[2] Paul J. Smith,[2] Daniel R. Matthews,[3] Paul Rees[4] and Huw D. Summers.[4,*]**

[1]*School of Medicine, Swansea University, Singleton Park, Swansea, SA2 8PP, U.K.*
[2]*School of Medicine, Cardiff University, Heath Park, Cardiff, CF14 4XN, U.K.*
[3]*Randall Division, Guy's Medical School Campus, King's College London,SE1 9RT, U.K.*
[4]*Multidisciplinary Nanotechnology Centre, School of Engineering, Swansea University, Swansea, SA2 8PP, U.K.*
[*]*Corresponding author: H.D.Summers@swansea.ac.uk*

**Abstract:** We report a fluorescence lifetime imaging technique that uses the time integrated response to a periodic optical excitation, eliminating the need for time resolution in detection. A Dirac pulse train of variable period is used to probe the frequency response of the total fluorescence per pulse leading to a frequency roll-off that is dependent on the relaxation rate of the fluorophores. The technique is validated by demonstrating wide-field, real-time, lifetime imaging of the endocytosis of inorganic quantum dots by a cancer cell line. Surface charging of the dots in the intra-cellular environment produces a switch in the fluorescence lifetime from ~ 40 ns to < 10 ns. A temporal resolution of half the excitation period is possible which in this instance is 15 ns. This stroboscopic technique offers lifetime based imaging at video rates with standard CCD cameras and has application in probing millisecond cell dynamics and in high throughput imaging assays.



**OCIS codes:** (170.0170) Microscopy; (170.6920) Time-resolved imaging; (120.3890) Medical optics instrumentation; (170.1530) Cell analysis; (170.2520) Fluorescence microscopy.

## References and links

1. F. S. Wouters, P. J. Verveer, and P. I. Bastiaens, "Imaging biochemistry inside cells," Trends Cell Biol. **11**, 203-211 (2001).
2. K. Suhling, P. M. W. French, and D. Phillips, "Time resolved fluorescence microscopy." Photochem. Photobiol. Sci. **4**, 13–22 (2005).
3. R. Cubeddu, P. Taroni, and G. Valentini, "Time-gated imaging system for tumor diagnosis," Opt. Eng. **32**, 320-324 (1993).
4. C. G. Morgan, A. C. Mitchell, and J. G. Murray, "Nanosecond Time-Resolved Fluorescence Microscopy: Principles and Practice," Proc.R. Microsc. Soc. **1**, 463–466 (1990).
5. E. P. Buurman, P. Sanders, A. Draaijer, H. C. Gertitsen, J. J. F. van Veen, P. M. Houtpt, and Y. K. Levine, "Fluorescence lifetime imaging using a confocal laser scanning microscope," Scanning **14**, 155–159 (1992).
6. I. Bugiel, K. Konig, and H. Wabnitz, "Investigation of cells by fluorescence laser scanning microscopy with subnanosecond time resolution," Lasers Life Sci. **3**, 47–53 (1989).
7. X. F. Wang, T. Uchida, D. M. Coleman, and S. Minami, "A 2-dimensional fluorescence lifetime imaging-system using a gated image intensifier," Appl Spectrosc. **45**, 360–366 (1991).
8. K. Dowling, M. J. Dayel, M. J. Lever, P. M. W. French, J. D. Hares, and A. K. L. Dymoke-Bradshaw, "Fluorescence lifetime imaging with picosecond resolution for biomedical applications," Opt. Lett. **23**, 810-812 (1998).
9. J. R. Lakowicz, H. Szmacinskia, K. Nowaczyka, K. W. Berndta, and M. Johnson, "Fluorescence lifetime imaging," Anal. Biochem. **202**, 316-330 (1992).
10. R. M. Clegg, G. Marriott, B. A Feddersen, E. Gratton, and T. M. Jovin, "Sensitive and rapid determinations of fluorescence lifetimes in the frequency domain in a light-microscope," Biophys. J. **57**, A375–A375 (1990).
11. D. R. Matthews, H. D. Summers, K. Njoh, R. J. Errington, P. J. Smith, P. Barber, S. Ameer-Beg, and B. Vojnovic, "Technique for measurement of fluorescence lifetime by use of stroboscopic excitation and continuous-wave detection," Appl. Opt. **45**, 2115-2123 (2006).
12. Y. Sakai and S. Hirayama, "A fast deconvolution method to analyze fluorescence decays when the excitation pulse repetition period is less than the decay times," J. Lumin. **39**, 145-151 (1988).

#107281 - $15.00 USD Received 6 Feb 2009; revised 13 Mar 2009; accepted 15 Mar 2009; published 18 Mar 2009



13. M. Müller, R. Ghauharali, K. Visscher, and G. Brakenhoff, "Double-pulse fluorescence lifetime imaging in confocal microscopy," J. Microsc. **177**, 171-179 (1994).
14. H. Nyquist, "Certain topics in telegraph transmission theory," Trans. Am. Inst. Electr. Eng. **47**, 617-644 (1928).
15. T. Ng, A. Squire, G. Hansra, F. Bornancin, C. Prevostel, A. Hanby, W. Harris, D. Barnes, S. Schmidt, H. Mellor, P. I. H. Bastiaens, and P. J. Parker, "Imaging protein kinase Cα activation in cells," Science **283**, 2085-2089 (1999).
16. O. Holub, M. J. Seufferheld, C. Gohlke, Govindjee, and R. M. Clegg, "Fluorescence lifetime imaging (FLI) in real time – a new technique in photosynthesis research," Photosynthetica **38**, 581-599 (2000).
17. A. V. Agronskaia, L. Tertoolen, and H. C. Gerritsen, "High frame rate fluorescence lifetime imaging," J. Phys. D **36**, 1655-1662 (2003).
18. D. J. Stephens and V. J. Allan, "Light microscopy techniques for live cell imaging," Science **300**, 82-86 (2003).
19. B. Dubertret, P. Skourides, D. J. Norris, V. Noireaux, A. H. Brivanlou, and A. Libchaber, "In vivo imaging of quantum dots encapsulated in phospholipid micelles," Science **298**, 1759-1762 (2002).
20. J. K. Jaiswal, H. Mattoussi, J. M. Mauro, and S. M. Simon, "Long-term multiple color imaging of live cells using quantum dot bioconjugates," Nature Biotech. **21**, 47-51 (2002).
21. A. Hoshino, K. Hanaki, K. Suzuki, and K. Yamamoto, "Applications of T-lymphoma labelled with fluorescent quantum dots to cell tracing markers in mouse body," Biochem. and Biophys. Res. Commun. **314**, 46-53 (2003).
22. Y. S. Liu, Y. H. Sun, P. T. Vernier, C. H. Liang, S. Y. C. Chong, and M. A. Gundersen, "pH-sensitive photoluminescence of CdSe/ZnSe/ZnS quantum dots in human ovarian cancer cells," J. Phys. Chem. **111**, 2872-2878 (2007).
23. Y. H. Sun, Y. S. Liu, P. T. Vernier, C. H. Liang, S. Y. Chong, L. Marcu, and M. A. Gundersen, "Photostability and pH sensitivity of CdSe/ZnSe/ZnS quantum dots in living cells," Nanotechnology **17**, 4469-4476 (2006).
24. S. J. Clarke, C. A. Hollmann, Z. Zhang, D. Suffern, S. E. Bradforth, N. M. Dimitrijevic, W. G. Minarik, and J. L. Nadeau, "Photophysics of dopamine-modified quantum dots and effects on biological systems," Nature Materials **5**, 409-417 (2006).
25. S. R. Cordero, P. J. Carson, R. A. Estabrook, G. F. Strouse, and S. K. Buratto, "Photo-activated luminescence of CdSe Quantum dot monolayers," J. Phys. Chem. **104**, 12137-12142 (2000).
26. N. E. Korunska, M. Dybiec, L. Zhukov, S. Ostapenko, and T. Zhukov, "Reversible and non-reversible photo-enhanced luminescence in CdSe/ZnS quantum dots," Semicond. Sci. Technol. **20**, 876-881 (2005).
27. M. Nirmal, B. O. Dabbousi, M. G. Bawendi, J. J. Macklin, J. K. Trautman, T. D. Harris, and L. E. Brus, "Fluorescence intermittency in single cadmium selenide nanocrystals," Nature **383**, 802-804 (1996).
28. C. D. McGuinness, K. Sagoo, D. McLoskey, and D. J. S. Birch, "A new sub-nanosecond LED at 280nm: application to protein fluorescence," Meas. Sci. Technol. **15**, L19-L22 (2004).

## 1. Introduction

Fluorescence imaging of biological material at tissue and single cell level is one of the most widely used techniques in biomedical science [1]. The use of fluorescence lifetime imaging (FLIM) has become particularly important because contrast based on a fluorescence decay rate rather than absolute intensity avoids signal variation due to effects such as inhomogeneous labelling, fluorophore diffusion or quenching and provides differentiation of tissue auto-fluorescence [2]. Spatial analysis of biological processes can also be achieved with a wide range of functional lifetime-based probes that report on key chemical markers such as oxygen, calcium or pH. FLIM may be implemented using either a time or frequency based measurement. In the time domain an ultra-short laser pulse provides impulse excitation followed by temporal resolution of the detected fluorescence [3,4]. This can be implemented with a single channel detector using scanning microscopy [5,6] or in wide-field using multiple channel detectors such as gated CCD cameras [7,8]. In the frequency domain the lifetime is extracted from analysis of the phase shift and demodulation of the fluorescence with respect to a modulated excitation [9,10]. In all of the current FLIM techniques there is a requirement for temporal resolution and synchronisation of excitation and detection signals. We report a new approach that uses what is in effect a Dirac pulse train for excitation and derives lifetime based image contrast using time-integrated fluorescence. This 'stroboscopic' technique therefore completely removes the need for time resolved detection or synchronisation making FLIM faster, cheaper and easier to implement on existing fluorescence microscopes. We have

#107281 - $15.00 USD Received 6 Feb 2009; revised 13 Mar 2009; accepted 15 Mar 2009; published 18 Mar 2009

previously demonstrated the use of stroboscopic excitation to determine fluorescence lifetime in a non-imaging mode and explored the resolution and sensitivity of the technique [11].

The extraction of lifetime-based contrast for strobe-FLIM is based on the interaction of fluorophores with a periodic train of optical impulse excitations. In the case where the impulse frequency is greater than the fluorescence relaxation rate, the time-integrated response of the system becomes dependent upon the relaxation process. A short excitation repetition time such as this is normally avoided as it leads to incomplete recovery of the system [12]. Here we deliberately use the limited time cycle to inhibit fluorescence decay and so maintain a finite, minimum excited state population of fluorophores. This leads to a decrease in the absorption of the excitation signal and a non-linear fluorescence response to increasing excitation frequency: the time-integrated fluorescence is described by the exponential of the ratio of fluorescence decay rate to excitation pulse frequency. The system establishes a dynamic equilibrium in which each pulse cycle is identical and a balance is maintained between the energy transferred from the impulse and the energy released by fluorescence decay. Reducing the impulse period lowers the amount of energy absorbed during the cycle and therefore reduces the integrated response signal per impulse excitation. The schematic in Fig. 1 shows the time and frequency domain functions for strobe-FLIM analysis of a fluorophore with a single exponential decay rate, γ.

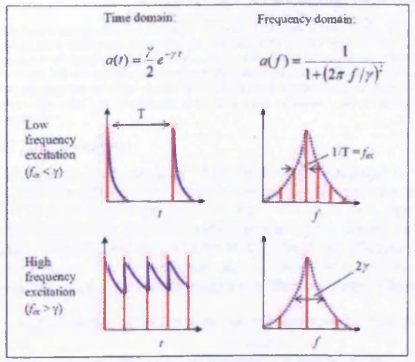


Fig. 1. Schematic of the stroboscopic excitation technique in time and frequency domains.

In the frequency domain the lifetime analysis may be viewed as a form of Fourier synthesis in which the temporal response of the system is reproduced by the frequency sampling imposed by the measurement. The impulse train maintains its waveform under Fourier transformation with the period, T and frequency spacing, $f_{ex}$ of the pulse train being inversely proportional thus in strobe-FLIM the system is sampled by a multiple set of discrete frequencies and its response is dictated by the relative values of γ and $f_{ex}$ (see equation 1). When the excitation period is very much greater than the fluorescence lifetime ($f_{ex} << \gamma$) the frequency sampling becomes quasi-continuous and a near-true representation of the decay waveform is achieved. This equates to repetitive time-domain lifetime measurement and produces a fluorescence pulse train that is linearly proportional to the excitation frequency and hence integrated fluorescence, Sc is independent of $f_{ex}$. Towards the high frequency limit for excitation ($f_{ex} \geq \gamma$) the pulse train resembles the frequency domain technique in that the temporal excitation signal Fourier transforms to a dc plus single frequency component and

#107281 - $15.00 USD Received 6 Feb 2009; revised 13 Mar 2009; accepted 15 Mar 2009; published 18 Mar 2009



produces a corresponding sinusoidal component within the time domain system response. The limited sampling produces a constant dc background with associated absorption saturation which leads to a frequency dependent Sc. Thus the stroboscopic technique sits between the time and frequency domain methods using a frequency-swept, periodic impulse excitation which equates to the traditional analyses in the limit, and in bridging them provides the unique capability of time resolution with time integrated detection.

A rate equation based analysis of these temporal dynamics can be used to obtain an analytical description of the total fluorescence per excitation cycle:

$$S_c = \kappa \left[ \frac{e^{2\alpha P} - 1}{e^{2\alpha P} - e^{-\frac{\gamma}{f_{ex}}}} \right] \left( 1 - e^{-\frac{\gamma}{f_{ex}}} \right) \quad (1)$$

where γ and $f_{ex}$ are the fluorescence relaxation rate and excitation frequency respectively, P is the number of excitation events per impulse, κ is a collection efficiency and α an excitation efficiency. The term in square brackets in equation 1 is a ratio of the number of excitation events per pulse and the maximum number of excitation events possible for all fluorophores in the ground state i.e. it represents an excitation efficiency determined by the constant presence of excited state fluorophores. The second bracketed term describes the reduction in total fluorescence due to the incomplete decay. A theoretical analysis of the measurement of fluorescence lifetime via the time integrated signal has been presented previously based on the use of a double-pulse excitation [13]. In this case because only two pulses are used the system must be excited to transparency to ensure an equal excited state population immediately following each of the impulses or alternatively corrections made to account for the non steady-state excitation. By introducing a periodic impulse train we allow the system to reach a cyclic equilibrium in which each impulse response is identical through natural evolution of the fluorescence excitation and decay dynamics. This essentially allows us to implement the technique using excitation powers well below (< 10%) what is required to produce fluorescence saturation [11].

## 2. Results

### *2.1 Frequency response of integrated fluorescence*

An example of time inhibited fluorescence decay in response to a periodic impulse excitation is shown in Fig. 2(a). The fluorescence emission from 705 nm wavelength, CdTe / ZnS quantum dots (QDs) in aqueous solution is time resolved using a streak camera detector over a range of excitation frequencies. The impulse train is provided by a picosecond pulse, from a white-light laser via a 600 nm short pass filter (Fig. 2(a).). The response at 1 MHz shows complete inter-pulse recovery of the fluorescence and a single exponential fit to the data (Fig. 2(b).) indicates a QD relaxation rate, γ = 23 ± 2 MHz (τ = 43 ± 4 ns). A simple, single component fit is adopted as this equates to the stroboscopic methodology. Due the limited relaxation rate at the higher excitation frequencies ($f_{ex}$ > 10 MHz ) there is incomplete relaxation to the ground state. In this example the peak fluorescence intensity is independent of frequency indicating excitation to saturation. A fit to the frequency roll-off in the total fluorescence per pulse (Fig. 2(c).), using equation 1 in the high excitation limit ($e^{2\alpha P} >> 1$), gives a value of γ = 21 ± 4 MHz, in good agreement with the directly time-resolved value. The accuracy of the γ measurement is determined by the relative range of the frequency sweep and the level of intensity noise in the fluorescence signal. Because the frequency roll-off can be described in terms of frequency sampling, a frequency domain formulation of the familiar Nyquist sampling theorem [14] can be adopted to assess the measurement maximum, $\gamma_{max}$ (minimum τ). Incomplete sampling arises when giving $\gamma_{max} = 2f_{max}$., which for this work equates to 60 MHz ($f_{max}$ = 30 MHz).

#107281 - $15.00 USD Received 6 Feb 2009; revised 13 Mar 2009; accepted 15 Mar 2009; published 18 Mar 2009

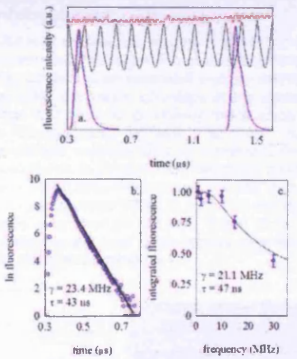


Fig. 2. (a) Streak camera data for excitation frequencies of 1 MHz (blue trace), 10 MHz (black trace) and 30 MHz (red trace) illustrating the inhibited fluorescence decay of 705 nm quantum dots in response to a periodic impulse; (b) a single-exponential fit to the complete inter-pulse recovery of the 705 nm quantum dots under 1 MHz excitation and (c) the frequency roll-off of integrated fluorescence per pulse as the inter-pulse period is reduced to less than the quantum dot lifetime. The solid line is a best-fit to the data using equation 1, the parameter values of which are shown.

### *2.2 Fluorescence lifetime imaging*

The experimental setup for implementation of the stroboscopic technique for lifetime imaging is shown in Fig. 3(a). The pulsed laser is directly coupled to a fluorescence microscope via the lamp port and wide-field images are collected via a 40x, 0.75 N.A. lens using a 20 ms exposure time. The beam passes through spectral filters to remove the red and infra-red part of the spectrum and a focusing lens that is adjusted to achieve full illumination of the image field. The excitation power density within the central, 50x50 μm area of the image is 500 W $cm^{-2}$. In this mode we adopt a ratio metric measure (a 'frequency ratio') for image contrast of $R = \frac{30\, I_{1MHz}}{I_{30MHz}}$ where I is the image intensity, for a fixed exposure time, at the appropriate excitation frequency. We then define a characteristic frequency of the system, $f_0$ using the measured response at 30 MHz: $f_0 = 30 \ln\left[\frac{R}{(R-1)}\right]$. This empirical approach provides a measure of the frequency response of the system and avoids inappropriate identification of a fluorescence 'lifetime' with the associated assumption of a single, exponential decay. Whilst $f_0$ does not directly equate to $\gamma$ it does provide a quantitative assessment of the dynamics of the fluorescence response. Thus the important point in relation to practical lifetime microscopy is that the frequency ratio, R will correlate with the fluorescence decay and so provides image contrast related to the lifetime rather than intensity of fluorescence. The frequency-ratio image requires measurement of just two images with ~ 20 ms exposure time and so lifetime based imaging can be achieved at video rates. The images in Fig. 3 show strobe-FLIM of inorganic (705 and 611 nm QDs) and organic (Cy-5) fluorophores deposited and dried onto glass cover slips to form touching boundaries between the two species. The fluorescence intensity and ratio images are shown in Fig. 3(b-e). there is a clear discrimination in the ratiometric images between the three fluorophores. The 611 nm QDs (CdSe/ZnS) have a 1/e lifetime of ~ 35 ns

#107281 - $15.00 USD Received 6 Feb 2009; revised 13 Mar 2009; accepted 15 Mar 2009; published 18 Mar 2009



(measured from time resolved, streak camera trace) leading to a mean R value ~ 2, the contrast of these with the longer lifetime 705 nm dots (CdTe/ZnS), with mean R ~ 3, can be clearly resolved. The origin of the large fractional range in R values for both QD types (~ 100% variation) is unclear but may be due to density fluctuations in the nanoparticle films. The decay rate of the Cy-5 is well in excess of the experimental range ( ~ 1 GHz) and so a linear frequency response with R ~ 1 is measured in this case.

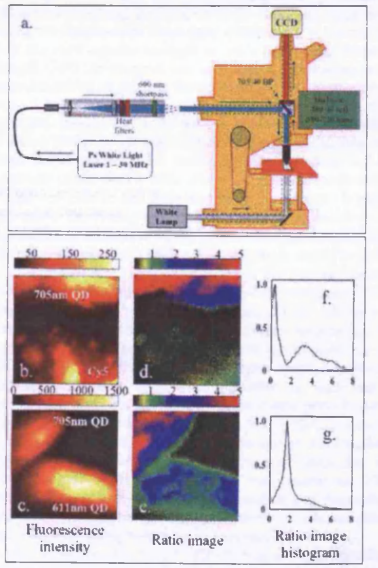


Fig. 3. (a) Experimental setup illustrating the laser input at the upper lamp input-port and the spectral filters used for imaging; (b) 50 x 50 μm, fluorescence intensity images of 705 nm QDs and Cy-5 dye and (c) 705 nm and 611 nm QDs; (d) ratio images derived from intensity images taken at 1 MHz and 30 MHz excitation frequencies for 705 nm QDs and Cy-5 and (e) 705 nm and 611 nm QDs; (f) histograms of pixel-to-pixel variation in R for 705 nm QDs and Cy-5 and (g) 705 nm and 611 nm QDs. In both cases the distribution is bi-modal illustrating the ability of stroboscopic imaging to distinguish the fluorophore pairs from their lifetime.

The maximum intensity variation in successive images is ± 5% (single pixel variation) and so the error margin in R is ± 7%. The characteristic frequencies for the 611 nm and 705 nm QDs are 29 ± 3 MHz and 12 ± 1 MHz respectively. A statistical analysis of the frequency ratio is also shown in Fig. 3(f-g). in the histograms of the pixel-to-pixel variation, each histogram represents data summed from three images. A bi-modal distribution is obtained in each case with the broader, 705 nm QD peak clearly discernible from the lower ratio 611 nm QD and Cy5 maxima.

#107281 - $15.00 USD Received 6 Feb 2009; revised 13 Mar 2009; accepted 15 Mar 2009; published 18 Mar 2009

*2.3 Imaging fluorescence dynamics in living cells*

FLIM has been successfully used for live cell imaging [15]. Whilst real-time, live-cell FLIM has been successfully demonstrated [16, 17] it is a challenging technique to apply to living cells as the potentially long exposure times associated with the determination of a decay time can lead to photo-damage [18]. The major advantage of the strobe-FLIM technique is its speed of image acquisition and so it is potentially much easier to apply to live cell applications. To validate this hypothesis we used it to image the endocytic uptake and processing of 705 nm wavelength, colloidal QDs by a human Osteosarcoma cell line (U-2 OS). Whilst QDs have been shown to be photo and bio-stable enough to be used as multi-generational (over 5 generations) fluorescent reporters [19, 20] there have been reports of a reduction in fluorescence efficiency when placed in cells [21] and their fluorescence lifetime has been shown to be sensitive to local pH [22, 23]. Indeed these nanoparticles have been conjugated to dopamine molecules and used as bio-sensors informing on intra-cellular redox potential via changes in the QD quantum yield [24].

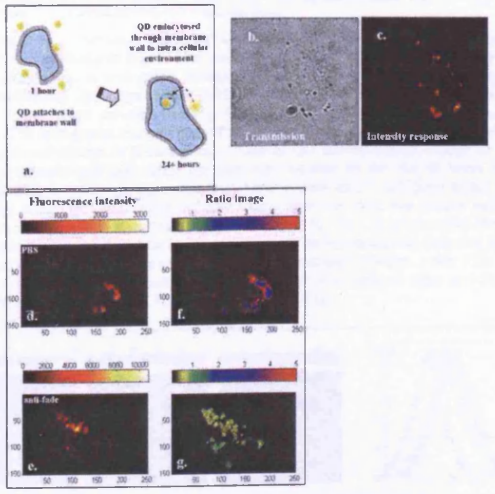


Fig. 4. (a) schematic of the QD uptake and localisation within intra-cellular vesicles via endocytosis: (b) typical 50 x 50 μm, transmission and (c) fluorescence intensity images of a single cell: (d) 50 x 30 μm intensity image of a cell, fixed in PBS 24 hours following QD uptake and (e) intensity image of a cell fixed in Prolong® Gold, anti-fade reagent 24 hours following QD uptake: (f) corresponding ratio images for cells fixed in PBS and (g) anti-fade reagent.

The fundamental process underlying these effects is charge transfer to and from surface states on the nanoparticle. When charge neutral the dots exist in a 'bright' state with high radiative efficiency, subsequent charge capture into surface traps leads to a 'dark' state in which rapid non-radiative relaxation is dominant [25, 26]. For individual dots this leads to a 'blinking' of the fluorescence as charge is transferred to and from the dot surface [27]. For QD ensembles the cumulative effect is a quantum yield and fluorescence lifetime that is dependent upon the redox potential of the local environment. The uptake of QDs via endocytosis and their subsequent encapsulation within acidic organelles therefore provides an ideal system in which to look for fluorescence lifetime changes.

Our initial work adopted the approach of Sun et al. [23] and used fixed cells in different buffers to demonstrate the potential of strobe-FLIM to provide spatially resolved read-out of redox state. The delivery of the dots by endocytosis leads to their concentration within discrete sub-cellular compartments (fig. 4(a-c).). We image the QD fluorescence from cells that are fixed at 24 hours post loading, at this point in the endocytic cycle there is peri-nuclear, punctate localisation of the fluorescence from QDs within the endosomal compartments. The reduction potential of the intra-cellular medium is controlled by the introduction of an anti-fade reagent – Prolong® Gold (Invitrogen); this is designed to act as an anti-oxidant with the aim of reducing photo-bleaching of organic fluorophores. When used with QDs the opposite is achieved as chemical reduction by the anti-oxidant charges the dots and so reduces the quantum yield (QY) [24]. Images (50 x 30 micron field) of the QDs within fixed cells in phosphate buffered saline (PBS) or anti-fade solutions are shown in Fig. 4(d). and 4(e). The results for cells fixed in pH neutral, PBS buffer indicate R values ~ 2-3 ($f_0$ ~ 16 MHz) indicating that the lifetime of the dots is little altered by the process of cellular targeting and uptake. The ratio images of cells in anti-fade reagent show a linear, R response indicating a fluorescence lifetime below the system resolution of 15 ns as expected given the dominance of short lifetime, non-radiative relaxation within surface charged dots. Continuous monitoring of R as the anti-fade agent is added to a PBS buffered sample shows an immediate reduction in fluorescence intensity and a switch in R from 2-3 to 1. We are confident therefore that the low R values are due to the external agent rather than cellular processes. To corroborate these results the cells were also imaged using time domain FLIM within a scanning, time-correlated, single photon counting (TCSPC) system (Nikon microscope with Becker and Hickl acquisition system). Two-photon excitation at 850 nm wavelength was used with an average power of 800 mW and an image acquisition time 2 minutes. For the cells fixed in PBS there is a continuous base-level count and no reliable tau value can be obtained. We attribute this to fluorescence build-up from previous excitation periods due to QD lifetimes well in excess of the TCSPC repetition time of 12.5 ns. The TCSPC results for the cells fixed in anti-fade reagent indicate a decay lifetime of ~ 300 ps and so confirm that the observation of R = 1 with strobe-FLIM is due to lifetime reduction below the resolution of the measurement. These fixed-cell experiments establish that, within the 10-100 ns lifetime regime of QDs, strobe-FLIM is able to provide spatial resolution of fluorophore dynamics and in the example shown allows correlation of intensity changes within the cellular environment with QY changes and a corresponding reduction in fluorescence lifetime.

Imaging of live cells was done over 5 days, maintaining the U-2 OS cells at 36.5 ± 0.2° C on a heated microscope stage within sealed chambers on a multi-well plate. The excitation power was once again 500 $Wcm^{-2}$ and lifetime based ratio metric imaging was done at 4 frames per second (2 Hz ratio imaging) using 20 ms exposure times on a daily basis. Whilst a detailed analysis of the cell cycle dynamics under these conditions was not undertaken there was clear evidence of progression through mitosis and hence cell proliferation throughout the time period. Thus it was possible to undertake live cell FLIM without marked photo-induced cell perturbation and with minimal cell death.

#107281 - $15.00 USD Received 6 Feb 2009; revised 13 Mar 2009; accepted 15 Mar 2009; published 18 Mar 2009



#107281 - $15.00 USD Received 6 Feb 2009; revised 13 Mar 2009; accepted 15 Mar 2009; published 18 Mar 2009

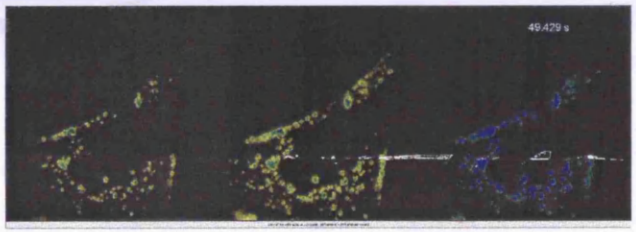


Fig. 5. (Media 1) shows 140 seconds of imaging time at x10 speed. From left to right, the first two images are the raw data taken at 1 MHz and 30 MHz repetition rates respectively and the final image is the frequency ratio, R. Rapid motion of the QD loaded vesicles can be seen and this temporal resolution is maintained in the ratio image.

A time-lapse movie covering 140 seconds of cell imaging using fluorescence intensity and intensity ratio, R is shown in Fig. 5. The imaging speed is sufficient to avoid blurring due to whole cell motion and is even quick enough to capture the rapid intra-cellular dynamics of endosome trafficking. The longer term dynamics are given in Fig. 6 where ratio metric images taken at 1, 2 and 5 days are shown in Fig. 6(a-c). together with histograms of the R values (fig. 6(d).). The histograms are averages of 4 cell images taken at each of the time points. There was minimal change in R during the process of QD internalisation, indeed the absolute fluorescence intensity and ratio metric measure was constant for the first 48 hours following QD loading. This is not surprising as the Qtracker® system used is designed to provide long term stability within live cells. Over the full 5 days however there was a clear reduction in fluorescence intensity and a corresponding change in R. This is presumably due to QD degradation with associated surface charging leading to an increased non-radiative decay rate and a concomitant reduction in quantum yield and fluorescence lifetime. After 100+ hours in the cell the QD fluorescence intensity is reduced to ~ 1/3 of its original value and the mean R value reduces from ~ 2.5 ($f_0$ ~ 15 MHz) to 1.9 ($f_0$ ~ 22 MHz).

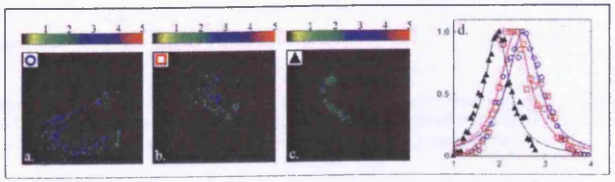


Fig. 6. (a) 30 x 30 µm, Ratio images of live cells at 24 hours post QD loading, (b) 48 hours post QD loading and (c) 120 hours post QD loading; (d) the histograms of the R variation, the symbols on the insets of fig. 6a-c relate each trace to the corresponding acquisition time. The three histograms show a systematic reduction as the QDs are degraded within the cells leading to a reduced QY and a shorter τ as non-radiative relaxation routes become active.

## 3. Discussion

The novelty of strobe-FLIM is its ability to provide temporal analysis using time integrated fluorescence; this removes the need for specialist detectors making it straightforward and relatively cheap to install; future development could see the implementation of relatively inexpensive, mass manufactured, LED light sources [28] for excitation making it truly low-cost. Implementing lifetime measurement using only excitation control also removes any requirement for synchronisation of excitation and detection signals and so strobe-FLIM is also easy to implement requiring only standard, wide-field fluorescence images from a CCD camera. The method cannot provide a complete description of the fluorescence decay relying rather on empirical measures that parameterise the fluorescence dynamics. The temporal resolution obtained is determined by the laser pulse frequency; and whilst this may be higher than reported here e.g. 1 GHz mode-locked Nd:YAG lasers are available; it is likely to remain in the nanosecond rather than picosecond range available using time domain FLIM. Strobe-FLIM therefore complements existing techniques in providing rapid lifetime imaging, implemented with minimal adaptation of a standard microscope, in a format that retains the sensitivity and pixel density of fluorescence intensity imaging. Analysis is based on the ratio of two image frames and so the method is inherently capable of providing video rate FLIM. The technique is ideally suited for applications requiring fast, robust image analysis such as the mapping, on sub-second timescales, of molecular interactions within live cells or rapid measurement in high throughput systems of lifetime-based switching assays with digital readout. Because the stroboscopic technique is detector independent its flexibility could also provide lifetime measurements across a broad range of fluorescence-based analysis systems such as endoscopy or flow cytometry.

## 4. Methods

### *4.1 Microscopy*

All images were acquired in wide field using a standard Nikon fluorescence microscope with a 40x magnification objective. Detection was via a Hamamatsu Orca CCD camera using a 20 ms exposure time. A Fianium white light laser was used for excitation and was coupled into the microscope via the lamp housing. A 600 nm short pass filter and 480/40 nm bandpass dichroic mirror were used to spectrally filter the excitation beam whilst a 705/40 nm bandpass detection filter was used. For live cell lifetime imaging, the laser pulse frequency was initially set to 1 MHz and an image acquired after a 100 ms delay to allow the system to stabilise. The laser pulse frequency was then switched to 30 MHz and after a further 100 ms stabilisation a second image was acquired. There was no discernible photobleaching due to this stabilization delay in fact repeated imaging over a minute could be achieved whilst maintaining fluorescence intensity stability. Image matrices were stacked in memory to minimise CPU load of the controlling PC. Image processing involved the simple subtraction of a fixed background, and division of the 30 MHz matrix by the 1 MHz matrix (scaled by 30x to keep the number of pulses per acquisition for the two laser pulse frequencies the same).

### *4.2 Cell preparation*

The human osteosarcoma cells, U-2 OS (ATCC HTB-96) were cultured under in McCoy's 5a medium supplemented with 10% foetal calf serum (FCS), 1mM glutamine, and antibiotics and incubated at 37° C in an atmosphere of 5% $CO_2$ in air. For imaging experiments, cells were grown at a density of $1x10^5$ cells $ml^{-1}$ on top of a 24x24 No. 1.5 coverslip (RA Lamb) in a 6 well plate (BD Falcon™) to a confluency of 60-70%. Cells were loaded with commercially available targeted nanocrystals using the Qtracker® 705 Cell Labeling Kit (from Invitrogen; Catalog Number - Q25061MP) at 4 nM. The QD labelling solution was added to the cells and incubated for 1 hour at 37° C before washing twice with full growth media. One set of Qtracker® 705 loaded cells coverslips was immediately fixed (1h pos-loaded cells) and another let to incubate for 24h. Cells were fixed with 4% paraformaldehyde in PBS for 30 min at 4° C. Following fixation the coverslips were then mounted onto slides, directly with ProLong® Gold antifade reagent (P36930, Invitrogen) and in PBS, for this a square well of approx 150 µl volume was shaped with adhesive plastic tape on the slide, finally for both cases the coverslips were fixed in place using clear nail polish. Live samples were pre-prepared in silicone multi-well plates, and sealed with a glass slide and cover-slips and mounted individually on a temperature controlled stage (TCS).

#107281 - $15.00 USD Received 6 Feb 2009; revised 13 Mar 2009; accepted 15 Mar 2009; published 18 Mar 2009



#107281 - $15.00 USD Received 6 Feb 2009; revised 13 Mar 2009; accepted 15 Mar 2009; published 18 Mar 2009
(C) 2009 OSA

## Appendix

**Analytical derivation of stroboscopic response:**
The analysis proceeds by considering an ensemble of $N_T$ systems with microstates 1 and 2 under excitation. The time dependent rate equations for such an ensemble are:

$$\frac{dN_2}{dt} = I_p(N_1 - N_2) - \frac{N_2}{\tau} \quad [A1]$$

$$\frac{dN_1}{dt} = -I_p(N_1 - N_2) + \frac{N_2}{\tau} \quad [A2]$$

where $\tau$ is the relaxation lifetime between upper state 2 and lower state 1 and $I_p$ is the excitation rate per system. If we introduce n as the factional number of systems in the upper state; $n = N_2 / N_T$ we obtain an expression:

$$\frac{dn}{dt} = I_p(1-2n) - \frac{n}{\tau} \quad [A3]$$

We consider the excitation to be a periodic impulse of duration $T_p$ and period T. After an initial transient the ensemble will achieve a dynamic equilibrium and respond with a periodic output of fixed amplitude. Using the assumption of $T_p << \tau$ (i.e. an impulse excitation) the excitation of the ensemble becomes temporally separate from the relaxation and equation 3 can be solved by separately integrating the rate equation during the excitation pulse and during the ensuing relaxation.

i.e. $$\int_{n_l}^{n_u} \frac{1}{(1-2n)} dn = \int_0^{T_p} I_p dt \quad [A4]$$

and $$\int_{n_u}^{n_l} -\frac{1}{n} dn = \int_0^{T} \frac{1}{\tau} dt \quad [A5]$$

where $n_l$ is the fraction of systems in the upper state immediately before the excitation pulse and $n_u$ the fraction immediately after the pulse. Using the results of the integrals in equations A4 and A5 the change in n during a single cycle, $\Delta n = ( n_u - n_l )$ can be found:

$$\Delta n = \tfrac{1}{2} \frac{\left(e^{2I_pT_p} - 1\right)}{\left(e^{I_pT_p} - e^{-\frac{T}{\tau}}\right)} \left\{1 - e^{-\frac{T}{\tau}}\right\} \quad [A6]$$

*Relation to measured parameters*

To translate this analysis to experiment the parameters, $\Delta n$ and $I_pT_p$ have to be related to a measurable. The change in n is proportional to the integrated output signal per excitation period. A dc detector would therefore return a signal, $S_{dc}$ per unit time which is proportional to the average value of $\Delta n$ over one period. The term $I_pT_p$ represents the total number of excitation events during a single impulse and is related to measurable physical quantities by:

#107281 - $15.00 USD Received 6 Feb 2009; revised 13 Mar 2009; accepted 15 Mar 2009; published 18 Mar 2009



$$I_pT_p = \eta_{ex} \frac{E_p}{E_q} \frac{\sigma}{A} \quad [A7]$$

Where $E_p/A$ is the excitation pulse energy per unit area, $\eta_{ex}$ is the delivery efficiency of that energy to the ensemble, $E_q$ is the energy of the excitation quanta and $\sigma$ is the absorption cross-section of the 2-level system. The total fluorescence signal per pulse can therefore be represented by:

$$S_c = \kappa \frac{\left(e^{2\alpha P} - 1\right)}{\left(e^{2\alpha P} - e^{-\frac{1}{f_{ex}\gamma}}\right)} \left\{1 - e^{-\frac{1}{f_{ex}\gamma}}\right\} \quad [A8]$$

where $\kappa$ is a detection constant relating the measureable output to the number of relaxation events i.e. the energy released from the ensemble, $\alpha$ is an excitation constant linking the incident power to the excitation impulse function and the temporal dynamics of the excitation and fluorescence response are represented by a pulse frequency, $f_{ex}$ and a relaxation rate, $\gamma$. Equation [A8] provides a means to determine $\gamma$ from steady state measurements of the output signal.

**Acknowledgments**

This work was funded by the Engineering and Physical Sciences Research Council, U.K. under grant no. EP/E013104/1, 'Stroboscopic excitation fluorescence lifetime imaging' and the Research Councils U.K. on the Basic Technology programme under grant no. GR/S23483/01 'Optical Biochips'.

#107281 - $15.00 USD Received 6 Feb 2009; revised 13 Mar 2009; accepted 15 Mar 2009; published 18 Mar 2009
(C) 2009 OSA